

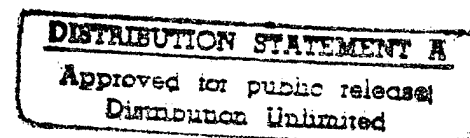
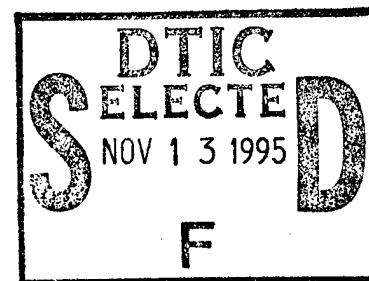
ADD 432365

N80-21420

SPACECRAFT MATERIALS IN SPACE ENVIRONMENT

Proceedings of a Symposium held at ESTEC, Noordwijk,
The Netherlands, 2 - 5 October 1979

19951108 198



DEPARTMENT OF DEFENSE
PLASTICS TECHNICAL EVALUATION CENTER
ARRADCOM, DOVER, N. J. 07801

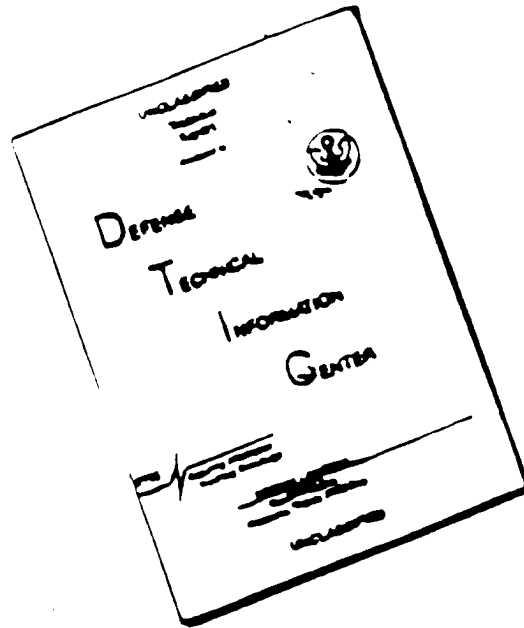
DTIC QUALITY INSPECTED 5

U.S. DEPARTMENT OF COMMERCE
National Technical Information Service

NTIS®

1068C
38901
38893

DISCLAIMER NOTICE



THIS DOCUMENT IS BEST
QUALITY AVAILABLE. THE COPY
FURNISHED TO DTIC CONTAINED
A SIGNIFICANT NUMBER OF
PAGES WHICH DO NOT
REPRODUCE LEGIBLY.

*MSG DI4 DROLS PROCESSING - LAST INPUT IGNORED

-- 1 OF 1

DTIC DOES NOT HAVE THIS ITEM

-- 1 - AD NUMBER: D432365
-- 5 - CORPORATE AUTHOR: EUROPEAN SPACE AGENCY PARIS (FRANCE)
-- 6 - UNCLASSIFIED TITLE: SPACECRAFT MATERIALS IN SPACE ENVIRONMENT,
--10 - PERSONAL AUTHORS: DAUPHIN, J. ; GUYENNE, T. D. ;
--11 - REPORT DATE: OCT 02, 1979
--12 - PAGINATION: 338P
--14 - REPORT NUMBER: ESA-SP-145
--20 - REPORT CLASSIFICATION: UNCLASSIFIED
--21 - SUPPLEMENTARY NOTE: PROCEEDINGS: ESA SYMPOSIUM, 'SPACECRAFT
-- MATERIALS IN SPACE ENVIRONMENT', EDITED BY J. DAUPHIN AND T. D.
-- GUYENNE, 2-5 OCT 79, NOORDWIJK, THE NETHERLANDS. SPONSORED BY
-- EUROPEAN SPACE AGENCY, PARIS, FRANCE. (SEE PL-38894 - PL-38901).
--22 - LIMITATIONS (ALPHA): APPROVED FOR PUBLIC RELEASE; DISTRIBUTION
-- UNLIMITED. AVAILABILITY: NATIONAL TECHNICAL INFORMATION SERVICE,
-- SPRINGFIELD, VA. 22161. N80-21420.
--33 - LIMITATION CODES: 1 24

-- END Y FOR NEXT ACCESSION

END

Alt-Z FOR HELP3 ANSI

3 HDX 3

3 LOG CLOSED 3 PRINT OFF 3 PARITY

~~Add~~ 432365 - 432373

N80-21420 thru N80-21450

esa SP-145

December 1979

Spacecraft materials in space environment

Proceedings of a symposium held at
ESTEC, Noordwijk, The Netherlands
2-5 October 1979

Accession For	
NTIS CRA&I	<input checked="" type="checkbox"/>
DTIC TAB	<input type="checkbox"/>
Unannounced	<input type="checkbox"/>
Justification	
By <i>DTIC-AL memo</i>	
Distribution / <i>11-2-95</i>	
Availability Codes	
Dist	Avail and/or Special
<i>A-1</i>	

REPRODUCED BY
NATIONAL TECHNICAL
INFORMATION SERVICE
U.S. DEPARTMENT OF COMMERCE
SPRINGFIELD, VA. 22161

european space agency / agence spatiale européenne

8-10, rue Mario-Nikis, 75738 PARIS 15, France

Cover picture shows an ultraviolet degradation test of Spacelab pallet thermal control samples.

SPACECRAFT MATERIALS IN SPACE ENVIRONMENT
(ESA SP-145 – December 1979)

Symposium organised by: J Dauphin, Head of Materials Section,
ESTEC Product Assurance Division

Proceedings published by: ESA Scientific & Technical Publications Branch
ESTEC, Noordwijk, The Netherlands

Edited by: J Dauphin & T D Guyenne

Printed by: ESTEC Reproduction Services
793637

Copyright © 1979 by European Space Agency
ISSN: 039-6566

Distribution Office: ESA Information Retrieval Service
8-10 rue Mario-Nikis, 75738 Paris

Price Code: C2(75 FF)

CONTENTS

OPENING SESSION

WELCOME ADDRESS

M Trella, ESA Technical Director

ix

OPENING ADDRESS

A Rémondrière, Deputy Manager of CNES Toulouse Space Centre

xi

INTRODUCTION

J Dauphin, Head of Materials Section, ESTEC

xiii

SESSION I

METHOD OF ANALYSIS

Co-chairmen: J F Lafay & R.G. Moss

OFFGASSING AND ODOUR TESTS OF NON-METALLIC MATERIALS FOR SPACE CABINS

WR Eckert, NATEC GmbH, Hamburg - Germany

3

THE METALLURGICAL EXAMINATION OF SPACECRAFT MATERIALS FAILURES

BD Dunn, ESA, ESTEC, Noordwijk - The Netherlands

5

THERMAL ANALYTICAL METHODS FOR CHARACTERISATION OF RESINS, PREPREGS AND COMPOSITES

H D Stenzenberger & M Herzog, Technochemie GmbH, Dossenheim - Germany

23

DISCUSSION

38894

SESSION II

NEW MATERIALS DEVELOPMENTS

Co-chairmen: J Berry & D F Hall

NEW SPACE MATERIALS DEVELOPMENTS IN THE UNITED STATES

WL Lehn, Wright-Patterson Air Force Base, Ohio - USA

37

ADVANCED CARBON FIBRE COMPOSITES FOR SPACECRAFT USE

D H Bowen, AERE, Harwell - UK

49

SOME MATERIAL REQUIREMENTS FOR FUTURE PROJECTS (paper not available)
R Pacault & G Whitcomb, ESA/ESTEC, Noordwijk - The Netherlands

PAINTS, POTTING COMPOUNDS AND SILICONE VARNISHES WITH LOW
 OUTGASSING IN SPACE ENVIRONMENT
J C Guillaumon & J Guillin, CNES, Toulouse - France 38895

63

DISCUSSION

SESSION III

CLEANLINESS & CONTAMINATION PRACTICE

Co-chairmen: M McCargo & H E Hintermann

COATING & CONTAMINATION EXPERIMENT ON LDEF
L Preuss & W Schaefer, MBB GmbH, Munich - Germany

71

PRELIMINARY FLIGHT RESULTS FROM P78-2 (SCATHA) SPACECRAFT
 CONTAMINATION EXPERIMENT
D F Hall & A A Fote, Aerospace Corp., El Segundo - USA

81

METEOSAT CLEANLINESS CONTROL PRINCIPLES
P G Edwards & J Marcoux, ESA/Earth Observation Programme Office, Toulouse - France

91

ASSESSMENT OF SHUTTLE PAYLOADS GASEOUS ENVIRONMENT
 CONTAMINATION AND ITS CONTROL
J J Scialdone, Goddard Space Flight Center, Greenbelt - USA

101

CLEANLINESS ASPECT OF THE ARIANE PAYLOAD BAY
M Desloire & R Jaeger, CNES, Erry - France

117

SESSION IV

CLEANLINESS & CONTAMINATION THEORY

Co-chairmen: D A Nutt & A Paillous

SPACE CONTAMINATION ASSESSMENT STUDY - FIRST APPLICATION TO
 PRESENT PROJECTS
B Tatry, CNES, Toulouse - France

131

THE RELATIONSHIP OF CONTAMINATION MASS DEPOSITION TO OPTICAL
 PROPERTY CHANGES ON SPACECRAFT SURFACES (paper not available)
C R Maag, JPL, Pasadena - USA

EVALUATION OF KINETIC OUTGASSING UNDER VACUUM FOR POTTING
 COMPOUNDS AND PAINTS

J Guillin, CNES, Toulouse - France

38896

139

CONTAMINATION ENHANCED ELECTROSTATIC DISCHARGE MECHANISMS
J A Jeffery & C R Maag, JPL, Pasadena - USA

38897

145

DISCUSSION

SESSION V

MATERIALS IN VARIOUS PROJECT TYPES

Co-chairmen: J J Scialdone & J Dauphin

MATERIALS REQUIREMENTS FOR SPACELAB AND SPACELAB PAYLOADS <i>J E Bennett & M D Judd, ESA/ESTEC, Noordwijk - The Netherlands</i>	161
MATERIALS POLICY FOR ADVANCED SCIENTIFIC SPACECRAFT <i>R Thomas, ESA/ESTEC, Noordwijk - The Netherlands</i>	167
OTS/ECS MATERIALS POLICY <i>P J H Molloy, British Aerospace Dynamics Group, Stevenage - UK</i>	175
METEOSAT CLEANLINESS CONTROL ACHIEVEMENTS <i>M L Reynolds & J Kieffer, ESA/Earth Observation Programme, Toulouse & Matra, Vélizy - France</i>	181
DISCUSSION	

SESSION VI

ENVIRONMENTAL EFFECTS - CHARGING UP

Co-chairmen: J Guillin & M L Minges

ELECTROSTATIC CHARGING & SPACE MATERIALS <i>F Levadou & J Bosma, ESA/ESTEC, Noordwijk - The Netherlands</i>	189
SURFACE DISCHARGE ARC PROPAGATION AND DAMAGE ON SPACECRAFT DIELECTRICS <i>K G Balmain, University of Toronto - Canada</i>	209
THE CHARGING AND DISCHARGING OF SPACECRAFT DIELECTRICS <i>D K Davies, Electrical Research Association Ltd., Leatherhead - UK</i>	217
DISCUSSION	

SESSION VII

ENVIRONMENTAL EFFECTS - RADIATION

Co-chairmen: J Guillin & M L Minges

EFFECTS OF RADIATION ON POLYMERS & THERMAL CONTROL COATINGS <i>J Bourrieau & A Paillous, CERT/DERTS, Toulouse - France</i>	227
RANGE & INTERACTION OF LOW-ENERGY PROTONS IN METAL AND METAL OXIDE THERMAL CONTROL MATERIALS <i>S A Greenberg & M McCargo, Lockheed Palo Alto Res. Lab. - USA</i>	247
AN ANALYTICAL APPROACH TO EVALUATION OF SPACE RADIATION EFFECTS ON MATERIALS FOR LONG-LIFE MISSIONS <i>J Moacanin, A Gupta & W F Carroll, JPL, Pasadena - USA</i>	255

SPACE ENVIRONMENTAL EFFECTS ON POLYMER MATRIX COMPOSITES
R C Tennyson, J S Hansen, B Uffen, D Morison & G Mabson, University of Toronto -
Canada

263

DISCUSSION

SESSION VIII

MATERIALS FOR SPECIFIC APPLICATIONS
Co-chairmen: L Preuss & D Verdin

EFFECTS OF SPACE CHARGED PARTICLE ENVIRONMENT ON OPTICAL COMPONENTS & MATERIALS

J Bourricau & M Roméro, CERT/DERTS, Toulouse - France

275

USE OF ULTRA-LIGHT ADHESIVE FOR METAL HONEYCOMB BONDING
J Chanteranne, Aérospatiale, Les Mureaux - France

38899

287

HIGH-TEMPERATURE RESISTANT MATERIALS FOR SPACE MOTORS
J J Choury, SEP, Saint-Médard-en-Jalles - France

38900

293

WACKER RTV-S691: A SILICONE ADHESIVE WITH LOW OUTGASSING RATE
W Hechtel, Wacker-Chemie GmbH, Munich - Germany

38901

305

THE USE OF MoS₂-LOADED GREASES IN ANTENNA DESPIN MECHANISMS UNDER SIMULATED SPACE ENVIRONMENT
B H Baxter, British Aerospace Dynamics Group, Stevenage - UK

309

DISCUSSION

LIST OF PARTICIPANTS

321

OPENING SESSION

WELCOME ADDRESS

Professor M Trella

ESA Technical Director & Director of ESTEC, Noordwijk, The Netherlands

I am very pleased to welcome you to this first ESTEC Symposium on Spacecraft Materials. We would like to consider it an opportunity to compare our understanding, our knowledge and our experience, and we hope also as a source of future contacts, because the topic with which we are going to be involved for the next three and a half days is growing more rapidly in importance than we all could have expected.

This, in combination with the increasing number of new missions, was really the reason why we have taken the initiative to organise this Symposium; in addition, one of the major functions that we in ESTEC have is specifically that of providing support to the Agency's projects. We have perhaps therefore become aware of the increasing importance of the materials problems more quickly because of these considerations. It is not at all a simple task to find the necessary solutions, because space materials have grown to the point of becoming an important new branch in materials technology, a branch for which when we started our studies, there was virtually no literature. We had to strive ourselves to achieve an understanding to unravel the chemical/physical phenomena, the influence of particular parameters, and the behaviour of particular materials.

We have been faced in our projects with a number of surprises, and unforeseen phenomena that have proved extremely difficult to master, for the simple reason that we have no post-launch access to the materials. This is a burden that we can hardly carry alone, since it requires an effort that is far beyond our in-house capacity.

In the last 12-13 years, we have however acquired some understanding of this field and accumulated a number of important results. We therefore believe that we can contribute something to this exchange of views and we hope to foster a spirit of mutual co-operation in the coming days. In this connection, I am very pleased to see so many specialists here in our midst, coming not only from our European countries, but also from the United States and Canada.

Among the eight sessions that will occupy the next three and a half days, session I has been

devoted especially to investigation and analysis methods for materials behaviour, and another has been focussed on the effects of materials on the space environment; sessions VI and VII will deal with the effects of environment of the materials, while session VIII is devoted to particular materials for specific applications.

In selecting the papers we have tried to allow sufficient time for a comprehensive exchange of views during the discussion period which, I think, will play an essential role in making this meeting a particularly fruitful one.

On the basis of the quality and size of the attendance, I really believe that our high expectations will not be disappointed, and I wish you all every success in your deliberations.

OPENING ADDRESS

A Rémondère

*Deputy Manager of the Toulouse Space Centre
Head of Projects and Technical Research, CNES, Toulouse, France*

The last Symposium dealing with Materials for Space needs was organised in Toulouse, by CNES and DERTS, five years ago, in June 1974. I still remember this Symposium, which like today's, drew together many attendees from a number of countries. It was the first meeting of its kind in Europe and many of those lectures showed how interesting were the theoretical studies, the simulation techniques, laboratory tests and in-flight experiments, and highlighted the amount of work still outstanding.

The first Symposium demonstrated the high level of expertise being developed in Europe. At the same time, an event that certainly stuck in the minds of many people at that Symposium was the U.S. movie about Skylab, showing some typical in-flight results concerning contamination phenomena. The comparison between the models prepared by U.S. engineers and these in-flight results was, I remember, particularly interesting.

During the same week, the Toulouse Symposium dealt with materials for spacecraft and materials for semiconductors. It was perhaps too broad and the problems were too different. I think it a good idea that this new Symposium restricts itself to the single topic of 'Materials for Spacecraft'. I have read both the programme and the abstracts, and I think this Symposium looks very promising.

I would like to underline how the need for an effort on Materials for Spacecraft has increased in Europe between the two Symposia, by looking for example at the following missions being considered during the last year in Europe, and the corresponding problems :

Low Earth Orbit

- Offgassing and toxicity problems with materials used in the Spacelab crew compartment.
- Contamination and its disturbing effects on the properties of optical surfaces in the case of Earth observation satellites (French SPOT Project).

Geosynchronous Orbit

- Following the first European telecommunication satellites, like Symphonie (F + FRG) and OTS (ESA), the required operational lifetimes for our future telecom satellites will increase from 3-5 years to 7-10 years, a requirement that involves :

- stability to vacuum and radiation environment,
- low outgassing,
- reduced electrostatic charging effects.

We must also take note of the increasing trend in installed power, which introduces new problems for thermal control.

Aside from the telecommunications missions, there are meteorological satellites, such as Meteosat, and their need for cleanliness, particularly for the infrared channels.

Planetary missions

An example of this kind of mission is the International Solar Polar Mission (ISPM). The constraints are considerable : broad range of temperatures, exposure to very high levels of radiation during the Jupiter swing-by, etc.

The need is always the same :

- to find the right material for a given use,
- to obtain good confidence in the material performances by test and simulation,
- to ensure that the spacecraft is built according to specification and with space qualified materials, and
- to extract all possible information from successes and from failures.

Meeting this need involves a large endeavour. That is why I must underline the necessity of cooperation between the different countries. By coordinating activities, and by examining the results together, it will be possible to achieve improved efficiency.

Taking in account the increasing importance of the materials behaviour both for the reliability and the availability of applications satellites and for the success of scientific satellite missions, I think that we might well have to meet again sooner than five years hence. Three years would seem to me to be a good compromise.

I wish the Symposium every success, and I hope that all the participants will find it interesting and worthwhile.

INTRODUCTION

J Dauphin

*Head of Materials Section, Product Assurance Division
ESA/ESTEC, Noordwijk, The Netherlands*

SOME THOUGHTS ABOUT MATERIALS FOR SPACE

Materials policy has emerged with difficulty over the history of space activities. In the beginning, spacecraft were made utilizing existing technologies and the need of a special approach to materials was not recognized. Such an attitude can be traced to several reasons :

- The only strict requirement for materials was on the mass and this was already dealt with in many industries, particularly aeronautics. The knowledge of vacuum effects was rudimentary, that of radiation forgotten and the others unknown.
- Industry normally tends to favour the use of well-known technology and is reluctant to innovate particularly for a "one of its sort" item.
- Project managers are also rather conservative and can be driven to adopt new approaches only if old ones are shown to be inadequate.
- There is a lack of incentive, when compared to the mass production industry, to avoid firstly over designing with consequent cost increases, and secondly, failures after production which are expensive to repair and lead to damaged reputations.

Over a long period an evolution has taken place towards a more professional approach to materials problems due mainly to the more stringent requirements put on space hardware and to the experience gained through failures during tests or missions. It is now normal practice that these problems are dealt with by specialists right from the very beginning of a project and have a sizeable influence in the trade-offs to be made.

We even arrive at a point in time where the availability or not of a material with a given set of properties can determine the feasibility or not of a given spacecraft : two examples of future missions studied by NASA and ESA can be given to

illustrate this, the "solar sail" which requires the existence of large quantities of extremely thin film with special mechanical/optical properties and the "solar probe" which depends for its survival of the availability of materials capable of screening out the infernal temperature of the sun's corona.

The large space structures which are now leaving the domain of science fiction to enter, in the near future, our day to day life will no doubt also be the source of exciting new materials problems.

In this sense there is a bright future for Space Materials Specialists except if the energy crisis prevents our civilization expanding further.

Let us now review some of the steps which should be followed to ensure that materials and their associated processes will be adapted to the requirements of a given mission. This type of "philosophical lecture" is, in general, the lot of the oldtimer in an assembly. I hope I still do not look quite like that but having been almost 15 years engaged in this space materials business, I start feeling like that.

DEFINITION OF NEEDS

Ideally the description of each item to be built should contain a section covering the requirements to be put on materials, i.e. define the one or few critical properties which will be used as selection criteria for this specific use. There is no need to accumulate large detailed specifications, frequently copied from the US-MIL series, if it's only for the sake of having paperwork to show : How many times we see as a criterium for space materials, the fact that they should not be "nutrient to fungi" and at the same time complete omission of UV degradation and/or outgassing properties. Manufacturing space hardware is different from making military equipment to be used for months in the tropical jungle!

It is evident that accumulated experience in the task of defining the properties required and analogy in material functions must be used to reduce the number of cases to be studied. The most difficult part is often to define the environment and its possible effects since many parameters have to be considered, some of them being completely or partially unknown. In this case safety factors must be allocated but this should not lead to gross overdesign. Environments before launch, i.e. during manufacture, test, transportation, must also be considered. Another important aspect to be analysed in defining materials requirements are the interfaces: couples of materials in contact, EMC specifications, influence of test levels, cleanliness requirements, etc.

In summary, materials requirements must come from an evaluation of their functions, their environments and their interfaces.

SELECTION, QUALIFICATION AND PROCUREMENT

When a space project is starting, it is generally too late to think of any new materials development. At best it will be possible to modify slightly some existing materials for the purpose. Incidentally this proves that research on new materials should be triggered well in advance with some kind of prophetic view over the needs of future projects. Materials specialists are therefore bound to use what exists on the commercial market and here lies the difficulty since up to now and for the foreseeable future space is not a very exciting market for materials producers: the quantities used are measured at best in Kg and not in tons or tens of tons as they would like! It is true that some "advanced" materials are made available and sometimes become indispensable for space use but at a high cost and at a risk of withdrawal from the market without warning: these are the prices to pay for our low consumption. In general, the materials specialists will be faced with the task of selecting commercial material to suit the designer's aims. There now exist a number of guidelines to help him in such a task and also batteries of screening tests which are fully specified. The existence of past experience is useful but should not lead to excessive conservatism, it is partly the duty of the Material Specialist to promote the use of new and more efficient materials. If nothing of this kind had been done in the past, we would still be cutting flintstones in the Vézère Valley...

Another snag is the "Qualification"... In the space world, this can mean anything between the evidence of good performance with past spacecraft and the corridor rumour heard during the last trip to NASA... A good practice would be never to use the word "Qualified" alone but say or write "Qualified by such or such authority for such or such application" and always give a dated reference. It is not evident that a material qualified by Peugeot in 1926 to make bicycles is applicable to an X-ray detector in EXOSAT...

There is also an art in the granting of a waiver; a waiver is the proof, like a sin, that the world is not perfect-and as such will occur often in every project-but like a sin, it must be committed

reluctantly, regretted deeply and not repeated... if possible. A waiver granted for a given application in a given project is not necessarily justified - and in many cases it is just the contrary - in another context.

In the case of off-the-shelf equipment it is frequent that materials control becomes impractical, the cost implied by changes would negate the advantage of having a standard item... The only way out of this problem is to qualify at the equipment level but remembering always that not only the item must fulfill its function in the relevant environment but also, and even more, not disturb other functions in the spacecraft. Materials present in a so qualified equipment do not become qualified individually by this method and their use in any other case must be assessed.

MANUFACTURE AND QUALITY CONTROL

Mass production over the last decade has seen the institution of stricter quality control; rules have been fixed; detailed procedures of manufacture and inspection evolved... I am, however, convinced that all this, which is implemented in our contractor's premises for their main productions should not be applied directly and blindly to space hardware. The production we are interested in, is of limited quantity and realized over a relatively short time span. The environment that the hardware will have to endure is not necessarily more demanding than in many ground applications but is certainly very different and well-known classical specifications may not be adequate.

We certainly need a good documentation for making space hardware but this must be specific. Concerning materials the main areas to be covered are Incoming Control, Storage and Life Control, Application Processes. Anyway, even with the best documentation, the quality of the product will depend on the availability of skilled, well-trained staff in the production as well as in the inspection area. This staff must be indoctrinated towards high quality production and must receive corresponding incentives; he must understand fully what he is doing and the underlying reasons. This is particularly true in the area of cleanliness control where self-discipline from the staff is the only way to ensure a really clean product. I read somewhere that "The Watchmakers of the XVIIIth. century had no clean room... but they produced perfectly clean movements", I could add that they probably did not even have written procedures'.

FAILURES AND FEEDBACK OF EXPERIENCE

Whatever we do to ensure very high quality production we will encounter failures and some of them will be caused by materials. In this case the most remarkable is the burst of panic which occurs in the concerned project. This is understandable but this state of panic should not be followed by Materials Specialists... You would not like to see the doctors and nurses get into panic at a road accident!

The first need, and this is still far from being always realized, is that the failure be properly documented (circumstances, environment, value of

physical parameters...) and that sample (s) of the failed item reaches a competent and experienced analyst. In most cases he/she will be able to trace the cause of failure and recommend a recovery action if it is at all possible. Remember however that an ad-hoc fix is not a qualified procedure for the future, even if it works!

In the materials area, luckily enough, failures are generally detected during tests on the ground before the mission commences and this permits a thorough analysis to be done. Experience in the utilization of materials is therefore growing and avoidance of similar errors on subsequent projects possible. Where a failure occurs in space its analysis is far more complicated particularly when it is not a go/no-go failure but a mere degradation of performance. The housekeeping instrumentation on board is frequently insufficient to allow an unequivocal determination of the cause. In addition, I must stress that the feedback from flying spacecraft rarely reaches the materials specialists. Improvements in that area would be welcome.

CONCLUSIONS

This, I hope, will be a fair introduction for the coming symposium where several specialists will now give you more detailed views on the different materials problems they meet. I want, however, to explain why we excluded some areas of Materials Science and Technology from our programme. This is not "racism"... In the area of semi-conducting materials we expect the component industry to be in a better position than us to solve their materials problems and we count on our colleagues working in the Space Electronic Components to assess the performances of what is proposed on the market. In the area of Launchers there are also lots of interesting materials... but rather far away from the ones we meet when making spacecraft. Up to now the launchers are not staying for long time in space, and we can consider them only as transportation vehicles for our hardware... However with the advent of the Shuttle times are changing! The area of Materials Physics in Space has been a pet subject over the last few years, for the moment it has been mainly oriented at trying to fabricate in space materials for ground use... which is exactly the reverse of what concerns us. But here again the times are changing and manufacture of large space structures in space could become an active area for the future technologist.

We will keep that in mind for the next event... and in the meantime wish you all a fruitful symposium.

SESSION I

ANALYSIS METHODS

Co-chairmen: J.F. Lafay & R.G. Moss

OFFGASSING AND ODOUR TESTS OF NON-METALLIC MATERIALS FOR SPACE CABINS

W R Eckert

NATEC - Institut für Naturwissenschaftlich-Technische Dienste GmbH, Hamburg, Germany

ABSTRACT

The description of test methods for non-metallic materials to be used in the construction of space cabins is presented. The Offgassing Test involves heating a sample in an enclosed chamber. A sample of the atmosphere surrounding the material under test is taken for analysis. The analysis is performed by gas chromatography and combined gas chromatography/mass spectrometry. The purpose of this test and the also described Odour Test is to provide details of trace contaminants released into the atmosphere by materials such that an assessment can be made with respect to safety hazards involved in the use of such materials.

Keywords: Offgassing Test, Odour Test, Non-metallic Materials, Space Cabins, Analysis of Contaminants, Gas Chromatography

1. INTRODUCTION

One of the many tests imposed on materials proposed for use in the construction of Spacelab and Spacelab Experiments is the Offgassing Test. This test involves heating a sample in an enclosed chamber at a predetermined temperature (usually 50°C) for a period of 72 hours. After this time the chamber is allowed to cool to room temperature and a sample of the atmosphere surrounding the material under test is taken for analysis. The analysis, which involves the use of gas chromatography and combined gas chromatography/mass spectrometry is required to quantitatively identify all contaminants present in concentrations above a certain defined level. The purpose of this test is to provide details of trace contaminants released into the atmosphere by materials such that an assessment can be made with respect to safety hazards involved in the use of such materials.

2. OFFGASSING TEST

The test chamber with a volume of 2.6 l is made out of glass. The lid of the chamber has three ground glass joints, one each for a transducer, a stop cock, and a sampling septum. Lid and chamber will fit together by faceground joints with an O-ring of Viton in between. Six clamps press the lid onto the chamber.

The transducer measures the pressure and temperature inside the test chamber. The accuracy of the transducer is $\pm 0.05 \text{ kp/cm}^2$ and $\pm 1^\circ\text{C}$. Pressure and temperature of the test chamber are recorded by an electronic 12-point printer.

The chambers were leak checked at 65°C during 24 hours, as well as at room temperature at a pressure of 10 Torr during 24 hours. The pressure-values of both tests did not change more than 10 Torr. In order to verify that no gases occur in the chamber during heating, the chamber was cooled to room temperature and a sample of air was taken and analysed. Total organics and carbonmonoxide did not occur in detectable amounts.

The sample under investigation is placed into a test chamber and the chamber connected to the gas rack. The gas rack consists of a tube with four adaptors to connect four test chambers. Both ends of the tube are fitted with valves. One end is connected via a 13 X molecular sieve cartridge to a cylinder with test atmosphere, while the other end is connected via a liquid nitrogen trap to a vacuum pump capable of producing less than 10 Torr in the test chamber. Evacuation of 4 chambers simultaneously is accomplished in less than 10 minutes.

After evacuating to 10 Torr or less, the test chamber is pressurized to 690 Torr with a test atmosphere having the following composition:

23.8 % oxygen, purity $\geq 99.998 \%$
76.2 % nitrogen, purity $\geq 99.9992 \%$
<0.05 % vpm carbonmonoxid

The chamber is now exposed in an oven to a temperature of 50°C for a time period of 72 hours, allowing time for initial warm up. Up to 6 test chambers fit into the oven. The test temperature is reached after 2 hours. The temperature of the oven is measured with a thermometer and proved to be well regulated (50.0°C \pm 0.5°C). Following the isothermal exposure, the test chamber is allowed to return to room temperature and then removed from the oven. The test chamber is pressurized on the gas rack to ambient atmospheric pressure with test gas. Then a known volume of the atmosphere surrounding the material under test is taken for analysis.

The separation of carbonmonoxide, methane, and total organics is performed by a first injection into the gas chromatograph. There are three columns connected by means of a six-port valve. The first column is packed with activated aluminiumoxide. It separates methane and carbonmonoxide from organics with two or more carbon atoms whereby the latter are held back. The second column is packed with molecular sieve 13 X. It separates methane from carbonmonoxide. The third column is packed with a nickel-catalyst which reduces carbonmonoxide to methane. After this methane and carbonmonoxide (as methane) are detected by the flame ionization detector. Once methane and carbonmonoxide have been eluted from the columns, the total organics with two or more carbon atoms are back-flushed from the first column, and eluted towards the detector and calculated as pentane equivalents. Taking a 1-ml gas sample out of a 2.6 l test chamber with a 10-g test sample the following detection limits can be achieved:

0.3 µg/g carbonmonoxide
0.08 µg/g pentane equivalents

The separation of the total organics into the different components is performed on a second gas sample using a column packed with Porapak Q. The calculation as pentane equivalents of each component is done in the same manner as for the total organics.

Certain criteria of acceptability are established:

- a) The maximum level of carbon monoxide in the tested configuration shall not exceed 25 µg per g of sample.
- b) The maximum level of total organics in the tested configuration shall not exceed 100 µg per g of sample.

All offgassing components exceeding 10 µg per g must be identified using the gas chromatograph/mass spectrometer combination.

3. ODOUR TEST

Gaseous contaminants given off by materials having passed the above mentioned test can still create nauseating and irritating odours. The purpose of the Odour Test is to determine the odour characteristics of materials proposed for use in the construction of space cabins. A specially trained pool of personnel exists. Each member of the pool is capable of detecting a series of basic odours.

A panel of five members is selected from the pool for odour evaluations, only subjects of good health becoming members. Members of the pool shall not participate on the panel if their sense of smell is affected in any manner such as recent smoking, ingestion of highly flavoured foods, and exposure to pungent vapours.

Odour evaluation on sample materials must be performed in a room actively ventilated and free from extraneous odours.

Each of the five members of the panel has to judge individually the undiluted atmosphere of the test chamber.

Criteria of acceptability are as follows:

<u>Member rating</u>	<u>Numerical rating</u>
Undetectable	0
Barely detectable	1
Easily detectable	2
Objectionable	3
Irritating	4

A total score of 25 or less for the sum of 10 odour evaluations (5 panelists x 2) is passing; a total score above 25 fails the material.

THE METALLURGICAL EXAMINATION OF SPACECRAFT MATERIALS FAILURES

B D Dunn

ESA/ESTEC, Noordwijk, The Netherlands

ABSTRACT

Several failure analyses performed in the ESTEC metallurgical laboratories are summarised in this paper. The normal techniques applied during these evaluations include low power and scanning electron microscopy, microprobe analysis and metallography. Spacecraft hardware may suffer from all the classical metallurgical failure modes, such as fatigue, stress corrosion, hydrogen embrittlement, etc., but metallic particle contamination has also proven to be an area for concern.

Small companies, which do not employ their own materials specialists, could benefit greatly from advice from national research establishments. The majority of problems discussed in this paper do not result from overload or underdesign and it is recommended that Review Boards convened to assess suspect or failed hardware do not bypass the materials laboratory. Remedial actions, based on intuition rather than hard facts, and untested, last minute "improvements" are blessed with a 100% failure rate and may contribute to launch delays.

installed on-board engineering or qualification model spacecraft, so that the results and recommendations can be fed back to project designers and engineers. This procedure will, hopefully, eliminate future problems with flight model spacecraft.

The classic failure modes, e.g. fatigue, stress corrosion cracking and overload, have been frequently identified during the past ten years of our laboratory work. The object of this paper is to outline some of the areas of concern by summarising several case histories of actual spacecraft failures. This quasi tutorial review may also demonstrate the usefulness of the SEM and the importance of microscopic examination of polished samples cut from failed or suspect components (i.e. metallography)

INTRODUCTION

Analyses of spacecraft failures which result from metallurgical faults generally follow the traditional guidelines applicable to all engineering failures. The Scanning Electron Microscope (SEM), the Energy-Dispersive X-ray Analyser (EDAX) attached to the SEM, and metallography are the main tools used by the Metallurgy Group of the ESTEC Materials Section.

Failures originating from shortcomings in design, choice of metal, or process procedure, may occur during spacecraft fabrication, assembly, integration and environmental life testing. The failure analysis is viewed as a constructive task intended to identify failure modes and causes. This can only be achieved when sufficient information is available about the history of the failed part since its manufacture. Fortunately, the high degree of surveillance by the Product Assurance teams of European Space Agency (ESA) contractors usually enables proper documentation of most details pertinent to a failure. A knowledge of the operating stresses and environment is of great help in the diagnosis of a failure mechanism.

The majority of our analyses are made of hardware tested at equipment level, but some defective items also originate from units which have been



Fig. 1 - SEM photograph of fatigue striations on the fracture surface of a failed satellite structure (Al 6061-T651) following vibration-testing. Crack propagation is in direction of arrows (from test house report).

EXAMINATION OF FRACTURE SURFACES

The failure mode of spacecraft materials can often be assessed by detailed examination of the fracture surfaces. The Scanning Electron Microscope (SEM) is an invaluable tool in such failure investigations because it extends both the depth of field and the magnification obtainable by conventional light microscopes. Fracture surfaces rarely require special preparation for SEM inspection. Only when thick corrosion products or other non-conductive substances are present in the area of examination will a thin layer of gold be applied to prevent electrical charging effects.

Fractures often leave characteristic markings from which the cause of a component failure may be quickly deduced. However, for accurate identification of failure modes, fractography should always be followed by metallographic examination.

Fig. 1 details the fatigue striations as seen in the SEM on the failed surface of a satellite structure following vibration-testing. The fracture path is perpendicular to the stress axis and each of the parallel striations has resulted from a single stress cycle. The density of the striation spacings and their definition also provide information about the loading conditions.

Fig. 2(a) highlights the appearance of typical stress corrosion cracks found in a high strength aluminium alloy test specimen which was stressed to 75% of the material's yield point and then exposed to a saline environment for 80 days. Some corrosion pitting was observed adjacent to this specimen's surface. A stress concentration had developed at the root of the deepest pit and promoted stress corrosion cracking (SCC) along this alloy's rather large grain boundaries. Fig. 2(b) shows the characteristic, very small dimple shapes at the centre of the specimen. They result from tensile overloading and the ductile

failure of the alloy. These SCC test samples originate from part of the test programme undertaken to qualify the SPACELAB structure. The overall results categorised this Al 2219-T 851 alloy, including its weldments, to have a high resistance to SCC.

DISCLOSURE OF THERMAL HISTORY FROM MICROSTRUCTURE

Halfway through the trial firing of an apogee boost motor (ABM), the outer case material was observed to breach and fail catastrophically. An anomaly was known to exist in the ablative case-liner which separated the propellant from the Ti-6Al-4V case material, but it was considered important to perform a metallurgical failure analysis to ensure that no local defects had been present within the titanium alloy case before rupture.

Two metal samples were carefully cut from the case wall: one adjacent to the failure initiation site and the other from a region through which the crack had propagated. The fracture surface at the origin of the fracture was photographed (arrowed in Fig. 3a) and both samples were then mounted, polished and lightly etched in a solution of HF, HNO₃ and water to reveal the material's microstructure.

The case-wall thickness is clearly seen to have necked down prior to failure. Such extreme ductility of this particular alloy will only occur within the temperature range 800 - 1000° C, when it is known to undergo superplastic deformation. The most significant observation made during this examination was the existence of two markedly different microstructures within the failed case material. Well away from the rupture initiation site, the microstructure (Fig. 3b) is seen to consist of the typical room temperature stable ($\alpha + \beta$) structure. However, in the vicinity of the rupture, a wholly martensitic (α') structure exists (Fig. 3c). The ternary phase diagram of this alloy dictates that it is necessary for the Ti-6Al-4V composition to be heated to a temper-

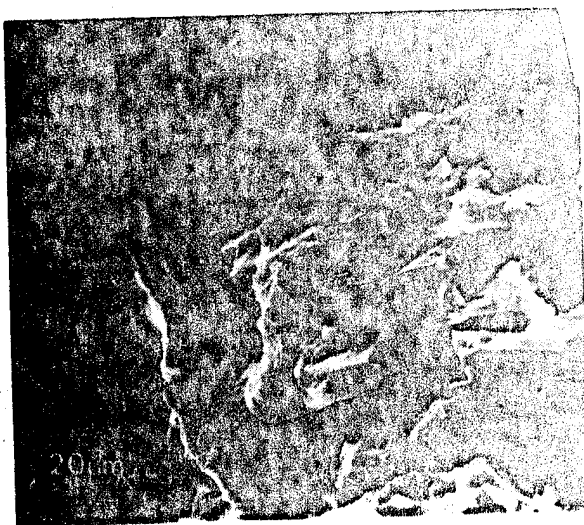


Fig. 2a - Intergranular cracking attributed to stress corrosion;



Fig. 2b - Ductile dimple fracture following tensile overloading of Al 2219-T851 plate.

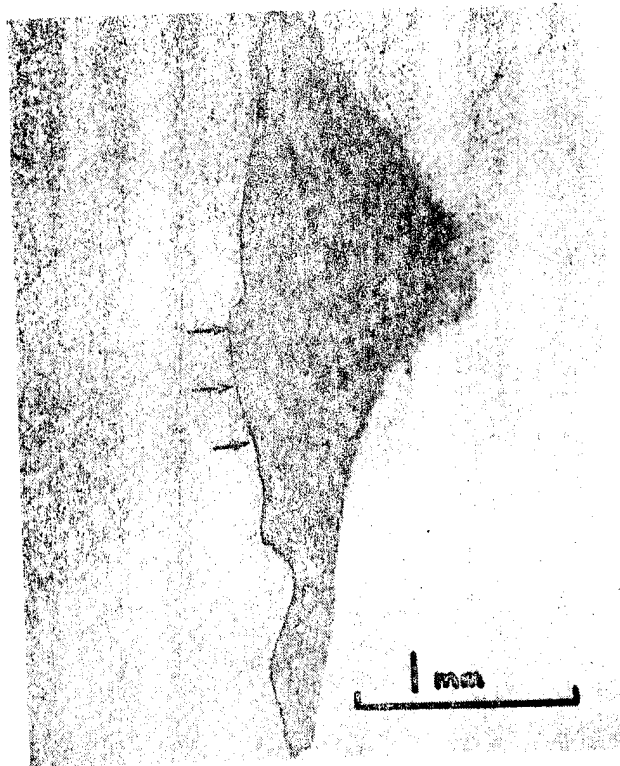


Fig. 3a - Origin of ABM case fracture.

ature between 910 and 1000° C for the ($\alpha + \beta$) structure to transform completely into the single β high temperature phase.

The partial phase diagram of this alloy system is shown in Fig. 3d; the fully β region is denoted by location 'A'. The microstructures which result from heat-treating this alloy in various manners are shown schematically. On slow cooling from the β phase, the resultant ambient temperature microstructure would appear as a mixture of martensite (α') and primary (α). On fast cooling to ambient temperature, the β phase is replaced by a totally martensitic (α') structure.

Phase diagrams are the metallurgist's "blueprints". For any combination of metals, a characteristic form of phase diagram is obtained. For instance, when a piece of polished alloy is viewed under a microscope and then heated or cooled at its equilibrium rate, the observer will notice microstructural changes which may include phase modifications corresponding to the alloy's phase diagram. In practice, alloys are rarely cooled at equilibrium rate and, as shown in Figs. 3b and 3c, divergencies from the conditions indicated by the phase diagram are frequently considerable. From experience and consultation of other data, e.g. time-temperature-transformation diagrams, it is possible for the metallurgist to assess metastable structures which result from non-equilibrium cooling.

Examination of the failed ABM case proved that there were no defects in the case structure and that it had been heat-treated correctly. However, as a result of abnormal burning of the propellant,

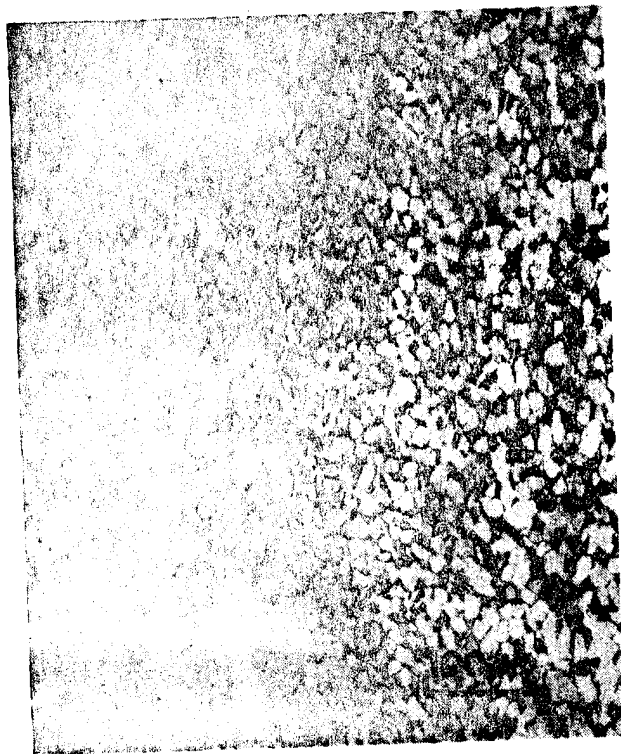


Fig. 3b - Typical microstructure of the case 2-phase ($\alpha + \beta$) possessing small grain size.



Fig. 3c - Microstructure at origin of fracture is large grain and fully martensitic.

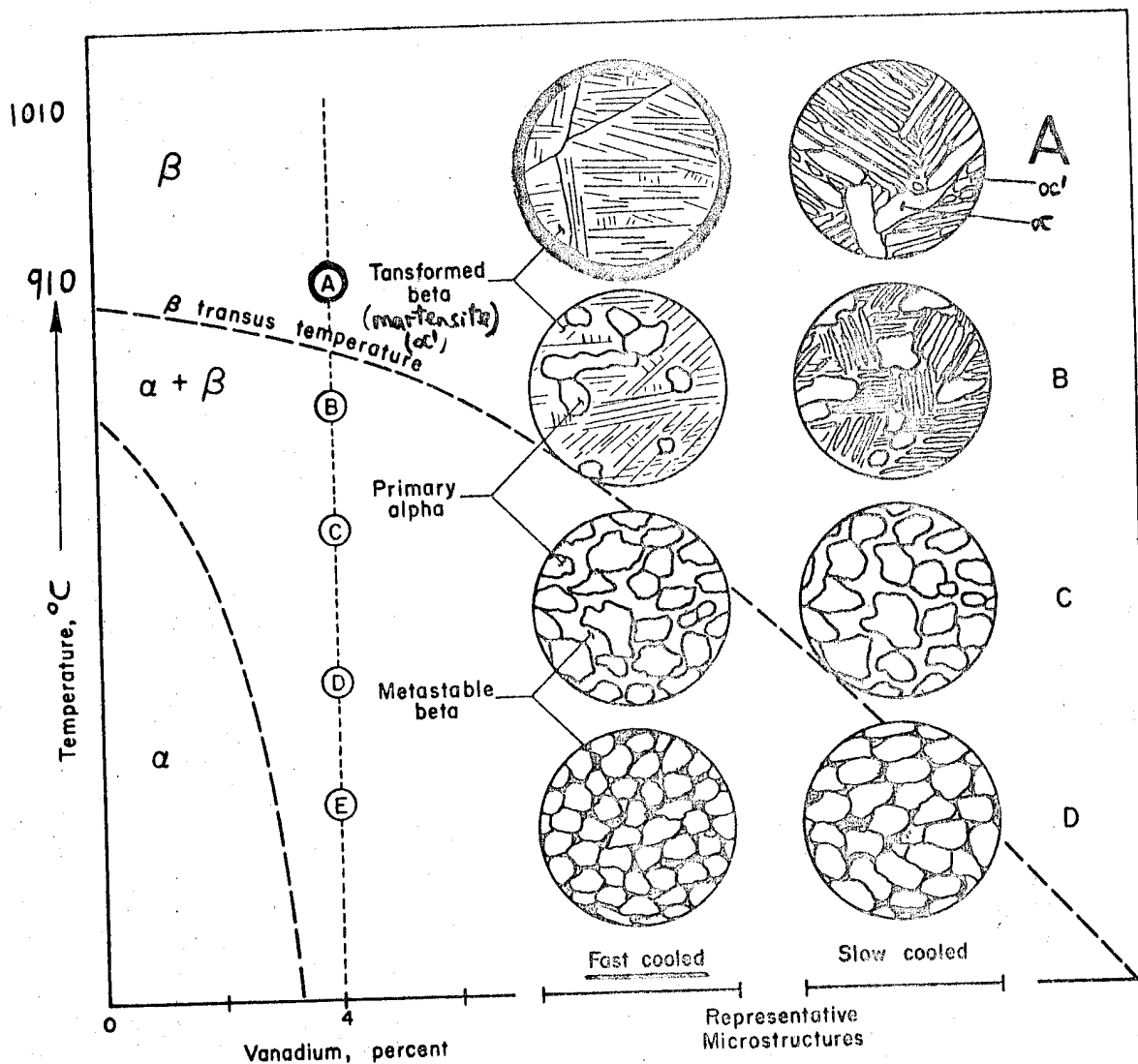


Fig. 3d - Partial phase diagram of the Ti-6Al-4V system and schematic representation of microstructures resulting from fabrication of Ti-6Al-4V at various temperatures (from Ref. 1).

a hot spot occurred in the case and reached a temperature of 800°C . This caused the case to plastically deform and aggravate the liner problem. The microstructure shown in Fig. 3c illustrates that the rupture initiation site must have reached a temperature of approximately 1000°C for the $(\alpha + \beta)$ to transform completely into β phase. At this temperature, the case initiated a fissure which propagated due to the case's internal pressures. After case rupture, the hot spot must have cooled rapidly, so that the β phase fully transformed into the meta-stable martensitic structure.

MECHANICAL DAMAGE REVEALED BY MICROSTRUCTURE

Fig. 4a shows a flexible wave-guide from a batch which, at final inspection, was rejected due to the occurrence of small pin-holes adjacent to the tube-to-flange soldered joints. These defects were visible only at X10 magnification. The tube

material was solution-treated beryllium copper and the pin-holes were limited to the first two tube convolutions.

At the start of the investigation, two reasons had been put forward by the wave-guide manufacturer: first, the tubes had been supplied with drawing defects which had opened out by the heat dissipated during the soldering operation, and - second - the strong soldering flux required to produce smooth and bright solder fillets had chemically corroded the tube. Another opinion was that the soft solution-treated alloy had been penetrated by sharply cornered tooling jigs used to bend the tube into its spacecraft configuration. After forming, the assembly had been precipitation-hardened at 315°C for two hours and then soldered to the flange at 240°C .

The defective region was microsectioned and polished (see Fig. 4b). It can be seen that at

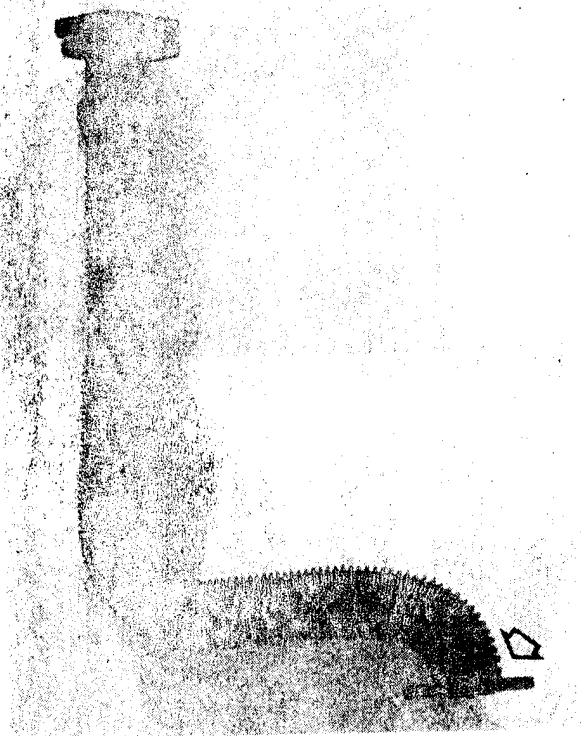


Fig. 4a - General view of flexible wave-guide showing position of pin-hole (arrowed).

least two of the convolutions were damaged and that in these regions the section thickness of the tubing was greatly reduced and hence mechanically weakened.

Complete beryllium copper removal had occurred at the pin-hole site. The detail of one of the defective areas (etched, Fig. 4c) shows the damaged internal wall of the tube to have slightly collapsed. This indicates that a compressive force had been applied to the tube surface. Also, the microstructure of the undamaged tube is shown to consist of non-deformed equiaxed grains. In the damaged region, the grains have been slightly deformed; they contain a high density of parallel slip bands and mechanical twins which change direction from grain to grain. Such features are characteristic of mechanical damage that must have occurred subsequent to the precipitation treatment because, at 300° C, they would have been annealed out.

At this stage, it was possible to rule out the initial judgement that penetration had been caused by forming or corrosion. A visit to the manufacturer's shop-floor revealed that an inexperienced soldering operator had assembled this particular batch of waveguides. Many of his fillets had contained more solder than was normal. By means of pulling a fine cord, loaded with abrasive grit, around the fillets, he was able to remove the excess solder and produce a clean bright fillet. In doing so, this action had also produced wear and excessive thinning of the waveguide tube. The characteristic slip lines and deformation twins in the microstructure (Fig. 4c) had accurately indicated that abrasion and pin-hole formation had been introduced at a stage after the final heat treatment of the tube.

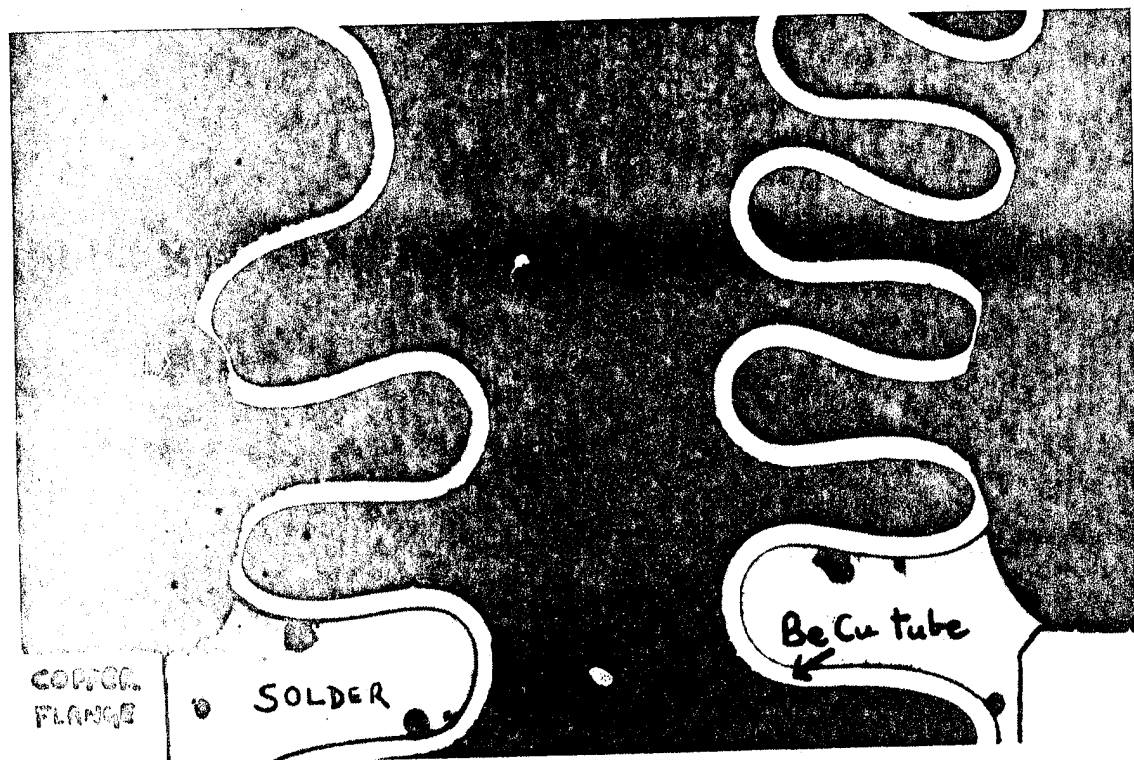


Fig. 4b - Full cross-section of defective region showing solder fillet and location of pin-hole (arrowed).



Fig. 4c - Etched microstructure of beryllium copper in region of pin-hole. Grains are generally equiaxed, but have deformed beneath abraded region and contain a high density of slip and twin bands.

ASSESSMENT OF APPROXIMATE CHEMICAL COMPOSITION FROM MICROSTRUCTURE

It is a mandatory ESA requirement (2) that Printed Circuit Boards (PCB's), to be assembled by soldering support eutectic composition tin-lead finishes which have been electroplated and then fused onto their high-purity electrolytic copper conductors. From experience to date, hot oil fusing of tin-lead finishes has proved to be a controllable process. One ESA-qualified supplier has, however, encountered systematic problems resulting in rough, fused tin-lead finishes containing a large degree of porosity (Fig. 5a). A metallurgical investigation was instigated to determine the severity of the problem and recommend a procedure which would eliminate the observed defects (3). Microsections (Fig. 5b and 5c) were analysed by EDAX and line-scan attachments to a SEM. Wet chemical analysis confirmed the presence of slight copper contamination and a hyper-eutectoidal composition of the tin-lead; tin being 69.4% whereas the eutectic composition of pure solder is 62.9%.

The detailed photomicrographs highlight several large, partially sealed pores in the cross-sectioned coating; the normal copper-tin intermetallic layer is just visible (A and B of Fig. 5b, respectively). The microstructure of the plated-through hole shown in Fig. 5c also details severe porosity (A) and a fine laminated eutectic structure (C). This phase distribution would be expected in a tin-lead alloy containing 69% tin, the relative volumes of "islands" and eutectic being given by the tin-lead binary phase diagram.

The surface cavities and spherical pores associated with the rejected boards are considered to result from the volatilisation of occluded organic materials during the hot oil fusion process. At some time during solder fusion, before the alloy had cooled to its solidus temperature, the presence of tin-rich dendrites had entrapped gas pockets which would otherwise have been released at the liquid solder-to-oil interface. A revised plating procedure eliminated all trace contaminants and, once fused, provided a microstructure of almost exact eutectic composition (Fig. 5d). No surface imperfections were observed on PCB's made to this revised procedure.

THE EFFECT OF INCLUSIONS WITHIN THE MICROSTRUCTURE OF EXPLOSIVELY DEFORMED MATERIAL

Pyrotechnic or "electro-explosive" devices are used extensively in spacecraft to push or pull loads, to pull switches and pins, and to cut cables, wires and release mechanisms. ESA utilises various forms of such explosive actuated devices. They consist generally of a cylindrical body containing a pyrotechnic charge and an ignitor which can be fired by lead wires. The high pressure gases which are developed inside the cylinder as a result of firing cause a piston or bellow to move forward within a few milliseconds.

Fig. 6a shows the end of a fired satellite cable cutter cylinder; the round imprint has been caused by a piston rod attached to a cutter blade (their relative positions have been superimposed on the photograph). It is highly desirable to prevent spent explosive from contaminating the spacecraft or its environment by ensuring that these devices retain their hermeticity after

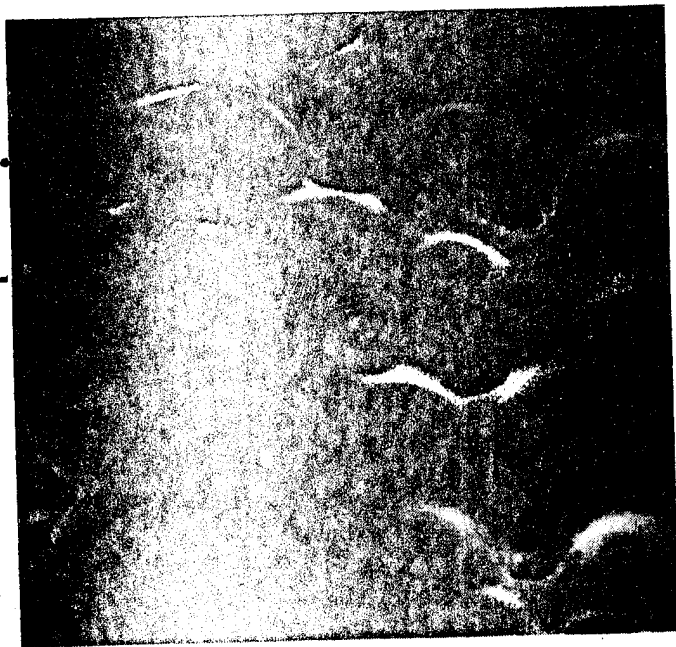


Fig. 5a - SEM photograph of PCB track surface showing the dendritic appearance and associated porosity within the fused tin-lead finish.



Fig. 5b - The microsection details the porosity seen on the track surface.

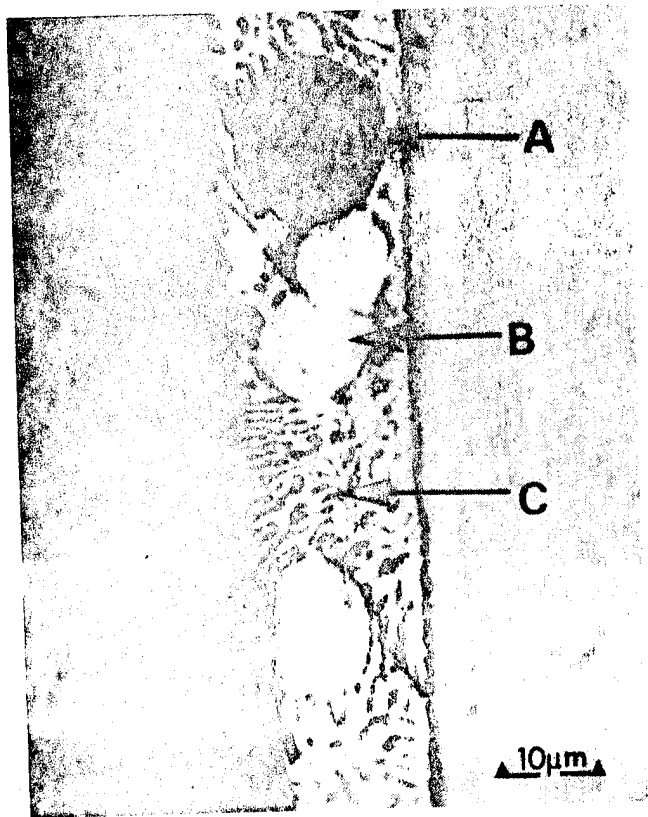


Fig. 5c - Porosity also exists within the plated-through hole of this reject board.

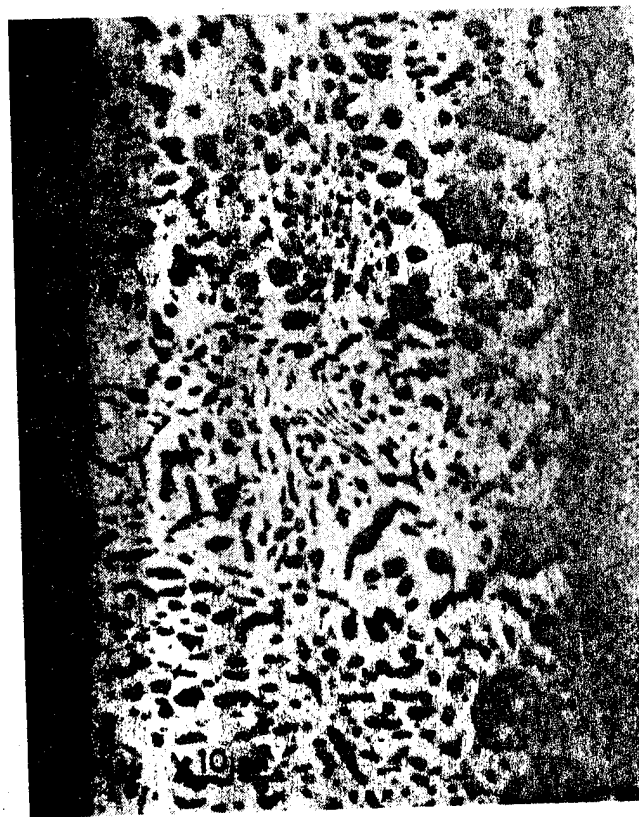


Fig. 5d - Properly plated and fused holes should contain a fully eutectic tin-lead microstructure.

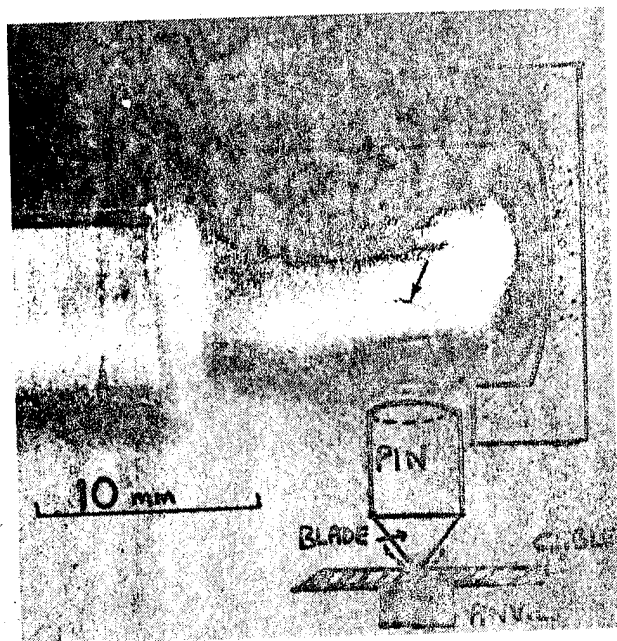


Fig. 6a - Photograph of pyrotechnic cutter found cracked (arrowed) and leaking after firing.

firing. The Inconel alloy cylinder shown in this figure, as with many prototypes, developed cracks (arrowed) during firing and this resulted in the escape of a considerable quantity of contaminants.

The metallographically prepared section shown in Fig. 6b reveals a high propensity of micro-porosity extending through the thickness of the cylinder wall.

Additional examinations and testing determined the mode of cylinder failure. The cylinders were found to have been machined from commercial purity Inconel 600 in bar form. This Ni-Cr-Fe alloy exists as a stable solid solution. The rather high carbon and sulphur content which is permitted by commercial specifications can give rise to inclusions of chromium carbide and nickel sulphide. Longitudinal sections made from bar stock showed such inclusions to be numerous and as having generally a high length-to-width ratio. Closer examination of the leaking cartridge revealed that each microvoid in the structure was associated with an inclusion (see Fig. 6c). These voids have formed by the pressure differences caused when the shock wave of the explosion passed over the inclusion and created microcracking, separation and cavitation at the inclusion-to-matrix interface. It is thought likely that cracks have formed after firing due to the high gas pressures within the cylinder. These cracks are seen to propagate through the Inconel in a ductile transgranular manner, linking the microvoids and so forming a continuous leak path.

Rigorous quality controls were imposed to ensure that only high-purity "clean" alloy was procured for the manufacture of additional cylinders. These were successfully tested and their hermeticity and freedom from microvoiding is attributed to the almost total absence of inclusions within the new stock material.

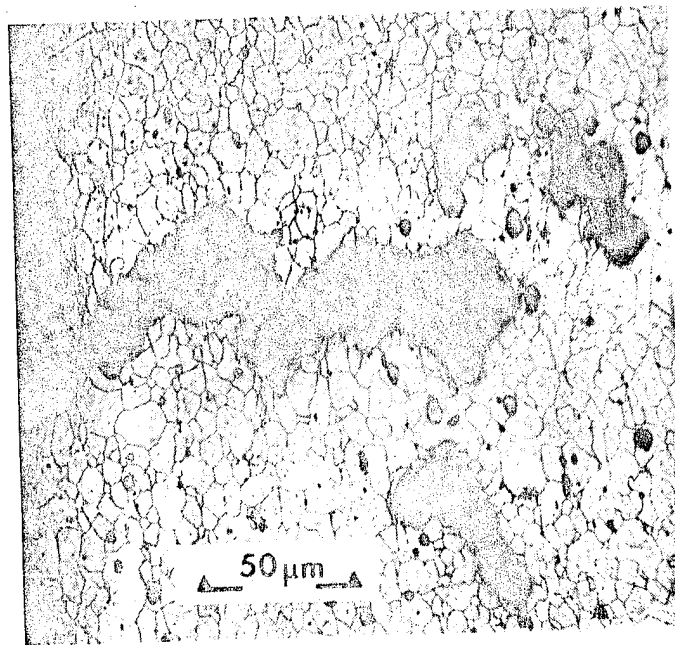


Fig. 6b - A transverse section highlights severe porosity.



Fig. 6c - The detailed examination shows inclusions (arrowed) surrounded by microvoids - the major crack has propagated in a ductile manner as evidenced by the deformed Inconel grains.

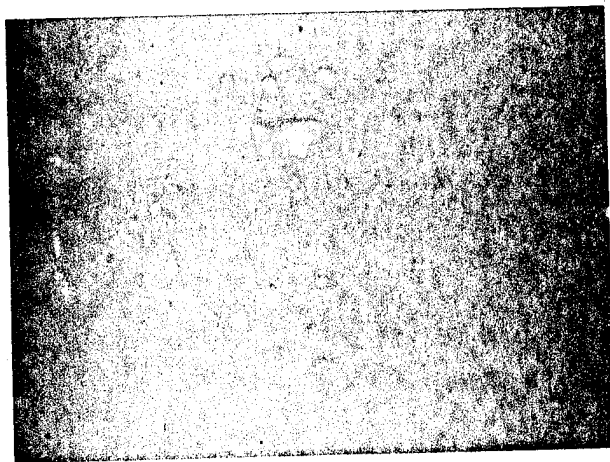


Fig. 7a - Side-view of brass bifurcated terminal on component side of PCB (arrow highlights typical lack of solder and crack in solder fillet)

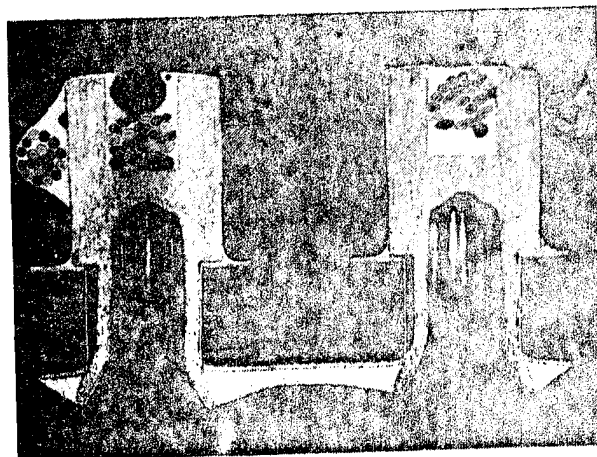


Fig. 7b - Section through two adjacent terminal pins.

FRACTURE RESULTING FROM MATERIAL THERMAL EXPANSION

MISMATCH

The following photographs highlight the most common cause of solder joint cracking in PCB's. These defects are associated with the use of solder-mounted brass terminal pins which develop cracks in their solder fillets within hours or days after assembly. They give cause for concern, particularly when noticed subsequent to the finished PCB being passed as visually acceptable at some inspection point. Fig. 7a shows a typical crack which had grown through 360° around this post. Microsections revealed that all posts soldered to this board contained cracks at the upperside solder fillet (Fig. 7b).

The detailed micrograph (Fig. 7c) shows that the underside solder fillet is still intact and, because plated-through holes have been utilised, the electrical continuity of this circuit had not been affected. These terminal pins had been machined from brass stock without a barrier layer of copper or nickel to prevent the zinc constituent of the brass from diffusing through the tin-lead finish and oxidising at the surface. Brass components which become covered by a thin layer of zinc oxide have almost zero solderability, even when highly corrosive fluxes are employed.

Fig. 7c shows that poor pin solderability prevented complete solder flow into the plated-through hole. Solder was applied with difficulty to both sides of the PCB. The lack of solder in the plated-through hole reduces the mechanical strength of this connection. During solder assembly of the terminal post into the PCB, or later during soldering of a wire to the post, heat will be dissipated into the PCB laminate and this will expand an order of magnitude more than the metallic parts of the joint. Upon cooling, the board laminate shrinks to its original dimension and creates a tensile force that stresses the solder joint. Due to the temperature excursions during soldering, the dimensional displacement of joints made to 1/16 inch thick boards can be 100 microns. The mean-time-to-failure or cracking is dependent upon the length of time the soldering iron remains

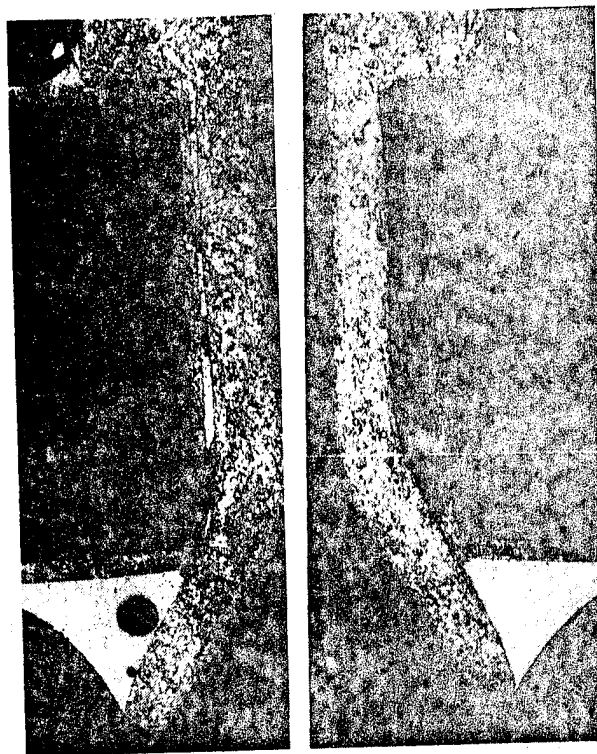


Fig. 7c - Cracked solder fillets (arrowed) on upper side of PCB and lack of solder penetration.

in contact with the conductive surfaces and the thickness of the non-metallic (PCB) media. Successful joints are only achieved by employing terminal posts of excellent solderability (e.g. solder-plated bronze or, when brass cannot be avoided, an intermediate barrier layer of at least 3 microns copper or nickel to prevent zinc diffusion to the surface). Soldering times and temperatures should also be kept to a minimum. The use of clip-on heat sinks has also proved to be of advantage when making secondary connections.

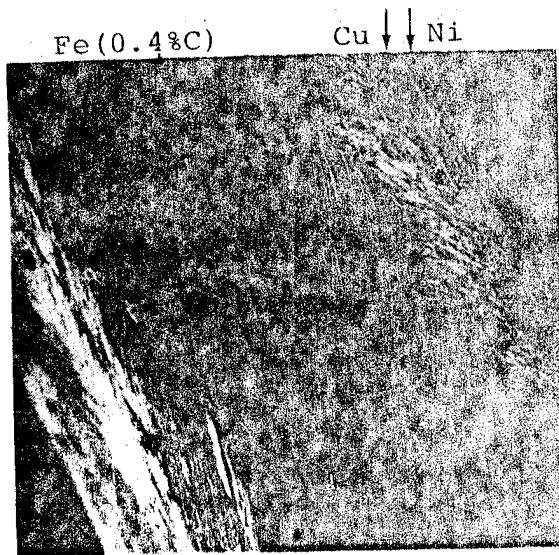


Fig. 8a - SEM fracturograph of prematurely failed steel spring showing plated layers and "delaminated" appearance of matrix.

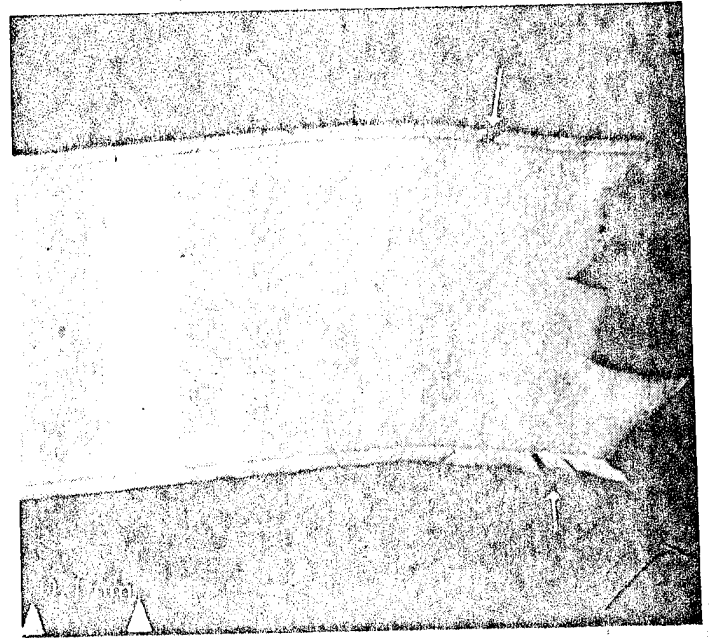


Fig. 8b - Longitudinal microsection made through fracture surface presented in Fig. 8a.



Fig. 8c - Extremely fine crack beneath plated layers.

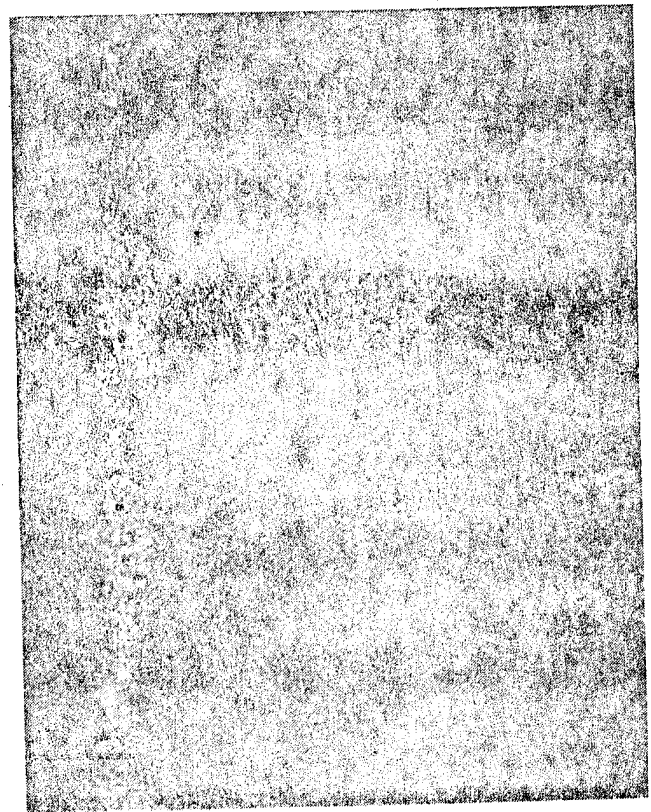


Fig. 8d - Internal microcracks formed by hydrogen and probably initiated adjacent to elongated inclusions in the rolled steel (lightly etched in 2% Nital).

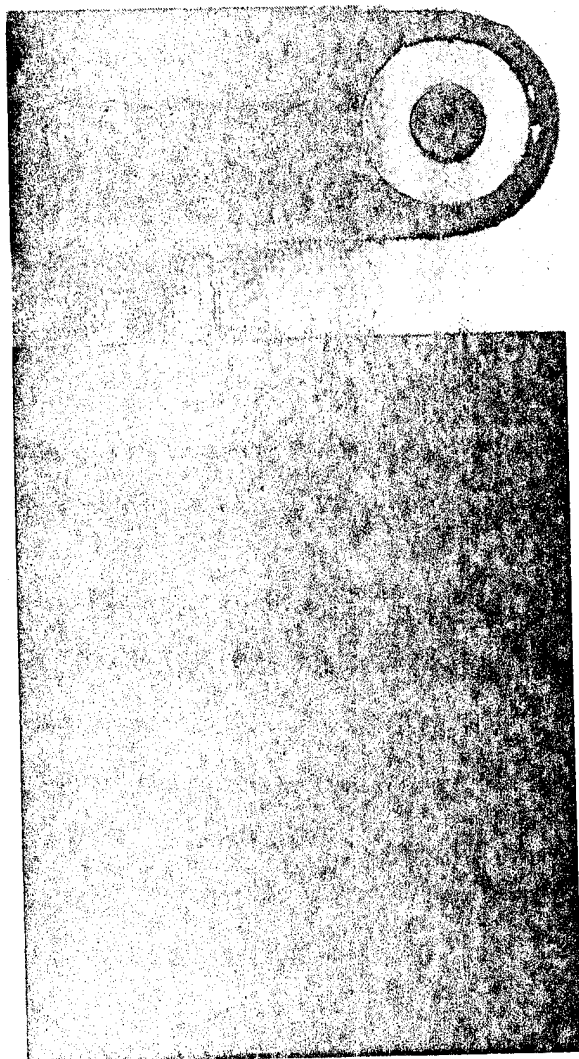
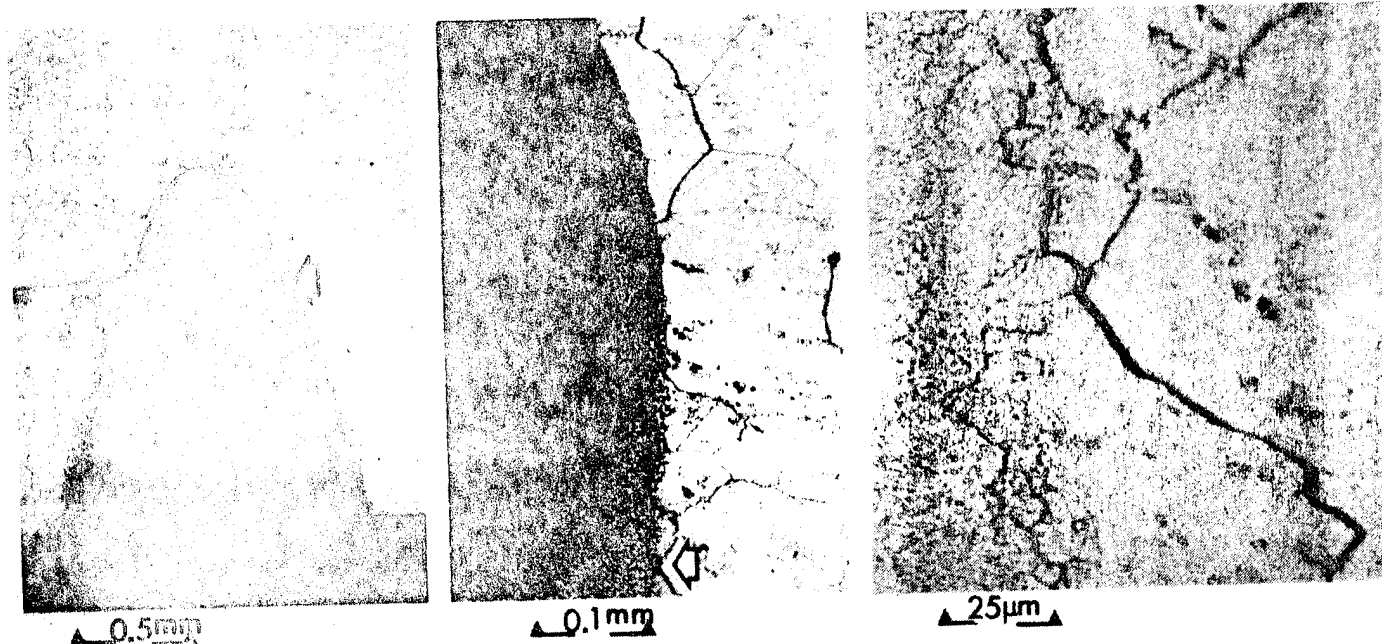


Fig. 9a - Strut intended for satellite structure. Tube and machined lug (both A12618) joined by EB welding. This strut had been stored non-loaded for six months. After integration, a similar strut failed along the path denoted by dotted line.

Fig. 9b - Photomicrographs progressively detail a continuous network of hairline cracks which surround and propagate into the weld pool; several intergranular cracks also exist in the HAZ.



HYDROGEN EMBRITTLEMENT OF SPRING STEEL

Several small springs which had been installed for two days within the equipment of an engineering model satellite were heard to snap into two halves prior to equipment level testing. The metallurgical analysis found the failed springs to have been fabricated of a standard 0.4% carbon low alloy spring steel which had been hardened and tempered, descaled and finally plated with, first, copper and then nickel. The spring fracture surfaces were examined in a SEM (Fig. 8a) and seen to consist of delaminated bands separated by dimpled rupture regions. The fracture path direction had followed along machine marks and some deep scores which existed on the nickel surface which are detailed in the microsection shown in Fig. 8b.

Based on a review of the spring processing procedure in conjunction with examination of the highly magnified steel microstructure (Figs. 8c and 8d), the primary failure of the springs was attributed to hydrogen embrittlement. These springs had been conditioned by heating to 900° C, oil quenched, and then immediately tempered at 250° C to produce the required hardness and spring properties. The subsequent cleaning and plating process stages generated hydrogen in its atomic form at the steel surfaces. Atomic hydrogen will rapidly diffuse through the metal lattice and, when uniformly distributed, is non-damaging. However, once the springs were installed on the spacecraft, they became loaded and, under the influence of applied stress, the hydrogen diffused to areas of stress concentration (e.g. internal sites of inclusions and dislocations). In these locations, the atomic hydrogen recombines to form molecular hydrogen as shown in Fig. 8d. This molecular hydrogen generates exceedingly high pressures which facilitate cracking. In most rolled steel sheets, banded structures containing fine, elongated inclusions are common. It is probable that the microcracks or delaminations visible in this microstructure result directly from the combined interaction of stress and the generation and accumulation of gaseous hydrogen at the inclusion-to-matrix interfaces. Once the density of microcracks had sufficiently impaired the load-bearing capability of the spring, the final failure occurred by overstress with the regions between the microcracks tearing in a ductile manner as shown by the dimpled zones on the fractograph.

Hydrogen embrittlement can be eliminated by a simple baking procedure which rattles out any absorbed atomic hydrogen before it can recombine as gaseous hydrogen. A recommended practice⁽⁴⁾ for "hydrogen bake-out" was successfully employed in the process of fabricating replacement springs. This consisted of heating the parts for three hours at 190° C within an hour of the plating operation and taking all necessary precautions to avoid flexing the articles before they were baked.

PROBLEMS ASSOCIATED WITH RESIDUAL STRESSES IN WELDMENTS

Electron beam (EB) welding is frequently employed during spacecraft construction and it is particularly suitable for weldments that are bodies of rotation, e.g. pressure vessels and tubular assemblies. The welding motion is mechanised and generally narrower weld widths - and therefore reduced distortion and heat-affected zones (HAZ) - are produced. It should be remembered that even EB welds will contain certain residual stresses which are caused by expansion differentials, shrinkage of the weld metal as it solidifies, and subsequent contraction due to uneven cooling. The design of one spacecraft structure included a strut manufactured by EB welding an aluminium alloy tube to an end piece lug which had been machined from the same high strength precipitation hardening alloy Al 2618.

Fig. 9a shows the appearance of this painted cylindrical weldment; the section shows that adequate weld penetration has fused and welded the end of the tube to the end-piece without the need for a filler metal. During integration, this weldment was observed to fracture under very low loading conditions. The crack path had propagated through the weld region in a manner superimposed on the micrograph.

As part of this failure investigation, an as-welded, but never loaded, strut was microsectioned. This sample was lightly etched (Fig. 9b) to reveal the presence of a fine network of cracks at the weld pool-to-parent metal interface. Some large, secondary intergranular cracks have also formed in the HAZ. It was later confirmed that cracks did not exist in newly made weldments. In fact, they had initiated and grown at some stage during the strut's 6-month storage period. In this case, the reasons for crack initiation and growth are believed to be twofold. The strut material is a rather complex precipitation-hardening alloy which undergoes various submicroscopic changes during fabrication. The alloy adjacent to the weld pool (HAZ) heats up during the welding operation and undergoes a localised solution treatment. At room temperature, the residual stresses, which have been set up within the material as a result of weld metal contraction, cause the solution-treated HAZ to gradually harden due to natural strain ageing. Unfortunately, such a condition may become embrittled, particularly if exposed to a mildly corrosive environment. It should be noted that, following the welding process, these struts had been chemically cleaned, alodined and finally painted. It is likely that these corrosive processing environments caused crack initiation sites which later were to grow by a stress corrosion mechanism.

Based on the failure analysis results, subsequent struts were carefully heat-treated in a furnace immediately after the welding operation. The residual welding stresses, which can reach levels as high as the yield strength of the welded structure, were sufficiently relieved during this heat cycle. At the same time, the solution treated HAZ was modified to a state of controlled higher strength owing to precipitation-hardening. No further cracking problems were experienced after the adoption of this post-weld heat treatment procedure.

CORROSION-RELATED FAILURES

Corrosion has to be considered during all manufacturing and pre-launch phases of spacecraft. Certain equipment may have to be designed to also withstand strongly corrosive environments during its useful life of possibly 10 years in orbit. Such equipment includes battery units, heat pipes and systems, and pressure vessels containing liquid fuels. Excepting emergency conditions, space hardware on-board the NASA Shuttle, e.g. SPACELAB, will not be exposed to uncontrolled terrestrial environments. However, pre-launch phases and ground storage periods for re-usable spacecraft may be long and it has been necessary to develop and implement a plan which ensures that all structural or load-bearing metals are adequately protected from general surface corrosion and stress corrosion cracking. Assessments are generally made by accelerated testing, using saline solutions (e.g. 3% NaCl).

For electrical connections, it is highly desirable to select metallic combinations from the approved couples detailed in Fig. 10. However, it is also important to note that many of the less noble metals shown in this tabulation require additional protection from general surface corrosion in the form of platings, conversion coatings, anodic films, paints, etc.

Until recently, magnesium alloys with their high strength-to-weight ratios have been frequently

selected for the construction of spacecraft structures and the housing of electronic systems. New ESA spacecraft requirements now stipulate generally that all units must be electrically grounded to their structures and, at the same time, possess an adequate surface protection system. This has led to the virtual exclusion of magnesium from present spacecraft design. Commercial conversion coatings, such as DOW 7, may be suitably conductive, but, being thin, they frequently give rise to corrosion problems (see Fig. 11).

This photograph shows the effect of slight condensed moisture on an experiment housing constructed of magnesium after equipment qualification by thermal cycling. The white, dust-like corrosion product was also considered to be a contamination hazard.

Contamination of an aluminium alloy cooling loop by a few minute particles of copper swarf (Fig. 12) has been identified as promoting the failure of this system.

Connection of copper, or its alloys, to aluminium is a most unfavourable galvanic couple, particularly in aqueous environments. In this instance, a small number of hemispherical pin-holes, originating from the inner surface of the channel, have been produced by the localised corrosion cell set up between the cathodic copper particle and the aluminium. Away from the pin-holes, the aluminium surfaces have not been corroded.

Group No.	Metallurgical category The metals having the greater negative EMF will tend to corrode and form oxides	EMF between a standard electrode and sea water	Compatible couples Maximum potential difference for	
			A) 0-25 V Non-cleanroom environment	B) 0-5 V Clean-room or hermetically sealed environment
1.	Gold, solid or plated; gold-platinum alloys; wrought platinum	+0.15	•	•
2.	Rhodium plated on silver-plated copper	+0.05	•	•
3.	Silver, solid or plated on copper; high silver alloys	0	•	•
4.	Nickel, solid or plated; monel metal and high-nickel-copper alloys; titanium	-0.15	•	•
5.	Copper, solid or plated; low brasses or bronzes; silver solder; German silver; high copper-nickel alloys; nickel-chromium alloys; austenitic high corrosion-resistant steels	-0.20	•	•
6.	Commercial yellow brasses and bronzes	-0.26	•	•
7.	High brasses and bronzes; naval brass; Muntz metal	-0.30	•	•
8.	18% chromium type corrosion-resistant steels	-0.35	•	•
9.	Chromium or tin plated (non-porous) metals; 12% chromium type corrosion-resistant steels	-0.46	•	•
10.	Tin-lead solder; solid or plated;terne plate	-0.50	•	•
11.	Lead, solid or plated; high lead alloys	-0.55	•	•
12.	Duralumin type aluminium wrought alloys	-0.60	•	•
13.	Iron, wrought grey or malleable; Armco iron; plain carbon and low alloy steels	-0.70	•	•
14.	Aluminium, wrought alloys other than Duralumin type; aluminium case alloys of the silicon type	-0.75	•	•
15.	Aluminium, cast alloys other than silicon type; cadmium platings (generally not approved for space-use)	-0.80	•	•
16.	Hot dipped zinc plate (generally not approved for space-use)	-1.05	•	•
17.	Zinc, wrought; zinc-base die casting alloys; zinc plate (generally not approved for space-use)	-1.10	•	•
18.	Magnesium and magnesium-base alloys, cast or wrought	-1.60	•	•

Fig. 10 - Compatible couples for bimetallic contact.

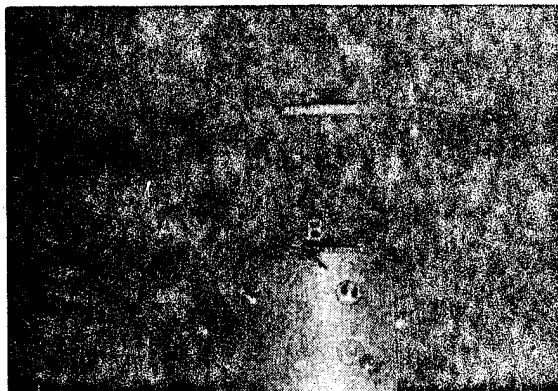


Fig. 11 - Magnesium housing finished with DOW 7 showing corrosion along bottom surface of ring (A) and around the threaded stainless steel helicoil inserts (B).

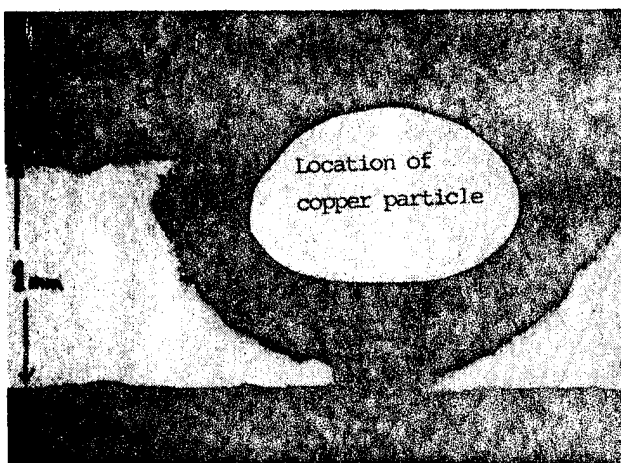


Fig. 12 - Copper (cathodic) surface contamination has resulted in severe pitting and leakage of an aluminium cooling channel.

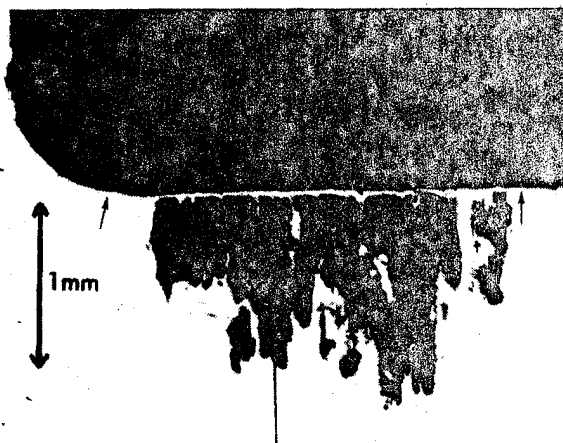


Fig. 13 - Pitting corrosion of aluminium alloy 2014-T6 enhanced by local porosity in 8 micron thick nickel plating, after 30 days in saline solution.

Fig. 13 details a severe corrosion pit within aluminium alloy 2014-T6. This part had been nickel-plated and subjected to a saline solution for 30 days as part of a qualification programme. The nickel plating was intended to provide the surface protection system, but - like many nickel plates - it contained microscopically fine cracks resulting from high residual stresses in the plating and caused the substrate to become exposed. In these locations, galvanic corrosion of the aluminium is enhanced by the large nickel area (EMF difference between Al 2024 and nickel is approx. 0.45V). This particular alloy also contains a high copper composition and the deep lamellar corrosion channels observed in Fig. 13 result from selective galvanic attack between undissolved cathodic particles of CuAl_2 and the alloy matrix.

The choice of metals for specific corrosive environments may be made by referring to corrosion handbooks. Unfortunately, important details are occasionally overlooked. Two brief, historical accounts are now given to illustrate the use of incompatible metals in contact with corrosive environments.

Problem No. 1 was caused by battery cells which had been installed in a satellite and were found to have developed slight leaks (Fig. 14a). The potassium hydroxide electrolyte had seeped out onto the cell tops and formed a white deposit which was analysed to be potassium carbonate, the reaction product between the electrolyte and carbon dioxide from the atmosphere. The central terminal posts of these battery cells are separated from their case bodies by a ceramic insulator. The cell construction materials had been designed to ensure proper matching of expansion coefficients. A strong metallisation system which could be painted onto the ceramic insulator had been selected. This would then be fired and subsequently brazed to form a reliable ceramic-to-metal seal. The metallisation chosen for the alumina ceramic was molybdenum-manganese metallic powder. During firing, the powder sinters together; the manganese component is oxidised, and this reacts with the alumina and its secondary siliceous phases to form a fluid glass (in the $\text{MnO-Al}_2\text{O}_3\text{-SiO}_2$ ternary system). This liquid then penetrates between the grains of the alumina and encompasses the molybdenum metallic particles. The exposed, electrically conductive molybdenum particles could then be plated with nickel. Copper-silver eutectic preforms were used to subsequently braze the ceramic into the Kovar cell cap. To satisfy long-life requirements, it was necessary for these seals to be completely inert to the cell electrolyte, a solution of potassium hydroxide, in the presence of oxygen, hydrogen and applied potentials up to 1.5V. Short-term, accelerated tests on the seals produced satisfactory results, but did not promote the actual failure mode which had initiated long-term cell leakage. The failure analysis of the leaking cells (Fig. 14b) revealed that the minute amount of free molybdenum in the metallisation was being chemically dissolved and leached out by the potassium hydroxide electrolyte. The leak path has a width of between 0.5 and 2 microns and complete penetration of these caps had occurred within 18 months after final assembly. Additional cells were developed utilising a titanium active metal metallisation in conjunction with the silver-copper braze and these have remained hermetically sealed for more than five years.

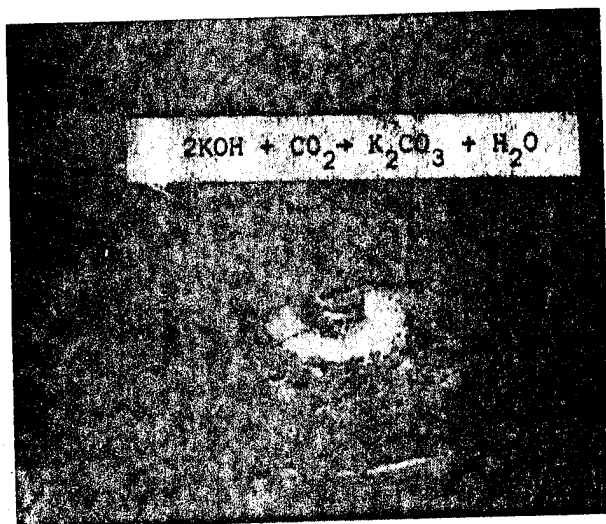


Fig. 14a - White crystalline potassium carbonate on surface of leaking ceramic-to-metal metal seal on terminal of nickel-cadmium battery cell (potassium hydroxide electrolyte).

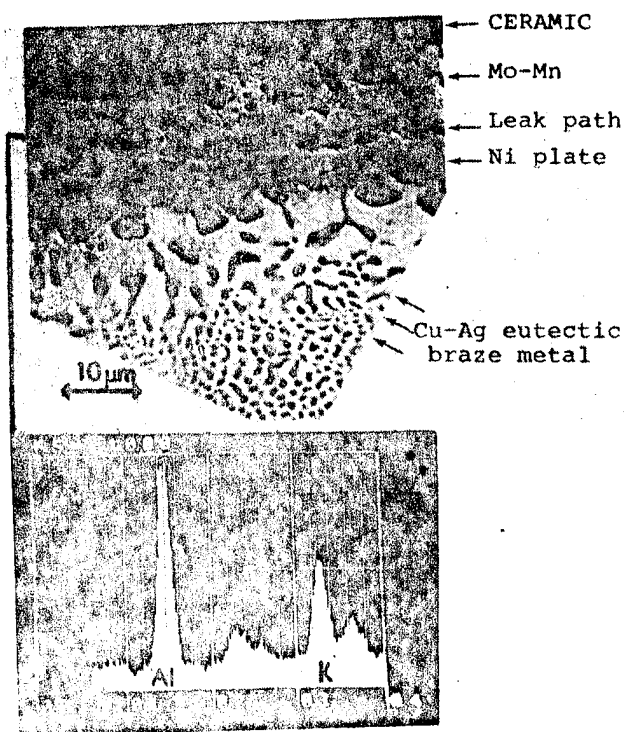


Fig. 14b - SEM photomicrograph of section made through leaking battery terminal. The Energy Dispersive X-ray analysis of marked area identifies the presence of Al, K, Ni, Mn and low Mo. The displayed low wavelength distribution highlights two large potassium peaks.

Problem No. 2 concerns incompatible materials which may be introduced unwittingly into fully satisfactory units. Reaction control systems, which are based on hydrazine fuel, suffer from severe material limitations because very few metals have been found to be compatible with hydrazine or its decomposition products. Qualified thruster designs were noted, during particular service tests, to operate at an unacceptably high temperature. All the existing thruster construction materials were known to be compatible with hydrazine; however, to increase the thermal dissipation of heat from thruster chambers, a small modification was made to existing hardware. This consisted of tagging thin copper ribbons onto the outside surface of each thruster chamber by means of a very small electron beam weld. Unfortunately, the depth of weld penetration was far greater than imagined, as shown in Fig. 15. Copper is seen to alloy with, and penetrate along, the grain boundaries of the chamber material. Local penetration of copper caused it to appear on the inside surface of the chamber. Thruster firings introduced hydrazine into the copper-contaminated areas and, within a few minutes, the chambers were observed to leak due to the rapid dissolution of copper by the reactive hydrazine.

Armed with this knowledge, satisfactory modifications were implemented by relocating the position of the copper ribbons to less critical parts of these thrusters.

SOME SOURCES OF METALLIC CONTAMINATION PARTICLES

The control of contamination has led to increases in the reliability and precision of spacecraft. Much effort is made to utilise materials, particularly organic ones, with very low outgassing properties. It is also necessary to ensure particle cleanliness by employing a contamination control procedure involving the use of clean rooms, laminar airflow facilities, clean packaging,

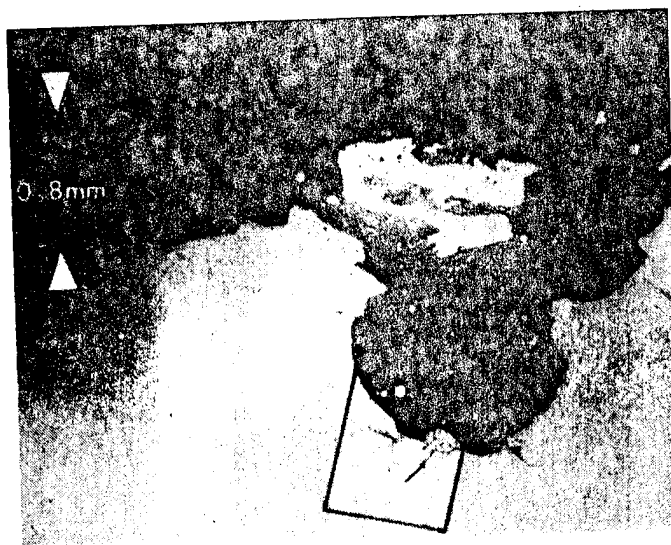


Fig. 15 - 0.8 mm thick copper ribbon electron beam welded to superalloy. Note extent of alloying and depth of grain boundary penetration.

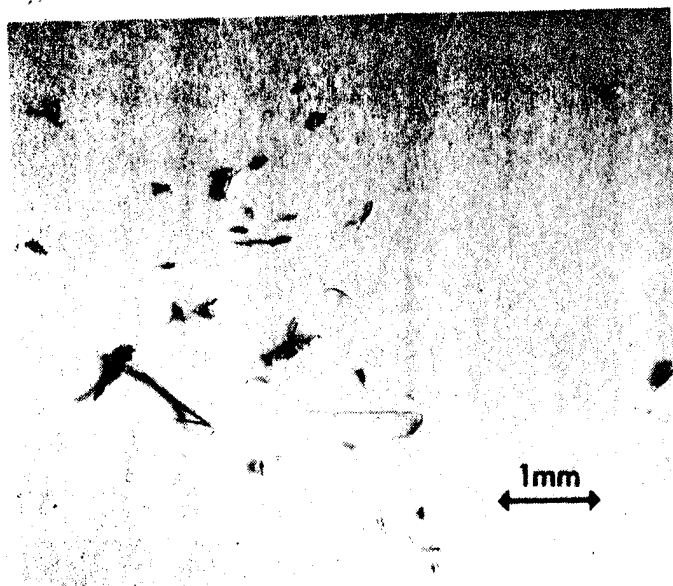


Fig. 16a - Silver slivers generated from the torque loading of titanium bolts into silver-plated titanium stiff-nuts; these cause electrical short-circuits and must be removed by vacuum cleaning.

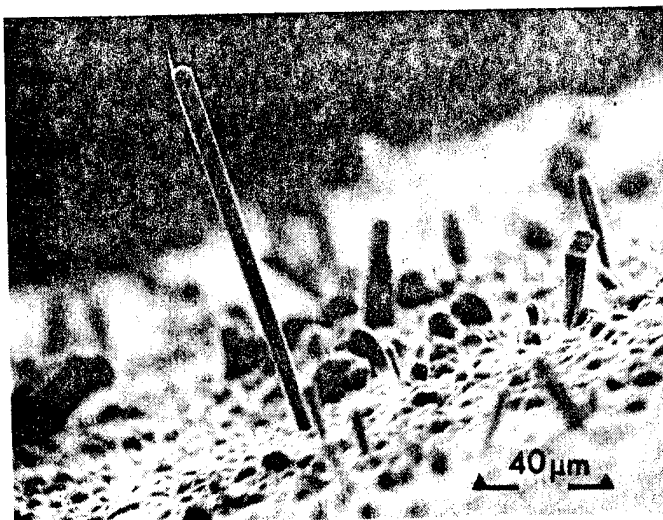


Fig. 16c - Filamentary growths of single crystals, termed "whiskers", growing on cadmium, zinc and tin-plated components. The whiskers shown here on tin-plated crimp connectors were seen to grow after their barrels had been deformed by a crimping tool. Some whiskers have been found⁽⁵⁾ to grow to lengths exceeding 2 mm and they can carry currents up to 32 mA before burning out. As spacecraft electronics progressively employ reduced spacing between conductors, any undetected whiskers which become detached during launch vibration may float under zero gravity to cause short-circuits.

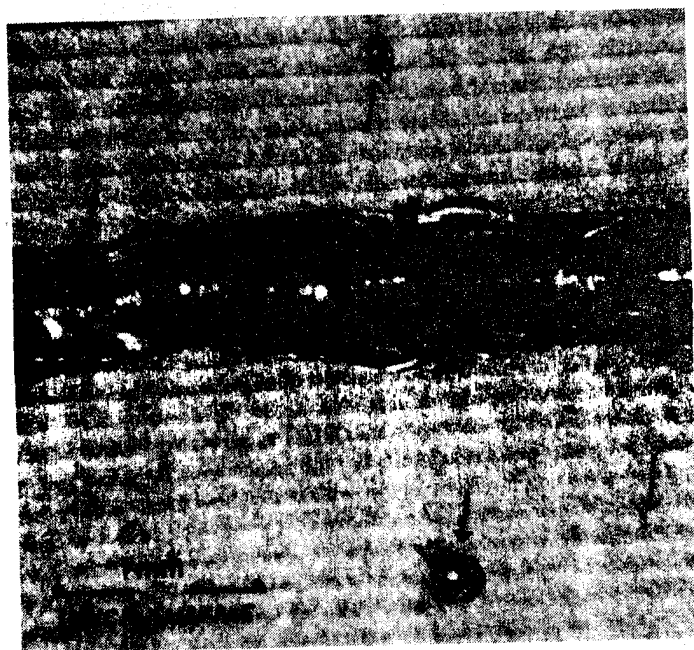
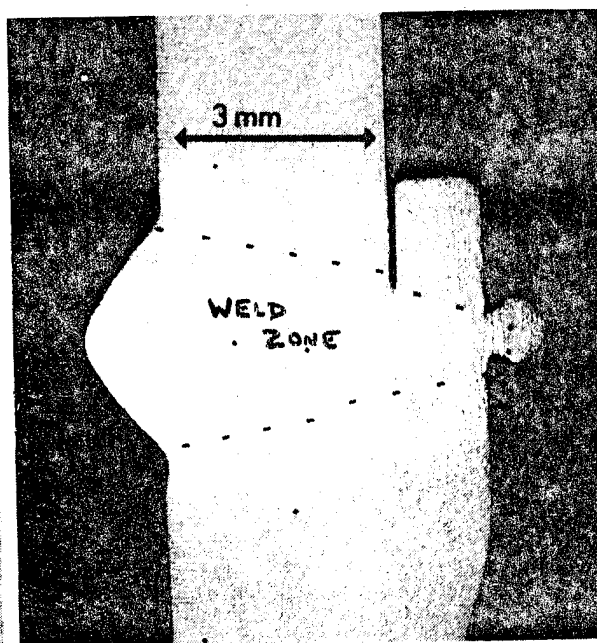


Fig. 16b - The internal surface of a Ti6Al4V propellant tank after EB welding. The failure analysis revealed weld overpenetrations and the release of weld splutter particles which were



loosely adhering to the inside tank wall surface. Vibration could cause particle detachment resulting in blockage of this spacecraft propellant system.

special monitors and the like. One aspect which should not be overlooked is the generation of metallic particle contamination, the sources of which may range from the very obvious to the highly illusive. Three highly problematic sources of metallic particle contamination, recovered from recent spacecraft, are illustrated in Fig. 16. They show respectively: Figures 16a, b and c.

It is strongly recommended⁽⁵⁾ that surfaces which may support stress-induced whisker growth, such as tin, cadmium and zinc, be excluded from spacecraft design and replaced, if possible, by a tin-lead alloy.

DISCUSSION AND SUMMARY

In practice, the majority of materials for specific spacecraft applications are chosen by designers and engineers who may only have a superficial knowledge of material science. It happens only too often that a metallurgist is brought in after failures have occurred. As a result of the continuously growing sophistication of spacecraft, brought about particularly by the flying of advanced technologies and the requirement for longer lifetimes, ESA now requests that the prime contractor for each project employ a team of materials specialists⁽⁶⁾. This team must be declared in the first phase of the project. Several of the smaller companies engaged to manufacture hardware such as mechanical devices and electronics lack the availability of materials specialists. In these cases, it is essential that materials information and test laboratories are close at hand, possibly at national research establishments, to give advice and to perform tests on technology samples with the aim of choosing materials and production methods that are both economic and reliable.

The review of specific metallurgical failures presented herein may put project engineers, designers and managers on the alert for problems, probable causes and the modes of some materials failures. Unfortunately, the diagnoses indicate only too

often that failures could have been prevented at the design state or during production if there had been sufficient consultation between the engineer and the materials specialist. It should also be stated that much time and money may be wasted by exasperated managers and engineers who attempt to conduct failure investigations during failure review boards and make recommendations based on intuition whilst bypassing the laboratory failure analysis. It must be stressed here that the majority of failures described in this paper do not result from overload, but stem mainly from fundamental shortcomings in design, choice of material or choice of process procedure.

The metallurgical analysis plays an indispensable role in the post-mortem diagnosis of spacecraft hardware failures. Metallographic techniques together with adequate knowledge of the background of a problem area are equally indispensable in the clarification and rectification of the material factors that affect the modes of failure.

References

1. MIL -HANDBOOK-697A, "Titanium and Titanium Alloys", June 1974.
2. ESA PSS-50/QRM-17E, "Test Specification for Two-sided Printed Circuit Boards, Fused Tin-Lead Finished".
3. Dunn, B.D., "Metallurgical Evaluation of Tin-Lead Finishes on PCB's", Trans.Inst. Metal Finishing, 1977, Vol. 55, p. 86.
4. ASTM Standard B 242-54 (reapproved 1971), "Preparation of High-Carbon Steel for Electroplating".
5. Dunn, B.D., "Whisker Formation on Electronic Materials", ESA Sci. Tech. Rev., Vol. 2, No. 1, 1976, pp. 1 - 10.
6. ESA PSS-19/QRM-16, "Qualification of Materials and Materials Lists Applicable to Space Projects".

THERMAL ANALYTICAL METHODS FOR CHARACTERISATION OF RESINS, PREPREGS AND COMPOSITES

H Stenzenberger & M Herzog

Technochemie GmbH-Verfahrenstechnik, Dossenheim, Germany

ABSTRACT

This paper provides the DSC characteristics of 7 model epoxy resin curing agent combinations. In addition, the DSC-cure behaviour of a typical autoclave grade high temperature bismaleimide resin is evaluated.

The calculation of cure cycles based on DSC-data and time-temperature profiles of a commercial autoclave are demonstrated for 2 epoxy resins and a polyimide resin material.

For a new high temperature epoxy resin formulation based on TGDDM and m-Aminobenzoic acid hydrazide it is demonstrated that Differential Scanning Calorimetry (DSC) can be used to define the state of advancement of the resin and therefore to control the quality of carbon fibre unidirectional prepregs. Thermal Mechanical Analysis techniques are advantageously used to develop postcure cycles.

Keywords: Differential Scanning Calorimetry, expansion coefficients, thermosetting resins, cure cycle calculation.

1. INTRODUCTION

Fibre reinforced composite materials are of increasing importance in many aerospace and aircraft applications as a result of the requirement for lighter weight structures. Graphite fibre composites are accepted materials now, because they offer a very high strength to weight ratio and stiffness to weight ratio, as compared with conventional metallic structural materials. The usual technology to mould complicated spherical parts needs prepreg materials as precursors. They consist of the reinforcing fibres either unidirectional or as a woven fabric impregnated with a thermosetting resin formulation. The resin is sometimes B-staged, e.g. reacted to a small degree to make it non-liquid at ambient temperatures and suitable for being processed by a low pressure (4-7 MPa's) autoclave moulding procedure. As a consequence of the rapid introduction of advanced resin composites into the production of structural components in aircrafts and spacecrafts, the development of advanced quality assurance criteria became extremely important. During the early period, acceptance criteria for prepregs were based on performance tests such as mechanical properties of moulded test coupons, gel time, resin contents, flow properties and tackiness. Nowadays,

it is accepted by the industry that the chemical composition of the resins used must also be part of the quality assurance control. Chemical analytical methods like thin layer chromatography (Ref.1), high pressure liquid chromatography (Refs. 2,3,4), infrared spectroscopy, C-13 nuclear magnetic resonance, chemical analysis and end group titrations are used more and more. Great attention is paid to Differential Scanning Calorimetry (DSC), since this method provides information which is related to the chemical reaction of the matrix during cure.

Described in a recent publication are the instrumental techniques for developing epoxy cure cycles by using DSC (Ref.5). A mathematical model for evaluating recommended cure cycles is provided for one commercial epoxy resin system (NARMCO 5208). The investigations performed during the course of this work are directed toward the correlation between the chemical composition of the resin binder matrix and the thermal analytical (DSC) behaviour. DSC is also applied to calculate the cure cycle of a commercial graphite epoxy-prepreg (Code 92 of Fothergill and Harvey), a polyfunctional epoxy and a thermosetting polyimide resin. To demonstrate the applicability of DSC as a quality assurance control method, the ageing behaviour of a 350°F prepreg system based on tetraglycidylmethylenedianiline (TGMDA) and m-aminobenzoic acid hydrazide (ABH) is followed by DSC. TMA-analysis is used to measure coefficients of linear thermal expansion for both laminates and neat resins to obtain information about postcuring requirements.

2. EXPERIMENTAL

2.1 Resins investigated

Three typical epoxy resin base materials, e.g. tetraglycidylmethylenedianiline (TGMDA) (Ciba Geigy MY 720), bisglycidylbisphenol A (Ciba Geigy CY 209) and an epoxy novolac resin (Bakelite 0302) were used in this investigation. Methylenedianiline (MDA), diaminodiphenylsulfon (DDS) and m-aminobenzoic acid hydrazide (ABH) were used as curing agents for the model epoxy-curing agent combinations. In addition to these model compounds a commercial prepreg resin formulation was made available by Fothergill and Harvey (Code 92) for this investigation.

The chemical structures of these model compounds are provided in Table 1.

MATERIAL	VENDOR	EQ. Wt	STRUCTURE
CY 209	CIBA GEIGY	150	
MY 720	CIBA GEIGY	127	
EPN 0302	BAKELITE	144	
MDA	CIBA GEIGY (H 7972) 4356		
DOS	ROUSSEL UCLAF 6203		
ABH	TECHNOCHIMIE 3780		

Table 1. Chemical structures of epoxy-resins and curing agents

A thermosetting polyimide resin formulation which can be processed as a hot melt, Code H 795, has been developed recently by Technochemie for graphite fibre prepreps and was included in this study for comparison.

2.2 Sample preparation

The epoxy resins and curing agents were dissolved in Aceton at low temperature to obtain a homogenous mixture of the reactants. The solvent was stripped off in a vacuum at 50-70°C, and the resinous residue obtained was directly used for DSC measurements. The mixtures contained 4-8% by weight of residual solvent. The PBMI (H 795) hot melt resin was free of residual solvent for the thermal analysis investigation. The commercial EP-resin Code 92 was delivered as a solution in a low-boiling solvent. DSC samples were obtained after solvent removal in the usual way.

2.3 Instrumental

A Du Pont Thermal Analyser (900) with a Differential Scanning Calorimetry (DSC) module was employed. The thermal mechanical analyser (TMA) model 941 was used for the CTE measurements.

2.4 Differential Scanning Calorimetry (Method of Carpenter)

Differential Scanning Calorimetry covers the measurement of the heat evolved during an exothermic reaction like epoxy (EP) or polybismaleimide (PBMI) resin cure. The DSC-thermogram - a typical scan is given in Figure 1 - provides the profile for the rate of energy released for a programmed heating rate. Following the procedure of Carpenter (Ref.5) within this DSC-curve several characteristic temperatures can be defined.

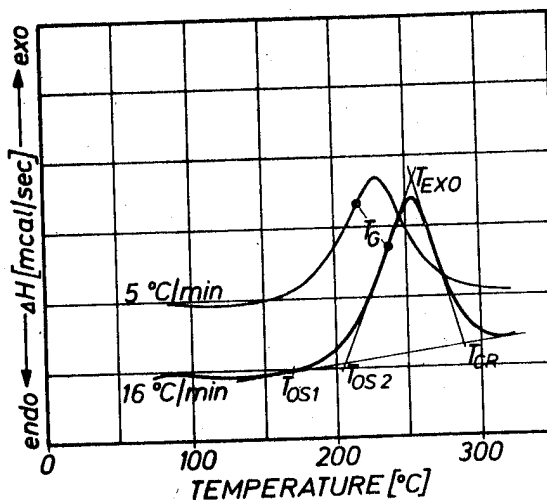


Fig.1 Differential Scanning Calorigramme of a thermosetting resin.

T_{OS1} (onset temperature) - this is the temperature where the first detectable heat is released, it is the onset temperature for the curing reaction.

T_{OS2} (onset temperature) obtained by extrapolating the front side of the exotherm curve to the base line.

T_{GEL} (gel temperature)

T_{EXO} (exotherm peak temperature)

T_{CR} (complete reaction temperature) obtained by extrapolating the back side of the exotherm curve to the base line.

The values for the four temperatures (T_{OS} , T_{GEL} , T_{EXO} , T_{CR}) depend on the heat up rate and are related to the heat up rate by equation (1) (Doyle approximation, Ref.6)

$$\log \phi = \frac{A}{T} + B \quad (1)$$

ϕ = heat up rate (°C/min)

T = Temperature (T_{OS} , T_{GEL} , T_{EXO} , T_{CR})

A = Constant, related to the activation energy

B = Constant which is related to the Arrhenius frequency factor.

The constants A and B of equation (1) can be determined from the best straight line through a plot of $\log \phi$ vis $1/T$. These data obtained dynamically can be converted to the following isothermal relationship

$$t = cT^2 10^{-A/T} \quad (2)$$

t = time (minutes)

T = isothermal hold temperature (°K)

c = constant

Because the DSC-trace represents the various states of advancement of the resin during cure, one point of this trace defines the gel temperature for the specific heating rate condition. The knowledge of the equation (2) for the event of gel allows

the calculation of the gel-temperature for any cure cycle by treating the dynamic parts (heating up) of the cure cycle as a series of isothermal holds.

$$\sum_{T_0}^{T_{GEL}} \frac{\Delta t}{t} = 1 \quad (3)$$

t = time

Δt = fractional time

A detailed example to calculate the pressure application point for curing the commercial Code 92 epoxy resin prepreg is provided later. This technique will also be applied to the system MY 720/ABH and the polybismaleimide resin H 795.

3. RESULTS AND DISCUSSION

3.1 DSC behaviour of model epoxy resin-curing agent compositions

The effect of the heating rate on the DSC-trace for the resin Araldit MY 720 cured with MDA, DDS and ABH is provided in Figures 2-4 and in Table 2. It is apparent that the characteristic temperature points (T_{OS} , T_{EXO} , T_{CR}) are shifted to lower temperatures when the heating rate is decreased. The influence of the chemistry (chemical reactivity) of the curing agent on cure behaviour is apparent from Figure 5. Diaminodiphenylsulfon (DDS) is of much lower reactivity than Diaminodiphenylmethane (MDA), therefore the exotherm peak maximum occurs at higher temperatures under the same set of curing conditions (DSC-heating rate). It is well known that basicity of the DDS amino groups is much less than the basicity of the MDA amino groups, which influences the amino-epoxy cure reaction velocity. Both resin systems show a single curing exotherm.

As was to be expected, a quite different DSC-profile is obtained for the cure of Araldit MY 720 with m-Aminobenzoic acid hydrazide (ABH). The curve has a bimodal character e.g. two very good separated peaks are present due to two different chemical reactions with different activation energies. The curing agent ABH has two different chemical functional groups which differ extremely in their chemical reactivity. The comparison with the DSC-profile of the MY 720/MDA system leads to the conclusion that the first maximum is relevant for the epoxy aromatic amine reaction, while the second peak is responsible for the hydrazide-epoxy cure. It is of interest to note that all three epoxy-MDA resins provide DSC-profiles (heating rate 15°C/min) with a single maximum at temperatures around 166 to 186°C (Table 2) as can be seen in Fig. 6. It has to be noted at this point that the characteristic temperatures of the DSC-profile can change slightly with variations in the ratios of the reactants.

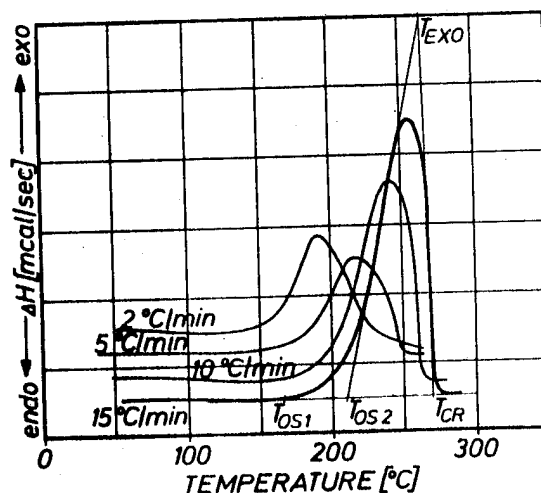


Fig. 2 DSC-thermogramme for MY 720/DDS resin

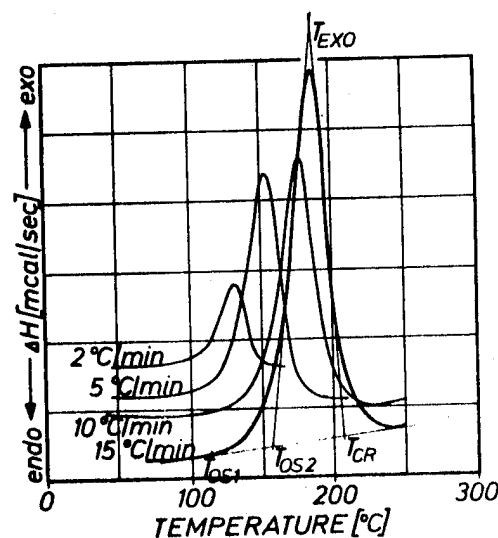


Fig. 3 DSC-thermogramme for MY 720/MDA resin

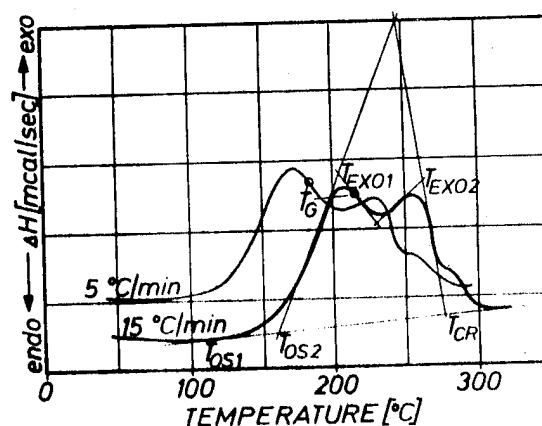


Fig. 4 DSC-thermogramme for MY 720/MDA resin

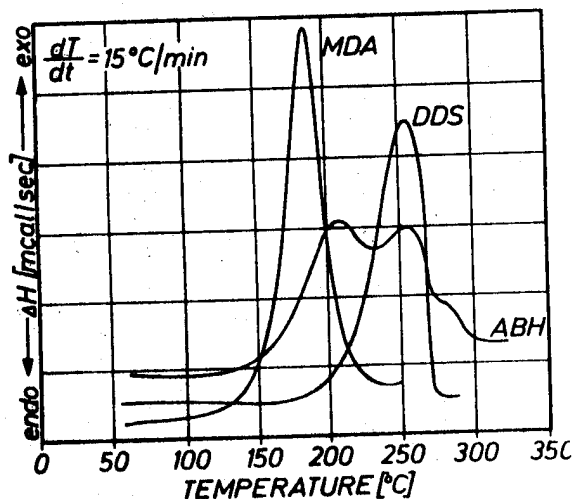


Fig. 5 DSC-traces of MY 720 resin with various curing agents

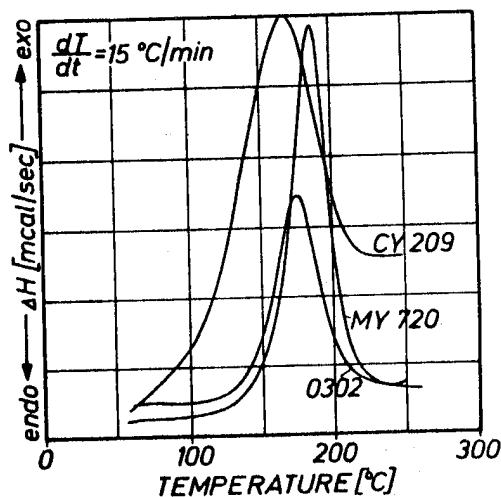


Fig. 6 DSC-traces of epoxy resins cured with methylenedianiline (MDA)

Resin	ϕ (°C/min)	Temperature (°C)				
		T_{OS-1}	T_{OS-2}	T_{EXO-1}	T_{EXO-2}	T_{CR}
CY 209 MDA	2	60	80	115		139
	5	75	100	138		173
	10	80	105	158		194
	15	86	113	166		207
CY 209 ABH	1.92	65	83	137		205
	5.0	85	100	167		223
	10.0	100	112	187		240
	15.3	110	137	202		249
MY 720 MDA	1.91	75	108	132		146
	5.0	95	127	155		174
	10.90	105	150	178		198
	15.3	115	156	186		207
MY 720 DDS	1.90	115	158	192		232
	4.93	137	178	227		250
	10.0	155	200	253		261
	15.3	170	211	264		270
MY 720 ABH	1.94	105	111	151	219	247
	4.94	110	123	170	235	251
	10.6	123	143	190	250	266
	15.2	135	160	205	262	277
O302 MDA	1.90	70	100	124		149
	4.90	85	112	143		170
	10.10	105	132	166		193
	15.4	110	142	175		205
O302 DDS	1.92	116	146	178		213
	4.90	125	161	200		237
	10.10	150	178	217		256
	15.2	170	187	229		268
H 795	2.04	130	165	212		252
	5.32	145	182	230		270
	13.2	160	199	245		282
	16.18	170	207	255		288

ϕ = heating rate

Table 2 DSC data for Araldit CY 209 & MY 720 resins, EPN O302 resins and Polyimide resin Code H 795

The cure of polybismaleimide resins has been extensively investigated in our laboratory (Ref.7) and also by others (Ref.8). Typical DSC-profiles of the new resin formulation H 795 for two heating rates are provided in Figure 1 (DSC-data points see Table 2). As compared with epoxies, the shape of the curve is somewhat different, e.g. polymerization proceeds within a broader temperature range terminating at higher temperatures. Higher T_{CR} values indicate that higher cure temperatures are necessary to obtain a complete setting.

3.2 Heat of polymerization

The area under the DSC curve is a measure for the heat of polymerization (ΔH_{pol}). For all systems of this investigation, the heat of polymerization has been determined. All samples were scanned immediately after preparation to prevent prepolymerization. The values obtained are provided in Table 3. Apparently, the highest values were obtained for the polyfunctional epoxy system MY 720 cured with DDS and ABH (~ 600 J/g) and the lowest for the bisphenol A-type resin cured with MDA. Attention should be paid to the initial oxirane concentration of the epoxy curing agent mixture in comparison with the heat evolved during cure. The oxirane concentration in all systems is in nearly the same range ($5-6 \cdot 10^{-3}$ mols/g EP resin) but the polymerization energies vary significantly. It can be concluded that the polyfunctional epoxy provides the highest crosslink density after complete cure and therefore offers outstanding high temperature properties.

The H value for the H 795 polyimide resin cannot be compared with the epoxy resins because a different curing reaction mechanism is involved (polymerization of terminating maleimide end groups).

Resin	C A	E P C	ΔH_p
CY 209	MDA	$4.93 \cdot 10^{-3}$	219 - 246
CY 209	ABH	$5.26 \cdot 10^{-3}$	257 - 275
MY 720	MDA	$5.80 \cdot 10^{-3}$	446 - 449
MY 720	DDS	$5.44 \cdot 10^{-3}$	592 - 642
MY 720	ABH	$6.19 \cdot 10^{-3}$	602 - 629
O302	MDA	$5.12 \cdot 10^{-3}$	386 - 396
O302	DDS	$4.75 \cdot 10^{-3}$	319 - 350
Code 92	composition unknown		380 - 430
H 795			212 - 240

CA = Curing agent
 EPC = Epoxy concentration (Mol. oxirane/g resin)
 ΔH_p = Polymerization energy J/g

Table 3. Heat of polymerization of EP-resin-curing agent combinations.

3.3 Ageing of EP resin prepregs

Differential scanning calorimetry is applicable to characterize the state of advancement of the prepreg material. For this part of our work we used the MY 720/ABH resin formulation because of the known composition. Prepregs were prepared by a filament winding process and the resin was applied onto the fibres by impregnation bath techniques from a 65% by weight solution in methyl-ethyl-ketone. The dried prepreg contained around 2% of residual solvent and all other properties met the German Luftfahrt Specification LN 29971 for uni-directional graphite prepregs. Samples of the prepreg and the neat resin (same batch as used for the prepreg fabrication) were aged in those Al-pans which were used for DSC measurements. The residual heat of polymerization obtained for the aged samples are provided in Table 4 and plotted in Fig. 7 as a function of ageing time and temperature. Both the neat resin and the prepreg are almost stable at -18° for around 156 days (about 5 months) e.g. only a 10% loss in polymerization energy occurs. The ageing temperature of 20°C (room temperature) is not usual for storing prepregs but was used in this programme to demonstrate the drastic decrease of the polymerization energy under this ageing condition, which is accompanied by a rapid loss of handling properties like tackiness and drapability. The DSC thermogrammes of the aged neat resin and prepreg samples again showed the difference in the chemical reactivity of an aromatic amino group and the hydrazide group of the m-aminobenzoic acid hydrazide curing agent. The cure exotherm responsible for the epoxy amino reaction disappeared (peak maximum at around 190°C) while the second exotherm remained unchanged.

A t	Neat Resin Ageing temperature			Prepreg Ageing temp.	
	20°C	$+4^\circ\text{C}$	-18°C	20°C	-18°C
0	602	602	602	610	610
8				558	
15	502				
26	427				
38	372			414	
54	310				564
67		511			
89				398	
156	300	396	607	348	548
270			474		492

A t = Ageing time (days)

Table 4. Heat of polymerization of aged MY 720/ABH neat resin and prepreg samples.

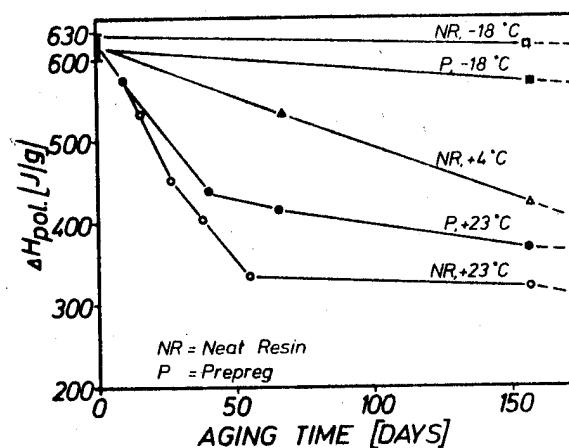


Fig. 7 Ageing of MY 720/ABH resin and prepreg.

3.4 Cure cycle calculation by use of DSC data

Autoclave moulding is the technology widely used for the fabrication of complex components. High quality composites need the timely application of the consolidation pressure well before the resin has gelled. Within this part of our work, it was demonstrated that the pressure application point within a preselected time-temperature profile (which is the temperature profile of the autoclave during cure) can be calculated by following the procedure described previously (Ref.5)

3.4.1 Epoxy resin Code 92 The first step was the determination of the isothermal gel times for the neat resins by use of the experimental procedure described in DIN 16945. These isothermal gel times for resin Code 92, MY 720/ABH and the PI-resin H 795 at various temperatures are provided in Table 5.

T (°C)	Gel-times (mins)		
	Code 92	My 720/ABH	H 795
80	60 - 64	-	-
100	15	-	-
120	4	80	-
140	-	32	-
160	-	12	60
170	-	-	30
180	-	-	15

T = temperature

Table 5. Isothermal gel times according to DIN 16945

By use of two time-temperature pairs for isothermal gel the isothermal gel equation was calculated (e.g. the constants A and c of equation (2) for the Code 92 resin were calculated).

Isothermal gel equation for Code 92 resin

$$t_{\text{(mins)}} = 1.0871 \times 10^{-6} \times T^2 \times 10^{4475/T} \quad (4)$$

The next step was the determination of the kinematic gel equation. To perform this, the kinematic gel-temperature for the heating rate of 2°C/min was determined (for Code 92 resin, the value of 110°C was obtained) followed by the calculation of the constant B of equation (1).

Kinematic gel equation for Code 92 resin

$$\log \phi = \frac{-4475}{T_{\text{gel}}} + 11.98384 \quad (5)$$

Having derived the isothermal gel equation, the gel point for any given time-temperature profile can be calculated. The calculation of the point at which gel occurs for a typical cure cycle (Fig.8 - this cure cycle was provided by the component fabricator Dornier-System Friedrichshafen) for prepreps of the resin Code 92 taken step by step is:

- 1). Heat up to 75°C, heating rate 2°C/min

$$\sum_{293}^{348} \frac{10^{4474.89/T}}{1.0871 \times 10^{-6} \times T^2} = 0.061$$

2. Hold 20 minutes at 75°C

$$\frac{20}{t_{\text{gel}}} = \frac{20}{95.23} = 0.210$$

3. Heat up to 120°C, heating rate 2°C/min

$$\sum_{348}^{T_{\text{gel}}} \frac{10^{4474.89/T}}{1.0871 \times 10^{-6} \times T^2} = \frac{0.729}{1.000}$$

The event of gel takes place during step 3). The summation of step 3) is obtained by

$1 - (0.061 + 0.210) = 0.729$ so that the calculation of T_{gel} is possible. T_{gel} was found to be 107°C. This is the temperature where pressure has to be applied. The results of the calculations are in very good agreement with the actually used curing cycle. (Pressure application at 110°C).

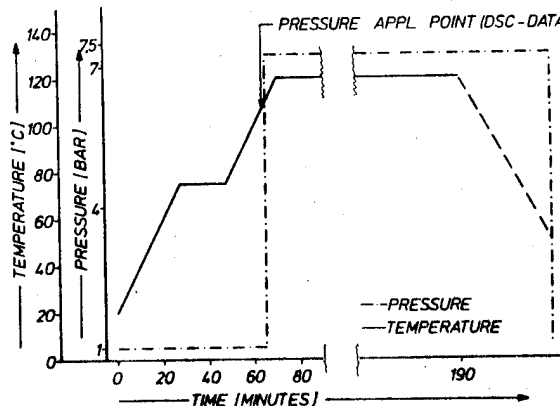


Fig.8 Autoclave cure cycle of Code 92 prepreps

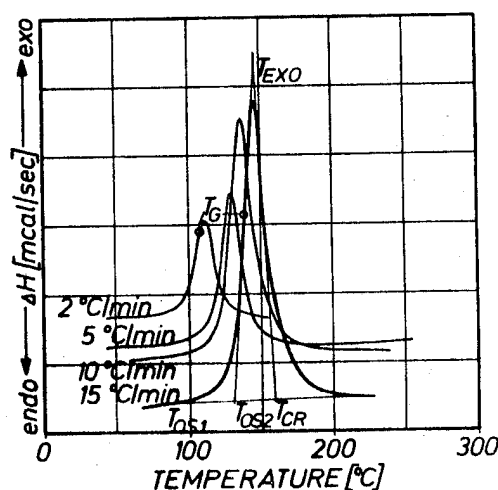


Fig.9 DSC-traces of Code 92 prepreps

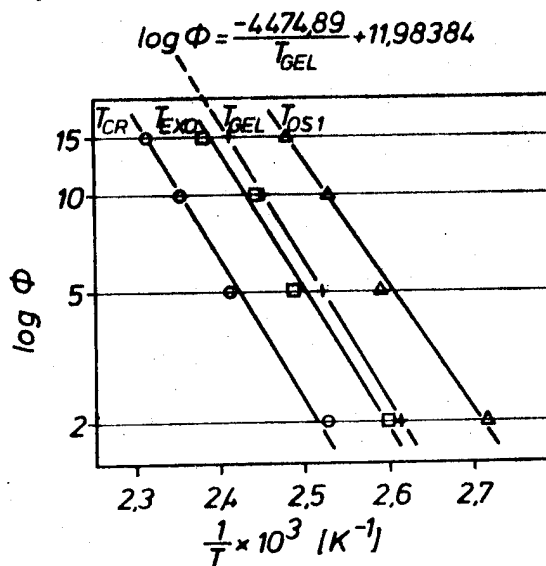


Fig.10 DSC-data plots for Code 92 prepreps

3.4.2 Resin MY 720/ABH The isothermal and kinematic gel equation for this system has been determined in the same way as described before for Code 92 prepreg. The kinematic gel temperature for a heating rate of 2°C was found to be 162.5°C .

Isothermal gel equation for MY 720/ABH

$$t(\text{mins}) = 4.04168 \times 10^{-13} \times T^2 \times 10^{3579.34297/T} \quad (6)$$

Kinematic gel equation for MY 720/ABH

$$\log \phi = \frac{-3579.34297}{T_{\text{gel}}} + 8.51551 \quad (7)$$

For the time-temperature profile in Figure 12, the gel point was calculated as follows:

Fraction of gel

- 1) Heat up to 140°C in 40 mins

$$\sum_{293}^{413} \frac{10^{-3579.34297/T}}{4.04168 \times 10^{-3} \times T^2} = 0.23149$$

- 2) Gelation occurs during the isothermal hold at 170°C

$$\frac{x}{t_{\text{gel}}} = \frac{x}{32} = \frac{0.76851}{1.00000}$$

This means that gel occurs after 64.59 minutes after the start of the cure cycle. The actual pressure application during composite moulding is performed well before gelation takes place.

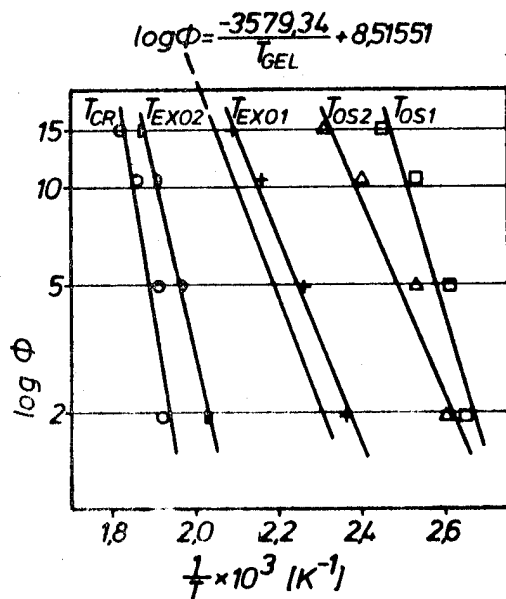


Fig. 11 DSC-data plots for MY 720/ABH resin

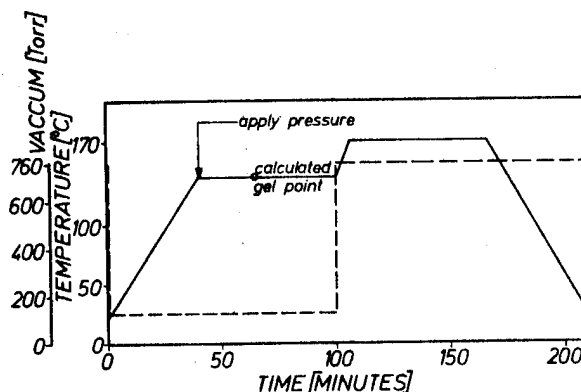


Fig.12 Autoclave cure cycle for MY 720/ABH resin

3.4.3 PI-Resin Code H 795 The typical autoclave cycle for this thermosetting PI-resin is provided in Figure 13. The application of the moulding pressure is performed 60 minutes after starting the cycle.

The isothermal and kinematic equations were calculated by using the isothermal gel times of Table 5. For a heating rate of $2^{\circ}\text{C}/\text{min}$, the gel temperature was found to be 202°C .

Isothermal gel equation for resin H 795

$$t(\text{mins}) = 1.97569 \times 10^{-18} \times T^2 \times 10^{6152.69519/T} \quad (8)$$

Kinematic gel equation for resin H 795

$$\log \phi = \frac{-6152.69519}{T_{\text{gel}}} + 13.25407 \quad (9)$$

The event of gel during the cure cycle given in Figure 12 was calculated as follows:

Fraction of gel

- 1) Heat up to 170°C in 50 mins ($\phi = 3^{\circ}\text{C}/\text{min}$)

$$\sum_{293}^{443} \frac{10^{-6152.69519/T}}{1.97569 \times 10^{-18} \times T^2} = 0.34863$$

- 2) Hold at 170°C for one hour. (During this step gelling occurs)

$$\frac{x}{t_{\text{gel}}} = \frac{x}{10.0} = \frac{0.65137}{1.00000}$$

$x = 19.55$ mins (e.g. gelation occurs after 19.55 mins at 170°C).

Within this cure cycle, pressure has to be applied well below the gel point. In fact, the pressure is applied after 60-65 mins from the start of the cycle. This cycle was used to mould graphite fibre laminates which provided the properties given in Table 6.

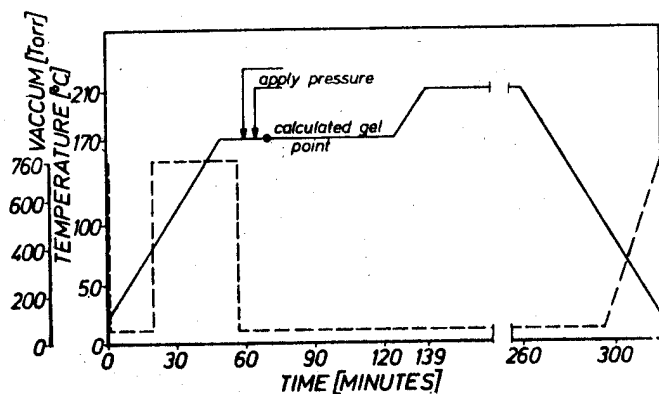


Fig. 13 Autoclave cure cycle for H 795 prepreps

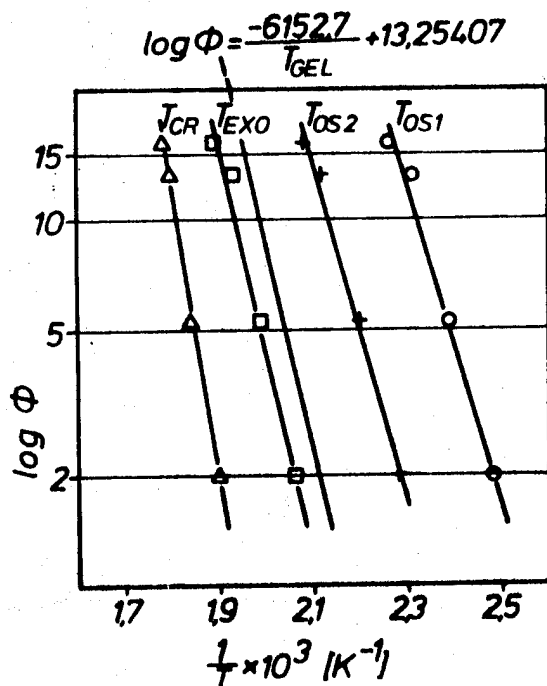


Fig. 14 DSC-data plots for H 795 resin

Property	Unit	-55°C	Value 25°C	250°C
Fibre content	Vol. %		59 ⁺¹	
σ_{BO}	N/mm ²	1439	1646	1378
E_{BO}	KN/mm ²	119.5	121.3	84.4
σ_{B90}	N/mm ²	64	81	31
E_{B90}	KN/mm ²	9.24	8.71	7.60
ILSS (1a)	N/mm ²	86	81	49
ILSS (1b)	N/mm ²	37	48	44

 σ_B = flexural strength E_B = flexural modulus

a = (0°)

b = (0° ± 45°)s

l = span to depth ration 5 : 1

Table 6. Properties of H 795 - T 300-3000 laminates (LN 29971)

The examples given show how DSC can be applied to quantitatively define cure cycles for autoclave moulding. If the gel equations are known for a resin system, the gel points for every time-temperature cure profile can be calculated indicating the latest point for the application of the moulding pressure to get adequate flow. The techniques described can of course also be applied to other characteristic temperatures of the DSC profile e.g. for the temperature of the reaction termination (T_{CR}) which then allows the calculation of cure times for isothermal conditions.

3.5 Coefficients of thermal expansion

Within a recent programme sponsored by ESTEC (Ref.9) coefficients of thermal expansion (CTE) of the constituents of graphite laminates, e.g. neat resins and unidirectional layers, became of interest to calculate in-built stresses that occur during manufacture of carbon fibre composites. It is well stated in the literature that the resin type (Ref.10) and the fibre content of the composite (Ref.11) influence the CTE's in both the fibre direction and perpendicular to the fibre direction of a unidirectional layer.

For this programme, it was of interest to know whether postcure does or does not influence the CTE's of the neat resin. Vice versa, information about postcuring requirements could be obtained from CTE determinations.

3.5.1 Resin Code 92 Neat resin samples were cured according to the recommendation for Code 92 prepreps for 4 hours at 50°C then for 2 hours at 125°C (cure cycle 1). Other samples were held for 4 hours at 120°C (cycle 2) and others were cured at a temperature of 140°C for 4 hours, and CTE's measured in the temperature range of -80°C to +90°C.

Temp. °C	Expansion coefficient $\alpha \times 10^6$		
	Cure cycle 1	Cure cycle 2	Cure cycle 3
+90	-	-	102.4
+80	-	96.5	-
+70	103.6	90.5	85.7
+50	85.7	82.2	78.6
+30	75.0	76.2	70.3
+10	73.8	71.5	66.7
-10	66.7	65.5	59.5
-30	59.5	58.4	52.4
-50	54.8	52.4	46.4
-70	42.9	41.7	42.9

Cure cycle 1 : 4 h 50°C + 2 h 125°C
 Cure cycle 2 : 6 h 60°C + 4 h 120°C
 Cure cycle 3 : 6 h 60°C + 4 h 140°C

Table 7. Coefficients of thermal expansion for Resin Code 92

The recommended cure cycle 1 provided a CTE profile which indicated a glass transition temperature of approximately 60°C. The absolute values for the expansion coefficient are high as compared with other EP-resins (MY 720/ABH, $25 = 48 \cdot 10^{-3}/^\circ\text{C}$).

The comparison with the cure cycle 2 shows an overall decrease of the CTE values mainly in the high temperature region between +30 to +90°C. Further increase of the cure temperature to 140°C for an additional 4 hours again gave a lowering of all CTE's but the knee point which indicates the glass

transition temperature is again present but shifted to a higher temperature (80°C).

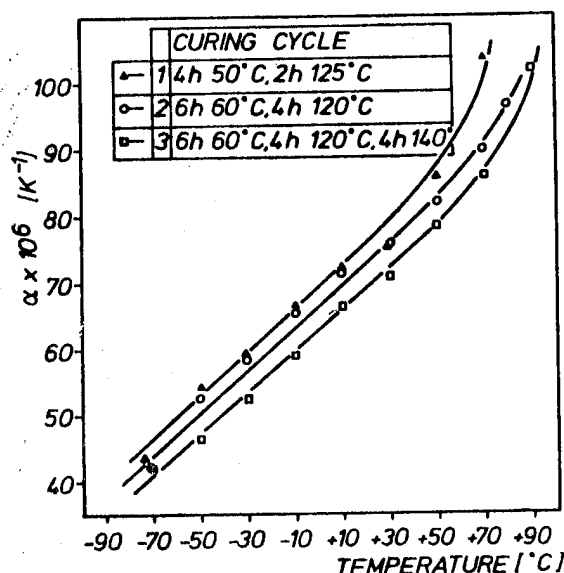


Fig.15 Expansion characteristics of EP-resin Code 92

3.5.2 Resin CY 209/MDA (HT 972) The CY 209/HT 972 system cured at 125°C for 2 hours provided a CTE-temperature profile which is nearly linear up to 40°C (Figure 16, Table 8). At higher temperatures a drastic increase of α (CTE) is apparent.

Temp. °C	Expansion coefficient $\alpha \times 10^6$		
	Cure cycle 1	Cure cycle 2	Cure cycle 3
+90	97.4	76.2	66.7
+70	76.1	67.9	63.2
+50	66.2	59.5	61.9
+30	56.7	54.8	59.5
+10	55.5	50.0	53.5
-10	50.0	45.3	48.8
-30	47.2	41.7	44.4
-50	42.5	38.1	42.4
-70	37.8	36.9	40.5

Cycle 1 : 4 h 50°C + 2 h 125°C
 Cycle 2 : 20 h 45°C + 7 h 120°C
 Cycle 3 : 20 h 45°C + 7 h 120°C + 4 h 140°C

Table 8. Coefficients of thermal expansion for CY 209/HT 972 resin.

Postcuring for 7 hours at 120°C (cure cycle 2) again provided an overall lowering of the CTE-values; the knee point at around 40-50°C is still present. If this resin is postcured for an additional 4 hours at 140°C (cure cycle 3) a totally expansion-stable material up to 100°C is obtained.

The comparison between the Code 92 formulation and resin CY 209/MDA shows that postcuring at 140°C is more effective for the CY 209 resin providing a material that performs up to 100°C as far as CTE stability is concerned. For Code 92 resin, the T_g is shifted up to 80°C during postcure, but the maximum use temperature should not exceed 80°C. The comparison of these two resin systems with respect to their correlation between postcure conditions and CTE-performance apparently demonstrates the validity of this thermal analytical method.

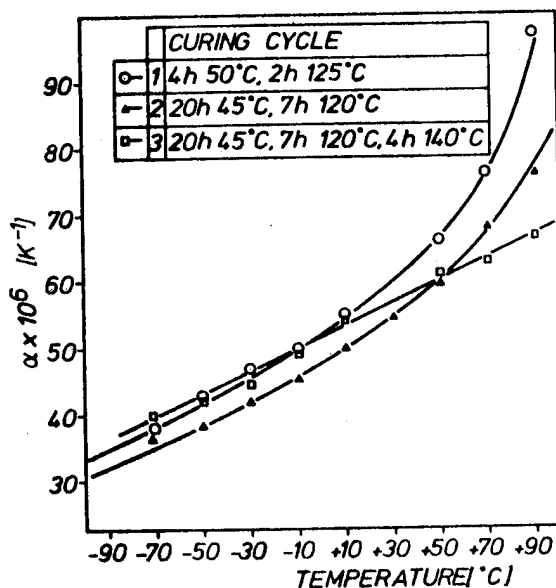


Fig.16 Expansion characteristics of EP-resin CY 209/HT 972.

3.5.3 Unidirectional laminates. The CTE of a unidirectional layer is mainly influenced by the resin matrix, also the temperature dependency is correlatable to the resin property. The CTE values for unidirectional Code 92 resin laminates, which were cured under the conditions of the component fabricator, are presented here in Table 9 and Figure 17.

Laminate FM 1207		Laminate FT 1206	
Temp. °C	$\alpha \times 10^6$	Temp. °C	$\alpha \times 10^6$
-80	29.88	-70	30.25
-60	31.20	-50	32.35
-40	34.95	-30	35.29
-20	36.50	-10	38.24
0	38.20	+10	39.49
+20	38.20	+30	41.17
+40	43.00	+50	47.50
+60	46.53	+50	47.50
+80	46.91	+70	50.42

FM = high modulus fibre laminate
 FT = high strength fibre laminate

Table 9. Expansion coefficients of Code 92-unidirectional laminates.

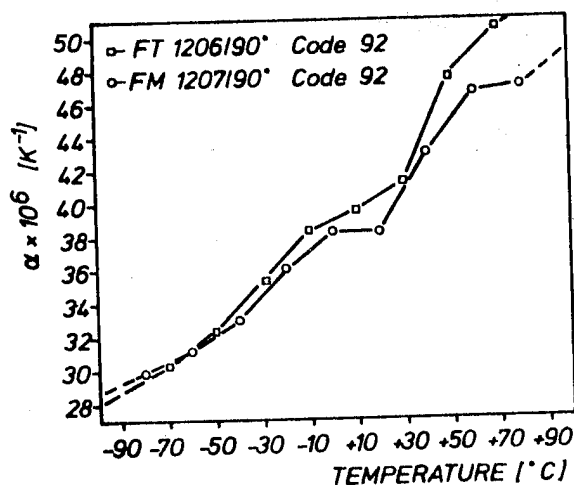


Fig.17 Expansion characteristics of Code 92 UD-laminates

The CTE's in fibre direction were found to be $-1.05 \pm 0.2 \times 10^{-6}$ cm/cm/°C and $-0.41 \pm 0.2 \times 10^{-6}$ cm/cm/°C for high modulus and high strength fibres respectively. Perpendicular to the fibre direction, the expected temperature dependency could be measured.

4. CONCLUSION

Thermal analytical methods like Differential Scanning Calorimetry (DSC) and Thermal Mechanical Analysis (TMA) are methods which can be used either as a tool for research in the early state of development to follow and define the cure behaviour of thermosetting resins and prepregs thereof. DSC is also applicable as a quality assurance control method for resins and prepregs. DSC data are also important from the fabrication point of view because production relevant parameters like gel within a given time-temperature cycle and isothermal cure times can be calculated. TMA (Thermal Mechanical Analysis) gains insight into the post-curing requirements for a resin or a laminate made thereof.

5. ACKNOWLEDGEMENTS

The authors wish to acknowledge support of parts of this work by ESTEC under Contract No.2930/76/NL/PP(SC).

6. REFERENCES

1. May C A, Hadad D, Browning C E, 33rd Annual Tech. Conf., RP/Composite Inst., SPI 15D (1978), Washington D.C.
2. Hadad D, 22nd National SAMPE Symposium and Exposition 22, 301-11 (April 1977) San Diego.
3. Hagnaurer G L and Setton J, J.Liquid Chrom. 1(1) 55-73 (1978).
4. Halpin B M, Sprouse J F and Hagnaurer G L, 33rd Annual Tech.Conf., RP/Composites Inst., SPI 15G (1978), Washington D.C.
5. Carpenter J F, Instrumental Techniques for Developing Epoxy Cure Cycles, 21st National SAMPE Symposium and Exhibition, Los Angeles, CA 1976.
6. Doyle, J.Appl.Polym.Sci. 6 639, 1962.
7. Stenzenberger H D, Appl.Polym.Symp. 22, 77-88 (1973).
8. Barton J M, Knight G J The Thermal Analysis of some addition type polyimides, RAE Technical Report 75082 (1975).
9. Schneermann M W, Stenzenberger H D, Evaluation of in-built stresses during manufacture of elements made of carbon fibre reinforced plastics, Final Report of ESTEC Contract No. 2930/76/NL/PP(SC).
10. Yates B, McCalla B A, Sargent J P, Rogers K F, Phillips L N, Kingston-Lee D M, J.Mater.Sci. 13 (1978) 2217.
11. Yates B, Overy M J, Sargent J P, McCalla B A, Kingston-Lee D M, Phillips L N, Rogers K F, J.Mater.Sci. 12 (1977) 718.

DISCUSSION

G.R. ter Haar (Fokker VFW) :

As a user of materials we are only faced with the results of the work of your laboratory. Is there no possibility of having a feedback, e.g. to improve odour or toxicity, from your laboratory, because I suppose there must be significant knowledge and data available because of your long experience in this field.

W. R. Eckert.

The laboratory is just doing test without knowing details of the samples.

J. Dauphin (ESA) :

There exist some possible methods of improving in the same way that we improve outgassing parameters, but as far as I know nothing has been attempted in this direction. For complete equipment a careful selection of cleaning agents can help.

R.L. Moss (Ford Aerospace) :

All of our spacecraft have used conformal coatings on every printed circuit board, and normally on microcircuits. Are you aware of any ESA or other European spacecraft which have used bare circuit boards or microcircuits, and if so, which ones ?

M.L. Minges (AFML, USA) :

What are your views on the use of conformal coatings on printed wiring boards as contrasted to microcircuits in the USA ?

B. Dunn:

All component-assembled printed-circuit boards used on ESA spacecraft are cleaned, then electrically tested and finally conformally coated. Great care must be taken to ensure that the correct coating material is applied. Many of the clear epoxy resins require curing cycles which may damage components - especially those containing glass-to-metal seals. One transparent polyurethane conformal coating (a Solithane^(R) mixture) has been extensively tested in our laboratory. It is room-temperature curing and meets the ESA outgassing requirements. Also this coating has a low engineering modulus so that it did not promote thermal fatigue of components or solder joints during our thermal cycling tests. To my knowledge hybrid and integrated circuits are always contained within hermetically sealed packages and these microcircuits in Europe are not conformally coated.

D.K. Davies (ERA Technology Ltd.) :

Protection of circuitry by organic layer coating is not universally acceptable owing to microphony problems on high-sensitivity circuits in high-vibration environments. Our investigations have shown that the signals arise from interfacial charge transfer and may be exacerbated by the thermal cycling of the structure.

B. Dunn:

Your comment is probably true for microcircuits. Conformal coatings on printed circuit boards are desirable and they will prevent short circuits by loose pieces of wires, metallic slivers or carton fibres. However, they do not suppress the growth of whiskers which might be growing on tin-plated surfaces.

A.J. Clarke (MSDS) :

Have you attempted to relate maximum heat of polymerisation with minimum outgassing ? If this relation was established then the use of thermal analysis to define cure schedules, presumably could become an ESA requirement. This is not practical at present in the composite fabricating industry.

H. Stenzenberger:

I agree with you on the heat of polymerisation that I did show ; the comparison was made for resins that had nearly the same epoxy content. We chose the exact equivalent proportions between the curing agent and the resin system. The optimisation for a special resin curing agent combination can be made by running different ratios between curing agent and resin, then by looking which concentration gives the maximum heat of polymerisation : this composition will be the best for this combination of resin and curing system. But I am not sure whether or not this composition is good with respect to the outgassing.

A.J. Clarke (MSDS) :

We have found some strange results with resin systems. We have not looked into it thoroughly, but we have found that you do not necessarily have a high-temperature curing to achieve minimum outgassing and I think that it is in contradiction to what one would normally expect.

H. Stenzenberger:

This is the problem that you have when you deal with epoxy resins at high temperatures. High-outgassing rates can also occur because if you get a high-curing temperature you might degrade the epoxy resin, i.e. you might come into the range where you get concurrently to your curing reaction and a degradation of your material and this can in fact produce low molecular species that will give you higher outgassing rates.

D.H. Bowen (Harwell) :

You mentioned that MY 720 cured with ABH is a 'high flow' system. Is this a function of the curing agent and does the fact that the first exotherm occurs before the gel-point make it difficult to control the cure schedule ?

H. Stenzenberger:

a) All model resin formulations presented in the paper based on MY 720 are 'high flow' system. Nevertheless, the curing agent can influence the flow properties e.g. low-melting low-molecular weight resin soluble curing agents will provide better flow than high-melting high-molecular weight curing agents. Therefore ABH contribute positively in comparison with DDS.

b) Our experience with this curing agent does not indicate disadvantages with respect to controlling the cure schedule. The fact that gel occurs after the first curing exotherm indicates that the first reaction is mainly a linear chain growing reaction which occurs in advance to the cross-linking reaction.

D.H. Bowen (Harwell) :

Could you please comment on the relative merits of DSC and dielectrometry as a means of establishing cure schedules ?

H. Stenzenberger:

Dielectrometry is the method of choice to monitor the curing of components while DSC is from my point of view, the method of choice to characterise prepregs and resins. Correlations between DSC and dielectrometry are preferably evaluated during the cure cycle development to define the state of the resin advancement within the dielectrogramme.

J. Dauphin (ESA) :

In your experience with commercial products did you observe a good constance of the quality of prepregs ?

H. Stenzenberger:

The results that were obtained in our laboratory on one commercial prepreg show a very good constance as far as the DSC properties are concerned. The problem with respect to mould prepregs to composites is the residual solvent content which in fact influences the gel behaviour of the prepreg, e.g. the gel point on the DSC trace can shift to higher or lower temperatures. Till now this effect is not fully evaluated.

SESSION II

NEW MATERIALS DEVELOPMENTS

Co-chairmen: J. Berry & D.F. Hall

NEW SPACE MATERIALS DEVELOPMENTS IN THE UNITED STATES

W L Lehn

Air Force Materials Laboratory

Coatings and Thermal Protection Materials Branch, Wright-Patterson Air Force Base, Ohio, USA

ABSTRACT

The development and evaluation of transparent conductive coatings, conductive bulk materials and grounding techniques for application to high resistivity dielectric spacecraft materials to eliminate or control spacecraft charging is discussed. Techniques for the application of thin transparent conductive indium oxide, indium/tin oxide and other metal oxide coatings to Kapton, FEP Teflon, OSR and solar cell coverglasses are presented. The development of conductive bulk glass and stable low outgassing fabric type thermal control coatings as spacecraft charging control materials is presented.

Keywords: Thermal Control, Conductive Anti-static, Transparent Coatings, Spacecraft Charging, Contamination, Adhesive

to 100°K or lower markedly increasing the contamination problems of the optics, baffles and sensors. The passive thermal radiator coatings and materials necessary to maintain these low temperatures are also extremely contamination effect sensitive. Contamination and its deleterious effects has in fact been identified as the operational life limiting factor of many future satellites.

Spacecraft operating at synchronous orbit are subject to spacecraft charging of external surfaces when exposed to magnetic sub-storm electrons. Discharge/breakdown of these high, up to 19,000 volt, surface charges can cause disruption or even catastrophic failure of various electronic systems or subsystems. Damage to the physical and radiative properties of materials and enhanced contamination due to surface charge related attraction of contaminant species may also occur. Conductive spacecraft materials are necessary in order to control or limit these charging effects.

The major goals of current materials development programs are: the development of conductive thermal control materials and approaches to control or eliminate spacecraft charging and the development of low contamination potential spacecraft materials, adhesives, potting compounds, etc., and related technology to maintain the cleanliness of sensitive satellite components.

1. INTRODUCTION

Current spacecraft thermal control materials R&D activities in the U.S. are directed to the development of these materials and associated technology which will meet or solve the leading, pacing, materials requirements and problems of current and future extended life/survivable satellites and space vehicles. The most important materials requirements are: long-term, 7-10 years, stability to the vacuum and ultraviolet and particulate space radiation environment; tailorable thermo-optical properties of solar absorptance and emittance; reduced spacecraft charging effects, particularly for satellites operating at synchronous altitude; and low contamination potential (low outgassing). These requirements are mutually inclusive. As the design goal operational life times of satellites have increased from 3-5 years to the present 7-10 years; the sensitivities, resolution and long-term operational performance of various optical, electro-optical and other sensor systems and subsystems have also increased. For example, the operational temperatures of current and future satellite infrared sensor systems have decreased

2. APPROACH TO THE PROBLEM

Based upon past experience and the high level of risks involved, spacecraft designers are reluctant to apply new materials for critical applications on satellites, particularly if they are required to operate for 10 years. Unless adequate actual space flight performance data on these materials are available the designer will utilize materials with known performance characteristics. This has had the effect that much of the satellite materials research in the last few years is based upon modifications of known state-of-the-art materials, which would be expected to have a minor negative influence on the overall materials performance if the expected

gain were not realized. This observation is apparent in the work that follows. The majority of the work presented below is based upon exploratory development efforts performed under U.S. Air Force sponsorship as part of the conductive spacecraft materials development program (Ref. 1).

3. MATERIALS DEVELOPMENT EFFORTS

3.1 Development of transparent conductive coatings

Conductive transparent coatings from semiconductor-metal oxides represent one route to controlling electrostatic charge buildup on dielectric thermal control materials while having a minimal effect on the thermo-optical properties of solar absorptance and emittance (Ref. 2). Thin films of indium and indium/tin oxide have been most commonly used. The conductivity of these coatings is critically dependent upon the proper oxygen-metal stoichiometry and the properties are strongly dependent on the condition of the substrate and deposition process.

Thin films of 90% indium oxide/10% tin oxide (ITO) and indium oxide (IO) have been deposited on 3 mil Kapton, 5 mil FEP Teflon and OSR and coverglass tiles of fused silica and borosilicate using Magnetron, DC and RF sputtering and resistive heating vapor deposition techniques. Deposition has been demonstrated both reactively by Magnetron and DC sputtering and by resistive heating from In/Sn and In targets in a controlled oxygen and argon atmosphere and non-reactively from metal oxide targets.

Visible absorptance and infrared emittance measurements of ITO reactively sputtered onto FEP Teflon, as conductive coatings in thicknesses up to 900Å⁰, show a definite thickness dependence. Emittance, solar absorptance and transmittance in the visible region are shown in Figure 1 as a function of the coating thickness.

Indium oxide and aluminum oxide coatings have been deposited in thicknesses down to 100Å⁰ by resistive heating vapor deposition onto FEP Teflon and Kapton films and microsheet tiles. These films were slightly dark due to oxygen deficiencies. After heating in air at about 220°C for a period of 15 minutes, the coatings were highly transparent with sheet resistance in the 10⁸ohm/square range, Table 1. IO coatings can be prepared by reactive Magnetron sputtering in a controlled oxygen and argon environment using RF, or more conveniently DC biasing. Properties of IO coatings deposited using this later technique are summarized in Table 2. Figures 2 and 3 show the transmittance and reflectance of typical 100Å⁰ coatings on microsheet reported in Table 2. Average values of transmittance and reflectance for these coatings weighted over the Johnson curve of solar energy density are 0.87 and 0.12 respectively.

Magnetron sputtering was used to deposit clear ITO on various substrates using the DC bias. Table 3 compares the resistances of ITO and IO coatings as prepared and after two weeks. The apparent greater change in surface resistance of the ITO, compared to IO after two weeks, has been further investigated and both coatings seem to have comparable short term shelf life stability.

In general, Magnetron reactive sputtering from the metal or metal alloy in controlled oxygen-argon atmosphere with DC bias appears to be the preferred method for producing conductive, reproducible transparent coatings of IO and ITO on polymeric dielectric materials. The resulting coatings have low surface resistivities and very little effect on the optical properties. Experience indicates that Magnetron sputtering can be scaled up with little loss in coating characteristics. Therefore, scale up from current 12" to 12" to full, more practical 36" to 48" widths of material should be possible with a minimum effort.

The conductive coatings of IO and ITO applied to Kapton and glass substrates are, in general, quite durable and stable to handling and abrasion. Similar coatings applied to FEP Teflon are relatively soft and must be handled with care to prevent loss by abrasion and handling. Additional optimization is in progress.

IO and ITO conductively coated FEP Teflon and Kapton films have been tested under electron irradiation in a charging control facility. Bulk (I_p) and surface (I_R) conduction currents were recorded for beam potentials between 2 Kev and 20 Kev. Initial maxima and steady state values for IO and ITO coated 3 mil Kapton and 5 mil FEP Teflon are shown in Tables 4 and 5. Surface potential measurements using a Monroe electrostatic voltmeter following irradiation at beam potentials of 10 Kev, 15 Kev and 20 Kev showed surface potentials of less than 5 Volts. Larger samples, 12" X 12", of ITO on FEP Teflon and Kapton have been tested under electron irradiation with average current densities up to 2nA/cm² and electron energies up to 30 Kev. The 100Å⁰ and 200Å⁰ thick coatings, with surface resistances up to 10⁹ohm, demonstrated characteristic charge control properties with no evidence of discharges.

Combined electron and solar UV irradiation for 1000 hours of coated and uncoated FEP Teflon films caused the same relative decrease, 2%, in transmittance indicating that the decrease was due primarily to degradation of the FEP, i.e. the conductive coatings are stable.

3.2 Development of conductive glass

A conductive lithium borosilicate glass, designation GE-ITL, was developed several years ago by General Electric under Air Force sponsorship (Ref. 2). This material is considered a substitute glass for OSR's and

solar cell covers to prevent static charge buildup because of its good transmission and resistance to high energy (beta) radiation. A comparison of the transmittance of the material with fused silica and borosilicate glass is shown in Figure 4. A block of this glass was poured, annealed, cut and polished into 1" square wafers about 0.25 mm (10 mil) thick. A silvered OSR prepared from this material had an absorptance of 0.12 and emittance of 0.86 (Fig. 5). Bulk resistance measurements give a value of 10^{11} ohms and eliminate the need for transparent conductive coatings and interconnects or chamfering and conductive fillets in order to effect a durable continuous conductive path from the front surface to ground. Optimization of this material is being pursued. Electron irradiation tests of an OSR array of conductive mirrors of silvered GE-ITL at beam energies of 2 to 20 Kev and 10 nA/cm^2 beam density showed no significant charge buildup.

3.3 Conductive adhesives

Conductive, space qualified adhesives are required to physically and electrically bond OSR's, solar cells and other conductively coated dielectric surfaces to ground to prevent the buildup of static charges. Because of the nature of these materials, they are a leading potential source of spacecraft contaminants. A conductive, low outgassing, graphite loaded adhesive has been developed and evaluated for bonding conductively coated OSR's. The adhesive composition consisted of RTV 566 or 560 silicone filled with 13% by weight of 0.25 mm chopped graphite fibers, Hercules HMS. The RTV 566/HMS fiber formulation produced a resistivity of about $7.5 \times 10^4 \text{ ohm-cm}$. Used in combination with IO or ITO coated OSR's, it has been shown to provide a space stable system which provides a reliable conductive path between the coating and the grounded surface support, Figure 6.

In another study, efforts to lower the outgassing potential of DC 93-500 and RTV 567 by chromatographic separation of the low molecular weight species did not produce materials with significantly improved outgassing properties. Since these materials are already pretreated by the manufacturer for minimum outgassing, further treatment produces marginal reduction in total weight loss. Batch production of many of these materials dictates quality control checks before use in critical applications. Filler studies indicate that the graphite fiber fillers produce increased conductivity in silicones at lower loadings than silver powders or silver coated glass spheres.

Recent studies at ONERA/CERT under an AFOSR (Ref. 2) grant have explored the feasibility of a conductive adhesive technique for the electrical interconnection of transparent ITO coated materials. Good electrostatic performance and the durability of the components combining ITO coated metallized Kapton and aluminum foil ground straps by means of a silver (CHO-bond 1029B) loaded silicone (RTV

566A plus RTV 566B catalyst) have been achieved. A heated tool was designed and developed and is used to cure the electrical joint, Figure 7. A prequalification test program has confirmed the stability of the interconnects formed and the potential application of this technique to operational satellites.

A program to develop low outgassing/low contamination potential potting compounds for spacecraft electrical applications will be initiated shortly.

3.4 Fabric spacecraft charging control materials

High purity silica fabrics have been proposed for application as stable, low outgassing thermal control coatings to control the effects of electrostatic charging of satellites at synchronous altitudes (Ref. 4). These materials have exhibited very quiet behavior, non-arcing, under electron beam bombardment at energies to at least 30 Kev. Secondary emission conductivity has been proposed to explain this excellent behavior. Secondary electrons produced by the primary electron beam are thought to be a cloud of free charges in the voids between the silica, Figure 8, which can migrate and conduct the charge through the fabric to the conductive back surface or edge attachment. Secondary emission is enhanced due to the extremely high surface area encountered by the incident electrons and the enhanced efficiencies of secondary production as the higher energy electrons are decelerated due to the many collisions to energies more favorable for efficient secondary production. Electron bombardment induced surface conductivity probably also contributes to the discharging process. Applicability of this material is limited to operational type satellites since surface potential studies indicate surface potential of greater than 100 volts, which could not be tolerated on many scientific satellites.

While the fabric may be directly bonded to the spacecraft, the adhesive used could migrate to the fabric surface and lead to unstable optical properties under space radiation or serve as a source of contaminants. A composite structure obtained by laminating, at 280°C , the fabric to an impervious aluminum foil backing with a thin film of FEP as an adhesive has been developed. The subsequent composite is then bonded to the satellite surface. A conductive adhesive must be used to electrically bond the metallic layer of the composite to the satellite surface. Lamination of the fabric to the aluminum causes some fabric aluminum contact due to the thin interlayer and allows charge to be carried to the aluminum foil.

Evaluation of the spacecraft charging characteristics of the fabric type coatings is being actively pursued at ONERA/CERT as part of the program under the AFOSR grant.

The secondary emission conductivity proposed to explain the excellent antistatic behavior of the fabric type thermal control coating is in accord with the conclusion and recommendation of a recently completed review, *Spacecraft Charging Studies in Europe* (Ref. 5). The report specifically recommends that the role of secondary emission in controlling the potential of electron irradiated surfaces be investigated and that the development of space stable materials with a secondary yield greater than unity for incident multi Kev-electrons would be particularly important. Variations of the fabric approach may play a key role in the development of such improved materials.

3.5 Paint type thermal control coatings

Research toward the development of paint type thermal control materials has been rather limited in recent years with two exceptions. Both of these efforts were NASA related programs.

A silicate-bonded zinc orthotitanate (ZOT) thermal control coating for space applications has been developed under NASA sponsorship by IITRI (Ref. 7). The material is reported to be superior to the zinc oxide pigmented S-13G/LO silicone and Z93 silicate based materials. The material is readily applied by spraying and cures at room temperature. Solar absorptance to emittance ratios as low as 0.12 can be achieved and the change in solar absorptance after 1000 ESH of UV exposure, is less than 0.01. The material has been proposed for use on a number of satellites, but as mentioned above, actual in-orbit performance data is limited.

A series of electrically conductive paint type thermal control coatings have been developed for use on the International Sun Earth Explorer (ISEE) spacecraft by workers at NASA/Goddard Space Flight Center, Table 6. Required stability in space called for bulk resistivity less than $1 \times 10^5 \text{ ohm-cm}^2$, absorptance less than 0.67 and normal emittance of 0.90 after exposure to approximately 4×10^{16} proton/cm² of solar wind particles and 5300 ESH. These coatings are formulated with mixed alkali silicate binders and doped, conductive zinc oxide pigments (Ref. 8). Formulations of these materials were qualified in laboratory tests and have been applied and are flying on ISEE spacecraft as well as on SCATHA. Specific performance data have not been published.

Laboratory simulation tests indicate that the non-conductive paint type coatings do develop surface charges when applied over conductive substrates, but are "leaky" and do not discharge by arcing. As expected, the conductive materials do not charge.

3.6 Materials space flight experiments

Actual in-orbit materials operational performance data is essential to the accep-

tance and application of new materials for critical spacecraft applications and as guidelines for the development of new and improved materials. Of particular concern to the materials developer is the very limited materials performance data in the geosynchronous spacecraft charging environment. The ML12 thermal control/contamination experiment was designed to correlate the degradation of thermal control materials and contamination rates of the spacecraft surfaces in this environment (Ref. 9). Preliminary flight results from this experiment, launched on the Air Force P78-2, SCATHA (Spacecraft Charging at High Altitudes) satellite will be covered in another paper.

The SCl Charging Electrical Effects Analyzer and Satellite Surface Potential Monitor experiment also launched on the SCATHA satellite, is designed in part to measure the electrical potential buildup on spacecraft materials such as Kapton, FEP, fabric coatings and OSR's. The experiment is reported to be operating satisfactorily but no details are available at this time.

An extensive matrix of thermal control materials and polymeric films will be flown as part of the DOD/LDEF Satellite Materials Experiment, S80-1, to provide low altitude in orbit materials performance data.

4. SUMMARY

Investigation on the development and optimization of new and improved spacecraft materials to control and eliminate spacecraft charging and the development of low contamination potential materials is continuing. Approaches for the development of new materials have been mentioned. Data from actual in-orbit operational performance of spacecraft materials will be useful in the correlation of laboratory and space data and provide guidelines for the development of new materials.

5. REFERENCES

1. Lehn W L 1977, Conductive spacecraft materials development program, Proceedings of the Spacecraft Charging Technology Conference, AFGL-TR-0051, NASA TMX-73537, pp. 559-567, National Technical Information Service, Springfield VA.
2. Benaissa B, Levy L, Paillous A, & Sarraill D, Satellite spacecraft charging materials, in press.
3. Schmidt R E & Eagles A E 1979, Spacecraft Charging Technology - 1978, pp. 524-555, AFGL-TR-0082, NASA Conference Publication 2071, Scientific and Technical Information Office, NASA.
4. Eagles A E et al May 1975, Fabric Coatings: A New Technique for Spacecraft Passive Temperature Control, AIAA paper #75-668, AOAA 10th Thermophysics Conference, Denver CO.

5. Belanger V J & Eagles A E 1977, Proceedings of the Spacecraft Charging Technology Conference, AFGL-TR-77-0051, NASA TMX-73537, pp. 655-668, National Technical Information Service, Springfield VA.

6. Wren G L, Johnstone A D, & Johnson J F E 1979, Spacecraft Charging Studies in Europe, EAORD-TR-79-4, DDC AD #A069967.

7. Harada Y & Walker D R 1979, Inorganic Zn₂TiO₄ thermal control coatings, Science of Advance Materials and Process Engineering Series, Vol. 24, Book 2, pp. 936-944.

8. Shai M C 1977, Formulation of electrically conductive thermal control coatings, Proceedings of the Spacecraft Charging Technology Conference, AFGL-TR-0051, NASA TMX73537, pp. 613-620, National Technical Information Service, Springfield VA.

9. Hall O F, Borson E N, Winn R A & Lehn W L 1975, Experiment to Measure Enhancement of Spacecraft Contamination by Spacecraft Charging, NASA SP-379, National Technical Information Service, Springfield VA.

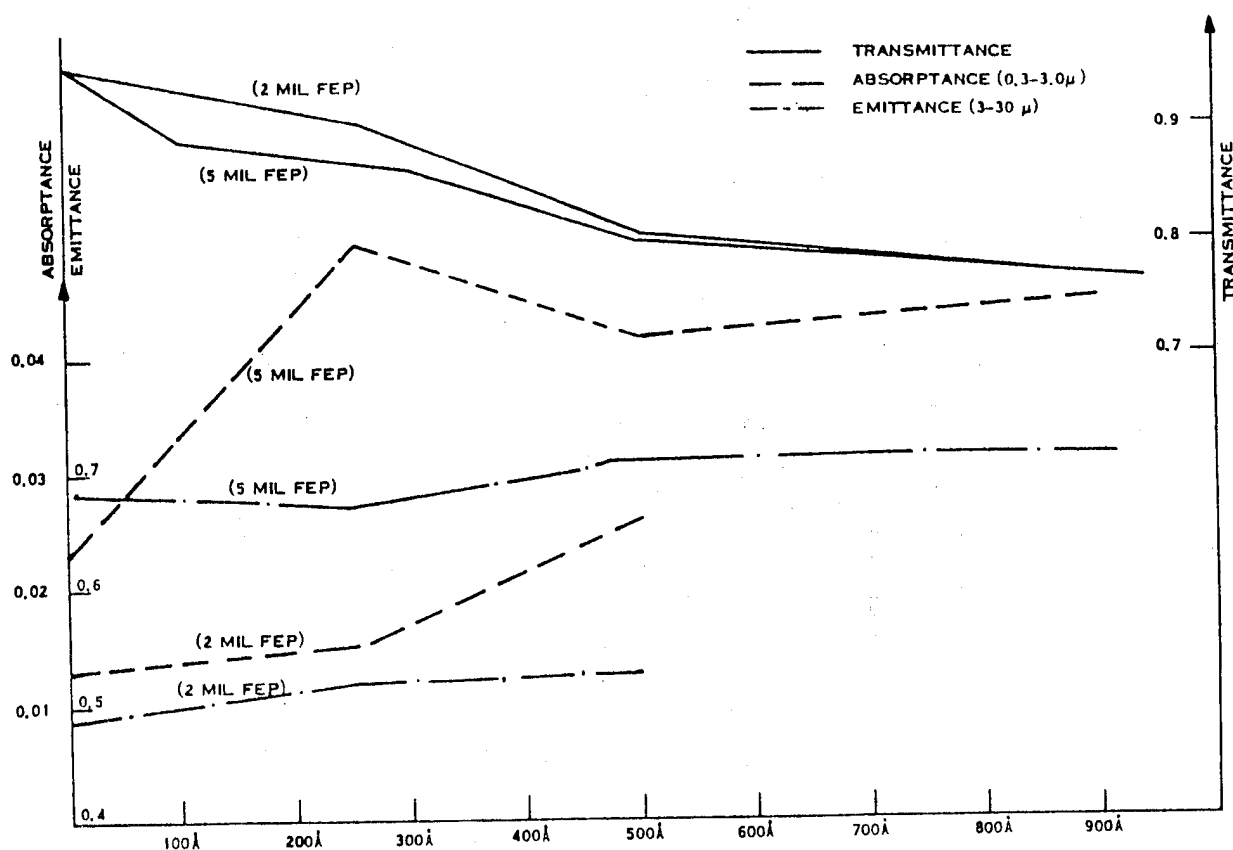


Figure 1. Optical Characterization of ITO Coating Thickness Dependence

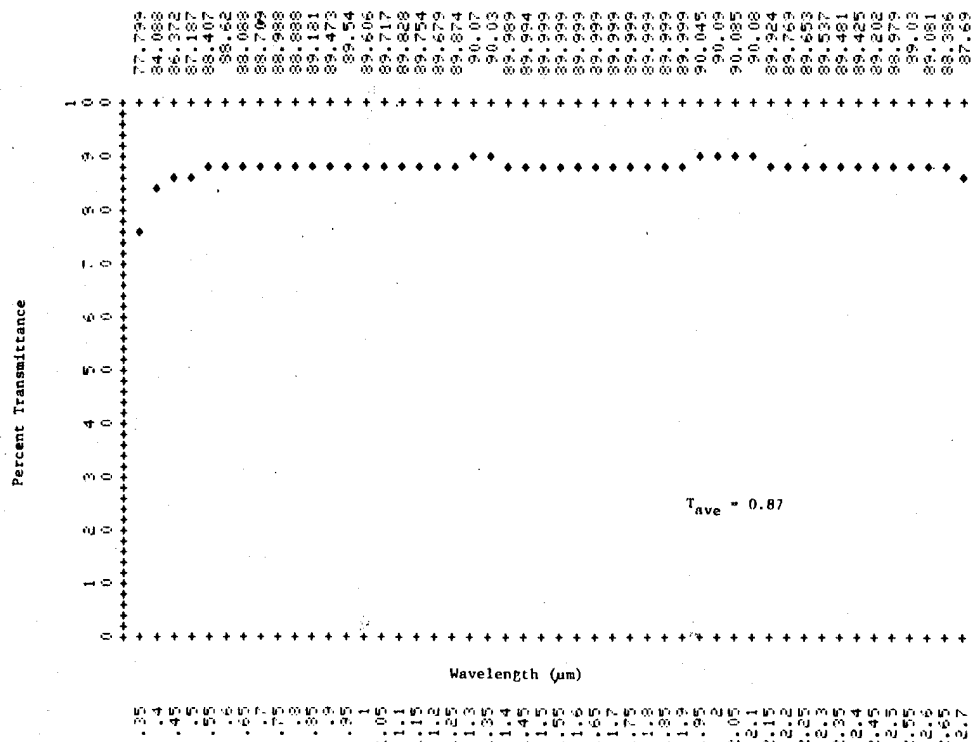


Figure 2. Percent Transmittance of 100A° IO Coated 0211 Microsheet

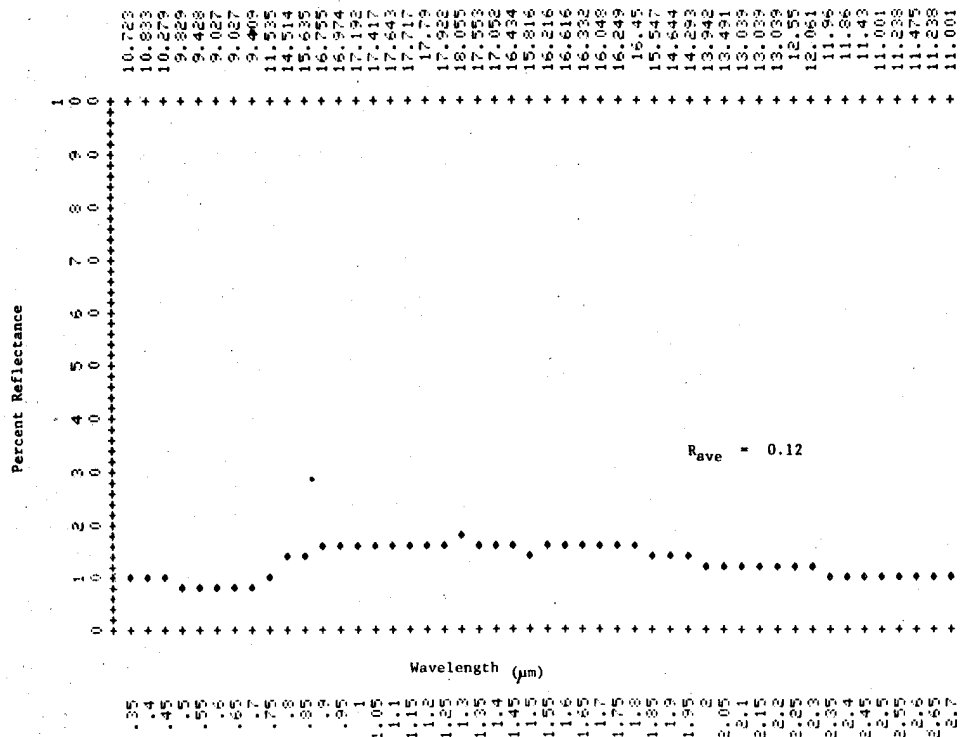


Figure 3. Percent Reflectance of 100A° IO Coated 0211 Microsheet

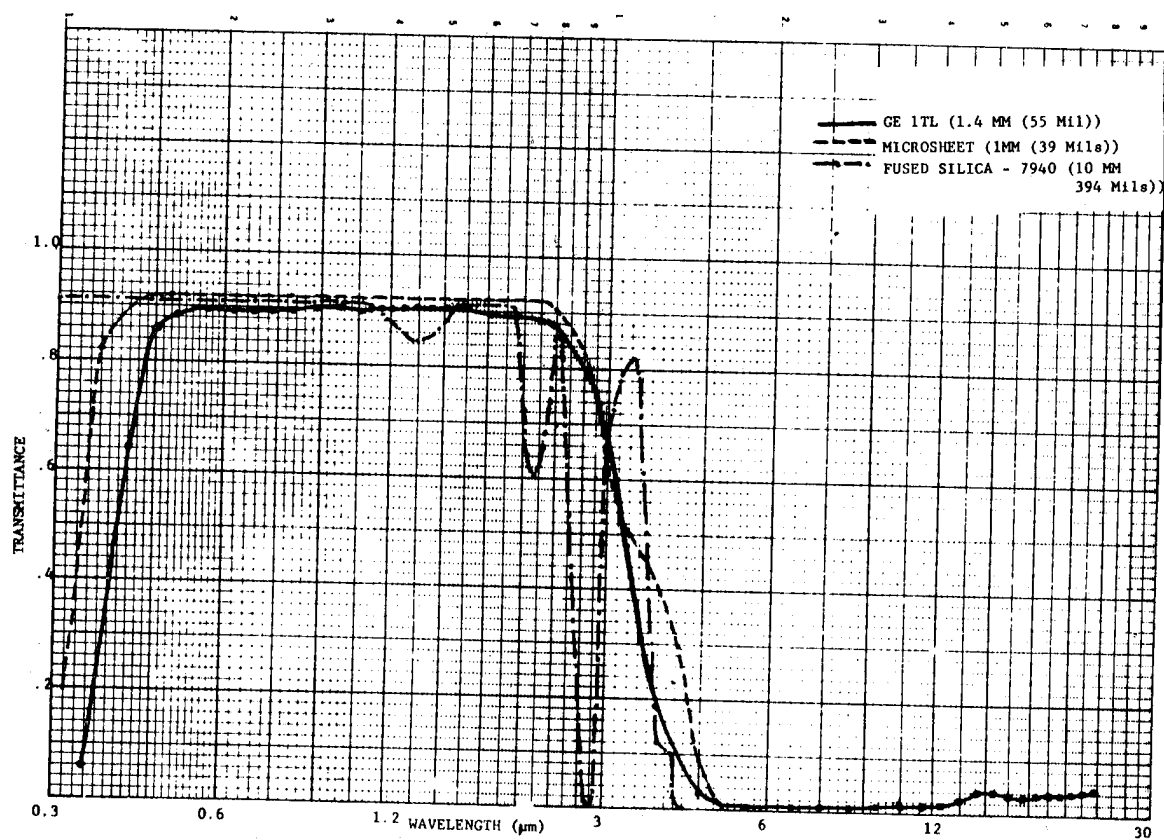


Figure 4. Transmittance of Fused Silica, Borosilicate and GE-1TL Glass

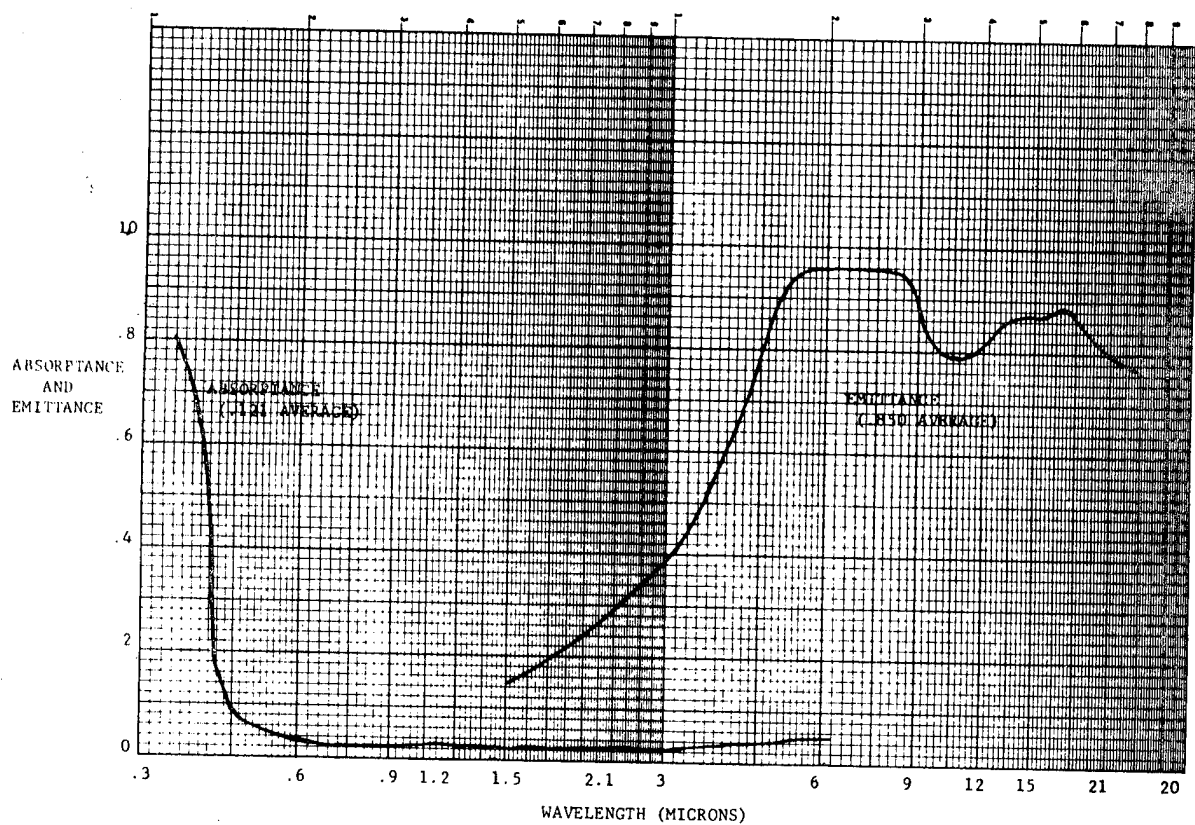


Figure 5. Solar Absorptance and IR Emittance of GE-1TL Glass (10 Mil)

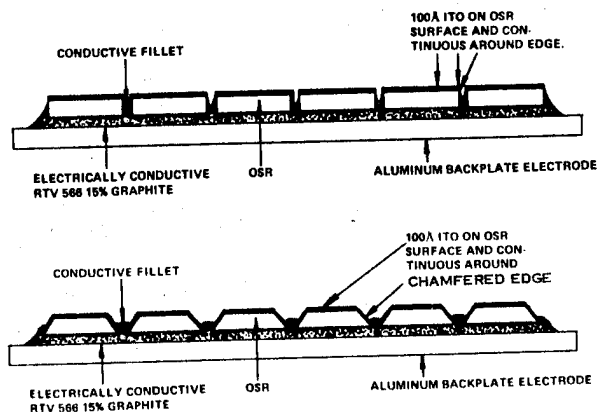


Figure 6. Continuous Antistatic Grounded OSR Configurations

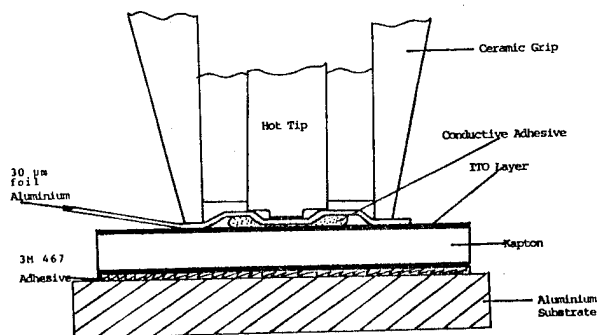


Figure 7. Conductive Adhesive/ITO Heated Tool Bond Formation

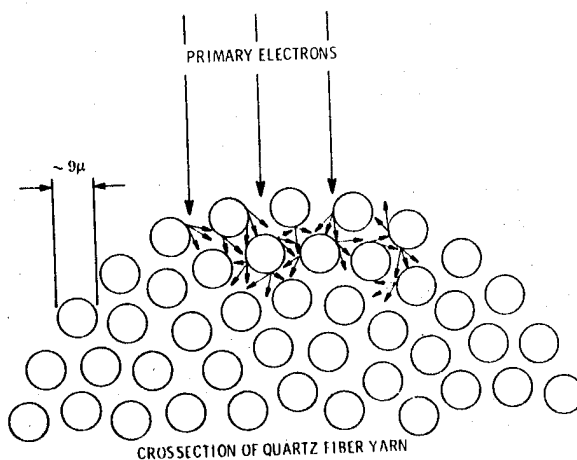


Figure 8. Quartz Fabric Thermal Control Coating Yarn Cross Section

MATERIAL	DEPOSITION RATE	BACKGROUND OXYGEN PRESSURE	TAPE (2) TEST	HEAT AT 425°F/ 15 MIN.	TRANSPARENCY	SURFACE RESISTIVITY (3) $\Omega /$	SUBSTRATE
Al_2O_3	25A/MIN.	5×10^{-5} TORR	P(1)	YES	NO DETECTABLE INCREASE IN TRANSMISSION BEFORE AND AFTER TESTING	5×10^7 TO 5×10^8	KAPTON
In_2O_3	25A/MIN.	1×10^{-4} TORR	P	YES		5×10^7 TO 5×10^8	KAPTON
In_2O_3	25A/MIN.	1×10^{-4} TORR	P	YES		5×10^7 TO 5×10^8	FEP
Al_2O_3	250Å/MIN	5×10^{-5} TORR	P	YES		5×10^7 TO 5×10^8	MICROSHEET
In_2O_3	250Å/MIN	1×10^{-4} TORR	P	YES		5×10^7 TO 5×10^8	MICROSHEET
In_2O_3	250Å/MIN.	1×10^{-4} TORR	P	YES		5×10^7 TO 5×10^8	MICROSHEET

Table 1. Summary of Vacuum Vapor Deposited Transparent Conductive Oxide Films

Run#	Substrate	Thickness	Carrier Gas *		Surface Resistance (Ω)	Transmittance Comments
			Ar	O ₂		
1	Microsheet Kapton FEP Teflon	100Å	31	11	Non. Cond.	Clear
2	Microsheet Kapton FEP Teflon	100Å	32	9	18K 14K 30K	Clear
3	Microsheet Kapton FEP Teflon	"	"	"	10K 10-14K 10-30K	Clear
4	Microsheet Kapton FEP Teflon	300Å	"	"	1K 1K 4-7K	Very Light Tan

* Units of flow rate in cc/min

Table 2. Properties of Indium Oxide Coatings Using Magnetron Sputtering with DC Biasing

Deposition	Thickness Å	Substrate	Resistance (As Deposited) (Ω)	Resistance (2 Weeks Later) (Ω)
I T O	300	Microsheet Kapton FEP	10 - 20K 10K 4K	10 - 20K 700K 200K
I T O	100	Microsheet Kapton FEP	30 - 40K 10K 2 - 5 MEG	5 - 10 MEG 2 - 5 MEG 20 - 50 MEG
I O	300	Microsheet Kapton FEP	1 K 1 K 4 - 7 K	2 K 2 K 16 - 40 K
I O	100	Microsheet Kapton FEP	10 K 10 - 14 K 10 - 30 K	100 K 50 - 100 K 70 - 100 K

Table 3. Indium Tin Oxide (ITO) and Indium Oxide (IO) with DC Biasing

Beam Potential (kV)	IO FEP Teflon (Sample No. 44)					ITO FEP Teflon (Sample No. 37)				
	I_D^c		I_R		I_S	I_D		I_R		I_S
	Max.	S. S. ^b	Max.	S. S.	S. S.	Max.	S. S. ^b	Max.	S. S.	S. S.
2	0.05	0.03	11	11	180	0.8	0.05	99	26	240
6	0.1	0.02	220	150	90	2.2	0.05	270	150	125
10	0.25	0.02	360	200	75	2.6	0.05	280	200	90
15	0.4	0.02	300	200	55	3.5	0.05	450	310	90
20	0.65	0.02	300	200	45	4.5	0.05	470	340	85

^a All currents in units of nanoamperes^b Steady State^c I_D = bulk conduction current I_R = surface conduction current I_S = secondary collector currentTable 4. Summary of Current Measurements of IO and ITO FEP Teflon^a

Beam Potential (kV)	IO-Kapton (Sample No. 40)					ITO-Kapton (Sample No. 36)				
	I_D^b		I_R		I_S	I_D		I_R		I_S
	Max	S. S. ^d	Max	S. S.	S. S. ^c	Max	S. S.	Max	S. S.	S. S.
2	0.2		150	120	280	nm ^d	nm	nm	nm	nm
6	1.4	0.03	540	330	100	21	0.1	630	420	160
10	3.4	nm	570	340	90	4.3	0.05	630	450	nm
15	8.1	0.02	600	360	70	9.9	0.05	750	460	nm
20	12.6	0.02	500	360	60	6.0	0.05	690	570	nm

^a All currents in units of nanoamperes.^c Steady state.

^b I_D = bulk conduction current
 I_R = surface conduction current
 I_S = secondary collector current

^d Not measured.Table 5. Summary of Current Measurements of IO and ITO Kapton^a

	AREA RESISTANCE ρ_d (ohm-m ²)	ABSORPTANCE \bar{a}	EMITTANCE e
NS 43G	1.7×10^3	.38	.90
NS 53B	1×10^3	.52	.87
NS 43E	2×10^3 ohm-m ²	.57	.89
NS 43C	1×10^5 ohm-m ²	.20	.92
NS 55F	6×10^4 ohm-m ²	.57	.91

Table 6. Summary of Environmental Test Data of Electrically Conductive, Thermal Control Coatings

PRECEDING PAGE BLANK NOT FILMED

N80-21425

ADVANCED CARBON FIBRE COMPOSITES FOR SPACECRAFT USE

DH Bowen

Atomic Energy Research Establishment
Materials Development Division, Harwell, Oxfordshire, UK

ABSTRACT

Basic methods for the preparation of carbon fibres are presented and the relationship between fibre properties and structure is described. Carbon fibre composites with carbon, metal and resin matrices are briefly reviewed and examples of applications for resin composites in spacecraft are described. Finally, the possible course of future developments is discussed.

Keywords: Carbon Fibres; Structure; Properties; Carbon, Metal and Resin Matrices; Dimensional Stability; Applications.

1. INTRODUCTION

High performance carbon fibres have been available commercially for about fifteen years. Developed primarily for use in aircraft structures, they are now being employed in a wide range of applications, many of which lie outside the aerospace field. As far as spacecraft structures and components are concerned, the fibres and their associated composites represent a family of materials with almost ideal properties in many respects. The specific strength and stiffness are greater than for most other constructional materials and consequently offer substantial weight savings, and the fibres also possess useful thermal properties that can be exploited to provide lightweight components with good dimensional stability under variations in temperature.

This paper traces briefly the development of carbon fibres and their properties and illustrates some of the advantages of using carbon fibre composites in current and projected types of spacecraft.

2. BACKGROUND TO CARBON FIBRE DEVELOPMENT

The first two elements in each of Groups IIIA and

IVa of the Periodic Table possess high degrees of covalent bonding and low densities and considerable effort has been devoted to finding ways in which the intrinsic strength and elastic properties of such elements, or their compounds, can be used for structural purposes. The development of glass fibre technology in the 1940's and 1950's illustrated some of the advantages to be gained from combining strong fibres with polymers of relatively low strength and stiffness and the last two or three decades have seen the development of other types of fibrous reinforcement, such as boron, carbon, silicon carbide and aluminium oxide, and their use to improve the properties of a variety of weaker materials, notably polymers and aluminium alloys.

Of the inorganic materials available commercially as strong fibres carbon has the lowest density and it also possesses the important technological advantage that it is present as a constituent in most man-made textile fibres. In the late 1950's and early 1960's, several groups of workers, notably in Japan, the USA and the UK, foresaw the possibility of processing a polymeric textile fibre to yield a carbonaceous fibre with a structure approximating to that of single crystal graphite. Most subsequent work has consequently centred upon identifying ways of transforming a textile fibre - an established and relatively low-cost product, into a material possessing greatly superior properties.

3. BASIC PRODUCTION METHODS FOR HIGH MODULUS FIBRES

The graphite crystal structure is shown in Figure 1. To realise in a carbon fibre the high intrinsic strength and stiffness deriving from the C-C bond in the basal plane of this structure (Ref. 1), it is necessary to induce a high degree of preferred orientation of the individual crystallites of which the fibre is composed. Since the strong covalent bonds lie in the basal plane it is evident that the fibre structure must consist of oriented regions in which the basal planes are parallel to the fibre axis. Most precursors when pyrolysed however, give rise to a carbonaceous material with a relatively poor degree of preferred orientation and even graphitisation at temperatures in excess of 2000°C does little to improve the structure.

Two methods are available for producing a high

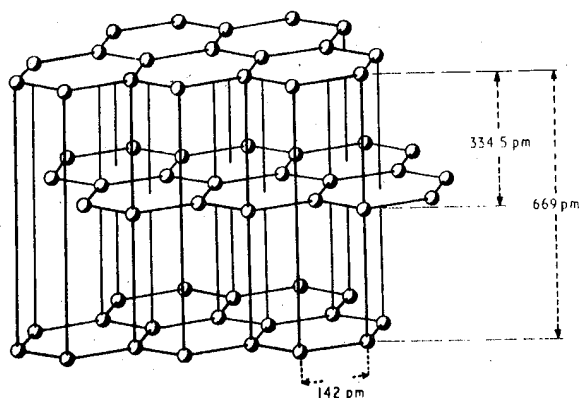


Figure 1. The graphite crystal lattice

degree of preferred orientation. One is stress graphitisation and the other relies on the identification of a polymer precursor whose molecular structure can be aligned and maintained during pyrolysis sufficiently well to yield a well-ordered graphitic structure in the resulting fibre. Practical realisation of these possibilities, particularly the second, during the early 1960's first made available carbon fibres of high specific strength and stiffness. These events in turn triggered off a new industry as well as a world-wide effort on carbon fibre composites technology.

Stress graphitisation involves controlled stretching of the fibre at temperatures in excess of 2000°C and extensions of 200 to 300% have been employed at temperatures up to 2750°C . This induces a greater degree of preferred orientation in the fibre structure and also results in some densification so that both elastic modulus and strength are improved. The principle has been demonstrated with fibres based on rayon (Ref. 2) and petroleum pitches (Refs. 3,4) and tenfold increases in modulus and fourfold improvements in strength have been noted. Stress graphitised fibres derived from rayon have now been produced in the United States for several years and represent some of the highest modulus fibres commercially available. No high performance fibres produced by stretching pitch-based fibres have yet appeared commercially.

The selection of a polymer fibre with an appropriate molecular structure as a precursor to the graphite structure had its origins in work by Shindo and coworkers (Refs. 5,6) in Japan in the late 1950's. They showed that fibres produced by heat treatment of polyacrylonitrile (PAN) possessed an appreciable degree of preferred orientation and a higher modulus than could be obtained from cellulose without hot-stretching. Polyacrylonitrile (PAN) forms a ladder polymer on heating at temperatures around 200°C and if heating is carried out in an oxidising atmosphere, cross-linking reactions can occur between adjacent groups of ladder polymer with the formation of a six-membered ring structure. The structure has, at this stage, a greater intermolecular spacing than the C-C bond length in the graphite crystal structure. However, on further heating in an inert atmosphere, the ring

structure is gradually converted, with the evolution of volatile compounds of hydrogen, nitrogen, oxygen and carbon, to sheets of material having increasingly the character of basal plane graphite. The extent to which graphitisation occurs, and the spatial order of the hexagonal layers, then depends primarily on the final temperature to which the material is heated in an inert atmosphere.

Although the Japanese work showed that a PAN precursor could give rise to better carbon fibre properties than other polymer precursors, the crucial step upon which most commercial carbon fibre production is now based was identified in the mid 1960's by Watt, Phillips and Johnson (Refs. 7,8) working at the Royal Aircraft Establishment in the UK. This step was to apply tension to the PAN filaments during the initial stage of oxidation at 220°C so as to maintain, or even increase, the molecular alignment of the ladder polymer and the subsequent sheets of ring structure that develop from it, parallel to the fibre axis. The application of tension during the oxidation stage makes the attainment of high modulus and strength possible without the need for any further stretching at subsequent stages in the heat-treatment cycle, and in particular, it obviates stretching at temperatures above 2000°C , as required in the case of rayon. The RAE process thus transfers the stretching stage from a high to a low temperature with a consequent decrease in the capital cost of manufacturing plant and a simplification in the fibre handling arrangements.

Most types of man-made fibres in quantity production, such as glass or textile fibres, are produced directly by melt or solution spinning requiring little, or any, further processing. Carbon fibres are intrinsically more expensive to produce since the cost of pyrolysis, and the control of molecular structure during pyrolysis, must be added to the cost of production of the precursor. Opportunities for reduction in manufacturing costs exist, however, in a number of directions and since the evolution of the basic PAN manufacturing route some ten years ago, a considerable amount of research and development has been devoted to reducing manufacturing costs and improving product quality. For example, various co-polymer formulations of PAN (Ref. 9) have been explored with a view to developing the appropriate graphitic structure at minimum process times and temperatures. An alternative approach has been to use the cheap textile grades of PAN (Ref. 10), in quantity production for the clothing and furnishing industries, as precursors. Much of the detail of this work, however, has not been published for commercial reasons.

One approach that has received considerable attention, notably by the Union Carbide Corporation (Ref. 11) in the USA, has been to explore further the possibility of using pitch as a precursor, using pre-treatments that would obviate the need for high temperature stretching in order to develop high modulus and strength. Two advantages of pitch as a precursor are that the raw materials prior to spinning may be a cheap by-product of other chemical manufacturing processes or of petroleum refining; and secondly that a higher carbon yield could result upon pyrolysis, thereby providing a higher output for a given plant size and precursor input. The carbon yield from

pyrolysis of PAN is typically 50-55%. Thus, pitch-based fibres might be cheaper to process than PAN-based, provided a means can be found to develop an oriented molecular structure at suitably low temperatures.

Progress in this direction has undoubtedly been made (Refs. 12,13) by converting part of the pitch to mesophase or a liquid crystal state. By heat treating certain types of pitch, it is possible to induce the formation of liquid spherules containing layers of oriented molecules aligned in the same direction. These spherules are known as mesophase regions. If a pitch containing suitable proportions of mesophase is spun into fibre form, the mesophase regions are drawn into elongated fibrils parallel to the fibre axis and possess a highly oriented molecular structure. On pyrolysis, these regions convert to graphite possessing a degree of preferred orientation similar to that achieved from the pyrolysis of PAN. Consequently, a fibre of high modulus and strength can be produced from pitch without the necessity of stretching at high temperatures to produce the requisite degree of crystallite orientation.

4. CARBON FIBRE STRUCTURE AND PROPERTIES

4.1 Elastic Modulus and Relationship with Structure

Typical carbon fibre properties are displayed in Table 1. From the known elastic constants of the graphite single crystal (Ref. 14) the modulus within the layer planes is of the order 1000 GNm^{-2} and this value clearly represents an upper limit to what might be achievable in a carbon fibre. Reference to Table 1 indicates how close it has proved possible to approach this limit, particularly in the case of hot-stretched fibre. A number of models (Refs. 15,16) have been proposed to account for the observed elastic modulus of carbon fibres in terms of their structure as determined by X-ray diffraction and electron microscopy studies. In general, these models depict carbon fibres as consisting of a series of stacks or ribbons of hexagonal planes extending large distances parallel to the fibre axis. There is little systematic order in the stacking of adjacent layers and although, in a high modulus fibre, the misorientation angle between the normals to the hexagonal planes (the c-axis direction) and the fibre radius is less than $\sim 10^\circ$, the broadening of X-ray diffraction lines indicates a spread of misorientation angles amongst individual layer planes. Most models consequently depict the structure as a series of extended ribbons or layers whose orientation relative to the fibre axis varies along the axis. As to be expected from these models, voids would exist between adjacent layers of different orientation and this is reflected in the fibre density values in Table 1 compared to the density of single crystal graphite ($2,500 \text{ kg m}^{-3}$). The table also shows how the density of the fibre increases as the modulus increases and the structural models suggest that increasing the graphitisation temperature, or hot-stretching, are effective in both increasing the degree of preferred orientation of the layer planes and reducing the incidence of voids and boundaries between adjacent layers. Fourdeux et al. (Ref. 15) have shown that excellent agreement exists between the misorientation model and the observed axial Young's modulus of a series of carbon fibres derived from PAN, rayon and pitch.

The picture of the axial structure of a carbon fibre and its influence on modulus is therefore fairly comprehensive. The transverse structure, in other words, the disposition of the layer planes in the fibre cross-section, is less well understood. Optical birefringence studies (Ref. 17) and plasma etching (Ref. 18) of fibre cross-sections have indicated a core with radial symmetry surrounded by an outer sheath with a predominantly circumferential structure. Figure 2, taken from Reference 18, shows one interpretation

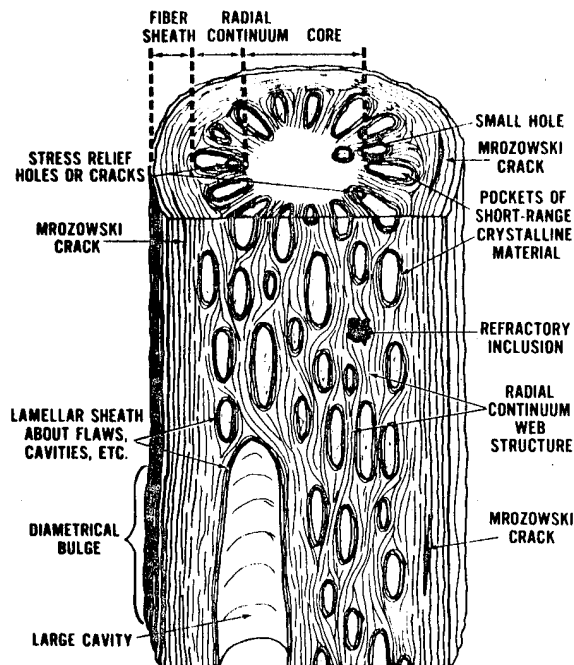


Figure 2. Proposed model of carbon fibre structure

tion of the fibre structure. Considerable variations from this simple picture exist however, depending on the final heat-treatment temperature of the fibre and on the type of precursor, i.e. whether based on rayon, PAN, or pitch. PAN-based fibres also show marked morphological differences depending upon whether the precursor fibre was spun from a solution or melt, and whether it was spun into a coagulating bath or air dried. Thus, fibres with circular, 'dog-bone' and bean-shaped cross-sections have been produced. Commercially, however, fibres with circular cross-sections have been preferred because of the relative ease with which specifications for fibre quality and properties can be established and checked for a simple geometry.

4.2 Thermal Expansion Behaviour

The similarity between the carbon fibre structure and that of the graphite single crystal suggests that the fibres should exhibit similar thermal expansion behaviour and this is observed. Graphite crystals exhibit highly anisotropic behaviour (Ref. 1), the basal plane expansion

ORIGINAL PAGE IS
OF POOR QUALITY

coefficient (α_a) being very small ($\sim 1.2 \times 10^{-6} \text{ }^\circ\text{C}^{-1}$) and becoming negative below 400°C , whereas the coefficient perpendicular to the basal plane (α_c) is positive at all temperatures and is relatively large ($\sim 28 \times 10^{-6} \text{ }^\circ\text{C}^{-1}$). The absolute values of expansion coefficients for carbon fibres depend on the fibre type, the closest approach to the single crystal values being obtained in the most highly graphitised fibres, i.e. those heat-treated to the highest temperature. Table 1 lists typical values. The lower transverse value is a consequence partly of the distribution of c-axes about the fibre axis and partly of the microscopic imperfections in the fibre structure.

4.3 Fibre Strength

The theoretical strengths of crystalline solids can be shown to approximate to $E/10$, (where E is Young's modulus) by an expression due to Orowan (Ref. 19) which estimates the energy required to break the cohesive forces between adjacent atoms. Thus an idealised carbon fibre with the structure of a perfect graphite single crystal could be expected to display a strength $\sim 100 \text{ GNm}^{-2}$. Reference to Table 1 shows that in practice, fibre strengths fall well below the value determined by the C-C bond in the layer planes and this shortfall is associated with the presence of imperfections in the structure.

A number of studies have been carried out with the aim of identifying strength-limiting flaws in fibres. Johnson (Ref. 16) and Johnson and Thorne (Ref. 20) showed that fracture of fibres frequently originated at voids in the cross-section and that such voids could often be attributed to the presence of inclusions in the precursor fibre. Sharp and Burnay (Ref. 21) have produced, from observations by transmission electron microscopy, direct evidence that diclinal voids in high modulus fibres occur at the site of particular inclusions and have concluded that the voids are produced by volatilisation of inorganic impurities above $\sim 1600^\circ\text{C}$. Reynolds and Sharp (Ref. 22) have postulated that failure at diclinal voids occurs as a result of shear stresses developed in the mis-oriented crystallites surrounding such voids.

Using carefully filtered PAN solutions and spinning the precursor fibres in a dust-free atmosphere, Moreton and Watt (Ref. 23) were able to produce carbon fibres in which internal flaws were virtually eliminated. Fracture strengths consequently increased by about 80% compared to a fibre produced by conventional methods and fractographic studies indicated that failure of the 'clean-spun' fibres was then initiated at surface flaws. Supporting evidence for the importance of surface flaws comes from experiments in which increases in fibre strength have been observed following etching (Ref. 24) treatments. These treatments presumably are instrumental in altering the morphology of surface flaws and hence increasing the stress at which cracks propagate from them.

So far, little insight has been gained into the detailed nature of surface flaws. Fibres derived from rayon and PAN have highly convoluted surfaces which make identification of incipient failure sites almost impossible by microscopical techniques. It is conceivable that the mechanism suggested by Reynolds and Sharp of shear failure from regions of greater than average crystallite misorientation could account for the initiation of failure at the fibre surface. Other theories (Refs. 25, 26, 27)

postulate regions of ribbon wrinkling around microvoids or the disordered regions shown in Figure 2 as the source of crack initiation and there is scope for considerably more work to improve understanding on this point. The highest strengths so far produced in an elongated graphitic structure of high aspect ratio have been achieved in graphite whiskers. Bacon (Ref. 28) has demonstrated strengths up to $\sim 20 \text{ GNm}^{-2}$ and these values represent the closest approach to the theoretical strength yet attained.

It is of considerable technological interest to consider what order of strength may ultimately be achievable in a carbon fibre. In the absence of a well-substantiated theory of fibre strength, accurate predictions are not possible, but some indication may be derived from work by Morita et al. (Ref. 29) and by Hughes et al. (Ref. 30). Both groups adopted special processing procedures, not specified, for polyacrylonitrile fibres and obtained carbon fibre strengths, deduced from measurements on resin composites, in the region 3.7 to 4.3 GPa. Reference to the data in Table 1 for high strength fibre shows that a considerable improvement over the properties of fibres currently produced commercially is possible. The properties of commercial fibres have shown a steady improvement over the years with regard to both absolute values and the consistency of properties and it is to be expected that additional improvements will follow as manufacturing procedures are further refined.

5. CARBON FIBRE COMPOSITES

Carbon fibres, of course, form only one of a series of reinforcing fibres available for use in composite materials. Other high performance reinforcements include glass and aramid fibres, boron and silicon carbide fibres formed by vapour deposition on to a carbon or tungsten filament, and metal wires. Although there are certain realms where a particular reinforcement is uniquely suitable, to some extent each reinforcement is in competition with the others and careful appraisal is required to determine which material will fall within a given set of technical and economic constraints. Similarly, a variety of matrix materials are available. As far as carbon fibres are concerned, only two matrix materials have so far reached significant commercial application - polymers and carbon itself. A considerable effort has also been devoted to the development of carbon fibre reinforced metals and, to a lesser extent, to carbon fibre reinforced ceramics and hydraulic cements.

It is not within the scope of this article to review the vast literature concerning the science of composite materials and reference should be made to a number of excellent treatises on this subject (Refs. 31, 32). Instead, it is intended to indicate, where work is still in the development stage, what progress has been made, and to review briefly present and future spacecraft applications. Reinforced carbon and metals are considered first, followed by the most widely used material, carbon fibre reinforced plastics, (CFRP).

5.1 Carbon Fibre Reinforced Carbon

Although properties may vary widely, depending on starting materials and method of manufacture,

bulk carbons and graphites have generally poor mechanical properties. Flexural strengths are typically less than 40 MNm^{-2} and Young's modulus usually does not exceed 20 GNm^{-2} (Ref. 33). There is thus considerable potential for upgrading the properties of such materials by reinforcing with carbon fibres. Fabrication usually consists of first making a composite using resin that, on pyrolysis, will yield a high residue of carbon. Suitable resins include phenolics, furanes and epoxy-novolacs. On pyrolysis, the loss of volatiles from the resin gives rise to a porous carbon matrix and hence a poor bond strength, and to achieve high mechanical properties it is necessary to densify the matrix. Densification methods involve successive re-impregnations with resin followed by further pyrolysis operations, or deposition of carbon in the pores from the vapour phase (chemical vapour deposition), or a combination of both methods. For the highest strength composites the chemical vapour deposition process is probably superior because in addition to filling internal pores, surface cracks and flaws can be healed by deposition of carbon. Both densification processes are relatively slow however, and hence carbon/carbon composites are inherently more expensive than CFRP. A paper by Hill et al. (Ref. 34) gives details of the effects of various resin reimpregnation and chemical vapour deposition treatments and shows that longitudinal flexural strengths and Young's modulus values of $\sim 1800 \text{ MNm}^{-2}$ and $\sim 190 \text{ GNm}^{-2}$ are achievable using high strength and high modulus fibres respectively.

For aerospace use, the principal applications for this type of material are in rocket-motor cases (Ref. 35), for ablative purposes on re-entry vehicles, and for aircraft disc brakes. The principal advantage over CFRP is the high temperature capability and it is difficult to envisage use of reinforced carbon in spacecraft for other than very special purposes.

5.2 Carbon Fibre Reinforced Metals

Three principal reasons can be presented to justify attempting to incorporate carbon fibres in metals. The ability of carbon to maintain its strength to high temperatures suggests that carbon fibres might be effective in reducing creep in nickel-based alloys used in gas turbine engine technology and hence would increase operating temperatures. Secondly, the high specific strength and modulus of the fibres make them attractive for upgrading the mechanical performance of the low density non-ferrous alloys and thirdly, the combination of mechanical and tribological properties of carbon fibres suggest the possibility of improving the performance of the low melting point alloys widely used for bearings. Thus the matrices most extensively studied have been nickel, aluminium alloys and lead-tin alloys, although some work has been carried out on other metals including cobalt and titanium (Ref. 36), chromium (Ref. 37) and magnesium (Ref. 38).

One of the major problems with high temperature composites is the chemical compatibility of dissimilar materials at the fibre/matrix interface. Many metals form carbides or have a finite solubility for carbon and both processes may be expected to degrade the properties of the reinforcing fibres. Baker (Ref. 39) has reviewed the subject of chemical compatibility and Old and Nicholas (Ref. 40) have considered the prospects

generally for carbon fibre reinforced metals. With regard to nickel and its alloys, there is conflicting evidence in the literature about the extent to which degradation in mechanical properties of the composites occurs after heating to $\sim 1200^\circ\text{C}$ in vacuo, but little doubt that some degradation occurs. This is attributed primarily to the solubility of carbon in nickel. More serious however, is the fact that in air, oxidation of the fibres in the nickel matrix occurs rapidly at temperatures above $\sim 600^\circ\text{C}$, particularly where fibre ends are exposed at a surface.

In contrast to nickel, there is evidence, both from free-energy considerations and from experiment, to suggest that an aluminium matrix would give some protection to the fibres from oxidation up to $\sim 450^\circ\text{C}$ although there would still remain the problem of oxidation where fibres intersect the surface of a component. Despite this limitation, considerable development work has been devoted to fabrication methods for carbon fibre reinforced aluminium and to evaluation of properties. One of the most successful developments appears to be that reported by Harrigan and Goddard (Ref. 41) in which carbon fibre tows, previously treated chemically to promote wetting, were infiltrated with molten aluminium to form a composite wire. The wire can then be formed into sheet or bulk material by liquid phase hot-pressing or diffusion bonding. Tensile strengths up to 700 MNm^{-2} have been quoted for wire incorporating 28.5% of fibre by volume, and retention of strength at elevated temperatures, as indicated in Figure 3, is reported to be significantly better than for un-reinforced alloys.

For spacecraft use, the principal advantages of carbon fibre reinforced aluminium alloys over reinforced resins are likely to be the improved high temperature performance, reduced moisture pick-up, freedom from outgassing effects, higher electrical and thermal conductivities and possibly easier joining techniques. Such materials are only just becoming available commercially in the USA and it remains to be seen to what extent they will find application for other than military spacecraft. They are likely to remain more expensive than reinforced plastics owing to their more difficult fabrication technology.

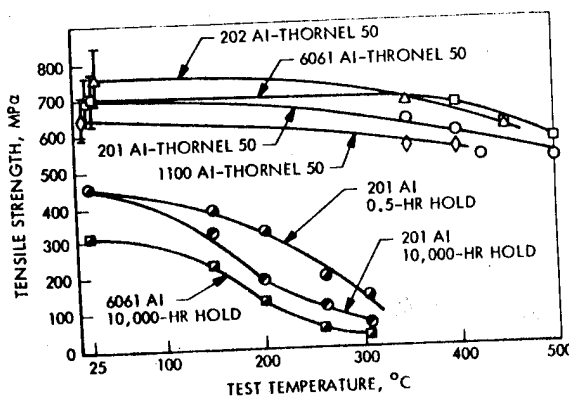


Figure 3. Effect of carbon fibres on the high temperature strength of aluminium alloys (from Ref. 42)

5.3 Carbon Fibre Reinforced Plastics (CFRP)

5.3.1 Mechanical Properties. The high specific stiffness and strength of CFRP make it potentially one of the most useful materials for aircraft and aerospace vehicle construction although much patient and detailed work has been necessary to evolve the principles of design and manufacture in highly anisotropic materials. Figure 4, based

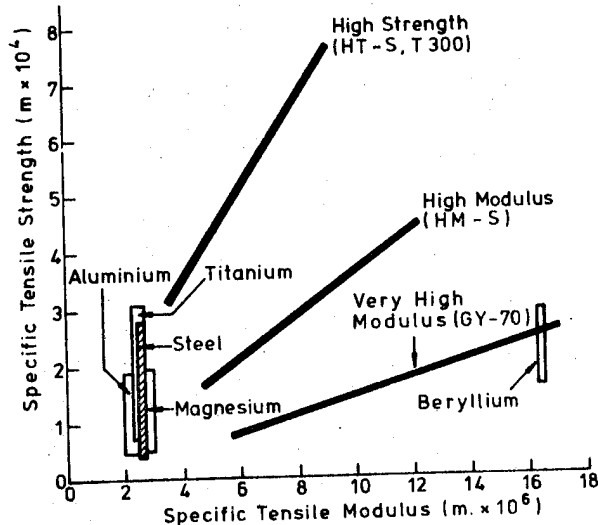


Figure 4. Representative values for the specific strength and modulus of carbon fibre composites

on Reference 43, summarises the relative specific properties of CFRP deriving from various grades of fibres, compared with those of structural metals. Typical absolute values are quoted in Table 2. The greatest benefit attaching to fibre composites is obtained when the design permits the use of unidirectional fibres and the properties of unidirectional forms of CFRP are represented by the right-hand ends of the property bars in Figure 4. However, relatively few components are subjected to principal stresses in one direction only and some degree of isotropy, at least in two dimensions, is required to meet stress distributions experienced in practice. This can be achieved by building up sections from thin laminae with the fibres in each ply oriented in appropriate directions and the left-hand ends of the property bars in Figure 4 represent the specific values for symmetrical laminates designed to give near-isotropic properties in the plane of the laminate. Design procedures for laminates are now well established (see e.g. Refs. 32 and 44) although there is little doubt that considerably more work remains to be done - on such problems as the development of greater confidence in design procedures, the achievement of greater quality control in fabrication processes and the development of better inspection and evaluation techniques - both destructive and non-destructive. Some of the advantages, and problems, attaching to the use of fibre reinforced composites in aerospace structures have been discussed by Fray (Ref. 45), and Reference 46 is a review, containing extensive property data, conducted for ESA of the use of CFRP in spacecraft structures.

5.3.2 Dimensional and Environmental Stability. Although the high specific strength and stiffness of carbon fibre composites are obviously advantageous, many satellite components, such as communications antennae, waveguides, microwave filters and optical equipment are required to display a high degree of dimensional stability over long periods of exposure to a high vacuum, to solar and particle radiations, and, in particular to temperature variations which, from full solar irradiance to eclipse can range from $+100^{\circ}\text{C}$ to -100°C (Ref. 47), for components at the surface of the spacecraft.

Properly formulated and cured thermosetting resins, particularly epoxies, are generally stable under space conditions and a number of products have been shown to give rise to acceptable levels of volatiles in outgassing tests. Radiation levels in space are such that significant degradation of matrix materials is unlikely to occur over currently projected spacecraft lifetimes (Ref. 48) and the major factors influencing dimensional stability are temperature variations and the effects of moisture absorbed prior to launch.

5.3.3 Thermal Expansivity. By careful laminate design, the low axial expansion coefficient of carbon fibres can be exploited, despite the high degree of anisotropy and the relatively large expansion of matrix resins ($\sim 50 \times 10^{-6} \text{ }^{\circ}\text{C}^{-1}$), to produce laminates with in-plane expansion coefficients close to zero.

Detailed measurements of thermal expansion coefficients for various types of laminate are described in References 49 to 52 and representative values are shown in Table 3 for unidirectional and pseudo-isotropic laminates made with three grades of fibre - high strength, high modulus and ultra-high modulus. Figure 5 (Ref. 46, Vol. 2) shows that there is

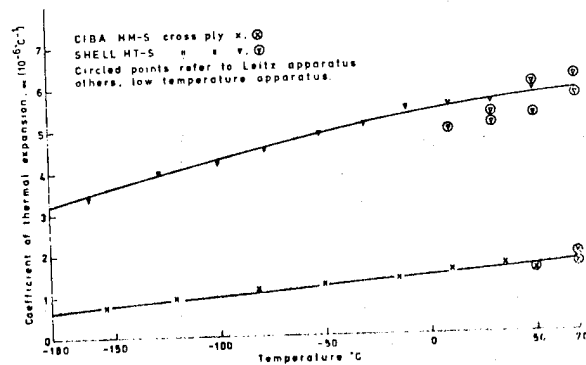


Figure 5. Coefficients of Expansion for Cross-Ply Laminates as a Function of Temperature

only a small temperature dependence for the expansion coefficients of (0,90) laminates over the range of temperatures likely to be experienced in spacecraft components so that some confidence may be attached to the design of thermally stable structures from CFRP.

The magnitude of thermally-induced dimensional changes has been studied by Goggin (Ref. 53) and Freund (Ref. 54) in relation to spacecraft applications. The main conclusions from these investigations are that carbon fibre composites provide adequate stability for components required to maintain moderate dimensional tolerances, such as microwave antennas and some metering structures, but that thermally-induced changes are too large for the construction of, say, optical reflectors. One reason for this is the relatively large expansion coefficient perpendicular to the plane of a laminate which is determined primarily by the matrix expansion. Kedward (Ref. 55), has analysed the distortion that can occur in laminates as a result of temperature changes.

5.3.4 Moisture Effects. A topic to which considerable attention has been directed in recent years has been the possible effects of absorbed moisture on the properties and behaviour of CFRP. For spacecraft the major concern arises from the difficulty of protecting resin-based materials from moisture absorption during storage on Earth and the possibility of irreversible changes accompanying the loss of vapour after launch. The effect of moisture absorption on the mechanical properties of CFRP has been reviewed in a recent ESTEC contract (Ref. 56). Exposure to high relative humidities causes those mechanical properties controlled by the matrix to decrease and the effect is more serious at high temperatures. Properties dominated by the fibres tend to recover when water vapour is removed, but transverse properties do not return to their pre-exposure levels. The degradation appears to be due to absorbed water causing the resin to swell, possibly giving rise to internal micro-cracking and disruption of the fibre-resin bond. Any degradation of the fibre-matrix bond would be expected to influence shear behaviour sensitively and Figure 6 (Ref. 57) illustrates

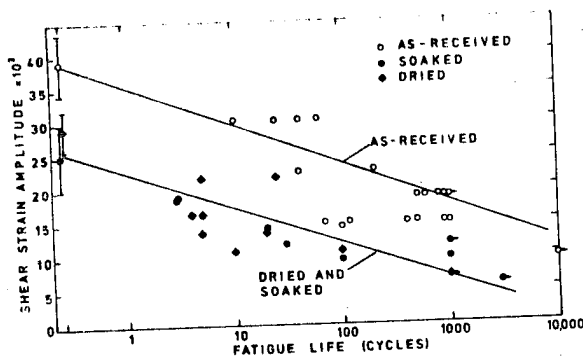


Figure 6. Fatigue lives of CFRP under constant shear strain amplitude cycling after various treatments

the effects of water immersion and subsequent drying on fatigue life under constant amplitude shear strain cycling.

As might be expected from a resin swelling phenomenon the absorption (or desorption) of moisture has a significant influence on dimensional

stability. Reference 43 quotes a linear expansion of 20 ppm in the plane of a (0/45)_g laminate made with GY70 fibre, and 1400 ppm along the normal to the plane during a period of ~140 days exposure to a relative humidity of 50% at 24°C. It may therefore be necessary to store critical components in a moisture-free environment prior to launch, or to seal the surface with an impermeable membrane. Metal foils or vapour deposited coatings may be effective and Figure 7 illustrates

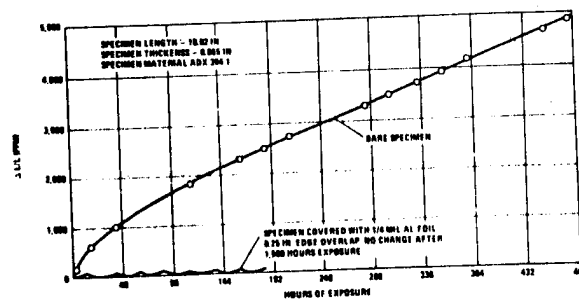


Figure 7. Dimensional changes for foil-covered and unprotected CFRP exposed to moisture

the improvement to be gained by covering the surface of a CFRP test piece with aluminium foil (Ref. 43).

5.3.5 Tribological Properties. Extensive studies of the tribological characteristics of CFRP have been conducted by Lancaster and his coworkers (Refs. 58,59). These show carbon fibre reinforced epoxide resins and some reinforced thermoplastics to have extremely low coefficients of friction and rates of wear when sliding against a steel counterface in both lubricated and non-lubricated conditions. So far, there has been little commercial exploitation of the tribological properties of carbon fibres, but their ability to operate under dry conditions make them a candidate for spacecraft use provided that other components can be protected from wear debris that is electrically conductive. Gotch (Ref. 60) describes experience with CFRP gears in rail transport and Reference 61 describes the processing of a carbon fibre reinforced plastic intended for gear applications in spacecraft.

5.3.6 Applications of CFRP. The principal uses of CFRP in spacecraft thus far have been for components rather than spacecraft structures and where combinations of weight saving and dimensional stability give advantages over conventional materials. One of the earliest significant components to be launched was the high gain antenna for the Viking spacecraft mission to Mars in 1975 which consisted of carbon fibre/epoxy resin skins bonded to an aluminium honeycomb core (Ref. 62). Factors in the design of the Marots L-band antenna, of similar construction, have been described by Jones (Ref. 63). The testing of the Marots antenna and some of the materials problems encountered in its development, have

been described by Dunn and Collins (Ref. 64). The Intelsat IV series of communication satellites contained a small amount of carbon fibre stiffening on an aluminium member of the antenna support structure and the Intelsat V East and West spot beam antennas will be of carbon fibre construction. A detailed description of the design and fabrication of a CFRP antenna for the Nimbus-G/Seasat-A satellite is given in Reference 65.

An excellent example of the weight saving potential of CFRP is cited in Reference 66 dealing with the development of microwave filters and waveguides for spacecraft. Frequency stability requirements demand the use of a material of low thermal expansion coefficient in narrow band channel filters and Invar has customarily been the principal material of construction since its linear expansion coefficient is $\sim 1.0 \times 10^{-6} \text{ } ^\circ\text{C}^{-1}$. Its density however is $8.0 \times 10^3 \text{ kg m}^{-3}$ and the use of CFRP can effect a fivefold saving in weight. The paper reports tests on thermal and environmental exposure and indicates that approximately 100 devices have operated successfully in orbit for more than two years.

The use of CFRP generally in spacecraft in the United States prior to 1974 has been reviewed by Mayer (Ref. 67) and more recent work has been described by Prunty (Ref. 43). Potential applications for metal matrix composites in spacecraft have been reviewed by Armstrong and Johnson (Ref. 68).

Practical, or proposed, structural applications for CFRP in spacecraft are too numerous to review in detail within the scope of this article. Table 4 lists typical examples with references for further reading.

6. FUTURE POSSIBILITIES

Now that the advantages of carbon fibre materials are being demonstrated in flight hardware, their use will almost certainly extend to other components and parts of spacecraft structures. The amounts of fibre required for such purposes are likely to remain small, but at least one projected space application could create a major market. As an alternative to launching individual spacecraft built on Earth, considerable attention is now being directed, particularly in the USA, to the possibility of constructing much larger craft or platforms in space, using the Shuttle Orbiter to transport materials and equipment to low earth orbit. Such platforms may be used as large communications satellites capable of handling vastly increased amounts of data and providing, for example, point-to-point facsimile transmission services (electronic mail), direct broadcast TV, personal radio-telephonic communications and direct access to data banks on a national or continental scale. Other possible uses include greatly expanded earth resource survey activities, space manufacturing facilities and the collection and transmission to earth of solar energy. The latter could take the form of reflected radiation in the visible region of the spectrum to illuminate say, city areas at night; or radiation in the visible and infra-red to assist crop growth in selected areas (Refs. 69,70,71).

A major subject currently under investigation is the possibility of constructing a 5 GW solar

power source in geostationary orbit by the end of the century (Refs. 72,73,74). The support structure for the solar collectors/converters would, according to one concept, occupy an area of 82 km^2 , and weigh $\sim 36,000$ tonnes. This mass is only a small fraction of the mass of a terrestrial power station of comparable output, but since the existing Shuttle is capable of lifting only 25 tonnes into orbit, the achievement of large solar power sources will depend on the development of launch vehicles of much larger carrying capability and much lower launch costs per unit weight. The economics of carrying out the structural work in low earth orbit and subsequently transporting the entire structure to geostationary orbit have been studied (Ref. 75), as has the possibility of deriving the structural materials (e.g. aluminium alloys) from lunar minerals (Ref. 76), since the low gravitational forces on the moon would considerably reduce launch costs. Apart from the problems and costs of transporting materials for the Solar Power Source, a reduction in the costs of photovoltaic cells by two, or three, orders of magnitude will be required.

6.1 Beam Building Experiments

Several schemes have been proposed for manufacturing, in space, the basic structural elements from which space platforms will be fabricated. Most are based on a triangular truss (Figure 8) produced automatically by a machine located in

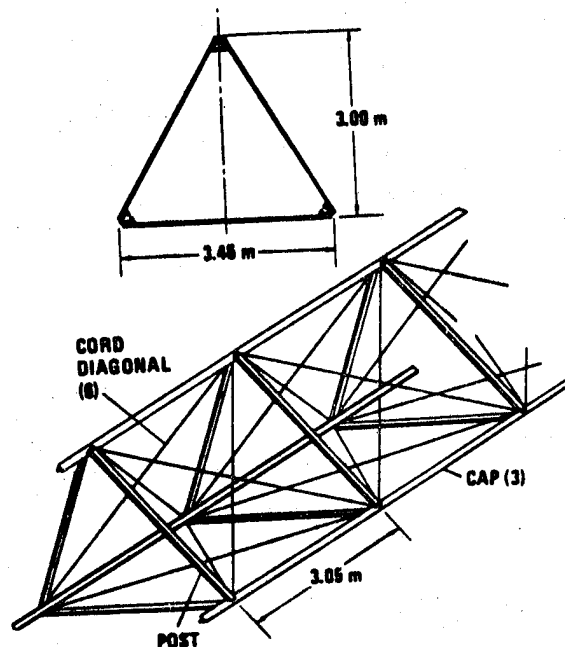


Figure 8. Example of beam envisaged for in-space fabrication (from Ref. 43)

the Shuttle Orbiter. Such machines would be capable of producing beams of any desired length and platforms could be constructed by linking parallel beams with cross-beams of identical

construction. The most advanced development is an experimental machine built by Grumman (Ref. 77) which uses coiled aluminium strip as feedstock and roll-forms it into stringers to which are attached cross-braces by spot-welding. A possible problem with aluminium is the thermal distortion that could arise as a result of temperature differences when only one surface of the structure receives radiation from the sun. Carbon fibre composites, on account of their very low longitudinal thermal expansion coefficients, offer a solution to this problem. Table 5 (from Ref. 43) compares the thermal deflections for various materials and coatings at one end of a 200 m cantilever of triangular cross-sections when two surfaces are exposed to solar radiation and one is in shadow. It appears likely that in practice, in contrast to demonstration experiments, large structures will be built from carbon fibre materials rather than light alloys and one study (Ref. 78), by General Dynamics Convair Division, envisages structural elements thermoformed in space from a carbon fibre reinforced thermoplastic, where joining could be accomplished by ultrasonic welding techniques. An important step in the beam building programme is the plan ~1983 to erect a trial structure 10 m x 30 m in orbit with the machine located in the Shuttle (Figure 9).

keys to lower prices and although a development such as the Solar Power Satellite could lead to a dramatic expansion from the present world market size of ~3-400 tonnes per annum, the advent of the SPS is much too problematical, to enable credible predictions to be made. A somewhat less tentative basis for anticipating a significant improvement in market potential comes from the automotive industry's current interest in weight reduction and Table 6 (Ref. 79) gives one assessment of the relative size of markets for carbon fibre in the future.

In addition to saving weight, the ability to mould complex one-piece components in CFRP can show a net cost saving over forms of construction involving assembly of a large number of metal components. As an example, Lubin and Dastin (Ref. 80) have described in detail the fabrication and testing of the main landing gear strut door for the F-14A aircraft. They have concluded that the use of carbon fibre results in a 10% weight saving and that a 15% cost reduction over aluminium alloy is possible in production. Costs for the production of composite components for the aircraft industry have been analysed by Reinert and Meade (Ref. 81) who have concluded that despite rising materials, labour costs and inflation, improved manufacturing techniques and parts integration will lead to a continuing downward trend in the cost per kg of composite structure.

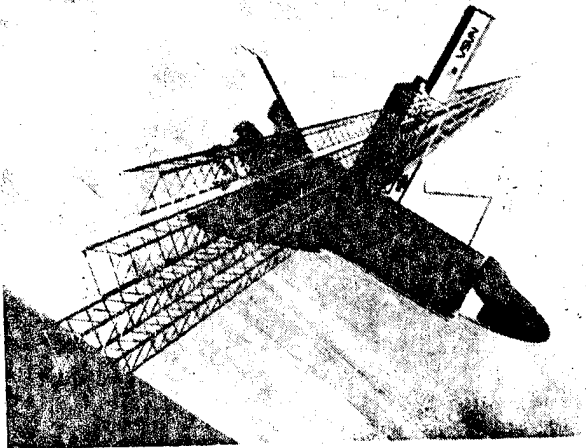


Figure 9. Illustration of the fabrication and assembly of a 200 m long platform by a beam building machine located in the Shuttle Orbiter

6.2 Future Price Structure

Although it is acceptable to pay a higher premium for weight-saving materials in spacecraft than in most other engineering structures the price of carbon fibres is clearly a factor that will determine the extent of their use. Prices have, in fact, fallen by an order of magnitude since the fibres were first introduced commercially. It is not within the scope of this article to examine probable price levels in the future, but it is at least pertinent to consider what factors may lead to further reductions. The size and stability of the market are almost certainly the

Table 1. Approximate Properties of Major Carbon Fibre Types

Fibre Type	Precursor	Young's Modulus GNm ⁻²	Tensile Strength GNm ⁻²	Diameter μm	Density kg m ⁻³	Strain to Failure σ/E %	Longitudinal Expansion Coefficient* x 10 ⁻⁶ °C ⁻¹
High strength	PAN	200-250	2.5-3.0	8	1770	~ 1.2	-0.75
High modulus	PAN	300-360	1.7-2.5	8	1900	~ 0.6)
	Rayon	390	1.9		1860	~ 0.5) -1.25
	Pitch	380	1.4			~ 0.4)
Ultra-high modulus (hot-stretched)	PAN	530	1.7		1960	~ 0.3	
	Rayon	525	2.5		1820	~ 0.5	

* Transverse expansion coefficient $\sim 20 \times 10^{-6} \text{ }^{\circ}\text{C}^{-1}$ (Ref. 91)

Table 2. Typical Mechanical Properties for Uni-directional Carbon Fibre Composites Containing ~60% Fibre by Volume (Ref. 46)

Property		High Strength Fibre Composite	High Modulus Fibre Composite	Very High Modulus Fibre Composite
Long tensile modulus	GNm ⁻²	124-172	200-290	290-350
Transverse tensile modulus	"	6.9-9.0	6.1-7.6	5.9-6.8
Long tensile strength	MNm ⁻²	1240-1520	550-1020	460-1540
Transverse tensile strength	"	16-53	13.8-50	17-31
Density	kg m ⁻³	1.54x10 ³	1.61x10 ³	1.63x10 ³

Table 3. Representative Thermal Expansion Coefficients for ~60 v/o Fibre Composites (Ref. 43)

Type of Laminate	High Strength Fibre Composite	High Modulus Fibre Composite	Very High Modulus Fibre Composite
Unidirectional			
Longitudinal	-0.7	-0.8	-0.9
Transverse	29.2	29.2	28.8
Pseudo-isotropic			
Longitudinal	2.2	0.6	≈ zero
Transverse	2.2	0.6	≈ zero

Table 4. Typical Applications for CFRP in Spacecraft

Application	References
Antennas - fixed	62, 63, 64, 65, 82, 84, 85
Antennas - deployable	68
Microwave filters and waveguides	66, 82
Pressure vessels	86, 87
Booms for deploying equipment from spacecraft	46, 88
Supports for optical and microwave components	89, 90
Optical telescopes and benches	43
Rocket motor cases	
Thrust cones	
Solar panel support frames	

Table 5. Deflections of a 200 m Cantilever Beam Exposed to Solar Irradiance

Material	Surface Coating	C.T.E. ppm °C ⁻¹	ΔT(max) °C	Tip Deflection m
Aluminium	White paint	22	57	16.45
Carbon fibre/epoxy				
High strength fibre (Type AS)	White paint	2.6	57	1.95
	Bare	2.6	140	4.78
Very high modulus (Type GY-70)	White paint	0.2	57	0.14
	Bare	0.2	140	0.32

Table 6. Pattern of Growth for Carbon Fibres in Major Markets (tonnes)

Market	1975	1980	1985
Aerospace	40	130	720
Automotive	N ^a	900	11,200
Other	50	500	2,000
Total	90	1,530	13,720

Source: Industry estimates

a - negligible or none

b - sporting goods, EDP equipment etc.

REFERENCES

- See e.g. Reynolds W N 1968, *The Physical Properties of Graphite*. Elsevier.
- Bacon R & Schalamon W A 1969, Physical properties of a high modulus graphite fibre made from a rayon precursor, *High Temperature Resistant Fibres from Organic Polymers*. (Ed. J Preston) Interscience, New York, 293.
- Hawthorne H M, Baker C, Bentall R H & Linger K R 1970, *Nature*. 227.
- Hawthorne H M 1971, Structure and properties of strain-graphitised glassy carbon fibres, *Proc Int Conf on Carbon Fibres*. Paper 13. The Plastics Institute, London.
- Shindo A, Fujii R & Sengoku M and Japanese Bureau of Industrial Technics 1962, *Jap. Patent* 4405.
- Shindo A 1961, *Graphite Fibres*, Rep. Osaka Ind. Res. Inst. 317.
- Watt W, Phillips L N & Johnson W 1966, High strength, high modulus carbon fibres, *Engineer*. London. 221 (5757) 815.
- UK Patent 1110791, 1968.
- Fitzer E & Heym M 1976, Carbon fibres - the outlook, *Chemistry & Industry*. 663.
- Prescott R, Goan J C, Hill J E, Joo L A & Martin T W 1972, High performance carbon fibre tows, *Proc 27th Annual Technical Conf. Soc Plastics Ind Inc, USA*.
- Forsyth R B 1974, New low cost 'Thornel' fibres from pitch precursor, *SAMPE*.
- US Patent Nos 3,919,376 and 3,919,387 1975.
- Singer L S 1977, High modulus carbon fibres from mesophase pitch, *Proc Conf on Ultra High Modulus Polymers*. 251, Santa Margherita, Ligure.
- Seldin E J & Nezbeda C W 1970, Elastic constants and electron microscope observations of neutron-irradiated compression-annealed pyrolytic and single crystal graphite, *J Appl Phys*. 41, 3389.
- Fourdeux A, Perret R & Ruland W 1971, General structural features of carbon fibres, *Proc Carbon Fibres, Their Composites and Applications*. Paper 9. The Plastics Institute, London.
- Johnson J W 1969, Factors affecting the tensile strength of carbon-graphite fibres, *Applied Polymer Symp* 9, 229.
- Knibbs R H 1972, The use of polarised light microscopy in examining the structure of carbon fibres. *J Microscopy*. 94, 273.
- Barnet F R & Norr M K 1974, The etching of carbon fibres to show structure, *Proc Carbon Fibres - Their Place in Modern Technology*. Paper 6. The Plastics Institute, London.

19. Orowan E 1949, Fracture and strength of solids, *Rep Prog Phys.* 12, 185.
20. Johnson J W & Thorne D J 1969, Effect of internal polymer flaws on strength of carbon fibres prepared from an acrylic precursor, *Carbon.* 7, 659.
21. Sharp J V & Burnay S G 1971, High voltage electron microscopy of internal defects in carbon fibres, *Proc Carbon Fibres - Their Composites and Applications.* Paper 10. The Plastics Institute, London.
22. Reynolds W N & Sharp J V 1974, Crystal shear limit to carbon fibre strength, *Carbon.* 12, 103.
23. Moreton R & Watt W 1974, Tensile strengths of carbon fibres, *Nature.* 247, 360.
24. Thorne D J 1974, Carbon fibres with large breaking strain, *Nature.* 248, 754.
25. Feughelman S M 1973, The fracture mechanism of carbon fibres, *J Mater Sci.* 8, 1119.
26. Tyson C N 1975, Fracture mechanisms in carbon fibre derived from PAN, *J Phys D.* 8, 749.
27. Rose P G 1976.
Proc 2nd Int Carbon Conf. Baden-Baden.
28. Bacon R 1960, Growth, structure and properties of graphite whiskers, *J Appl Phys.* 31, 283.
29. Morita K, Miyachi H, Kobori K & Matsubara I 1977, Carbon fibres with large breaking strain, *High Temperature - High Pressures.* 9, 193.
30. Hughes J D H, Morley H & Jackson E E 1977, Carbon Fibre Composites which Approach Theoretical Strength. AERE-R.8727.
31. Broutman L J & Krock R H (Eds) 1975, *Composite Materials.* Vol. 1-8, Academic Press.
32. Jones R M 1975, *Mechanics of Composite Materials,* McGraw Hill, New York.
33. Mantell C L 1968, *Carbon and Graphite Handbook,* Interscience.
34. Hill J, Thomas C R & Walker E J 1974, Advanced carbon-carbon composites for structural applications, *Proc Carbon Fibres - Their Place in Modern Technology.* Paper 19, The Plastics Institute, London.
35. Parmee A C 1971, Carbon fibre/carbon composites - some properties and potential applications in rocket motors, *Proc Carbon Fibres - Their Composites and Applications.* Paper 38. The Plastics Institute, London.
36. Jackson P W 1969, Studies of the compatibility of graphite and other fibres with metal matrices, *Metals Eng. Quart.* 9 (3) 22.
37. Lumley E J & Gillin L M 1970, Preprint of 4th Australian Ceramic Conference. August.
38. Maire J, Gremion R, Rappeneau J & Jouquet G 1971, Composite materials with a metallic matrix and carbon fibres, *Proc Carbon Fibres - Their Composites and Applications.* Paper 15. The Plastics Institute, London.
39. Baker A A 1975, Carbon fibre reinforced metals - a review of the current technology, *Mat Sci & Eng.* 17, 177.
40. Old C F & Nicholas M G 1974, Prospects for metal matrix composites, *Proc Carbon Fibres - Their Place in Modern Technology.* Paper 13. The Plastics Institute, London.
41. Harrigan W C & Goddard D M 1975, Aluminium graphite composites effect of processing on mechanical properties, *J Met.* 27 (5) 20.
42. Harrigan W C & French W W 1975, *High Temperature Creep Properties of Aluminium Graphite Composites.* Aerospace Corporation Report ATR-75-(9450)-2.
43. Prunty J 1978, Dimensionally stable graphite composites for spacecraft structures, *SAMPE Quarterly.* 9 (2) 41 January.
44. Greenwood J H 1977, German work on GRP Design, *Composites.* 8 (3) 175.
45. Fray J 1976, The special problems of high performance structures, *Proc Reinforced Plastics Congress.* Paper 20, 199. British Plastics Fed., London.
46. ESRO CR(P)507 Vol 1; ESRO CR(P)598 Vol 2; 1974, *Final Report on the Use of CFRP in Satellite Structures.*
47. Dauphin J 1973, Materials Problems in Space, *Int J Environmental Studies.* 4, 109.
48. ESA PSS-07 (QRM-01) Issue 4 1978, *Guidelines for Space Materials Selection.* Section 11.6, p.32.
49. Fahmy A A & Ragai A N 1970, Thermal Expansion of graphite-epoxy composites, *J Appl Phys.* 41, 5112.
50. Freeman W T & Campbell M D 1972, Thermal expansion characteristics of graphite reinforced composite materials, *Proc Composite Materials: Testing and Design (Second Conference).* ASTM STP 497, 121.
51. Geiler D E 1973, Analysis, test and comparison of composite material laminates configured for isotropic low thermal expansion, *Proc 28th Ann Tech Conf Society of the Plastics Industry Inc.* Paper 8-D.
52. Rogers K F, Phillips L N, Kingston-Lea D M, Yates B, Overy M J, Sargent J P & McCalla B A 1977, The thermal expansion of carbon fibre reinforced plastics. Part 1. The influence of fibre type and orientation. *J Mat Sci.* 12, 718. Part 2. The influence of fibre volume fraction, *J Mat Sci.* 13, 433, 1978. Part 3. The influence of resin type, *J Mat Sci.* 13, 2217, 1978. Part 4. Ply multi-directional effects. *J Mat Sci.* 13, 2226, 1978.

53. Goggin W R 1974, Thermomechanical stability of graphite/epoxy composites, *Appl. Optics*. 13, 444.
54. Freund N P 1975, Measurement of thermal and mechanical properties of graphite-epoxy composites for precision applications. *Proc Conf on Composite Reliability*. ASTM STP 580, 133.
55. Kedward K T 1976, Thermally induced deformation of laminated composite structure, *Composites*. 7, 21.
56. Rickett M F, Hancox N L & Minty D C C 1978, An Investigation into the Hydrothermal Degradation of Carbon Fibre Composites. ESA CR (P) - 1100
57. Phillips D C, Scott J M & Buckley N 1978, The effects of moisture on the shear fatigue of fibre composites, *Proc 2nd Int Conf on Composite Materials*. Met Soc AIME. 1544.
58. Giltrow J P & Lancaster J K 1971, Properties of carbon fibre reinforced polymers relevant to applications in tribology, *Proc Carbon Fibres - Their Composites and Application*. Paper 31. Plastics Institute, London.
59. Lancaster J K 1972, Lubrication of carbon fibre reinforced polymers: Part 1 - Water and aqueous solutions; Part 2 - Organic fluids, *Wear*. 20, 315.
60. Gotch T M 1970, Engineering applications of reinforced thermoplastics in rail transport - carbon fibre reinforced plastic gears and bearings, *Proc Conf on Reinforced Thermoplastics*. Solihull, Birmingham. October.
61. Phillips D C & Scott J M 1976, The Selection and Processing of Carbon Fibre Reinforced Acetal for Gear Applications in Satellites. AERE-R.8351 (ESTEC Contract No. 2255/74AK).
62. Young J W & Dougherty T A 1976, Application of composite materials for fabrication of spacecraft communication antennas, *Proc XXVII International Congress of the International Astronautical Federation*. Anaheim, California. 833.
63. Jones W L 1975, The Marots antenna subsystem, *Proc Antennas for Aircraft and Spacecraft*. 107. Conf Pub 128. Institute of Elec Engrs. London.
64. Dunn B D & Collins D S 1978, Materials investigation for a failed spacecraft antenna, *ESA Journal*. 2 (3) 223.
65. Knoell A & Krumweide G 1978, Structural development of the Nimbus G/Seasat-A SMMR graphite epoxy antenna reflector. *Proc 2nd Int Conf on Composite Materials*. Met Soc AIME. 1377.
66. Hammond M G & Farrell K 1978, Graphite epoxy composite material components for satellites, *Proc 2nd Int Conf on Composite Materials*. Met Soc. AIME. 1392.
67. Mayer N J 1974, Carbon composites in space vehicle structures, *Proc Carbon Fibres - Their Place in Modern Technology*. Paper 39. The Plastics Institute, London.
68. Armstrong H & Johnson RR 1978, Organic and metal matrix composites for spacecraft applications, *SAMPE Quarterly*. 13. January.
69. NASA CR 150720-3, April 1978, *Space Industrialisation*. Vol 1-4, Rockwell International Corp, Downey, Calif.
70. NASA CR 150752-5, April 1978, *Space Industrialisation*. Vol 1-4, Science Applications Inc, Huntsville, Ala.
71. NASA CR 155203, 1977, *Industries in Space to Benefit Mankind. A View over the Next 30 Years*. Rockwell International Corp, Downey, Calif.
72. Glaser P E 1977, Solar power from satellites, *Physics Today*. 30 (2) 30.
73. NASA TM X-73344, 1976, *SPS. Engineering and Economic Analysis Summary*.
74. NSS-P-76006 1975, *Space-Based Solar Power Conversion and Delivery Systems (Study) - Engineering, Analysis Data Compilation*. Grumman.
75. Graff W J & Huang C J 1976, *Solar Power Satellites: An Analysis of Alternatives for Transporting Material to Geosynchronous Orbit*. NASA Grant NGT 44-005-114.
76. Waldron R D, Erstfeld T E & Criswell D R 1979, The role of chemical engineering in space manufacturing, *Chemical Engineering*. 86 (4) 80.
77. Muench W 1978, Automatic fabrication of large space structures - the next step, *Proc AIAA Conf Large Space Platforms - Future Needs and Capabilities*. Los Angeles, Calif. September.
78. See e.g. NASA CR 151730, May 1978, *Space Construction Automated Fabrication Experiment Definition Study*. Vol. 2. General Dynamics Convair Division.
79. 1977, Reinforcements (fibrous), *Modern Plastics International*. 46. July.
80. Lubin G & Dastin S 1974, Carbon fibres can be cost effective - an example, *Proc Carbon Fibres - Their Place in Modern Technology*. Paper 37, The Plastics Institute, London.
81. Reinert H S & Meade L E 1976, Application of advanced composites in place of conventional materials, *SAMPE Quarterly*. 7, 8.
82. Dharan C K H 1978, Mechanical and thermal behaviour characterisation of composite materials for communications spacecraft, *Proc 2nd Int Conf on Composite Materials*. Met Soc AIME. 735.

83. Stonier R A & Hillesland H L 1974, Fabrication of a graphite/epoxy antenna for the Viking orbiter spacecraft, *Proc 19th Annual SAMPE Symposium*. April.
84. Kudo M, Nemoto Y & Wickert A N, Han C C & Ford D 1976, The design of the communications antenna for CS, *Proc. AIAA/CASI 6th Communications Satellite Systems Conference*. Montreal. April 5-8.
85. Robinson E Y, Stonier R A & Lofgren C L 1974, Development of a unique graphite/epoxy antenna sub reflector, *Proc Composite Materials: Testing and Design (Third Conf.)*. ASTM STP 546, 632.
86. Hamstad M A, Chiao T T & Patterson R G 1975, Fatigue performance of metal-lined graphite epoxy pressure vessels, *Composites*. 249.
87. Lark R F 1977, *Recent Advances in Lightweight Filament Wound Composite Pressure Vessel Technology*. NASA N77 33265.
88. Dunbar D R, Robinson A R & Kerrison R 1978, Graphite/epoxy booms for the space shuttle remote manipulator, *Proc 2nd Int Conf on Composite Materials*.
89. Randolph R E, Jenson L C & Martin W 1977, Graphite epoxy reflector support truss for Applications Technology Satellite (ATS). *Proc 4th SAMPE Nat Tech Conference*. Palo Alto. 209.
90. Corvelli N 1978, Metering trusses for a large telescope, *Proc 23rd Nat SAMPE Symposium*. Anaheim, Calif. May 2-4.
91. Goggin P R 1971, *The Thermal Expansion of Carbon Fibre Reinforced Resins*. AERE-R.6875.

N80-21426

PAINTS, POTTING COMPOUNDS AND SILICONE VARNISHES WITH LOW OUTGASSING IN SPACE ENVIRONMENT

J C Guillaumon & J Guillin

Centre National d'Etudes Spatiales, Toulouse, France

ABSTRACT

With a purifying process developed at the Centre National d'Etudes Spatiales we have produced paints, potting compounds and varnishes with low outgassing under vacuum. Paints were made from purified silicone - coated binders showing a good stability under U.V. irradiations. These paints may be cold coating (α/E about 0,20) or hot coatings (α/E about 1) : their thermo-optical and outgassing properties are studied ; environment tests (thermal cycling, moisture resistance and U.V. irradiations) are also carried out.

Silicone products usable as adhesives for bonding filters on solar cells, potting compounds for electronic modules mastics and isolation varnishes, etc... have been obtained by the same purifying process. Mechanical, optical and outgassing properties are also studied.

Keywords : paints, conductive paint, silicone, purified, outgassing

1. INTRODUCTION

The organic products, polymer resins are often used in space technology because their specific properties are practically without equivalent : mechanical and electrical properties and also lightness.

These products are used like potting compounds, adhesives, binders for paints.

Inconvenience of organic products is their outgassing under vacuum if they are compare to mineral products.

Indeed, many commercial resins do not satisfy selection criteria which are used : a material which is heated at 125° C under vacuum $\leq 10^{-6}$ torr during 24 h does not have a weight loss $> 1\%$ and the volatile condensable materials (V.C.M.) at 25° C are not $> 0,1\%$ of initial weight.

Sometimes, it is possible to reduce the weight loss and V.C.M. with particular cures : heating under high vacuum for example.

Our work has been to obtain low outgassing materials by purification of commercial resins presently silicone resins which do not need any particular treat-

ment to be used.

In this paper, we shall study purification influency on weight loss and V.C.M. and then we shall give the properties of obtained products.

2. PURIFICATION INFLUENCY ON VACUUM WEIGHT LOSS AND V.C.M.

We ascertain that the outgassing products of commercial resins are composed of uncleanness, light molecules and oligomers which may be eliminated by purification.

In the past we used distillation methods with a mechanical pumping system (ref. 1) but this did not give satisfactory results because resins had to be heated at 250° C which is very close to the silicones decomposition temperature.

IITRI (ref. 2,3) has purified RTV 602 of General Electric Co by this method. The distillation parameters were : temperature 150° C, pressure 10^{-6} torr and cure time 24 hours.

We have obtained different degrees of purity related to the number of cures with our method. We have studied influency of number of purification in relation to total weight loss (T.W.L.) and percentage of V.C.M. for RTV 141 produced by Rhone Poulenc.

The purified resin has been reticulated with 10 % of the weight of catalyst 141 B and the polymerisation has been made at room temperature.

The values of weight loss and V.C.M. are shown in Table 1. The curves concerning influency of the number of purification are given in appendix.

Table 1

Number of purifications	Total weight loss (%)	V.C.M. at 25° C (%)
0	1.27	0.40
1	0.69	0.22
2	0.43	0.12
3	0.33	0.08
4	0.41	0.05
5	0.37	0.05

These results show that total weight loss and V.C.M. are greatly decreased from the first purification and at the third cure we consider that the result is satisfactory. The next cures improve only slightly the results.

3. OBTAINED PRODUCTS

3.1 - Potting compounds and varnishes

We have used our purification method (three successive cures) for miscellaneous commercial products. Table 2 gives results and conditions of curing for T.W.L. and V.C.M. of purified or not purified resins and varnishes.

The purification does not bring modifications for their mechanical or electrical properties ; we have only observe an increase of viscosity of not reticulated resin.

3.2 - Paints

With two purified silicone binders we have prepared two white paints and one black paint.

3.2.1. PSG 120 FD CNES. The composition of this paint is the same that PSG 120 ASTRAL ; the binder is RTV 121 purified.

- thermo-optical properties

- . solar absorptance $\alpha_s = 0.17 + 0.02$
- . hemispherical emittance $\epsilon = 0.88$

- accelerated ageing

- . moisture resistance : after five days in a hot and humid atmosphere (90° C, 90 % H.R.) the coating shows no failures, not even tiny unstuck spots
- . thermal cycling under vacuum ($\leq 10^{-6}$ torr) : after 200 thermal cycling (cycle time 1 h 30) between - 100° C and + 100° C it has no cracking of the surface

outgassing test : three series of PSG 120 FD paint were prepared from three series of purified binders and application was made to thin sheets of aluminium alloy coated with P 128 ASTRAL primer. Results are shown in table 3 and it is possible to compare with PSG 120/P 128 cure at room temperature :

T.W.L. at 125°C = 1.3 % to 1.4 %
V.C.M. at 25°C = 0.2 %

Table 3

Drying conditions	T.W.L. (%)	V.C.M. (%)
120h/t.a.	0.70	0.03
120h/t.a.	0.79	0.05
120h/t.a.	0.80	0.03
120h/ta+24h/60°C	0.43	0.03
120h/ta+24h/60°C	0.49	0.03
120h/ta+24h/100°C	0.24	0.02
120h/ta+24h/100°C	0.24	0.03

. U.V. resistance :

after UV irradiation of 1000 esh at 25° C :

$$\Delta\alpha_s = 0.06$$

after UV irradiation of 1000 esh at 25° C then 72 h at atmospheric environment : $\Delta\alpha_s = 0.011$

3.2.2. S1 CNES paint. This paint has been completely conceived at CNES ; the binder is purified R4-3117. The paint properties applied without primer on aluminium alloy (AU4G) follow :

- thermo-optical measurements

- . solar absorptance $\alpha_s = 0.20 + 0.02$
- . hemispherical emittance $\epsilon = 0.86$

- accelerated ageing

- . moisture resistance : after five days in a hot and humid atmosphere (90° C, 90 % H.R.) the coating shows no failures; not even tiny unstuck spots

Table 2

Produit		Taux de dégazage en % (TWL)	Condensables en % (VCM)	Conditions de polymérisation
SYLGARD 182	sans purification	1.23	0.32	10pA + 1pB t.a.
	avec purification	0.36	0.09	10pA + 1pB 72 h/60° C
SYLGARD 184	sans purification	1.92	0.50	10pA + 1pB t.a.
	avec purification	0.39	0.08	10pA + 1pB t.a.
RTV 184	sans purification	0.81-0.83	0.23-0.33	A.R. ESTEC
	avec purification	0.32	0.06	10pA + 1pB t.a.
R 4-3117	sans purification	1.60	0.41	t.a.
	avec purification	0.46	0.008	t.a.
RTV 147/148	sans purification	1.10	0.28	t.a.
	avec purification	0.42	0.09	t.a.
RTV 121	sans purification	≈ 4	0.7 à 0.8	t.a.
	avec purification	2.17	0.15	t.a.

- thermal cycling under vacuum ($<10^{-6}$ torr) : after 200 thermal cycling (cycle time 1 h 30) between -100°C and $+100^{\circ}\text{C}$ it has no cracking of the surface
- climatic + thermal cycle accumulated tests : same conditions as above : it has no cracking of the surface
- outgassing tests : S1 paint with and without P 123 ASTRAL primer has been tested, both types dried during five days at room temperature
- without primer :
T.W.L. at 125°C = 0.09 %
V.C.M. at 25°C = 0.02 %
- with primer :
T.W.L. at 125°C = 0.45 %
V.C.M. at 25°C = 0.00 %
- U.V. resistance :
after UV irradiation of 1000 esh at 25°C :
 $\Delta\alpha_s = 0.15$
after UV irradiation of 1000 esh at 25°C then 72 h at atmospheric environment : $\Delta\alpha_s = 0.11$

3.2.3. S2 CNES paint. Like S1, this paint has been conceived at CNES. The binder is purified R4-3117. The properties of this black paint applied without primer on aluminium alloy (AU4G) follow :

- thermo-optical measurements
 - solar absorptance $\alpha_s = 0.97 \pm 0.02$
 - hemispherical emittance $\epsilon = 0.90$
- accelerated ageing
 - moisture resistance : after five days in a hot and humid atmosphere (90°C , 90 % H.R.) the coating shows no failures, not even tiny unstuck spots
 - thermal cycling under vacuum ($<10^{-6}$ torr) : after 200 thermal cycling (cycle time 1 h 30) between -100°C and $+100^{\circ}\text{C}$ it has no cracking of the surface
 - climatic + thermal cycle accumulated tests : same conditions as above : it has no cracking of the surface
 - outgassing tests : S2 paint with and without P 123 ASTRAL primer has been tested, both types dried during five days at room temperature
 - without primer :
T.W.L. at 125°C = 0.87 %
V.C.M. at 25°C = 0.04 %
 - with primer :
T.W.L. at 125°C = 2.92 %
V.C.M. at 25°C = 0.04 %
 - U.V. resistance :
after UV irradiation of 1000 esh at 25°C :
 $\Delta\alpha_s = 0.005$
after UV irradiation of 1000 esh at 25°C then 72 h at atmospheric environment $\Delta\alpha_s = 0.003$

3.2.4. CNES white conductive paint. This paint is presently being developed and it is not quite qualified. The binder is purified R4-3117. The properties of this paint applied without primer on aluminium alloy (AU4G) are the following :

- thermo-optical measurements
 - solar absorptance $\alpha_s = 0.28 \pm 0.03$
 - hemispherical emittance $\epsilon = 0.82$
- electrical properties

DERTS has measured surface resistivity and surface potential following specifications described in ref. 4

- surface resistivity : this data was obtained with 1, 10 and 40 Volts at atmospheric pressure and under vacuum.
The value R is expressed in Ω/\square (table 4).

Table 4

Conditions	1 V	10 V	40 V
A l'air	2.4	2.4	2.4
24 h sous $P < 10^{-6}$ torr	2.2	2.2	2.2
48 h sous $P < 10^{-6}$ torr	2.4	2.4	2.4
72 h sous $P < 10^{-6}$ torr	2.4	2.4	2.4
5 jours sous $P < 10^{-6}$ torr	2.1	2.1	2.1

- surface potential : electron beam energies used during irradiations were 10 KeV and 20 KeV of intensity of 0.1 nA and 2 nA. Surface potential are given in the table 5.

Table 5

Energy (keV)	Intensity (nA/cm ²)	Surface potential
10	0.1	$P < 10\text{ V}$
20	0.1	$P < 10\text{ V}$
10	2	$P < 10\text{ V}$
20	2	$P < 10\text{ V}$

- outgassing test
T.W.L. at 125°C = 0.08 % (room temp. cure)
V.C.M. at 25°C = 0.01 %

- U.V. resistance
after UV irradiation of 1000 esh at 25°C :
 $\Delta\alpha_s = 0.12$
after UV irradiation of 1000 esh at 25°C then 72 h at atmospheric environment : $\Delta\alpha_s = 0.08$

4. CONCLUSIONS

In this paper we have shown that it is possible to obtain low outgassing products by purification before reticulation of commercial silicone resins. This purification does not modify the properties of polymerised resins.

Paints prepared from purified binders have good thermo-optical properties and stability under accelerated ageing with the exception of S1 and white conductive paint which are degraded during U.V. irradiation.

We are studying the replacement of binder R4-3117 in order to improve the U.V. stability for these paints.

For white conductive paint we are searching to reduce solar absorptance by using other pigments and at which time we shall qualify this paint.

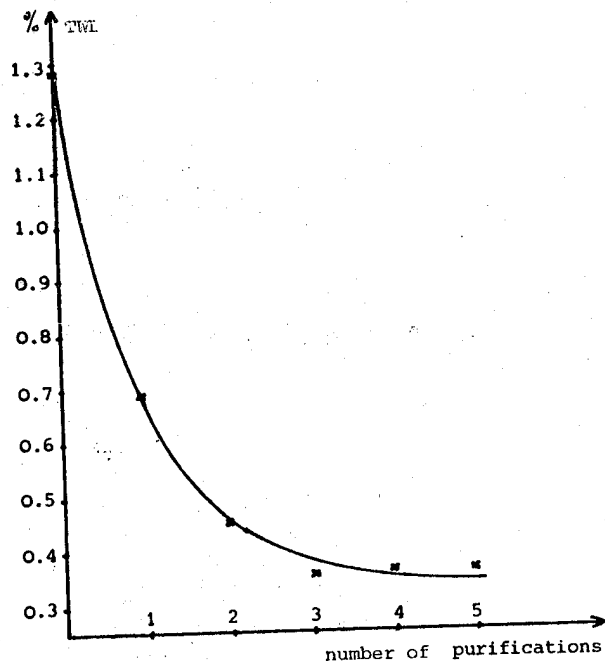
REFERENCES

1. Guillaumon J.C., Guillin J. 1974, Réduction du dégazage des silicones par purification, *Colloque international "Evaluation de l'Action de l'Environnement Spatial sur les matériaux"* Toulouse 17-21 Juin 1974, p. 271-280
2. Triannual Report IITRI U-6002-90, July 1970, *Development of Stable Thermal control coatings*, by Gilligan J. and Zerlaut G.
3. NASA TN D-6892, August 1972, *Achievement of a low-outgassing white paint system for spacecraft thermal control*, by Seidenberg B., Park J.J., Clatterbuck C.
4. Document ONERA/CERT/DETS/CR/REV/02

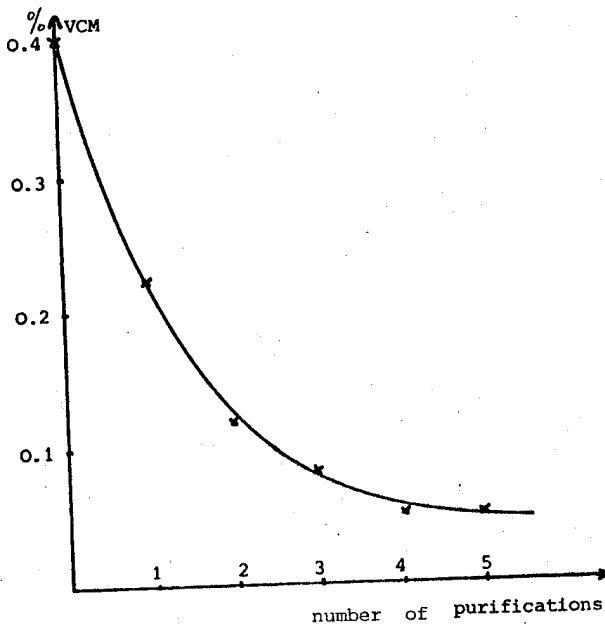
ANNEXE

RTV 141 - INFLUENCY OF NUMBER OF PURIFICATIONS

1. Total weight loss



2. Volatile condensable materials



DISCUSSION

J. Dauphin (ESA/ESTEC) :

Do you consider NDT methods to protect against accidental misprocessing which are probably the main cause of accident on TWT's potting ?

M. L. Minges:

At the current time the appropriate term would be carefully process and quality control (QC) during TWT fabrication followed by an extensive burn-in, thermal vacuum and electrical performance tests rather than 'NDT'. Some of the issues we will be studying include :

- 1) Simplifying the construction procedures and making the critical materials more 'forgiving' in terms of process control.
- 2) Trying to understand and remove latent defects in the materials that do not show up early as 'infant mortality' effects. What to expect for the long term (thousands of hours of operation) is a critical question to be addressed in our new programme.
- 3) NDT methods will be considered in connection especially with such issues as mentioned in (2) above.

R.L. Moss (Ford Aerospace) :

Are you looking at any new materials for potting TWT's ? If so, which ones ?

M. L. Minges:

As I mentioned in the talk, the first activity on our new programme is assembling an analytical modelling scheme which deals adequately with the combined effects of mechanical, thermal and electrical variables.

- For the near term (2-3 years) we expect not only modifications of state-of-the-art materials will be practical (e.g. perhaps change in type and amount of filler materials to better balance mechanical-thermal-electrical properties).
- For the longer term (3-5 years), we will consider other programmes to develop truly new materials. High adhesion will surely be an important feature of any such new material.

D. Verdin (Harwell) :

In polymer films coated with conductive oxides giving low surface potentials on electron irradiation, what is the fate of incident electrons which have sufficient energy to penetrate below the surface and build up sub-surface charged layers?

W. L. Lehn:

A. Meulenbergh at COMSAT has proposed a buried sub-surface charge layer. Electret is a known classical material. If the sub-surface charge breaks down, 'treeing' and clouding in FEP Teflon, for example, will occur with loss in optical and material properties. In addition, if sub-surface breakdowns occur, material will be ejected and

constitute a potential contaminant to nearby surfaces. People at USAF ESD at Cambridge feel that very high dielectric fields can easily be built up in most dielectric materials (10^6 V) under charging conditions which can then discharge by more than one route. That, in addition to surface conductivity and bulk conductivity, is really required to prevent charge build-up and subsequent discharging.

S. Bosma (ESTEC) :

What will be the future policy of AFML, considering spacecraft charging? Will AFML still support research activities in this field of investigation?

W. L. Lehn:

AFML will continue to sponsor work in the spacecraft charging materials area, dependent upon relative availability of funds and priorities. This area of spacecraft contamination is receiving increased attention and therefore the funds available for charging are lower.

F. Levadou (ESTEC) :

What is the effect of temperature on the electrical conductivity of conductive glass?

W. L. Lehn:

This effect has not been measured but it would be expected to be reduced on cooling. The materials were used in a 'cold' application and the electrical conductivity would be lower than in other applications.

W. Schaefer (MBB) :

Is the electrical conductivity of the glass under development achieved by means of a kind of doping, and if so does this doping not reduce the stability of the glass for high-energy space radiation?

W. L. Lehn:

The glass being developed is a doped lithium borosilicate. More than one dopant is added. The high-energy space radiation stability of the final formulation is expected to be good, but will have to be evaluated before the material can be approved for application. There is still a significant amount of development to be done before any applications can be seriously considered.

D.K. Davies (ERA Technology Ltd) :

1) Some of the coatings show a two-order increase in resistivity on storage. Do you have an explanation?

2) Aluminised polymer films are degraded on electron bombardment owing to discharge erosion of the conductive layer. Do you envisage similar problems with the metal-oxide conductive layers?

W. L. Lehn:

1) Early samples showed an increase in resistivity, but later specimens showed much lower changes. Measurement techniques are usually only $\pm 10^2$ in the measurements being made. Sample preparation is important. The chamber must be conditioned when changing from one coating to another.

2) The longest instability of IO and ITO coatings under electron irradiation have not been fully investigated, but will surely have to be examined before full material qualification. There is an adhesion problem of ITO and IO to FEP Teflon at this time and this is of greater concern.

L.P. Preuss (NBB) :

Can you give any information about crack formation in the ITO on polymer foils especially on FEP Teflon at elevated temperatures (e.g. above 80°C)? If so, how can such cracks be avoided?

W. L. Lehn:

Crack formation has not been specifically investigated, particularly since the coatings are transparent. The ITO and IO on FEP Teflon are prone to removal by handling and rubbing, but adhere well to Kapton. This will have to be examined.

D.F. Hall (The Aerospace Corp.) :

You stated in your paper that Astroquarts exhibits low charging levels in ground tests. I believe such results have been obtained at several laboratories using the customary $j = 10^{-9}$ amp/cm² levels of incident electron beam current density. This intensity is usually taken as representative of maximum arrival rates to be encountered during magnetic substorms near geosynchronous altitude. However, the Satellite Surface Potential Monitor (SSPM) portion of the SCI experiment on PD8-2 (SCATHA) has measured charging levels of several

kilovolts on the Astroquarts sample when j was in the 10^{-10} to 10^{-11} amp/cm² range. Subsequently similar charging levels on Astroquarts have been demonstrated at the Aerospace Corp. in laboratory simulations at these levels (which are probably more typical of geosynchronous orbit current densities).

In my view, these space and ground results demonstrate the need to vary j over the 10^{-12} to 10^{-9} amp/cm² range in dielectric charging measurements associated with geosynchronous spacecraft materials test programmes.

J. Dauphin (ESA) :

Could glass reinforced by carbon fibre solve the problem of anisotropy of expansion coefficient of reinforced materials and the absorption of water leading to deformation?

D. H. Bowen:

The use of glass as a matrix certainly reduces the internal stresses resulting from differential expansion coefficients of fibre and matrix and the lower expansion coefficient of the glass is effective in reducing the anisotropy in expansion behaviour, compared to resin composites. Although there are no experimental data, reinforced glasses would not be expected to show moisture absorption effects. The same could be said of metal matrix composites on carbon/carbon composites.

I. Stenzenberger (Technochemie) :

Is there any information available about property changes of neat resins which are used for graphite composites?

D. H. Bowen:

The literature on hydrothermal degradation of composites has been reviewed recently under ESTEC contract and this report contains references to the effects of moisture on bulk resins.

SESSION III

CLEANLINESS & CONTAMINATION PRACTICE

Co-chairmen: M.McCargo & H.E. Hintermann

COATING AND CONTAMINATION EXPERIMENT ON LDEF

L Preuss & W Schäfer

Messerschmitt-Bölkow-Blohm GmbH, Ottobrunn, Germany

ABSTRACT

Geosynchronous satellites in general will have lifetimes of 7 years and more. Such mission periods require a reliable thermal control based on space stable SSM. Flight measurements showed higher α_s -degradation than measured on the ground. This can be explained reasonably assuming in flight secondary degradation effects additionally to colour centers formation. By means of a flight experiment on the LDEF and additional ground experiments degradation of thermal coatings (SSM etc.) developed in the F.R.G. shall be investigated. The flight experiment as well as the ground experiment test samples and values to be measured will be presented.

Keywords: degradation, SSM, combined effects, contamination, surface charging

public of Germany shall be measured, the coatings under investigation shall be qualified. Additional accompanying ground experiments shall help to clarify the influence of secondary effects on the total α_s -degradation, especially the influence of contamination and/or surface charging (surface charging effects are negligible small in the low altitude Earth orbit of LDEF). By means of the four ground experiments

- EUV-investigation
- near UV solar simulation
- Contamination experiment
- Investigation of charging effects

each of the different effects contributing to the total α_s -degradation in a geostationary orbit simultaneously (combined effects) shall be investigated separately.

1. INTRODUCTION

Advanced communication satellites in general will have lifetimes of 7 years and more. Such mission periods require a reliable thermal control of the satellites which will be based on longterm, space stable thermal control coatings with low α_s , ϵ_H -ratio (α_s = solar absorptance, ϵ_H = hemispherical emittance). Even the so called Second Surface Mirrors (SSM), the most stable low α_s , ϵ_H -coatings yet known, showed much higher α_s -degradation in flight than expected and measured on the ground. A reasonable explanation of this discrepancy between flight and ground measurements can only be given assuming in flight secondary degradation effects caused by contamination and differential charging of the SSM surface as well as by a combination of both effects in addition to the colour center formation in the dielectric material of the SSM itself. By means of a suitable flight experiment on the LDEF (Long Duration Exposure Facility) the critical degradation effects of selected thermal control coatings, especially of flexible SSM, developed in the Federal Re-

2. EXPERIMENT OBJECTIVE

The objective of the coating and contamination experiment is twofold:

1. Determination of the combined effects of
 - UV-irradiation especially
 - o near UV (down to 1700 Å)
 - o far UV (EUV down up to some 100 Å)
 - Outgassing and resulting contamination
 - differential charging
- on special thermal coatings (SSM) and solar cells with and without Conductive Coatings (CC) developed in the F.R.G. with the objective of the preparation of

- Design criteria
- Techniques and testing methods
- 2. Space Qualification of all coatings under investigation

3. FLIGHT EXPERIMENT

3.1 Components to be investigated

Within the framework of a development program sponsored by the BMFT/DFVLR-BPT various coatings have been developed (Ref. 1 and 2) which shall be tested and flight qualified by means of the MBB LDEF-experiment defined in Ref. 3.
These are:

- flexible SSM consisting of 125 μm thick FEP-Teflon foil with
 - o Ag-Reflector and Inconel-protection-layer on the rear side
 - o Interference-Filter ($\text{Al}_2\text{O}_3/\text{ZnS}$ -layers) on the front face
- flexible SSM consisting of 125 μm thick FEP-Teflon foil with
 - o Ag-Reflector and Inconel-protection-layer on the rear side
 - o Interference-filter ($\text{Al}_2\text{O}_3/\text{ZnS}$ -layers) above a 1 μm PMMA-intermediate-layer on the front face
 - o doped In_2O_3 -layer about 100-150 \AA thick on the Interference-filter surface
- Cobalt black selective absorbers (CoS_x)
- Solar cell modules with doped In_2O_3 -layers on the coverglasses, electrically connected

In addition some well known reference samples shall be tested to allow a good interpretation of the flight results.
Reference components to be tested are:

- flexible SSM consisting of 125 μm thick FEP-Teflon foil with
 - o Ag-reflector and Inconel-protection-layer on the rear side
- rigid SSM (OSR) consisting of 200 μm thick fused silica platelet with
 - o Ag-reflector and MgF_2 -protection-layer on the rear side.
- Solar cell module
- black paint Chemglaze Z 306 (sun sensor)

3.2 Measurements

Following values shall be measured during the LDEF-flight (measurement initiate and sequence will be described in chapter 3.3):

- the temperature of the test samples to determine the α_x -degradation as a function of mission time and UV-radiation dose
- the electrical resistance of the doped In_2O_3 -layers to determine the electrical degradation as a function of mission time and UV-radiation dose
- the short circuit current of the solar cell modules as a function of temperature, mission time and UV-radiation dose
- the amount of deposited contaminants on the SSM by means of the measurement of Quartz Cristal Microbalance (QCM)-beat frequency as a function of mission time

3.3 Experiment design

3.3.1 Mechanical design: The mechanical design of the complete experiment is shown in Figure 1. In the experimental tray the Experiment Exposure Control Canister (EECC) with the active test samples is arranged on the right side. Here the EECC is open (measuring position) exposing the samples to the space environment. On top of the left side of the tray a cover sheet with larger passive test samples (same type like the active samples) is attaches by means of bolts. The electronic box and the batteries are attached under the cover sheet and the bottom plate respectively. The active test samples, that means samples which shall be measured during the flight, are

- α_x -degradation measurement samples
 - o 2 solar cell modules (4 cells each) with Conductive Coating (CC) on the cover glasses, electrically connected
 - o 1 solar cell module (4 cells) without CC
 - o 2 SSM with Interference Filter (IF)
 - o 2 SSM with IF + CC
 - o 1 SSM without IF
 - o 2 CoS_x -Samples
 - o 1 OSR (OCLI)
 - o 1 Chemglaze Z 306-sample (black paint)
- Contamination measurement samples
 - o 1 QCM cristal surface with thin Al_2O_3 -layer (outer surface of SSM with IF)
 - o 1 QCM cristal surface with thin In_2O_3 -layer (outer surface of SSM with CC)

The active test samples are held in suitable calorimeters.

The passive test samples, (sample size: 90 x 100 mm except solar cell module) that means samples which will be measured only before launch and after retrieval on the ground, are:

- 3 solar cell modules (4 cells each) with CC on the coverglasses electrically connected
- 1 solar cell module (4 cells) without CC
- 4 SSM with IF
- 4 SSM with IF + CC (between FEP Teflon foil and IF a very thin PMMA-layer)
- 1 SSM with IF + CC (without PMMA-layer)
- 1 SSM without IF
- 4 CoS_x-samples
- 1 OSR-sample (OCLI)
- 1 Chemglaze Z 306-sample (black paint)

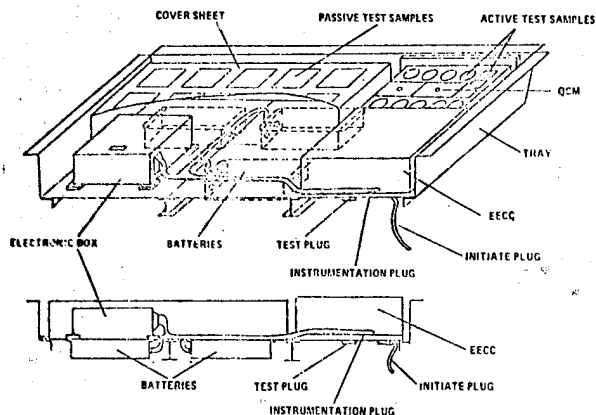


Figure 1. LDEF Flight Experiment S 1002 Mechanical Design

The weight break down of the S 1002 Experiment is shown in Table 1.

The total weight of 68.9 kg is well below the specified upper weight limit for the tray of 77.6 kg. The other LDEF System guidelines given in Ref. 4 also will be fulfilled by the experiment (e.g. lowest predicted resonance of the experiment mounted on a firm base shall be > 50 Hz).

3.3.2 Thermal design A passive thermal control concept has been selected so that a heat path from the outside to the inside of the LDEF exists as desired by NASA LDEF

COMPONENTS	WEIGHT (G)
1 EECC	32900
1 CALORIMETER SUPPORT	934
1 QCM-CALORIMETER	168
9 COATING-CALORIMETERS	961
3 SOLAR CELL-CALORIMETERS	166
1 BOTTOM PLATE	11463
1 COVER + COATING SUBSTR.	4496
1 ELECTRONIC BOX	5837
1 BATTERY 7,5 V	3490
1 BATTERY -28 V	3400
1 BATTERY 28 V	3400
2 QCMs	227
CABLING	1133
COATINGS	116
MULTILAYERINSULATION	200
TOTAL WEIGHT	68891

Table 1. S 1002 Experiment Weight Break-down

project office. A detailed thermal design analysis conducted proved the feasibility of the concept. Table 2 shows the most essential coating data of the 48 node model used for the design analysis and the thermal coatings selected respectively. Following insulation measures have been taken in addition:

- multilayer insulation between
 - o coating support and housing of coating calorimeters A and B
 - o solar cell module support and housing of solar cell module calerimeter
- spacers between
 - o coating support and guard ring of coating calorimeters A and B
 - o guard ring and housing of coating calorimeters A and B
 - o solar cell module support and housing of solar cell module calorimeters
 - o electronic box and bottom plate

The design cases for the thermal design are given in Table 3.

Table 2. Most essential coating data of the selected thermal coatings
(48 node model)

COATING DISTRIBUTION

NODE NO.	NODE DESCRIPTION	COATING	$\alpha_{EXT.}$	$\epsilon_{EXT.}$	$\epsilon_{INT.}$
			COLD CASE -4 °C COLD CASE -15 °C	HOT CASE 50 °C HOT CASE 66 °C	
1B	LDEF-INTERIOR				
2B	LDEF-STRUCTURE				
3	TRAY SIDE OPP. 7	ANODIZED Al	.3	.15	.15
4	8				
5	9, 10				
6	11				
7	BOTTOM PLATE EECC DRAWER	INT. PARTS	.2	.75	.9
8	EECC CANISTER	BLACK PAINT	.2	.75	
9	7.5 V BATTERY	EXT. PARTS	-	.57	
10	E-BOX	ANODIZED Al	-		
11	+28/-28 V BAT.				
12	EECC CANISTER RAD. SHIELD	ANOD. Al / Al	.3	.16	.06
13	EECC PRESS. PL. RAD. SHIELD	ANOD. Al / Al	.3	.16	.05
14	EECC CANISTER	MOST ANOD. Al	.2	.75	.75
15	EECC DRAWER			.05/.75	.05-.86
16	EECC PRESSURE PLATE			.75	.3-.75
17	7.5 V BATTERY	BLACK PAINT	-	-	.9
18	-28 V BATTERY		-	-	
19	+28 V BATTERY		-	-	
20	ELECTRONIC-BOX	INT. PARTS BL. PAINT EXT. PARTS Au	-	.07	
21	COVER TOP	ANOD. Al	.5	.56	.56
22		ANOD. Al, SSM	.36	.62	
23		ANOD. Al, SSM	.36	.63	
24		ANOD. Al, CoS _x /SOL. CELLS	.67	.41	
25		ANOD. Al, BL. PAINT	.56	.6	
26	4 SIDES	ANOD. Al	.5	.56	
27					
28					
29		ANOD. Al	.27	.7	.7
30	CALORIM. SUPP. EXT. PART	ANOD. Al	-	-	.7
31	CALORIM. SUPP. INT. PART		.1	.74	.28
32	QCM-CALORIMETER	EXT. PART SSM INT. PART Al-SiO _x	.25	.08	.08
33	QCM MEAS. CRYSTAL	ZnS	.4	.76	.28-.6
34	EXT. PARTS OF 5 CALORIM.	SSM, BL. PAINT OSR, SOL. CELLS	-	-	.05-.75
35	INT. PARTS OF 5 CALORIM.	Ni, KAPTON, Al-SiO _x	-	-	
36	COAT. CAL. A COAT. SUPP.	SSM/Al-SiO _x	.1	.74	.28
37	GUARD RING	SSM/Al-SiO _x	.1	.74	.28
38	HOUSING	PASSIV. Ti	.78	.18	.18
39	MLI TOP	Ni	-	-	.05
40	MLI SUPP. PL.	Al-SiO _x	-	-	.28
41	COAT. CAL. B COAT. SUPP.	CoS _x /Au	.96	.09	.03
42	GUARD RING	CoS _x /Au	.96	.09	.03
43	HOUSING	PASSIV. Ti	.78	.18	.18
44	MLI TOP	Ni	-	-	.05
45	MLI SUPP. PL.	Al-SiO _x	-	-	.28
46	SOL. CELL CAL. COAT. SUPP.	SOL. CELLS/KAPTON	.75	.79	.6
47	HOUSING	BL. PAINT/Al-SiO _x	.97	.9	.28
48	MLI TOP	KAPTON	-	-	.75

Table 3. Design Cases for the S 1002 Thermal Design

DESIGN CASES

● COLD CASE NON-OPERATING

- LDEF INTERIOR, NODE 1B: -4°C
- LDEF STRUCTURE, NODE 2B: -23°C
- EARTH RADIATION ACC. REF. 4, TABLE 2.2, SURF. 3 & 9
- SOLAR RADIATION ACC. REF. 4 "THE DIRECT SOLAR EXPOSURE OF LDEF", FIG. 9, SURFACES 4/8, 2/10 = 0°

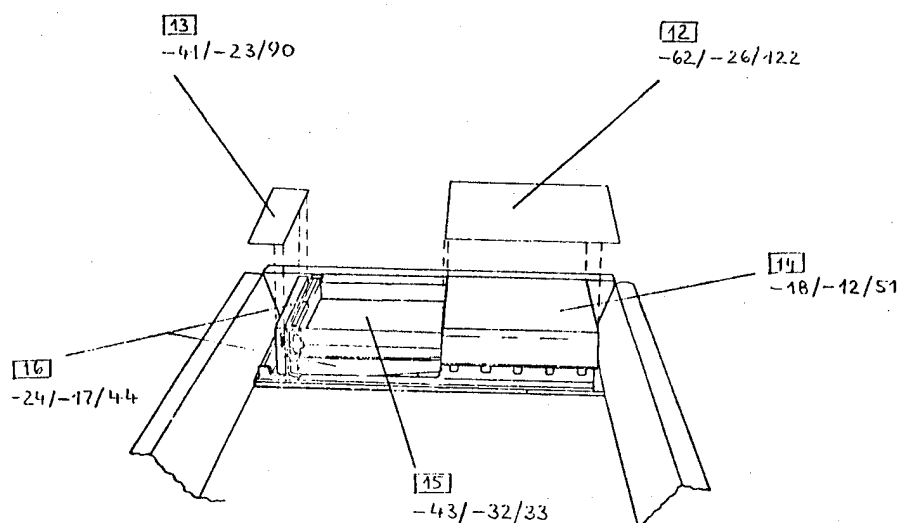
● COLD CASE OPERATING

- LDEF INTERIOR, NODE 1B: -7°C
- LDEF STRUCTURE, NODE 2B: -15°C
- EARTH RADIATION ACC. REF. 4, TABLE 2.2, SURF. 3 & 9
- SOLAR RADIATION ACC. REF. 4, "THE DIRECT SOLAR EXPOSURE OF LDEF" FIG. 9, SURFACES 4/8, 2/10; = $-30^{\circ}, 30^{\circ}$

● HOT CASE OPERATING

- LDEF INTERIOR, NODE 1B: 50°C
- LDEF STRUCTURE, NODE 2B: 66°C
- EARTH RADIATION ACC. REF. 4, TABLE 2.3, SURF. 3 & 9
- ALBEDO RADIATION ACC. REF. 4, TABLE 2.3, SURF. 3 & 9
- SOLAR RADIATION ACC. REF. 4, TABLE 2.3, SURF. 3 & 9

Figure 2 and 3 show some of the predicted orbit temperatures for the 3 critical design cases defined in Table 3.

Figure 2. Predicted Orbit Temperatures ($^{\circ}\text{C}$) for the EECC

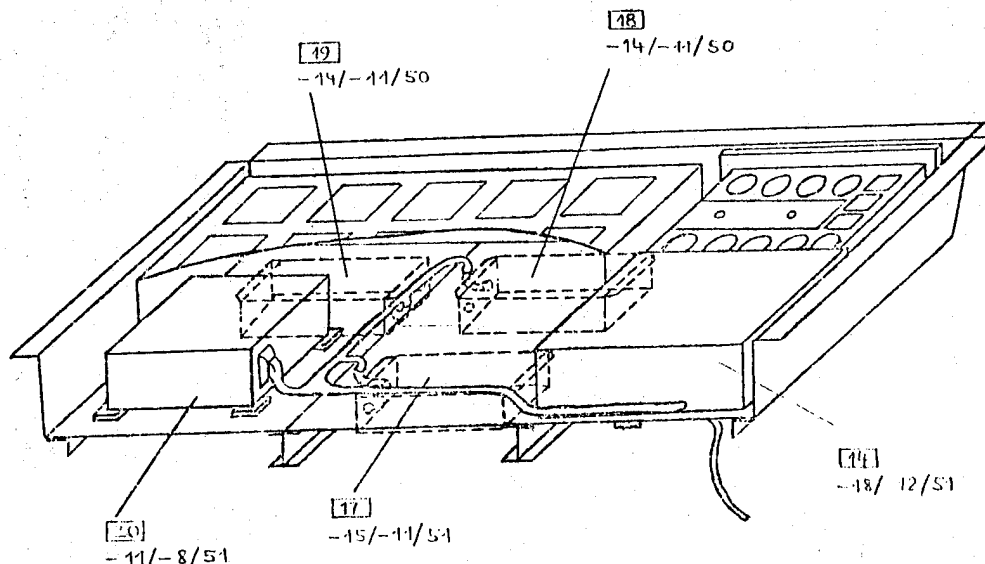


Figure 3. Predicted Orbit Temperatures ($^{\circ}\text{C}$) for the Batteries and the Electronic Box

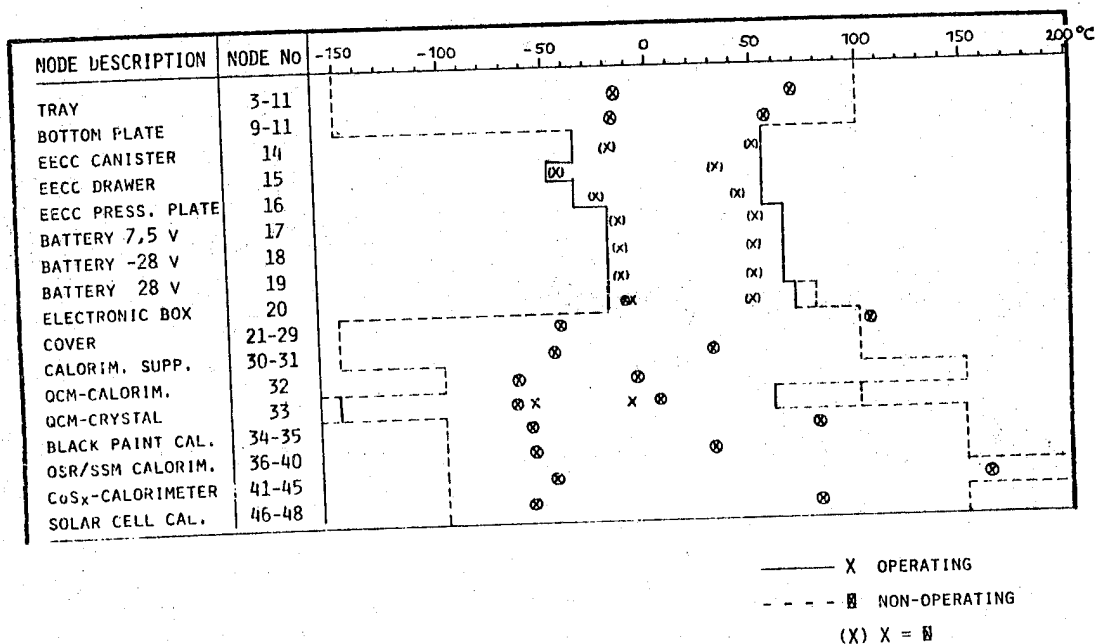


Figure 4. Temperature Comparison Prediction vs. Specification

Figure 4 gives a comparison between the predicted and the specified temperatures. The dotted line represents the specified non operating temperature limits. As can be seen all temperatures remain within the specified temperature ranges except the uncritical cover in the non

operating case.

The analysis also shows a suitable behaviour of the different calorimeters used within the experiment.

3.3.3 Electrical design. Figure 5 shows the electronic block diagram. On the left side of the diagram the 4 kinds of scientific measurements executed by the active part of the experiment can be seen, that means:

- solar cell short circuit current (2 x)
- temperature measurements (32 x)
- surface resistance measurements (2 x)
- beat frequency of QCM's (2 x)

In addition to these measurements some housekeeping data will be recorded like voltages and temperatures (not shown in the diagram).

From the solar cell short circuit current a threshold signal is generated which starts the measurement cycle always at a solar intensity of 0.5 solar constants when the sun is rising. All the analog signals get multiplexed by the analog multiplexer (MUX) and converted into digital signals (A/D). These signals and those from the QCM-frequency counters and the mission time counter get multiplexed by a digital multiplexer (MUX) and will be recorded by being programmed into an "Electrically Alterable Read Only Memory" (EAROM).

The power required will be supplied by three batteries:

- two batteries for the measurement electronics which is only activated for short measurement cycles (initiated by the threshold signal).
- one battery which drive the timer continuously up to a 1 year mission.

The timer activates the threshold electronics at predestinated times as shown in Figure 6.

These are 3 h, 6 h, 12 h, 1 day and so on up to 32 days and then every 32 days up to 256 days after the opening of the BECC drawer which happens 8 days after release of LDEF into the orbit.

Depending on the launch date there can be a period of about 18 days where the maximum solar intensity will be less than 0.5 solar constants. If the timer wants to start the experiment at such a time, he will not get a threshold signal. The timer then waits 8 days and tries again to start a measurement cycle. This procedure will be continued (probably not more than two times) until there is enough sun intensity to start and execute a measurement cycle.

The measurement cycle consists of 8 measurements (64 data words each) every 2.8 minutes. After the completion of the 8th measurement of each cycle the recording will be stopped. It will be continued with the QCM-beat frequency measurement 48 minutes later. This is necessary in order to have a period without sun where the space facing quartz of the QCM cools down to the same temperature as the reference quartz.

The dotted line shows the maximum sun intensity diagram. The varying sun intensity does not create steady state temperatures as they are necessary for the evaluation of coating degradation. These values only can be derived by calculation with the results from transient temperature measurements near the maximum sun intensity (Therefore 8 measurements per cycle).

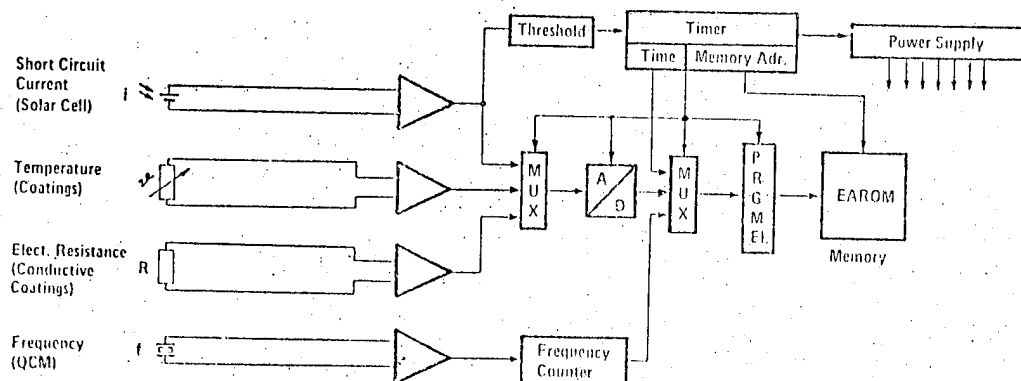
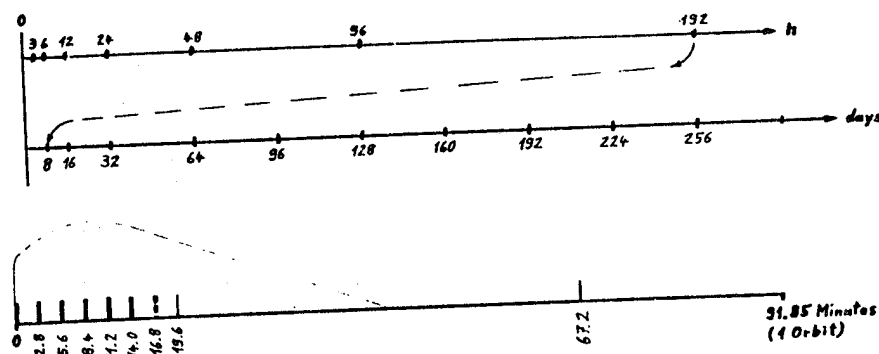


Figure 5. Electronic Block Diagram of the S 1002 LDEF Flight Experiment



$$8 \text{ Bit} \times 64 \text{ Words} \times 8 \text{ Measurements} \times 16 \text{ Meas. Cycles} = 65\,536 \text{ Bit}$$

$$2^6 \times 2^3 \times 2^4 = 8 \text{ k Bytes}$$

Figure 6. Measurement Time Diagram of the S 1002 LDEF Flight Experiment

4. GROUND EXPERIMENTS

Following accompanying ground experiments will be conducted:

1. EUV-Investigation at the IPW (Fraunhofer Gesellschaft)
 - o irradiation of all sample types of the Flight Experiment with the simulated sun radiation in the far UV-range (below 1700 Å including the most essential lines like the Lyman-α-line) and in-situ measurement of α_s (α_λ)
2. Near UV Solar Simulation (MBB)
 - o irradiation of all sample types of the Flight Experiment with the simulated sun radiation in the near UV-range (down to 1700 Å) and in-situ measurement of α_s (α_λ) and el. resistivity (if applicable)
3. Contamination Experiment (MBB)
 - o measurement of the Volatile Condensible Material as a function of sample temperature (only SSM and solar cells)
4. Investigation of Charging Effects (NASA/LeRC - MBB)
 - o determination of sample charging, surface potential and discharge characteristic (only SSM and solar cells)

5. DEVELOPMENT STATUS

Figure 7 shows the milestone plan for the LDEF-Experiment S 1002. As can be seen the flight experiment is in the integration phase which will be completed end of October 1979. After qualification tests the experiment will be stowed at MBB under clean conditions (dry Nitrogen atmosphere). Final functional tests at MBB will be conducted before delivery to NASA KSC to verify that experiment has survived without damage the long stowage period. Test and measurement facilities for the EUV- and contamination experiments not available at the begin of the program are designed, facilities assembly is near completion, so that all ground experiments can be started begin of 1980. A pretest program in the EUV-irradiation facility with the developed flexible SSM will deliver additional data concerning UV-stability and will ensure the proper function of the facility. This pretest program will be finished end of February 1980.

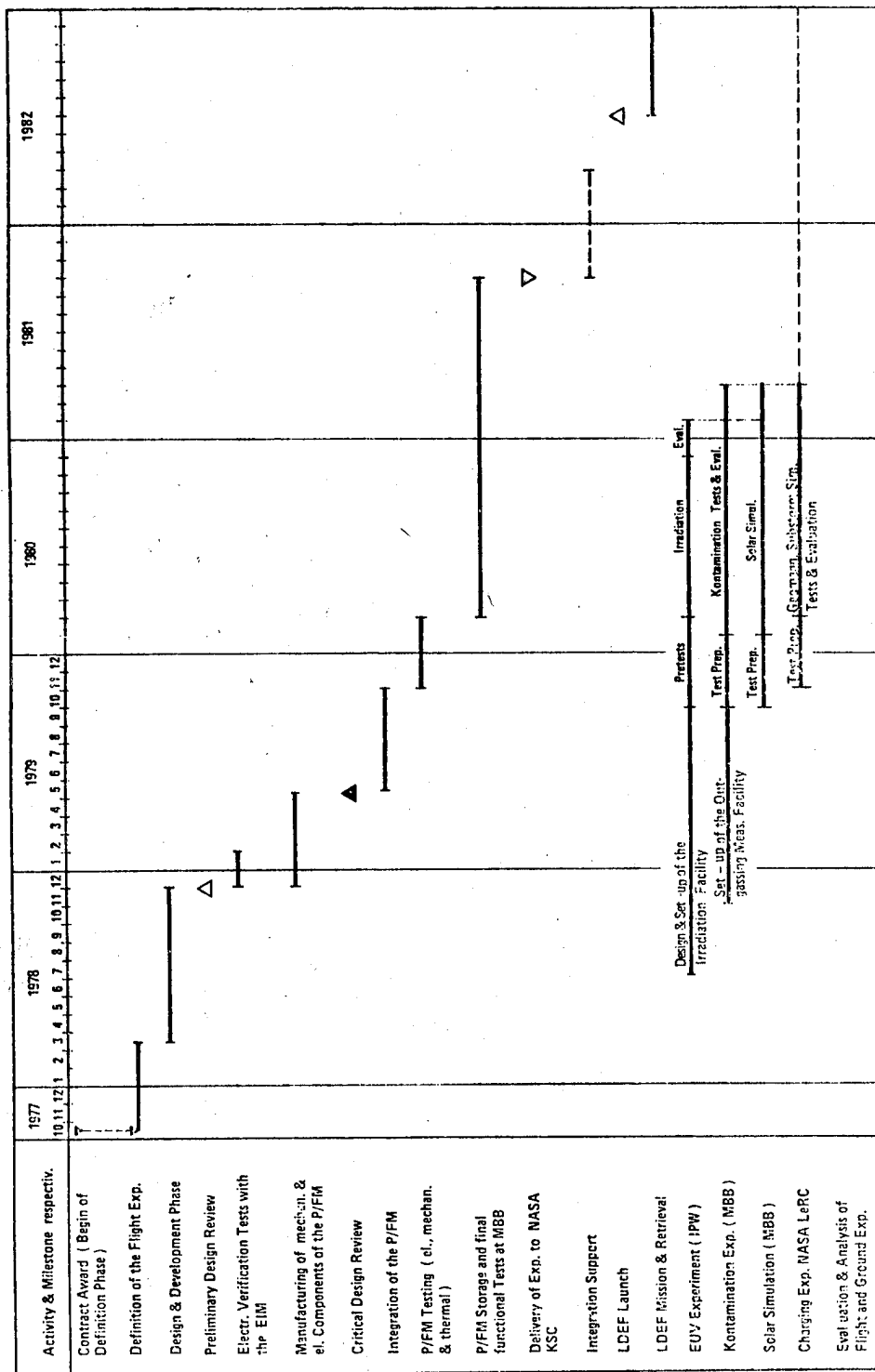


Figure 7. MBB - LDEF Experiment (S 1002) Time Schedule

6. REFERENCES

1. Behrendt A, Jungk H O, Klopfer A, Scholz H 1977, Entwicklung und Untersuchungen von schwarzen Beschichtungen zur Thermalkontrolle, II. Phase, Schlußbericht PHILIPS GmbH, DFVLR-BPT-Vertrag: 01 TB 065 A - Z 12 WRT 2074
2. Husmann K O, Preuss L et al 1980, Qualifikation flexibler SSM hoher Langzeitstabilität, 3. Phase, Schlußbericht MBB, DFVLR-BPT-Vertrag: 01 TB 067 B - AK/RT - WRT 2076
3. Goedtke P et al 1978, Raumflugerprobung von Oberflächenbeschichtungen (LDEF), Detaillierte Definition des MBB-LDEF-Experiments, Abschlußbericht MBB, DFVLR-BPT-Vertrag: 01 TD 037 - AK/RT - WRT 2077
4. LDEF Project Office 1978, LDEF Experimenter Users Handbook, NASA LaRC Hampton, Virginia
5. Goedtke P, Husmann K O, Popp H, Schäfer W 1977, Entwicklung und Herstellung von Oberflächenschichten mit langer Lebensdauer für die Thermalkontrolle von Raumflugkörpern, 2. Phase, Schlußbericht MBB, DFVLR-BPT-Vertrag: 01 TB 055 A - V 12 WRT 2074

ACKNOWLEDGEMENTS

The authors would like to express their gratitude to the BMFT/DFVLR-BPT which sponsored several development programs at MBB under the DFVLR-BPT-Contract Nrs. 01 TD 037 - AK/RT - WRT 2077, 01 TB 067 B - AK/RT - WRT 2076, 01 TD 048 A - AK/RT - WRT 2077 and 01 TD 019 B - AK/RT - WRT 2079. Large portions of the data for this paper resulted from this programs.

Thanks are due to P B Seidl from the IPW and G-U Folgner, P Goedtke, Dr. K O Husmann from MBB who made essential contributions especially to the ground experiments. Recognition also is due to W Mehltreter who developed the electronics and to G Stickel responsible for the PA of the flight experiment.

N80-21428

PRELIMINARY FLIGHT RESULTS FROM P78-2 (SCATHA) SPACECRAFT CONTAMINATION EXPERIMENT*

DF Hall & AA Fote

The Aerospace Corporation, El Segundo, California, USA

ABSTRACT

The ML12 experiment was launched on January 30, 1979, on United States Air Force (USAF) Space Test Program P78-2 spacecraft, SCATHA (Spacecraft Charging at High Altitudes). It was designed to determine if spacecraft charging contributes significantly to the rate that contaminants arrive at exterior spacecraft surfaces.

The experiment consists of two mass detectors and two trays of calorimetrically mounted thermal control coatings samples. "Quick-look" data from the first 6 months on orbit indicate that the vehicle has gradually accumulated a mass, which has not yet reached a magnitude sufficient to measurably affect α_s of the spacecraft surface materials. However, two black paint samples appear to have undergone bleaching, and two fabric samples have experienced some transitory degradation.

Keywords: Spacecraft Contamination, Spacecraft Charging, Spacecraft Thermal Control Coatings, SCATHA.

1. INTRODUCTION

During the last decade, malfunctions of spacecraft operating near geosynchronous altitude have been attributed to noise pulses generated by arcing between differentially charged members of the spacecraft. The realization of the nature of the problem grew out of on-orbit measurements of spacecraft charging (Refs. 1, 2), studies of correlations between anomalous spacecraft behavior and geomagnetic conditions (Refs. 3, 4), and experimental and theoretical investigations (Refs. 3-7).

Another source of difficulty with the operation of spacecraft, namely, the problem of contamination

of critical surfaces, may also be aggravated by the occurrence of charging. In addition to line-of-sight contaminant trajectories usually considered for synchronous altitude spacecraft, a negatively charged vehicle can electrostatically reattract molecules released from the vehicle if they become photoionized while still within range of the vehicle's electric field. Such a trajectory is shown in Figure 1. Inasmuch as the electric field from a charged vehicle can extend tens to hundreds of meters in the very dilute plasma at synchronous altitude, the molecule can arrive at almost any point on the vehicle. Theoretical estimates suggest that this mode may be important for spacecraft outgassing at typical rates, but the multitude of simplifying assumptions required in such calculations render them of uncertain validity (Refs. 8, 9). A major goal of ML12 is to determine the extent to which this mode of contaminant transport has engineering significance.

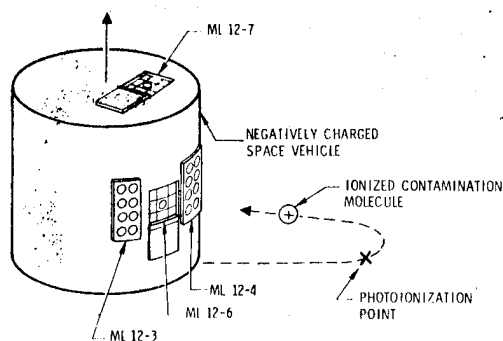


Figure 1. Negatively Charged Vehicle Reattracts Contaminant

2. THE P78-2 SPACECRAFT

The P78-2 spacecraft is managed and funded by the United States Air Force (USAF) Space Test Program. It is one element of a cooperative National Aeronautics and Space Administration (NASA)/United States Air Force program to investigate various aspects of the electrical charging and discharging of geosynchronous

*Work supported by the United States Air Force Materials Lab, Coatings and Thermal Protection Materials Branch, WPAFB, OH 45433.

spacecraft surfaces (Ref. 10). The program is known as SCATHA (Spacecraft Charging At High Altitudes).

The P78-2 was launched on January 30, 1979, into a 176- by 43,278-km transfer orbit. On February 2, it was injected into a 27,578- by 43,288-km, 7.9 deg inclination final orbit. The vehicle, pictured in Figure 2, is a right cylinder approximately 1.75 m in both length and diameter.

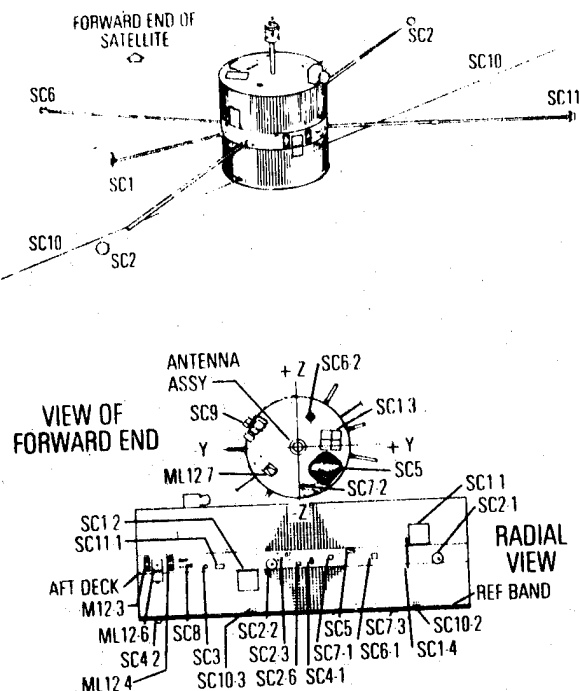


Figure 2. P78-2 Space Vehicle

The objectives of P78-2 are to measure (1) the environment that leads to charging, (2) the characteristics of the vehicle plasma sheath, and (3) the effects of charging on vehicle subsystems (Refs. 4, 11). To achieve these objectives, it carries a complement of six charged particle experiments, electron and positive ion emitters, magnetic and electric plasma field detectors, satellite surface potential monitors, instruments to characterize electrical discharges, and the ML12 contamination experiment (Ref. 11).

3. THE ML12 EXPERIMENT

The ML12 experiment was designed to: (1) determine whether or not spacecraft charging increases the contamination rate, and if so, by what means; (2) distinguish between the changes of selected thermal control coatings caused by contamination and those caused by degradation; (3) determine the effects of the space environment on spacecraft contaminants, i.e., lowering of the vapor pressure, darkening of the adsorbed film, and removal of material; (4) compare P78-2 observations with the results of terrestrial and other in-space degradation and contamination experiments; (5)

identify the effects of specific contaminant releasing events such as thruster operations and boom deployments.

To accomplish these goals, two sensor types are used. One type is a combination retarding potential analyzer (RPA) and temperature controlled quartz crystal microbalance (TQCM). With it, distinction can be made between charged and uncharged arriving molecules, and information can be obtained concerning the temperature dependence of the contaminant adsorption and desorption rates. The other sensor type exposes samples of different spacecraft thermal control coatings (TCCs) to the arriving contaminants and continuously measures the solar absorptances (α_s) of these samples. Changes in α_s of space-stable samples will be ascribed to contamination, whereas changes in α_s of the other samples will be ascribed to a combination of contamination, photochemical, and radiation effects. Upon ground command, some of the samples go through a heating sequence designed to roughly determine the temperature at which the contaminants are desorbed.

As shown in Figures 1 and 2, there are two of each type of sensor on the satellite. Both of the TCC trays (ML12-3, ML12-4) and one of the RPA/TQCMs (ML12-6) view radially. The other RPA/TQCM (ML12-7) views axially from the "forward" end of the space vehicle. The three ML12 sensors mounted on the vehicle belly band between the SC2 and SC11 booms have a nearly clear field of view. The fourth sensor, mounted flush with the forward end of the vehicle, has a portion of the main communication antenna within its field of view.

The following sections describe these instruments in more detail and present some preliminary results from them. The results are preliminary in that they are based on the very small fraction of flight data currently accessible to the experimenters, and in that the analysis of these data is incomplete.

4. THE RPA/TQCM EXPERIMENT

4.1 Instrument Design

The RPA/TQCM construction is shown in Figure 3. A photograph of the flight hardware appears in Figure 4. The RPAs were designed and fabricated at The Aerospace Corporation; the TQCM sensors were supplied by Faraday Laboratories, La Jolla, California (Ref. 12). The TQCM sensor

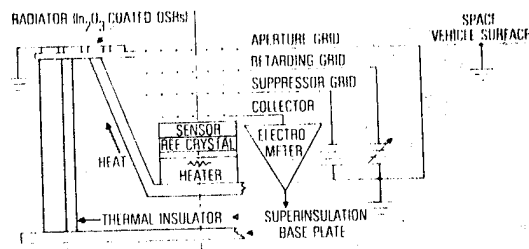


Figure 3. Diagram of the RPA/TQCMs (ML12-6 and ML12-7)

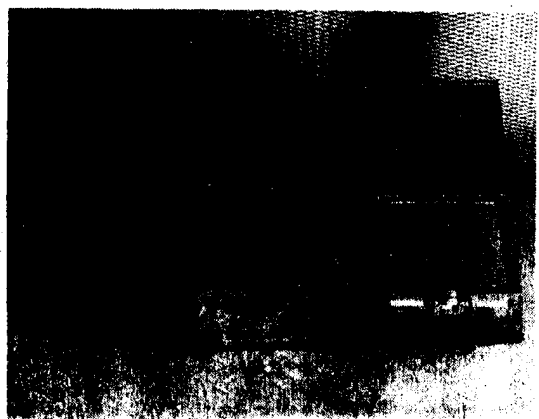


Figure 4. Photo of ML12-6 and ML12-7 With Protective Covers Released. Mirror Radiators Surround the Sensor Apertures.

has a field of view of approximately 2.24 sr (50-deg half-angle cone), and the RPA has a coaxial field of view of approximately 3.5 sr (59-deg half-angle cone).

The TQCM sensors are two AT-cut, 15-MHz, optically polished crystals with aluminum electrodes. The sensitivity is $1.6 \times 10^{-5} \text{ g m}^{-2} \text{ Hz}^{-1}$; therefore, for the $\pm 1.0 \text{ Hz}$ telemetry resolution and an integration time of 1 hr, the net sensitivity is approximately $1.6 \times 10^{-5} \text{ g m}^{-2} \text{ hr}^{-1}$. This corresponds to the deposition of a 0.016 nm thick uniform film of unity density per hour. Preliminary flight data suggest that the oscillator stabilities will justify longer integration times. The maximum mass loading for which the sensor crystal will still oscillate is approximately 1 g m^{-2} .

The TQCMs are radiatively cooled but can also be operated at elevated temperatures by the use of heaters. The radiators are silvered, fused-silica, second-surface mirrors coated with electrically conducting indium oxide connected to the spacecraft ground. This prevents electrostatic charge buildup on the radiator surface. The TQCM sensor heaters can be commanded from the ground to maintain one of five predetermined temperatures in the range of -60 to +70°C. "Controller Off" is a sixth command state, which produces temperatures of approximately -40°C in ML12-6 and about -95°C in ML12-7. Precision helium-filled, platinum, resistance thermometers, which are linear to $\pm 0.5\%$, indicate the TQCM temperature.

The TQCM receives molecules through a gridded aperture in the RPA collector. The aperture grid is normally grounded to minimize defocusing of incoming ions. Together, the four RPA grids will intercept approximately 35% of the incident contaminant flux.

The retarding potential grid is commanded from the ground to one of the following potentials: +500, +100, +10, +1, 0, -1, -10, or -100 V. Alternately, it may be commanded to cycle through these values, dwelling 8 s at each potential.

An approximately 1 cm^2 annular collector plate (located immediately above the sensing crystal), in combination with an electrometer and guard ring circuitry, measures currents in the range of 10^{-12} to 10^{-8} A with a resolution of $\pm 10^{-12} \text{ A}$. This is approximately 6×10^{10} to 6×10^{14} electrons $\text{m}^{-2} \text{ s}^{-1}$ or the equivalent in ionized molecules.

Of course, the electrometer will detect the arrival of both condensable and noncondensable ions.

4.2 Preliminary RPA/TQCM Experiment Results

Qualitatively, the RPA currents respond to grid voltage commands in the expected manner. For instance, when the vehicle frame is known to be negatively biased by approximately 400 V with respect to the ambient plasma potential, commanding the retarding grid to +500 V reduces the ion current recorded by the electrometer. Similarly, when the vehicle is positive, larger negative grid potentials diminish the electron current recorded. Detailed analysis of the RPA data has not yet begun.

The continuously shadowed ML12-7 TQCM recorded mass accumulation ranging between 0 and $11 \text{ ng cm}^{-2} \text{ day}^{-1}$ during the early weeks on final orbit when its temperature was about -95°C. On March 29, 1979, its temperature was increased to -30°C, and since that date it has been commanded to temperatures between -30 and +25°C. No mass accumulated on this detector at these temperatures. At this writing, a week of ML12-7 operation at -60°C and at approximately -95°C is planned for the period of late July to early August, 1979.

The ML12-6 TQCM sensor, which initially was operated at about -40°C, began experiencing mass accumulation soon after final orbit was achieved. This higher temperature was reached in the case of ML12-6 with no applied heater power because the sun line is maintained between 85 and 95 deg to the vehicle spin axis. The mass accumulation rate was initially about $17 \text{ ng cm}^{-2} \text{ day}^{-1}$ and gradually diminished to approximately $12 \text{ ng cm}^{-2} \text{ day}^{-1}$ by the end of June, suggesting that the source of this material is diffusion limited. The accumulation rate was relatively insensitive to sensor temperature over the -40 to +70°C range, suggesting that either the material initially had a high desorption energy or that sunlight quickly transformed it into a material with a high desorption energy. Experiments in which the sensor temperature is varied are being continued. Analysis will be made of the changes in crystal beat frequency that occur rapidly when the temperature commands are issued. When corrections are made for the sensor's frequency-temperature characteristics, which were obtained during ground tests, it should be possible to determine if any mass was desorbed during rapid positive temperature changes.

Quick look, "raw" data in tabular form are available for a few brief periods (of less than 1 hr) of spacecraft charging. Enhanced accumulation rates are usually not evident from casual

inspection of these data. When the 24 hr/day magnetic data tapes from the vehicle become available, a computer will be used to search for longer and larger charging events and to analyze statistically the RPA/TQCM data.

5. THE TCC EXPERIMENT

5.1 Instrument Design

The instrument consists of three interconnected units designated as ML12-3, ML12-4, and ML12-5. These units are a modification and augmentation of hardware originally designed and fabricated at TRW Systems, Redondo Beach, California (Ref. 13). The ML12-3 and ML12-4 are the sample trays (Figure 5) that carry eight 1.25-in.-diameter samples each. The ML12-5 carries the electronic circuitry required to monitor the TCC coupons.

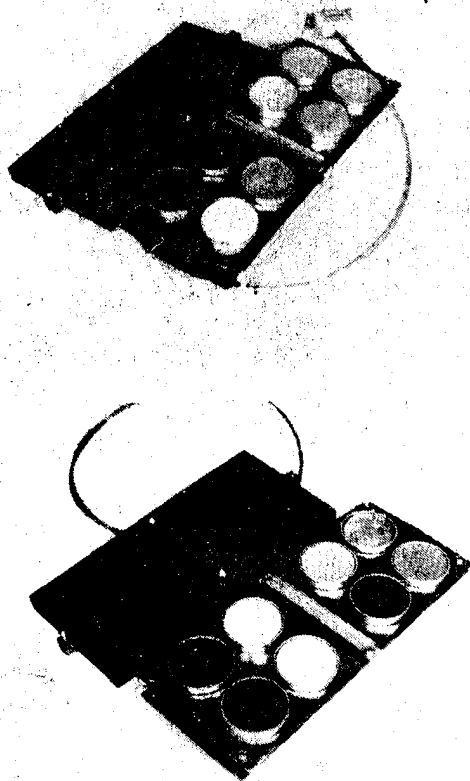


Figure 5. Photos of Flight TCC Trays. Dust Covers and Fine Thermocouple Leads Were Removed Before Launch

On the trays, each test sample is mounted on an aluminum disk by the use of diluted Eccobond EC57C conducting epoxy (except for the fabric/tape sample) (Figure 6). Thermal isolation is accomplished by having the disk supported by three 14-mil o.d. stainless steel tubes, which are thermally insulated from the base of the cup by fiberglass sleeving. The length and diameter of the instrumentation leads to the disk were also chosen to minimize conduction. The tubing and wires together give approximately a 9×10^{-4} W/K thermal conduction coefficient. The volume enclosed by the disk and cup walls is filled with a combination of multilayer and open-cell polyurethane insulation. The radiation coupling coefficient between the disk and cup is approximately 7.9×10^{-12} W/K⁴. The underside of each aluminum disk carries two heaters in series and three thermistors. The heaters, which are actually strain gauges, were chosen because of their low temperature coefficient of resistance. The heaters are included for the purposes of pre-flight calibration and to allow thermal desorption cleaning of six of the samples on orbit. The three thermistors span low, medium, and high temperature ranges. On half of the samples, one of the three thermistors is monitored based upon the expected temperature range. On the other samples, two of the thermistors are monitored. In addition, there are two thermistors located on each of the sample trays to measure the temperature of the supporting cups.

The electronics package, ML12-5, contains an ohmmeter circuit for measuring the resistance of the thermistors. It also contains a stepping circuit for sequential scanning of each of the 14 thermistors on the samples and trays and of two fixed resistors on the tray. The ML12-5 converts the thermistor resistances into a 0.0- to 5.1-V signal, which is then transmitted to the spacecraft telemetry system. Finally, ML12-5

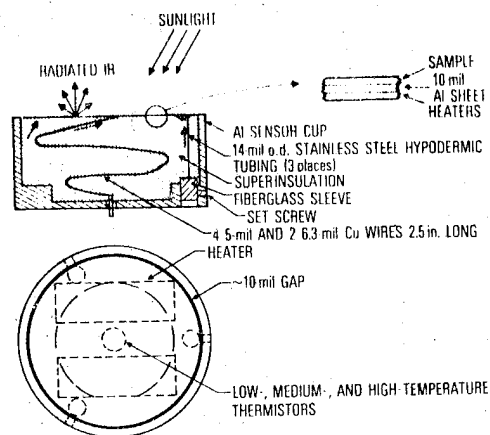


Figure 6. Arrangement for Mounting the TCC Sample Disks in the Cups

generates, on command, a programmed heating sequence for six of the samples. This sequence consists of four heating/cooling cycles, each of which achieves a higher equilibrium temperature than the preceding cycle. The cooling cycle allows us to determine if any change in α_s has occurred during the heating due to desorption of contaminants.

5.2 Sample Selection

The sixteen samples chosen for testing are given in Table 1. These samples were chosen for a number of reasons:

1. To provide a wide range of initial α_s and ϵ (emittance) values in case a given contaminant is invisible for particular substrates.
2. To include materials that are expected to be relatively space stable in the absence of contamination. This refers to the polished Al samples, the Au sample, and the optical solar reflector (OSR) samples.
3. To provide for some redundancy to allow checks for consistency. Thus, two black and two polished Al samples, one on each tray, were included.
4. To allow for the comparison of similar materials. Thus both OSR and OSR coated with a conductive In_2O_3 layer were included. Similarly, both an In_2O_3 -coated, a Au-coated, and an uncoated aluminized Kapton were chosen. Two thicknesses of silvered Teflon, 2 mil and 5 mil, are present. Finally, two samples of Astroquartz fabric, one with a FEP/Al backing and one without such a backing, are being tested.
5. To test a new material. To our knowledge the In_2O_3 /Kapton/Al sample has not been flown before.

6. To include samples identical to those studied in the satellite surface potential monitor (SSPM) package on board P78-2, which is designed to measure the amount of charging of TCC samples. These samples are the aluminized Kapton, the OSRs, the Au sample, the Au-coated Kapton, an Astroquartz fabric, and the 5 mil silvered Teflon.

5.3 Data Reduction

The temperature of a sample is determined by Eqs. 1, 2

$$C_v(T) \frac{dT}{dt} = F(T_c^4 - T^4) + C(T_c - T) + \epsilon A_s(T_o^4 - T^4) + \alpha_s S\phi(t) + P \quad (1)$$

$$\phi(t) = AE \sin \omega t \text{ for } 0 \leq \omega t \leq \pi;$$

$$\phi(t) = 0 \text{ for } \pi \leq \omega t \leq 2\pi \quad (2)$$

where

T = sample temperature

T_c = tray temperature

T_o = surrounds temperature

F, C = thermal coupling constants between the sample and tray

ϵA_s = emissivity times sample area times Stefan-Boltzman constant

$C_v(T)$ = heat capacity of sample

Table 1. Flight samples for ML12

-3 Tray	-4 Tray
Grafoil (Union Carbide, GTA Grade)	10 nm Au on Kapton/Al (Sheldahl)
Black Paint (3M401C10)	Astroquartz Fabric(J.P.Stevens 581)/FEP/Al
OSR (OCLI SI-100 Mirror)	In_2O_3 /OSR (OCLI SI-100 Mirror)
Vacuum Deposited Au on Al	In_2O_3 /Kapton/Al (General Electric)
Diamond Polished 2024 T3 Al	Diamond Polished 2024 T3 Al
FEP(5 mil)/Ag (Sheldahl)	Black Paint (3M401C10)
FEP(2 mil)/Ag (Sheldahl)	Astroquartz Fabric(J.P. Stevens 581)/Tape (Sheldahl 405900)
Yellow Paint (NASA Goddard No. NS43G)	Kapton(5 mil)/Al (Sheldahl)

$\Phi(t)$	= radiant power falling on sample
ω	= rotational velocity of spacecraft
E	= solar irradiance
α_s	= solar absorptance
S	= factor between 0 and 1 to account for shading due to spacecraft booms
P	= power applied via sample heater
t	= time

Albedo and earth emission are expected to be negligible at near synchronous orbit and have been left out of Eq. 1.

Under normal space conditions, $P = T_o = 0$. The solution of this equation is then given by

$$T = T_{ind} + \Delta T \quad (3)$$

where T_{ind} is the solution of the time independent equation

$$F(T_c^4 - T_{ind}^4) + C(T_c - T_{ind}) + \epsilon A(T_o^4 - T_{ind}^4) + \alpha_s SAE/\pi = 0 \quad (4)$$

and ΔT is given by

$$\Delta T = \begin{cases} -\gamma + [\gamma\beta/(1-e^{-\beta})]e^{-\frac{\beta Y}{\pi}} + \gamma\beta(\frac{\beta}{Y}\sin\theta - \cos\theta) & 0 \leq \theta \leq \pi \\ -\gamma + [\gamma\beta/(1-e^{-\beta})]e^{-\frac{\beta Y}{\pi}} e^{\beta} & \pi \leq \theta \leq 2\pi \end{cases} \quad (5)$$

where

$$\theta = \omega t$$

$$\omega = \text{angular velocity of spacecraft}$$

$$\beta = \pi [C + 4 T_{ind}^3 / (F + \epsilon A)] / C_{\nu}$$

$$\gamma = EA\alpha_s / \beta C_{\nu}$$

For the data shown under results, α_s was calculated from T_c and T by the following procedure:

1. Assume $\Delta T = 0$, $T_{ind} = T$
2. Calculate α_s from the time independent equation (Eq. 4)
3. Calculate ΔT using above value for α_s
4. Calculate $T_{ind} = T - \Delta T$ using above value for ΔT
5. Return to Step 2

5.4 Preflight Calibrations and Calculations

The use of Eqs. 4 and 5 to calculate α_s requires a calibration of each of the sample and tray thermistors, a determination of the thermal coupling constants C , F , and ϵA , a measurement of the heat capacity C_{ν} of each sample, and a calculation of the shading factors S as a function of spacecraft orientation with respect to the sun.

The 24 sample and 4 tray thermistors were calibrated against precision copper constantan thermocouples (two used per tray) by placing the trays in a commercial temperature-regulated oven/refrigerator and by recording resistances and temperatures over the range of 203 to 388 K. The data were fitted to the equation

$$T = \sum_{i=0}^4 C_i (\ln R)^i \quad (6)$$

by a least squares routine. The standard errors of the fits varied between 0.05 K and 0.27 K; all but three of the 28 values were less than 0.13 K. In comparison, the resolution of the spacecraft telemetry system yields an uncertainty of ± 0.5 K.

The determinations of C , F , ϵA , and C_{ν} described below were performed in an ion-pumped vacuum chamber containing a liquid nitrogen cooled shroud surrounding the trays. The shroud was painted black to ensure proper radiative coupling between it and the samples. The trays were held in a temperature controlled aluminum holder and kept near room temperature to duplicate the conditions expected on orbit. Under these conditions $\phi(t) = 0$ and $T_o = 77$ K (see Eq. 1).

The thermal coupling constants C , F , and ϵA were determined by applying a measured amount of current to the sample heaters and by measuring the equilibrium temperatures T and T_c . By doing this at five different power levels, five sets of data were generated that were used to obtain C , F , and ϵA from Eq. 4. A least squares technique was used, with P as the dependent variable. Under space conditions, we would normally have $P = 0$ and $\phi(t) \neq 0$ in Eq. 1, whereas during calibration $P \neq 0$ and $\phi(t) = 0$. Thus P plays the same role during calibration that $\alpha_s \phi(t)$ plays on orbit. In space, $\phi(t) \sim 0.324$ W. By forming the ratio $\sqrt{\Delta P^2} / 0.342 \alpha_s$, where ΔP^2 is the average value of the error ΔP in the least squares fit, a good estimate of the expected error $\Delta \alpha_s / \alpha_s$ from this source can be obtained. The values of $\Delta \alpha_s / \alpha_s$ calculated in this way are given in Table 2. These errors should be compared to the random errors as given in Section 4. The larger error for one of the fabric samples on tray 4 is the result of a thermistor having become defective on that sample during calibration. Scheduling limitations did not allow for replacement and recalibration of this thermistor. However, the error is comparable to the random error introduced due to telemetry resolution (see below). Furthermore, the temperature of this sample on orbit is monitored by an undamaged backup thermistor.

To determine C_{ν} , heater power was applied, and the data were recorded in the form of temperature

Table 2. Percent and absolute error in α_s due to uncertainties in the heat leak calibration.

	$\frac{\Delta \alpha_s}{\alpha_s} (\%)$	$\Delta \alpha_s$
ML12-3		
Grafoil	0.09	0.001
Black Paint	0.21	0.002
OSR	0.44	0.000
Au on Al	0.69	0.001
Polished Al	0.64	0.001
FEP (5 mil)/Ag	1.14	0.001
FEP (2 mil)/Ag	1.10	0.001
GSFC yellow	.29	0.001
ML12-4		
Au/Kapton/Al	0.07	0.000
Fabric/FEP/Al	1.37	0.003
In ₂ O ₃ /OSR	0.20	0.000
In ₂ O ₃ /Kapton/Al	0.19	0.001
Polished Al	0.64	0.001
Black Paint	0.17	0.002
Fabric/Tape	6.95	0.016
Kapton (5 mil)/Al	0.26	0.001

versus time (30-sec intervals). This enabled the calculation of dT/dt for use in Eq. 1. The values of dT/dt were calculated by fitting seven consecutive data points (T versus t) to a parabola using a least squares routine. The derivative of the parabola at the center data point was taken as the value of dT/dt there. With dT/dt determined, and with T , T_c , and P measured, Eq. 1 can be solved to give C_v as a function of temperature. The resulting heat capacities of the samples are usually between 1.0 and 2.0 J/K. The heat capacities of the 1.25-in. diameter, 10 mil thick supporting aluminum disk alone should be 0.45 J/K. Thus, the experimentally determined values of C_v for the sample assemblies seem quite reasonable.

The shading factors S are a function of the angle ρ between the spacecraft spin axis and the sun. Maximum shading occurs for the Grafoil and GSFC samples at $\rho = 90^\circ$ and represents a 10% drop in radiation. Values of S were calculated by Systems, Sciences, and Software for $80^\circ < \rho < 100^\circ$ in 1-deg steps for each of the 16 samples (Ref. 14). The samples are not shaded for ρ outside this range.

5.5 Random Error Analysis

An analysis of the degree of random error to be expected in calculating α_s has been performed. For each sample, the various input parameters that are used in the equations were varied by amounts equal to the resolution inherent in the 8-bit telemetry processing, and the percent change in each calculated value of α_s was noted. The parameters of importance are: (1) the data from the first two channels that are used in converting telemetry voltage to resistance of the thermistors; (2) the tray temperature; (3) the sample temperature; and (4) the shading factor. The last source of error depends upon the spacecraft orientation and arises from both the 1-deg resolution of the table of shading values versus ρ and the uncertainty of the angle ρ at a given time. The total errors due to these sources as given by the square root of the sum of the squares of each are listed in Table 3. These tables were used to determine the error bars shown on the data plots. We expect to reduce the size of some of the random errors by obtaining better estimates of ρ and by selecting data from times when knowledge of ρ is not so highly critical (for example, when $\rho \approx 93^\circ$).

Subsequent publications will address systematic experimental errors.

5.6 TCC Experiment Results

The results, to date, of the calculations of α_s from the time of launch are plotted in Figures 7 - 9. For the first 12 plots it is possible to draw a straight line of zero slope that "captures" all of the error bars. Thus, within experimental error, no degradation of any of these 12 samples has been demonstrated so far.

In Fig. 8, the last two plots indicate a increase in α_s of 0.01 for the Fabric/FEP sample and 0.05 for the Fabric/Tape sample during the first 50 days on orbit. The α_s values appear to be stable for the succeeding 100 days.

The α_s values of the two black paint samples are plotted in Fig. 9. The data indicates an approximately constant α_s for about the first 60 days on orbit followed by a decrease in α_s of about 1.7% per month for the next 3 months.

With all of the samples, reduction of data from additional days and refinements in the calculations are expected to yield more definitive results.

6. SUMMARY AND CONCLUSIONS

Since the time of launch, extensive analyses have been performed on the accumulated raw flight data for the ML12 TCC samples. Due to the

Table 3. Percent and absolute error (in parentheses) in α_s due to random errors.

ρ	≤ 87	88	89	90	91	92	93	94	95	≥ 96
Grafoil	2 (0.013)	3 (0.020)	8 (0.052)	8 (0.052)	6 (0.039)	6 (0.039)	3 (0.020)	2 (0.013)	2 (0.013)	2 (0.013)
Black Paint	1 (0.009)	1 (0.009)	2 (0.018)	6 (0.055)	6 (0.055)	4 (0.037)	4 (0.037)	2 (0.018)	2 (0.018)	1 (0.018)
OSR	12 (0.010)	12 (0.010)	12 (0.010)	12 (0.010)	12 (0.010)	12 (0.010)	12 (0.010)	12 (0.010)	12 (0.010)	12 (0.010)
Au on Al	5 (0.010)	5 (0.010)	5 (0.010)	5 (0.010)	6 (0.012)	6 (0.012)	6 (0.012)	5 (0.012)	5 (0.010)	5 (0.010)
Polished Al	6 (0.009)	6 (0.009)	6 (0.009)	6 (0.009)	6 (0.009)	6 (0.009)	6 (0.009)	6 (0.009)	6 (0.009)	6 (0.009)
FEP (5 mil)/ Ag	7 (0.009)	7 (0.009)	7 (0.009)	7 (0.009)	7 (0.009)	7 (0.009)	7 (0.009)	7 (0.009)	7 (0.009)	7 (0.009)
FEP (2 mil)/ Ag	11 (0.009)	11 (0.009)	11 (0.009)	13 (0.011)	13 (0.011)	12 (0.010)	12 (0.010)	12 (0.010)	11 (0.009)	11 (0.009)
GSFC Yellow	3 (0.010)	4 (0.014)	4 (0.014)	5 (0.017)	6 (0.021)	6 (0.021)	3 (0.010)	3 (0.010)	3 (0.010)	3 (0.010)
Au/Kapton/Al	2 (0.011)	2 (0.011)	6 (0.032)	6 (0.032)	5 (0.027)	2 (0.011)	2 (0.011)	2 (0.011)	2 (0.011)	2 (0.011)
Fabric/FEP/ Al	3 (0.008)	3 (0.008)	3 (0.008)	6 (0.015)	6 (0.015)	4 (0.010)	3 (0.008)	3 (0.008)	3 (0.008)	3 (0.008)
In ₂ O ₃ /OSR	16 (0.014)	16 (0.014)	16 (0.014)	16 (0.014)	16 (0.014)	16 (0.014)	16 (0.014)	16 (0.014)	16 (0.014)	16 (0.014)
In ₂ O ₃ /Kapton/ Al	4 (0.016)	4 (0.016)	4 (0.016)	4 (0.016)	4 (0.016)	4 (0.016)	4 (0.016)	4 (0.016)	4 (0.016)	4 (0.016)
Polished Al	10 (0.014)	10 (0.014)	10 (0.014)	10 (0.014)	10 (0.014)	10 (0.014)	10 (0.014)	10 (0.014)	10 (0.014)	10 (0.014)
Black Paint	1 (0.010)	1 (0.010)	1 (0.010)	2 (0.019)	2 (0.019)	2 (0.019)	2 (0.019)	2 (0.019)	2 (0.019)	1 (0.010)
Fabric/Tape	5 (0.012)	5 (0.012)	5 (0.012)	7 (0.017)	7 (0.017)	6 (0.014)	5 (0.012)	5 (0.012)	5 (0.012)	5 (0.012)
Kapton (5 mil)/ Al	2 (0.010)	2 (0.010)	6 (0.031)	6 (0.026)	5 (0.010)	2 (0.010)	2 (0.010)	2 (0.010)	2 (0.010)	2 (0.010)

unavailability of data tapes thus far, these analyses have been carried out by hand from quick look data provided by the USAF Satellite Control Facility. A detailed evaluation of the random errors introduced into the calculations of the solar absorptivities from the raw data was also performed. These errors are caused primarily by the resolution of the telemetry system and by uncertainty in the amount of shading of the samples due to the spacecraft booms. Reduction of the uncertainty due to shading is anticipated when more accurate spacecraft attitude data become available.

Temporal data has been presented for the 16 TCC samples as of five months into the flight. Because the satellite spins, 3.14 hours are required to accumulate one equivalent sun hour. Most samples exhibit α_s constant within the current uncertainty of the measurement. During this time period the quartz crystal microbalance adjacent to the TCC trays has indicated a contaminant buildup equivalent to a 15 nm thick film (assuming uniform coverage and unity density). Suspect organic contaminants of this thickness, photo degraded or not, would be

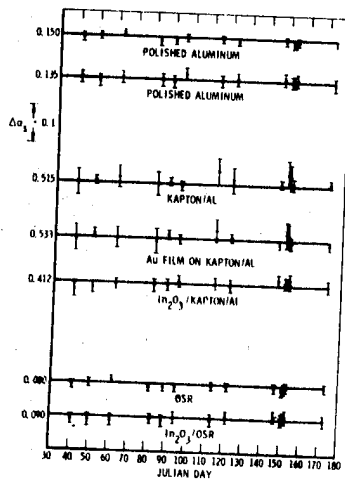


Figure 7. Solar absorptances from day of launch (day 30)

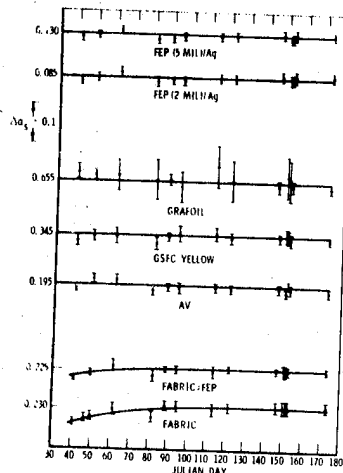


Figure 8. Solar absorptances from day of launch (day 30)

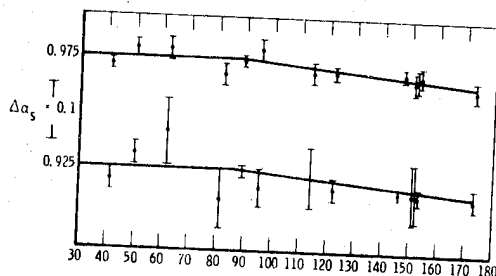


Figure 9. Solar absorptances of black paint samples from day of launch (day 30)

expected to be transparent (Ref. 15). The lack of any observable change in the solar absorptances of most of the TCC samples is consistent, therefore, with the TQCM data.

Both quartz fabric samples exhibit a small increase in α_s during the first month on orbit. Both 3M black paint samples have exhibited an approximate 5% decrease in α_s . Since it would be somewhat surprising for these samples alone to be affected by the presence of a thin contaminant film, this decrease is most likely due to degradation. Bleaching of black paints has been intimated on previous flights (Refs. 16, 17) and so its occurrence on P78-2 is not unreasonable.

7. ACKNOWLEDGMENTS

Undertakings as large as a flight experiment usually require the labors of many people; in this instance the numbers exceeded three dozen, all of whom made important contributions. The following individuals are due special thanks for their assistance: D. Prince, AFML, TCC sample procurement, measurement, and mounting and sponsor representative; W. Chater, Aerospace Corp. design and fabrication of much of the flight electronics; D. Jones, Aerospace Corp., mechanical fabrication, design and testing; P. Fleischauer, Aerospace Corp., assistance with program management and testing; R. Corbin, J. Goldman, J. Hribar, and W. Kalinowski, Aerospace Corp., calibration and environmental testing; D. Clark, Aerospace Corp., system testing and orbital operations; J. Vellinga, Martin Marietta Aerospace, payload integration. The authors of Refs. 12 and 13 supplied important portions of the flight hardware under contract to AFML.

8. REFERENCES

1. DeForest S E & McIlwain C E 1971, Plasma Clouds in the Magnetosphere, *J Geophys Res* Vol 76, 3587.
2. DeForest S E 1972, Spacecraft Charging at Synchronous Orbit, *J Geophys Res* Vol 77, 651.
3. McPherson D A, Cauffman D P, & Schober W R 1975, Spacecraft Charging at High Altitudes: SCATHA Satellite Program, *J Spacecraft and Rockets* vol 12, 621-626.
4. Rosen A, ed 1976, *Spacecraft Charging by Magnetospheric Plasmas*, Prog in Astronautics and Aeronautics vol 47, AIAA, MIT Press, Cambridge, Mass, and London.
5. Rosen A 1976, Spacecraft Charging: Environment-Induced Anomalities, *J Spacecraft and Rockets* vol 13, 129-136.
6. Pike C P & Lovell R R, eds 1977, *Proc Spacecraft Charging Technology Conference*, AFGL-TR-77-0051, NASA TMX-73537, National Technical Information Service, Springfield, Vir.

7. Spacecraft Charging Technology - 1978 1979, AFGL-TR-79-0082, NASA Conference Publication 2071, Scientific and Technical Information Office, NASA, Washington D. C.
8. Cauffman D P 1973, Ionization and Attraction of Neutral Molecules to a Charged Spacecraft, TR-0074(9260-09)-1, The Aerospace Corporation, El Segundo, Calif.
9. Hall D F, et al. 1975, Experiment to Measure Enhancement of Spacecraft Contamination by Spacecraft Charging, NASA SP-379, National Technical Information Service, Springfield, Vir.
10. Lovell R R, et. al. 1976, Spacecraft Charging Investigation: A Joint Research and Technology Program, Spacecraft Charging by Magnetospheric Plasmas, A. Rosen, ed., Prog in Astronautics and Aeronautics vol 47, AIAA, MIT Press, Cambridge, Mass and London.
11. Stevens J R & Vampola A L, eds 1978, Description of the Space Test Program P78-2 Spacecraft and Payloads, SAMSO-TR-78-24, National Technical Information Service Springfield, Vir.
12. McKeown D, et al. 1977, Temperature Controlled Quartz Crystal Microbalance System, AFML-TR-77-83, AFML/MBE, Wright-Patterson Air Force Base, Ohio.
13. Luedke EE & Kelley LR 1972, Development of Flight Units for Thermal Control Coatings Experiment, AFML-TR-72-233, AFML/MBE, Wright-Patterson Air Force Base, Ohio.
14. Steen P G 1978, SCATHA Experiment Shadowing Study, SSS-R-78-3658, Systems, Science and Software, La Jolla, Calif.
15. Jones P F & Borson E N 1971, The Effects of Deposition and Irradiation of Contamination from the Outgassing of Silastic 140 RTV, TOR-0059(6129-01)-56, The Aerospace Corporation, El Segundo, Calif.
16. Carroll W F, Mariner V Temperature Control Reference Design, Test, and Performance, AIAA Paper No. 68-791, AIAA 3rd Thermophysics Conference, 24-26 June 1968, Los Angeles.
17. Millard J P & Pearson, Jr. B D, Optical Stability of Coatings Exposed to Four Years Space Environment on OSO-III, AIAA Paper No. 73-734, AIAA 8th Thermophysics Conference, 16-18 July 1973, Palm Springs, Calif.

N80-21429

METEOSAT CLEANLINESS CONTROL PRINCIPLES

P G Edwards & J Marcoux

European Space Agency, Earth Observation Programme Office, Toulouse, France

ABSTRACT

The development history of METEOSAT cleanliness control is described, from its first steps to the final comprehensive form. Details of the resulting design features, material selection control and pre-launch/launch contamination control are given. Control techniques and procedures are described: example (manufacturing techniques; test techniques; materials selection problems are given to illustrate these. Cleanliness goals feasibility and their cost effectivity are discussed.

Keywords: METEOSAT, contamination, cleanliness control, materials selection, radiometer.

1. INTRODUCTION

From the inception of the METEOSAT programme, particular attention was drawn (1) to the potential contamination hazards involved in the fabrication, launch and operation of a spacecraft whose primary payload, a scanning radiometer, contains optical and, in its radiative cryogenic cooler, critical thermo-optical surfaces. The contractor was required to reduce the in-orbit self contamination of the spacecraft by :

- design features - isolating sensitive areas from contamination sources
- materials selection - reducing contamination sources
- pre-launch and launch contamination control - keeping the initial contamination of the sensitive equipment to the minimum

2. DEVELOPMENT HISTORY

During the pre-development phase of the METEOSAT programme, product cleanliness assurance and control was not a well defined discipline, experience from previous ESRO projects being rather limited. Consequently, the initial requirements (1) were restricted to materials selection and screening method (2) (3).

The radiometer, as previously mentioned, is the most critical on-board item (being the primary payload): it is also the most sensitive to contamination. The safeguarding of the prime mission was soon recognised as a vital element in the project development and accordingly a range of studies were commenced to :

- collect applicable experience and expertise
- redefine materials selection policies
- identify and assess contamination sources or effects, and sensitive areas or operations, in order to improve design, adapt facilities, refine manufacturing or test procedures, modify pre- and post-launch operations
- eventually, to implement an overall cleanliness control plan to reach goals identified and quantified from the above studies

Applicable data on in-orbit contamination and control methods was gathered from various space agencies (NASA, ESRO, CNES, DFVLR), research centres (especially DERTS) and programme contractors. In addition, a specific contract was let to an experienced specialist in the field (A.D. Little) for the most critical area, i.e. the cooler of the radiometer.

A configuration study of the METEOSAT radiometer and cooler, prepared by DFVLR (4) and consisting of a theoretical estimation of the minimum and maximum contamination fluxes from all potential contamination sources and at sensitive surface areas. It resulted into a clear and timely identification of critical 'sinks' and 'sources'.

As far as materials selection policy was concerned, the following basic principles were agreed, in the absence of more specific knowledge of contaminant criticalities :

- consider the (just developed) ESRO standards as a baseline (1) (2)
- adhere strictly to accept/reject criteria
- screening tests on all unknown materials (liable to produce contaminants)
- batch tests on any accepted material liable to variability in out-gassing properties
- functional (goods receipt) tests on all accepted materials
- thorough materials/processes approval procedures, using formal materials/processes lists

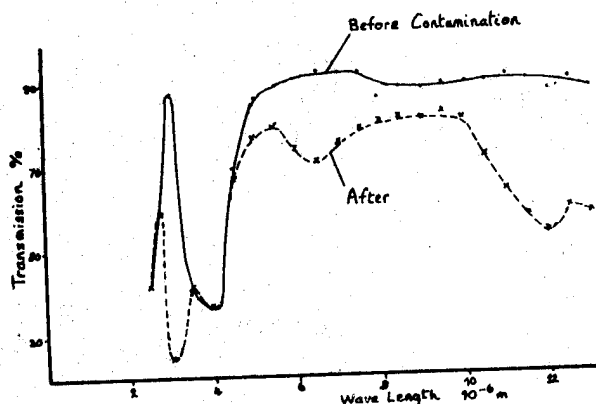
The identification and assessment of contamination sources or effects was the most difficult and costly stage in the development of the METEOSAT contamination controls. The main effort was to assess degradation of optical and thermo-optical surfaces under simulated in-orbit contamination and radiation environments.

AERE Harwell (5) conducted degradation tests on the following elements of the radiometer :

- primary mirror reflective coating (Ag/ThF₄ optical thickness $\lambda/2$ for $\lambda = 5000\text{\AA}$)
- cooler cone non-radiative (reflective) surface (Au)
- cold optical window (Ge)

The principal conclusions suggested that, when a VCM flux is present during irradiation, performance degradation occurs up to $0.7\mu\text{m}$, but IR performance is little affected (up to $15\mu\text{m}$).

DFVLR (6) generated dynamic contaminant fluxes in their evaluation of the contamination effects on the cold optics and the cooler, under simulated space environment. Fig. 1 shows some of the typical results.



Sample: 2mm Ge, at -175°C . Exposure 24 hrs
 Contaminant: H₂O ($4\mu\text{g}/\text{hcm}^2$) CO₂ ($0.06\text{ g}/\text{hcm}^2$)
 Flux VCM ($0.5\mu\text{g}/\text{dcm}^2$)
 Contaminant: $114.6\mu\text{g}/\text{cm}^2$
 Layer

Fig. 1 - Transmission Losses of an Optical Window

The study's principal conclusions were :

- water is the most important contaminant on cooler surfaces and the cold optical window (Ge), and deposits as thin as $1\mu\text{m}$ leads to significant performance degradation
- specular reflectance degradation induced by water contamination is not appreciably modified by other contaminants or by changes in the environment
- water contamination can be readily removed by heating the affected surfaces to moderate temperatures

All the above activities were used in the preparation of materials processes and chemical cleanliness requirements (7) (9) and the establishment of the METEOSAT cleanliness control plan (8).

3. DESIGN FEATURES

The principal design features selected to reduce in-orbit self contamination of the spacecraft are summarised as follows :

3.1 Radiometer Design

- radiometer interior and cooler sealed (quasi-hermetically) from rest of spacecraft in respect of line-of-sight contamination fluxes
- jettisonable⁺ covers provided for radiometer and cooler apertures (⁺after station acquisition and 'off-gassing' period)
- gas purge system for pre-launch operations
- decontamination heaters in radiative cooler (permitting a temperature rise from 77°K to 320°K , and providing an effective means of evaporating off volatile contaminants)
- hermetic sealing of lubricated mechanisms (scanning gearbox)
- venting of cooler superisolation
- multilayer termination at structure interface
- number and dimensions of holes for suspension wires optimisation to meet conflicting requirements = thermal, mechanical, cleanliness

3.2 General Spacecraft Design

- use of a separable apogee boost motor, such that a few seconds after firing the spent ABM case is removed from the vicinity of the spacecraft
- 'line-of-sight' sealing of the lower face of the spacecraft
- cable cutters hermetically sealed and qualified in this respect

3.3 Non-flight Features

- solar panel covers
- earth, sun sensor covers
- thruster caps
- hermetic, positively pressurised spacecraft transport container
- use of a 'super-clean' fairing on the THOR-DELTA 2914 launch vehicle
- specific anti-contamination protecting devices during handling and testing (thermal cycling) of filters 6.3µ, anti-reflecting coatings of Ge windows, filters supports

4. MATERIALS SELECTION

In an attempt to reduce the contamination source to the minimum possible, a rigid materials selection and control policy was adopted (2) and following the initial studies during the pre-development (53) specific METEOSAT materials and processes selection requirements (7) were developed. Contractors were required to submit materials lists which would be subject to ESA evaluation and result :

- material approval
- material rejection
- out-gassing test required

The outgassing test (3) using the ESTEC micro equipment or similar would in turn result in material approval or rejection. The limits total weight loss 1%, volatile condensibles 0.1% by weight (3) were maintained - however the rigidity of their application as rejects criteria was modified by the intended application. For example, a structural adhesive, with limited free surface area and zero view factor to VCM sensitive areas could be tolerated with a marginally high VCM - however, a solar cell adhesive, with a large free surface area and large view factor to sensitive areas, could not, and in fact as low as possible out-gassing figures were used as a principal factor in its selection.

Where experience had shown materials to have variable out-gassing properties, the contractor was required to submit samples for each batch.

Finally for all materials, contractors were obliged to make quality control checks for each batch on receipt - the nature of the checks following the type of material.

Table 1 provides some statistics on the materials list eventually developed for METEOSAT. One can note that in the 15 classes of materials there are some 507 types, and for a type many are used in different applications by different contractors. Note the importance of the application process which can lead to an acceptable or unacceptable item. Typical cases are conformed coatings and paints.

Screening tests (3) have been performed on 400 different materials samples by ESTEC, out of which 160 types only have been approved. Cost of a sample test amounts to 100 AU.

5. PRE-LAUNCH AND LAUNCH CONTAMINATION CONTROL

5.1 Contamination Control Plans

Initially limited to particulate contaminants, contamination controls were progressively extended and developed to include monitoring and control of all contamination types, shortly after start of the hardware development and manufacturing phases.

The METEOSAT cleanliness control plan (8) covers the various phases of the programme :

- design: . materials: application, procedure, selection
 . shapes, tolerances, venting paths, on-board heaters, purging system
- manufacturing: . personnel training, facilities, special tooling
 . procedures: inspection, control, cleaning
- integration, test, handling: . contamination monitoring, purging
- launch operations: . super-clean fairing
- orbital operations: . decontamination procedure

This plan met the requirements of the Chemical Cleanliness Specification (9), whose quantitative requirements are expressed in Tables 2 and 3 in terms of cleanliness level goals and monitoring requirements. In addition it contains detailed requirements such as access, 'cleanability' of equipment, and, for certain units, factors affecting design, manufacturing, testing and/or operation. Methods of monitoring techniques and contamination control are referred to, and the definition of a Cleanliness Control Board is made.

5.2 Clean Room Requirements

For the normal satellite AI & T activities, class 100,000 conditions were observed - however for operations involving work on the radiometer with the baffle cover removed, class 1000 conditions were imposed.

Chemical contamination failure level was taken as $1 \times 10^{-7} \text{ g/cm}^2$. Manufacture and Assembly of the radiometer and cooler demanded, for various critical operations, rigid control at class 100 under laminar flow conditions (cooler elements assembly contamination sensors incoming inspection, multilayer manufacturing, cooler integration) (13). Except for critical items such as sensors and solar panels the remaining equipment was manufactured under less stringent conditions (generally class 100,000).

TABLE 1 - MATERIALS LIST BREAKDOWN

MATERIAL CLASS	No. OF TYPES	APPLICATION SIZES			
		0-1g	1-50g	50-500g	> 500g
Adhesives	32	5	18	7	3
Adhesive Tapes	18	3	11	4	-
Coatings and Varnishes	10	2	9	6	-
(Glasses)	(4)				
Lubricants (external)	8	3	4	1	-
Lubricants (sealed)	1	-	-	-	1
(Metals)	(200)				
Paints and Inks	13	4	4	4	2
Plastics and Metallised Films	11	2	6	-	4
Potting and Sealing Compounds	8	1	10	7	1
Reinforced/thermoset Plastics	49	-	17	20	12
Rubbers and Lacings	12	1	7	4	-
Thermoplastics and sleeving	36	4	33	7	-
(Wires, cables, ribbons, foils)	(39)				
(Miscellaneous, incl. mechanical components)	(66)				

TABLE 2 - CLEANLINESS LEVEL GOALS

ELEMENTS	TYPES	At delivery	After acceptance of S/C	After launch completion
TELESCOPE BAFFLE AND TELESCOPE COVER (Internal sides)	VCM g/cm ²	4 x 10 ⁻⁷	7.10 ⁻⁷	8.10 ⁻⁷
	DUST (N > d)/cm ²	5.10 ³ d ^{-2.2}	10 ⁴ d ^{-2.2}	2.10 ⁴ d ^{-2.2} (0.1%)
COOLER COOLER COVER (Internal side)	VCM g/cm ²	4 x 10 ⁻⁷	7.10 ⁻⁷	8.10 ⁻⁷
	DUST (N > d)/cm ²	5.10 ² d ^{-2.2}	10 ³ d ^{-2.2}	2.10 ³ d ^{-2.2} (0.01%)
EDA, DOWN PART AND CENTRAL BELT (External sides)	VCM g/cm ²	10 ⁻⁷	5.10 ⁻⁷	10 ⁻⁶
	DUST (N > d)/cm ²	4.10 ⁵ d ^{-2.2}	6.10 ⁵ d ^{-2.2}	8.10 ⁵ d ^{-2.2} (5%)
Other Internal SPACECRAFT elements	VCM g/cm ²	10 ⁻⁷	5.10 ⁻⁷	10 ⁻⁵
	DUST (N > d)/cm ²	4.10 ⁵ d ^{-2.2}	6.10 ⁵ d ^{-2.2}	8.10 ⁵ d ^{-2.2} (5%)
SOLAR GENERATOR	VCM g/cm ²	10 ⁻⁷	2.5 10 ⁻⁷	10 ⁻⁶
	DUST (N > d)/cm ²	3.10 ⁵ d ^{-2.2}	4.10 ⁵ d ^{-2.2}	5.10 ⁵ d ^{-2.2} (3%)
SENSORS	VCM g/cm ²	1.7 10 ⁻⁷	2.2 10 ⁻⁷	10 ⁻⁶
	DUST (N > d)/cm ²	3.10 ⁵ d ^{-2.2}	4.10 ⁵ d ^{-2.2}	5.10 ³ d ^{-2.2} (3%)

Table 3 - NATURE AND FREQUENCY OF SYSTEM LEVEL INSPECTIONS

ACTIVITIES	ENVIRONMENT CONTROL										TELESCOPE	COOLER	SOLAR GENERATOR
	Before and/or after activities		If critical elements are										
			OPEN				CLOSED						
			VCM	DUST	VCM	DUST	VCM	DUST	VCM	DUST			
Integration Checkout Measurements Storage	W on walls and handling facilities 4 SI/5 days	4 DC/day for 5 days	1 SI/5 days 2 SI/10 days 1 SI/through-out activities	DC permanent	2 SI/10 days 2 SI/through-out activities	1 DC/4 hours	SI or W cover	SI or W cover	VCM	VCM	W/masks 1 SI panel at end of activity		
Vacuum Test	<u>VACUUM CHAMBER</u> W on walls before and after <u>PREPARATION ROOM</u> W on walls and 4 SI/5 days	4 DC/day for 5 days	2 SI/through-out activities without covers	DC permanent	2 SI/10 days 2 SI/through-out activities	1 DC/4 hours	SI or W/cover	SI or W cover					
Mechanical tests	W on walls and handling facilities 4 SI/5 days	4 DC/day for 5 days			2 SI/10 days 2 SI/through-out activities	1 DC/4 hours					1 SI/panel after test		
Transportation	W on container before and after 2 SI after												
Launch Preparation	W on walls and handling facilities 4 SI on inner face	4 DC/day for 5 days	IF NEEDED 1 SI/5 days 2 SI/10 days 1 SI/through-out activities	IF NEEDED 1 DC/hour	2 SI/10 days 2 SI/through-out activities	1 DC/4 hours					1 SI/panel before launch		
Fairing	W on inner face												

- DC Counting of atmospheric dust
- SI IR analysis of a contamination sensor
- W IR analysis of a molecular deposit as collected by cleaning.
We refer to all molecular surface deposits as VCM.

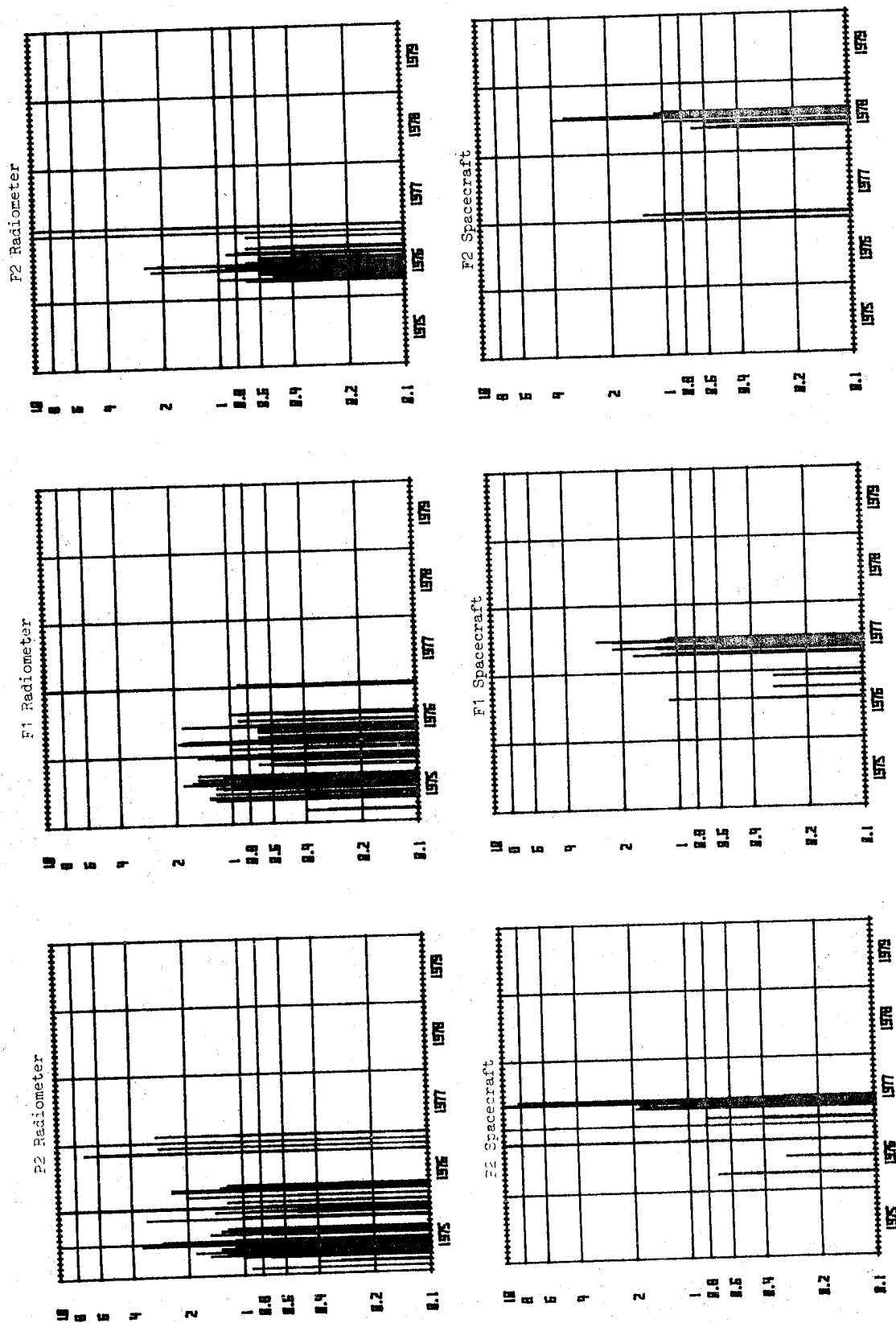


Fig. 2 - Contamination Sensor Results in 10^{-7}g/cm^2

5.3 Packaging/Cleaning

Uniform packaging and pre-integration cleaning methods were used across the consortium - solvent surface cleaning, sealed double bagging under nitrogen and with inclusion of dessicant, inspection and recleaning on opening.

Specific anti-contamination techniques were developed during manufacturing and qualification testing of processes such as anti-reflecting coatings, mirrors substrates, optical filters. These techniques involved specific handling instructions, additional cleaning steps, lengthy substrate preparation, special handling tools.

An example of a specific anti-contamination technique is given in Appendix 1 for mirror substrates.

5.4 Monitoring Techniques

Particulate contamination: a continuous or frequent periodic particulate count has been performed during all satellite integration activities up to launch. Only one or two instances has occurred where the class 100,000 limits have been approached - due to clean room equipment failure - were shown subsequently not to have contaminated the spacecraft appreciably.

Chemical contamination: the most significant aspect of contamination for the radiometer, a regular series of controls has been carried out during the radiometer manufacture and the satellite integration. For the most part these controls were carried out using both wipes and sensors. Fig. 2 and Table 4 show, as histograms, the results obtained for the radiometer and the spacecraft integration, for each of the spacecraft models (qualification, Flight 1 and Flight 2). The significance of their findings is discussed elsewhere.

Table 4 - Averaged Contamination Levels

Model	Radiometer	Spacecraft
F2	1,33	2,76
F1	0,90	$0,95 \times 10^{-7} \text{ g/cm}^2$
F2	0,97	0,96

We can mention, however, the results of an experiment carried out by our contractor after a certain experience of variably dissimilar results between monitoring contamination levels with wipes and with sensors (10). This experiment (set-up shown in Fig. 3) compared the two monitoring methods under a controlled contamination environment: its results (see Table 5) suggest that little reliance can be placed on the correspondence of the two methods, and that of the two methods, the sensor approach gave the more consistent result.

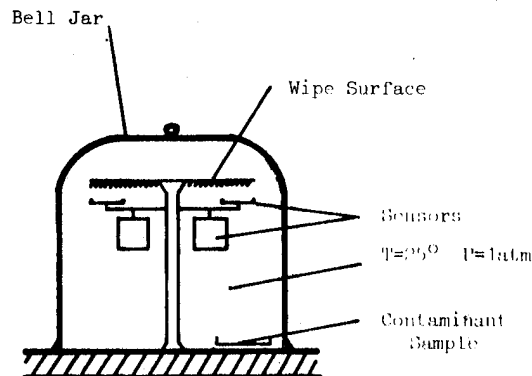


Fig. 3 - Sensor/Wipe Comparison Test

6. PROBLEMS ENCOUNTERED

To enumerate all the problems or incidents with impact on cleanliness control occurring during the METEOSAT programme is, of course, impracticable here. However, to demonstrate typical problems encountered during the programme, 4 examples are hereunder described: relating to materials, processes and contamination control procedure.

6.1 Rejection of Basic Adhesive for Solar Generator

The adhesive (SY186 + primer 023) initially proposed for the METEOSAT solar generator had been previously used on other solar generators and was part of a qualified fabrication procedure of which the adhesive's intrinsic properties (viscosity, cure, pot life) formed a critical part.

Nevertheless, the adhesive was rejected due to its rather poor outgassing properties, the large surface area and critical application: a replacement (DC93-500) was chosen which, although having the requisite outgassing characteristics, required additional testing, new tooling, modifications to the fabrication procedure, etc. This change met with opposition (10 months of technical negotiations) from the contractor, and resulted in significant cost and planning impacts.

This example underlines that it is neither cheap nor easy to impose cleanliness constraints on contractors or programmes: there is a strong tendency to use the already 'proven' method even if data shows that it is insufficient. Cleanliness design control, with materials' selection, needs to be instigated right from the start of the programme.

6.2 Scanning Mechanism Sealing

The scanning mechanism of the radiometer telescope is an oil lubricated system, essential in the image-taking function. Containing a "dirty" product, it had to be correctly filled up and

CONTAMINANT	PERIOD OF EXPOSURE (days)	SENSOR CONTAMINATION LEVELS ($\mu\text{g}/\text{cm}^2$)			WIPE CONTAMINATION LEVELS ($\mu\text{g}/\text{cm}^2$)			CORRELATION FACTOR
		Hydrocarb	Esters	Silicone	Hydrocarb	Esters	Silicone	
Hydrocarbon (Pump Oil)	7	0,126	0	0	0,18	0	0	0,7
	16	0,022	0	0	0,00013	0	0	0,006
	17	0,105	0	0	0	0	0	0
	24	0,063	0	0	0,04	0	0	0,6
	32	0,062	0	0	0,02	0	0	0,3
+ Ester (Dibutyl Phtrlate)	19	*	0,04	0	*	*	*	*
	26	0,026	0,165	0	0,079	0,0095	0	0,3/0,06
+ Silicone (DC200-dimethyl Silicone)	34	0,8	0,119	4,2	*	*	*	*
	49	3,1	0,31	6,66	0,0052	0	0	0,002/0/0

(* not measured)

Table 5 - Sensor/Wipe Comparison

hermetically sealed. Several contamination problems were encountered during the development tests. The following chart of operations defines the steps of the qualified process, each of them being defined in a specific procedure. Figure 3 illustrates the complet set-up of this single, but critical, operation. Duration ~3 days.

PROCESS OPERATIONS SEQUENCE

1. Outgassing of:
 - a) equipment + test equipment
 - b) silicone oil (DC FS 1265)
2. Filling operation
 - 4 major steps:
 - a) 500 cc filling
 - b) bellows heating (bubble-free/gas pocket elimination)
 - c) partial pressurization
 - d) filling up (about 100 cc)
3. He pressurization
4. Crimp-sealing
5. Leak test.

The procedure was developed on a 1:1 scale model made with a transparent body.

6.3 Cooler Gold-plating Process

This problem relates to the early detection of defects observed after metallization of cooler components. This plating, critically important for cooler performance, is highly dependent for its ultimate quality on cleanliness control during the process. Defects were found by visual (e.g. white spots, surface diffusion) and by physical test (e.g. poor adhesion). The necessary improvements were made by an iterative process whose major steps were:

- modification of tools and test equipment,
- redesign of cooler components to meet process equipment capabilities,

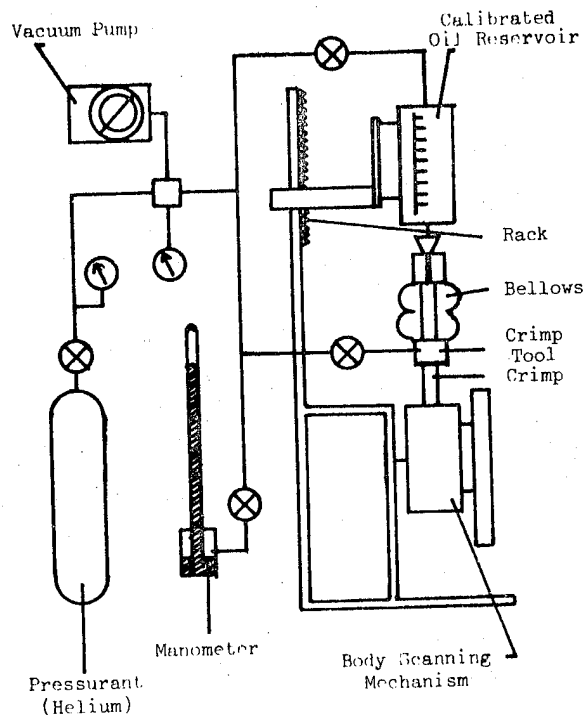


Fig. 4 - Scanning Mechanism Sealing Process

- qualification testing of process,
- sample metallization,
- improvement to pre-cleaning procedure,
- additional process steps (baking at 120°C),
- additional process steps (ultrasonic cleaning),
- implementation of contamination sensing during process,
- additional cleaning,
- packaging improvements.

No single contamination problem was identified during the course of this process development: rather a problem whose solution demanded a multiplicity of controls and steps. Contamination control is a system problem, and the system must deal with all aspects to be effective.

6.4 Radiometer Thermal Vacuum Test Contamination

A contamination problem, induced by paint particles from the inner chamber wall, occurred during thermal vacuum testing of the radiometer. Here the pattern of corrective and preventive action took a different course as the problem was well identified. However, the potential cost/planning impacts are potentially very high in this case as irreversible damage to the test-item was threatened. The maximum care must be taken during these system or sub-system tests - and the rôle of product assurance personnel is here a vital step in diminishing the risk. It is unfortunate that the concentration of effort tends to be on the side of the user, rather than the test house in this respect: greater involvement by project P.A. in thermal vacuum facility procedures and preparation may be indicated.

7. DISCUSSION AND CONCLUSIONS

The activities recorded in this paper have led to an acceptable in-orbit performance (11). The development of cleanliness goals and requirements, integration, test and operations have had heavy impacts on cost and schedule - it is difficult to make a good estimate as the effects of cleanliness control occur at every stage of the programme, but limiting cost consideration to materials screening tests, degradation studies, in-situ contamination measurements and implementation of the Cleanliness Control Plan, not less than 1% of spacecraft overall cost is involved.

The goals defined appeared to be realistic; as Fig. 2 show (and Table 4), global contamination levels of the order of 10^{-7} gcm⁻² are practicable. Whether this order of contamination is, for METEOSAT application, just adequate or much better than necessary, is an open question.

For new programmes having spacecraft embarking contamination-sensitive equipment, our recommendation is that a product cleanliness assurance system be established at a very early stage. As in many other domains, prevention is better than cure; and in fact may be the only solution. Therefore, the project should consider cleanliness throughout design, manufacturing, integration and launch phases, and should not believe that clean rooms are a sufficient solution.

8. APPENDIX

Mirror Substrate Cleaning Procedure

Hereafter are listed the basic cleaning steps implemented before the metallisation process of the telescope mirrors :

1. Degreasing in a bath containing :
 H_2SO_4 : 60cc
 Potassium Ferricyanide 60g/l
 Volume bath : 1 l. max
 Temperature : 25°C max
2. Rinsing in desionised water
3. Neutralisation in - distilled water 2/3
 - ammonia 1/3

4. Immersion in - ethanol 95/96°C 2/3
 - ammonia 1/3
5. Drying with optical cleansing tissue or surgical quality hygroscopic cotton
6. Mechanical cleaning :
 - smooth polishing with hygroscopic cotton and aluminium powder (granulometry 3µ)
 - repeat step 4 to eliminate residues of previous step
 - drying cleaning
7. Visual control at ambient + about 5 hours stabilisation necessary for large size mirrors
8. Elimination of static charges
9. Final cleaning as per step 5

10. REFERENCES

1. ESRO MET/SA/SPEC-01, Issue 3, rev. Sept 1974
 'Performance Specification for the METEOSAT Satellite'
2. ESTEC QRM-01, Issue 1, rev. 3
 'Guidelines for Spacecraft Materials Selection'
3. ESTEC QRM-02, Issue 1, rev. 1
 'Screening Test Method Employing Thermal Vacuum for Selection of Materials'
4. DFVLR Contract no. 1930/73/CG
 'Configuration Study of the METEOSAT Radiometer and Cooler with respect to the Contamination of Sensitive Surfaces'
5. HARWELL CR(P)847
 'Degradation of METEOSAT Radiometer Primary Mirror by Contamination and Radiations'
6. DFVLR Contract no. 2234/74/CG
 'Experimental Study on the Contamination Degradation effects on the Optical and Thermo-optical Performances of critical parts of the METEOSAT Radiometer in Orbit'
7. SNIAS SR9, rev. A of 10.4.76
 'METEOSAT - Selection, Procurement and Control of Materials and Special Processes'
8. SNIAS 81/83 TJA, Issue 3 of 4.4.74
 'METEOSAT - Chemical Cleanliness Control Plan'
9. SNIAS SR6A, rev. F/RO2 of 12.7.74
 'METEOSAT - Chemical Cleanliness Control Specification'
10. SNIAS 800/CA 44 of 16.6.77
 'Essais de Contamination Contrôlée'
11. M. Reynolds/J. Kieffer ESTEC 2-4.10.79
 'METEOSAT Cleanliness Control Achievements' Symposium on Spacecraft Materials
12. BERTIN CR(X)1006
 'Etude de Synthèse des Actions de Propreté engagées pour la réalisation du Radiomètre cryogénique passif du Radiomètre du satellite METEOSAT'

PRECEDING PAGE BLANK NOT FILMED

N80-21430

ASSESSMENT OF SHUTTLE PAYLOADS GASEOUS ENVIRONMENT CONTAMINATION AND ITS CONTROL

J J Scialdone

Goddard Space Flight Center, Greenbelt, Maryland, USA

ABSTRACT

A prediction of the in-orbit gaseous environment and the contamination it could produce on cryogenic and room temperature surfaces of payloads in the shuttle bay has been carried out. The time-varying environment was obtained by the superposition of the calculated shuttle environment for a discrete time and payload induced environments measured in large space chambers. The payloads will dictate the environment with the exception of periods when the attitude motors and water-release operations are in operation. Representative contaminant surface accretions have been calculated for flights 1 week and 1 month long for payloads having the largest source of outgassing and an orbit of 200 km. Based on the magnitude of the sources, their molecular natures, the decay rate with time, the sticking coefficients, the view factors, and the temperatures of the surfaces being contaminated, a number of calculations were made. These calculations led to a number of results. To reduce the contamination hazards, investigations have been performed on delaying the exposure of critical surfaces, on the effect of using vented helium as a counterflow to ingested oxygen in telescopes, on the effect of varying sublimation temperatures and times on the removal of condensed oxygen, and on the waiting time for normalization of the environment after operation of the control motors and/or evaporator. This document concludes with a list of precautions that can be taken during the design and operational phases of an instrument to limit the contamination to acceptable levels for short-duration Spacelab flights.

1. INTRODUCTION

Instruments and payloads carried by the Space Transportation System (STS) will be in a different space environment than that of the present satellites. This environment can degrade the observations and the measurements of the sources of energy being monitored. The degradation can be caused by the intervening gaseous and particulate medium that exists between the source and the instrument or by the deposits of this medium on thermo-optical surfaces. The most affected surfaces are those at cryogenic temperatures. The deposits may change the radiative properties of the surfaces, induce loss of optical transmittance, and produce light scattering and false indications of sources. The environment of payloads in the STS is dictated by the STS propulsion, life-sustaining, and power-generating systems and by material outgassing and shedding of particulates.

A preliminary assessment of the induced and natural environment of the STS with payloads has been performed. Its magnitude, deposit on surfaces, and controllability have been investigated. A generalized approach has been used to develop these data so that it may be used in the design and planning of instruments and payloads. Case-by-case detailed analyses must be performed later, when measured data on the STS environment and the particular design of the payloads will be available.

In this document, the gaseous environment for a payload or payloads in the STS were derived by the superposition of the calculated self-induced environment of the STS and the induced environment of a number of spacecraft, measured in large vacuum chambers. The density, direct fluxes, and column densities of the Shuttle and payloads were derived as a function of time, orbital altitudes and lines of sight. The contributions of the STS evaporator and vernier-control systems (VCS) are included.

Deposits of these molecular sources on surfaces at room and cryogenic temperatures were calculated, with attention to contamination of telescopes and, in particular, to the proposed cryogenic limb interferometer radiometer (CLIR). However, the calculations and relative plots in this document are general and can be used for any payload if geometrical factors and surface temperatures are known. The times during which contaminant deposits are possible were obtained from the expected magnitude of the contaminant after 10 hours in orbit, modified by the geometrical view factor between the source and the surface, the surface temperature, and the nature of the contaminant. The maximum deposit and the time for its eventual disappearance were estimated. The effect of delay in the exposure of a surface to the contaminant was evaluated. A list of the expected contaminant deposits on surfaces with direct or limited view (CLIR instrument) of the contaminant is provided. The deposits are based on the most severe expected environment of a general class of payloads in the STS at a 200-km altitude. The effect of surface temperatures, the nature of the contaminant (H_2O or DC-705 silicone oil), the flight duration (1 week to 1 month), and the delay in exposure time were considered. Deposit rates from the emissions of the VCS and evaporator and from the natural oxygen were calculated. Methods for reducing cryogenic surface contamination using He as a purging gas or temperatures required for subliming the deposits were investigated. Also, the time required for the environment to become acceptable after the emission from a source such as the VCS and the evaporator was considered. The

estimated environment was compared with the criteria limits on the environment suggested by the scientific community for satisfactory measurements and observations. Finally, a number of suggestions for limiting contamination through design and operational control are included.

2. CONTAMINATION CRITERIA

Early in the Shuttle program, the scientific community set certain mission objectives and recommendations regarding the induced molecular and particulate contaminant emanating from the Shuttle. Volume X of Ref. 1 lists the maximum allowable induced environment levels or criteria, which were subsequently clarified and expanded by the Contamination Requirements and Development Group (CRDG). The criteria * state that it is a design and operational goal for the Orbiter and Spacelab to control the environment within the following limits:

- Column density

10^{11} to 10^{12} cm^{-2} , $\text{H}_2\text{O} + \text{CO}_2$

10^{13} cm^{-2} , $\text{O}_2 + \text{N}_2$

10^{10} cm^{-2} , other gases

- Particulate emission

<1 discernible particle per orbit entering 1.5×10^{-5} steradian (sr) field-of-view along any line within 60 degrees of the Z-axis (discernible particle is 5μ diameter within 10 km)

- Molecular deposition

$<10^{-5}$ $\text{g}/\text{cm}^2/30$ days/ 2π sr on 300-K surface

$<10^{-7}$ $\text{g}/\text{cm}^2/30$ days/0.1 sr on 300-K surface

$<10^{-5}$ $\text{g}/\text{cm}^2/30$ days/0.1 sr on 20-K surface

$(10^{-5} \text{ g}/\text{cm}^2/30 \text{ days} \approx 10^{12} \text{ molecules}/\text{cm}^2/\text{s}$ average flux)

≈ 1 -percent optical degradation in infrared through ultraviolet by condensibles

- Background brightness

Continuous emissions or scattering not to exceed 20th magnitude/sec² in the ultraviolet (equivalent to 10^{-12} B @ $\lambda = 360 \times 10^{-9}$ m).

The Particle and Gas Contamination Panel (PGCP) has used these criteria as the basis for the contamination control of the Orbiter. This panel is implementing recommendations for design changes, material selections, contamination control, and flight and ground contamination monitoring.

3. SHUTTLE-INDUCED ENVIRONMENT DATA

Figure 1 shows the Shuttle configuration with the vent locations and sources of contamination. Martin Marietta Aerospace and Johnson Space Center have used the Shuttle Payload Contamination Evaluation Program (SPACE) to model the Shuttle environment. Among other things, the model includes the geometries, the materials outgassing, and the various vent sources. It provides an estimate of the gaseous characteristic of the Shuttle and estimates of contaminant deposits on surfaces.

Parameters of interest were calculated along lines of sight (LOS) identified in terms of the angles, θ and Φ , as shown in Figure 1. The origins of the LOS are at $X=28.12$ m, $Y=0$, $Z=12.88$ m. The data for the materials outgassing were obtained from previous experiences with the outgassing of the Skylab, from some tests on outgassing of sample materials, and by averaging the results of the 24-hour, 125°C volatile condensable material/total mass loss (VCM/TML) selection criteria tests on sample materials. Other sources, such as the evaporator, VCS, and cabin leak rates, were obtained from analytical estimates, tests, or previous experiences with similar systems.

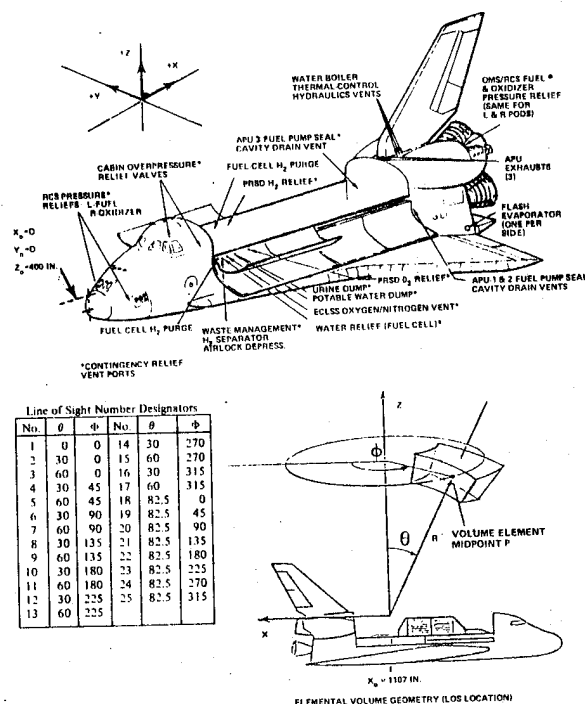


Figure 1. Shuttle Configuration Showing Vent Locations, Sources of Contamination, and Lines of Sight.

The data for the plots in Figures 2, 3, and 4 were provided by the PGCP panel at Johnson Space Center or collected from Refs. 2 and 3. These data were obtained using the Space Computer Program. Figure 2 shows the density versus distance for the Shuttle at a 400-km orbit. It shows that the densities produced by the evaporator and the VCS along LOS-1 and LOS-5 are maximum at about 10-15 m from the Shuttle origin. Their magnitudes, 10^{-11} - 10^{-12} g/cm^3 , are equal to pressures of about 7×10^{-6} to 7×10^{-8} torr. The maximum densities produced by material outgassing at maximum temperatures are 8×10^{-15} g/cm^3 ($\sim 10^{-8}$ torr) for the early flight desorption and 2.5×10^{-15} g/cm^3 ($\sim 10^{-9}$ torr) for outgassing beyond 10 hours in flight. The densities for low temperature conditions are also shown.

Figure 3 shows the column densities along various LOS for the Shuttle at a 400-km orbit produced by the same sources as before. These column densities are the integrated values of the density in a column 1 cm^2 of area from the surface of the Shuttle to infinity. As shown, the columns for the VCS and evaporator are in the 10^{14} cm^{-2} range, which are higher than the 10^{12} cm^{-2} columns considered acceptable. The plot shows that the columns produced by the materials outgassing of the Shuttle meet the criteria for the chosen conditions. Figure 4 shows the

*Contamination Requirements and Development Group, Marshall Space Flight Center, July 22, 1975.

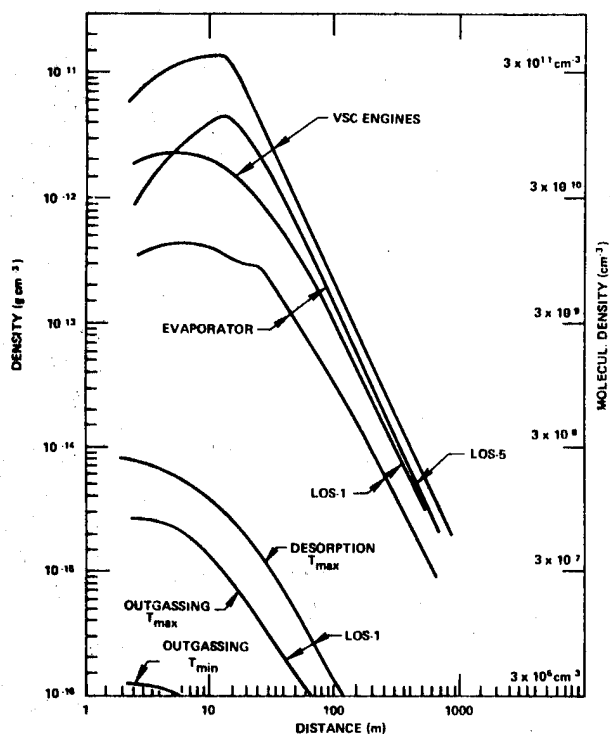


Figure 2. Shuttle Density Versus Distance at 400-km Orbit

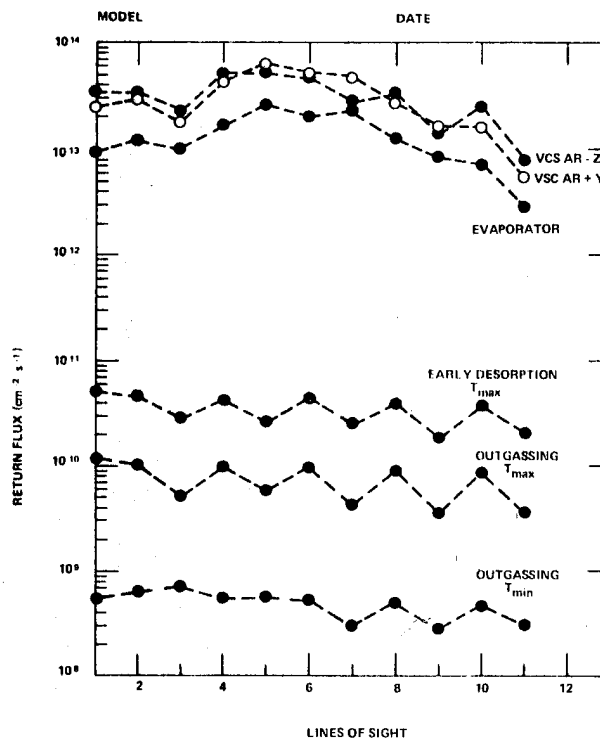


Figure 4. Shuttle Return Flux Versus LOS at 400-km Orbit

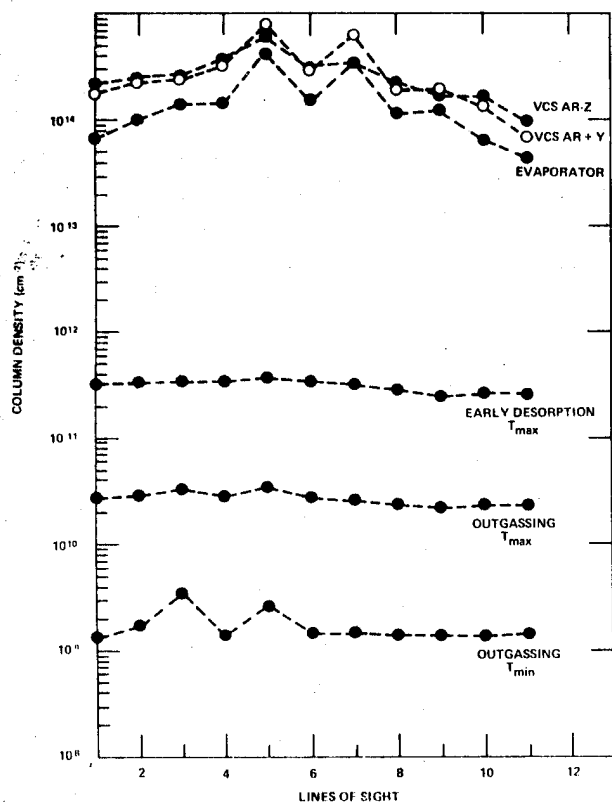


Figure 3. Shuttle Column Density Versus LOS at 400-km Orbit

return fluxes of the several sources produced by their scattering with residual ambient molecules at 400-km. These molecules may condense or adsorb on the surfaces on which they impinge if the conditions of temperature are favorable. The return fluxes at this altitude are approximately 1/32 of the returns expected at 200 km. Figure 4 shows that the return fluxes of the evaporator and VCS are about 3 orders of magnitude higher than those produced by the outgassing.

The data shown in these Figures 2, 3, and 4 apply to a 400-km orbit. For lower orbits, the return fluxes caused by ambient scattering will increase as shown in Figure 5 (Ref. 4). At 300 km, the return is approximately 4 times larger than at 400 km, and, at 200 km, the return is about 32 times larger for the assumed source radii of 1 m or more. At these altitudes, the ambient scatter predominates over the self-scattering of the sources, which may become important at altitudes higher than 400 km. The density and column density are not affected by altitude being a function of the source strengths. However, as shown in Figure 6, their distributions with distance change. For orbits higher than about 200 km, the density is quasi-constant for about 1 m from the source. On the other end, for altitudes near 100 km, the density drops rapidly beyond 10 to 15 cm. These considerations could be helpful for instruments such as a telescope or probe. Moving out the entrance of the instrument 10 to 15 cm could provide much lower densities at the entrance when operating at lower orbits.

The molecular compositions of the sources from the Shuttle and payloads are estimated as follows. Early desorption from materials may consist of about 60-percent H_2O , 25-percent H_2 , 10-percent CO_2 , and the rest O_2 and other molecules. Long-term outgassing will consist almost entirely of unreacted monomers and polymer chain fragments. The average molecular

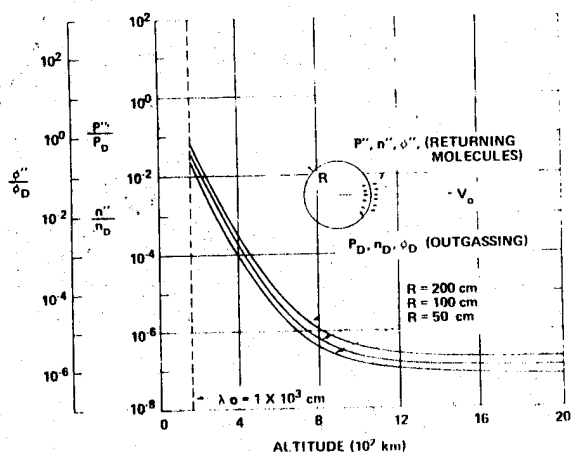


Figure 5. Density, Pressure, and Flux Ratios at the Spacecraft Surface, Produced by Outgassed Molecules Returning to the Satellite (for $\lambda_0 > 21 R$)

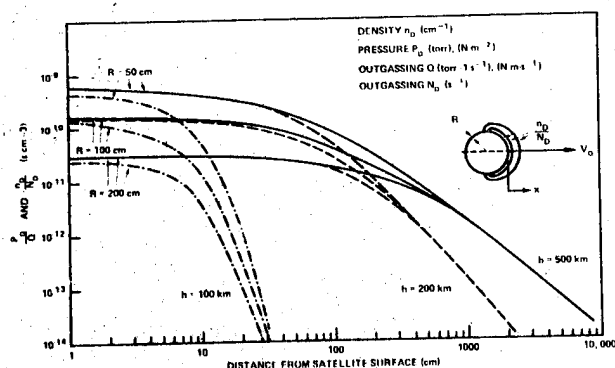


Figure 6. Pressure and Density Produced by Outgassing Versus Distance from the Spacecraft Surface

mass may be about 100-g/ mole. The evaporator source is entirely water. The VCS and the reaction-control system (RCS) sources will consist of about 30-percent H_2O , 30-percent N , 10-percent CO , 20-percent H , and the rest O , NO , H_2 , and some nonvolatile materials. (Although it is not shown in the plots, the RCS induces magnitudes 100 times or more than the VCS.)

4. SATELLITE-INDUCED ENVIRONMENT DATA

Payloads carried by the Shuttle will be exposed to the environment created by themselves and the Shuttle. The molecular and particulate environments produced by the payloads are not known at this time. They cannot be evaluated until data on the payload designs, missions, functions, etc., are known. Calculations similar to those performed for the Shuttle will be needed. Some specific estimates of the global environment have been made for the Shuttle with the Spacelab and with Defense Support Satellite (Refs. 5 and 6). These estimates are based on conditions that exist during certain periods of the flights and some assumptions on the magnitudes of the outgassing sources. In this document data from past experience on satellite-induced environments are used to generate generalized payload environments. These environments, together with that estimated for the Shuttle, can provide expected global environments for future payloads.

The author obtained data on spacecraft-induced environments from tests in large vacuum chambers. Measurements were made on the Canadian Technology Satellite (CTS), the Interplanetary Monitoring Platform (IMP-H) and the Atmospheric Explorer D (AE-D). The CTS weight was 340 kg, and its configuration could be assumed to have an equivalent spherical radius of 1.37 m. The IMP-H weighed about 260 kg and approached a cylinder 1.57 m long with a 1.6-m diameter. The AE-D satellite weighed 679 kg and approximated a cylinder 1.14 m long with a 1.36-m diameter. Figure 7 shows the polar flux, density, and equivalent pressure at 1-m distance and in a plane through the CTS (Ref. 7).

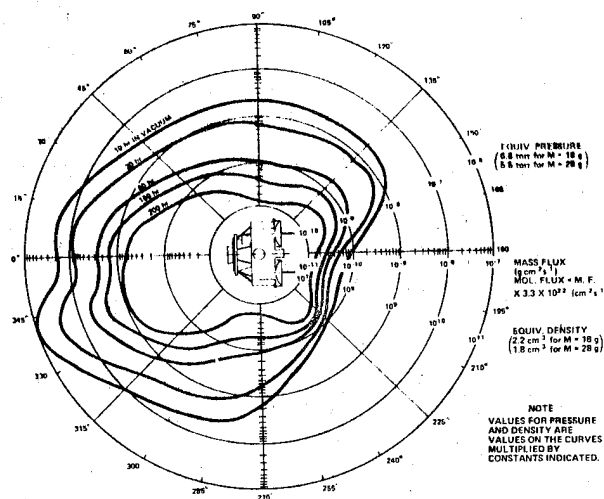


Figure 7. Polar Flux, Density and Pressure Produced by the CTS at 1 m from its Equivalent Surface (equivalent orbit is 300 km)

These parameters were measured as a function of time with two back-to-back mounted quartz crystal microbalances (QCM), cooled at LN_2 temperature. From geometrical considerations and chamber temperatures, the test simulated the outgassing conditions of the spacecraft when orbiting at 300 km. Figure 8, taken from Ref. 8, shows test results with the IMP inside the same large chamber. In this case, the integrated outgassing flux versus time was obtained with the two back-to-back mounted tubulated ion gages while the spacecraft was slowly rotating. Mass spectrometer measurements during these tests indicated that the outgassing consisted of about 90-percent condensibles, $M < 44$ g/mole, during the first 10 to 20 hours. Later, the condensibles were about 50-percent of the outgassing, and there was an increasing fraction of larger molecular-weight products. Complementary information on spacecraft outgassing was obtained from tests on the AE-C (Ref. 9) and from data such as those listed in Table 1 (Ref. 4).

Figure 9 shows the measured changes in outgassing rates as a function of time and angular positions from the CTS test. The measurements were taken for a period of about 150 hours, beginning after the spacecraft had been in the chamber for about 10 hours. Most of the outgassing curves in this plot show a decay with time according to a $t^{-1.5}$ - $t^{-1.8}$ law, with the exception of the angular positions at 190 and 235 degrees, which show a rate approaching a $t^{-1/2}$ law. These laws reflect a diffusion-controlled outgassing process. In fact, the solution of the equation for diffusive outgassing of a slab of material is an exponential function of time that approaches a $t^{-1/2}$ slope for an initial period of time and then changes to a slope whose asymptote is a $t^{-3/2}$

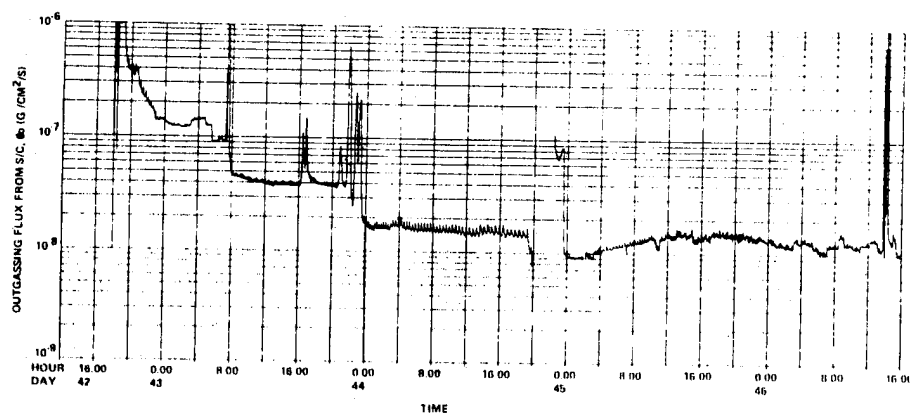


Figure 8. IMP-H Spacecraft Outgassing Flux, ϕ_o , Versus Time at its Surface

Table 1
Estimated Satellite Gaseous Parameters

Satellite	Parameter									
	Satellite Radius R_s (cm)	Altitude h (km)	Neutral Concentration n_0 (cm^{-3})	Pressure P_0 (torr)	Mean Free Path λ_0 (cm)	Outgassing (even calculated)			Molecular Mass M (g)	Temperature T (K)
						Q ($\text{torr}\cdot\text{L}\cdot\text{s}^{-1}$)	\dot{m} ($\text{g}\cdot\text{s}^{-1}$)	N ($\text{molecules}\cdot\text{s}^{-1}$)		
Gemini 3	200	160	5.24×10^{10}	4.13×10^{-6}	2.5×10^3	4.3×10^9	4.7×10^{-3}	1.12×10^{20}	18	293
Gemini 2	200	300	1.72×10^9	1.95×10^{-7}	1×10^5	1.43×10^1	1.4×10^{-7}	4.78×10^{20}	18	293
Apollo	200	300	1.72×10^9	1.95×10^{-7}	1×10^5	3.06×10^1	3×10^{-7}	1.01×10^{21}	18	293
ATM	300	400	3.98×10^8	3.98×10^{-8}	1×10^6	1.02×10^2	1×10^{-3}	3.3×10^{21}	18	293
IMP 2	~50	200	1.5×10^{10}	1.35×10^{-6}	8×10^1	2×10^9	5×10^{-3}	6.68×10^{19}	18	293
ISIS 1	~55	575	4×10^7	4×10^{-9}	1×10^7	9×10^{-1}	9×10^{-4}	3×10^{19}	18	293
Nimbus (TWS)	~70	1100	9.45×10^4	1.08×10^{-10}	1×10^9	8.9×10^{-3}	8.9×10^{-6}	2.8×10^{17}	18	293

Calculations

Satellite	Parameter												
	Mean Free Path (cm)		Molecular Concentration (cm^{-3})				Pressure (torr)		Reverse Pressure (torr)		Thick. ($\text{cm}^{-2} \cdot \text{s}^{-1}$)		Mass Column Density (g/cm^2)
	Desorbed λ_D	Reflected λ_R	Desorbed n_D	Reflected n_R	Reverse n	Reflected P_R	Desorbed P_D	Reverse Pressure P	Desorbed \dot{P}_D	Reverse \dot{P}_R	Desorbed \dot{Q}_D	Reverse \dot{Q}_R	
Gemini 3	1.0×10^2	6×10^2	7.95×10^{10}	7.1×10^9	4.9×10^8	6.22×10^{-6}	2.15×10^{-7}	1.8×10^{-8}	2.83×10^{14}	1.96×10^{14}	1.96×10^{10}	1.96×10^{13}	2×10^{-12}
Gemini 2	5×10^3	3.5×10^3	2.6×10^9	2.83×10^{10}	1.13×10^8	2.94×10^{-7}	8.65×10^{-7}	3.45×10^{-9}	4.13×10^{15}	4.8×10^{13}	4.8×10^9	4.8×10^{13}	6.9×10^{-12}
Apollo	5×10^3	3.5×10^3	2.6×10^9	6×10^{10}	2.9×10^8	2.94×10^{-7}	1.84×10^{-7}	6.12×10^{-9}	2.4×10^{15}	9×10^{13}	9.6×10^9	9.6×10^{13}	1.4×10^{-11}
ATM	4.5×10^8	3×10^5	5.25×10^8	2.3×10^{11}	1.71×10^8	6×10^{-8}	7.14×10^{-6}	5.32×10^{-9}	9.25×10^{15}	8.8×10^{13}	8.8×10^9	8.8×10^{13}	3.2×10^{-11}
IMP 2	4×10^2	2×10^3	2.25×10^{10}	5.26×10^{10}	6.6×10^8	2.03×10^{-6}	1.6×10^{-6}	2×10^{-8}	2.1×10^{15}	3.3×10^{14}	3.3×10^{10}	3.3×10^{14}	3.9×10^{-12}
ISIS 1	5.5×10^5	4×10^8	6×10^7	2.4×10^{10}	1.55×10^5	6×10^{-9}	7.2×10^{-7}	4.66×10^{-11}	9.7×10^{14}	8×10^{10}	8×10^6	8×10^{10}	1.8×10^{-11}
Nimbus	6.5×10^7	4×10^8	1.4×10^6	1.68×10^8	1.6×10^1	1.62×10^{-10}	8.3×10^{-9}	8.3×10^{-10}	6.75×10^{17}	1.68×10^7	1.68×10^7	1.68×10^7	1×10^{-14}

*A monolayer of H_2O , 5.27×10^{19} molecules cm^{-2}

[†]Number column density expressed in cm^{-2}

curve (Ref. 10). The time at which the two slopes intersect is dictated by the thickness and diffusion coefficient of the material. This would indicate that the outgassing at the two angular positions with the $t^{-1/2}$ decay eventually decay like the others according to $t^{-3/2}$. In Figure 9, the total outgassing of IMP-H shown in Figure 8 has been superposed on the outgassing

rates of the CTS and its outgassing decay also shows a similar time dependence. The outgassing was not measured during the early hours of vacuum exposure because the large amount of outgassing at those times would rapidly saturate the measuring instruments. The early outgassing consists mainly of gases desorbed from the surfaces. This early outgassing decays rapidly to a much lower rate within 1 to 2 hours.

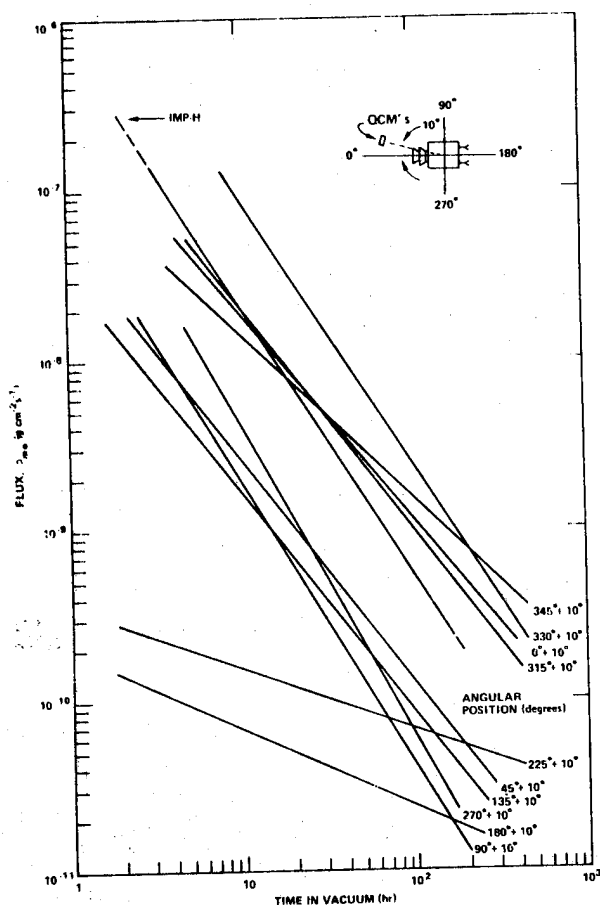


Figure 9. Mass Flux at 1 m from CTS and IMP-H Spacecraft Equivalent Surface

5. SHUTTLE OUTGASSING TIME DEPENDENCE

Figures 2, 3, and 4 show the shuttle environment calculated for a 400-km orbit and at discrete times. The curve labeled "Early Desorption" is taken as the outgassing conditions that exist during the first 10 hours of flight, whereas the curve labeled "outgassing" appears to correspond to the outgassing conditions after 100 hours. In the absence of definite outgassing versus time definition of the Shuttle outgassing, it is suggested that its outgassing versus time may be similar to that of the CTS and IMP-H. There are some supportive arguments for this assumption. According to some results of outgassing measurements of the Skylab and the Orbiting Geophysical Observatory (OGO) reported in Ref. 3 for the early hours of the flight, the outgassing could be represented by an exponential decaying function with a time constant of about 18 hours. This was followed by another exponential with a much longer time constant. For 100 hours, using the exponential with an 18-hour time constant, the drop in outgassing rate is comparable to the drop indicated by the $3/2$ function. For a 10-hour span, the drop from the same exponential equals that given by the $1/2$ function.

The long-term outgassing can be associated to a slow rate of degradation of the material. Another supportive argument to the assumption may be provided by recent tests (Ref. 11) on the RTV 560 silicone rubber used extensively for thermal protection of the Shuttle. These tests showed that the outgassing of this

material followed the classical diffusion-controlled process. In view of these considerations, it is assumed that the Shuttle outgassing decays similarly to that of the CTS and IMP-H (i.e., approximately with a $t^{-3/2}$ law). This decay should be valid for a period from sometime before 10 hours to a time at which this outgassing curve intersects the long-term outgassing. The magnitudes for "early desorption" will be assumed to exist at 10 hours. Regardless, it will be seen later that the total environment for the payloads will be dictated by their own outgassing.

6. PAYLOADS REPRESENTATION

As mentioned, the Shuttle payload environment was obtained by combining the Shuttle data shown in Figures 2, 3, and 4 with the experimental data from the mentioned spacecraft. The Shuttle data for early desorption were taken to exist at 10 hours, and the outgassing was a long-term condition. The magnitudes were taken at a 1-m distance from the origin along LOS (lines of sights) showing maximum values. The IMP-H, which may simulate a scientific payload, and two configurations of the CTS technological satellite are representative payloads. One configuration is a CTS-Maximum (CTS-M) that represents a spacecraft that includes a spent solid motor with 10-hour outgassing rate corresponding to the maximum flux shown in Figure 7. The other, designated CTS-Average (CTS-A) and representing an average spacecraft of that type without a spent motor, has a flux at 10 hours that corresponds to the integrated average of that shown in Figure 7. Additional data on combined Shuttle payload environment were obtained from Ref. 5, which provided predictions for early desorption and later outgassing of the STS with the long module one pallet (STS/LMOP) at 200- and 250-km orbits.

7. EVALUATION OF THE SHUTTLE PAYLOAD ENVIRONMENT PARAMETERS

Data for the Shuttle at a 400-km orbit, for CTS and IMP-H at a 300-km orbit, and for the STS/LMOP at a 200- to 250-km orbit have been reevaluated for altitudes of 200, 300, and 400 km. The following established relationships have been used for each parameter.

The direct flux is given by

$$\phi_D = n V_D \quad (\text{cm}^2 \text{ s}^{-1}) \quad (1)$$

where n (cm^{-3}) is the density, and

$$V_D = \sqrt{\frac{8RT}{\pi M}} = 1.45 \times 10^4 \sqrt{\frac{T}{M}} \quad (\text{cm s}^{-1}) \quad (2)$$

is the mean outgassing velocity of the molecules of molecular mass, M (g/mole), and temperature, T (K).

The ambient scattered return fluxes, ϕ_R ($\text{cm}^2 \text{ s}^{-1}$), were obtained from Refs. 4 and 12:

$$\frac{\phi_R}{\phi_D} = \frac{R}{\lambda_0} \left(\frac{V_s}{V_D} + 1 \right) \quad (3)$$

where R (cm) is the radius of the emitting source, λ_0 (cm) is the ambient, mean-solar-activity, mean free path (Ref. 13), V_D (cm s^{-1}) is the mean outgassing molecular velocity, and V_s is the orbital velocity. This relationship appears in Figure 5.

The column density, N_c (cm^{-2}), is approximated in Ref. 12 by

$$N_c = \frac{\lambda_0}{V_s} \phi_R \sim \frac{\phi_D R}{V_D} \sim nR \quad (\text{cm}^{-2}) \quad (4)$$

The molecular self-scattering flux, ϕ_{ss} ($\text{cm}^{-2} \text{s}^{-1}$), which is complementary to the ambient scattering, was evaluated by using the approximate relation (Ref. 12)

$$\phi_{ss} = \frac{1.78 \times 10^{-2}}{V_D} \sigma R \phi_D^2 \quad (\text{cm}^{-2} \text{s}^{-1}) \quad (5)$$

where σ (cm^2) is the molecular cross section, and the other terms are the same as before.

8. SHUTTLE PAYLOAD COMBINED ENVIRONMENT

The following paragraphs describe the predicted molecular environments of the Shuttle and of the Shuttle with representative payloads CTS-A, CTS-M, IMP, and LMOP with reference to Figures 10 through 13. The predicted parameters are density, column density, direct flux, and return fluxes.

8.1 Density

As shown in Figure 10, the presence of payloads in the bay increases the density of the STS at 1 m by orders of magnitude. The density is dictated by the payloads until their rates of outgassing are the same as those of the STS. The calculated data for the STS and the STS plus the LMOP include a long-term density value. These have been incorporated and are shown on the respective density plots. The natural ambient densities at 200, 300, and 400 km are indicated for comparison.

Payloads similar to the CTS-M will induce densities equal to the ambient density at 300 km after 7 days in orbit. Those similar to the IMP and the CTS-A will have the same equivalent density after 50 to 60 hours and 15 to 20 hours, respectively. The STS/LMOP payload will be in a density equal to the 300-km natural density after many days. Note that the decay rates ($t^{-3/2}$) used here are faster than the linear or square root decays that may also exist. Also, the presence in the bay of additional payloads with similar, same order magnitude outgassing will not significantly change these environments.

The densities that the VCS and the evaporator induce, which are maximum at about 12 m from the bay, are also shown. These are always greater than those that the payloads produce with some exceptions during the early hours of the flight. However, the large densities will dissipate rapidly after the emissions stop, as will be discussed later. The densities along different lines of sight and different distances can be deduced from Figure 2.

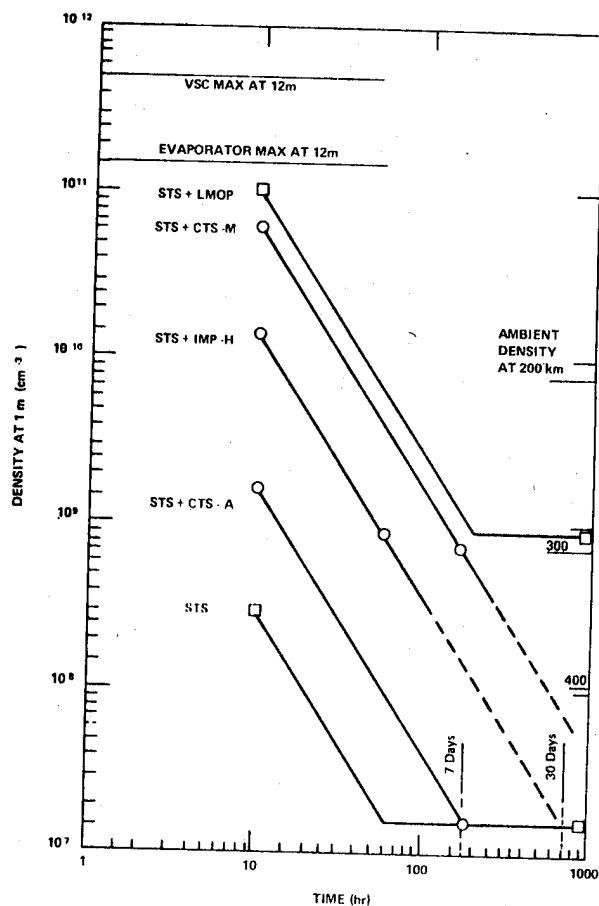


Figure 10. Density Versus Time at 1 m for STS with Payload

8.2 Column densities

Figure 11 shows the column densities versus time that result from combining the Shuttle and payloads. Disregarding the molecular constituents of the columns, the criteria goal of the 10^{12} cm^{-2} H_2O column will be met within 10 hours with CTS-A, within 35 hours with the LMOP, within 10 hours with IMP-H, and in about 30 hours for a payload with the CTS-M characteristics. However, the H_2O content of the column is estimated at about 60 percent after 10 hours in orbit and less than 10 percent thereafter. With this estimate, the criteria are met when the total column has a value of about 10^{13} cm^{-2} , which would exist for most of these payloads within 10 hours after launch. Although the columns produced by the VCS and evaporator are considerably higher than the criteria, they will exist only during their operations and for a few minutes thereafter.

8.3 Direct fluxes

Figure 12 shows the direct fluxes at 1 m that are produced by the STS and payloads. The fluxes for the STS and the STS/LMOP were calculated from the densities shown in Figure 2, using appropriate values for temperatures and molecular weight, and from the return fluxes and column densities given in Ref. 5. The direct-flux calculations assume that the sources are from cylinders. The full reflection of the outgassing from the bay liner increases the fluxes by a factor of 2 without affecting the order of magnitude. These calculated

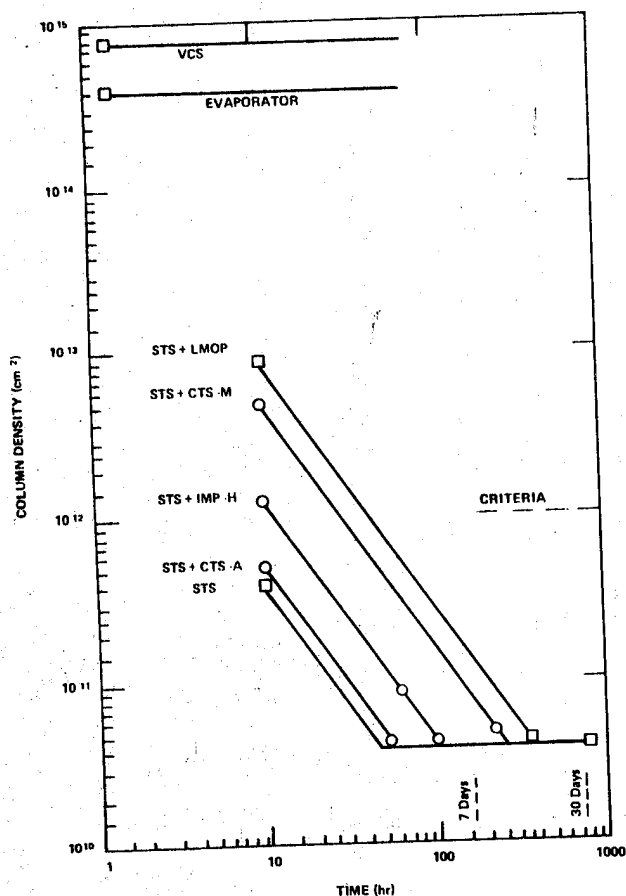


Figure 11. Column Density Versus Time for STS with Payload

fluxes, with data on view factors, nature of the constituents, and temperatures, can provide estimates of contamination risks on surfaces. For comparison, Figure 12 shows the flux that corresponds to a monolayer of H_2O . The monolayer flux will be established after 35 to 40 hours for the LMOP and CTS-M and after 10 to 12 hours for the IMP-H. Figure 12 also shows self-scattering magnitude of the flux from the STS/CTS-M. Its magnitude is about three orders of magnitude less than the direct flux and one order less than the ambient scatter at a 400-km orbit (Figure 13).

8.4 Return fluxes

In addition to the direct fluxes, return fluxes are produced from the scattering of the emitted molecules with the ambient molecules and particles. The return flux is a function of the source magnitude of the molecule cross sections and of the ambient density. It decreases with orbit altitudes and becomes quasi-constant at orbits above 600 to 700 km. Figure 13 shows the estimated returns on a 2π surface for altitudes of 200, 300, and 400 km for the STS, for the STS with the payloads, and for the VCS and evaporator.

The recommended goal of a return flux not larger than 10^{12} molecules/cm² (corresponding to H_2O accumulation of 1100 monolayers in 1 week) will be achieved for a 200-km orbit after 7 days by the Shuttle with the CTS-M, IMP-H, and LMOP and after about 40 hours for the Shuttle with the CTS-A. For a 300-km orbit, 10^{12} cm⁻² is achieved after 60 hours by the IMP,

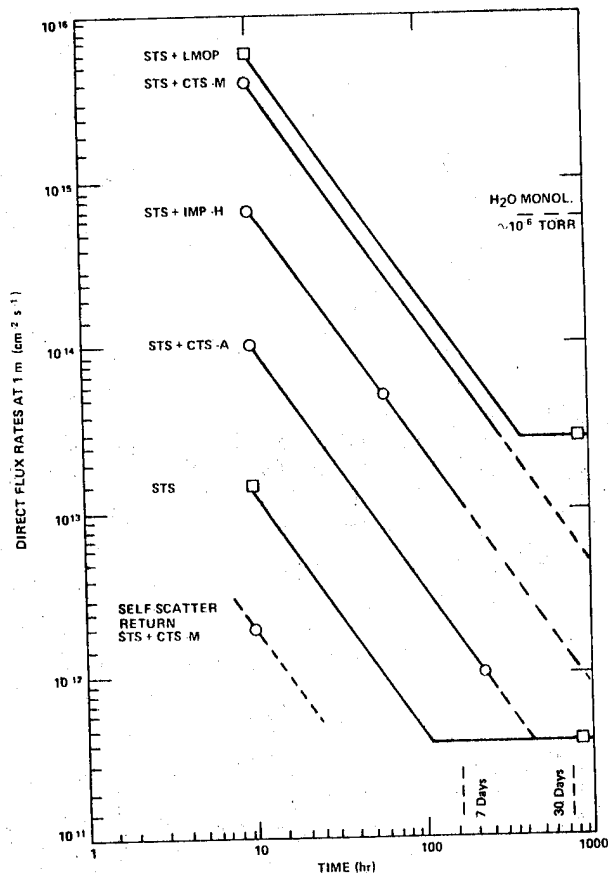


Figure 12. Direct Flux at 1 m Versus Time for STS with Payload

after 140 hours by the CTS-M, and after 12 hours by the CTS-A. At 400 km, the criteria are achieved earlier. The STS alone achieves the criteria within 2 hours at 400 km and within 12 hours at 200 km. The STS/LMOP shows a long-term compliance with the criteria. The return from the VCS and evaporator will not meet this criteria at any of the altitudes considered. As indicated previously, the magnitude of self-scattering within the emitted flux of the STS/CTS-M was shown for convenience in the plot for the direct flux. It is about one order of magnitude less than the ambient return flux for this payload at a 400-km orbit.

9. SURFACE CONTAMINATION

The gaseous environment to which payloads in the Shuttle bay will be exposed (as derived in the previous pages) can be used to estimate contaminant deposits on critical surfaces. In addition to the source and the nature of its constituents, additional data are needed on the temperature of the surface and its geometrical view factor with respect to the source. The following paragraphs discuss contamination on surfaces in the bay that have direct or limited view of the source and are at normal or cryogenic temperatures. In particular, it discusses the probable contamination of CLIR (Ref. 14), which has been proposed as an instrument to be carried on the Shuttle. CLIR includes a telescope with detectors at 10 K, a 25-cm diameter mirror at 30 K, and a baffle at 115 K. The view factor of the mirror is approximately 6.2×10^{-2} . However, before the deposits can be estimated, the tools for the calculations must be reviewed and developed.

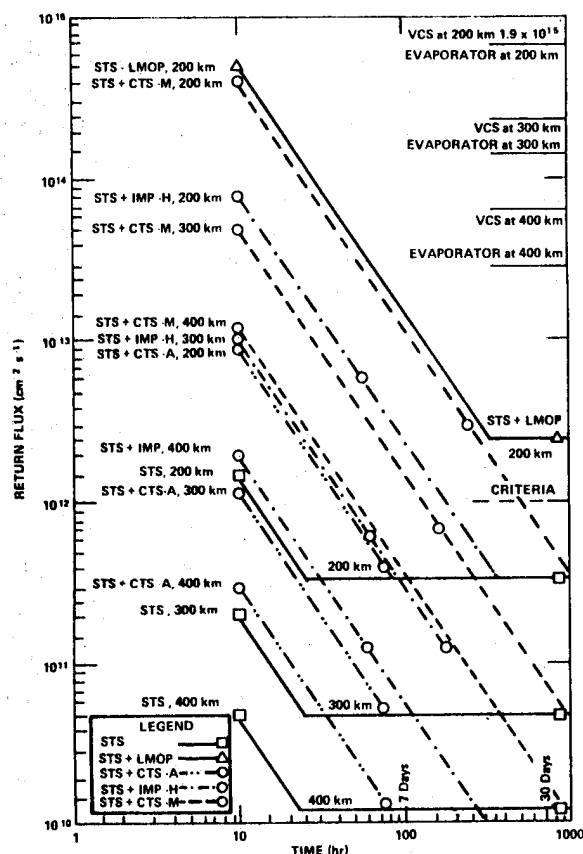


Figure 13. Molecular Return Flux Versus Time and Orbit for STS with Payload

Although the outgassing consists of many different molecules, the analysis and calculations for its deposit and reemission from surfaces has been carried out as if it were an equivalent single material. The contaminant source has been assumed to consist mainly of material having characteristics similar to water and to include some low vapor-pressure materials similar to the DC-705 silicone oil. This oil has an equivalent average vapor-pressure and activation energy.

10. THEORY

The flux of contaminant impinging and sticking on a unit surface, ϕ_i , is a function of the strength of the source, the view factor, γ , and the sticking (accommodations) factor, α . For a variable source, it can be expressed as

$$\phi_i = \alpha \gamma \frac{\phi_{10} t_{10}^n}{t^n} \quad (\text{cm}^2 \text{ s}^{-1}) \quad (6)$$

where n is the exponent of the source decay function, which has a magnitude of ϕ_{10} ($\text{cm}^2 \text{ s}^{-1}$) at time t_{10} (s). The subscripts "10" in these two terms indicate that reference values at 10 hours have been chosen. Any other set of values could have been used. The sticking coefficient, α , is close to 1 for the sources and surface temperatures under considerations. Ref. 15 contains a list of its values. The flux of contaminant that leaves the surface, ϕ_L , can be expressed in different forms,

depending on whether it is a sublimation (evaporation) or a surface desorption process. For an evaporation, it is given by the Langmuir expression,

$$\phi_L = \frac{3.52 \times 10^{22}}{\sqrt{MT_s}} \beta P_s \quad (\text{cm}^2 \text{ s}^{-1}) \quad (7)$$

where $\beta \sim 1$ is the evaporation coefficient, P_s (torr) and T_s (K) are the equivalent saturated vapor pressure and temperature of the material, molecular mass, M (g/mole), on the surface at T_s . In a desorption process, the flux is

$$\phi_L = \frac{N}{\tau_0} e^{-\frac{E}{RT_s}} \quad (\text{cm}^2 \text{ s}^{-1}) \quad (8)$$

where $N(\text{cm}^{-2})$ is the number of molecules adsorbed on the unit surface, $\tau_0 \sim 10^{-13}$ (s) is the oscillation period of the molecule on the surface at room temperature, E (cal/mole) is the activation or binding energy of the molecule on the surface (depending on the nature of the molecules and somewhat on the surface), and R (cal/mole/K) is the gas constant. The grouping, $\tau = \tau_0 E/RT$ (s), is the residence time of the molecule. An integration of the foregoing desorption flux equation gives the molecular density on the surface, σ (cm^{-2}), as a function of time, t (s):

$$\sigma = \sigma_0 e^{-\frac{t}{\tau}} \quad (\text{cm}^{-2}) \quad (9)$$

where σ_0 (cm^{-2}) is the initial deposit density. Applying the conservation of mass, the rate of molecules accreting or leaving the surface per unit time is

$$\frac{dN_a}{dt} = \phi_i - \phi_L \quad (\text{cm}^2 \text{ s}^{-1}) \quad (10)$$

For condensation on the surface, $\phi_i > \phi_L$, and the relation for this case will be

$$\frac{dN_a}{dt} = \alpha \gamma \frac{(\phi_{10} t_{10}^n)}{t^n} - \frac{3.52 \times 10^{22}}{\sqrt{MT_s}} \beta P_s \quad (\text{cm}^2 \text{ s}^{-1}) \quad (11)$$

The accumulation reaches its maximum when $dN_a/dt=0$. Thereafter, the second term, ϕ_L , predominates, and the molecules leave the surfaces. The time, t_m , corresponding to maximum accumulation is

$$t_m = \left[\alpha \gamma \phi_{10} t_{10}^n \right]^{1/n} \left[\frac{\sqrt{MT_s}}{3.52 \times 10^{22} \beta P_s} \right]^{1/n} \quad (\text{s}) \quad (12)$$

Therefore, knowing the depositing material properties (P_s , M , T_s) and the source intensity, one determines the time when accumulation stops and the contaminant begins to leave the surface (if not affected by radiation). The number of molecules N , on the surface as a function of time can be found by integrating equation

10 between t_i , the time of initial exposure to the flux, and time t . The integration for positive values of n gives:

$$N = \alpha \gamma \phi_{10} t_{10}^n \int_{t_i}^t t^{-n} dt - \frac{3.52 \times 10^{22}}{\sqrt{MT_s}} \beta P_s (t - t_i) \quad (\text{cm}^{-2}) \quad (13)$$

For $n < 1$,

$$N = \frac{\alpha \gamma \phi_{10} t_{10}^n}{1-n} \left[t^{1-n} - t_i^{1-n} \right] - \frac{3.52 \times 10^{22}}{\sqrt{MT_s}} \beta P_s (t - t_i) \quad (14)$$

For $n = 1$,

$$N = \alpha \gamma \phi_{10} t_{10}^n \ln \frac{t}{t_i} - \frac{3.52 \times 10^{22}}{\sqrt{MT_s}} \beta P_s (t - t_i) \quad (15)$$

For $n > 1$,

$$N = \frac{\alpha \gamma \phi_{10} t_{10}^n}{n-1} \left[t^{1-n} - t_i^{1-n} \right] - \frac{3.52 \times 10^{22}}{\sqrt{MT_s}} \beta P_s (t - t_i) \quad (16)$$

Equation 16 is applicable to sources decaying as $t^{-3/2}$, which we have used in the description of the payloads environment. If the flux leaving the surface, as given by the Langmuir expression, is greater than the impinging flux, condensation cannot occur. However, a number of monolayers can form on the surface by virtue of short-range surface forces. The mass conservation in that case is

$$\frac{dN_s}{dt} = \frac{\alpha \gamma \phi_{10} t_{10}^n}{t^n} - \frac{N_{AD}}{\tau} \quad (\text{cm}^{-2} \text{ s}^{-1}) \quad (17)$$

which, for the maximum number of adsorbed molecules when $dN_s/dt = 0$, gives

$$N_{AD} = \frac{\alpha \gamma \phi_{10} t_{10}^n}{t^n} \tau \quad (\text{cm}^{-2}) \quad (18)$$

This equation indicates a sequence of equilibrium conditions. The molecules on the surface will be maximum when the flux is maximum at the earliest exposure, and the quantity is strongly affected by $\tau = \tau_0 \exp E/RT_s$. Although the molecules will be leaving the surface as the impinging flux decays, a number of them will remain. The number of molecules left depends on the binding energy that can be effective up to several monolayers, on the surface temperature, and on the residual flux. The time of maximum deposit, t_m , found previously is indicative of the time

when the residual deposit will eventually be dictated by the adsorption process.

In all of the foregoing, the effects of radiation exposure on the deposited material, which may affect the energies of sublimation and desorption and the characteristics of the material, have been ignored because of lack of information.

Figure 14 is a plot of the time of maximum accumulation of a flux, $\alpha \gamma \phi_{10}$, which is decaying as $t^{-3/2}$ and impinging on a surface at T_s . The flux is specified by: (1) the sticking coefficient, obtainable from literature; (2) the view factor, γ , calculable from geometry; and (3) the magnitude of the source, ϕ_{10} , conveniently taken at $t_{10}=10$ hours in this case. The time is strongly dependent on the saturated vapor pressure P_s of the contaminant, corresponding to the surface temperature, T_s . The plot includes equivalent fluxes, $\alpha \gamma \phi_{10}$, varying from 10^9 to $10^{17} \text{ cm}^{-2} \text{ s}^{-1}$ for contaminants considered to be H_2O and equivalent fluxes of DC-705 silicone oils varying from 10^{12} to $10^{17} \text{ cm}^{-2} \text{ s}^{-1}$. The latter material is included as a representative of very low vapor-pressure materials. Their vapor pressures have been calculated from the Clapeyron equation, $\ln P_s = A - B/T_s$, with $A=10.48$ and $B=2680$ for H_2O and $A=12.11$ and $B=6424$ for DC-705. The times corresponding to 1-week and 1-month flights are shown for reference.

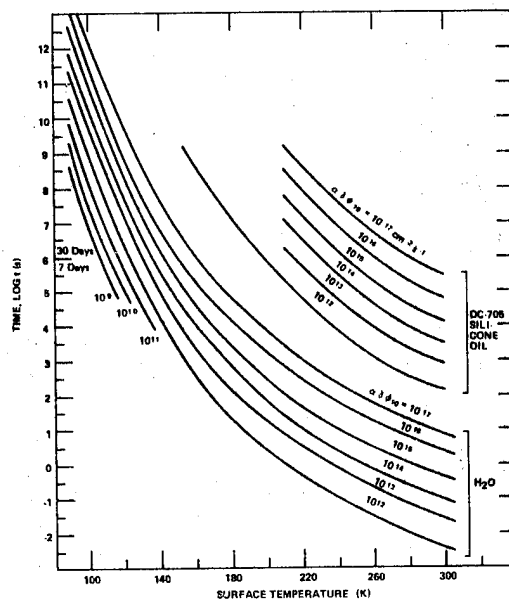


Figure 14. Time for Maximum Deposit of H_2O and DC-705 Oil on a Surface at $T(K)$ for Flux Decaying as $t^{-3/2}$ and Having a Value $\alpha \gamma \phi_{10}$ at 10 Hours

Figure 15 is a plot of the percent of accumulation on a surface as a function of time. It was obtained from equation 16. It shows that 70 percent of the total is deposited within 10 hours and 90 percent is deposited in 100 hours. For a 1-week mission, the deposit is 92 percent, and for a 1-month mission, it is 96 percent of the full accumulation. Figure 16 shows the deposit (cm^{-2}) or the thickness (cm) taken to be H_2O on a cryogenic surface as a function of time and equivalent flux. This was obtained from equation 16 with the second term assumed to be negligible.

Figure 17 shows the effect of delaying the exposure or cooling down of the surface. For a surface exposed 40 hours after the

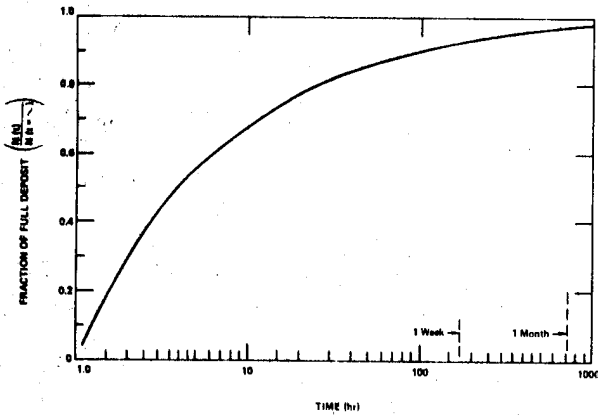


Figure 15. Fraction of Full Outgassing (deposit) Versus Time for Source Decaying as $t^{-3/2}$

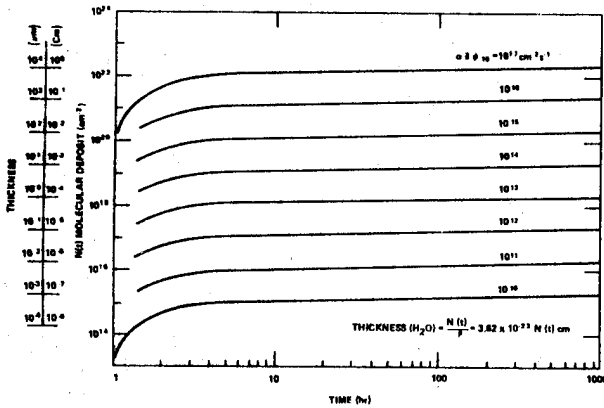


Figure 16. Maximum Molecular Deposit on Surface Versus Time for Contaminant Flux Decaying as $t^{-3/2}$ and Having a Value $\alpha\gamma_{0.10}$ at 10 Hours

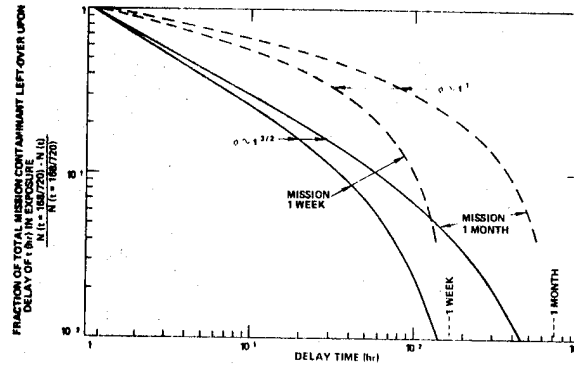


Figure 17. Fraction of Total Contamination Remaining when Surface is Exposed or Cooled Down t (hr) after Mission Starts

mission starts, the deposit will be about 9 percent of that expected in 1 week and 13 percent of that for 1 month. For comparison, the plot shows similar information for a source that decays linearly with time. A source decaying as $t^{-1/2}$ will require longer delay times than the linear relation to provide the same reduction in deposits.

11. PREDICTED CONTAMINANT DEPOSITS ON SHUTTLE PAYLOADS SURFACES

Assuming that the Shuttle bay environment is dictated by payloads similar to the CTS-M or LMOP and that an instrument such as the CLIR telescope is among the payloads, the contaminant deposits on its critical surfaces can be estimated. The results of these calculations for a 200-km orbit are listed in Table 2 and discussed in the following paragraphs.

11.1 Early stages of flight

The gaseous conditions existing in the Shuttle bay during the early stage of flight with the door closed or open, can be estimated by using the equations or plots of Figures 10, 11, 12,

Table 2
Instrument Contamination Predictions for Shuttle with LMOP/CTS-M-Type Payload at 200-km Orbit
(Surface view factors: $\gamma = 1$, direct surface/CLIR telescope forward baffle; $\gamma = 6.2 \times 10^{-2}$, CLIR mirror)

Gaseous Sources	Time in flight	Pressure (torr)	Density (cm ⁻³)	Flux (cm ⁻² s ⁻¹)	Column Density (cm ⁻²)	Return Flux (cm ⁻² s ⁻¹)	Deposit (cm) or Deposit Rate (cm/s)				Remarks
							$\gamma = 1.0$		$\gamma = 0.062$		
							Direct	Return	Direct	Return	
-Early outgas Closed bay door Open door 0.1% NVR ⁽²⁾	1 hr	(8 × 10 ⁻⁴) ⁽¹⁾	(2.6 × 10 ¹³)	(3 × 10 ¹⁷)							on T _s = 293 K for ~ 700 s, d ≈ 10 ⁻³ d max after 191 hr
	1 hr	(1 × 10 ⁻⁴)	(3.5 × 10 ¹²)	(1.5 × 10 ¹⁷)	(2.5 × 10 ¹⁴)	(1.4 × 10 ¹⁴)					
	1 hr	(1 × 10 ⁻⁷)	1 × 10 ⁸	5 × 10 ¹²	8 × 10 ⁹	5 × 10 ¹¹	9.12 × 10 ⁻⁵	1.1 × 10 ⁻⁶			
-Outgassing	1 hr-1 week		1 × 10 ¹¹	5 × 10 ¹⁵	8 × 10 ¹²	5 × 10 ¹⁴	5 × 10 ⁻²	4.0 × 10 ⁻³	3.1 × 10 ⁻³	2.5 × 10 ⁻⁴	on T _s <135-140 K (on T _s > 135 K for <10 ⁵ s)
	1 hr-1 month		1 × 10 ¹¹	5 × 10 ¹⁵	8 × 10 ¹²	5 × 10 ¹⁴	5.5 × 10 ⁻²	4.4 × 10 ⁻³	3.4 × 10 ⁻³	2.73 × 10 ⁻⁴	
	40 hr-1 week		1 × 10 ¹¹	5 × 10 ¹⁵	8 × 10 ¹²	5 × 10 ¹⁴	4.5 × 10 ⁻³	3.62 × 10 ⁻⁴	2.8 × 10 ⁻⁴	2.25 × 10 ⁻⁵	
	40 hr-1 month		1 × 10 ¹¹	5 × 10 ¹⁵	8 × 10 ¹²	5 × 10 ¹⁴	6.8 × 10 ⁻³	5.5 × 10 ⁻⁴	3.4 × 10 ⁻⁴	3.4 × 10 ⁻⁵	
-VCS 0.1% NVR	Any		(5 × 10 ¹¹)		(8 × 10 ¹⁴)	(1.95 × 10 ¹⁵)		5.8 × 10 ⁻⁸ cm/s		3.6 × 10 ⁻⁹ cm/s	on T _s <150 K indefinitely on T _s = 293 K indefinitely
	Any		(5 × 10 ⁸)		(8 × 10 ¹¹)	(1.95 × 10 ¹²)		1.6 × 10 ⁻⁹ cm/s		1.0 × 10 ⁻¹⁰ cm/s	
-Evaporator	Any		(1.5 × 10 ¹¹)		(4 × 10 ¹⁴)	(8 × 10 ¹⁴)		2.38 × 10 ⁻⁸ cm/s		1.48 × 10 ⁻⁹ cm/s	on T _s <140 K indefinitely
-Ambient oxygen in velocity vector	Any	(P _e = 1.4 × 10 ⁻³)	(4 × 10 ⁸)	(1.2 × 10 ¹⁵)			$\alpha=1$	7.5 × 10 ⁻⁶			on T _s <15 K
							$\alpha=1.37 \times 10^{-2}$	1.0 × 10 ⁻⁶ cm/s			

⁽¹⁾Numbers in parenthesis indicate values at that time; others are values at 10 hours

⁽²⁾NVR = Nonvolatile residues (Dk-303 silicone oil)

and 13. Extrapolating the curves to 1 hour in flight, the following conditions should exist in the bay: density, about $3.5 \times 10^{12} \text{ cm}^{-3}$; direct flux, about $1.5 \times 10^{17} \text{ cm}^{-2} \text{ s}^{-1}$; column density, $2.5 \times 10^{14} \text{ cm}^{-2}$; and return flux (with bay door open), about $1.4 \times 10^{16} \text{ cm}^{-2} \text{ s}^{-1}$. For convenience, Figure 18 is included to permit rapid conversion from molecular flux rates to mass flux rates. The indicated density at 1 hour corresponds to a pressure of about 1.08×10^{-4} torr. The contamination on a surface at 290 K that may occur during this period is estimated as follows. Figure 14 shows that, for H_2O fluxes of 1.5×10^{17} , the deposits on a 290-K surface occur for less than 100 seconds. Therefore, the maximum deposit is about 10^{19} cm^{-2} or less than 10^5 monolayers of H_2O . After 100 seconds, these monolayers evaporate quite rapidly because of the high H_2O vapor pressure at 290 K, but the surface may retain a few monolayers by virtue of surface forces.

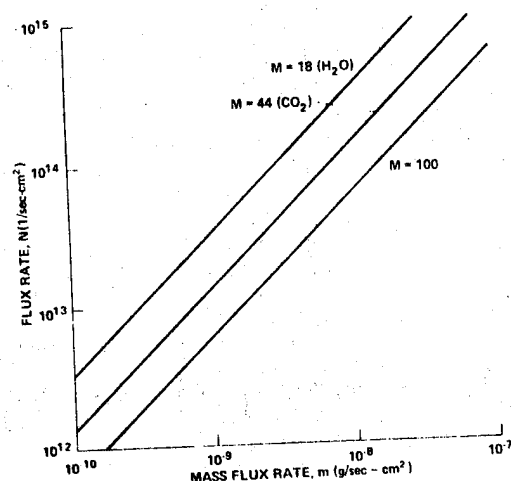


Figure 18. Conversion Data from the Mass Flux Rate, m , to the Number Flux Rate, N ($1/\text{cm}^2\text{-sec}$)

However, if the foregoing flux includes a fraction, say 0.1 percent, of the so-called volatile condensable materials (VCM) as per material selection criteria, this material will accumulate on a 290-K surface. The accumulation should last for a period of 7.7×10^2 seconds, as shown by Figure 14 for a DC-705 flux, $\alpha\gamma\phi_{10}$, at 10 hours of 5×10^{12} (Figure 12). The deposit will be about $9.12 \times 10^{-5} \text{ cm}$ thick because the direct flux of this material has a value of 1.5×10^{14} at 1 hour. In addition, when the bay door is open, the return flux, which, for VCM material, has a value at 10 hours of 5×10^{11} (Figure 13), contributes to the deposit. The deposit of this flux should continue for 10^2 s , and the deposit will be $1.1 \times 10^{-6} \text{ cm}$ on the exposed surfaces at 290 K. Thereafter the total VCM deposit thickness of $9.2 \times 10^{-5} \text{ cm}$ will decrease with time. After a week to 191 hours, the thickness should be about $9.2 \times 10^{-8} \text{ cm}$. This was calculated using equation 8 for $E=25 \text{ kcal/mole}$ and $T_s=290 \text{ K}$, resulting in a residence time of 10^5 s .

11.2 Outgassing deposits on cryogenic surfaces

The outgassing direct flux at 10 hours is about $5 \times 10^{15} \text{ cm}^{-2} \text{ s}^{-1}$ (Figure 12), and the return flux at 200 km at the same time is about 5×10^{14} (Figure 13). Neither of these sources will accrete on normal-temperature surfaces as shown by Figure 14, which indicates a very short t_m . But, for a surface at less than 140 K, the time of accumulation is longer than a 1-week or 1-month

mission. The total accumulation can be obtained from Figure 16. In fact, the deposit for the direct flux ($\alpha\gamma\phi_{10} = 5 \times 10^{15}$) for a 1-week mission will be $5 \times 10^{-2} \text{ cm}$. The return flux ($\alpha\gamma\phi_{10} = 5 \times 10^{14}$) will produce a thickness of $4 \times 10^{-3} \text{ cm}$ during the same period. This thickness could result at the forward baffle of the telescope where the temperature is less than 140 K.

The corresponding deposits on surfaces with a view factor of $\gamma=6.2 \times 10^{-2}$, such as those for the CLIR telescope, will be $3.1 \times 10^{-3} \text{ cm}$ for the direct flux ($\alpha\gamma\phi_{10}=3.1 \times 10^{14}$) and $2.5 \times 10^{-4} \text{ cm}$ for the return flux ($\alpha\gamma\phi_{10}=3 \times 10^{13}$). These deposits will be about 10 percent higher for a 1-month mission, as shown in Figure 15. To show the effect of delaying the exposure on the cooling down of the surfaces, Table 2 shows the deposits calculated for a delay of 40 hours. They are approximately one order of magnitude lower than those calculated for the immediate exposure at 1 hour. Figure 17 shows the delaying effect. Note that the foregoing calculations were made assuming H_2O as the gaseous fluxes. However, according to Figure 14, they are valid for any material with vapor pressures less than those of H_2O . If the surfaces are at $T_s > 140 \text{ K}$, the accumulations could terminate before the end of the mission. The calculations would be carried out in the same manner using Figure 14 to obtain t_m , and Figure 16 or equation 16 to obtain maximum deposits for a span of time t_m .

11.3 Deposit rates of VCS and evaporator products

Return fluxes from the evaporator and VCS at 200-km orbits are 8×10^{14} and $1.95 \times 10^{15} \text{ cm}^{-2} \text{ s}^{-1}$, respectively, as shown in Figure 13. The H_2O from the evaporator will deposit at a rate of $2.38 \times 10^{-8} \text{ cm/s}$ on a cryogenic surface $T_s < 140 \text{ K}$ with direct view of the flux, such as that of the forward baffle of the telescope. The deposit rate on the mirror ($\gamma=6.2 \times 10^{-2}$) will be $1.48 \times 10^{-9} \text{ cm/s}$. The corresponding rates for the VCS products are 5.8×10^{-8} and $3.6 \times 10^{-9} \text{ cm/s}$, respectively. These magnitudes are of the order of monolayers per second. There will be no deposits on surfaces at $T > 140 \text{ K}$ of the mostly H_2O content of the outgassing products. However, if the VCS products are estimated to contain a 0.1-percent low-vapor-pressure material, they could deposit at a rate of $1 \times 10^{-10} \text{ cm/s}$ on a surface with $\gamma=6.2 \times 10^{-2}$ field of view and $1.6 \times 10^{-9} \text{ cm/s}$ on a direct-view surface.

11.4 Oxygen deposits on cryosurfaces

At 200 km, the natural concentration of O is $4.05 \times 10^{15} \text{ m}^{-3}$ and O_2 is $1.91 \times 10^{14} \text{ m}^{-3}$ (Ref. 13). The average velocities of O and O_2 are 1.5 km/s and 1.08 km/s, and their temperatures vary between 900 K at night and 1600 K during the day. For a pseudomaxwellian flux distribution, the flux at the mirror of the telescope pointing in the direction perpendicular to the velocity vector will be $\phi=1/4\rho V\gamma$. For $\rho=4 \times 10^{15}$, $V=1.5 \text{ km/s}$ and $\gamma=6.2 \times 10^{-2}$, the flux is $9.3 \times 10^{12} \text{ cm}^{-2} \text{ s}^{-1}$, which corresponds to a pressure of 4.58×10^{-8} torr as per Langmuir equations with $T=1500 \text{ K}$ and $M=16$. Because the vapor pressure of O_2 at 30 K is about 1.2×10^{-7} torr, accumulation of oxygen should not occur at the mirror-surface temperature or on surfaces at 100 K. If, however, the telescope is pointed along the velocity vector, the oxygen flux on any surface of the telescope is $\rho V=3.2 \times 10^{15} \text{ cm}^{-2} \text{ s}^{-1}$ where $V=8 \text{ km/s}$. This is equivalent to 1.4×10^{-5} torr. Consequently, it should accrete on surfaces at $T_s < 35 \text{ K}$ at a rate dictated by the sticking coefficient. For the unity coefficient, the rate is about $7.54 \times 10^{-8} \text{ cm/s}$. Ref. 16 indicates that the sticking coefficient C_n of O_2 at temperature

$T_s = 300$ K on a surface at $T_s = 20$ K is 0.86. Further, Ref. 16 gives the relation $(1-C)^T = (1-C_0)^{T_s}$ for the evaluation of C at a temperature, T , of the gas for the same surface temperature. Assuming that the temperature of the gas is proportional to the square of its velocity, the temperature of the oxygen at 8 km/s could be equal to 42666 K. The sticking coefficient from the foregoing relation can be calculated to be 1.37×10^{-2} , and the O accretion rate in this case could be 1.02×10^{-9} cm/s. The heat inputs produced by these fluxes to the surface were estimated to be about 2.2×10^{-7} cal/cm²/s, which are equal to the emissive power of a blackbody at 20 K (Ref. 15).

12. METHODS FOR REDUCING CONTAMINATION

The following paragraphs describe some of the measures that can be used for alleviating the contamination predicted previously. The discussion of these measures is complemented with a list of suggested design and operational contamination controls. The methods of contamination control discussed in detail are:

(1) purging the telescope; (2) periodic sublimation of deposited materials; and (3) time required for protecting the surfaces both during and after operation of the evaporator and the VCS systems.

12.1 Gaseous purging

To protect the telescope mirror and baffle from incoming natural oxygen or other materials, one may employ He gas vented by the telescope at 100 K as a counterflow to the contaminant. The amount of He needed for the purging to be effective must now be estimated. The traverse time of the incoming O to reach the mirror is L/V , where L is the telescope tube length and V is the spacecraft velocity. To prevent the molecules from reaching the mirror, the mean collision of the gases in the tube should be several times less than the traverse time. The mean free path (mfp) of the purging gas should be

$$\lambda_p < \frac{L}{V} \quad (19)$$

where $v = \sqrt{8KT/\pi m} = (1.45 \times 10^4) \times \sqrt{T/M}$ (cm/s) is the average velocity of the purging He, which, at 100 K corresponds to a velocity of 7.25×10^4 cm/s. Therefore, for $L=100$ cm, $V=8$ km/s, and the He velocity as above, the mfp should be less than 9 cm. From the kinetic theory, the mfp of a gas is given by

$$\lambda = \frac{KT}{\sqrt{2} \pi \sigma^2 P} \quad (\text{cm}) \quad (20)$$

where K is the Boltzman constant, σ is the cross section of the molecule, and T and P are its temperature and pressure, respectively. With the appropriate constant and cross section of the He, the equation reduces to $\lambda = 4.89 \times 10^{-5} T/P$ (cm), where T (k) and P (torr). Equating the two mfp relationships, the required pressure for the purging gas is

$$P > \frac{1}{\sqrt{2} \pi \sigma^2} \frac{V}{L} \sqrt{\frac{\pi M K T}{8 N}} > 3.37 \times 10^{-9} \frac{V}{L} \sqrt{MT} \quad (\text{torr}) \quad (21)$$

With the specified geometry and gas, the above indicates that the pressure should be greater than 5.4×10^{-4} torr. The throughput of a gas at pressure P through a tube of area A , diameter D , length L , and velocity V can be estimated as:

$$Q = \frac{4}{3} \frac{D}{L} \left(\frac{1}{4} A v \right) \frac{P}{KT} \quad \left(\frac{\text{torr } \ell}{s} \right) \quad (22)$$

This equation for $D=25$ cm, $A=487$ cm², $L=100$ cm, $T=100$ K, $V=7.25 \times 10^4$ cm/s and $P=5 \times 10^{-4}$ torr, indicates a requirement of more than 1.6 torr ℓ /s. This corresponds to a mass flow rate,

$$\dot{m} = \frac{QM}{P_0 V_0} = 3.75 \times 10^{-4} \text{ g/s} \quad (23)$$

where $P_0=760$ torr, $V_0=22.4$ ℓ /mole, and $M=4$ g/mole. Therefore, for some beneficial effects of the purging with He at 100 K, a flow greater than 32.5 g/day is required.

12.2 Sublimation of condensed oxygen

During operation of the telescope, natural oxygen condenses on optical surfaces at $T < 30$ K. The temperature and time required for subliming a given accumulation from the surface must now be estimated.

The rate of removal of molecules, ϕ_L , from a surface at T_L is the difference between the rate of sublimation, ϕ_s , and the rate of molecules impinging on the surface; i.e.,

$$\sigma_L = \phi_s - \phi_i = \phi_L \left(1 - \frac{\phi_i}{\phi_s} \right) = \frac{P_L}{17.14} \sqrt{\frac{M}{T_L}} \left(1 - \frac{P_i}{P_L} \sqrt{\frac{T_L}{T_i}} \right) \quad (\text{gem}^{-2} \text{ s}^{-1}) \quad (24)$$

Equation 24 is obtained by using the Langmuir equation. The oxygen flux on the mirror at an altitude of 200 km was previously calculated to be equal to $P_i = 1.4 \times 10^{-5}$ torr. The pressure, P_L (torr), and temperature, T_L (K), are the saturated vapor pressure and temperature of the oxygen. At $T_L = 40$ K, P_L is about 10^{-3} torr, which is much greater than the equivalent impinging pressure of $P_i = 1.4 \times 10^{-5}$ torr. At a 40-K surface, the oxygen will not condense but will leave at a rate

$$\sigma_L = \frac{P_L}{17.14} \sqrt{\frac{M}{T_L}} = 3.68 \times 10^{-5} \quad (\text{gem}^{-2} \text{ s}^{-1}) \quad (25)$$

As previously indicated, oxygen condensation for 1 day was estimated to be 6.48×10^{-3} cm/day $\approx 5.76 \times 10^{-3}$ g/cm² day for the unit sticking coefficient. Therefore, the time required for subliming a 1-day accumulation with a surface at 40 K will be about 156 seconds.

12.3 Waiting time after VCS and evaporator operation

An estimate of the time required after the operating of these systems for their scattering fluxes and column densities to

become acceptable can be obtained as follows. The column density, N , can be expressed as

$$N \approx \frac{\dot{N}}{4\pi v R} \quad (\text{cm}^{-2}) \quad (26)$$

where \dot{N} (s^{-1}) and v (cm s^{-1}) are the effluent rate and its velocity, and R (cm) is the reference radius of the source. If the reference radius is assumed to be increasing linearly as $R=R_0+vt$, the column density at time, t , is related to the density, N_0 , corresponding to radius R_0 as:

$$N = \frac{N_0}{1 + vt/R_0} \quad (27)$$

Hence, an instrument that is $R_0=6$ m away from a source with an effluent velocity of $v=530$ m/s will see a column density of $10^{-6}N_0$ about 1 minute after the source effluent was terminated. Waiting this time before exposing an instrument or making measurements should provide both good observations and protection from contamination.

13. DESIGN AND OPERATIONAL CONTAMINATION CONTROL

From the previous analysis, it is apparent that contamination hazard is greatest during the early hours of flight and while the evaporator and VCS are being used. Considerable amounts of contaminants, including ambient oxygen, will collect on cryogenic surfaces. The magnitude of the deposits can be substantially reduced if certain design and operational precautions are taken. Some of these are:

- Protect cryogenic surfaces with dust covers and doors to inhibit ingestion of gases and particles and to limit the exposure to periods when the environment is acceptable.
- Monitor the gaseous environment with instruments that simulate the temperature of the critical surface. Instruments suitable for this purpose may be quartz crystal microbalances, water vapor radiometers, and calorimetric devices. They can measure the molecular flux rate to determine the advisability of exposing the critical surface.
- Include internal monitoring (e.g., inside a telescope) to provide data on total deposit. These data can be used for recalibrating an instrument.
- Provide energy sources that can be used to maintain a surface at elevated temperatures and to sublime existing contaminant deposits.
- Use cryogases to purge the system. This may prevent some contaminant molecules from reaching the surface.
- Sufficiently vent insulation materials, lubricated motors, and other sources away from critical surfaces.
- Expose systems and materials to vacuum, bake, and purging before using them in space, preferably a short time before.
- Select materials with low outgassing, as determined from actual tests on their rates of outgassing versus time, or, if this is not possible, VCM material selection tests. Note that the VCM test does not provide outgassing rates or ensure that the material will be acceptable in actual use.
- Extend the entrance of a telescope or probe as far as possible from the bay where the density is lower. This is more effective at low-orbit altitudes.
- Gimbal-mount pointing instruments so that they remain fixed to the object while the Shuttle is changing attitude. This can prevent the instrument from pointing in the velocity vector and reduce the VCS operations.
- Use gravity-gradient altitude flights so that there will be fewer VCS/RCS firing.
- Use flights with lower bay temperatures because outgassing is strongly dependent on temperature.
- Use flights with lower power requirements to reduce the amount of water generated by the power cells, and hence, the number of flash evaporator operations, or use flights that carry ample water-storage capabilities.
- When acceptable, use high-altitude flights because the ambient scattering return fluxes are an order of magnitude lower at 400 km than at 200 km, there is less chance of contamination.
- Do not point instruments in the velocity vector because the return fluxes are maximum in the velocity vector. Also, avoid looking toward the Shuttle cabin. Some water vapor will be escaping through the structural joints of the cabin.
- Avoid measurements and critical surface exposure during RCS/VCS and evaporator operations or other intentional venting. Wait 2 or 3 minutes after these operations before uncovering instruments and making measurements.
- Delay cool-down, exposure, and measurements for as many hours as possible. For example, exposing a surface 40 hours after flight initiation can reduce contaminant deposits by about 90 percent.
- Use dedicated flights that include instruments and payloads concerned with contamination.
- Use previously flown Shuttles, preferably those that have been recently flown. They have been exposed to vacuum and degassed, especially of highly volatile materials. Avoid recently retiled orbiters.
- Monitor fluxes at the instrument entrance because the flux rates at that location are a measure of the column density and of the degree of contaminant hazard. Variable temperature monitors can be used to obtain information on the nature of the contaminant.
- Use the results of the induced-environment contamination monitor (IECM). This package of

instruments, designed for mapping and measurement survey during several early flights, may indicate a best location for the instrument.

- Investigate synergistic effect of other payloads on the instrument. Perform detailed analysis on the environment at the instrument location. A knowledge of the sources outgassing, their temperatures, their view factors, contaminant transport mechanisms, operational modes, etc. is necessary.
- Be informed in advance of flight plans or obtain real-time information on RCS/VCS/evaporator and other venting operations so that protective actions can be taken.

14. SUMMARY OF THE RESULTS

With reference to the various plots and Table 2, the environment and contamination prediction for payloads in the Shuttle bay can be summarized as follows:

While the bay doors are closed, the pressure is of the order of 10^{-3} - 10^{-4} torr within 1 hour of the beginning of the flight. With the doors open, the pressure should be about 10^{-4} torr in the vicinity of the payloads, and the column density should be about $2.5 \times 10^{14} \text{ cm}^{-2}$. During the 1 to 2 hour transition period, surfaces at room temperatures should acquire a few monolayers of H_2O retained by surface forces. For a short period of 10 to 15 minutes, however, about 10^{-5} - 10^{-6} cm of low-vapor-pressure materials (VCM) should accumulate on these surfaces. This material will leave very slowly and, at the end of 1 week of flight, should be about 10^{-8} cm or less. If the surfaces are cooler than 290 K, this material will continue to accumulate for a longer period and its release will be correspondingly much slower.

Directly exposed surfaces at $T < 135$ to 140 K will be covered with a 5×10^{-2} cm thick deposit after a 1-week flight or 10 percent more after a 1-month flight. For a cold surface as above, but having a 6.2×10^{-2} view factor as for the CLIR mirror, the foregoing deposits are reduced in proportion. With the telescope deployed beyond the bay area, the scattered flux deposits a thickness of 4×10^{-3} cm on the forward baffle and 2.5×10^{-4} cm on the mirror for the 1-week flight. If the cool-down or exposure is delayed by 40 hours, the foregoing deposits will be about 9 percent of the above. Column densities on the order of 10^{12} cm^{-2} should be established 30 to 40 hours into the flight.

While the evaporator and the VCS are operating, the column densities are 10^{14} - 10^{15} cm^{-2} . The return flux of the VCS at 200 km will deposit at a rate of about $5.8 \times 10^{-8} \text{ cm/s}$ on a surface at $T < 150$ K with direct field of view and at about $3.6 \times 10^{-9} \text{ cm/s}$ on the telescope mirror. The water constituent of the VCS will not accrete on a surface at room temperature. However, its estimated 0.1 percent content of VCM will accrete at a rate of $1.6 \times 10^{-9} \text{ cm/s}$ on these surfaces ($1 \times 10^{-10} \text{ cm/s}$ on surfaces with a 6.2×10^{-2} field of view).

The 100-percent water constituent of the evaporator will condense at $T_s < 140$ K at a rate of 2.38×10^{-8} on direct surfaces and at a rate of $1.48 \times 10^{-9} \text{ cm/s}$ on surfaces with $\gamma = 6.2 \times 10^{-2}$. With regard to the ambient oxygen, if the telescope is pointed in the velocity vector, it will deposit on surfaces at $T < 35$ K at a rate between 7.5×10^{-8} and $1 \times 10^{-9} \text{ cm/s}$, depending on the sticking coefficient.

Although directional fluid leaks, improper direct venting of compartments, coolant leaks, motor leaks, etc. have not been considered, they would increase the contaminant hazard.

In addition to postponing as long as possible the exposure or the cool-down of the critical surface, the contamination can be minimized by: (1) exposing the surface to a noncontaminating gaseous purging flow; (2) periodically subliming the contaminant deposits; (3) protecting the surface during gaseous emissions (VCS/evaporator) and (4) reexposing the surface after the environment returns to normal. To minimize the ingestion of natural oxygen and other contaminants in the telescope, vented He gas at 100 K can be used as a counter flow to the contaminants. For the CLIR telescope and for an orbit of 200 km, the He pressure in the telescope tube should be greater than 5×10^{-4} torr. This can be accomplished by providing an He flow greater than 32 g/day.

The calculated daily accretion of oxygen on the telescope mirror at 30 K ($5.7 \times 10^{-3} \text{ g/cm}^2/\text{day}$) can be removed by heating the surface to 40 K for about 3 minutes. This assumes that the surface and the deposited oxygen have not been changed by a chemical surface reaction aided by impinging radiations. The waiting period for resuming observations and surface exposure after the operation of the VCS/evaporator and other emissions is estimated to be about 2 minutes.

15. CONCLUSIONS

The gaseous environment in which payloads and instruments will be exposed in the bay of the Shuttle Orbiter has been predicted. The prediction is based on the Shuttle discrete-time calculated molecular environment, and the measured, time-varying environment produced by a number of spacecraft in large vacuum chambers. The environment includes molecular density, directional fluxes, column density, and scattering fluxes contributed by material outgassing and emissions from the vernier control system and flash evaporator. These parameters are developed for different orbit altitudes and as a function of time. These predictions indicate that, with the exception of periods when the attitude motors and the evaporator are being used, the environment of a payload is dictated by the onboard payloads. It is also concluded that this environment is not significantly affected by the number of payloads in the bay. Rather, it is controlled by its self-induced environment or the maximum source nearby. The predictions provide representative environments that can be expected at a payload and estimate the times when certain recommended environmental criteria are met. The data can be used to estimate the degree of contamination that may result on critical surfaces. In fact, on the basis of a maximum estimated environment, contamination deposits have been calculated for a flight lasting 1 week or 1 month and for cryogenic and normal surface temperatures. These predictions include the effects of the field of view, the sticking coefficient, and the nature of the contaminant. For this purpose, a generalized method of estimating the deposits has been developed. It requires a knowledge of the source magnitude at a known time, its decay function, its chemical nature, and the temperature of the surface being contaminated. A specific calculation for the environment and the expected contaminant deposits on the surfaces of the CLIR have been performed and discussed. Included are an estimate of the rates of natural oxygen on the telescope optical surfaces and the effect of delaying the exposure or cool-down on the total deposits. Methods of reducing contamination, such as He purging of the

telescope, sublimation of accumulated deposits, and time required for normalization of the environment after large gaseous emissions, have been investigated. These and other methods that can be used in designing and during flight operations have been listed.

In conclusion, in the absence of more detailed calculations to be performed later when more is known on the Shuttle and the specific payloads, this document has attempted to: (1) provide a general characterization of the molecular environment of the payloads in the bay of the Shuttle, (2) provide methods for estimating the degree of contamination on critical surfaces, and (3) indicate methods for alleviating it.

16. REFERENCES

1. JSC-07700 1974, *Space Shuttle Program, Space Shuttle System Payload Accommodations*, Vol. X and XIV, Rev. C, Lyndon B. Johnson Space Center.
2. Leger L et al 1978, Space Shuttle Contamination Overview, *J. Environmental Sciences*.
3. NASA CR-151365 1977, *Orbiter/Payload Contamination Control Assessment Support*, by Rantanen R O & Strange-Jensen D A.
4. NASA TND-6645 1972, *Self-Contamination and Environment of an Orbiting Spacecraft*, by Scialdone J J.
5. Bareiss L E 1978, Verification Approach for the Shuttle/Payload Contamination Evaluation Program - Space-Lab Induced Environment, *AIAA/IES/ASTM 10th Space Simulation Conference, Bethesda, Maryland*, Paper 78-1606.
6. Final Report Contract NAS9-15335 (NASA) 1978, *Shuttle Orbiter-IUS/DSP Satellite Interface Contamination Study*, by Rantanen R O & Strange D A.
7. NASA TND-7597 1974, *Time Dependent Polar Distribution of Outgassing from a Spacecraft*, by Scialdone J J.
8. NASA TND-7492 1974, *Gas Flow Analysis During Thermal Vacuum Test of a Spacecraft*, by Scialdone J J.
9. Scialdone J J 1974, The Outgassing and Pressures in a Spacecraft, *Proceedings Institute of Environmental Sciences - 20th Annual Meeting, Washington, D.C.*, 164.
10. Henry R P 1969, Mesure Des Taux De Degazage, *Le Vide*, No. 144, 316.
11. Liu C K & Glassford A P 1978, Kinetics Data for Diffusion of Outgassing Species from RTV 560 Silicone Rubber, *J. Vacuum Science and Technology*, 15 (5), 1761.
12. NASA TND-8438 1977, *Correlation of Self-Contamination Experiments in Orbit and Scattering Return Flux Calculations*, by Scialdone J J.
13. National Oceanic and Atmospheric Administration/NASA/USAF 1976, *U.S. Standard Atmosphere*, 1976.
14. Spectroscopy Facility Definition Team (NASA/GSFC) 1978, *Cryogenic Limb-Scanning Interferometer and Radiometer (CLIR)*.
15. NASA TP-1177 1978, *Theoretical Contamination of Cryogenic Satellite Telescope*, by Murakami M.
16. Dawson J P 1966, Prediction of Cryopumping Speeds in Space Simulation Chambers, *J. Spacecraft*, 3 (2), 218.

CLEANLINESS ASPECT OF THE ARIANE PAYLOAD BAY

M Desloire & R Jaeger

Centre National d'Etudes Spatiales, Eery, France

ABSTRACT

The present paper deals with the mission particularities of the ARIANE launch vehicle with respect to the non-contamination aspect : brief time during which the launch vehicle components and the payload bay remain in the vicinity of each other, evolution of the pressure level, ... The specifications and the precautions considered at the time of conception of the nose fairings and the equipments bay regarding the selection of materials, surface treatments, the equipments and the wiring are presented. The integration procedures and those of cleaning and transport aspects of the equipments bay and the nose fairings are touched upon in addition to the precautions taken during their integration on the launch vehicle. We wish to add that the cleanliness of the payload bay will finally be evaluated during the qualification flights of the ARIANE vehicle by means of transducers installed on the technological capsule.

1. INTRODUCTION

The space missions, in general, are quite complex which call for severe and sophisticated measures in order to minimise, as far as possible, the risks involved due to pollution or contamination. Particular accent is given, in this paper, on this cleanliness aspect of the payload bay of the ARIANE launch vehicle. The payload bay of a launch vehicle, in view of its relative importance, must be particularly conceived so as to avoid pollution or contamination of the payload bay during the mission by dust or volatile materials. This payload bay, in the context of ARIANE launch vehicle is restricted by the nose fairings and the equipments bay with its payload adapter. The following sections of the paper deal with

- . the presentation of the ARIANE payload bay,
- . the contamination specifications at system level,
- . the particularities of the launcher mission,
- . the precautions taken during conception, manufacturing, integration and transport,
- . cleanliness assurance at launch site,
- . and the measurements during flights.

2. PRESENTATION OF THE ARIANE PAYLOAD BAY

The general layout of the payload volume under the nose fairings along with the vehicle equipment bay with its payload adapter is shown in Fig. 1.

The payload volume is restricted by :

- . the nose fairings, with - or without - acoustic insulation Figures 2 - 3
- . a membrane shield at the top of the 3rd stage
- . the vehicle Equipment Bay- Figure 4
- . the Payload adaptor : single or double (SYLDA)

3. CONTAMINATION SPECIFICATIONS AT SYSTEM LEVEL

The following are the specifications, considered at system level, with regard to the contamination aspect :

3.1 The organic deposit on the payload contributed by the materials used in its neighbourhood must not exceed 2 mg/m^2 (as measured in accordance with the procedure - ESA - PSS15/QRM 05T). This specification ensures that the vapour release of the materials of VEB and nose fairings, during flight, will have no injurious effect.

3.2 The use of Test : ESA-PSS 09/QRM 02T is recommended for the materials acceptance (see list ESA-PSS 07/QRM 01).

3.3 The pyrotechnic systems and retrorockets of the 2nd stage (liable to pollute the payload) must comply with the following requirements :

- Heat flux : 2 kW/m^2 max. (with a peak of 10 kW/m^2 authorized for a maximum period of 3s)
- Integrated particle flux : $< 1 \text{ g/m}^2$
- The retrorockets must not generate organic deposits in excess of 2 mg/m^2 on the payload.

3.4 The upper part of ARIANE vehicle will be integrated under clean tent in compliance with the following conditions :

- The V.E.B. will be cleaned on the launch vehicle under a clean tent prior to the payload installation.
- The nose fairings will be cleaned on the ground under clean tent before being installed.
- The payload container will be opened under clean tent.

3.5 The clean tent shall assure the following atmospheric conditions :

- Temperature : $25^\circ\text{C} \pm 2^\circ\text{C}$
- Relative humidity : $\leq 50 \%$
- Filtration : Class 100 000 (U.S. Fed. Std. 209b)

3.6 The payload and nose fairings, as mentioned above, will be placed in position under a clean tent. After installing the nose fairings the volume surrounding the satellite will be air-conditioned via the umbilical connector of the nose fairings. The payload compartment will be isolated from the cryogenic 3rd stage by means of a membrane shield (helium conditioning of the H8 forward bay). The ventilation fluid will be dry air, having the following characteristics :

- Filtration : adapted to the particular requirements of the mission (should at least comply with Class 100 000)
- Temperature : adjusted, according to requirements, within a range of 15° - 20°C (while being injected under nose fairings)
- Relative humidity : < 50 %
- Air Flow : 3000 kg/h

4. PARTICULARITIES OF THE LAUNCHER MISSION

The following are the characteristics specific to the ARIANE launcher mission.

4.1 The short durations during which the nose fairings and the vehicle equipment bay remain in the vicinity of the payload (in course of flight) are as follows :

- Nose fairings : ≈ 240 secondes)
- V E B : ≈ 840 secondes) (see Fig. 5)

4.2 The external and internal pressures with respect to the fairings are high and evolutive and are as follows :

- 4.2.1 External pressure at lift-off : 10^5 Pa) see
 " " at 150 s : 10^2 Pa) Fig.
 " " at 240 s : 10^{-2} Pa)
 (fairings separation)

- 4.2.2 Internal pressure at 150 s : around $2 \cdot 10^2$ Pa
 " " at 240 s : around 1 Pa

4.2.3 At the instant of fairings separation, the "mean free path" of molecules is $\approx 0,1$ mm, which means that the off-gassing and the out-gassing flow of the materials is laminar.

4.3 Comparison between out-gassing test and launcher mission

The out-gassing test shall comply with the procedure PSS 07/QRM 02 T. The out-gassing rate and the out-gassing mass are assumed to respect the following expressions :

out-gassing rate $q = K_1 e^{-E/RT}$ (Arrhenius law)

$q = K_2/t^{1/2}$ (diffusion phenomenon)

out-gassing mass $W = K e^{-E/RT} \int_0^t \frac{dt}{t^{1/2}}$

ie, $W = 2 K e^{-E/RT} \cdot t^{1/2}$

Where

T = temperature of out-gassing materials

t = time

For an assumed value of $E = 10$ K. cal/mole, the following table presents the comparison of out-gassing mass during launch and that observed during the test PSS07/QRM 02 T.

WLAUNCH= t	T t	30°C	40°C	60°C	90°C	125°C
80 s		0,00055	0,00095	0,00251	0,00591	0,03
100 s		0,00063	0,00107	0,00284	0,00670	0,034
700 s		0,00165	0,00285	0,00753	0,01773	0,09
24 H		0,0185	0,0316	0,0836	0,197	1

Let us recall that the test conditions are :

t = 24 hours

T = 125°C

Condenser temperature = 25°C

Vacuum $\approx 10^{-3}$ Pa

4.4 The following two examples demonstrate the satisfaction of the specification with regard to the payload contamination aspect.

4.4.1 1st Example sandwich Rear cone of the Fairings
 The following are the conservative assumptions made for the purpose :

- view factor between rear cone and payload : $F = 1$
- Material at the limit of acceptable level after test : $W = 1$ % = 10^{-2}
 PSS 09/QRM 02 T) VCM = 0,1 % = 10^{-3}
- Payload temperature : 25°C
- Lower cone inside temperature : $T = 40^\circ\text{C}$
 (during t = 80 s) (see Fig. 5 and 7)
- Good vacuum : $\approx 10^{-3}$ Pa
- Mass of material considered : $M = 10^6$ mg/m²
 (i.e thickness = 10^{-3} m)

with the above assumptions, the contamination on the payload may be estimated as

$$\begin{aligned} \text{VCM (payload)} &= \text{VCM (test)} \times M \times F \times \frac{W_{\text{Launch}}}{W_{\text{test}}} \\ &= 10^{-3} \times 10^6 \times 1 \times 0,00095 \\ &= 0,95 \text{ mg/m}^2 < 2 \text{ mg/m}^2 \end{aligned}$$

4.4.2 2nd Example : Painting of the VEB Equipments
 The following conservative assumptions are considered :

- View factor between Equipments and Payload (The entire VEB deck plate is covered by equipments and all the equipments are considered painted) : $F = 0,6$
- Payload temperature : 25°C
- Equipments temperature : $T = 60^\circ\text{C}$
 (during t = 700 s) (see Fig. 5 and 7)
- Paint at the limit of acceptable level after the test : $W = 1$ %
 PSS09/QRM 02T) VCM = 0,1 %
- Good vacuum : $\approx 10^{-3}$ Pa
- Mass of paint considered : $M = 5 \times 10^4$ mg/m²
 (i.e thickness = 50 μ)

The contamination on the payload, based on the above assumptions may be evaluated as

$$\text{VCM (payload)} = \text{VCM (test)} \times M \times F \times \frac{W_{\text{Launch}}}{W_{\text{test}}}$$

$$= 10^{-3} \times 5 \times 10^4 \times 0,6 \times 0,00753$$

$$= 0,22 \text{ mg/m}^2 < 2 \text{ mg/m}^2$$

5. PRECAUTIONS DURING CONCEPTION, MANUFACTURING, INTEGRATION AND TRANSPORT

5.1. Precautions at system level

The following precautions are taken into account at system level :

- The third stage is isolated from the payload bay by means of a membrane shield in order to prevent the diffusion of the cool Helium gas into the payload bay
- Care is taken to see that the organic materials in the payload bay are in low quantities (see Fig. 6)
- The temperatures inside the fairings are maintained relatively low (see Fig. 7)
- In view of the pollution from the exhaust of the retrorockets the payload bay is situated far away from these 2nd stage retrorockets ($\approx 12\text{m}$) and the burning time of the retrorockets is brief (1 seconde). In addition, these retrorockets are oriented at angle of $\approx 9^\circ$ with respect to the launcher axis (see Fig. 8)
- Ventilation of the payload bay before launch is achieved through air-conditioning (see Fig. 9) with the following characteristics :
 - . Temperature of air injected : adjustable between $15 - 20^\circ\text{C}$
 - . Relative humidity : $\leq 15\%$
 - . Filtration : class 100 000 (U.S Fed.Std. 209b)
 - . Air flow : 3000 kg/hour
- It may be noted that, at the user's request, local ventilation could be assured by adjusting the apertures in the ventilation tubing.

5.2 Precautions related to nose fairings

5.2.1 The following are the materials used for different sections of the fairings :

- Most of the fairing parts (nose cap, front cone, cylinder) are manufactured in Aluminium alloy without surface treatment
- Due to the radio-transparency requirement, the rear cone is manufactured in reinforced plastic material :
 - Kevlar + Glass/Epoxy (Elitrex-Prepreg).
 The fabrication is realised after curing for 90 minutes at 150°C .
- The bonding and sealing materials employed in limited quantities are :

Silastic 140 RTV and 738 RTV
Sylgard 186
Araldite AW 106/HV 953 U

It may be noted that these materials intended to assure the liaisons are employed in such a way that only insignificant portions are directly

exposed to the payload.

5.2.2 The separation system is leak-proof and does not cause any contamination (see Fig. 10).

5.2.3 The cleanliness of the nose fairings during manufacturing, integration and transport is assured in the following manner.

- Depending on the material, cleaning of individual parts is realised by trichloroethane (Chlorothene NU), white Spirit 100/140 or freon TF.
- Cleaning of various parts is undertaken during stage assemblies (especially areas which later become inaccessible).
- Final overall cleaning is assured by means of vacuum cleaner and trichloroethane (see Figures 11 and 12).
- Inspection according to the Technical Instruction ESA-PSS 15/QRM 05 T is assured : the total quantity of contaminants is about 10 mg/m^2 ; We believe that such small quantities do not contaminate the payload due to the fact that the fairings remain in the vicinity of the payload for a very short period and that during this period the pressure level is greater than 1 Pa.
- Packaging is done in hermetically sealed cover
- Transport is undertaken in pressurised (by azote) container.

5.3 Precautions related to V.E.B.

5.3.1 Materials employed

- All the structural parts are fabricated in aluminium alloy with chromic anodisation or alodine 1200.
- The paintings chosen for the equipments, if necessary, are PSG 120, PSE 109, ...

5.3.2 Payload separation system

The payload separation is achieved through the use of pyrotechnic "push-piston" and this separation system is confirmed leak-proof through tests realised at CNES/Toulouse (see Fig. 13).

5.3.3 The cleanliness of the VEB during manufacturing, integration and transport is assured in the following ways :

- clean cloth and vacuum cleaner are employed to ensure cleaning of structural parts before integration
- the equipments are cleaned before integration
- the integration is accomplished under tent with the help of gloves
- final overall cleaning is ensured
- packaging is done in plastic cover
- transport is assured in leak-proof container pressurized by azote.

5.4 Acoustic Insulation

The following precautions are observed in relation to the acoustic insulation during conception and transport :

5.4.1 Materials employed

- Glass fibers : "MICROLITE AA") (see
- covering film : "TERAL 18") (Fig. 14)

5.4.2 The acoustic insulation has been tested at SOPEMEA/Toulouse :

- under vacuum conditions : no contamination after 400 s
- after testing for random vibration ($0,07 \text{ g}^2/\text{Hz}$) under clean tent the air is always observed to be of class 100 000.

5.4.3 - cleaning before packaging is assured by vacuum cleaner and methanol

- Transport is done in sealed bags.

5.5 SYLDA (Double launch system)

The general view of SYLDA is shown on Fig. 15.

Materials used

- The structure is realised in honeycomb (face sheets in carbon fibers/Epoxy and core in aluminium). The carbon fibers prepeg corresponds to CARBOFORM HMS 87 (FOTHER GILL).
- Rings : in aluminium alloy
- Reinforcements : G 814 HTS 87 (BROCHIER)
- Internal bonding : REDUX 206 - 408 and 312L + 112 (see figure 16)

6. CLEANLINESS ASSURANCE IN GUYANA

This chapter deals with the assurance of cleanliness of the ARIANE Payload bay during launch preparation.

The upper floor of the preparation tower, called platform 8, can be transformed into a clean area by covering plastic curtains ; this being normally foreseen at J - 14 days.

Having done this, the following conditions prevail

Temperature : $25 \pm 2^\circ\text{C}$

Humidity : $50 \pm 10 \%$

Cleanliness Standard : 100.000

However as the VEB has been integrated at J - 37 days already, at the moment of creating clean conditions on platform 8 and latest before arrival of the satellite it may be necessary to clean the adapter and equipment surfaces.

The fairings shall arrive clean from Europe. At present an envelope that hermetically seals both half-fairings after cleaning in Europe is under study.

However should any incident occur necessitating a complete recleaning this can be done.

Its typical handling flow shall be :

From the assembly hall they will be conducted to the S3 - Satellite Assembly building-in its container. There they will be taken out and brought into the S3 - Cleanroom.

To protect these partially out door-operations a shelter will be installed in front of the S3-entrance.

In S3 can be achieved any control and cleaning that should be considered necessary.

After having removed the fairing containers from the shelter a can will be installed in front of

the entrance S3 and sealed to the building (see figure 17).

That can assures the following functions :

- give a volume to house the complete fairing and associated equipment under clean conditions

Dimensions : $5 \text{ m} \times 4 \text{ m} \times 9,70 \text{ m}$

- be clean according to standards and keep clean
- to store and to transport fairings
- allow sealed connection to S3 building
- receive conditioned air from S3
- allow lifting to platform 8
- allow sealed and rigid connection to the tower
- enlarge clean working space on platform 8 at fairing arrival until tower retreat.

Fairings having been inspected and/or cleaned they will be installed into the can and stay there until they are needed for integration. This in general will be necessary as fairings should leave S3-building at Payload arrival but enter platform 8 after payload integration to the launch vehicle.

For the period of storage the can will stay under shelter next to the S3 - entrance. It will be pressurized by clean air delivered from the S3 conditioning system.

When time comes to integrate fairings they will be transported in the can to the tower, and lifted up to the level of platform 8. There it will be sealed and fixed to the tower structure. Via the air-lock of platform 8 clean conditions remain after opening the can. Fairings then will be installed. (See figures 18 and 19)

We believe that the handling flow described and the means developed assure the cleanliness conditions required.

7. MEASUREMENTS DURING FLIGHTS

For all the four qualification flights of ARIANE launcher, it has been decided to put a quartz-crystal-microbalance (QCM) on the common CAT module (see Fig. 20) of the payload in order to evaluate the eventuality of payload contamination.

The following are the details concerning the measurements :

- Quartz microbalance for all the 4 experimental flights (CELESCO - IBC - QCM 710 A)
sensitivity = $4,4 \times 10^{-2} \text{ mg/m}^2 - \text{Hz}$
- solar sensors for LO1 and LO2 (RTC).

For further details the reader may refer to "SPACE CONTAMINATION ASSESSMENT STUDY - FIRST APPLICATIONS TO PRESENT PROJECTS" by B. TATRY, CNES.

8. CONCLUSIONS

In conclusion we believe to have done the necessary from the points of view of conception as well as precautions taken during fabrication, integration in Europe, transport and final integration in Guyana in order to ensure the available payload volume clean and pollution-free. The demonstration of this cleanliness will be made in the coming months during the qualification flights of the ARIANE launcher.

In case of need, specific to certain satellites, we are prepared to examine the additional optional precautions or remedial measures so as to further improve the cleanliness of the satellite.

ORIGINAL PAGE 18
OF POOR QUALITY

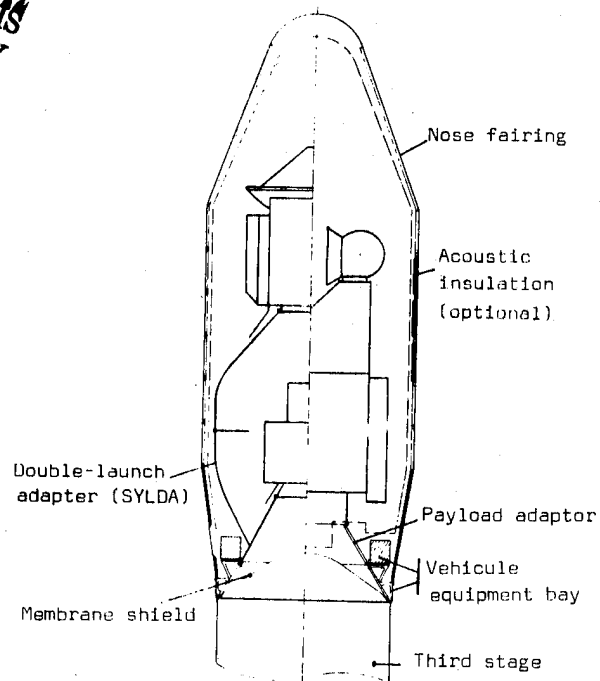
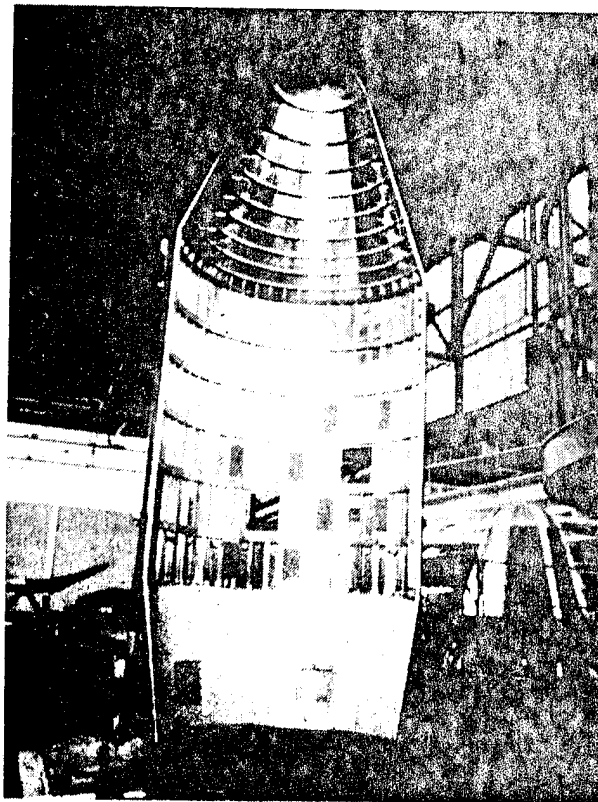
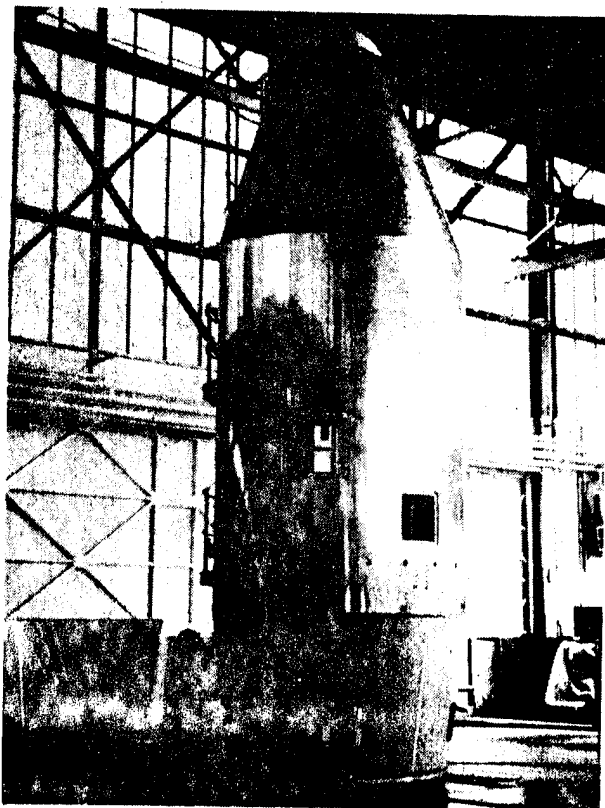


Figure 1. Payload volume



Figures 2-3. Nose fairing-external and internal views

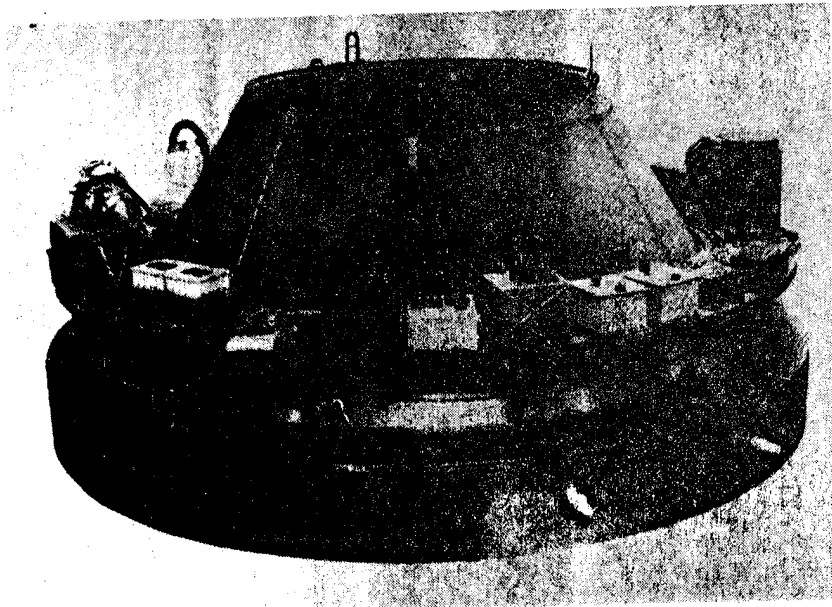


Figure 4. Vehicule Equipment Bay

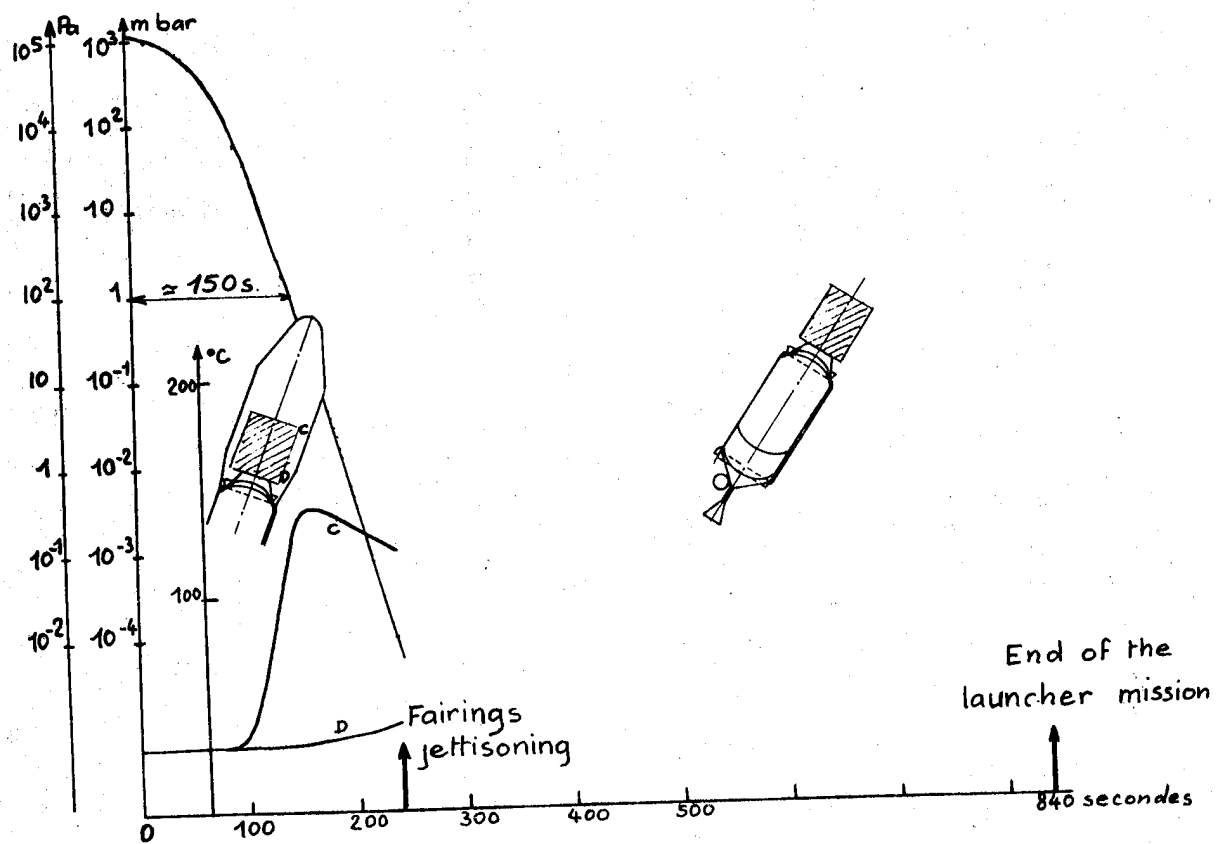


Figure 5. Pressure and temperature distribution during flight.

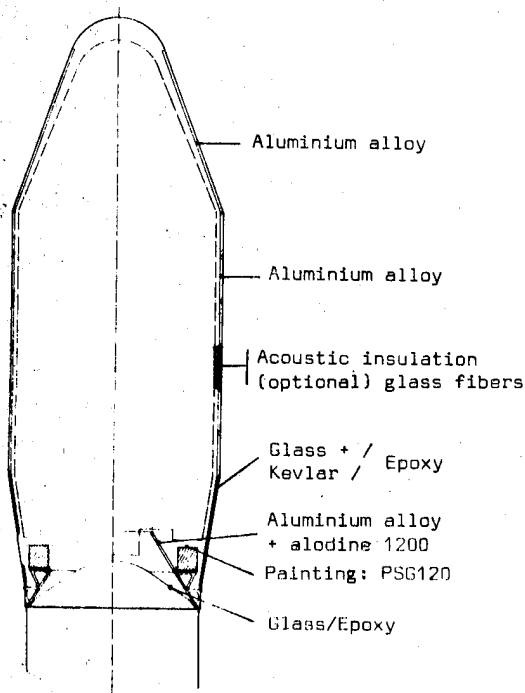


Figure 6. Materials used.

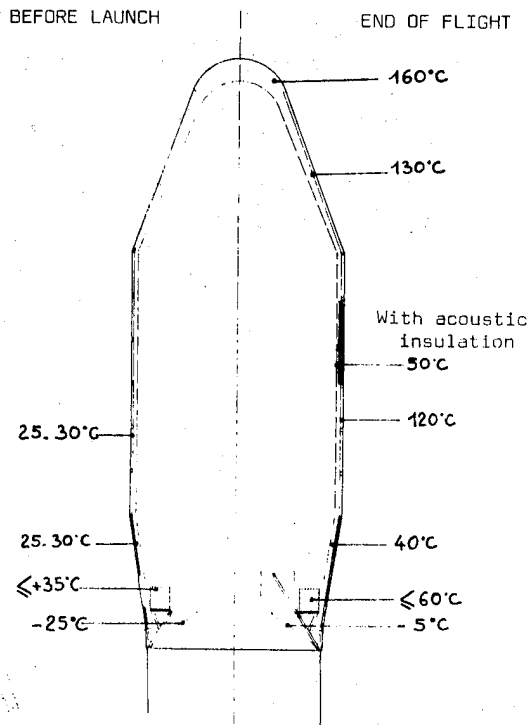


Figure 7. Temperatures in the payload volume.

ORIGINAL PAGE IS
OF POOR QUALITY

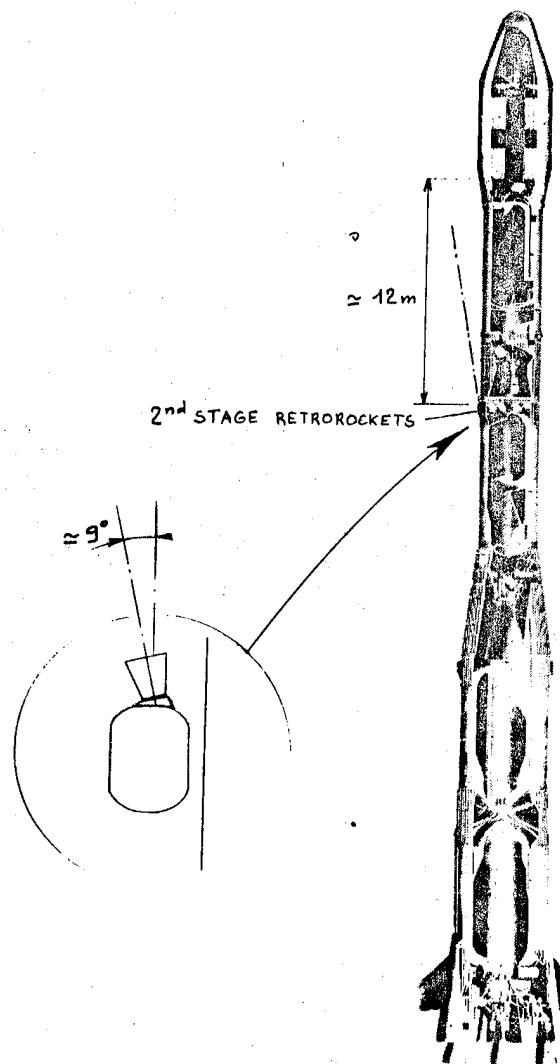


Figure 8. Location of 2nd stage retrorockets

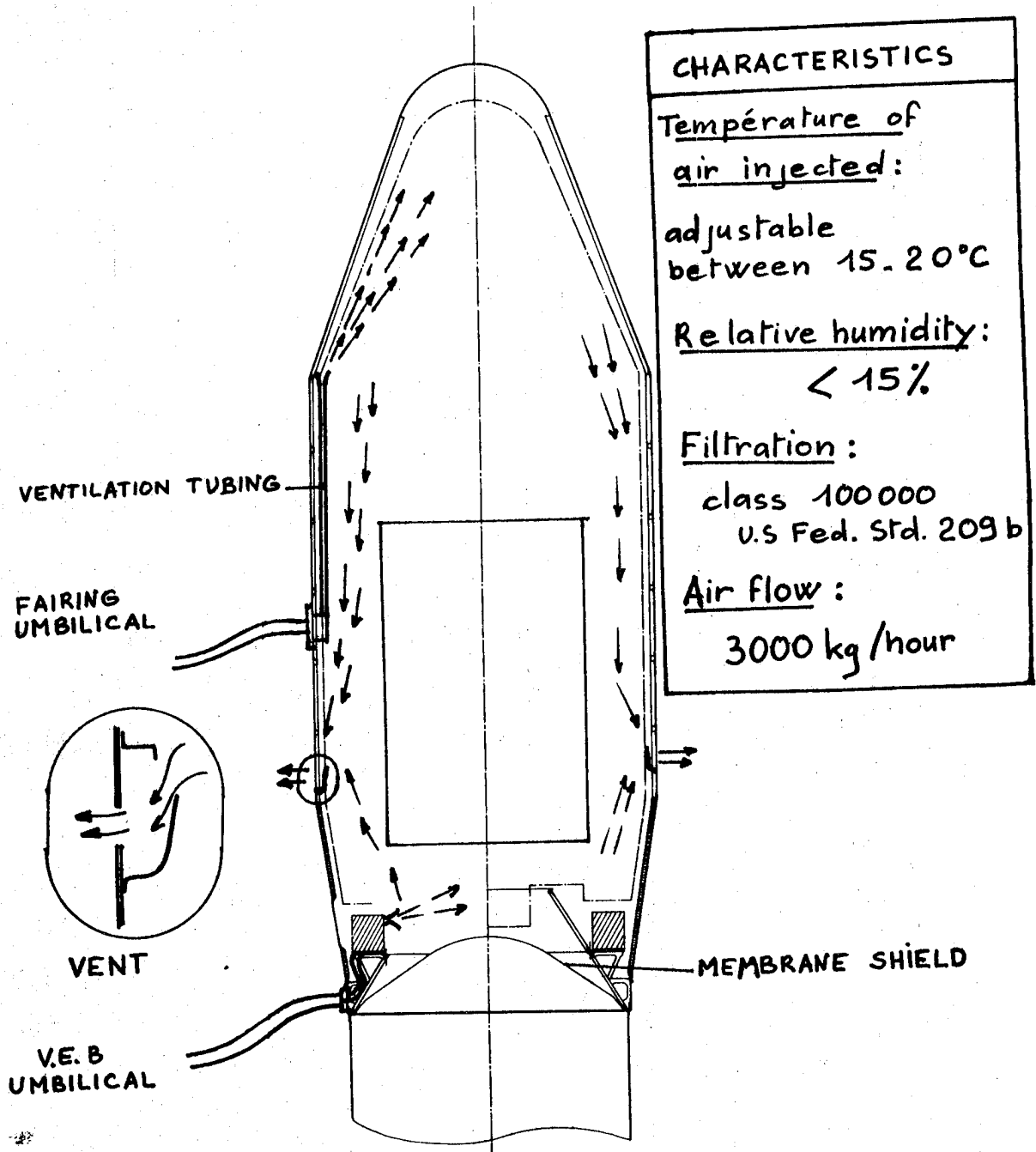


Figure 9. Ventilation of the payload before launch

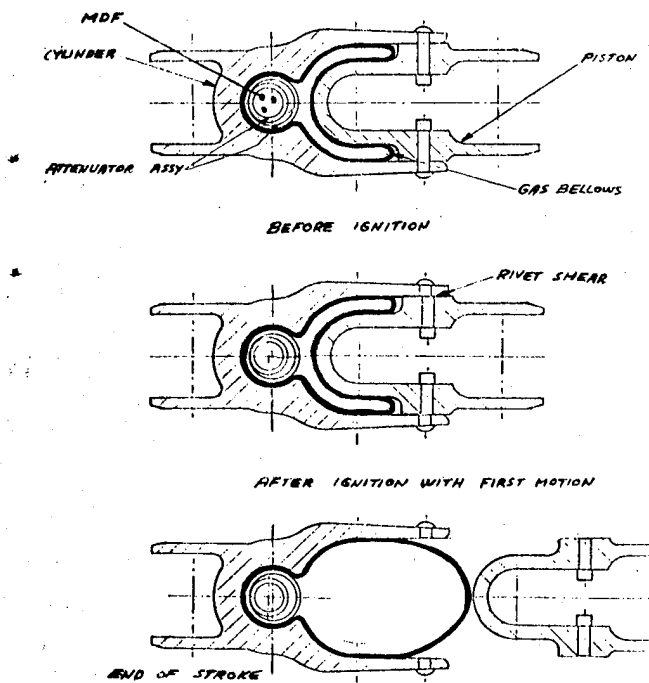


Figure 10. Fairing separation system.



Figure 12. Cleaning of the nose fairings



Figure 11. Cleaning of the nose fairings

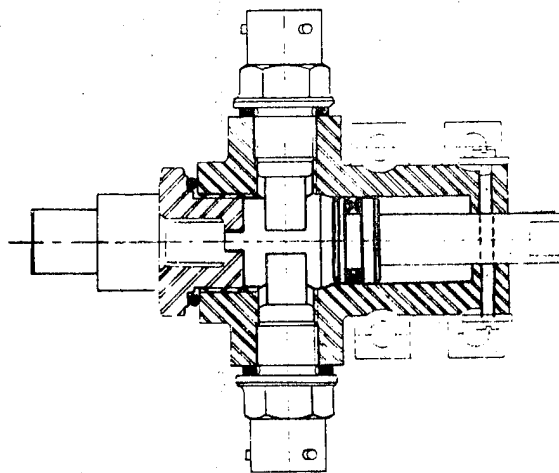


Figure 13. Payload separation system

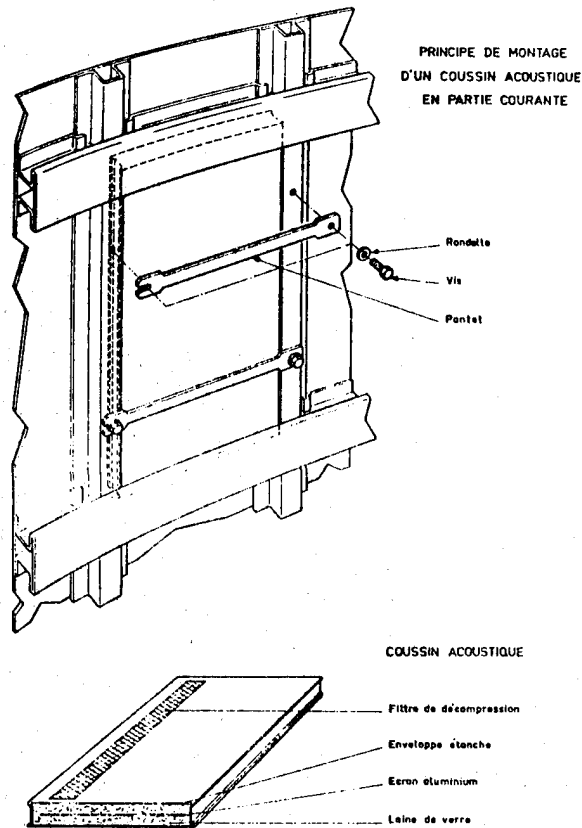


Figure 14. Acoustic insulation

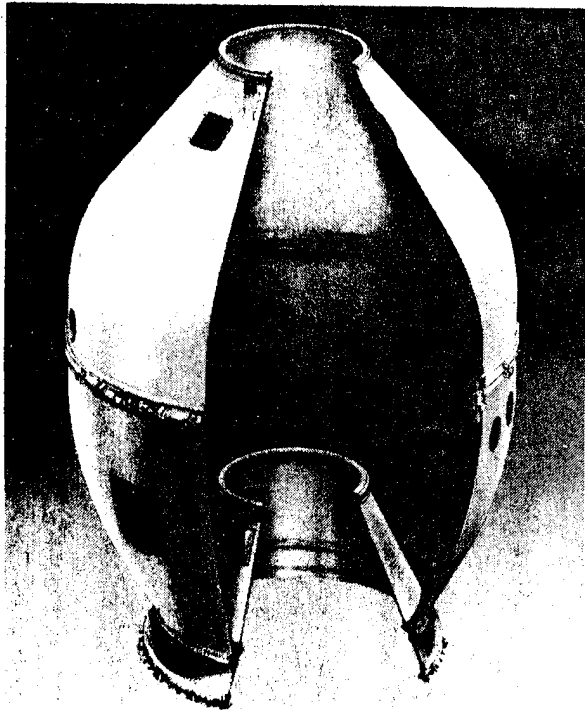


Figure 15. SYLDA.

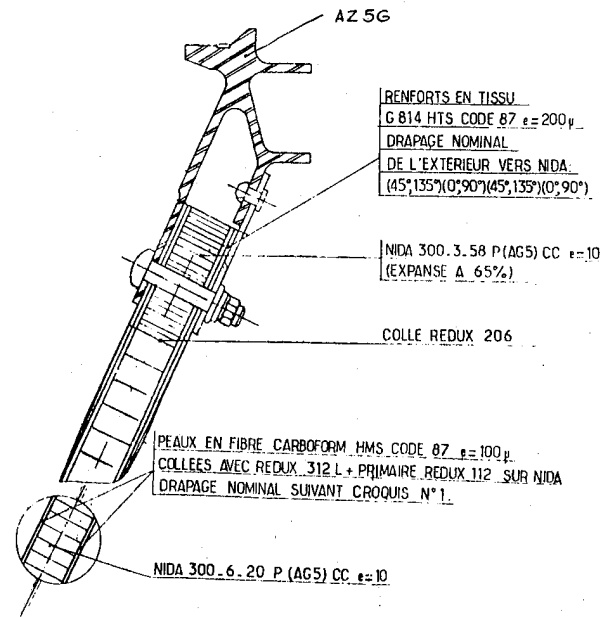


Figure 16. Details of SYLDA

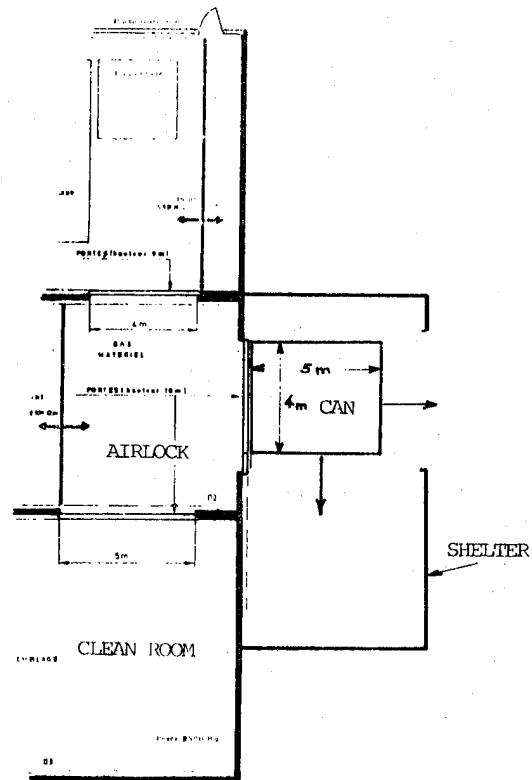


Figure 17. Building with shelter and can.

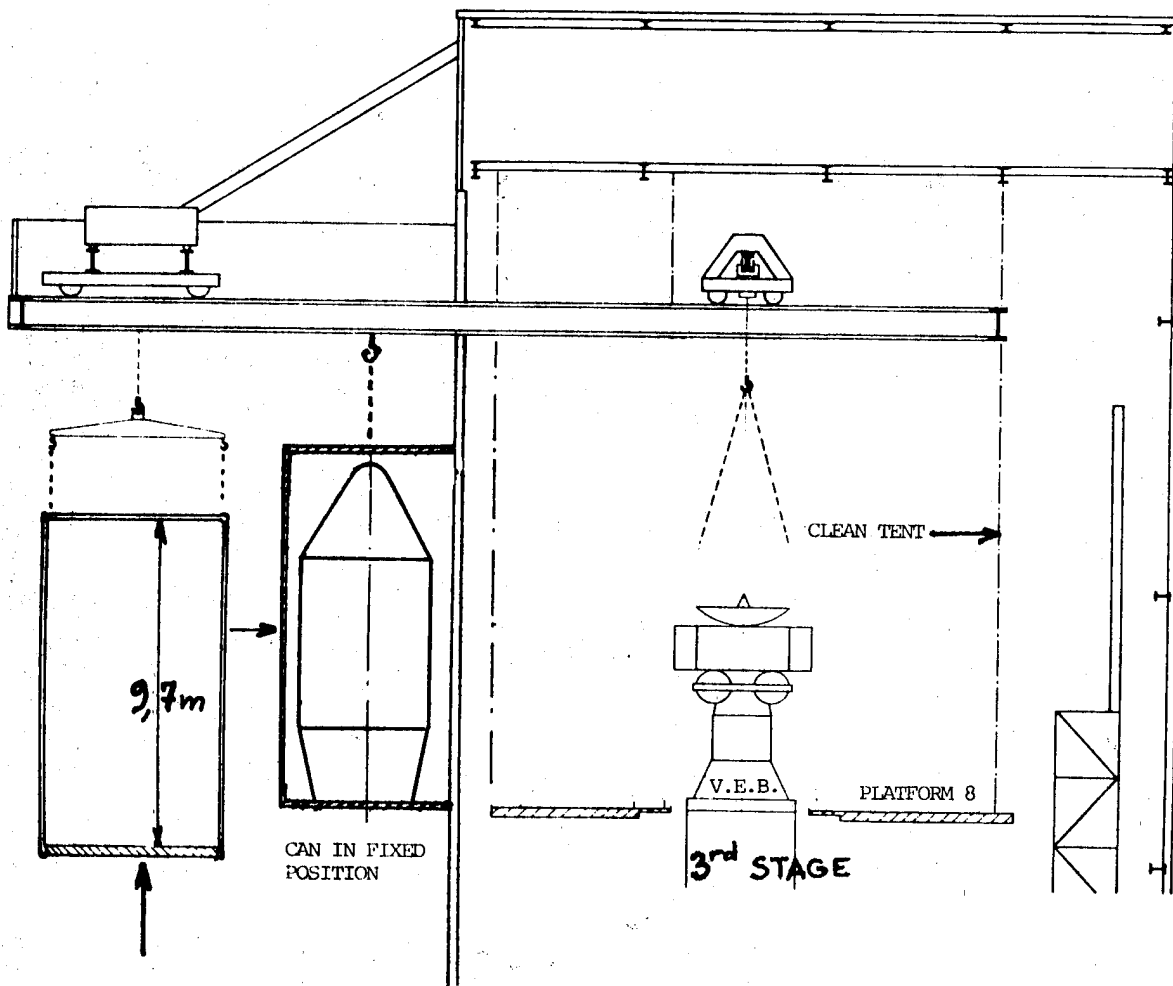


Figure 18.

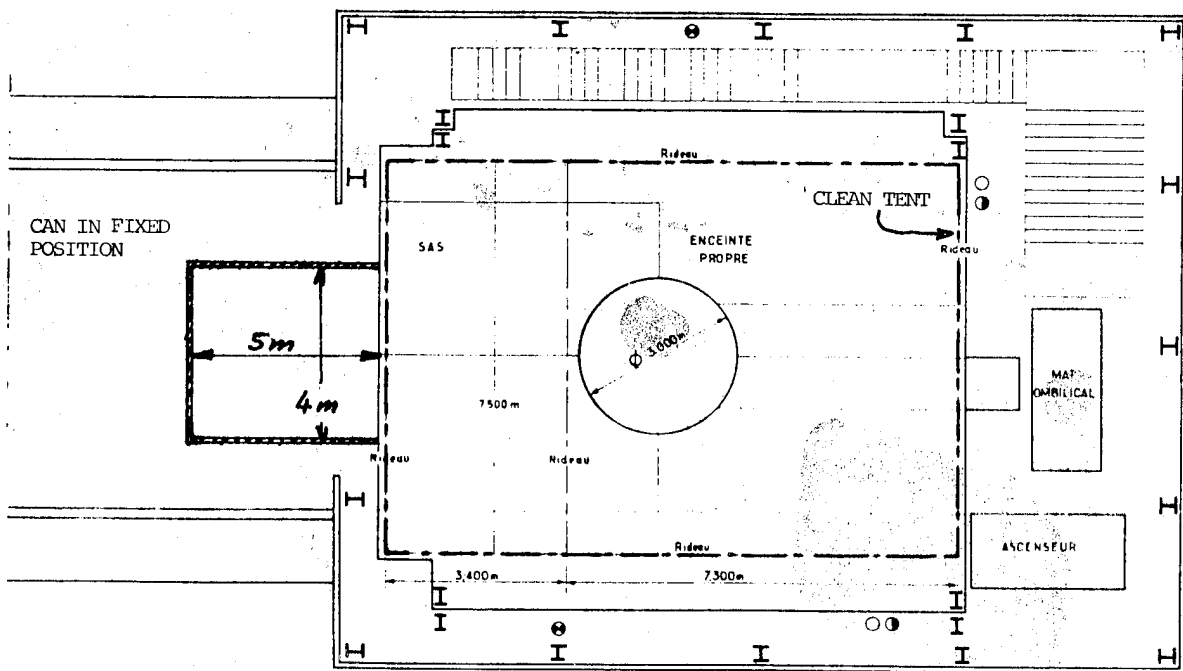


Figure 19. Plan of platform 8.

CAPSULE ARIANE TECHNOLOGIQUE

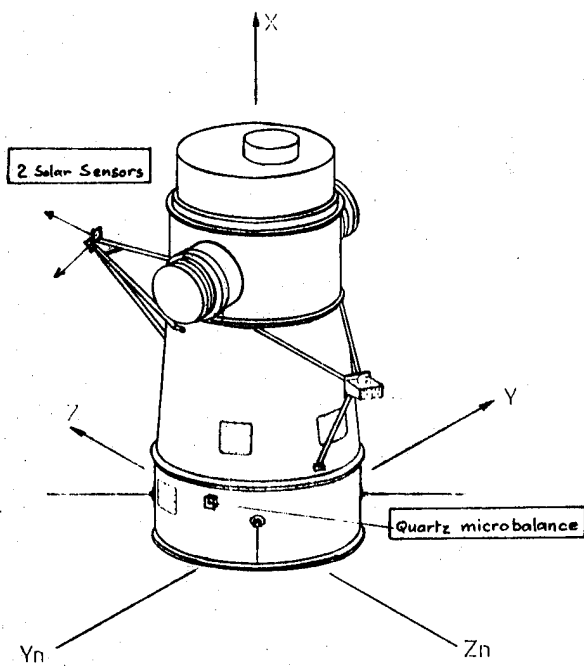


Figure 20. Measurement in flight.

SESSION IV

CLEANLINESS & CONTAMINATION THEORY

Co-chairmen: D.A. Nutt & A. Paillous

N80-21432

SPACE CONTAMINATION ASSESSMENT STUDY
- FIRST APPLICATIONS TO PRESENT PROJECTS -

B Taïry

Centre National d'Etudes Spatiales, Toulouse, France

ABSTRACT

The self induced atmosphere surrounding a space vehicle can limit or degrade the quality and resolution of optical observations or the surface properties. A contamination program has been developed to predict the induced environment and the deposits on a spacecraft. Major contaminant sources are modeled and transport functions are calculated. The preliminary version of the CONTAM program is applicable only for altitudes greater than 400 km. It is utilized for contamination assessment studies on the request of SIRIO 2 and SPOT projects. Also included is a presentation of the contamination experiment during the launch of ARIANE.

Keywords : Spacecraft contamination, Contaminants, Outgassing.

1. INTRODUCTION

As space projects develop in complexity and sophistication, the problems of interference from the self-induced local environment and the coating of optical or other surfaces becomes more severe. Therefore, extreme care must be taken to prevent the production of particulates, but as these particulates cannot be completely suppressed, it is essential to predict their behaviour. A model has been developed which predicts the deposits and the column density of the spacecraft due to its own outgassing or engines contaminants. This model can be applied to external or internal surfaces (cavities). Similar models have been previously developed (Refs 1, 2).

2. CONTAMINANT SOURCES

All the sources which eject particules or molecules are potential sources of contaminant. They are :

- a) non-metallic materials outgassing (the long term mass loss of the material upon exposure to space vacuum)
- b) early desorption from external surfaces (the initial high mass loss of adsorbed and absorbed volatiles, gases and liquids)
- c) thrusters exhaust plume (or vents)
- d) cabin atmosphere leakage
- e) other leakages (tanks, valves, ...) or anomalous sources.

These sources are treated as mathematical expressions which physically approximate the contaminant emission processes involved.

Any expression can be taken into account, with the two parameters : temperature T and time t .

2.1 - Outgassing

Non-metallic materials outgassing is modeled as a Lambertian source. The emission rate is a function of surface temperature of the material and time of exposure to the vacuum. Outgassing species are large molecular weight ($M \approx 100$ g) (Fig. 1).

2.2 - Early desorption

The early desorption rate decays more rapidly (≈ 100 h) than the outgassing. Primary constituents (H_2O , N_2 , CO_2 , O_2 , ...) are light ($M \approx 20$ to 30 g). It is also a function of surface temperature of the material and time of exposure to the vacuum.

2.3 - Thrusters plumes

The attitude and orbit control engines are considered as point sources. These point sources are expressed as an analytical function describing the mass flow as a function of distance and angle off the central axis of the source (Fig. 2). Attitude control systems or vents are more easily characterizable because their mass flow is usually well known.

The Table 1 presents the major sources of contaminants and their characteristics.

3. CONTAMINANTS TRANSPORT FUNCTIONS

Several flux can intercept a surface I (see Fig. 3). The irradiance can come by several pathes.

The total flux issued from the surface I is defined as the sum of :

- the own outgassing
- the reflection (the part that does not stick) of all the irradiant flux impinging on the surface.

Included in the following subsections are the analytical approaches currently employed to describe the transport of emitted contaminant molecules to locations of interest.

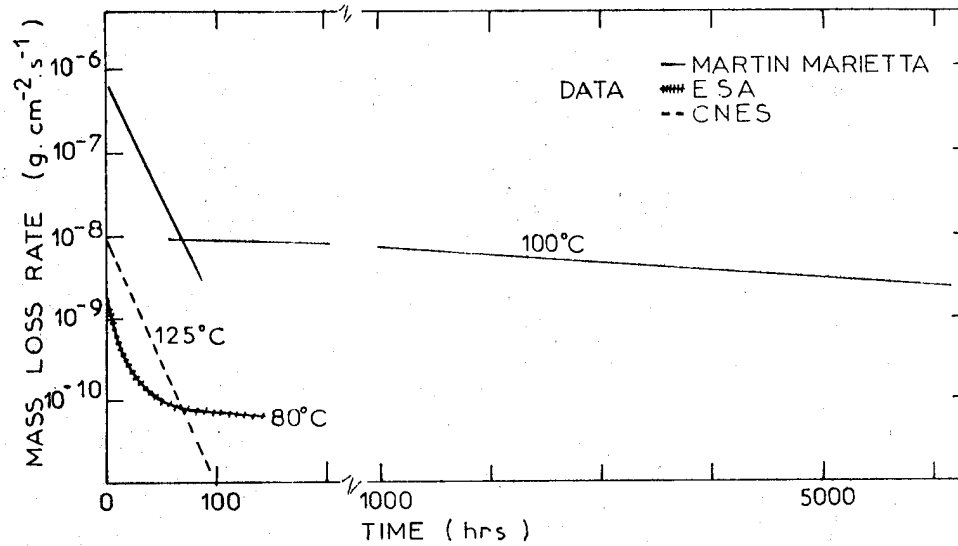


Figure 1. Early desorption and outgassing of paints

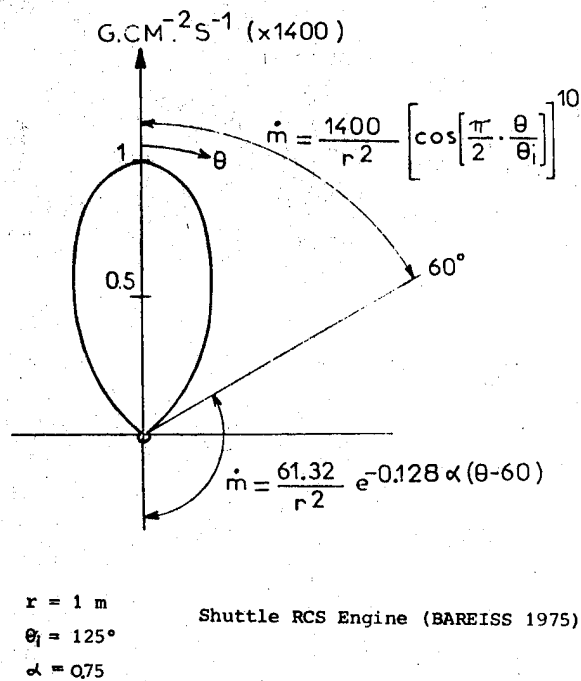
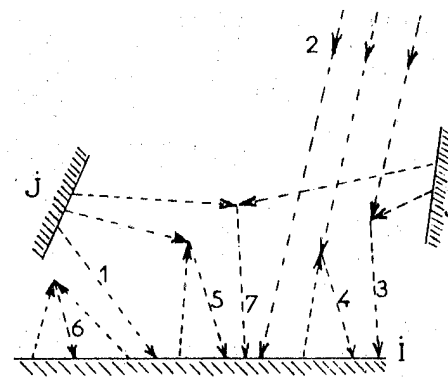


Figure 2. Engine plume



- 1 - Direct flux
- 2 - Direct ambient flux
- 3 - Direct flux scattered by ambient flux
- 4 - Own flux reflected by ambient flux
- 5 - Own flux reflected by direct flux
- 6 - Own flux auto-reflected
- 7 - Direct flux scattered by other direct flux

Figure 3. Different flux impinging on a surface

Table 1. Contaminant Sources

Source	Early desorption	Outgassing	Engines MMH/N ₂ O ₄	Vents
Location	External surfaces	External surfaces	T.B.D.	T.B.D.
Duration	Continu (100 h)	Continu >1000 h	Intermittent	Continu
Flux (G.CM ⁻² .S ⁻¹)	$1.59 \cdot 10^{-7} e^{-\frac{1053}{T}} e^{-\frac{t}{11760}}$ (ches)	$10^{-8} e^{-\frac{t}{4100}} e^{-\frac{T-100}{18}}$ (marlin marietta)		T.B.D.
Components	H ₂ O, H ₂ , CO CO ₂ , O ₂	Heavy molecules	T.B.D.	O ₂ , N ₂ CO ₂ , H ₂ O
Distribution	cos θ/r^2	cos θ/r^2	T.B.D.	cos θ/r^2
Velocity $\sqrt{\frac{2kT}{m}}$	30,4 $\sqrt{T(K)}$ (m.s ⁻¹)	12,9 \sqrt{T} (m.s ⁻¹)	3694 (m.s ⁻¹)	2220 $\sqrt{\frac{1}{M}}$ (m.s ⁻¹)
Mass molecular g	18	100	T.B.D.	29
Diameter	$\approx 3 \text{ \AA}$	$\approx 30 \text{ \AA}$	T.B.D.	$\approx 3 \text{ \AA}$

3.1 - Surface I to surface J direct transport

When the mean free path of the molecule emitted by I is larger than the distance between I and J, the trajectory of the molecule is a straight line. Surface sources such as outgassing, early desorption, compartment leakage are characteristically Lambertian (this assumption has been verified by experimental data obtained through numerous ground tests).

The line of sight transport for these sources can be considered analogous to black body thermal radiation. The geometric viewfactor is calculated to establish the percentage of mass emitted by a source J that is capable of impinging upon another surface I.

For these applications, the viewfactor is called the interception factor F (J,I) where :

$$F(J,I) = \frac{\text{number of molecules impinging on I}}{\text{total number of molecules emitted by J}}$$

With these considerations, one can calculate the flux impinging on a surface I, coming from all other surfaces J :

$$\mathcal{F}_I(i) = \sum_j \mathcal{F}_j \cdot \frac{A_j}{A_i} \quad (\text{g.cm}^{-2}.\text{s}^{-1})$$

\mathcal{F}_j total flux issued from the surface J (g.cm⁻².s⁻¹)

A_j, A_i areas of J and I (cm²)

This is the essential relation of the contamination modeling methodology.

3.2 - Ambient flux impinging on a surface I

The characteristics of the ambient atmosphere are given in several tables : ambient density, kinetic temperature, pressure, for each fundamental constituent.

The relative velocity of the ambient flux with the surface I of the satellite is equal to the orbital velocity of the satellite :

$$v \approx 7,9 \cdot \sqrt{\frac{r_0}{r}} \quad \text{km.s}^{-1}$$

r_0 : earth radius = 6371 km

r : orbit radius

The ambient flux impinging on a surface I is :

$$\mathcal{F}_A(i) = \mathcal{F}_A \cdot \cos \theta \quad \text{g.cm}^{-2}.\text{s}^{-1}$$

\mathcal{F}_A ambient flux (g.cm⁻².s⁻¹)

$0 \leq \theta \leq \frac{\pi}{2}$ is the angle between the velocity vector and the surface normal.

In fact, when the surface is parallel to the velocity vector, the ambient flux is not equal to zero (due to the ambient gas internal temperature), but in several cases the above assumption is valid.

3.3 - Direct flux scattered by ambient flux

When the mean free path of the emitted molecule is of the same order than the distance I,J, the molecule considered has a probability of collision with a molecule of another flux. The result of this collision is a probability for the emitted molecule to impinge the surface J (Fig. 4).

There are several approaches for modeling the scattering of two flux. We have choosen among the several models built by analysts. The HARVEY's model (Ref. 3) seems appropriate for our application because it takes into account the mean free path of the molecules, and then it is possible to consider the different species of molecules which compose the outgassing or other fluxes.

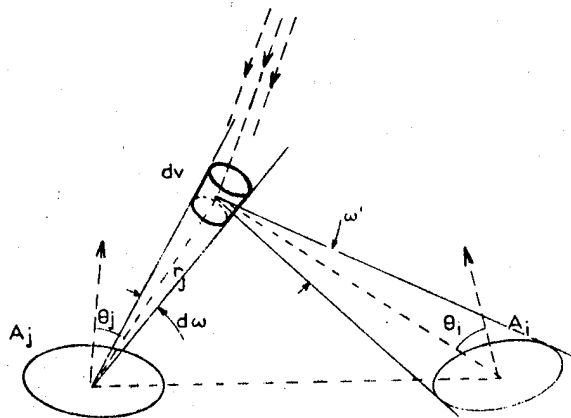


Figure 4. Interaction between two flux

The scattered flux is difficult to evaluate because of the multitude of paths each molecule can take, the details of the collision processes, and geometry factors such as shadowing.

As a first approximation, the HARVEY's model assumes that the molecules scattered to a surface undergo only one collision with an intervening molecule after being desorbed from an adjacent surface.

The collision processes are approximated by isotropic scattering in a reference frame attached to the emitting surface (laboratory frame).

Consider an area A_j emitting molecules into $d\omega$. The total emitted molecular flux \mathcal{F}_j leaving A_j is :

$$\mathcal{F}_j = \int_{\omega \leq \pi} H_j \cdot \cos \theta_j \cdot d\omega \quad 0 \leq \theta_j \leq \frac{\pi}{2}$$

H_j = total intensity of apparent flux ($\text{mol} \cdot \text{s}^{-1} \cdot \text{sr}^{-1}$)

The number of molecules scattered in distance dr_j is :

$$N = A_j \cdot H_j \cdot \cos \theta_j \cdot d\omega \cdot e^{-\frac{r_j}{\lambda}} \cdot \frac{dr_j}{\lambda} \quad (\text{mol} \cdot \text{s}^{-1})$$

by definition of the mean free path.

The part of the scattered molecules which enter ω' and impinge on I is :

$$A_j \cdot H_j \cdot \cos \theta_j \cdot d\omega \cdot e^{-\frac{r_j}{\lambda}} \cdot \frac{dr_j}{\lambda} \cdot \frac{\omega'}{4\pi}$$

and the molecular irradiance on area A_i is :

$$\frac{A_j}{A_i} \cdot H_j \cdot \cos \theta_j \cdot d\omega \cdot e^{-\frac{r_j}{\lambda}} \cdot \frac{dr_j}{\lambda} \cdot \frac{\omega'}{4\pi} \quad (\text{mol} \cdot \text{s}^{-1} \cdot \text{cm}^{-2})$$

or

$$d\mathcal{F} = \frac{A_j}{A_i} \cdot \frac{H_j}{4\pi} \cdot \cos \theta_j \cdot e^{-\frac{r_j}{\lambda}} \cdot \frac{\omega'}{\lambda r_j^2} \cdot dv$$

The total irradiance becomes :

$$\mathcal{F} = \frac{H_j}{4\pi} \cdot \frac{A_j}{A_i} \iiint_V \cos \theta_j \cdot e^{-\frac{r_j}{\lambda}} \cdot \frac{\omega'}{\lambda r_j^2} \cdot dv \quad (\text{mol} \cdot \text{cm}^{-2} \cdot \text{s}^{-1})$$

where the volume V is defined by the emitting beam $0 < \theta_j \leq \pi/2$ and the condition $\theta_i \leq \pi/2$.

3.4 - Other scatterings between flux

The interactions between the different flux (Fig. 3) can always be treated by the HARVEY's model or by another models (Refs. 4, 5). In most instances, these processes are secondary in nature when compared

to other mechanisms already cited.

3.5 - Second surface transport

Impingement on a surface by a contaminant flux results generally in deposition and reemission of the part that do not adhere. In addition, some of the deposited material can desorb with time under the influence of temperature variations of the surface.

3.5.1 Early desorption. The impinging flux on surface I $\mathcal{F}(J, I)$ issued from J surface is adsorbed :

- the adsorbed mass during time Δt is :

$$\mathcal{F}(j, i) \cdot S(j, i) \cdot \Delta t$$

$S(J, I)$ sticking coefficient = 1 if $T_I < T_J$
= 0 if $T_I > T_J$

- the desorbed mass can be expressed, for example, by :

$$5,83 \cdot 10^{-2} \cdot \gamma \cdot P_v \cdot \sqrt{\frac{M}{T}} \cdot \Delta t \quad (\text{g/cm}^2)$$

γ desorption coefficient

M molecular mass

P_v saturated vapor pressure

The deposited mass is the difference between the two. The emission distribution of the desorbed component is diffuse. The emission velocities are assumed to be the most probable velocity :

$$v = \sqrt{\frac{2 k T}{m}}$$

with T temperature of the emitting surface
 m mass of molecules impinging
 k BOLTZMANN constant

3.5.2 Outgassing. The sticking coefficient is a function of the temperature T_I and T_J . The Skylab derived relationship used in previous analysis is adopted :

$$S_{J, I} = \frac{T_J - T_I}{K} \quad (= 0 \text{ if } T_I > T_J)$$

with $K = 200$ for painting

Other laws can be utilized.

3.5.3 Reflection. In most instances, the effluents from the control system engines will not deposit on surfaces because of their temperature and the relatively high vapor pressure of the effluents. For this case, the reflection rate is equal to the impingement rate on the surface, and molecules exhibit diffuse scattering.

Specular scattering is hard to obtain and requires several conditions (unique gas, atomically smooth surface, no contamination, ultra high vacuum).

3.6 - Charged particles and small particles

They must be treated as particular cases (Ref. 6).

4. MODELING

The first step of our modeling approach and philosophy was to develop a model not too complicated, taking into consideration only the processes consistent with our present knowledge.

Only surface to surface direct transport is considered, that is to say only missions above a certain altitude (where mean free path is high) are looked at (above 300-400 km).

Indeed, the phases of ground handling, launch environment are not examined.

The contamination can deposit on surface or intercept the field of view of a sensor or experiment.

The aim of the modeling is to evaluate the deposits, usually expressed in terms of mass per unit area (g/cm^2) or thickness, and the so called column density (in g/cm^2 or molecules/ cm^2).

The surface to surface direct transport relation is utilized. The flux is integrated step by step.

The flow diagram of the computer model CONTAM is shown in figure 5.

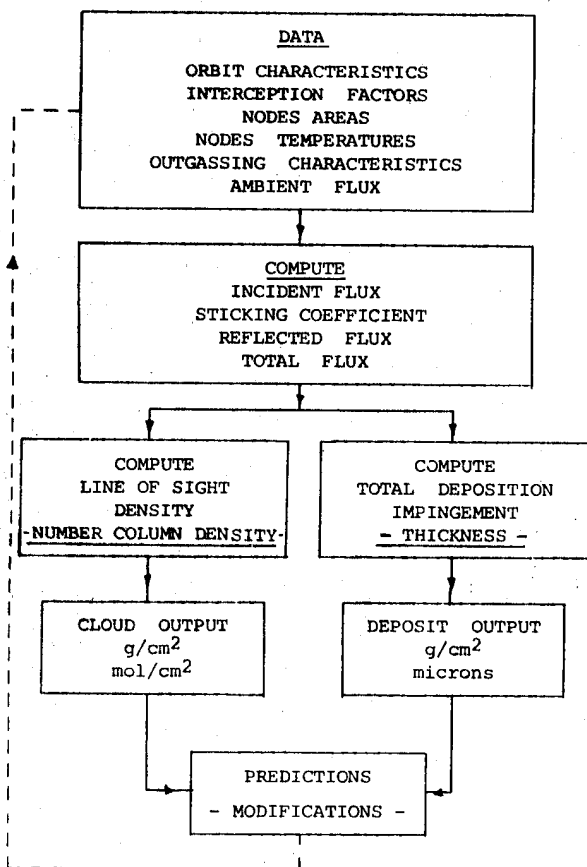


Figure 5. Flow diagram of CONTAM model

- The interception factors are calculated by the program CALMAR. The figure 6 shows two cases of calculation with diffuse and non diffuse emission.

- The temperatures are calculated by the program PROTERM.

- Others input are : areas of the nodes, outgassing rates, ...

- The choice of the nodes will depend upon the thermal model configuration. A contamination node will be defined by an homogeneous coating with homogeneous temperature, or by the exit of the nozzle of an engine.

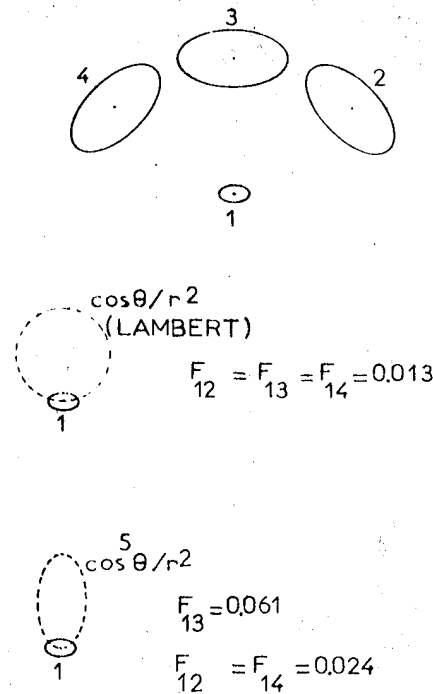


Figure 6. Example of interception factors calculated by CALMAR

Each open cavity (Fig. 7) is modeled separately. The holes are considered as particular nodes with sticking coefficient = 1 and without own outgassing. This nodes are considered as sources for the complete model (external). For the moment, cavities can be modelised only if the mean free path is larger than the bigger dimension of the cavity.

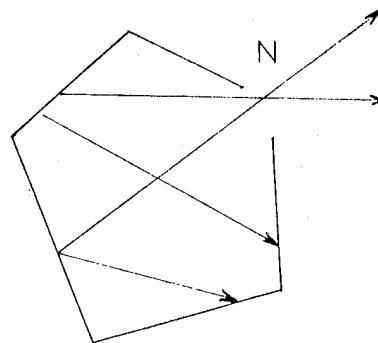


Figure 7. Open cavity

- Deposits are calculated by the above relation using the sticking coefficient.

- Column densities are derived in the following manner : consider a line of sight (direction of pointing of a telescope for example). Each section of a column around this line of sight (Fig. 8) is crossed by particles issued from adjacent areas J.

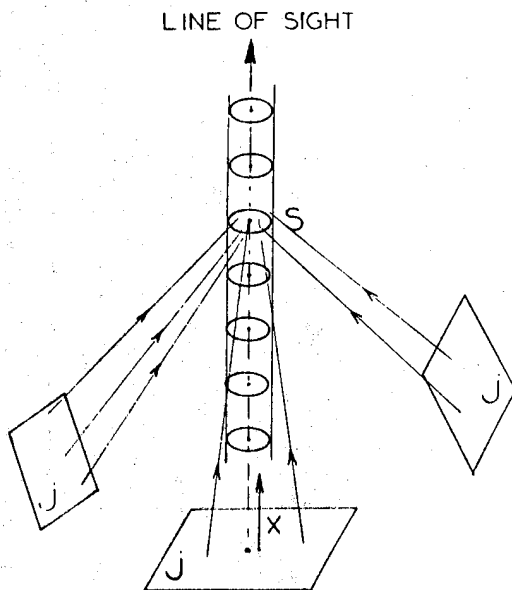


Figure 8. Line of sight

For a section S, the flux issued from J sources and crossing S is :

$$\sum_j \tau_j \cdot F_{(j,s)} \quad \text{g.cm}^{-2}.\text{s}^{-1}$$

and the density :

$$\text{DENS}(S) = \sum_j \frac{\tau_j \cdot F_{(j,s)}}{V_j} \quad \text{g.cm}^{-3}$$

By calculating this density at many sections along the line of sight, the mass column can be determined by integration :

$$\text{MC} = \int_{S=1}^{S=n} \text{DENS}(S) \, dx$$

x distance along the line of sight

V_j velocity of the source J molecules

Knowledge of the molecular constituents of the flux allows conversion of the mass column density into molecular number column density :

$$\text{NC} = \frac{\text{MC}}{m}$$

Deposits and column densities are expressed according to the time with a step of calculation $\Delta t \approx 10 \text{ mn}$.

5. APPLICATIONS

This model is applicable, at the present time, only for altitude above 300-400 km (where mean free path is high).

This is the case for the two projects where the CONTAM model is utilized :

- Project SIRIO 2 (E.S.A.) is a geostationary satellite. The LASSO experiment (Fig. 9) includes a laser reflector which temperature is low and there is a probability of deposit contaminants issued from :

- the A.B.M. (by autoretrodiffusion)

- A.O.C.S. engines (by autoretrodiffusion)
 - outgassing and vents located near the reflector.
- Present work consists in modeling the different contaminant sources. Included is the evaluation of the column density along the normal to the reflector.

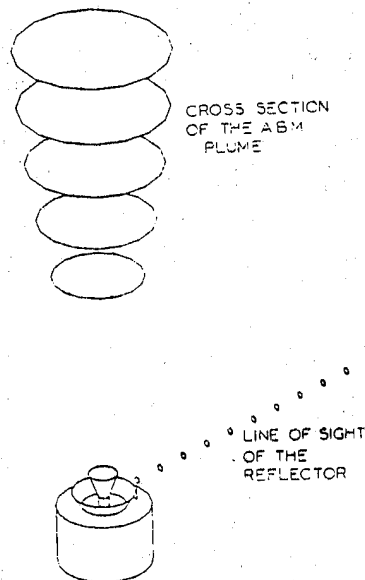


Figure 9. Graphic display of SIRIO 2 model

- Project SPOT (C.N.E.S.) is an earth observation satellite on a 800 km circular orbit. A contamination study has been done to calculate the deposits on the external surfaces and to evaluate the column density along the line of sight of the instruments. But due to the lack of experimental data, this study was made mainly to show the possibilities of the model.

More important is the evaluation of the deposits and the molecular cloud inside the High Resolution Visible (H.R.V.) instrument, due to its complicated geometry, the number of outgassing products and the critical optical surfaces present (work in progress).

Contamination problems on ARIANE - Flight experiment

To evaluate the eventuality of contamination of the payload during the launch of ARIANE, it was decided to put a quartz-crystal-microbalance (Q.C.M.) on the payload, at the surface of the CAT module.

This experiment was designed essentially to study the contamination during the firing of the retro-thrusters of the second stage of the rocket, and during the end of the launch.

There are two phases in the experiment :

- before the ejection of the fairing

In this phase, the condensable flux come from the inner part of the fairing. The pressure varies from atmospheric pressure to approximately 10^{-2} Torr at the ejection.

There are several sources of contaminants and several transfer mechanisms, due to the variation of the mean free path relative to the pressure.

- after the ejection of the fairing

During this phase, the sources of contaminants are the retrothrusters of the second stage and the early desorption of the payload and the top of the third stage.

This phase stops at the end of the telemetry (20 mn after launch).

Description of the Q.C.M.

The Q.C.M. is a model 700A (MK9) of CELESCO. It is used to measure small mass changes resulting from condensable efflux depositing upon a piezoelectric crystal. The condensing mass results in a predictable crystal vibrational frequency change. To relate crystal frequency changes to mass changes, other potential frequency effective phenomena must be considered. They are :

- temperature
- pressure
- solar radiation
- vibrations.

Figure 10 shows the influence of the first three parameters.

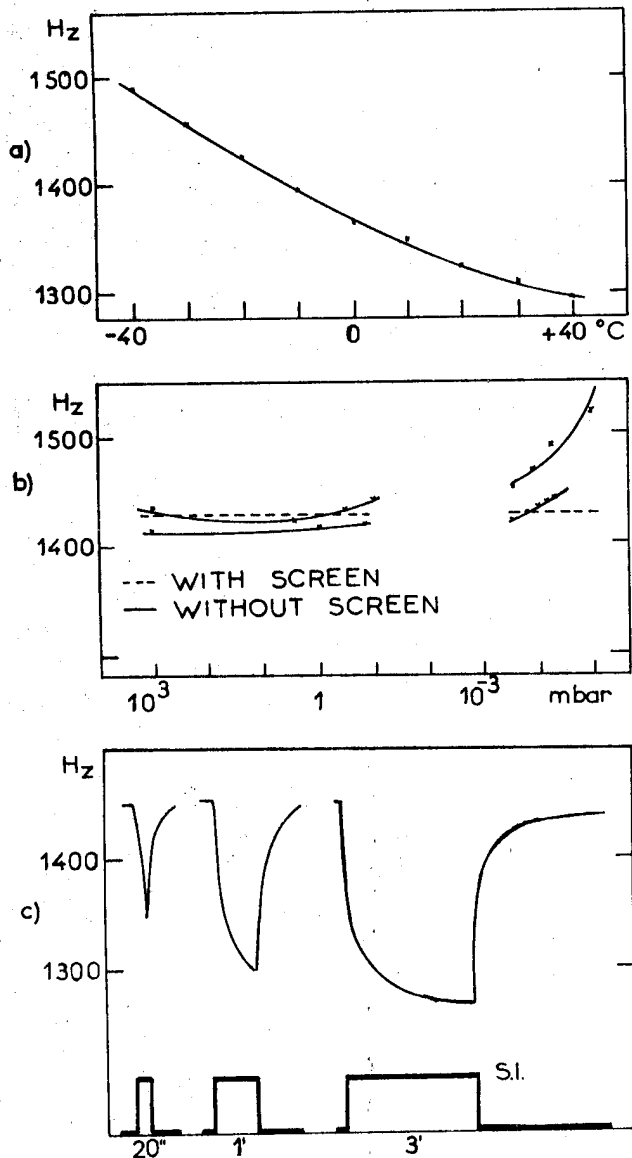


Figure 10. Q.C.M. Flight Model - Influence of :

- a) Temperature
- b) Pressure
- c) Solar Irradiance (S.I.)

The influence of vibrations is not perceptible. The frequency shift to deposited mass relationship is 2,26 Hz/A (for unit density). The cleanliness criteria has been fixed to $2,10^{-7}$ g.cm⁻², which corresponds to a shift of 45 Hz.

Unfortunately, the verification of the model will be complicated because there is only one Q.C.M.

But it is planned to use the results of the 3 planned flights and we hope a qualitative verification will be at least possible.

6. CONCLUSION

This paper is a first step towards a more sophisticated version which will take into account all the possibilities of scattering between all fluxes which are present inside or around a spacecraft.

But even in this preliminary approach, the credibility of this model is dependant upon the quality of the input data.

It is very important to note that it is necessary to have an important experimental support to validate the model.

Ground experiments and flight experiments are highly desirable.

The modeling activity will represent probably a necessary method to assess the space contamination when future heavy european spacecraft at low altitude will be designed.

7. REFERENCES

1. MARTIN MARIETTA MCR-75-202, 1975, *Payload/Orbiter contamination control requirement study*, Final report, by Bareiss, L.E., B. Ress
2. MARTIN MARIETTA MCR-77-107, 1977, *Orbiter/Payload contamination control assessment support*, by Rantanen, R.O., D.A. Strange Jensen
3. MASSACHUSETTS INSTITUTE OF TECHNOLOGY AD-A008-504, 1975, *Spacecraft self-contamination by molecular outgassing*, by Harvey, R.L.
4. NASA TN D-6645, 1972, *Self-contamination and environment of an orbiting spacecraft*, by Scialdone, J.J.
5. NASA N 76-18214, 1976, *Spacecraft self-contamination due to back-scattering of outgass products*, by Robertson, S.J.
6. NASA TN D-7590, 1974, *Dynamics and column densities of small particles ejected from spacecraft*, by Nauman, R.J.

N80-21433

EVALUATION OF KINETIC OUTGASSING UNDER VACUUM FOR POTTING COMPOUNDS AND PAINTS

J Guillin

Centre National d'Etudes Spatiales, Toulouse, France

ABSTRACT

The contamination evaluation computer model in space requires data on long term kinetic outgassing of materials under vacuum.

The weight loss under vacuum for potting compounds and thermal coating furnished by manufacturer or purified by ourselves has been measured by "micro-VCM" tests carried out at different temperatures and for periods as long as 2000 h. From these tests, equations of outgassing rates depending on time and temperature are proposed. It is pointed out that Arrhenius' equation is applicable for any temperature within the range studied and therefore it is possible to obtain "activation energies" for the total outgassing of these materials. The effects of the purifying process and of the polymerisation parameters (time, temperature) on outgassing energy and time dependance are studied.

Keywords : outgassing, potting compound, silicone, vacuum effect.

1. INTRODUCTION

The contamination evaluation computer model in space requires, in particular, the understanding of kinetic outgassing of materials during a long period. The "in-situ" continuous weight loss measurements with microbalance seem to be the most adjusted method but it is long and expensive. So, it was interesting to examine the possibility to obtain data with experimental weight loss measurements when the samples are weighted after a variable vacuum period at constant temperature (ref. 1).

2. EXPERIMENTS

To avoid the influency of water vapor readsorption we used commercial silicone resins or purified by ourselves like it is mentioned in another paper of this Symposium.

The resins are following :

- A - SYLGARD 184 of Dow Corning, polymerised at room temperature
- B - SYLGARD 184 purified at CNES, polymerised at room temperature

C - SYLGARD 184 purified, polymerised at room temperature then 24 hours at 100° C

D - SYLGARD 182 of Dow Corning, polymerised during 24 hours at 80° C

E - SYLGARD 182 purified at CNES, polymerised during 24 hours at 80° C

F - SYLGARD 182 purified, polymerised during 24 h at 100° C

Samples were cut out molded plates, their thickness was between two and four millimeters and their weight between 200 and 1000 mg.

Vacuum tests were conducted with an ionic pump (pumping speed : 200 l/s - pressure $\leq 10^{-6}$ torr) or sometimes with a micro-VCM equipment (ref. 2) including an oil vapor diffusion pump.

3. OUTGASSING KINETICS

Many papers show that the experimental outgassing rates decrease, depending on time, for non-metallic materials and during the first one hundred hours following approximate laws :

$$q = q_0 t^{-\alpha} \quad \text{or} \quad q = q_0 \exp\left(-\frac{t}{\tau}\right)$$

If we suppose that outgassing rates depending upon temperature, follow Arrhenius' equation into a recess interval of temperature (20 to 80° C for example) we may propose two types of equations :

$$q = q_0 t^{-\alpha} e^{-\frac{E}{RT}} \quad (1)$$

$$\text{or } q = q_0 e^{-\frac{t}{\tau}} e^{-\frac{E}{RT}} \quad (2)$$

with E "activation energy" of outgassing phenomena

t times

T temperature

R gas constant

α exponent of the source decay fonction

τ times constant

The integration of (1) between times 1 and t (for $\alpha \neq 1$) and equation 2 between times 0 and t gives the weight loss at constant temperature :

$$W = q_0 \cdot \frac{t^{1-\alpha} - 1}{1-\alpha} \cdot e^{-\frac{E}{RT}} \quad (3)$$

$$W = q_0 \cdot (-\gamma) \cdot (e^{-\frac{t}{\gamma}} - 1) \cdot e^{-\frac{E}{RT}} \quad (4)$$

For $t_1 T_1$ and $t_2 T_2$, we may write :

$$\frac{W_1}{W_2} = e^{-\frac{E}{R} \left(\frac{1}{T_1} - \frac{1}{T_2} \right)} \cdot \frac{t_1^{1-\alpha} - 1}{t_2^{1-\alpha} - 1} \quad (5)$$

$$\frac{W_1}{W_2} = e^{-\frac{E}{R} \left(\frac{1}{T_1} - \frac{1}{T_2} \right)} \cdot \frac{e^{-\frac{t_1}{\gamma}} - 1}{e^{-\frac{t_2}{\gamma}} - 1} \quad (6)$$

With (5) and (6) it is possible to determine E and α or E and γ if we know experimental measurements $W_i t_i T_i$ ($i = 1$ to 4) and then to calculate the weight loss in terms of the weight loss W_{REF} obtained during the reference time t_{REF} at T_{REF} , or then calculate the rate of outgassing :

$$q = W_{REF} \cdot e^{-\frac{E}{R} \left(\frac{1}{T} - \frac{1}{T_{REF}} \right)} \cdot \frac{1-\alpha}{t_{REF}^{1-\alpha} - 1} \cdot t^{-\alpha} \quad (7)$$

$$q = W_{REF} \cdot e^{-\frac{E}{R} \left(\frac{1}{T} - \frac{1}{T_{REF}} \right)} \cdot \frac{1}{\gamma \left(1 - e^{-\frac{t_{REF}}{\gamma}} \right)} \cdot e^{-\frac{t}{\gamma}} \quad (8)$$

4. RESULTS

Figures 1 to 6 show the experimental weight loss versus time for different constant temperatures and the calculated curves for these temperatures dating from (5) and (6) where W_2 is an experimental point corresponding to the highest temperature.

We verify a good agreement with predicted curves between 50 hours and 2000 hours ; it seems that the equation type $t^{-\alpha}$ is more accurate than exponential equation for SYLGARD 184 polymerised at room temperature, purified or not.

The table 1 shows the weight loss coefficient equations when weight loss is given in initial weight percentage. We observe that the predicted activation energy increase versus purity of SYLGARD 184 and the exponent α decrease for the $t^{-\alpha}$ equation.

Table 1

REF.	K ₁	K ₂	E ₁ cal.g mole ⁻¹	E ₂	T REF. °K	1 - α	γ HOURS
A	10.976	1.502	5420	3911	353	0.025	25.4
B	0.229	0.476	6319	7950	353	0.168	82.6
C	0.125	0.230	8605	6115	353	0.213	40.2
D	1.130	1.042	7298	7019	353	0.13	46
E	0.180	0.238	6029	4036	353	0.156	65.4
F	0.094	0.066	11680	11880	333	-0.26	20.4

$$W(\%) = K_1 \cdot \exp \left[\frac{-E_1}{1.98} \left(\frac{1}{T} - \frac{1}{T_{REF}} \right) \right] (t^{1-\alpha} - 1)$$

$$W(\%) = K_2 \cdot \exp \left[\frac{-E_2}{1.98} \left(\frac{1}{T} - \frac{1}{T_{REF}} \right) \right] (1 - \exp \frac{-t}{\gamma})$$

We have calculated the weight loss percentage of resins for tests at 125° C during 24 hours in order to see if it is possible to extend estimates out of our fixed gradient of temperatures. The Table 2 gives the experimental and calculated values. Except for F resin, the agreement seems correct.

Table 2

REFERENCE	PREDICTED LOG EXP	EXPERIMENT
A	2.18	1.86
	1.73	
B	0.43	0.40
	0.42	
C	0.28	0.34
	0.49	
D	1.32	1.23
	1.88	
E	0.14	0.26
	0.31	
F	0.48	0.26
	0.76	

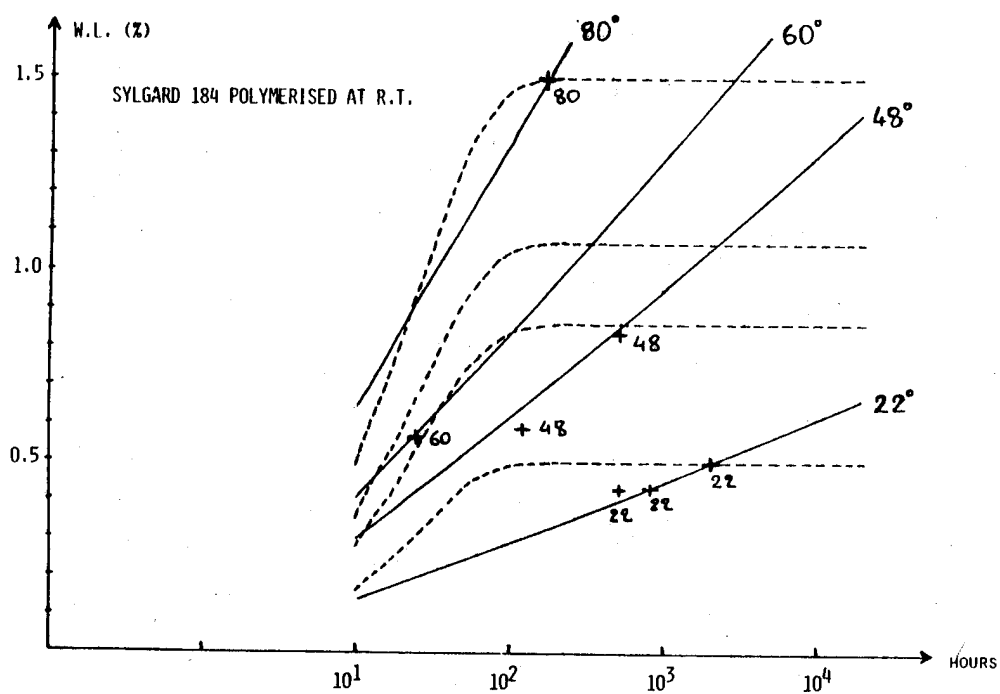


Figure 1

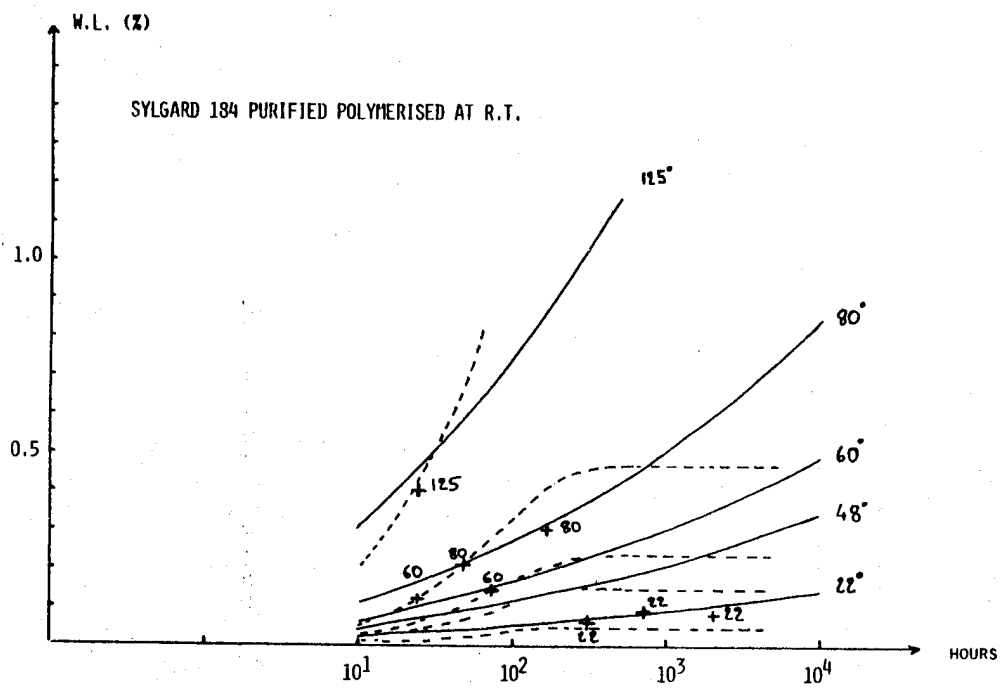


Figure 2

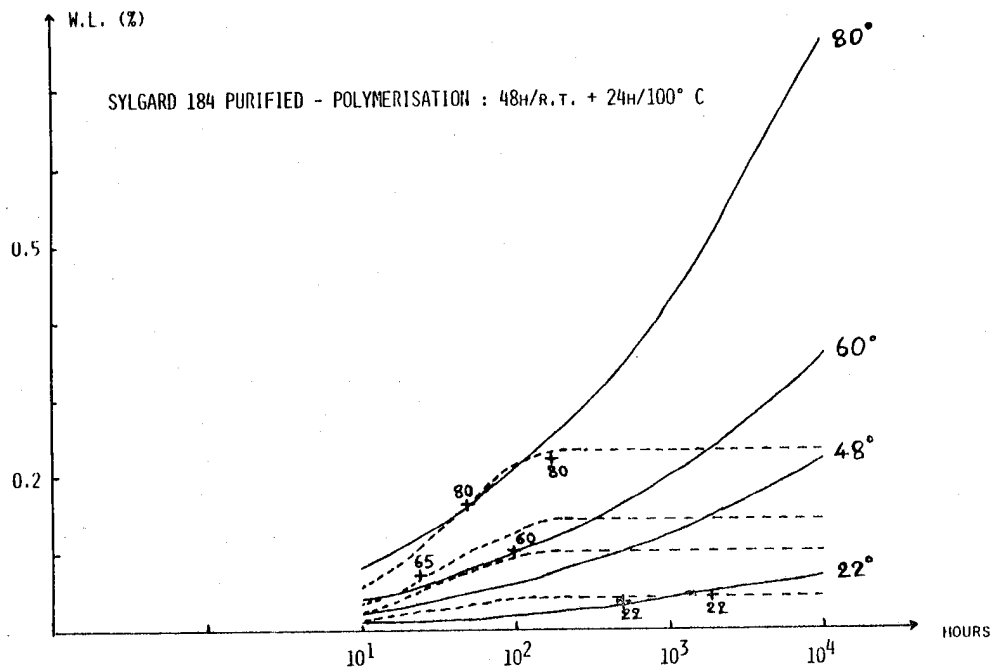


Figure 3

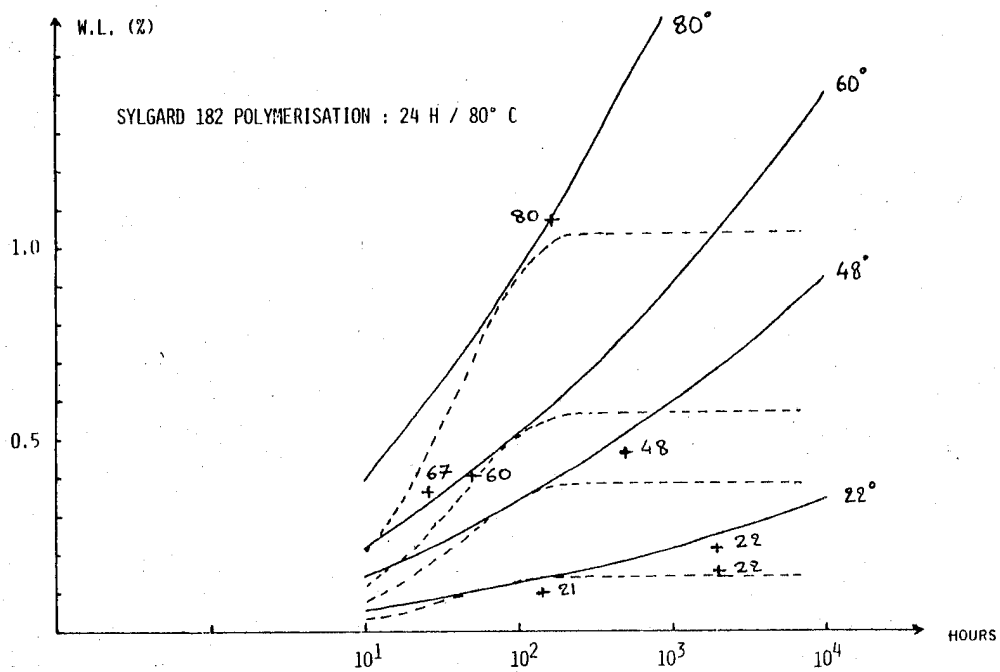


Figure 4

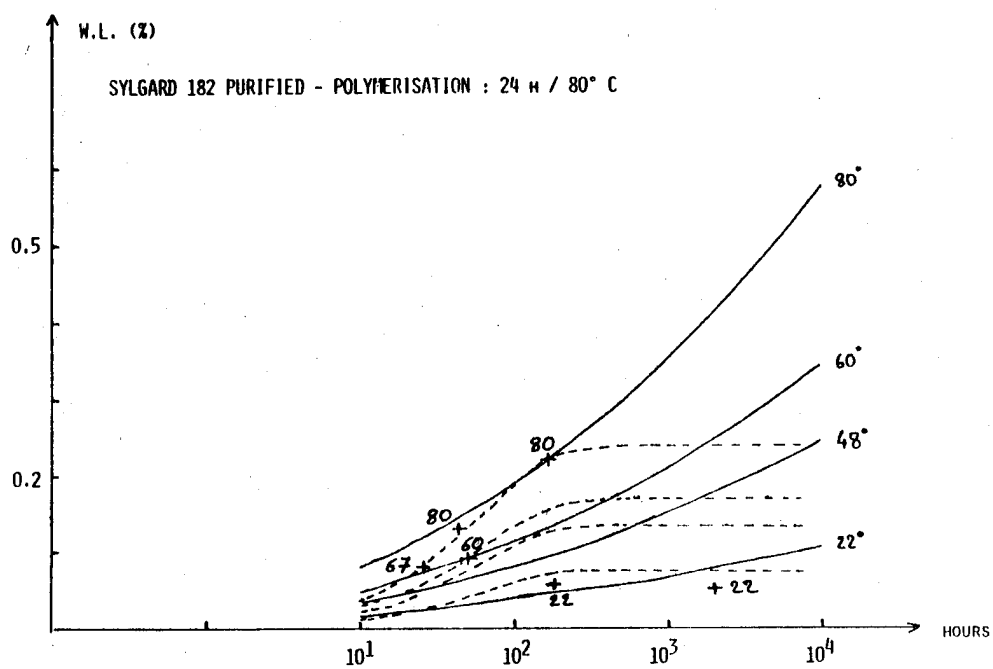


Figure 5

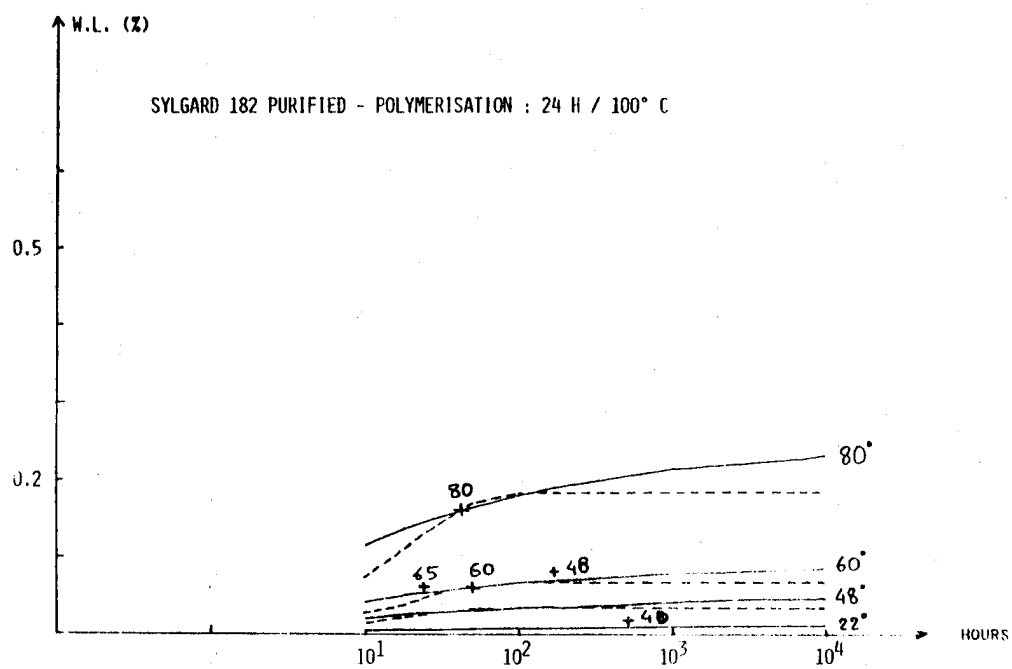


Figure 6

The experimental data at room temperature is shown in figure 7 in order to prove improvement of purified resins.

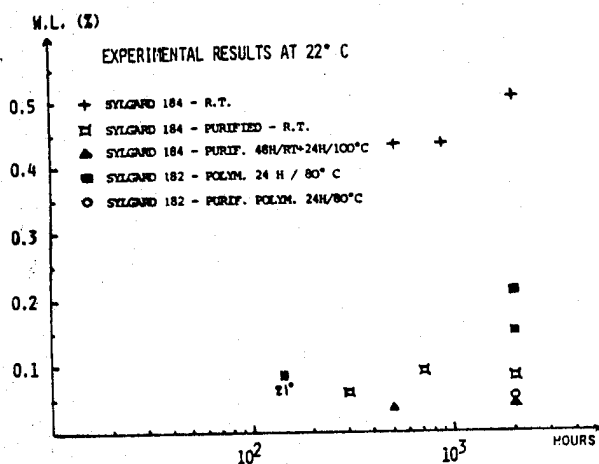


Figure 7

Figure 8 shows the calculated outgassing rates versus time at 20° C following equation 7.

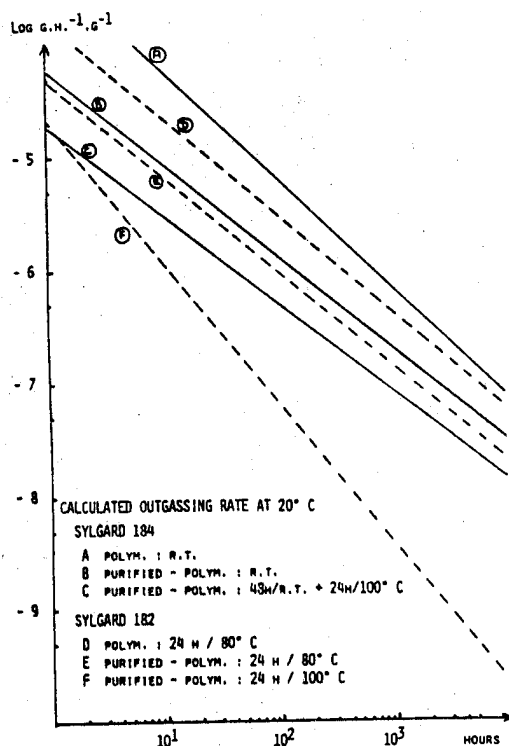


Figure 8

5. CONCLUSIONS

Starting with a small number of weight loss measurements we have shown that it is possible to estimate outgassing kinetic between 100 h - 2000 h and 20° C - 80° C for these silicone products. It will be possible to extend this method to another resins like epoxy - polyurethanes, etc... and charges silicones : paints for example.

We are presently testing paints type PSE 109/ P 123 primer, PSG 173/ P 123, PSG 120/ P 128 primer and PSG 120 FD/ P 128, S1 / P 123 CNES paints.

These tests show :

- the application field for proposed equations is smaller (activation energy variable versus temperature)
- desorption of water vapor must be taken into account
- it will be necessary to study weight loss evolution in relation to exposed areas rather than to initial weight.

6. REFERENCES

- J.J. Scialdone "Environment of a spacecraft produced by its own outgassing" Evaluation de l'action de l'environnement sur les matériaux - Toulouse, France, 17-21 juin 1974
- J. Guillin "Effets du vide sur les matériaux et contamination de l'environnement" AVIRES II, Lyon, France, 19-22 septembre 1972

N80-21434

CONTAMINATION ENHANCED ELECTROSTATIC DISCHARGE MECHANISMS

J A Jeffery & C R Maag

*Jet Propulsion Laboratory
Applied Mechanics Technology Division, Pasadena, California, USA*

With the advent of larger and more advanced spacecraft the two problems of ESD and contamination requires significant investigation in order to ensure the success of future missions. In addition there is a synergistic relationship between them such that one enhances the probability of occurrence of the other. And the action of both provides substantially more deleterious effects than the effects of both separately. Mechanisms for such a relationship will be discussed as well as applications to large advanced technology systems.

Keywords: ESD, Electrostatic Discharge, Contamination, Satellites, Thrusters

1. INTRODUCTION

The increased sophistication, sensitivity, and size of modern satellite systems has revealed many new hazards to satellite longevity. Two of the basic ones are the problems of Electrostatic Discharge and Contamination. The intent of this paper is to suggest that a synergistic relationship may exist between the two phenomena. The action of one process can increase the probability of the other, and both processes operating together can have a far more detrimental effect on survivability of space systems than both processes acting independently. There are many mechanisms which can explain this. Contamination may be enhanced by charging phenomena by the release of ions and vaporized materials from an ESD event which have the potential of redepositing on satellite surfaces (Ref. 1) or by the surface charge of the satellite causing reattraction and deposition of ionized thruster effluents or outgassed species that have become ionized. (Refs. 2,3,4) ESD may be enhanced by contamination by changing the surface conductivity of materials on the satellite and thereby affecting charge mobility. The effect of both phenomena simultaneously can have many times the impact of either separately. The understanding and prevention of these phenomena are essential to the success of

future missions which require lifetimes and sensitivity far greater than present systems. The state of the art in either field, however, is far from perfect and much investigation and technological development are necessary to insure the success of missions such as those being explored under advanced mission technology programs.

2. ESD OVERVIEW

Satellites at synchronous orbit have been observed to charge to large voltages as a result of the presence of charged particle currents associated with the spacecraft environment. In the local time sector from just before midnight to past dawn, a spacecraft at altitudes greater than $3 R_E$ will occasionally be immersed in a dense plasma cloud (N 1-10 particles/cm³) of energetic electrons (kT_e 5-20 keV). This phenomena is usually accompanied by localized fluctuations in the earth's magnetic field at high altitude magnetic observatories and is known as a magnetic substorm, in order to distinguish it from the worldwide fluctuations associated with a magnetic storm. In this environment, however, the spacecraft potential can range from zero to over 20,000 volts. ATS-5 has been observed to charge to negative voltages as great as fifteen thousand volts (15 keV) when the satellite is eclipsed by the earth. The spacecraft potential with respect to the plasma depends on the ambient parameters, the electrical and geometrical characteristics of the spacecraft, the state of illumination of the various sections, and the properties of the external surface materials used in the spacecraft.

If a satellite has insulating outer surfaces, those surfaces can charge to large differential voltages with respect to the spacecraft structure. The structure also can charge to large voltages relative to the environment, and thus create large electric fields at the surface of the spacecraft or internal to dielectric surface materials. Because of these large electric fields, electrical breakdowns

(discharges) may occur from the charged outer surfaces to the spacecraft frame. Where conductive spacecraft structures are electrically isolated from one another there exists the possibility of the accumulation of large amounts of charge which, due to the charge mobility of the conductive structure, will act as a single capacitive discharge transferring energy proportional to the capacitance and the square of the potential. This can be a serious threat to the operation of the spacecraft and has in fact caused the failure of at least one important satellite system.

Laboratory tests have shown that electrical discharges cause physical damage to dielectric materials used for satellite thermal control and solar power systems. The external surface of a spacecraft is complex and an extremely important subsystem of the satellite necessary for its adaption to the space environment. It must protect it from damage due to radiation and micrometeoroids, and is a key factor in the thermal balance of the spacecraft within the environment. Metallized polymeric films, because of their use in large area applications and multilayer configurations, are particularly vulnerable to static charge buildup and subsequent degradation from arcing. This arcing can cause removal of the metallized layer and vaporization of the polymeric film (Ref. 1) thus severely degrading the optical and thermal properties of the material. Additionally, this can cause contamination and degradation of adjacent thermal control, optical and other subsystems. Satellite charging can also cause the re-attraction of ionized outgassed species or ionized thruster effluents. (Ref. 2,3,4)

Discharges can also cause Electromagnetic Interference (EMI) which has been identified as a primary cause of satellite anomalous behavior. The RFI (radio frequency interference) emitted by an arc has the ability to couple into satellite electronics (via cable harnesses, connectors, etc.) and thereby cause anomalous voltage pulses resulting in erroneous data, false commands or system failures.

Many of the anomalies are in a nuisance category, and can be tolerated or corrected by a ground station command. There have been however, more serious incidences; one caused the loss of a complete satellite. This was caused by a power system failure during a very large geomagnetic substorm. Several other satellites have been saved only through quick ground station action when despun antenna platforms began to spin up. More frequent anomalies are, however, erroneous data, data frames, and spacecraft surface degradation.

The DSCS II satellites are probably the most significant examples illustrating the necessity to understand and prevent ESD. The first DSCS II satellite underwent a complete power failure coincidental with a severe geomagnetic substorm, and the satellite was lost. In addition, the DSCS II satellites have experienced several near losses and many less serious anomalies. There were several types: (a) spinup anomalies, (b) Reset Generator

Assembly (RGA), (c) Tunnel Diode Amplifier Logic (TDAL), (d) pressure transducer failure, (e) power converter switching, and (f) gimbal reset. (Ref. 5)

Simulated arc discharges were used to test a prototype spacecraft. Experimenters were able to cause every type of anomaly mentioned, except for the pressure transducer failure. The testing demonstrated that the anomalous behavior was the result of a change in the state of onboard flip-flop circuitry, probably caused by nearby ESD. In addition, the pressure transducer failure could have been caused by a direct arc discharge.

Potentially, the most serious was the spinup anomaly. DSCS II has a spinning cylinder for attitude stability and a despun platform which enables the antennas to be always oriented toward Earth. The spinup anomalies cause the despun platform to start spinning. If allowed to get too far, the antennas would not be Earth oriented most of the time and communication with the satellite would be lost. Commands from ground stations were able to despin the antennas and countermeasures were subsequently instituted to automatically despin the antenna if a spinup anomaly occurred.

Some of the anomalies of DSCS II were not correlated to geomagnetic indices or the dawn to dusk quadrant. These were, however, observed to be illumination and spin-orientation dependent. That is, the anomalies occurred more frequently when the satellite was in a certain orientation with specific sections illuminated. This fits in with the photoelectron dependence of the spacecraft charging theory, and is seen as a second type of ESD scenario.

Intelsat IV is a COMSAT satellite which has experienced the spinup anomalies described in the DSCS II section. It also has a despun antenna with a spinning cylindrical platform. Five spinup anomalies were observed coincident with geomagnetic substorms. Subsequently, software countermeasures were instituted to prevent satellite loss. During the first launches, the thermal blankets were not grounded and shielded wires were used minimally. No absolute grounding standard was used. Other anomalies not as serious as the spinup anomalies have been observed. Testing has shown that ESD could cause such anomalies. (Ref. 6)

Skynet 2B is a British Defense Communications satellite which has experienced a large number of anomalies. These anomalies are data omission, mistimed data, or errors in telemetered spacecraft parameters. The distribution of these anomalies does not show a daily local time preference, but it does show an increase during eclipse seasons in spring and autumn. This is interpreted to show significant dependence on photoemission effects and spacecraft sun angle. The presence of small apertures allows sunlight to enter and, through partial illumination, cause some surfaces to give off electrons while others remain charged. This condition, coupled with a

large number of switching devices, makes the satellite susceptible to ESD. In fact, repetitive anomalous telemetry data have been experienced. (Ref. 7)

The ATS-6 spacecraft has experienced no significant anomalies that are attributed to ESD. A UCSD instrument package was flown on the satellite to determine plasma fluxes and spacecraft potential. The experiment did indicate large fluxes and kilovolt potentials on the spacecraft. The lack of ESD anomalies can be explained in the basic design of the satellite. The Earth-viewing module was located in its own strong rf field. For this reason, the module employed extraordinary grounding, shielding, and rf sealing techniques. It was felt that, since the spacecraft was tested at twice the expected rf level, no ESD would be worse. The command system on the satellite required a data word to load a command and a separate data word to execute it. The circuitry required a 7.5-volt pulse to initiate logic currents and there were no stored onboard command sequences. Therefore, it was felt that this system also provided some immunity to ESD. Testing was done on each component as well as the whole spacecraft. The weight cost for such design procedures is not known, but it is significant. It has demonstrated though that known techniques, however extraordinary, can reduce or eliminate the problem with ESD. (Ref. 6)

Anomalous temperature rise rates on satellites has suggested the possibility of ESD degradation of radiator surfaces (Second Surface Mirrors). Studies have been done with the conclusion reached that ESDs damage radiator surfaces to some extent and appear to cause an increase in the α value. The degradation, however, was insufficient to explain the gradual temperature increase observed on operational sensors. Thus, it is probable that a contamination mechanism is a greater factor in surface degradation. This contamination could however be charging enhanced. (Ref. 8)

It has generally been concluded that there are basically three approaches that can be taken to deal with this problem. The first is to accept the fact that differential charging will occur and design or harden the spacecraft to its effects. Second, make the entire outside of the spacecraft including the solar panels electrically continuous and conductive, i.e., enclose it in a Faraday cage. Here the spacecraft will acquire a net charge; however, the charge will uniformly distribute itself and differential charging will not exist, hence, no discharges. Third, the design would include a method of distributing charge uniformly and would also provide through active or passive means, a mechanism for removing charge thus keeping the net spacecraft charge at zero.

The first approach described is the most practical in meeting requirements such as cost and readiness for the launch date where these are the controlling considerations consistent with program objectives. The basic guidelines to this type of hardening is that all conductive structures and subsystems are

electrically continuous to a unit point ground system even to the extent of including metal films in the multi-layer thermal blanket super insulation. This also has the added benefit of providing a Faraday cage around most of the spacecraft. Care must be taken to assure that exposed dielectrics are not degraded during the mission life and that discharges on these surfaces are sufficiently decoupled from sensitive electronics. All harnesses external to the spacecraft must be shielded where practical so that insulation breakdown will not compromise their function. Redundant logic can be employed in command and other sensitive circuitry.

In applying the methods of the second approach, consideration must be given to the use of conductive coatings over dielectrics. It should be possible to apply these coatings thin enough so that thermo-optical properties of the underlying dielectric would be minimally affected. It must be kept in mind that even if such coatings are possible there are other factors which may render them useless.

The third approach may also use thin coatings, however, here secondary emission characteristics must also be considered in addition to conductivity. In considering the current balance of a body in a plasma there are three components to achieve equilibrium. First, the incident charged particle current of electrons and ions; second, photoemission which is present when the body is illuminated; and third, secondary emission which is the most important of the three. If the secondary emission ratio of the surface is sufficiently high the net surface charge will be maintained near zero.

Other approaches to obtaining a more uniform charge distribution include the use of wire or other conductive grids. These techniques divide the dielectric surface into a matrix of small dielectric tiles each bounded by a ground plane. This reduces the area on the surface which can differentially charge and shortens the distance from any point on a dielectric to structure ground thus reducing the magnitude of individual discharges both in maximum voltage attained and charge transferred. Even though the total charge or the total capacitance, which are arithmetic sums of the smaller segments, available for discharge have not changed, the total energy has been significantly reduced. This is because the energy stored in a capacitor is proportional to the square of the voltage rather than being a linear function. Matrices of conductive paths through dielectrics to an underlying conductive layer would also offer this same type of control.

Active control of spacecraft charging involves the control of spacecraft potential by emitting charges from the satellite to balance the incoming environmental flux. Experiments have been flown on ATS-5 and ATS-6 to determine the effectiveness and problems of this technique. The primary difficulty is that electron emitters control only the spacecraft ground and surface conductively continuous with it. Isolated surfaces will still keep their charge

and hence the difference between their potential and ground will increase thus exacerbating differential charging and increasing ESD probability. An ion source can then be used to emit ions which can flow to the negatively charged surfaces and neutralize them. However, the serious contamination threat this poses is obvious.

The experiments on ATS-5 and ATS-6 have indicated that it is possible to control spacecraft potential by use of cesium ion thrusters as sources of both ions and electrons. On ATS-5 it has changed the spacecraft from a potential of a few kilovolts negative to about -20 volts. (Ref. 6)

3. CONTAMINATION OVERVIEW

High-performance optical systems and critical functional surfaces aboard advanced long-life spacecraft require effective contamination control measures to maintain performance stability and to ensure data accuracy. Contamination is said to exist if a spacecraft or launch vehicle produced material interferes with the intended performance of a surface or a sensor. The contamination can deposit on a surface and thus alter the absorptance, emittance, transmittance, reflectance or conductivity characteristics. The contamination can also intercept the field-of-view of a sensor or experiment and either scatter, emit or absorb electromagnetic radiation. Contamination can occur from either molecular species or particulate matter.

The sources of the molecular species are mass loss from nonmetallic materials, venting of confined spacecraft or experiment volumes, attitude control systems exhaust and operational venting or purging of systems such as fuel cells and sublimators. Anomalous sources such as leaks in coolant lines, propellant tanks and hydraulic systems also

contribute to the molecular induced environment. The major sources of particulates are sloughing off of particles acquired during ground handling and assembly, attitude control exhausts, overboard vents, leaks or purges of capable of condensing into particles upon vacuum exposure, abrasion of movable surfaces and micrometeoroid impacts.

Major contamination events may include: (1) ground-based initial contaminant loading during the factory-to-launch operational sequence; (2) launch vehicle interface effects during the launch/ascent/payload-deployment mission phase, vacuum-exposed outgassing-deposition, thruster impingement, venting, and release of particulates. A summary of the major contamination modes and sources encountered during spacecraft operations is presented in Table I.

An overview of general spacecraft contamination concerns shown in Table II indicates that three key issues must be carefully evaluated in order to develop an effective contamination control system and management plan:

- o Initial contamination budget - cleanliness level, including maintenance, handling, and other pertinent procedural factors.
- o Material selection - outgassing-deposition properties, pre-flight space conditioning being a possible means of contamination reduction.
- o Configuration and subsystem designs - avoidance of contaminant fluxes; implementation of on-board contamination preventive measures.

TABLE I
CONTAMINATION MODES

MODE	SOURCES
o Outgassing/Deposition (Molecular)	o Surface Desorption - Adsorption, Lubricants, Adhesives, and all Evaporable Surface Materials
o Cloud Formation (Molecular and Particulate)	o Leaks, Vents, Shuttle Interface
o Plume Impingements	o Leaks, Vents, Dust Recirculation Particle Dispersion
o Misc (Radiation, Electrostatic Forces, Proton Sputtering, Micrometeoroids)	o Solid and Liquid Engine Plumes
	o Atmospheric Particles, Electrostatic Discharge, Micrometeoroids

TABLE II

GENERAL SPACECRAFT CONTAMINATION CONCERNS

- o Deposition or Film Formation - Surface Physical/Chemical Property Changes; Optical and Thermal Performance Degradation
- o Plume Impingement or Particle Streams - Surface Erosion, Blast Damage
- o Particulate/Molecular Environments - Light Scattering and Absorption
- o Radiation, Proton Sputtering, Electrostatic Forces - Surface Outgassing, Contaminant Flux Trajectories

For the new generation of space vehicles within mission objectives of performing scientific experiments and observations over a long-life period, these issues may have to be evaluated based on stringent contamination constraints whereupon accurate contamination predictions become mandatory.

The sources of plume induced contamination from conventional liquid propellant engines can be grouped into four types:

- o Unreacted fuel or oxidizer vapor produced during preignition which forms clouds of droplets of about one to two microns in size, which usually cause hazy or smoke-like deposits.
- o Incompletely reacted fuel or oxidizer droplets which are too large to completely react in the chamber (up to several hundred microns in size), and which are centrally directed, pass through the throat and are accelerated to speeds of up to several thousand feet per second. If these droplets do not completely vaporize in the plume, they can deposit on or abrade a surface immersed in the plume.
- o Wall film produced by unburned propellant impinging on the chamber walls is propagated downstream under the influence of viscous forces from the expanding gas to the nozzle lip where it is ejected. If this wall film is able to move to the nozzle lip without being thermally destroyed, it will be thrown-off as large droplets in a direction roughly normal to the nozzle axis.
- o Combustion products, such as H_2O , CO_2 , MMH nitrate can condense in the plume or on cold surfaces immersed in the plume. These droplets, like the unburned propellant, can deposit on or abrade an immersed surface.

Bipropellant engines, due to incomplete combustion, generally produce all four types of contaminants, while monopropellant engines, if the catalytic bed is operating efficiently, generally render only condensibles as a

contaminant. During steady-state operation, a bipropellant engine produces unreacted propellant droplets, condensibles, and if the engine hardware is cold enough, wall film. Increasing combustion efficiency (i.e., optimizing fuel-oxidizer injector/chamber compatibility, etc.) can reduce the production of unreacted droplets and wall film. Unreacted vapor is limited to transient engine operation. Wall film, unreacted vapor, and unreacted droplets result from residual propellants in the injector and manifolds (dribble volume) downstream of the valves.

Following engine shutdown, when the chamber pressure decreases to the vapor pressure of the propellant, cold flow expulsion of the residual propellant is initiated. Since the oxidizer and fuel will have different vapor pressures, the initial expulsion of one will quench combustion. Contaminant production depends on how effectively the residual propellants are consumed following valve closure. If the engine is sufficiently hot at shutdown, some residual propellants will combust and diffuse into the vacuum environment. For cold engine shutdowns, combustion will quench earlier, resulting in more unreacted droplets, wall film, and unreacted vapor.

An optimum engine design is one which produces complete propellant vaporization upstream of the nozzle throat and eliminates manifold dribble volumes. Dribble volumes, however, will probably, never be eliminated completely, due to mechanical limitations. Complete propellant vaporization can be achieved by increasing chamber length; however, the more efficient mixing associated with increased chamber lengths, results in hotter wall temperatures, which degrades the film cooling effect and, ultimately, engine life. For these reasons, and the fact that condensibles will always be present in the exhaust plume and on cool surfaces immersed in the plume, plume induced contamination from liquid engines remain an area of continuing concern.

Attitude control thrusters operate in short pulses, and, thus, the steady state burn time is not long compared to the start-up and shut-down transients. For this reason, all three phases of the engine burn have to be analyzed. In addition, the fixed location of the thrusters on satellites mean that some sensitive surfaces will be located near the plane of the thruster exit, and thus, exposed to contamination from expelled nozzle wall film.

Solid Rocket Motors (SRM), Ion thrusters, and pulsed plasma thrusters (PPT) also exhibit contamination effects. The SRM's are distinguished by the large amount of solid particles ejected in its exhaust which constitutes an additional contaminant form. The IUS engines for shuttle assisted launches are SRM's and thus it is necessary to understand their contamination impact. The potential contamination problems from SRM's have been known for a considerable time and Borson and Landsbaum (Ref. 9) have indicated that their contamination potential is similar to that of liquid rockets except for the additional particulate contamination. Many

systems utilizing SRM's have reported problems or concern over contamination of these engines.

PPT's and ion thrusters because of their long useful life are prime candidates for future missions. They may be operated for thousands of hours without failure and thus are ideal as attitude control and station keeping devices as they are normally of small thrust. Average backflow contamination from a PPT was measured at 10^{-10} g-cm⁻²-pulse⁻¹ with an r-2 dropoff with distance from nozzle exit. Many atoms and ionized species such as carbon, fluorine, and iron have been observed as contaminants and some deposits could not be removed. Thus this thruster is also a prime candidate for contamination concern. (Ref. 10)

4. CONTAMINATION - ESD SYNERGISM

There are three basic mechanisms which explain the existence of a synergistic relationship between contamination processes and ESD phenomena.

The first of these was investigated by Yablowsky et. al., and concerns ESD's which release vaporized products and ions which deposit on other satellite surfaces as contaminants. Puncture discharges in silvered teflon were enhanced by electron beam irradiation and results indicated that both electrons and ions were emitted as well as vaporized teflon and silver. This vaporized material can be a serious source of contamination for other satellite surfaces as are the ions which may be reattracted to the satellite as described in the second mechanism to follow. The redeposition of these contaminants can have a significant deleterious effect on satellite lifetime and performance. It was however observed that as more discharges occur, less material is emitted. (Ref. 1)

The second mechanism involves the trajectories of charged particles in the electric field of a charged spacecraft. These particles are either outgassed materials, thruster effluents, or ESD ejecta (as described in the previous paragraph) which were ionized before emission or were subsequently ionized in space by solar UV or ambient electrons. In any case, if the spacecraft is charged these ions will tend to be reattracted to the satellite if they are ionized within the plasma sheath. D. P. Cauffman estimates that a total of 100 A will result in three months. N. J. Stevens, et.al. describes processes which may be included as a subset of this mechanism whereby contamination is enhanced by ESD. He describes it as an electrostatic precipitation effect whereby contaminants may be attracted to a charged spacecraft by (1) neutral molecules becoming polarized (but not ionized) by the electric fields, (2) acceleration of charged particles in space increasing the probability of ionization by collisions, and (3) the intense field at a surface actually may ionize outgassing molecules. Once these ions or particles are reattracted to the satellite surface they can have degradation effects. (Ref. 2,3,4)

The third mechanism involves the effect of contaminants on surface properties, particularly surface conductivity. The presence of a contaminant on a surface can effect the mobility of electrons. This is recognized to be one of the major problems with control of ESD. Dielectric materials trap electrons until such a charge builds up that an arc occurs radiating EMI and damaging satellite surfaces. As a submechanism of this it can be realized that a discharge can polymerize, darken, and otherwise change the properties of surface contamination so that it becomes even more deleterious.

Recently it was suggested by Scarf at an ESD workshop at JPL that certain discharges detected by the Plasma Wave experiment on the Jupiter Voyager spacecraft were coincident with hydrazine thruster firings. While several mechanisms can be used to explain such an effect, there clearly is an ESD - contamination relationship implicated. (Ref. 11)

Mechanism two is being directly investigated at present on the SCATHA satellite. The design of the ML12 experiment involves a combination of a retarding potential analyzer and a temperature controlled quartz crystal microbalance. Thereby differentiation between deposition of charged and uncharged species can be made and information can be obtained regarding adsorption and desorption rates of contaminants and their temperature dependence. The other instrument in the experiment has several materials of which the ϕ is monitored as a function of the depositing flux. Thus ML12 should be able to accurately determine if the charge state of a satellite contributes significantly to contamination deposition on exterior surfaces, thus determining the accuracy of mechanism two. (Ref. 12)

SCATHA also carries an experiment designated SC4 which involves particle beam systems. A Xenon ion gun is involved and return flux can be measured. (Ref. 12)

5. ADVANCED MISSION TECHNOLOGY PROGRAMS

This information has a great impact on any advanced mission technology programs within NASA. One of the new technology development areas is in the area of large deployable reflectors. Large (100 meter diameter) mesh antennas will be placed in geosynchronous altitude for studies in multi-beam communications. Most of these antennas will be erected in LEO and transported to the synchronous altitude by a low thrust orbit transfer propulsion system. It is highly probable that contamination from the numerous scenarios involving plume impingement will compromise the materials selection program for electrostatic discharge (ESD) control.

As the space shuttle will be the major transport vehicle to move material to Earth orbit and assemble and deploy future space systems, thruster effluents and other STS induced contamination will have an effect on these systems. The shuttle will only attain

low Earth orbit and some form of rocket system must be used to insert these large structures into higher Earth orbits and even geosynchronous orbits. These propulsion systems must almost certainly be low thrust so as not to destroy the structure and may be similar to the pulsed plasma thrusters previously discussed. A station keeping and attitude control system are also necessary for the structure to maintain proper orientation and position. This system would be used on an as needed basis and would require thrusters to be pulsed frequently while cold and hence more contamination prone. All of these factors, the STS transport and assembly, the orbit transfer, and the station keeping will all add to the contamination probability. In addition such structures have large quantities of VCM materials essential to their proper operation. These materials over the large lifetime of the antenna or platform will outgas substantial quantities of contaminants which will have an adverse effect on such a material. First they would certainly change the surface conductivity as previously discussed and may cause electrical signal interference should electrons become trapped in the materials. They could also have a corrosive effect on the dacron or they could have a stiffening effect causing the surface accuracy to be uncontrollable. It is also apparent that any direct or almost direct plume impingement during docking maneuvers or otherwise could tear or destroy parts of the system.

Once the contamination has deposited on such surfaces, it will be almost impossible to clean. It will be remembered that the PPT deposits discussed earlier were not removeable from hard metal surfaces and there is no reason to believe any other system is any better. It will then be impinged upon by ambient protons and electrons, UV radiation, and gamma rays. These will have an effect, possibly darkening and hardening the deposits and in the case of electrons can be a source of ESD arcs. Such arcing will of course have a degradation effect on the surface as well as providing additional contaminants for redeposition at other locations. The ESD events will also cause gold or other conductive coatings to be vaporized and destroyed in spots, thereby reducing conductivity additionally. Also surface charge will reattract ions and other particles to the surface for more contamination. The result can be seen to be multiplicative.

A study was conducted for NASA MSFC to determine the contamination impact of a typical docking maneuver of the space shuttle with a 25 KW power module. Thicknesses of contamination on sensitive surfaces and solar arrays were predicted to be as much as 35 microns (and will be even higher in spots because this number represents an average over the surface). (Ref. 13). Deposits of this magnitude cannot be ignored and it was felt that such a docking maneuver might produce torques significant enough to break off portions of the power module. Docking scenarios have subsequently been substantially improved but such contamination will continue to be an area of concern.

6. CONCLUSIONS

The long lifetime and expense of large space systems necessitate the development of contamination and ESD prevention or protection. It is obvious that one can enhance the other and thus attention must be given to solving both problems such that their interaction does not cause a multiplicative synergistic effect which reduces the effectiveness of such solutions. Obviously many measures need to be investigated of which plume shields, improved docking and undocking scenarios, and better materials and design are an essential part. It may be noted that plume shields and skirts have been used in many applications with significant reduction in contamination. The ESD problem is further still from solution. Active control of charging may not solve more problems than it causes. Thus it appears to be a problem of finding materials to do the job. In any event, these difficulties must be solved to insure the success of future missions, and the data from the SCATHA experiments will provide much needed insight into possible solutions.

Abstract Errata: the authors apologize to the principle investigators on SCATHA experiment SCI for the inaccurate reference to their experiment in the abstract publication which was the apparent result of a typographical error. It should be noted that SCI does not concern contamination reattraction as was indicated.

1. Yablowsky, E.J., Hazleton, R.C., and Churchill, R.J., 1978, Puncture Discharges in Surface Dielectrics as Contamination Sources in Spacecraft Environments, Proceedings of the USAF/NASA International Spacecraft Contamination Conference, Colorado Springs, 7-9 March, 1978, AFML-TR-78-190, 945-969.
2. Stevens, N.J., Roche, J.C., Mandell, M.J., 1978, NASA Charging Analyzer Program - A Computer Tool That Can Evaluate Electrostatic Contamination, Proceedings of the USAF/NASA International Spacecraft Contamination Conference, Colorado Springs 7-9 March, 1978, AFML-TR-78-190, 274-289.
3. SAMSO-TR-73-263 (Aerospace Corp.) 1973, Ionization and Attraction of Neutral Molecules to a Charged Spacecraft, Cauffman, D.P.
4. Barsh, M.K., et al. 1978, Contamination Mechanisms of Solid Rocket Motor Plumes, Procedures of USAF/NASA/International Spacecraft Contamination Conference, Colorado Springs 7-9 March 1978, AFML-79-78-190, 347-384.
5. Inouye, G.T. 1976, Spacecraft Charging Anomalies on the DSCS II, Launch 2 Satellites, Proceedings of the Spacecraft Charging Technology Conference, Colorado Springs, 27-29 October 1976, AFGL-TR-77-0051, 829-852.

6. Spacecraft Charging - A summary of an Investigator in Response to the Action Items of the Joint USAF/NASA Spacecraft Charging Planning Meeting, System Engineering Branch, Lewis Research Center, 13 March 1975.
7. Robbins, A. and Short, C.D. 1976, Space Environmental effects on the Skynet 2B Spacecraft, Proceedings of the Spacecraft Charging Technology Conference, Colorado Springs, 27-29 October 1976, AFGL-TR-77-0051, 853-864.
8. Nanevich, J.E., Adamo, R.C., and Scharfman, W.E., Satellite Lifetime Monitoring, Final Report Contract No. F04701-71-C-0130.
9. Borson, E.N., and Landshaum, E.M., A Review of Available Contamination Results, TR-0200 (4250-20), SAMS0-TR-69-82, AD-850122L, 15 Dec., 1968, Aerospace Corp., El Segundo, CA.
10. Maag, C.R., Overview of Pulsed Plasma Thruster Contamination Studies, presentation at JANNAF Plume Contamination Specialists Section, Anaheim Convention center, Anaheim, CA. 8 March 1979.
11. Scarf, F.L., Jupiter Plasma, presentation at Electrostatic Discharge workshop, Jet Propulsion Laboratory, Pasadena, CA., 2-4 October, 1979.
12. SAMS0-TR-73-263 (Aerospace Corp.) 1978, Description of the Space Test Program P78-2 Spacecraft and Payloads, Stevens, J.R. and Vanpola, A.L.
13. Maag, C.R. et al., Spacecraft Thermal Control Surfaces, Final Report Contract No. NAS-8-32637, April 1979.

DISCUSSION

J. Moacanin (JPL) :

Your LDEF experiments will be carried out in a Low-Earth-Orbit (LEO) environment, yet you are interested in effects in a geosynchronous orbit. Would you comment on the approach you plan to take in extrapolating LDEF data to the geosynchronous (GEO) environment?

L. Preuss:

The SSM to be tested in the MBR-LDEF Experiment are already qualified by ground tests (combined environment of electrons, protons and UV, vacuum, temperature). The approach we are planning for the extrapolation from Low Earth Orbit (LDEF-orbit) to GEO environment is as follows:

- investigation of the effects of
 - a) contamination
 - b) electrical discharging effects
 - c) far UV
 - d) near UV
 each separately, and
- comparing the results of
 - e) LDEF-flight experiment
 - f) related GEO tests available (from other satellites)

With the ground experiment results and analysing very carefully all results.

S.J. Bosma :

The extrapolation of LEO results to GEO results is limited, because syn-energistic effects are not taken into account.

A similar problem exists for ground tests. Do you perform your near and far - UV tests on the same test sample? Otherwise syn-energism will not be taken into account.

L. Preuss:

I agree that extrapolation of LEO results to GEO results is limited, as you mentioned. But at the moment, the LDEF Experiment is the only chance for putting our samples into orbit. We will perform the near and far-UV tests not with the same test samples, but with samples of the same type. The aim of the ground experiments is to investigate separately the effects of far-UV and near-UV and to compare them with the flight results (far + near-UV combined) on LDEF to determine testing criteria for future ground qualification tests.

A. Paillous :

DERTS has performed a radiation test using a combined environment facility for the OTS programme. Some results will be given in a subsequent session, together with in-flight degradation data. As DERTS has also planned and designed an experiment to be flown on LDEF, it will be possible to compare in-flight geosynchronous orbit degradation data, in-flight LDEF low-orbit degradation data, and laboratory degradation data.

L. Preuss:

The SSM to be tested and qualified in the MBR-LDEF-Experiments are already ground qualified for a long-term (10 years) GEO-Orbit mission. Flight results on LDEF, results from accompanying ground experiments and available ground test data for a simulated GEO-orbit as well as available related flight data will be compared and evaluated.

Because the reference SSM-samples of our LDEF-experiment (eg OCLI-OSR's) are well known in terms of flight - and lab - test data, a reasonable comparison of our SSM's on LDEF with in flight GEO-orbit degradation data of other SSM's (eg OCLI-OSR's) is therefore also possible.

L. Preuss :

Charging on SCATHA was predicted by the NASCAP charging analyser programme. On the other side charging sensors were installed in SCATHA. How is the agreement between predicted and measured charging on SCATHA? When will data be available in the literature?

D. F. Hall:

I do not think that these comparisons have been made yet. N. John Stevens of NASA Lewis Research Centre can best advise you of the schedule for NASCAP model validation and of publication plans. I would expect NASA Technical Reports (TRs) to appear on the topic, at least.

R. Moss (Ford Aerospace) :

To what do you attribute the differences in contamination results between the belly band and upper QCMs, particularly the lack of temperature sensitivity of the belly band QCM vs the distinct temperature sensitivity of the shadowed QCM? Also, why is there the gross difference in mass accumulation rates? Is there any relationship between charging events and mass deposition?

D. F. Hall:

The difference between the temperature sensitivities of the mass accumulation rates observed on the two QCMs is under investigation. The UV that falls on the belly band detector may activate the surface and/or polymerise the adsorbate to raise its desorption energy. I would not characterise the difference between the accumulation rate on the belly band detector and the -95°C shadowed detector as gross.

Regarding charging events, at this time I only have 'quick look' data for a few short (<1 hr) charging events. Casual inspection of these data does not reveal large changes in mass accumulation rates during these periods. A careful analysis of all charging events will be reported at a later time.

W. Schaefer (MBB) :

If I have understood correctly, the contamination rate of the contamination sensor facing space and sun irradiation was independent of sensor temperature. The fact, well known from laboratory tests, that condensable material will be cracked by the simulated high energy sun radiation (UV) could provide an explanation for your measurements, because after cracking contamination products cannot be removed from the surface of the sensor even by heating. Do you think that this could be true or have you another explanation for these measurements?

D. F. Hall:

This is a good hypothesis, but it requires that energetic photons arrive simultaneously with or very soon after the arrival of a low desorption energy molecule. Another hypothesis is that sunlight affects the material layer already on the detector, so as to strongly bind, perhaps chemisorb, incoming molecules. Finally, the molecules incident on the two detectors might be quite different.

W. Schaefer (MBB) :

- 1) Is SCATHA a clean satellite in the senses that both satellite and surfaces were carefully cleaned just before launch, that by proper material selection for all satellite components material, minimum contamination could be expected from the satellite itself, and that care has been taken to avoid contamination from the launcher?
- 2) If so, what special measures were taken to avoid contamination before contamination measurements started (in the final orbit)?

D. F. Hall:

P78-2 is probably quite representative of typical USAF spacecraft these days. MIL STO 1540A and 'visibly clean' requirements were in the spacecraft contract. The craft was cleaned at the launch site. The acoustical blanket in the payload fairing was subject to the special cleaning procedures occasionally used for contamination-critical USAF vehicles.

All ML12 sensors were covered until a few hours before launch, when the covers on the TCC trays were removed through a special door in the payload fairing. The cover on the ML12-7 TQCM was opened during the first pass of the transfer orbit after the experiment data collection had been initiated. The cover on the ML12-6 TQCM was opened about four days after launch, after the vehicle was inserted into final orbit and its angular velocity had been reduced from 60 to 15 rpm (final velocity is 1 rpm).

J. Bosma (ESTEC) :

A seven-year geosynchronous simulation (p^+ e^- and UV) showed bleaching effects of several black paints:

3M black velvet (401C10):	$\Delta\alpha_s = -0.010$ to -0.015
chemglaze 2306:	$\Delta\alpha_s = -0.015$
cuventin 306:	$\Delta\alpha_s = -0.020$

This bleaching effect is less than the data reported from SCATHA, so that the effect could be due to both bleaching and flaking.

D. F. Hall:

I expect to reduce the uncertainty bars in this data and compute α_s at more frequent intervals. The present data are not conclusive, but since rapid degradation appears to commence about the time of the start of the eclipse season, flaking would seem to be at least part of the story. Did the UV tests you report include the far UV?

C.N. Fellas (BADG) :

Could you give more details about the major charging event observed on 'Scatha', e.g. was it a slow build-up to the 8000 V, or a rapid charging event? Was there any discharge and any consequences from it?

D. F. Hall:

This event was observed during a pass which included an eclipse of a 45 minute duration. At the beginning of the pass, the craft frame potential was ~ -75 V with respect to the ambient plasma potential. As the vehicle was eclipsed by the Earth, the frame potential went immediately to several kilovolts. Apparently this potential would have persisted throughout the eclipse had the SC4 active charge control experiment not been run during portions of it. (Details regarding SC4 operations may be obtained from Herb Cohen at USAF Geophysics Lab). At the conclusion of the eclipse, the frame potential came to ~ -50 V.

C. Mori :

Concerning a possible mechanism of contamination involving ionisation and subsequent electrostatic re-attraction: are there any laboratory data suggesting that such a mechanism may indeed take place?

D. F. Hall:

The theoretical calculations and flight experience which form the bases for the ML12 experiment are discussed in References 1, 3, 8 and 9 of the paper. The calculations are necessarily based on gross simplifying assumptions. The flight data is a correlation between the thermal performance degradation of a USAF vehicle and periods favourable to spacecraft charging.

The importance of the electrostatic re-attraction mechanism depends on the rate and species of mass released from a vehicle, the photoionisation cross section of these molecules, and the dimensions of the vehicle's plasma sheath. The latter are of the order of tens to hundreds of metres and can be extremely complex. Meaningful laboratory simulation of this process is therefore not practical.

R. Thomas :

Could you please state your opinion on the long-term accuracy of QCMs in space. To what extent are the data to be trusted? Do other participants agree?

D. F. Hall:

There are two sources of error that I am aware of for QCMs in space. One is the QCM pick-up mass from its immediate environment either on the sensing crystal or on the reference crystal. That could be misinterpreted as a stuff coming in from the outside. This is one kind of error one has to

be alert to. The other kind of error has to do with the stability of the electronic circuitry, i.e. whether or not frequency changes are due to changes in voltages etc. I also believe people have looked at the effects of radiation by energetic particles on crystals. It is very important in any flight test of a quartz crystal microbalance that it be preceded by extensive ground testing so that one becomes well acquainted with the characteristics of the instrument. If the instrument is to see the sunlight then it is important that you know what effect that will have. Temperature gradient is induced in the exposed crystal and that leads to a frequency change of tens of hertz. We have that sun effect in our sun-exposed instrument and it is behaving in orbit very closely to the way it behaved in the laboratory source simulation test that we did. The getting of foreign material on the crystals from something local of course is subject to the design and you verify that you are clean by doing the test in a clean vacuum chamber. We believe that our instrument is clean in that respect. The stability of electronics can be addressed by varying input voltages etc. and by doing a long-term test to see how well the frequency is held constant with time. Our instrument had variations to the order of 1 or 2 Hz per week.

R. Thomas :

I think it would be useful if other people could give their experiences, but what I was really thinking of is the literature statements on QCMs flown which apparently indicate a reduction of contamination from what theoretically is a clean crystal. Therefore the values are certainly suspect to my mind.

D. F. Hall:

Are you referring to QCMs that were flown on the DSP satellite?

R. Thomas :

Probably so. I cannot be sure which one it is.

D. F. Hall:

That is the only one I am aware of in which a reduction occurred. I understand that it was a package that we put on in a rather rushed fashion onto an existing USAF operational spacecraft and that in fact adequate ground testing was not conducted ahead of time. Among various hypotheses that have been advanced, there is mass accumulation on the reference crystal which has the same effect as mass loss on the sensing crystal. In other flights, mass accumulation has been recorded (the first flight was, I believe, OGO-6 in early 1960). There was a quartz crystal microbalance on ATS-6 NASA Goddard experiment that had a mass accumulation.

All those experiments gave, I think, reasonable results as contrasted to the DSP case.

R. Thomas :

I take it that you have high confidence in your results, but I would like to ask if other contributors have the same opinion?

M. McCargo :

Is it true that the QCM has difficulty in picking up globules instead of film deposits? Does the QCM have difficulty picking up safe when the condensate goes into a globule on the surface?

D. F. Hall:

The way that the QCM works is that the crystal vibrates mechanically and you need to have an inertial coupling of the material that is sensed to the crystal in order for that mass to make itself felt. Therefore if you have a liquid or a particle that is not well adhered to the surface, you may get either a diminished effect or no effect at all, so the crystal is certainly most straightforward for solid films of material. You can use them with liquids but only when you have done a lot of calibration work with the particular liquid that you are using. There are QCMs made with special adhesive surfaces for the purpose of measuring particulates. The QCMs in the ML-12 experiment are not of that type; the exposed surface is aluminium.

Mr. Beere :

On the 3M black paint, you stated that the α value decreased; in this case is it always possible that it is in fact the emittance which is increasing?

D. F. Hall:

As I stated in my talk, what is actually measured is a temperature and therefore the ratio. I guess that it is possible that the emittance is increasing, but I think there are people present who are much more qualified than I to address that. So may I refer to a materials expert on that.

Mr. Bosma :

It is a fact that we did a seven-year degradation test at DERTS Toulouse for geosynchronous orbit. For several black paints — amongst others the 3M black velvet 401 C10, Chemglaze Z306 and Cuvertin 306 — we found bleaching effects. The degradation was around -0.10 to -0.15. Your degradation, which is a bit high, could be due also to flaking or something else.

Mr. Paillous :

I must confirm that when we measured the reflectance of samples, it was in situ and the samples were not in the middle of the sphere, but tangent to the sphere. This means that if our samples have shown a variation of diffusion, we can have recorded something that is not a variation of absorptance but only the change in specularities of the sample.

Mr. Greenberg :

It is pretty well established that the synchronous environment is significantly damaging to epoxy, which is the binder material in the 3M velvet. It does promote break-up of the binders. It is certainly not unreasonable to imagine damage at the pigment binder interface which could result in a change in scattering properties. I do not think it is unreasonable to expect changes like .02 and .03 in α .

D. F. Hall:

Is it not also true that in this particular paint, it is important that the application be done just right? There are microspheres of glass in the paint and when the spray is not done properly then the spheres are not near enough to the surface and therefore the properties may be less than optimum.

Mr Greenberg :

That is a very good point, that the surface is epoxy rich. You tend to create damage in the epoxy as you come into the eclipse, you may see slight spalling and your data seem to indicate that you are beginning to observe damage in the eclipse region. That is a possible explanation.

Mr Beere :

As a user of thermal-control coating I am particularly interested to know whether an information flow has been set up with ESA, and if not, could this be done?

D. F. Hall:

I guess the answer to that is yes. As I mentioned it in the talk, we plan to report all the analysis data that we can in the open literature, primarily, I guess, at AIAA meetings and in the *Journal of Spacecraft and Rockets*, but I am certainly quite anxious to share information with Europeans, as long as I get clearance from the Air Force.

R. Moss (Ford Aerospace) :

Did you consider any change in orbit after ABM firing and jettison to take the spacecraft away from the contaminant cloud from the firing?

P. G. Edwards:

No orbit change specifically related to avoidance of ABM plume cloud was made after ABM-F. However, a (~200) longitude drift orbit to the final geo-station was made over a period of two weeks.

Note also: As ABM case is ejected (at 1 m/s) a few seconds after completion of burn, this low-velocity contaminant cloud does not have a chance to form in the spacecraft vicinity.

J.A. Hanekamp (Fokker) :

For Meteosat a 'superclean' fairing was obtained. Questions:

- a) did the fairing have acoustic blankets inside?
- b) what was the final surface cleanliness of the inner side of the fairing (wrt particulates)?

P. G. Edwards:

- a) yes
- b) to maintain class - 100,000 conditions within the fairing - a particle distribution was not specified - visual inspection requirement only.

P.G. Edwards (ESA Toulouse) :

1. Do you have the particle size distribution for the second stage retro-rocket particulate contamination flux at payload level?
2. Have calculations been performed for the VCM contamination of the payload by upper cone and cylinder of fairing, especially with acoustic blankets fitted?

M. Desloire:

1. No
2. The acoustic blanket is not fitted on the upper cone.
We have not performed special calculations for the acoustic blanket fitted on the cylinder, but because t (time) and T (Temperature) are the same than for the rear cone the VCM result will be nearly the same (for our assumptions).

Note that the acoustic insulation is optional.

R. Moss (Ford Aerospace) :

How much contamination will there be from the payload bay in relation to the other payload? Does the fact that the bay is painted with a paint having 5.5% TML vs. your assumption of 1% TML - 1% VCM affect your analysis? How do you justify the assumption that cross contamination from other payloads is minor?

J. J. Scialdone:

The contribution of the payload bay is included in the base line data for the STS. The paint with a TML, as you indicate, may increase these baseline values and the corresponding environment for the payloads. As you see from the plots, the payloads induce a density that is order of magnitude higher than that now given for the STS. Regarding cross contamination, the contamination of a payload will be dictated by the conditions produced by the highest source.

A. Zwaal (ESTEC) :

When opening the payload bay doors, the spacecraft will be contaminated with a VCM of 10^{-4} g/cm². How do you know that evaporation takes place? For example what is the activation energy or vapour pressure of the contaminants?

J. J. Scialdone:

I have assumed that the contaminant may be water or a material having characteristics similar to the DC-705 silicone oil. The silicone oil has been taken as a representative of materials with a very low vapour pressure, ie the VCM portion of the material.

Mr. Tatry (CNES) :

How many (approximately) contaminant sources (paints, pottings, engines, vents...) have been taken into account and what percentage (approximately) of these sources have been investigated experimentally?

J. J. Scialdone:

The sources taken into account for the STS are listed in the Martin-Marietta document cited among my references. Kinetic data were available for many of them; others were estimated. For the payloads, the outgassing was experimentally obtained for the entire spacecraft. Therefore it includes all the sources.

H.E. Hintermann :

How has the sticking coefficient been determined? By radio-active tracer techniques? To what extent are these coefficients known for different substrate/gaseous species combinations?

B. Tatry:

I think for sticking coefficients we just took an example, but we have not done experimental work in this field. I think ESA can answer this question because they have done a lot of such work.

H.E. Hintermann :

I would like to know how it is done, and what has been done?

Mr. Zwaal:

I know what sticking coefficient means, but it is extremely difficult to measure; we have never tried because it is so complicated. What we measure is the amount of condensible products and from this one can never obtain the right sticking coefficient, because, what you measure is the difference between what has been absorbed and what has been left by evaporation. The exact sticking coefficient is difficult to determine.

Mr. Scialdone :

The effective sticking coefficient is established with a quartz crystal microbalance, the condensor of which is either at very low or another chosen desired temperature. You must first know the magnitude of the source of interest. In other words, the sticking coefficient becomes the ratio between what is condensed and the total incoming flux. The latter is measured via the QCM or an instrument at very low temperature, a temperature at which you condense everything. One must, of course, attempt to correct for viewing factors, distance, etc.

Mr. Nutt :

Are we saying that the sticking coefficient is never in fact really measured, ie. that it is only a theoretical coefficient?

Mr. Hall :

I think sticking coefficients can be measured especially if you use a shuttered source of material so that you can differentiate between what evaporates and what bounces. The origin of this distinction is that some molecules hit the surface and have a virtual zero residence time and almost bounce within 10^{-13} s, whereas others may reside for a period of time, a residence time, and then re-evaporate. When you use a shuttered system, so that you can chop the flux, you can by looking at the transient of what comes off from the surface or what is accumulated on the surface, calculate the sticking coefficient, but that is a very difficult experiment and probably more sophisticated than is really needed for the engineering calculations which are usually required.

Mr. Giori :

Did you measure the kinetics of outgassing as a function of sample thickness?

J. Guillin:

We used samples 2-4mm thick and these were the first results; I think that in future it will be necessary to study the influence of thickness, area and history of samples.

Mr. Giori :

It seems to me that outgassing is a diffusion-controlled process, and so when we are concerned with kinetics we must certainly take the total sample area per unit weight into account in any kinetic scheme.

Dr. J. Dauphin :

In fact we have looked a little bit at these phenomena and, when the outgassing is coming from the inside, it is effectively in a diffusion-controlled process. In principle you can apply the chemical law, ie. the rate depends on the inverse square of the thickness when you are working with a large area/thickness ratio.

Dr. J. Dauphin :

In addition to some results, you have shown two possible theoretical laws which apply. One is an exponential law which is frequently used; the other is a power law. I think that there are probably among the participants some people using something else (eg. Arie Zwaal). So it seems that there are a lot of different laws being used to interpret these data. For cost reasons, we can obtain the experimental data only for periods of say 100 or 200 hours. For those people using the Shuttle there is no problem, because they can calculate directly what they will get during a 7-day mission, but as soon as you speak of a real satellite, ie. one that is flying for several years, the extrapolation becomes totally different if you take one law or another. What I would like to ask Mr. Guillin is what law should be used, and I should like to address the same question to the floor.

J. Guillin:

Je suis tout à fait d'accord avec vos remarques. J'ai fait exactement les mêmes constatations que vous, à savoir qu'il n'y a rien de publié concernant le dégazage au-delà d'une à deux centaines d'heures. L'on avance seulement des hypothèses et personne ne les a vérifiées. C'est un pari à faire je pense. Je n'ai fait aucune considération théorique sur les équations de flux parce que je pense que les bases théoriques ne sont pas actuellement établies et j'ai préféré m'en tenir à deux types de lois de flux de dégazage que l'on voit couramment sur des essais expérimentaux, notamment la loi en t^2 .

Translation Dr. Dauphin :

As far as we know, there exists no law that has a physical basis, so we recognise that there is a need to find such a law. Mr. Guillin said he has used what he has found in the literature, which is the t^2 or the exponential law. Neither of these laws has a physical basis, and we are still waiting for something that permits a safe extrapolation.

Mr. Zwaal :

I have seen your method. This works only for a total mass loss in order of a few %, but how do you intend to measure low condensible amounts, say in the order of 0.01% or 10^{-3} %, because then you need completely different equipment. You cannot then make measurements of the condensible amounts with your equipment. I think we are nowadays more interested in condensible amounts than in total outgassing because total outgassing is a matter of the first hours, (we found mainly water desorption, which disappears after a few hours). You make measurements only for a few hours, but we are interested in long-term exposure and mainly in VCM's.

J. Guillin:

I have not measured VCM's, except when using micro-VCM equipment. We used very simple equipment, and we do not use the QCM for this test. I think that it is interesting to know the total weight loss and total outgassing if you want to know about the molecular cloud around the satellite.

Mr. Zwaal :

With present micro-VCM equipment, you obtain only one point on the condensible curve plus the origin. Since you have no intermediate point, you cannot extrapolate the curve. If you would mount 24 QCM's in the system, you would get the full curve ... And it would be good for the QCM manufacturers!

David F. Hall (Aerospace Corp) :

The 4th paragraph of Jeffery & Maag's abstract in the Symposium Programme makes reference to P78-2 (SCATHA) spacecraft results concerning contamination from thrusters. Data from the ML 12 Contamination Experiment on P78-2 relevant to thruster contamination have yet to be analysed and will be the subject of future papers by me. So far as I know, the SCl Experiment does not have the capability to detect contamination; a discussion of this point with Dr. Harry Koons, the SCl Principal Investigator, is suggested.

SESSION V

MATERIALS IN VARIOUS PROJECT TYPES

Co-chairmen: J.J. Scialdone & J. Dauphin

N80-21435

MATERIALS REQUIREMENTS FOR SPACELAB AND SPACELAB PAYLOADS

J E Bennett & M D Judd

ESA/ESTEC, Noordwijk, The Netherlands

The paper (to be presented in two parts) will discuss the various requirements applicable to the Spacelab project and will concentrate particularly on those requirements which are new to Europe. These new requirements arise because Spacelab is a manned reusable vehicle programme and will be used in conjunction with the NASA Orbiter. Similar requirements are applicable to the Spacelab Experiments and to other Orbiter cargoes. The measurement of these various material parameters will be briefly discussed and illustrated.

It is intended, in the first part of this presentation, to show and discuss how these various requirements are applied and implemented in practice using examples from the Spacelab development programme.

The second part of the presentation will focus on the first Spacelab Experimental Payload and illustrate how the approach described above has to be adapted to incorporate the needs and constraints of the Experimenter.

Part I by J.E. Bennett

For the benefit of those of you who are not familiar with Spacelab I would like to start with a brief description of the system. I hope from this you will begin to see the complexity of the hardware and therefore appreciate the task of ensuring that all the materials meet the requirements to be shown later.

The SL systems can firstly be broken down into the module and pallet. The pallet is a passive structure for supporting astronomy and solar physics experiments. The module is the container for a habitable environment where people can work in a "shirt sleeve" environment, in fact a laboratory with all the facilities that you would find on earth except gravity. The pallet is a "simple" framework construction, while the module is in fact two cylinders bolted together with end-cones fitted. One cylinder of the module is called the core segment and contains the additional sub-systems necessary for maintaining the environments, controlling experiments and collecting and transmitting data. These sub-systems being electrical power distribution (EPDS), command and data management (CMDs), and environmental control (ECs). The second cylinder is the experiment segment

which contains the necessary racks for locating experiments, for example the materials science double rack.

This so called modular construction allows the hardware to be flown in various configurations depending on the mission requirements. For example you could fly a module only, a long module plus pallet, a short module plus two pallets, or up to five pallets. You can obviously change these configurations depending on the precise mission requirements.

Additional hardware included in the programme is a high quality window for optical experiments and observations from within the module and an air-lock which provides access to space environment for experiments carried out within the module. For the pallet only mode the SL electronics and data handling equipments are mounted in a pressurised container (Igloo) mounted on the forward bulkhead of a pallet. The instrument pointing system (IPS) is a pallet mounted device which provides precision pointing for payloads that require greater pointing accuracy and stability than can be provided by the Orbiter alone.

When it was decided to design and build SL in Europe it brought with it requirements which, from a materials point of view, were new to European contractors. This is because SL is the first manned spacecraft to be built in Europe. The USA had accumulated experience on the Mercury Gemini, Apollo and Skylab projects. SL is also the first reusable spacecraft to be built in Europe and only the second in the world. We have defined a 10 year or 50 mission life requirement, admittedly with the possibility of maintenance. However, because of cost and turn-round time this has to be minimised.

SL was the first Shuttle payload to be built in Europe. So you can understand that this project introduced a new set of requirements to Europe which had to be understood by the Agency and Contractors and are now being learnt by experimenters.

I hope this introduction has given you some insight into the complexities of SL and why it brought with it new requirements. Before going into those requirements in detail I would just like to emphasise the size of the project. Somebody has calculated that in weight SL is

equivalent to the previous 13 satellite programs controlled by ESA.

I would now like to briefly describe just what these requirements are.

- 1) Flammability - This requirement arises basically from the tragic Apollo 1 fire. For SL the requirement is that material shall be non-flammable or self-extinguishing in either 21% oxygen (i.e. normal air) which is applicable to materials outside the module or 23.8% oxygen for materials used inside the module. The normal air requirement is to ensure that there is no danger of flame propagation during ground operations either on test or in the Shuttle payload bay. The enriched oxygen requirement is to ensure that there is no danger of flame propagation under orbit conditions. However if a flammable material has to be used for a particular application then we can only agree its use if it is remote from an ignition source or if it is isolated so that propagation will not occur.
- 2) Offgassing and Odour - I think this should be called toxicity for preference to avoid confusion which has and does occur with outgassing which is a different requirement. This requirement has been covered by Dr. Eckert in the first paper of session 1. It is sufficient here to state that we have managed to meet the requirement, of total organics < 100 μ grams/grm, carbon monoxide < 25 μ g/g and odour < 25, either by changing materials or where this was not feasible by baking the material either in air or under vacuum to remove toxic molecules. This bake then has to be carried out by the contractor on the actual SL hardware.
- 3) Outgassing - The SL requirement of TML 1.0% and VOM 0.1% is the same as previous ESA and NASA satellite programmes. This was therefore one of the easiest requirements to get the contractors to work to except that many still do not realise the correlation between mix ratio's, cure schedules and the outgassing characteristics. Because this requirement had been imposed previously on satellite programmes there is plenty of information available both from NASA literature and ESTEC test results. But it is worth noting that despite all the previous testing on materials ESTEC Materials Section have carried out something like 100 tests for SL.
- 4) Oxygen Compatibility - For SL this is of concern only for the oxygen control system which is manufactured in the US by Carleton Control and is basically similar to the Orbiter system. Here there is extensive test information available in JSC 02681 on oxygen compatibility.
- 5) Radiation Resistance - This is not too much of a problem for SL since it will fly only at an altitude of 300 km. and remain in space for only seven days at a time. It will become more important for follow on development projects which will fly at higher altitudes and for longer periods.
- 6) UV Stability - This is important for the external surfaces of the pallet and the outerlayer of the thermal blanket used on the module since these form the passive thermal control system. Too much degradation of their thermo-optical properties could lead to temperature control problems inside the module, thermal control problems for the experiments and indeed structure stress problems due to too high a thermal gradient.
- 7) Stress Corrosion Resistance (Rather important for a reusable spacecraft with 10 years life) - Again this requirement has grown out of the NASA experience on the Apollo and Saturn project where considerable time and money had to be expended in redesigns to overcome stress corrosion cracking problems. The reference document used for SL was the NASA MSFC 10M33107 Design Criteria for Controlling Stress Corrosion Cracking which has now been superseded by MSFC-SPEC-522A. There is also an ESA document (ORM-36) under preparation. All these documents group materials into high, moderate and low resistance to SCC. This rating is based on laboratory tests and in service usage. The problems have been to define European equivalents to the US listed alloys, and to find information about European alloys which would allow us to rate them in a similar way to the NASA document. Finally it has been difficult to get contractors to justify the use of materials which are not highly resistant. The design case is mostly high transient loads whereas to evaluate an SCC problem what is needed is an assessment of the lg load including, residual stresses from machining and heat treatment, assembly stresses as well as an assessment of the environment that the part will see during its 10 year life. I hope the above will become clearer in the example I will show you later however suffice to say that some of the common high strength aluminium alloys have a SCC threshold of less than 10% of yield in the short transverse direction and this can certainly be exceeded by assembly stresses alone. I also do not want you to think that the Americans have the latest information. For example we were rather concerned about the use of 5083 for part of the IPS. The contractor did some very good testing which convinced us that the material was acceptable. This was subsequently verified by NASA through the Alcoa Research Labs.
- 8) Galvanic Corrosion Resistance - Clearly most important for a spacecraft which is both reusable and has a 10 year life. It is important in both structural areas, e.g. the bolts holding the two cylinders together, and in electrical bonding applications.
- 9) General Corrosion Resistance - Again important for a spacecraft which is both reusable and has a 10 year life. Most of the high strength aluminium alloys are alloyed with copper or zinc and therefore have somewhat poor inherent corrosion resistance and require additional protecting in the form of anodising and/or painting.
- 10) Radioactive Materials are to be avoided for safety reasons. However low energy sources may be approved, for example as sensors provided they are properly packaged.
- 11) Elastomeric Materials and Potting Compounds - I have already mentioned the 10 year or 50

mission life requirement and this is particularly important with respect to elastomeric materials and potting compounds. Materials which do not retain their shape, adhesive properties or electrical properties must be avoided since they will cause safety problems due to structural or electrical failure or, as a minimum, high maintenance costs. Here you also have to remember the temperature extreme that some of the materials are expected to survive e.g. - 150°C to + 120°C for pallet materials. The non-metallic materials must also be moisture and fungus resistant since we do not want fungus growth inside SL. This would give rise to obnoxious smells and dangerous particles floating about in zero g.

- 12) Lubricants - This is obviously an important aspect for small mechanism and moving parts. It must be remembered that not only do these materials have to lubricate but they also have to meet the equally important outgassing and/or toxicity criteria depending on exactly where they are used. They also have to perform under the temperature extremes required e.g. - 150°C to + 120°C for pallet mounted equipment such as IPS.
- 13) Hydrogen Embrittlement - Attention must be paid to those metals which might be susceptible to this form of embrittlement or to processes which can give rise to hydrogen. We have already lost an ESA satellite due to this phenomenon occurring in a bolt on the launcher, so this is clearly a very dangerous form of failure which must be controlled during the design and manufacturing phases.
- 14) Shatterable and Flaking Materials - The use of glass, for example, is rather hazardous since a failure will lead to sharp particles floating in the atmosphere. We therefore have to be sure that such materials are enclosed such that, if there is a failure, then the particles are retained. Paints can also form a hazardous source of particles due to abrasion. We have therefore tried to both minimise the usage and to ensure that adhesion is high.
- 15) Fluid Compatibility - Materials which come into contact with for example the water and freon 21 used in the SL system cooling loops must be compatible with these fluids. If they are not compatible then the corrosion product will block the filters and damage pumps thus degrading the cooling performance and perhaps leading to a safety problem.
- 16) Restricted and Forbidden Materials : -

A) Beryllium and beryllium alloys)	
B) Titanium in contact with IO_2)	
C) Molybdenum for relays)	
D) Palladium in resistors)	Restricted
E) Ethylene glycol)	
A) Zinc and Cadmium)	
B) Cadmium plating)	
C) Mercury)	Forbidden
D) PVC)	
E) Certain alloys because of SCC)	
F) Carcinogens)	

Now a few examples of materials applications on SL to illustrate how some of these requirements are handled in practice.

Flammability. A number of contractors wanted to use conformal coatings for PCB's. It is unfortunate that most coating materials, except Silicones, are flammable. For the electronic boxes associated with the ECLS system the contractor wanted to use Scotchcast since they had experience of this system with their components and design rules. This material is flammable in 23.8% oxygen even when applied to a non-flammable PCB substrate. In order to meet the requirement the contractor overcoated the boards with a Silicone resin system which suppressed the flames. They preferred this approach rather than changing entirely to a silicone coating because as I said above they knew from previous projects that the Scotchcast was compatible with their design. To change completely would have meant re-evaluating the new coating system in terms of strength, electrical performance and compatibility with components. It must be emphasised however that the thickness of the Scotchcast is critical to the success of this approach. A thick coating would require retesting. An alternative approach was taken with the Remote Acquisition Unit (RAU) the contractor wanted to use Solithane 113 which again failed the requirement with respect to flammability.

Now the RAU is constructed from a series of frames mounted side by side with bolts through to form a closed box. Each frame contains two PCB's. Examination of the box showed that it was closed, though not sealed, and that it was of a rigid construction such that it would retain any burning particles. In order to prove this a simulated box was built with dummy PCB's and an ignitor system inside the box. Test results showed that because the box was closed ignition was virtually prevented because of the limited amount of oxygen available. Hence the material was acceptable without any design change.

A third example is a foam material used as insulation in the ECLS system. In order to pass the flammability test the material had to be fully encapsulated in self-adhesive aluminium foil. This encapsulation being enough to prevent ignition and anyway keep oxygen away from the material so that it would not burn.

Toxicity. The adhesive used to bond the insulating foam in place in the ECLS system has proved somewhat of a problem. In the basic toxicity test the material gave very high total organics and despite modifying the adhesive by making it in a reduced viscosity form, i.e. without filler the results would not come down to an acceptable level. Neither did the aluminium foil encapsulation or baking make any difference, we continued to find high total organics. The contractor has had to find an alternative bonding method.

Odour. The thermal blanket which is used as passive thermal control on the outside of the Module is also required to be used inside the Airlock. This means that it will be exposed to the Module environment and therefore not only does it have to meet the outgassing requirement

but also the offgassing (toxicity) requirement. We found that while the toxicity was acceptable, it in fact failed the odour. So rather than change the design for this one application we decided to bake the material until an acceptable figure was reached. Fortunately this proved possible.

Outgassing. The transformer used in the electronic box of the gyro unit for IPS were purchased from a standard product-line and had been used extensively in similar aircraft systems. Again to insist on a change of the potting material for the transformers would have implied changing an already established and reliable design. To overcome the problem a simple vacuum bake was introduced and proved to be satisfactory.

UV Stability. The paint used as the passive thermal control on the pallet has proved somewhat of a problem in this respect. Not that it decomposes or becomes brittle but its thermo-optical properties do degrade. The ESTEC Materials Lab have done extensive measurements on the rate of degradation and the effect of temperature on this degradation. We are therefore able to define the anticipated life of the paint system and the properties of the refurbished paint film. The exact number of missions to be flown between refurbishments will depend on the exact missions profiles.

Stress Corrosion Resistance. The frame for the gyro unit of IPS was found to be manufactured from the British alloy BSL 65 which is equivalent to 2014 T651. This alloy has low resistance to SCC the threshold being in the region of 8% of yield in the short transverse direction.

When this problem was found the contractor had already machined the FU frames. The contractor's previous experience on aircraft had been that this material was required because of its stability and their ability to machine it to close tolerances. A stress calculation showed that the SCC threshold was approached in the blind taped holes. The following actions were therefore agreed to solve the problem. The entire frame was shot peened thus inducing a compressive force into the surface, the compressive stress could be measured to be sure that it 'neutralized' the tensile stresses due to the design application. The frame was then treated with alodine, a chromate primer and a polyurethane top coat to ensure maximum protection against general corrosion. The blind taped holes were sealed with a polysulphide sealant. Finally the contractor demonstrated, by test, that should a failure occur in the frame then there were no subsequent hazards since the gyro unit would be retained in the cover of the unit.

On the other hand there are several applications where, because of the criticality, the material has had to be changed. For example the pins which hold the back-up structure for the Orbiter attachment fitting to the module. Secondly the closure hooks on the outer hatch of the airlock had to be changed.

Lubricants. An interesting lubrication problem is the cables used in the airlock to raise and lower the experiment table. Since these cables

are exposed to both the module and space environment the lubricant has to meet the outgassing and toxicity requirements. After some searching we have found a fluorosilicone lubricant which meets the requirements and appears to perform satisfactorily over the required temperature range. It appears also that the contractor has developed a suitable cleaning procedure to remove the original lubricant used during the winding of the cable and a technique to reimpregnate with the approved lubricant.

Hydrogen Embrittlement. The attachment pins or trunnions of the Pallet structure are manufactured from titanium and are chromium plated to provide a wear resistant surface of known friction coefficient as the interface with the Orbiter. Hydrogen is evolved during this plating process and could thus be absorbed into and embrittle the titanium with disastrous results.

Fortunately the contractor has been able to demonstrate that the chemical controls and post plating baking are sufficient to virtually eliminate this problem. This demonstration took the form of hydrogen analysis which showed approximately 50 ppm (material limit 125 ppm) and simple bend tests.

Shatterable and Flaking Materials. The Data Display Unit (DDU) which is part of the CDMS system has a cathode ray display tube. So to overcome the potential implosion problem the contractor has effectively constructed a foam filled container for the tube. The actual screen is encapsulated by bonding a layer of polycarbonate directly to the glass. The thermal insulation material used on the freon lines of the active thermal control is a silicate wool material which sheds particles and fibres. In order to prevent this the exposed surfaces are coated with a silicone rubber which meets the outgassing and flammability requirements.

Having reviewed these examples of how some of the SL materials have been controlled to meet the intent of the programme I would just like to touch on one other aspect.

The offgassing and odour test mentioned above is a screening test and in order to complete the assessment of the SL atmosphere with respect to toxicity we have a total offgassing test. In effect the SL module is treated as a black box with all systems powered and the air temperature at maximum, i.e. 28°C. Samples are then extracted, from the sealed module at regular intervals over a 3 day period. These samples are analysed to determine qualitatively what is present. These quantities are then compared with established MAC (Maximum Acceptable Concentration).

I hope this paper has given you some insight into the materials requirements for SL and hence for SL payloads and other Shuttle launch projects. I hope it has also indicated the clear need for more co-ordination at the beginning of a project, even during the proposal stage, between the structural engineer, the safety engineer and the materials specialists.

Part II by M.D. Judd

The First Space Payload (FSLP) is a multidisciplinary payload consisting of a wide diversity of experiments. At the present time construction is well advanced and in many cases virtually completed. In this second part of this presentation the materials control as applied to FSLP will be described and in particular attention will be focussed on any differences as compared to that applied to Spacelab Project. It must be stressed at this point that we are only considering FSLP here and the European part of the Payload at that. Subsequent programmes will adopt their own methods of materials control although the general requirements, with respect to stress corrosion, flammability, etc. will still have to be met.

Materials control for FSLP comes under the general area of Safety with overall responsibility for the European Payload resting with ESA/SPICE. The Payload is essentially divided into three parts with Safety Engineers at DFVLR, CNES and ESTEC, each covering a number of Experiments. ESTEC Materials Section, however, acts as a central point for materials questions and provides advice and assistance on request for all the Experimenters. This advice includes review of materials lists, provision of test facilities and assistance with the general day to day problems.

In order to discuss the materials control programme it is first necessary to look in some detail as to what actually makes up the Payload. At an early stage in the discussions on how best to utilise Spacelab it became clear that certain areas of scientific research created the most interest for the Scientific Community; areas such as Materials Science, Fluid Physics, etc.. Since in many cases experiments in such fields of study would require similar facilities, such as furnaces, vacuum supplies, etc., it soon became apparent that a certain number of facilities would be required to be used on more than one Spacelab mission. These facilities, principally the Materials Science Double Rack (MSDR), the Microwave Remote Sensing Experiment (MRSE), the Metric Camera and the Space Sled, were therefore incorporated in FSLP although once constructed they will be utilised in subsequent Payloads. For these Facilities therefore one is considering a reusable system. At the other end of the spectrum there are the Experiments that will use these facilities or are self standing in their own right. These Experiments will be flown on the FSLP only with no plans at present for subsequent flights. For these Experiments therefore one is considering equipment with a short lifetime. As can be imagined the existence of such a range of equipment in one Payload creates certain problems in the definition of a materials control programme which is suitable for the whole Payload.

So, therefore, what form of materials control has been implemented? Essentially SPICE have required that each Experimenter provides a standard materials list as per ESA specification QRM-16. This has then been reviewed by ESTEC Materials Section against available data (with respect to stress corrosion, flammability, etc.) and recommendations for acceptance/change, etc. done as per established procedures. In general this has worked well and especially so where the companies involved are well versed in Aerospace work. With the smaller experiments or with laboratories with

little or no aerospace experience this at first sight appeared to be yet another piece of paper to add to their ever increasing collection. However the advantages to all concerned soon became apparent and this has meant that for FSLP we have a detailed listing of all the materials which have been used.

In the cases where materials are unknown with respect to their properties of flammability, etc. alternatives have been suggested wherever possible. Unfortunately it is often the case that an Experimenter requires a particular material because it has specific property which is vital to the operation of this Experiment, and thus it is impossible for him to change. In these cases the materials have been tested, either singly or more often in configuration, in order to evaluate any hazards involved. This testing has been done at ESTEC on request. If the results of such tests indicate a potential hazard exists this is identified to NASA by SPICE using established procedures. Luckily very few cases such as this have arisen.

The biggest problems have been encountered in the area of commercial equipment. For reasons of cost and schedule many Experimenters wish to use commercial "off the shelf" equipment such as motors, cameras, tape recorders, etc.. In such cases it is, in general, impossible to obtain detailed listings of materials for evaluation and it is thus necessary to evaluate the unit as an entity for both flammability and offgassing.

In practice flammability is evaluated by a visual inspection of the unit concerned, normally in the presence of the Experimenter or the Safety Engineer. As a result of this inspection modifications to the unit may be required involving the inclusion of fire barriers, replacement of plastic outer cases by metallic ones, etc.. The ultimate in flammability tests, namely the destruction or attempted destruction of a complete unit has not yet had to be performed although the Test Engineer responsible for such tests lives in hope!

Such a visual inspection is unfortunately not possible for the evaluation of the extent of offgassing of a unit and this must be determined by testing. An earlier paper has described in detail the methods used for the measurement of the offgassing of materials and in a sense the testing required for these commercial units is an extension of the materials tests. There are, however, certain fundamental differences and the principal one concerns the need to test the unit in operation.

For these "off the shelf" items this is not too much of a problem since they are of small size and can be accommodated in a conventional vacuum oven (size ca 150 litres). In addition they do not require any forced cooling or auxiliary ground support equipment and thus only a small amount of auxiliary instrumentation. Atmosphere analyses are performed using adsorption traps and standard analytical procedures giving an absolute detection limit for organic contaminants of better than $1 \mu\text{g.m}^{-3}$. A standard procedure has been written for the performance of these tests and is similar to the one just incorporated by NASA in the B revision of Specification NHB 8060.1. At the time of writing the only data on

commercial units to be flown as part of the FSLP has been obtained at ESTEC. It should be added here that if a contaminant is identified which is considered as being of questionable toxicity the possibility exists of further investigation through an external contract arranged between SPICE and a well known toxicity testing centre in the U.K..

NASA/MSPC are in the process of, or have now written, a computer program for the prediction of the trace contaminant levels at certain times during Spacelab Missions. The input data required for this program is essentially three fold.

- 1) Contaminants generated by man - data available from NASA based on previous manned space programmes.
- 2) Contaminants generated by Spacelab and the Spacelab subsystems - data will be obtained by the total offgassing test on Spacelab Flight Unit (test procedure to be used has been qualified as a result of the successful test performed on EMI, May 1979).
- 3) Contaminants generated by the Payload - to be obtained by total offgassing tests of the Payload.

In cases where the Experiments are small then it is possible to use precisely the same procedure as described for commercial equipment. However, considerable problems are evident when one considers the facilities such as SLED, MSDR or Metric Camera which are of somewhat large size.

This question of size meant that the small chamber in the Materials Section could not be used. Fortunately there are several other test chambers of suitable dimensions inside ESTEC's Test Division as well as others outside ESTEC which could probably be used subject to cleanliness verifications (VIC-A of Test Division has, for instance, been shown to be clean enough for such tests). The biggest problem, however, concerned the need to test the Experiment in the powered up mode. When one considers, in the case of the MSDR, what this would entail (avionics cooling, fluid cooling, etc.) then it is immediately apparent that this is not feasible without the construction of a dedicated test chamber.

A compromise has therefore been reached whereby the Experiments will not be powered but that the chamber temperature will be ca 50°C in order to simulate the existence of hot spots throughout the equipment. It is felt that this test will give as meaningful assessment of the trace contaminant generation rates as is possible considering the inherent variability in such offgassing tests.

In conclusion it should be added that the materials control programme as described has been criticised by certain people with respect to costs and complexity. Perhaps we have required too much. It is certainly clear that the whole question must be reviewed before subsequent payloads are defined and in this context the lessons learnt on FSLP will be of significant help.

N80-21436

MATERIALS POLICY FOR ADVANCED SCIENTIFIC SPACECRAFT

R Thomas

ESA/ESTEC, Noordwijk, The Netherlands

This paper concentrates on material applications for the ESA contribution to the ST with other remarks made for ISPM and GEOS. These projects cover a wide range of missions and payloads. No account is taken of manned spacecraft, but some of the requirements of Shuttle as a launcher are mentioned.

Materials selection for the FOC, which is ESA's contribution to the ST, has to take into account a very low emission of condensable contaminants, low production of particles, high mechanical stability, wide temperature ranges, flammability, and stress corrosion cracking susceptibility control. To minimise the emission of VOM the standard WL and VOM test has been replaced by continuous measurement of VOM deposition on a QCM. The data are extrapolated to obtain an estimate of the orbital VOM deposit.

Materials chosen for ISPM will experience both severe thermal extremes and high levels of radiation. The spacecraft also carries a sensitive magnetometer which will govern the selection of materials near the sensor.

1. FOC MATERIALS SELECTION

1.1 Introduction

I propose to commence by describing the European part of NASA's Space Telescope. As you may know this is a 2.4m diameter Ritchey-Chretien telescope intended to be launched by the Shuttle at the end of 1983 into a 600 km circular orbit. It will support five scientific instruments of which the Faint Object Camera (FOC) is one (see fig. 1). As its title implies, the FOC is designed to capture faint images and, indeed, it is hoped to detect stars of magnitude 30 (compare this with TDIA's 1972 ability to see stars of magnitude 13). At this level of sensitivity, the physical, particular identity of light and photons is much more obvious and in fact the FOC operates by counting discrete photons. Light from the hypothetical magnitude 30 star should be detected at an average rate of .01 photons/second. Photo 1, showing one of Jupiter's moons, gives some idea of the imaging sensitivity of the FOC in earth orbit.

You will appreciate that at such low signal levels, losses due to contamination of the optical system must be reduced to the minimum for the duration of the expected 5 years of orbital operation before scheduled maintenance. The majority of this paper

will deal with the selection and treatment of materials to minimise deposition of condensates in the optical surfaces.

1.2 FOC Optics

A simplified layout of the FOC is shown in Fig. 2 which illustrates the position of one of the two detectors with its light path. The main mirrors are indicated, as is the filter wheel assembly which can introduce narrow band filters or attenuators into the light path as required. Thus there is a total of twelve reflecting or transmitting surfaces involved and contamination of only 5 nm thickness on each of these surfaces could reduce the detected light to only 1.3% of that incident on the first mirror (Ref. 1).

1.3 QRM-02 Tests

How can satisfactory performance be achieved and maintained for a period of 3 years on the ground and 5 years in orbit? The first step is the classical one of choosing the cleanest materials available subject to the constraints of the other design requirements. Experience with the QRM-02 test method which yields data for the total mass loss (TML) and collected volatile condensable materials (CVCM) emitted at 125°C and collected at +25°C in a test of 24 hours duration gives a very good indication of the more useful materials, but is subject to the criticisms that the test is not really representative of the actual operating conditions, and that it cannot be used to forecast long term contamination levels. Originally the FOC detector faceplate was held at -5°C during operation while the remainder of the Optical Bench Enclosure (OBE) was held at +20°C. Thus the QRM-02 emitter was 105°C hotter and the collector 30°C hotter than the real case with the danger that some molecular species would not be collected in the QRM-02 test while others would not be emitted in the real case.

1.4 Double QRM-02 Tests

The use of a double QRM-02 test that is a repeated test on one sample of material was considered. While this could give an indication of the rate of emission, the same criticisms regarding the reality of the test temperatures still apply, and the CVCM collected in the second test might be too small to measure reliably although remaining a contamination hazard to the FOC where large quantities of the source material could exist.

1.5 VBQC Tests

The method chosen was basically that described in Ref. 2, with all surfaces normally held at $+50^{\circ}\text{C}$ except for the QCM's which are held at -25°C . These temperatures still exaggerate the emitter and collector temperatures which now are identical at $+17^{\circ}\text{C}$ in the FOC, but this exaggeration is necessary if any significant measurements are to be obtained in the period of up to five days available for test (N.B. the same test time as for a double QRM-02 test). The risk that some molecular species are detected in the test but are unlikely to affect the FOC is regarded as both small and reasonable. The samples used can be large and in some cases can be realistic in dimensions and shape. This particularly applies when several materials are involved, e.g. a carbon fibre reinforced plastic tube containing potting material around the camera tube with its drive coils impregnated with another potting material will later be tested as a whole to verify the material decisions made. The data obtained are continuous and enable prediction of the likely contaminant production in the FOC lifetime.

1.6 VBQC Test Uncertainties

Naturally extrapolation from 100 to 44,000 hours demands a faith which may be misplaced and is certainly open to doubts regarding:-

- Contamination released by the test chamber.
- Sample emission not detected by the QRM.
- QCM drift errors.
- Sample contamination, e.g. from plastic bags, parting agents or finger prints.

Similar uncertainties affect most other test methods available for material selection but, until a greater body of experience is available, justification of this method will remain uncertain. Here the eventual return of the FOC for refurbishment after 5 years of orbital operation will represent a useful check on the assumptions and measurements made now. To those still bothered by the extrapolation alone it must be said that data are normally measured over two or more decades of hours and extrapolations are only for another two and a half decades. Thus for the usual equations involving logarithmic or power laws the extrapolation may be reasonable. One other uncertainty is that of re-emission of contaminants after original deposition on the QCM: it is argued that, providing the sticking co-efficient for a given molecule onto the QCM is similar to that for an optical surface, this leads to more realistic results than operating a QCM at exaggeratedly low temperatures such as that of LN₂.

1.7 VBQC Results

It is now proposed to discuss some of the more important test results and their interpretations but, first, it is here proper to acknowledge the vast efforts expanded by Arie Zwaal of ESTEC's Materials Division in aid of the FOC. Some of the data has occasioned considerable discussion concerning the interpretations but it is stressed that the opinions stated here are the author's. The most significant problems were anticipated as being the intensifier tube potting, the magnet material and paint likely to be necessary inside the OBE. Later it was found that the carbon fibre reinforced plastics represented a greater hazard than imagined from the QRM-02 test data. These cases will now be examined in some detail, see fig. 3 for an indication of the more significant contamination sources.

1.8 Intensifier Tube Potting

The first stage of the detector (see Fig. 4 for detector layout) uses a 3 stage image intensifier tube produced by EMI: this converts incident photons into electrons and accelerates the latter with voltages totalling 40 KV in a high permanent magnetic field. The electrons are converted into photons and then back to electrons by means of phosphors and photocathodes formed on thin mica plates inside the evacuated tube. The tube is potted inside a housing and the potting has the following functions:-

- Mechanical support with a high degree of stability over a typical exposure period of 10 hours.
- Critical damping during launch to obviate damage to the delicate mica plates and the junctions between the electrodes and the glass elements of the tube.
- Ability to withstand 40 KV without breakdown and to provide a very small leakage path to prevent unwanted accumulation of static charges.
- Since the potting material is very close to the detector faceplate a very high degree of cleanliness is essential.
- Opacity to reduce optical feedback from the output window to the faceplate (optical gains of 100,000 are involved).

More than 40 materials were evaluated for the first three parameters by EMI and of these four have been evaluated for cleanliness. These were Araldite CY-208 and Feldex R3, R6 and R7, the latter being EMI proprietary polyurethanes. ESTEC has also verified certain mechanical properties over the temperature range $+60^{\circ}\text{C}$ for the Araldite and the Feldex R6 (\approx R7).

The VBQC test data indicate that for the preferred Feldex R7 material as much as 120 mg of condensable materials may be emitted in 5 years. This is certainly an overestimate since in the real application the ratio exposed surface area: material mass is small whereas in the samples so far tested the reverse is true. An initial attempt to check the assumed diffusion through the material used a 13 cm long tube of Feldex R7, which was sealed at one end with a plug of DC-93500 1 cm thick, see Fig. 5. The sample was baked for 24 hours at 125°C in vacuum and immediately afterwards 16 samples were taken from positions along the length of the tube and then tested by the QRM-02 test method. It was hoped that a contamination gradient would be observed and from this to determine the efficiency of the DC-93500 plug as a seal to reduce the diffusion through the Feldex. So far the results have been ambiguous in that the samples were all too clean in respect of VCM production. This can be interpreted as:-

- Diffusion at 125°C is so rapid that the efficiency of the plug cannot be determined, and the predicted 120 mg is valid, or
- the material is very much cleaner than the sample originally tested (the latter may have been contaminated with a parting agent used to cast the sample).

These alternative interpretations are being examined in other ways to confirm the selection of Feldex R7 as the intensifier potting.

1.9 The Magnet

The intensifier needs a high permanent magnet field for its operation and this is provided by a rare earth epoxy material known as Hera. Again QRM-02 data showed this to be acceptable but the high mass and high surface area of the magnet might lead to high contaminant production. VBQC tests were performed on the material coated with Rutapox which was assumed to act as a diffusion barrier. These tests showed too high a level so it was then proposed to vacuum bake the material in an attempt to accelerate the outgassing. Tests on small blocks showed no measurable effect on the magnetic properties at temperatures as high as 100°C providing a good vacuum was maintained whenever the material exceeded 45°C (the presence of oxygen adversely affects the field strength at higher temperatures by oxidation of the rare earth). VBQC tests showed some improvement but still not to an acceptable level and it was then proposed to vacuum bake at 80°C and then coat with a room temperature curing epoxy. These results were in fact worse still and the present solution is to use this epoxy as an adhesive for aluminium foil on all exposed surfaces. Vacuum baking of a full scale magnet has shown that magnetic properties are adversely affected, hence vacuum baking of Hera is no longer proposed. The most recent VBQC test data shows a much more acceptable result, one which can only be improved by switching to a better room temperature adhesive. Figure 6 shows plots of the predicted data for the various configurations of the magnet material. This figure incidentally shows the benefit to be gained by space conditioning is not very large for this material, being only a reduction of 25% of that otherwise expected in 5 years.

1.10 Paint

The appropriate surface finish to be applied in the OBE has received a lot of attention as the area concerned approaches 11 m² and paints are well-known to be unsatisfactory when tested according to QRM-02. Black anodising, other black inorganic treatments and black teflonisation have been considered as alternatives, but cannot altogether replace paint. Table 1 shows the paints considered with test data where applicable. As may be expected, space conditioning at high temperatures appears the best solution, and the present recommendation is to use Chemglaze Z-306 without primer with a postcure of 24 hours/100°C/10⁻⁴ T. Adhesion tests on Aluminium foil, Mumetal and Kapton have been successful when this curing schedule is followed. It must be admitted that, for the cleaner materials, the predictions are less certain than usual for the condensates measured were so small that it is difficult to be sure they came from the sample and not the chamber walls.

The raw data often indicated a reduction in the deposit in the period 2 to 10 hours after start of the test, and best fit curves were sometimes power or even linear laws. The data presented in Table 1 are those obtained from a forced selection of a logarithmic law which normally is the best fit curve for paints with higher deposits. This forcing is justified if one recognises that a linear law implies material degradation which is less likely to occur at 50°C than at 100°C at which temperature a logarithmic curve is usually the best fit. While in this penitent mood, it is as well to point out that only one sample has been tested at each condition, that the 7D/RT cure is very sensitive to the environmental conditions, and that batch

to batch variations between paints can be larger than the differences predicted here. It is felt that the recommended cure stated above is tolerable for the FOC, but that much more work needs to be done for similar applications for future optical spacecraft. It is hoped that the results of work on paints done by MartinMarietta and BASD for other ST instruments will be available in the next four months to supplement the work reported here.

TABLE 1 : PAINTS

PAINT	CURE	TML %	CVCN %	TEST HR/°C	DEPOSIT RATE 10 ⁻³ g / HR	5 YEAR PRD. g/cm ²
COVERTIN-306	7D/RT	1.7	.04	100/50	1.5+1.6 Log _e ^t	.88
CHEMGLAZE Z-306 + PRIMER P123	7D/RT 18/80	1.7	.02	18/80 44/50	17+3.8 Log _e ^t -18+35 Log _e ^t	5.7 .34
AS ABOVE	7D/RT 43/100	AS ABOVE		43/100 61/50	5.0+7.0 Log _e ^t .0081+.08 Log _e ^t	7.1 .078
AS ABOVE BUT NO PRIMER	7D/RT 22/80	AS ABOVE		22/80 41/50	10.6+1.05 Log _e ^t .084+.12 Log _e ^t	1.4 .091
AS ABOVE	7D/RT	AS ABOVE		135/100	4.119.2 Log _e ^t	6.7
AS ABOVE	7D/RT	AS ABOVE		27/125	32+17 Log _e ^t	14.7
CHEMGLAZE Z306 + PRIMER 9924	7D/RT	2.3	.07	NO TEST	PLANNED	
CHEMGLAZE 2004 NO PRIMER	7D/RT +24/80	1.6	.03	110/50	-20+9.5 Log _e ^t	.82
NEXTEL 3M 401C 10	7D/RT	4	1.0 to .03	44/50	4.3+3.8 Log _e ^t	2.8

Table 2 shows the raw data obtained for Nextel 401-C10 with 7D/RT cure : column 3 shows the best fit CVCN curve leading to a prediction in 5 years of .045% of the original paint mass as the contamination deposit on a surface at -25°C. The data on the right-hand side gives the actual and best fit data for the TML. Both CVCN and TML can be expressed in % mass/unit time but more conveniently may also be expressed as deposit mass/emitter area.

TABLE 2 : CVCN DATA FOR : NEXTEL 401 C10
AT 50°C (NO PRIMER)

Temp.	-25°C	Log	Power	TML	Log	Power
	CVCN act	CVCN calc	CVCN calc	TML act	TML calc	TML calc
a	-	.00428	.00418	a		
b	-	.00384	.4449	b		
T hrs	Corr. Coef	.9909	.9663	C.C.		
1.4	.00197			4.644 x		
1.0	.00373	.00384	.00418	5.135 x		
2	.00579			5.471		5.473
3	.00707 x			5.632		5.633
4	.00877			5.728		
5	.00984	.01046	.00855	5.792		5.791
6	.01079			5.839		
7	.01167			5.875		
8	.01238			5.904		
10	.01351			5.948		5.946
12	.01439	.01313	.01164	5.979		
14	.01510			6.003		
16	.01569			6.023		
19	.01629			6.046		
22	.01674			6.064		
24	.01696	.01649	.01718	6.073		6.073
27	.01720			6.086		
30	.01740			6.098		
33	.01757			6.107		
36	.01768			6.115		
40	.01777			6.124		
44	.01785	.01881	.0225	6.131		6.131
100	.022			6.185		6.185
300	.026			6.228		6.228
1000	.031			6.253		6.253
3000	.040			6.265		6.265
10000	.045			6.272		6.272
43800			.485	6.277		6.277

PAINT DENSITY 1.3 mg/cm²O = .0041 + .0018 Log_e^t % or .27 + .24 Log_e^t mg/cm²TML = 6.26 - 1.181 Log_e^t %

x = bad data

ORIGINAL PAGE IS
OF POOR QUALITY

1.11 EHT Cable

Selection of a satisfactory EHT cable and its termination is difficult when it is to handle voltages as high as 40 KV. Special requirements here include: very good bonding to potting materials, reasonable flexibility and, of course, low outgassing. The choice fell between two materials, a highly flexible silicone rubber and a Polyolefin/polyvinylidene fluoride insulation which is very stiff, the former being "dirty" and the latter almost clean. However, it is possible to improve silicone rubber by vacuum baking, e.g. in a double QRM-02 test the CVM data improved from .35% to .06%. Fig. 7 shows the data obtained in a VBQC test after baking a sample for 5D/125°C/10⁻⁴T leading to a 5 year prediction of .0011%. Fig. 8 shows VBQC data for the stiffer cable: this gives .026% if not space conditioned and negligible if vacuum baked at 80°C for 24 hours.

1.12 Condensibles Budget

Table 3 shows a summation of the potential contribution from the major sources in the OBE of the FOC. The target value was 8 mg based on the area of optically critical surfaces in the FOC and the assumption that a deposit equivalent to 3 monolayers may be acceptable in the 5 years mission. It may be seen that this target is not met, with the chief offenders being the CFRP + honeycomb, the Hera, Kapton foil heaters and paint. The first may yet be improved once an edge sealed sample is tested although it is necessary to note that the sealing cannot be hermetic since the volume must vent. It is simply hoped that the rate of outgassing will be reduced by an order of magnitude. The value obtained for Hera is probably pessimistic since it should be possible to reduce the proportional length of the perimeter of the aluminium foil in the real case compared with that of the sample. Alternatively the use of a better room temperature curing adhesive may solve the problem. The data for the Kapton foil is suspect since the curve fitting to the data obtained in the test at 50°C after bakeout at 80°C is much too steep; a more probable 5 year prediction is .001% giving a budget contribution of only 3 mg: this test is to be repeated to verify this assumption, see Fig. 9.

TABLE 3 : CONDENSIBLES BUDGET

SOURCE	MASS GM	5 YR MGM	CVM S.C. MGM	Balance MGM	COMMENTS
CF+Al Honeycomb	12,500	37	24	13	Data from sample with-out edge sealing
Hera Magnet with Al foil sealing	6,400	16	None	16	
Chemglaze Z-306 No primer	8 M ² Max	60	54	6	Space Cond. 100°C/24 hrs min.
Harness (Tefzel)	7,000	165	~165	~1	
EHT Cables (Silicone rubber)	200	-	-	.16	Space Cond. 125°C/5D
EHT Cables (PVF)	300	78	~78	~1	
Actuators	11 off	.5	none	.5	
CF Structure	4,500	7.2	4.8	2.4	
GF Structure	2,000	4.5	3.0	1.5	
Feldex R7	1,600		none		see text
Preamp : Stycast 2651	216	4.1	0.3	4.1	No SC prop. enclosed source
Camera Tube Potting (DC93500)					Test at assembly level
Kapton Foil Heaters	1.8 M ²		260		SC 80°C/24H

While it seems possible to attain the budgeted contamination level it is less clear that this will not impact on the FOC performance. Data published recently (Ref. 3) indicates that a deposit of plasticiser equivalent to 8 mg on the FOC optical surfaces would only degrade the performance at 225 nm by 10% or so, would be acceptable, this differs from ref. 1 which indicates three times worse losses; this can only be confirmed by long duration testing in vacuum with a detector as sensitive as the FOC's.

1.13 Conclusions for FOC Materials Selection

These few cases discussed above have touched on one factor that can significantly modify the interpretation of the test data: this is shape or form. The intensifier potting has large bulk but a low surface area, hence contaminants have long diffusion paths; the "cigar" test was one attempt to simulate the real application. Paint is at the other extreme with a negligible diffusion path but very large area. The CFRP honeycomb composite is a combination of these extremes since at least half of the outgassing products must follow tortuous paths through the honeycomb cells and, once the ambient pressure has reduced to 10⁻⁵T, these paths can be regarded as infinitely long.

The chosen solutions to these potential contamination problems have been as varied as the applications, e.g. after:

- selecting the cleanest material available and acceptable from other design standpoints, then
- bakeout the contaminants, and/or
- seal the remaining contaminants in.

At system level a combination of bakeout and a fourth solution purging, is envisaged for the first entry into vacuum of the FOC but the efficiency of this bakeout is uncertain since the bakeout temperature has to be limited to only 45°C. Witness mirrors will be used to record the total contamination occurring during this and other integration and test activities, although the sensitivity of measurement is too low to confirm the correctness of the materials selection criteria given above. Should the mirrors indicate a problem then reconsideration of the possibility of introducing thermal cleaning of optical surfaces would be necessary.

2. ADVANCED SPACECRAFT CONCERNS

2.1 STS Payloads

Where the Shuttle is to be the launcher it is necessary to satisfy NASA in respect of its requirements for flammability and stress corrosion cracking (SCC) susceptibility of materials. Most European work in these fields has been in support of Spacelab where the presence of astronaut-scientists makes these requirements literally vital. However, for payloads like the FOC which is never powered in the presence of an astronaut, the flammability requirements should not be so onerous. At present formal applications for approval of each potentially flammable material are necessary but it is suggested that NASA should identify from the project material usage list only those materials regarded as hazardous in the general application after considering the environment relevant to the human interface with the equipment.

Similarly while it is well understood that metals exposed to a warm, humid, coastal environment can fail suddenly, with quite low loads it is not understood why SCC control must be rigorously applied to equipment always maintained in a clean, low humidity, atmosphere. SCC and flammability control need not always be rigidly enforced and must not if project costs are to be kept within reasonable bounds.

2.2 Magnetic Properties

Previous spacecraft such as HEOS, HELIOS and GEOS have required progressively stricter control of magnetic materials and ISPM will follow this trend. It is an unfortunate fact that electronic parts use Kovar in significant quantities and that no replacement is reasonably possible, hence magnetometer sensors are doomed to be supported remotely from the electronics, and thus to suffer severe thermal conditions. It was the GEOS experience that sample measurement of the magnetic properties of the electronic parts was largely ineffectual since no alternative parts were available and layouts could not be changed when the magnetic data became available: however, the integration of the thousands of individual magnetic fields tends to be self-cancelling at the sensor position.

2.3 EMI

Reduction of EMI will be ever more important on future scientific spacecraft and the use of the outer surface of the spacecraft as a conductive shield will become more usual, at least for geostationary spacecraft. In this respect neither GEOS I or II has suffered interference associated with high voltage surface discharges thought to be responsible for some Meteosat "events". This may be due to the care with which the outer surface was grounded. Fig. 10 shows part of the solar panel with the solar cell cover glasses with an outer Indium Oxide layer grounded via welded tabs to copper tracks leading to the "star point". Even quite small areas of potential insulation were grounded using VDA on Kapton foil with conductive cements leading to grounded surfaces. The contact with the VDA had to be protected with an overcoat of epoxy to prevent corrosion and, perhaps with an excess of zeal, these epoxy blobs were finally coated with a conductive black paint during the last 6 weeks before launch.

3. SUMMARY

The title of this paper was "Materials Policy for Advanced Scientific Spacecraft" yet most of the text has been restricted to one aspect of materials selection of one part of one advanced spacecraft. No apology is made for this restriction and it is admitted that the recommended materials policy for any spacecraft should be summarised by the latin words "ad hoc". In effect if the scientific requirements demand special attention for one aspect, then fulfil that demand, but avoid piling unnecessary constraints on the designer. Thus, for the FOC, the most important materials selection test seems to be the production of VCM as emitted at 50°C and collected at -25°C. For IRAS and the Space Telescope's Wide Field Camera the collector temperatures must be reduced since the critical surfaces are much lower so that water will be a significant contaminant. The use of thermal cleaning will be essential for these applications if not for the FOC.

Thus for spacecraft the materials policy like all other policies should be tailored and financed according to its needs.

References

1. Hass.G. and Hunter W.R. Laboratory Experiments to Study Surface Contamination, Applied Optics, September 1970, p. 2104.
2. Zwaal. A. - Outgassing Measurements on Materials in Vacuum using a Vacuum Balance and Quartz Crystal Balances, Proceedings of USAF/NASA International Spacecraft Contamination Conference AFML TR-78-190/NASA CP-2039 pp. 118-150.
3. Colony. J.A. - UV Absorption of Common Spacecraft Contaminants, GSFC TM-80551.

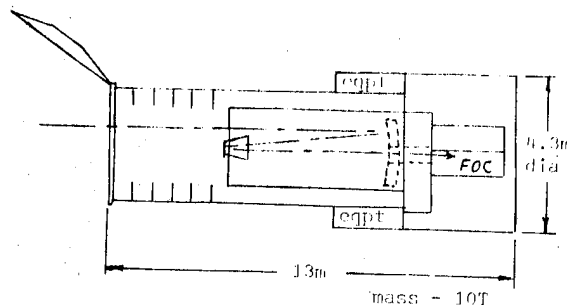


Fig. 1 - Space Telescope

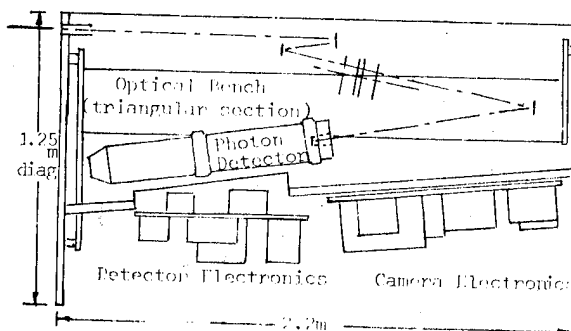


Fig. 2 - Faint Object Camera Layout

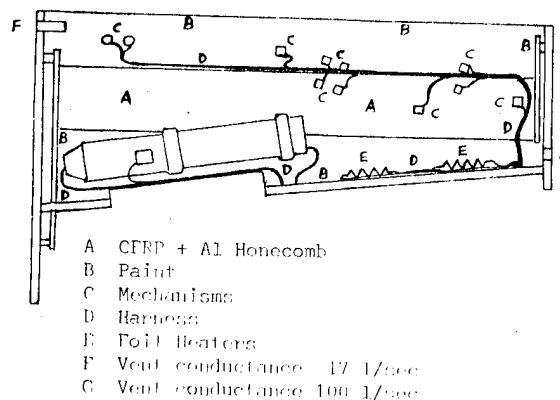


Fig. 3 - Contamination Sources

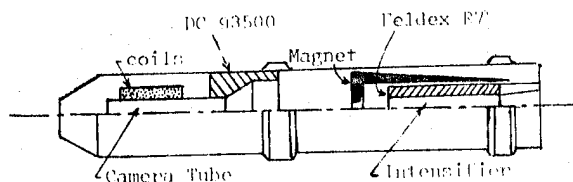


Fig. 4 - Detector Layout

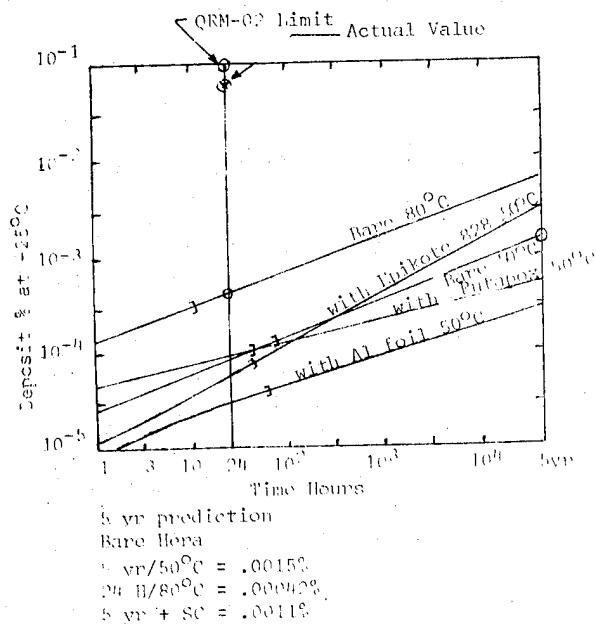


Fig. 6 - CVCM Data for HERA

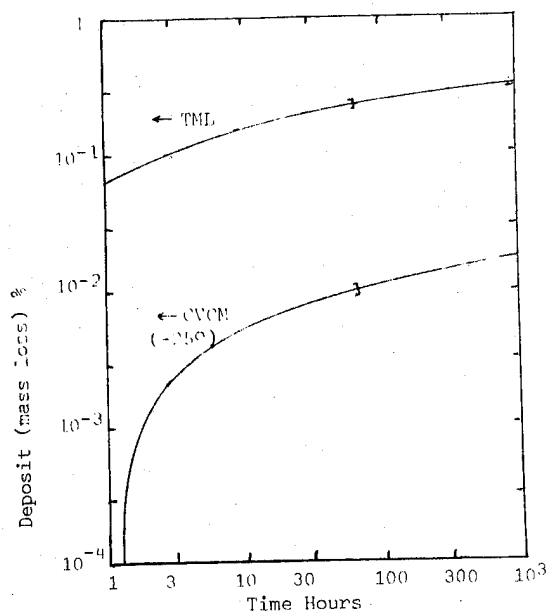
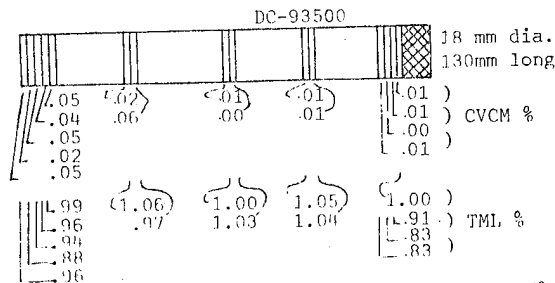


Fig. 8 - CVCM and TML Data for PVF EHT Table



Sample without postcure gave CVCM=.03%, TML 1.87%.

Fig. 5 - Foldex R7 "cigar test" after 24hr/125°C/

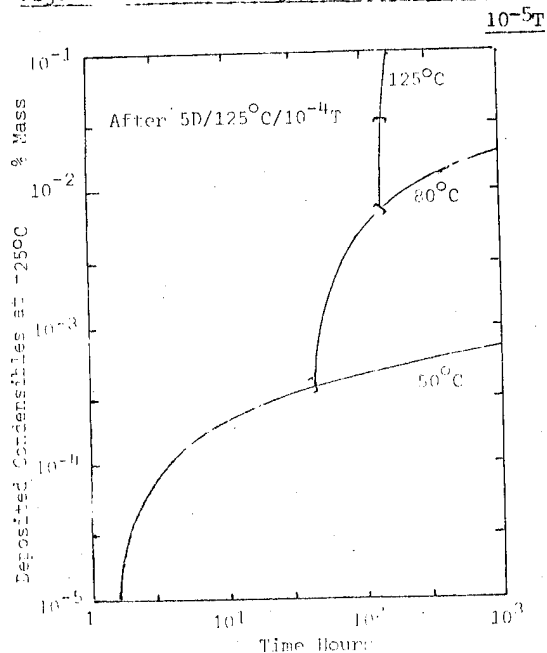


Fig. 7 - CVCM Data Silicon Rubber EHT Cable

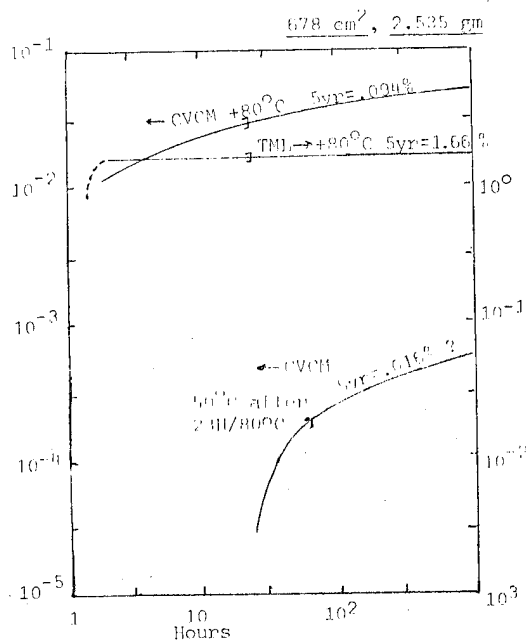


Fig. 9 - CVCM and TML Data for Kapton



Photo 1. Picture of Ganymede, one of Jupiter's moons, giving an idea of the imaging sensitivity of the FOC in earth orbit.

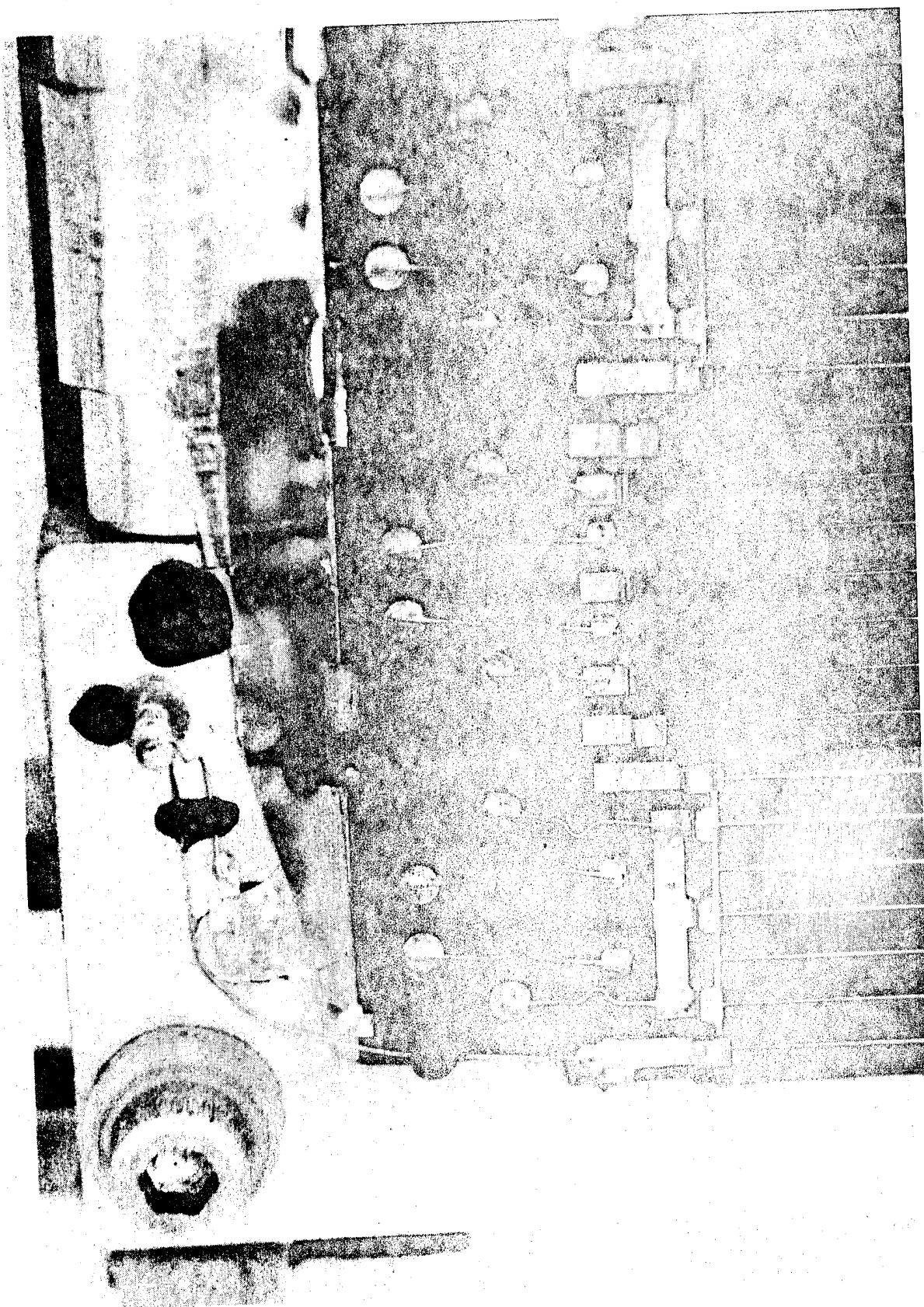


Figure 10. Surface grounding of the Geos solar panel.

N80-21437

OTS/ECS MATERIALS POLICY

P.J.H. Molloy

British Aerospace Dynamics Group, Stevenage, Hertfordshire, UK

ABSTRACT

This paper is written to describe the Materials Policy as used on an experimental communications satellite - OTS (ORBITAL TEST SATELLITE) - which was designed as the forerunner of a series of European Communications Satellites. The paper explains the methods by which this policy was implemented, its problems and its achievements.

The policy followed on subsequent communication satellites is discussed and also developments of techniques which are likely to influence future materials and process policies and their implementation.

Keywords: OTS Materials Policy, Problems, Results, ECS Materials Policy, Outgassing Study, Future Materials Policy.

1. INTRODUCTION

OTS (the Orbital Test Satellite) was the first major communications satellite to be managed and produced by BAe (British Aerospace). It is a 3 axis stabilised satellite which was launched into geostationary orbit in May 1978 - its primary use is as a test satellite for the European Post Offices (Eutelsat) and as such was planned as a forerunner of a series of European Communications Spacecraft which are under development at present.

The Materials control on OTS was thus extremely important to ensure a successful mission so as to give confidence to Eutelsat and ESA (our customer) that we could succeed in this new venture. The OTS materials control policy used was specified by ESA and is a derivative of the policy developed in the USA for control of spacecraft materials.

2. MATERIALS POLICY ON OTS

The aim of the policy was to ensure that materials used on OTS were suitable for the intended life in a space environment. The use of materials in space vacuum conditions and the effects of that environment on these materials is unfamiliar to the average engineer so that there is a need for education of this aspect of space engineering. In simple terms there are two basic effects not normally experienced on Earth - outgassing and extremes of temperatures.

Outgassing is the effect of vacuum conditions on materials causing them to outgas, i.e. gases will disperse, liquids will vaporise, and solids will release molecules only loosely held by molecular forces.

The effect of outgassing is to produce molecular products which can be harmful to sensitive surfaces (e.g., optical and thermal control surfaces, solar cells etc.) if they adhere on these surfaces. To combat this the amount of these products needs to be limited in order to control their harmful effects. To do this an accept/reject criteria on outgassing is necessary and all materials need to be tested for outgassing in a vacuum environment at a representative standard temperature. The accept/reject values set by ESA were 1% on Total Weight Loss and 0.1% on Volatile Condensable Materials irrespective of the quantity of material.

The standard temperature chosen for these tests (called Micro VCM tests) is for the material to be at 125°C and the receptor (to detect outgassing products) at 25°C. The test is run at 10^{-5} torr vacuum for 24 hours. A second effect of space conditions is that spacecraft surfaces can become very cold (due to the near absolute zero temperatures) or very hot if facing the sun - the lack of atmosphere means there is no convection of heat. The effect of extreme temperatures on spacecraft is to prevent the sophisticated electronic systems from working correctly and of course, in the extreme cases of overheating, being about failure of organic materials used. Heat will of course, accelerate the rate of outgassing.

0.3

The adverse effects of temperature can be overcome by selection and use of thermal control systems, techniques and materials - e.g., insulation materials, thermal blankets, thermal control surfaces, radiators, active and passive thermal control systems, heatpipes, etc.

The foregoing space related criteria had to be taken into account for OTS as were the normal (terrestrial) engineering criteria such as prevention of corrosion, control of plating and process methods, jointing materials and processes etc., always bearing in mind any peculiar effects which might arise due to the space environment.

Summarising then, the criteria used in approving materials were as follows:-

Compatibility with Space Environment
Corrosion prevention
Jointing materials and processes
Process controls
Unique effects (e.g., tin whisker growth)
Safety (e.g., use of toxic materials, Beryllium)

2.1 Implementing the Policy

To implement this policy, the Consortium (consisting of some 40 major companies arranged in levels - Prime Contractor, Co-Contractors, Sub-Contractors and suppliers) were required to draw up Material Lists. These lists had to specify every material used on the Satellite and were divided into several categories - adhesives, tapes, paints, coatings and varnishes, glasses, lubricants, metals, plastics and potting compounds. The lists had to give the type, manufacture, brief processing details, its application, location and operating environment of each material.

Sub-Contractors lists were reviewed by Co-Contractors and incorporated into single Co-Contractors lists which were supplied to BAe for approval. The Co-Contractors materials lists were reviewed and any outstanding points discussed with the Co-Contractors. When all materials were approved or when an agreed state had been reached the whole Spacecraft Materials List was submitted to ESA for review and approval.

2.2 Review of the Materials List

In order to approve a material in the Materials List, the outgassing data was checked and the user instructed to provide outgassing samples for checking if necessary. In addition to the outgassing check, the material would be checked against the other criteria, processing, plating, jointing methods, corrosion prevention, thermal finishes, cleanliness control, safety and unique effects.

The whole process involved dialogue by telex or telephone between Prime Contractor, Co-Contractors and Sub-Contractors with materials and/or processes being changed to meet the requirements. In the early days of the project the discussions took the form of regular meetings to which all the Co-Contractors (and sometimes their sub-contractors) sent materials representatives.

The meetings proved very useful on exchange of information concerning the ESA requirements, common materials problems, and passing on of information on new materials.

Review of the Materials List was a long and tedious process. Each material had to be checked using the above criteria.

The most troublesome area was outgassing. Meeting the 1% TWI and 0.1% VCM requirement was difficult in many instances - in some cases there was insufficient data or sometimes no alternative materials. Where insufficient data was available on a material and its associated process, samples had to be sent to ESA for testing.

Generally metals (with some exceptions - e.g., cadmium) have a very low outgassing product and can be accepted for space use without testing. However, organic materials generally need to be tested - the frequency of testing is dependent on the amount they outgas and their batch variability.

For instances, if a material had an outgassing product of say 0.5% TWI and 0.06% VCM and showed little batch variability then only occasional testing would be necessary. On the other hand, paints, foams, some types of adhesives invariably needed batch testing because their outgassing values can be close to the specification limit, batch variability is known to occur and slight processing differences can have a marked effect on outgassing. Many of the early materials had to be rejected for a host of reasons (outgassing, vacuum compatibility, processing, plating, etc.). It soon became apparent that processing could have a marked effect on outgassing and material properties and so in several instances, manufacturers had to change their processes to obtain acceptable materials.

2.3 Problems Found from the Materials List

1. In the early days of OTS several companies were using solders containing a high added antimony level (above 0.2%). This, when soldering alloys containing zinc, can lead to embrittlement as the zinc - antimony alloy causes the solder to become brittle. This was rejected with the result that manufacturing procedures had to be changed and a specific supplier arranged to provide low antimony solder. Users then had to re-train the soldering operators in the use of this new solder - this did not cause the problems envisaged as low antimony solders have better wetting properties.
2. Corrosion protection - the use of magnesium boxes on some equipments gave rise to several corrosion problems - in particular, achieving the correct thermal finish and corrosion protection was difficult especially around the feet of the boxes where an electrical grounding correction between the feet and the structure was necessary. In such cases it was often necessary to use a bonding strap to achieve the required electrical grounding as the corrosion protective finish was invariably non-conductive.

3. Galvanic couples - care was taken to ensure contact was not made between metals that could present a galvanic couple which could lead to corrosion during ground storage. Among the methods used was the use of organic and oxide films interposed between the relevant metals. The method adopted were completely successful - no galvanic corrosion problems arose throughout the programme.

4. Outgassing - As stated several problems arose in meeting the outgassing requirements. To highlight one of the problems on outgassing the following is given as an example. RTV 560 was listed in a Co-Contractors Materials List for use on the solar array panels.

The Qualification Model (QM) panels were built before the implications of this high outgassing material were realised and agreed. The concern was that besides possible contamination of the solar cells themselves there was also a distinct possibility of contaminating the SSM's (Secondary Surface Mirrors) thus upsetting the spacecraft thermal control system.

After much discussion involving manufacturing methods, pot life, planning schedules and their associated extra costs the adhesive was eventually changed to an acceptable one with lower outgassing values (RTV 566).

2.4 Other Materials Problems

1. Cleanliness - After manufacture of the QM structure panels and some Flight Model (FM) structure parts, oil was noticed on these panels. The source of this oil was traced to a leaky head on the milling machine used to mill out the panel insert holes. This caused a major problem as the QM Spacecraft was to be thermal vacuum tested with QM/FM equipments. A process was devised to remove the oil but no one knew for sure how far the oil had seeped into the honeycomb.
2. Cleanliness - When the QM Spacecraft was removed from the thermal vacuum chamber after thermal vacuum testing the lower half was covered in a thin layer of oil. On the SSM's this layer was like condensation of a fine mist. First thoughts were that the oil was from the vacuum chamber roughing pump oil. When this was discounted by checking the spectral characteristics of the two oils the other possibilities were considered - these were the oil contaminated panels, vacuum grease used to lubricate the equipment insert threads, ABM nozzle thermal blanket, oil from the overhead crane used to move the QM Spacecraft and in particular, the fired ABM Safe and Arm device which contained large amounts of lubricant.

When checked none of these oils and greases matched the characteristics of the contaminant. Only after extensive detective work was the culprit found. It turned out to be the release cables for the solar array mechanism.

During manufacture, these cables are oiled to facilitate the winding and twisting together of the wires and indeed oil is essential for use of these bowden type cables. It is estimated that these cables contained a total of less than one gm of oil and this was sufficient to cover the lower half of the spacecraft and parts of the vacuum chamber.

From this point on the cables were cleaned using a process that was specially developed to remove all traces of the lubricant. Removal of the lubricant does not compromise the operation of the cable as it is a "one shot" device.

3. Failure of TWT after launch - some months after launch one of the 6 Travelling Wave Tubes failed. It is not certain why this happened but one of the possibilities is that the leakage current has increased in the high voltage area. The possible cause of this is arcing in this area caused by outgassing or voids in the potting surrounding the high voltage terminals. This is under active investigation at BAe.

3. RESULTS OF MATERIALS POLICY ON OTS

Looking back over OTS now at the halfway point of its mission it has been demonstrated to be a successful satellite, and although one of its 6 TWT's has failed, the redundant TWT is still working. Several successful TV link-ups in Europe and N. Africa have been made by OTS including a recent teleconference between Geneva and London. More recently the Pope's visit to Ireland has been transmitted live to Britain via OTS. As to the results of the materials policy we can summarise these as follows:

1. No detected galvanic corrosion problems have been encountered.
2. Other than the TWT already mentioned, there are no detected problems due to outgassing i.e. no degradation of power, thermal control, pointing accuracy, etc.
3. There is a much greater understanding of the materials policy and requirements throughout Europe.
4. There is a far better understanding of the effects of space environment on materials and processes.
5. There is now a great amount of data on materials and processes - this coupled with the problems faced and experience gained on OTS now gives a lot of confidence in the use of materials for future space projects.
6. A great deal of investigation is under way to understand what went wrong with the TWT that failed to avoid a recurrence in the future.

It is also worth mentioning how important the success of OTS is on the Communications industry in Europe. Television and data transmission organisation in Europe are using its services more and more and as it establishes the concept of a reliable data link the demand will grow for further and better satellites of this type.

4. ECS POLICY

The current ECS policy is a direct follow-on from the OTS policy. It is, however, much easier in that most companies are now familiar with the requirements having had experience on OTS.

In addition, the data handling has been reduced in that the Co-contractors materials lists are now only compiled - this eases the task at Prime Contractor level but consolidation is still being performed at Co-contractor level. A great amount of effort is still expended, however, in reviewing each and every material for its application in space - batch sample testing (i.e., Micro VCM testing) of particular organic materials is still needed and this has placed considerable strain on the facilities we use at ESTEC. The pressure is growing for further test centres in Europe.

From OTS experience it has been noted how important processing of materials is. This has led to the requirement of separate processes lists for review and approval at Prime and Customer level. This can be tricky as in many cases processes are confidential. In such cases the processes may sometimes be reviewed on site. Where this has been refused to the Prime Contractor, the Customer has been asked to do this delicate task (with the undertaking of course to keep the knowledge gained confidential) and advise the Prime Contractor of the acceptability or not of these processes.

4.1 Review of the ECS Policy

With this increasing knowledge of materials and their properties in space comes an increasing curiosity as to how the original criteria were generated for approval of these materials. In this area the outgassing requirements are questioned particularly as this forms the major problem in approving materials.

As a step in this direction a crude analysis has been done on ECS to estimate the gross outgassing amounts and effects on the spacecraft. This shows that a maximum of 0.70 kg of outgassing product (containing 0.08 kg of VCM) will be produced within the satellite. This represents about one sixth of the theoretically allowable outgassing if we were to assume all materials in the satellite were on the limit of the outgassing requirements.

As the satellite is sealed in a VHF kapton layer the outgassing product will generally find its way out through the main openings in this layer, i.e., the battery cooling holes and the ABM cone support ring where there is no VHF shield.

4.2 Effects of Outgassing

The study indicated that the lightweight molecules (water, gases, etc.) would generally disappear into space - they would only remain attached to very cold surfaces and as there are no low temperature surfaces on ECS/MARECS this is not thought to be a problem.

The heavier outgassing molecules (called VCM as these are the ones that tend to condense) can cause problems because if they impinge on sensitive surfaces and remain on these surfaces (due to surface absorption or condensation) then given sufficient time these molecules may be polymerised by solar radiation etc. Once this happens they will not leave that surface. On sensitive surfaces this layer will cause performance degradation of that surface.

4.3 Minimising Outgassing Effects

Sometimes it is necessary (for all sorts of reasons) to use materials which do not meet the outgassing requirements of 1% TWL and 0.1% VCM. This can be reviewed favourably if the TWL requirement is just out of specification as this represents the non-condensibles. However, if the VCM is above 0.1% then this could present a problem as this outgassing product is the one that could be deposited permanently on sensitive surfaces.

The quantities of these products is important and that is why it is necessary to have an idea of the spacecraft total outgassing product. Not only is the quantity important, but also its configuration within the spacecraft so that it is possible to assess the path it will take as it outgasses. Once this has been done then steps can be taken to alter the path taken to minimise the effects of the outgassing.

This has been done on the ECS/MARECS structure where a fairly high VCM foam was necessary to join honeycomb sections together. Here perforations in the edge tape were left out at the areas where the foam came to the edge of the panels. By making the outgassing path much more difficult through the honeycomb it is considered that the harmful VCM products will either stay within the honeycomb or leak out so slowly as to make their effect negligible.

This technique will also be applied to the L-band antenna on MARECS. The thermal blankets on the rear surface of the antenna are to be sealed around the apertures in the antenna. This is to reduce the effect of outgassing from the antenna on the Infra-Red Earth Sensors which are mounted below the antenna and which look through the apertures in the antenna.

5. FUTURE POLICY

Having had 5 years experience of materials control on OTS and ECS and gained an appreciation of why the materials control is necessary, companies are taking a more positive interest on controlling materials and processes.

There is a wealth of data available, many more materials are now approved for space use and steps are being taken to consolidate this in some form. Computer listings come to mind and this is being done in order to reduce the clerical effort necessary for preparing materials and process lists. One can envisage data links between customer, Prime Contractor and Co-Contractors in this area.

Control of processes is becoming more important and approval of all processes is now being implemented. This can lead to problems of confidentiality, particularly in small specialist companies where these processes represent a large proportion of their expertise and investment. The criteria for selection of materials (particularly outgassing) is unlikely to change significantly in the foreseeable future. The "blind" screening method for material outgassing (i.e., the micro VCM test) has been demonstrated to be successful on many spacecraft and has worldwide acceptance. It forms the cornerstone for material selection for space use. However, because it is a blind screening method and takes no account of the amount of outgassing material involved it can be overtly restrictive where small amounts of material are used and possibly too lax for very large amounts of outgassing material.

In practise, it focuses attention on small amounts of material which are high outgassers and not on large amounts of low outgassers - even if the low outgassing from large amounts of material may far exceed the outgassing from the small amounts of high outgassers. This has become obvious on ECS when the total outgassing product was estimated.

In providing a total outgassing product as a guide, ones attention is not focused on the detail and thus the problem is viewed as a whole. From this standpoint the dynamic characteristics of the outgassing product can be utilised so that by slight modifications to spacecraft geometry, these products are directed away from any sensitive areas.

Using these techniques one could adopt a more flexible attitude to small amount of high outgasses - i.e., relax the 1% TWL requirement for small quantities of these products always bearing in mind the safeguards (including material integrity) necessary in doing this. The safeguards would be to have a limit on the total quantity of these materials per subsystem and per spacecraft, the relaxation would be only on TWL and not VCM and would not be allowed in high voltage areas (e.g., TWT's). In fact it would appear that the 1% TWL is perhaps too lax for these high voltage areas and needs to be tightened. It could also be said that an overall total amount of outgassing should be given as a target as it is theoretically possible to have very much larger outgassing levels than are currently being predicted.

More data is also needed on the rates of outgassing and the effects of temperature etc. on these rates. With this and an understanding of dynamic behaviour of the outgassing products within a given configuration the outgassing problem could be tackled in a much more scientific way.

Using this method and with a flexible materials policy the materials effort would be expended in a more valuable and constructive way, with greater understanding and more precise knowledge of outgassing effects to the benefit of all.

REFERENCES

1. Gross outgassing levels and effects on the MARECS and ECS spacecraft - MCS/004/PWN/0040/BAe, 1979.
2. Visit Report of P. Molloy to TRW - MCS/004/VIR/0023/BAe, 1979.
3. Polymers for Space Applications - Stanford Research Institute, 1967.
4. Self contamination and environment of an Orbiting Spacecraft, NASA TN D6645, 1975.
5. Contamination assessment and control in Scientific Satellites NASA TN D7433, 1973.

ACKNOWLEDGEMENTS

I am very grateful to the following for the help given to me in the preparation of this paper:-

Mr. K.J. Burton - Materials specialist at BAe for his support and technical advice on the content of the paper.

Mr. R.G. Staniforth - Project Manager (MARECS) at BAe for allowing me time and resources in presentation of the paper.

PRECEDING PAGE BLANK NOT FILMED

N80-21438

METEOSAT CLEANLINESS CONTROL ACHIEVEMENTS

M L Reynolds

ESA Earth Observation Programme Office
Toulouse, France

J Kieffer

MATRA Espace
Vélizy, France

ABSTRACT

An associated paper describes the cleanliness control programme derived for the Meteosat radiometer manufacturing, test and integration activities. This paper deals with the inflight behaviour of the equipment to assess the degree of success of the control programme.

As the Meteosat satellite was defined for application functions and not for technological activities, the analysis is necessarily derived from observed performance rather than through direct measurement.

Particular emphasis is made on the radiometer cooler as this is the most sensitive component of the system. As its function is highly dependent on surface properties, it is almost an ideal indicator of contamination.

Keywords: Radiometer, Infrared, Contamination, Cleanliness, Passive Cooling.

1. INTRODUCTION

Follow-up of the Meteosat's in-orbit exhibition of cleanliness/contamination is of significance both to interpret the observed performance and to evaluate the success of the pre-flight cleanliness control programme.

Our analysis activities have essentially been limited to the optical payload as this was judged to be the critical item and the most likely area to yield quantifiable results.

During the definition of the radiometer cleanliness control plan (see Edwards and Marcoux) our thinking was dominated by two general classes of potential problems:

- Optical surface contamination: i.e. contamination of the surfaces of mirrors, lenses, filters and windows resulting in efficiency losses and possible modifications to spectral responses.
- Thermo-optical surface contamination: i.e. contamination of surfaces whose optical properties are essential to the thermal control design. This is particularly limited to the

passive cooling system used to provide the correct working temperature for the infrared detectors.

2. GENERAL ANALYTIC APPROACH

The above classes of problems are clearly separated in effect and can thus be independently observed. Further, a physical separation and thus isolation of the instrument into two principle environmental cavities, the telescope cavity and the cooler cavity, considerably reduces the potential sources of a given problem.

Unfortunately, it was not possible to include dedicated inflight contamination monitoring equipment, hence analysis is dependent on interpretation of available data in the telemetry and image data streams. The task has been considerably aided by the development of an operational programme profile which permits service time-slots within the daily planning of satellite operations; a philosophy which has been very successfully exploited thanks to the enthusiasm of the Meteosat Operation Division of ESOC and the patient understanding of the Meteorological Users of the system.

3. OPTICAL SURFACE CONTAMINATION

3.1 Possible optical surface contaminants

Obviously a complete list of all possible contaminants would create dull reading and confuse the practical problem of post-launch analysis. Fortunately the problem can be reduced to a short list of simple molecular bonds with resonant characteristics corresponding to the optical wavelengths of interest. Examples of the spectra of such molecular or sub-molecular species are shown in Figure 1. These illustrations were chosen to show that similar contaminants can be expected in almost any satellite situation and are very characteristic of sample measurements made on Meteosat, with the added exception of ice which only exists as a stable deposit at low temperatures (below about - 100°C in hard vacuum), see Figure 2.

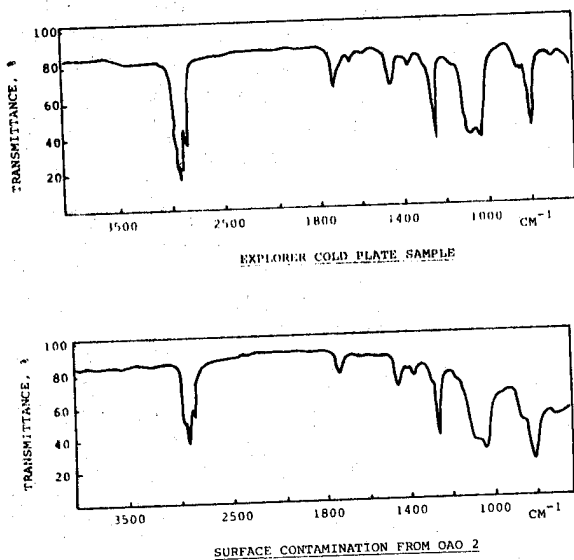


Figure 1 - Typical molecular spectra of satellite surface contamination

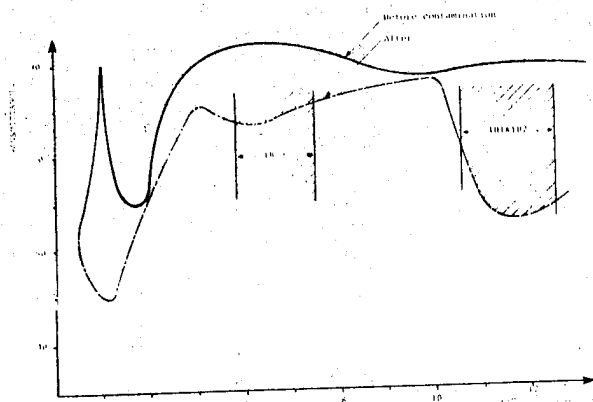


Figure 2 - Optical transmission loss resulting from an ice deposit of 97.8 $\mu\text{g}/\text{cm}$

The situation of a massive contamination build-up is not admitted to in this paper as it would result in a failure analysis rather than performance analysis.

Figure 3 shows the general arrangement of the Meteosat radiometer. This relatively complex configuration and thus differential local ambient environment leads to differing potential contamination problems. For example, the primary mirror is exposed directly to the local general spacecraft background whereas the secondary reflecting surfaces essentially only "see" the internal structure and equipment. Finally, the transmitting relay optics is mainly operating at the cryogenic tempe-

perature of the cooler. The optical cavity was protected by an ejectable cover for most of its ground life, the launch phase and the early orbit phase.

The major potential contamination sources are estimated to be possible micro-leakage of silicon oil from the scan drive assembly, outgassing or offgassing from the internal paint and, exclusively for the cold optics, water vapour contained in or entering the cooler cavity.

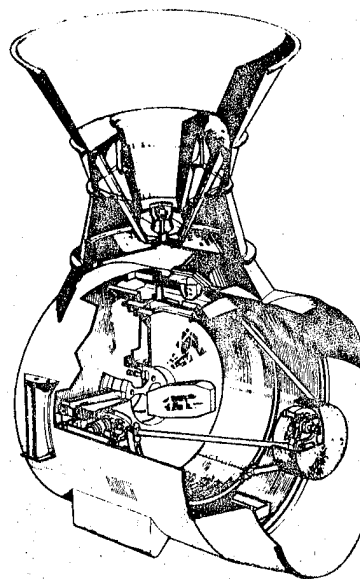


Figure 3 - Schematic of the Meteosat radiometer

3.2 Diagnostic means

Although contamination from any of the above sources will lead to loss of video signal, such a loss is not direct proof of contamination, as evidently loss of electronics gain would give the same first impression. However, various methods of data manipulation and measurement configuration provide means of differentiating the various phenomena. The methods identified utilise the following instrument characteristics:

- Internal electronic redundancy exists allowing a simple identification of gain loss resulting from a component or sub-circuit degradation,
- three grossly different spectral channels are available which allows a low-resolution spectral analysis to be performed,
- an internal black-body calibration source, which is only viewed by part of the optical chain, permits a rough localisation of a problem and hence a useful first-guess of the likely cause,
- Meteosat can view external sources of widely different temperatures; the sun, moon, earth targets and space, which permits a finer resolution, differential spectral analysis by using the known detailed spectral sensitivity differences between the redundant thermal IR channels and utilising the simple spectral

differences between the sources.

3.3 Analysis results

On the two occasions, to date, that measurable, unforeseen signal reduction has been experienced, both during the winters of 1977-78 and 1978-79 which is of significance as we shall see below, the above diagnostic techniques rapidly identified the most likely cause as ice deposition on the cold optics. On the first occasion this diagnosis was immediately confirmed by heating the optical elements above the ice sublimation point and thus restoring the signal level. By the time of the second event the confidence in the analysis was sufficient that an intervention by heating was delayed by four months to schedule it around other activities.

An interesting point to note, concerning this particular contamination problem, is that a certain degree of contamination by ice is now known to have been present in pre-flight thermal vacuum calibration testing. While the level was not a major problem for Meteosat it certainly could be for other cryogenic systems.

4. THERMO-OPTICAL SURFACE CONTAMINATION

4.1 Possible thermo-optical surface contamination

Figure 4 shows a schematic of the passive cooler arrangement. Cooling is achieved by a combination of radiation to space from the second stage and from low α surfaces on the first stage

and sun-shield. The view to space of the second stage is defined by the cooled conical reflector of the first stage. The sun-shield is geometrically configured to prevent any direct or reflected solar energy from entering the system. Thermal isolation is achieved by combinations of low conductivity mechanical support, low radiative coupling and a multi-layer blanket.

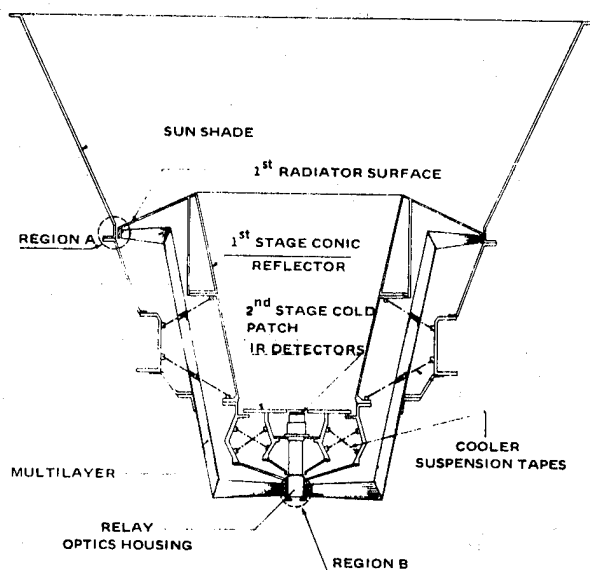


Figure 4 - Schematic of the Meteosat Radiometer cooler

The total arrangement was maintained as a closed cavity for most of its pre-launch life, for the launch phase and for two weeks after orbit acquisition by an ejectable cover. Thus the potential inflight contamination sources are limited to self-contamination or to contaminants from the outgassing cloud around the bottom of the satellite.

The major concerns during development of the equipment were essentially limited to self-contamination by water vapour (ice) and polymer formation on the sun-shield during periods of solar illumination. Ice contamination is a known problem from the NASA programmes (Nimbus and Landsat) and at least one incident of polymer formation has been suspected (ERTS) as a result of solar UV radiation interacting with a simple molecular contaminant.

4.2 Diagnostic means

Only three telemetered temperature measurement points are available for analysis which make precise interpretation difficult. However, with knowledge of design details and performance modelling a satisfactory analysis has been made.

The diagnostic technique cannot depend on monitoring the temperature evolution with time, as this is subject to seasonal fluctuations of greater magnitude than the effects of low-level contamination. However, satisfactory analysis is possible by monitoring the relative temperature evolution between the principal sub-assemblies. This is possible from the theoretical knowledge (confirmed by subsystem tests) that the second stage temperature is predominantly dictated by the first stage and that the first stage is similarly dependent on the sun-shield with a secondary contribution from the radiometer equipment plane, assuming nominal surface properties.

4.3 Analysis results

The space available for this paper only permits us to present a very brief overview of the analysis made on the passive cooler. For the reason we confine ourselves to the findings identified as surface contamination associated phenomena.

In normal operations the cooler second stage (i.e. detector assembly) is actively maintained at 90 K to avoid detector response variations. However, during the first six months of operation the system was allowed to free-run. Since that time the non-controlled temperature has been extrapolated from knowledge of the thermostat reference signal.

Figure 5 shows the relative evolution of the first and second stage temperatures as compared to two pre-flight equipment tests. Detailed differences are the result of equipment and test configurations and need not to concern us here. The important observations are that the inflight data has evolved in a completely consistent fashion even when the absolute temperatures have varied by many degrees, due to a decontamination as well as seasonal fluctuations. This leads to a confident conclusion that the thermal coupling

between these items has not been degraded by any measurable contamination.

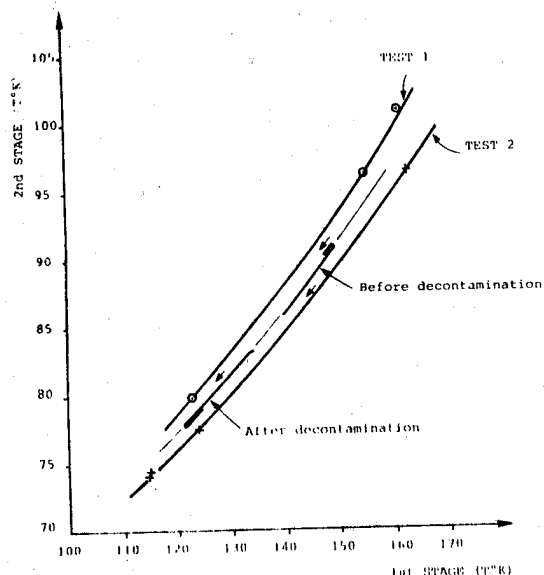


Figure 5 - Relative temperature evolution of cooler first and second stages

Figure 6 showing similar plots for the relative evolution of the first stage and sun-shield, a departure from nominal performance is immediately evident. The evolution is indicated by the small directional arrows. The total time elapse is approximately the first six months in orbit starting in early December 1977. A very rapid initial contamination is evident in the winter which continued, to a lesser extent, after a decontamination in late January, at a rate which decreases into the summer period. Similar but less dramatic results were observed in the following year.

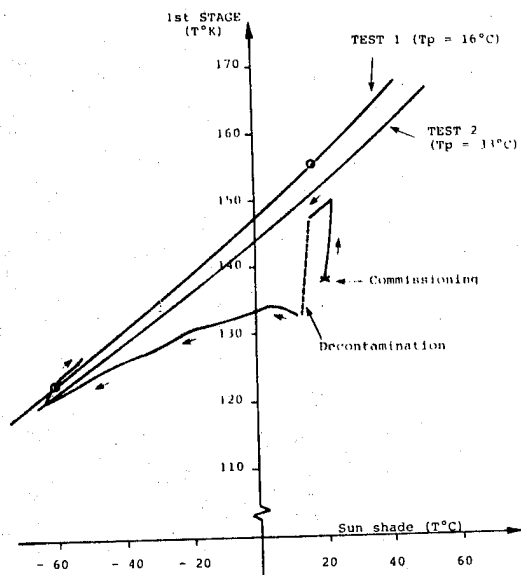


Figure 6 - Relative temperature evolution of cooler first stage and sun-shield

5. CONCLUSIONS OF ANALYSIS

Three distinct contamination phenomena have been identified in flight.

- Low but continuous contamination degrading the exterior thermal coupling of the cooler first stage to its surroundings
- similar but more rapid degradation in the winter months (approximately mid-November to mid-December)
- a contamination of the cold infrared relay optics also in the winter months.

All these problems are believed to be related to condensation of water vapour and all are reversible.

There remains the problem of identification of the source of the water vapour and the mechanism of contamination.

As the degree of re-contamination, following the thermal decontamination, has decreased with time it is evident that the source is finite. This has led to the assumption that the most likely source is the multilayer blanket (see Figure 3). Further, as there exists a thermal gradient from the top (region A) to the bottom (region B) with an average temperature which is maximum in the winter, it is hypothesised that the problem generating the loss of first stage performance is simply off-gassing from end A (average temperature greater than -100°C with maximum in winter) and re-condensation to ice on the local surfaces. Similarly, the loss of optical transmission is the result of off-gassing from end B, during the short period of winter when this region is above -100°C, and subsequent ice formation on the cold optics.

Lack of sufficient measurement points obviously limit this explanation to a "best guess". However, absence of an alternative theory lends support to this idea.

6. GENERAL CONCLUSIONS

With the exception of the water vapour problems it appears that the adopted cleanliness control programme was adequate for the Meteosat Programme. Obviously we cannot confidently state that it was necessary. However, the percentage cost in relation to the total programme (roughly 1 %) can, at the limit, be considered as reasonable assurance much in the same way as many of our quality assurance requirements.

It is possible that the water vapour problems could be avoided by design change. However, this has not been recommended for the following Meteosat(s) as the operation impact has not been major and because we are reasonably confident that an extended decontamination during the commissioning phase will minimise the problem to the level of insignificance.

DISCUSSION

K.J. Burton (BAC) :

What criteria are used to ensure that carcinogens are excluded from use in Spacelab? It would appear that almost daily the medical profession identifies another potential carcinogen, which must make the task very difficult.

J. E. Bennett:

During the design and manufacturing phase we are trying eliminate known carcinogen by reference to published literature eg. *Dangerous Properties of Industrial Materials* - Irving Sax. This is clearly supported by government safety inspectorates.

With respect to the final spacecraft, there is a total offgassing test. SL will be powered up and operated at maximum temperature. Samples are withdrawn from the atmosphere for analysis. The results from this analysis are reviewed by a team and toxicologist at JSC.

W.L. Lehn (USAF) :

What steps are taken to clean the outer β cloth layer of the insulation blanket? You said that an odour problem was noted but cured by heat treatments. Apparently this volatile odour was removed by this heating.

J. E. Bennett:

The contractor using the material does not take any particular precautions to clean the β -cloth; rather the thermal blanket is manufactured in a clean environment by operators using protective clothing.

Any size or similar coating is removed during the manufacture, probably prior to the application of the PTFE. It is certainly specified in the procurement specification.

W.H. Lehn :

Can Betacloth be cleaned?

J. E. Bennett:

Betacloth can be cleaned with isopropyl-alcohol, if care is taken to avoid too much wetting by using cloths. The Betacloth is relatively leak-tight.

J. Bourrieau (ONERA-CERTI-DERTS) :

Have you made studies in the field of radiation-induced spurious background in your detector assembly?

R. Thoman:

Yes, work is being done to measure the scintillation effects produced in the $M_j F_2$ face plate during normal orbital operation (operation in the South Atlantic Anomaly is expected to be impractical).

H. Hintermann (LSRH) :

What are the major reasons why, instead of black paints for radiation absorbance, inorganic coatings are used in certain instances, such as black copper, chromium or nickel?

R. Thoman:

Inorganic coatings are used on Invar and stainless steels; black teflonisation for nonmetal and black 'velvet' anodic treatment for aluminium have been considered, but paint seems necessary for Kapton and the carbon-fibre face sheets of the Optical Bench.

Mr. Greenberg :

I would like to put a question to all the authors and all the participants here who have an interest in contamination. Because I feel we have been a little bit too civilised, I would like to introduce a little controversy by first making a comment and then asking a question.

My comment is that I feel that many of us have been hiding very securely behind the VCM-type specification for materials and feeling rather confident that we can meet these requirements. However, it seems to me that we have very little basis for using VCM in specifying and qualifying materials, rather for using this procedure as a screening test since each functional system is going to behave somewhat differently.

My question to all is :

What direction should we take in the future to make more quantitative use of outgassing data, what sort of a data base do we need to be able to generate this kind of information, and what is our time frame?

Mr. Dauphin :

First, I must say that you have dropped what we in France call "Le pavé dans la mare". I think this also goes for a comment made by Mr. Malloy and to which I wanted to respond anyway. I agree completely with your first comment that the Micro-VCM method is entirely arbitrary, and it has only one thing in its favour: it has been used now for 12 years and we have accumulated a lot of data, which history has proved to be useful. But from there on I have always objected to people, including John Scialdone here, trying to make calculations from VCM data, because we do not know enough about the real kinetics to do that.

Now, what is the situation?

When you want to really calculate the spacecraft contamination, all the necessary tools exist at the present time: you have computer programs to model the spacecraft: you know, approximately, the law of propagation of the molecules, how they will condense etc. I do not say that you know this with high accuracy,

but you know enough for technological purposes. The only limiting factor, I think, is cost. The VCM test has a big advantage in that it costs practically nothing, and this is a reason why I think it will still be useful as a screening test for materials. But each time you will encounter a difficult problem, as for the Meteosat radiometer, the Space Telescope, etc. and you will be forced into running other type of tests. I think balance tests, QCM etc., are the only ones that can be useful at such times and which permit a correct analysis of the situation. The level of complexity of the analyses will depend on the type of item concerned; in the case of the Space Telescope where the enclosure is almost in thermodynamic equilibrium you can have something rather simple; when you have a satellite with openings, with different compartments, with appendices, etc., analysis can become very difficult, but if you have critical items you will have to do this type of test to pay for it.

Mr. Scialdone :

I should like to add something here. I am completely in favour of not using VCM, because of the obvious complex influences of thickness and surface areas etc., but what Jack is referring to is that I sometimes had to use that information in so far that there was no other data available. VCM is a good screening criterion, but that is all. We need the outgassing as function of temperature and time; that is the only way to foresee contamination levels. VCM does not give all the information; I am trying to get people to give at least energy of activation. I have made some attempts to derive energy of activation from the VCM and total material weight loss.

Mr. Greenberg :

Precisely, I agree. All I have heard about here has been VCM and that was an end; nobody was asking for more and that was the frightening aspect for me.

Mr. Dauphin :

Nevertheless, tests cost quite a lot: we can run a VCM test on a material for approximately 300 AU. As soon as we start a balance test on a material we assume a ten times higher cost.

Mr. Moss :

I agree with your statement, but we have to work in the real world, and the programme managers we deal with are 99% electrical engineers and they do not even understand material problems. I have found after some years I have been able to convince them that there are indeed materials and materials problems and outgassing is one of them and that they should be willing to pay for some material tests. Having educated them this far, I intend to continue educating them, and we all have to do the same, recognising that there are other useful

tests. Some organisations have run them for years, TRW have been running microbalance, weight-loss, measurements for years as a function of time and temperature; they have run them at various temperatures for up to 256 hours and they can plot weight losses and these curves are extremely useful. They are showing at least initial reaction rates and that is all very nice, but they run only one material a time, which is expensive. Earlier in the week somebody talked about spending 1% of the entire budget for a programme on materials; in my own company we do not even spend that much on materials control, and so what you are asking is a significant change in thinking and having tried to get programme office people to change their thinking and working at this for some years, all I can say is "good luck".

Mr. Reynolds :

I would like to add one further comment to that. It is very good to talk about quantifying VCM or quantifying outgassing. I think it is essential at the same time to quantify the effects of those, because without that you still have no control or no controlling influence.

Mr. Molloy :

This question on the validity of VCM tests is very serious. Take the example of the high VCM foam we used on L-band antenna on Marecs. If it had been within the 1%/0.1% specification, we would have taken no precautions to protect the IR sensors and we would not have been aware of whether there was any problem or not.

Mr. Dauphin :

Objection : After the first thermal test you would have seen the contamination.

Mr. Molloy :

But that would have been too late.

Mr. Dauphin :

No, there would have been another panic!

Mr. Thomas :

You can in fact get activation energies and make predictions. We run three different tests at different temperatures on the same material, a silicone rubber, the material temperature is 50, 80, 125 °C and the collector is always -25°C.

Mr. Minges :

Despite the logic of the view about a more quantitative approach, I do not see any particular trend within the Air Force now to actually do this.

SESSION VI

ENVIRONMENTAL EFFECTS – CHARGING UP

Co-chairmen: J. Guillin & M.L. Minges

N80-21439

ELECTROSTATIC CHARGING AND SPACE MATERIALS

J Bosma & F Levadou

ESA/ESTEC, Noordwijk, The Netherlands

The qualification of materials for space application is based on established criteria as thermal control ability, contamination effects, stability in space environment.

Spacecraft charging effects have emphasized the relevance of electrostatic cleanliness aspects of materials.

Since several years, the ESTEC Materials Section has been involved in research and development activities to study the effects of electrostatic charging on thermal control coatings.

This paper will illustrate that there is extensive progress in this field of investigation and that from the materials points of view electrostatic cleanliness can be implemented in a cost effective manner on future spacecraft projects. The materials will be discussed on the basis of experimental data obtained in house or under ESA contract.

A survey of the on-going activities in several major European laboratories on electrostatic charging and the future activities and policy of the Materials Section will complete the presentation.

1. INTRODUCTION

During the past decade there has been been considerable European effort to understand and solve the problem of spacecraft charging.

The recognition of electrostatic charging as a potential hazard to geosynchronous satellites has never been unanimous and the approach to the new phenomenon tends to vary from one project to another.

For scientific satellites the charging of the outer skin to moderate potential levels is already sufficient to disturb the operation of the experimental payload. Application satellites are less critical to charging, but subsequent discharging may cause malfunctions of various subsystems.

For the ESA Scientific Programme, it was evident that charging effects could be detrimental to various plasma experiments on geosynchronous satellites. Europe's answer to the problem was the development of a spacecraft with a conductive outer skin. The solution is based on the principle that application and interconnection of conductive surface materials will avoid

differential charging and establish a uniform potential on the spacecraft surface.

GEOS demonstrated that this approach was feasible; it was the first satellite to have a surface that is more than 96% conductive. (Figure 1)

GEOS was also a very costly step to solve spacecraft charging. It required the development of new conductive materials and the implementation of strict electrostatic cleanliness requirements.

The initial attitude of the application programme was often one of scepticism, partially brought about by the high costs involved to implement the GEOS solution.

While spacecraft charging could jeopardize the actual object of a scientific mission, application satellites can tolerate surface potentials of up to several hundreds of volts, provided discharges are avoided.

Elimination of discharges by selection of adequate materials proved to be difficult in the early phase of the application programme, because thermal control design was based on conventional materials. Many of these materials are non-conductive and will not support high potential levels. The subsequent discharges generate electromagnetic interferences, which are capable of upsetting logic circuitry and damaging electronic components.

Some projects regard electronics hardening as a sufficient measure to limit spacecraft anomalies induced by discharges. This solution, however, does not stop degradation of thermal control coatings and enhanced contamination due to the attraction of charged contaminants. These accumulated effects could become serious on long term missions.

The worst situation exists when no precautions are implemented on a spacecraft. Once in orbit, anomalies are often attributed to spacecraft charging without supporting evidence, which can create an over-reaction of the project concerned. (Figure 2)

It is obvious that no matter which approach a project prefers, spacecraft charging is essentially a materials problem.

Through the years ESTEC Materials Section has been

involved in research and development activities to study the effects of electrostatic charging on thermal control coatings.

The policy has been to characterize conventional materials and to search or develop new conductive solutions where necessary.

This paper will illustrate that there is extensive progress in this field of investigation and that from the materials point of view electrostatic cleanliness can be implemented in a cost effective manner on future satellite projects.

2. GENERAL MATERIAL REQUIREMENTS

Passive thermal control of spacecraft is accomplished by a wide range of surface finishes.

Conventional thermal control materials are generally characterized by four extremes :

1. Total Absorbers : Surfaces having high solar absorptance (α_s) and high infra-red emittance (ϵ), e.g. black paints.
2. Solar Absorbers : Surfaces having high absorptance and low emittance, e.g. black metals.
3. Solar Reflectors: Surfaces having low absorptance and high emittance, e.g. white paints.
4. Total Reflectors: Surfaces having low absorptance and low emittance, e.g. white metals.

Between these extremes there are so-called median ranges.

Ideally conductive thermal control materials should be developed to cover each category. For categories 2 and 4 the solution is straight forward because spacecraft surfaces having these particular thermo-optical properties tend to be metals that are themselves conductive.

Categories 1 and 3 include a variety of non-conductive materials : polymers, paints, composites, glass, quartz and fabrics. Many of these coatings were developed particularly for space application.

Finding conductive alternatives for these materials proved to be more problematic.

Space qualification requirements further limited the number of candidate conductive coatings. The ESTEC Materials Section maintains a strict guideline on the acceptance of materials for space application.

First a thermal control material is "prequalified", which implies that the outgassing properties are in agreement with ESA Specification PSS-09/QRM-02T (TWL : <1%, VCM < 0.1%)³ and that the material has successfully passed the following tests :

Decontamination
Humidity
Thermal Cycling
Thermal Shock
Vibration

Successfully means that changes of any relevant properties (i.e. solar absorptance, emittance, electrical conductivity, adhesion) are in agreement with the requirements of a specific satellite project. A thermal control material is "qualified" when it is first prequalified and then it has successfully passed the ultra-violet and particle irradiation tests as described in ESA Specifications PSS-37/QRM-06T⁽¹⁾ and PSS-34/QRM-07T⁽²⁾, "successfully" keeping the same definition as above.

3. MATERIALS CHARACTERIZATION FOR SPACECRAFT CHARGING

Spacecraft charging is a complex phenomenon which depends on the spacecraft plasma environment, the electrical properties of the surface materials and the geometrical configuration of the spacecraft outer surface.

The actual potential levels achieved will depend on various current components⁽⁴⁾ :

- Incident Ambient Electrons;
- Incident Ambient Ions;
- Photoemitted Electrons;
- Backscattered Electrons;
- Secondary Electrons.

These potential levels will vary for the different materials applied on the exterior of the spacecraft surface. If the differential potential exceeds, the breakdown voltage for the specific material geometries, a discharge will occur.

There are four basic locations for a discharge⁽⁴⁾ :

- Between adjacent metallic elements which do not have a common ground;
- Between a dielectric material and a metallic surface or backing;
- Between neighbouring dielectrics;
- Between an insulator surface and space.

From this short summary it is obvious that laboratory simulation of the electrostatic behaviour of materials is always subjected to various limitations.

Scaling factors, complex geometries, expected particles energy distribution are among others difficult parameters to incorporate in a test. The most common technique employed up to date is the exposure of a material to a normally incident mono-energetic electron beam in a vacuum chamber. This is a relatively simple approach to the complex problem of spacecraft charging, which already requires sophisticated instrumentation. The question arises : "How to interpret the results of small scale laboratory tests?" Compared to several other material properties which are relevant to space application e.g. thermo-optical properties, the electrostatic behaviour of a material depends very much on random conditions in the actual application. In particular discharging will depend on such factors as total area, adjacent materials, grounding techniques, etc.. Small scale laboratory tests should be considered as a screening test method to indicate the susceptibility of a material to spacecraft charging. The probability that a material will meet the electrostatic cleanliness requirements of a

satellite will depend on the number of simulation factors incorporated in a test. The actual performance of an integrated material can only be established by in-flight data and to a less extent by ground testing of spacecraft models. This is definitely the case for non-conductive materials which are susceptible to discharging. For conductive materials, small scale laboratory tests will already give fairly reliable information if the basic electrical properties of a material are adequate to meet the electrostatic requirements of a specific satellite project.

4. STANDARD TEST METHODS USED BY ESTEC MATERIALS SECTION

For prequalification testing of conductive materials surface and volume resistivities are the standard discriminating parameters used by ESTEC Materials Section (5), (6).

In general a conductive material is evaluated to meet the requirements of a scientific satellite; these are that an exposed spacecraft surface must allow the plasma currents to that surface to flow either to spacecraft ground or to the sunlight portion of the surface without generating potentials in excess of 1V.

Once the conductive material has passed the prequalification phase, its electrostatic behaviour is characterized in a simulated substorm environment.

Most of the ESTEC Materials Section simulation experiments have been performed under contract at DERTS Toulouse.

Several tests have also been performed in the Materials Section substorm facility. Both facilities will be described in more detail in the annexed "Survey of European Laboratories". Standard test parameters are :

- Surface Voltage Profile;
- Sample to Holder Leakage Current;
- Breakdown Transient Current;
- Photography of Discharge Patterns.

Recently the DERTS facility has been upgraded to measure :

- Secondary Emission Currents;
- Surface Leakage Currents.

Both facilities have the possibility of illuminating irradiated samples with ultra-violet light at solar simulation levels and modification of the sample temperature.

5. REVIEW OF TESTED MATERIALS

The materials will be discussed on the basis of experimental results in the following sections. This section will compile relevant basic information on the tested conductive materials. Test data will refer only to ESA sources. The data is presented as a summary for potential users.

5.1. Conductive Black Paints

5.1.1. Chemglaze H322.

- Nature : Polyurethane Paint, High Temperature Cure;
 - Manufacturer : Hughson Chemical Corp. U.K.;
 - Prequalified : On Kapton Substrate;
- (7) (8) (9)

: On Aluminium Side of Aluminised Mylar;
On Aluminium Side of Aluminised Kapton;
On Aluminised Kapton with Lesonal 01-66050 Primer;

- Qualified : Ultra-violet and Particle Irradiation for 3 year Geosynchronous Orbit;
(27) Solar Absorptance Degradation $\Delta\alpha_s = -0.03$.

- Electrical Properties : Surface Resistivity on
(5) (6) Aluminium Substrate :
 $\rho_s = 0.6 \text{ K}\Omega$;
Surface Resistivity on Kapton Substrate :
 $\rho_s = 5.5 \text{ K}\Omega$;

- Flight Experience : GEOS
ISEE-B
To be used on MARECS.

5.1.2 Chemglaze L300

- Nature : Polyurethane Paint, Room Temperature Cure;
- Manufacturer : Hughson Chemical Corp. U.K.;
- Prequalified : With Pyrolac P123 Primer;
(10) (11) (12) On Kapton;
On Aluminium Substrate;
On Aluminium Kapton Laminate;
- Qualified : No data available;
- Electrical Properties : Surface Resistivity on Aluminium : $\rho_s = 3 \text{ K}\Omega$
Surface Resistivity on Kapton : $\rho_s = 2.5 \text{ K}\Omega$
- Flight Experience : Recommended for ECS.

5.2 Solar Reflector Materials

5.2.1 Optical solar reflector (rigid)

- Nature : Quartz Substrate with Silver Reflector and a Conductive Top Layer of Indium-Tin-Oxide;
- Manufacturer : OCLI, U.S.A.;
- Prequalified : On Aluminium Substrate with DC 6-1104 Adhesive;
- Qualified : Ultra-violet and Particle Irradiation for 3 year Geosynchronous Orbit;
(27) Solar Absorptance Degradation :
 $\Delta\alpha_s = +0.03$;
- Electrical Properties : Surface Resistivity :
 $\rho_s = \text{K}\Omega$ -range;
- Flight Experience : GEOS.

5.2.2 Optical solar reflector (rigid)

- Nature : Cerium Doped Glass with Silver Reflector and a Conductive Top Layer of Indium-Tin-Oxide;
 - Manufacturer : PPE, U.K.;
 - Prequalified : On Aluminium Substrate with DC 6-1104 Adhesive;
 - Qualified : Ultra-violet and Particle Irradiation for 3 years Geosynchronous Orbit;
(27) Solar Absorptance Degradation :
 $\Delta\alpha_s = +0.02$;
 - Electrical Properties (16) : Surface Resistivity:
 $\rho_s = \text{K}\Omega$ -range;
- Electrostatic simulation test in combination with conductive adhesive RTV 566 loaded with Cho-Bond 1029B : Low surface potential and no discharges for 20-30 KeV electrons with current

densities 1-10 nA/cm².

- Flight Experience : ISEE-B.

5.2.3 Second surface mirror (flexible)

- Nature : 75 μ m Aluminised FeP Teflon with a Conductive Top Layer of Indium-Tin-Oxide;
- Manufacturer : FeP Teflon : Sheldahl U.S.
Indium-Oxide : Deposited by Balzers Liechtenstein;
- Prequalified : No;
- Qualified : Not complete;
Ultra-Violet Tests : (25);
Derts : 1000 ESH at Room Temperature $\Delta\alpha_s = + 0.02$;
Estec : 500 ESH at 80°C
 $\Delta\alpha_s = - 0.03$;
- Electrical Properties : (24) (25);
Surface Resistivity : K Ω -range;
Electrostatic Simulation Test : Surface Potential smaller than 10V, no discharges for 5 to 25 KeV electrons with current densities 1 to 5 nA/cm²;
- Flight Experience : No.

5.2.4 Second surface mirror (flexible)

- Nature : 125 μ m Silver FeP Teflon with a Conductive Top Layer of Indium-Tin-Oxide;
- Manufacturer : Sheldahl U.S.
- Prequalified : No;
- Qualified : Not Complete;
Ultra-violet Tests :
Derts : 1000 ESH at Room Temperature :
 $\Delta\alpha_s = + 0.05$;
Estec : 700 ESH at 80°C :
 $\Delta\alpha_s = + 0.03$
- Electrical Properties : Surface Resistivity : (24) (25) M Ω -Range;

5.2.5 White conductive paint NS43C

- Nature : Silicate Paint, Room Temperature Cure;
- Manufacturer : NASA Goddard U.S.
- Prequalified : On Aluminium Substrate; (21)
- Qualified : Not by ESA, but by Goddard for ISEE project;
2000 ESH UV and 4×10^{16} ρ /cm²
Solar Absorptance Degradation :
 $\Delta\alpha_s = + 0.12$
(Goddard Reference)
- Electrical Properties : Surface Resistivity on Aluminium Substrate :
 $\rho_s = 14 \times 10^6 \Omega$
Volume Resistivity :
 $\rho_v = 6.3 \times 10^5 \Omega m$
- Flight Experience : GEOS (small experiment) ISEE-A.

5.2.6 Silica Fabric Brochier 20766

- Nature : Woven Fabric Based on Medium-Purity Silica Fibers, Heat Treated at 800°C;
- Manufacturer : Brochier France;
- Prequalified : No;
- Qualified : Not Complete, Ultra-Violet Test : (24) (25) 900 ESH at Room Temperature :
 $\Delta\alpha_s = 0.12$

- Electrical Properties :
High secondary emission conductivity. Electrostatic simulation test : Surface potentials up to kV-range, no discharges occur for electron energies up to 15 KeV with current density of 1 nA/cm². At 20 KeV : small discharges;

- Flight Experience : No, but a high purity material "Astroquartz" manufactured by General Electrics U.S. has been flown on USAF satellites.

5.3 Conductive Aluminium Paints

5.3.1 Conductive PSG 173

- Nature : Silicone paint with aluminium pigment and silver flakes for conductive loading;
- Manufacturer : CNES/ASTRAL France;
- Prequalified : Not by ESA, but there has been a prequalification by CNES high outgassing rate;
- Qualified : No;
- Electrical Properties : Surface resistivity : <1 Ω ;
Electrostatic Simulation Test : Surface potential smaller than 10V, no discharges for 5 to 20 KeV electrons with current densities 1-5 nA/cm²;
- Flight Experience : No.

5.3.2 Conductive aluminium paint

- Nature : Silicone paint with aluminium pigment and silver powder for conductive loading;
- Manufacturer : Estec Formulation;
Silicone : Owens Illinois 650;
Aluminium pigment : Alcan MD5100;
Silver powder : XRP-1;
- Prequalified : In process;
- Qualified : No;
- Electrical Properties : Surface Resistivity : <1 Ω ;
- Flight Experience : Intended for Spacelab Experiment.

5.4 Multi-Layer Insulation Blankets

5.4.1 Conductive aluminised Kapton

- Nature : 125 μ m Kapton H film with aluminium reflector and a conductive top layer of indium-tin-oxide;
- Manufacturer : Aluminised Kapton : Sheldahl US;
Indium-Tin-Oxide : Deposited by General Electric U.S.;
- Prequalified : In combination with conductive grounding bonds consisting of aluminium straps with conductive adhesive RIV 566 loaded with Cho-Bond 1029B; (23)
- Qualified : No;
- Electrical Properties : Surface resistivity : K Ω -range;
Electrostatic Simulation Test : Surface potential smaller than 10V, no discharges for electron energies 5-20 KeV with current densities of 0.5 to 1.25 nA/cm²;
- Flight Experience : No.

5.5 Conductive Adhesives

5.5.1 Conductive RTV 566

- Nature : Silicone Rubber RTV 566 loaded with silver powder Cho-Bond 1029B;
- Manufacturer : Estec Formulation; RTV 566 : General Electric USA; Cho-Bond 1029B : Chomerics USA;
- Prequalified : For conductive grounding of aluminised Kapton tape (aluminium space exposed). For conductive grounding of ITO coated aluminised Kapton. For conductive adhering of OSR's;
- Qualified : Not applicable for underlying adhesive;
- Electrical Properties : Contact resistance of 100 $\mu\Omega$ layer between two aluminium plates : smaller than 10 Ω ;
- Electrostatic Simulation Tests : In combination with PPE conductive OSR (16). In combination with ITO coated aluminised Kapton (23). In both cases surface potentials smaller than 10V, no discharges for electron energies 5-20 KeV with current densities 0.5 to 1.25 nA/cm² for Kapton and 1 to 10 nA/cm² for OSR.

6. ELECTROSTATIC SIMULATION TESTS OF NON-CONDUCTIVE MATERIALS

6.1 General Behaviour of The Irradiated Sample

The impinging electrons on the sample surface cause a charge displacement in the conductive substrate which accounts for the initial high leakage current. This "displacement" current decays with time, because the incident electrons are partially retarded by a potential build-up on the sample surface.

There are two cases to be considered :

Case A The potential build-up is sufficient to decrease the number of incident electrons to a value which can be removed by leakage paths and secondary emission of the sample. An equilibrium potential is obtained which is lower than the breakdown voltage of the test material.

Case B The charge removal is at all times smaller than the number of incident electrons. The test sample will charge to the breakdown voltage of the sample at which time an abrupt drop in surface potential occurs. It is assumed that this is caused by a discharge of a large surface area. After the discharge the leakage current jumps to a high value and starts to decay until a new discharge takes place.

The discharges described in case B are identified as "large", in contradiction to "small" discharges, which do not considerably modify the surface potential and are assumed to be "point" discharges. This latter type can occur in both cases A and B.

6.2 Electron Irradiation Tests of OTS Thermal Control Coatings

6.2.1 Scope

These tests were performed at Derts Toulouse for various thermal control materials applied on the OTS geosynchronous satellite. The actual tests are

described in (13). This section gives a survey of the main results.

6.2.2 Materials tested

- 3 Mil silver FeP Teflon adhered to an aluminium substrate with 3M 467 tape;
- 3 Mil aluminised Kapton (with vent holes) adhered to aluminium substrate with RTV 566 conductively loaded with Cho-Bond 1029B;
- 3 Mil aluminised Kapton (without vent holes) adhered to aluminium substrate with RTV 566 conductively loaded with Cho-Bond 1029B;
- 3 Mil aluminised Kapton (without vent holes) adhered to aluminium substrate with RTV 566 silicone adhesive;
- Multilayer insulation blanket with external aluminised Kapton layer;
- OCLI OSR's adhered to aluminium substrate with RTV 566 silicone adhesive;
- Aluminium honeycomb with glass fibre/epoxy resin top layer coated with S13GLO white silicone paint.

6.2.3 Test conditions

The tests were performed in the earlier irradiation chamber at Derts Toulouse. The samples were irradiated with electrons of increasing energy, starting from 5 KeV up to 30 KeV with current densities of 0.1 nA/cm² to 2 nA/cm² until discharges were observed. When the conditions for electrostatic discharges are obtained, the sample remains irradiated and is allowed to discharge during 6 hours.

6.2.4 Test results

The test results are documented in Table I.

6.2.5 General observations

All tested samples demonstrated charging and discharging effects. The highest potential levels were achieved by the silver teflon sample.

Adhering of the aluminised Kapton sample with a conductive adhesive decreased the maximum potential level and the number of discharges as compared to a non-conductive adhesive mount. It also minimised the degradation effects on the aluminised Kapton.

The honeycomb coated with S13GLO showed the highest rate of large discharges, which started at a relatively low incident electron energy. Illumination with ultra-violet light showed a clear response of all Kapton samples. The leakage current increased and the surface potential was almost minimised. No discharges occurred during illumination.

The other samples showed no response, but this could be caused by the fact that the incident light did not contain wavelengths shorter than 320 nm.

6.3 Electrostatic Charging Tests of Conductive and Non-Conductive Optical Solar Reflectors

6.3.1 Scope

This research was performed to evaluate various ways of limiting electrostatic discharge effects on optical solar reflectors. The investigations have been published in detail in various recent reports (16) (17) (18) (19) (26).

This section will give a listing of the main conclusions.

6.3.2 Conclusions

The successive testing of different OSR/adhesive systems in ESTEC's Materials Section has indicated that both OCLI and PPE OSR's with a conductive indium-tin-oxide top layer in combination with a conductive adhesive are most reliable as regards their ability to withstand charging and discharging effects in a substorm environment. Such an OSR/adhesive system makes interconnection and conductive pads superfluous.

The backing of the OSR should definitely not be provided with a protective insulating layer. PPE standard non-conductive OSR's may be applied in combination with a conductive adhesive, provided that they are operated at room temperature or higher. OCLI standard non-conductive OSR's are not recommended for the same application since the high bulk resistivity of the quartz will cause charging and discharging. (Fig. 3, Fig. 4)
The conductive adhesive referred to is always the RTV 566 with Cho-Bond 1029B conductive loading.

6.4 Electrostatic Simulation Test of Improved Aluminised Kapton

6.4.1 Scope

Electrostatic discharge testing of a large sample of multilayer thermal blanket applied on OTS had indicated that evaporation of relatively large areas of the vacuum deposited aluminium on the back of the outer Kapton layer occurred as a result of numerous discharges. The solution proposed to this problem was to raise the thickness of the aluminium layer from 1000 Å (VDA) to 25 µm. (laminated)
The result of this test has been published in (20).

6.4.2 Conclusions

A small scale mono-energetic electron irradiation demonstrated that the improvement sought is indeed achieved.

The Kapton with 1000 Å aluminium showed considerable evaporation of aluminium after app. 80 discharges varying from 20 to 90 ampere peak current pulse. (Fig. 5).

The Kapton with 25 µm aluminium showed no visible degradation after app. 90 discharges of similar magnitude.

This is an example of how projects who prefer to harden electronics may also avoid extensive materials degradation due to discharging. It must be kept in mind, however, that this is only a short-term solution.

7. RESEARCH AND DEVELOPMENT PROGRAMME OF A CONDUCTIVE SOLAR REFLECTOR (24) (25)

7.1 Scope

In the frame of research and development, Materials Section have had different contracts with DERTS (Toulouse). The aim of one of these contracts was definition and realization of a thermal control coating having the following properties :

- low value of the ratio α/ϵ (cold coating);
- electrically conductive;
- space qualified.

The contract has been divided into two parts. The first phase was an evaluation of the possible different techniques. Three have been studied into detail :

- transparent conductive layers deposited on flexible polymeric materials;
- quartz tissues;
- conductive pigments or charges for a paint, or conductive flexible transparent materials used as SSM.

A critical study of the bibliography and a theoretical evaluation of the different solutions with some preliminary tests made in the DERTS laboratories have shown in what direction phase 2 will be directed.

Phase 2 has consisted in a deep study of mainly two different solutions with a follow-up on quartz tissue.

- FeP SSM covered with Indium Oxide;
The type which has been studied was a 3 Mil SSM manufactured by SHELDON on which an ITO layer has been deposited by BALZERS.
- Nafion film as an SSM.

Commercialized by DUPONT DE NEMOURS, Nafion is a fluorinated polymer of the perfluorosulfonic acid. Nafion could be used either as a pigment for a conductive paint or as a second surface metallized film. These two techniques had been studied during the first phase. The latter (SSM) has been chosen as the most promising.

Studies during the first phase have shown that the optical transmission of the Nafion film was improved if the film is washed in methanol. Also the transmission is improved either if the hydrogen of the acid function is exchanged by a metallic carbon, or if the film is treated by polyethylene-glycol.

These are the reasons why the following different solutions for Nafion have been tested during this second phase.

- Commercial film (type 125);
- Type 125 washed with methanol;
- Type 125 washed with methanol, sodic form;
- Same with an ITO layer;
- Type 125 washed with methanol, treated with PEG 1500;
- Same with ITO layer.

On all of these films aluminium has been vacuum deposited by DERTS. Nafion film has been prepared by IRCHA France to obtain the salt forms.

7.2 Tests and Measurements Performed

The following tests and measurements have been performed by DERTS on all samples :

- Measurement of electrical resistance including influence of a bending test over cylinders of various dimensions;
- Electrostatic simulation test consisting of
 - * measurements of surface potentials at different energy levels and currents of incident electrons;
 - * detection of discharges if any;
 - * effect of electron irradiation on electrical resistance;
 - * effect of bending on electrostatic behaviour;

- Measurement of reflectance;
- UV irradiation tests.

7.3 Results

The main results obtained during the contract are the following :

FEP SSM film. Coating with an ITO layer seems to be a very good conductive solution. The surface potential under electron irradiation is very low (<10 Volts), no detectable discharging and a very good stability under UV irradiation. Table II gives electrical resistance and Fig. 6 gives the change of solar reflectance with irradiation time.

The SSM prepared by BALZERS is more stable than the commercial one from SHELDON. In general it appears that the ITO layer acts like a UV filter and protects the film underneath. The UV degradation with ITO layer tends to be lower than without.

Nafion SSM film seems to be a promising solution, mainly the potassium sulfonate form. The surface potentials reached during electrostatic testing stay low (<350 Volts). These films are affected by UV irradiation. Complementing studies will certainly be necessary to improve the vacuum stability as well as the UV stability. Fig. 7 gives the change of electrical resistances under vacuum exposure. Fig. 8 and Fig. 9 give the change of solar reflectance with irradiation time.

Quartz tissue

The studies performed during the phase 1 of the contract show that the surface potentials for monoenergetic electron irradiation are rather high (up to KV-range). Lower values of the surface potential might be measured with polyenergetic beams including low energies (2 to 5 KeV). There appears to be no arcing risk for monoenergetic electron irradiation.

The degradation under UV irradiation of the tested medium purity fibres is high. Fabrics made of high purity Silica should have better UV-stability, the yarns can be procured at Quartz et Silice France. Fig. 10 shows the change of solar reflectance with UV irradiation time.

8. NEW GROUNDING TECHNIQUES BASED ON CONDUCTIVE ADHESIVES (14) (15) (23)

8.1 Scope

A variety of new conductive materials has been developed to avoid spacecraft charging effects. The deposition of a thin layer of indium oxide on a conventional thermal control material has become a favoured technique. One of the first applications of this technique was the indium oxide coated rigid optical solar reflector (OSR) which was flown on the GEOS and ISEE-B satellites. These OSR-panels consisted of small individual units (2 x 4 cm) which were each grounded or interconnected by 4 conductive tabs on each corner of the indium oxide surface. This method of a large ratio of grounding points to exposed thermal control surface gives a high reliability that the electrostatic cleanliness requirements will be maintained during satellite lifetime. This type of panel is however very

expensive and involves considerable labour due to the mounting and interconnection techniques. A solution to avoid interconnection is the mounting of the OSR's with a conductive adhesive. This option has already successfully passed electrostatic simulation testing, as has been described in section 6.3.

Following the general trend to cut expenses it is a logical step to apply indium oxide layers on the cheaper flexible polymer materials e.g. second surface mirrors (SSM) and multi-layer insulation blankets. These materials are provided as a sheet, which simplifies application techniques. It is obvious that more attention will be required for the grounding methods as not to increase application costs of the sheet material due to numerous grounding points as is the case with the OSR panel.

The minimum amount of grounding points will depend on several considerations: (22)

- Type of grounding point (shape, physical dimensions).
- Maximum permissible surface voltage on the satellite outer skin.
- Reliability of a grounding point in space conditions.
- Configuration of the grounding points over the thermal control coating.

ESTEC Materials Section has developed a grounding technique based on RTV 566 with CHO-bond 1029B conductive loading.

8.2. Bonding Method

As is common with many conductive silicone adhesives, the bond line must be very thin (app. 5 to 10 mil) and the cure must take place under pressure (200 gram load). The adhesive can be cured at room temperature, but curing at an elevated temperature (e.g. 160°C) is more rapid. So that pressure and a high temperature could be applied simultaneously to small awkwardly situated areas, a special heated probe was developed.

The tool is a Weller Weep-Tetronik solar station with the iron modified.

The face of the hot end has a raised area 0.7mm in height which when pressed down to the level of the ceramic grip produces a load. The stainless steel spring spanner increases or decreases the load by rotation.

The probe is held by the ceramic grip and the hot end applied to the desired place.

8.3. Examples of application

8.3.1. Grounding of aluminised Kapton Tape (14)

For the GEOS thermal control, aluminised kapton tape was applied for thermal trimming with the aluminised surface exposed to space.

Each tape segment had to be electrically interconnected and integrated segments grounded to the spacecraft structure. One solution which was however not flown, was with RTV566 + CHO-bond 1029B. The grounding system was based on the cutting of triangles in the tape to expose the underlying aluminium structure. Conductive adhesive was applied in the triangle, covered with an aluminium foil tab after which an earlier version of the heat probe was applied, to cure the adhesive. This grounding method passed pre-qualification.

8.3.2. Grounding of Indium-Tin-Oxide coated aluminised Kapton tape (23).

This investigation is part of a study to develop new methods of electrical connection for flexible second surface mirrors coated with ITO. The connection by mechanical means such as bolts or rivets is not successful due to the breaking of the very thin Indium-Tin-Oxide, with subsequent loss of electrical conduction.

The basic material is 5 mil aluminised Kapton on which a layer of I.T.O. has been deposited. An aluminium strap of 8mm width and 30mm thickness is bonded to the top layer by means of the conductive adhesive which is cured with the heat probe. This grounding method successfully passed pre-qualification testing.

A test panel of ITO coated aluminised kapton with four conductive adhesive bonded grounding straps followed the pre-qualification programme and was submitted to simulated substorm environment in the Derts laboratories in Toulouse. The results show that the panel surface potential did not exceed 10V and that discharges did not occur.

8.3.3. Conclusions The conductive adhesive system developed by ESTEC Materials Section is very versatile and can be used as a means of solving a wide variety of grounding problems. It has already been successfully pre-qualified for several applications.

9. FUTURE ACTIVITIES AND POLICY.

Up to now, materials characterization for spacecraft charging has been based primarily on mono-energetic electron beam irradiation. Future techniques should include the interaction of a low energy plasma with a charged surface. This type of experiment would represent a more realistic simulation of geosynchronous orbit conditions and could be performed on large test samples of materials, which have already passed standard electrostatic tests with mono-energetic beams. More data on additional environmental effects are needed, including:

- temperature effects,
- solar illumination effects,
- aging effects.

Recent studies have shown that secondary electron emission plays a major part in obtaining equilibrium conditions. More information on secondary emission characteristics of materials will be necessary. The utilisation of coatings with pronounced secondary emission to control surface potentials may be possible.

The ultimate policy should be to avoid substantial charging of the exposed surface. Even then there will still be the problem of enhanced contamination due to the attraction of charged contaminants. Besides changing the thermo-optical properties, these contaminants could also change the electrostatic behaviour of the surface. For the near future, ESTEC Materials Section intends to specify and develop a standard screening test method for the selection of space materials based on their electrostatic behaviour under exposure to a simulated geomagnetic substorm environment.

The avoidance of surface charging will become "state of the art" in future spacecraft projects. Breakdown voltage, secondary emission, surface and volume resistivities are amongst others, parameters which vary from batch to batch and a continuous screening of these properties for new, as well as conventional materials is evident.

REFERENCES

1. Dauphin J.
Guidelines for the simulation of the degradation of surface properties under combined UV/particle irradiation. ESA PSS-37/QRM-06T.
2. Dauphin J.
Guidelines for the simulation of materials degradation due to particle irradiation in space. ESA PSS-34/QRM-07T.
3. Zwaal A.
A screening test method employing a thermal vacuum for the selection of materials to be used in space. ESA PSS-09/QRM-02T.
4. Holman A.B.
Spacecraft charging standard.
S.A.I. Document CDRL 01 A2 July 1978.
5. Bosma S.J.
Evaluation of three methods of measuring the surface resistivity of Hughson conductive black paint. ESA TM170 November 1976.
6. Bosma S.J., Levadou F.
Measurement of the surface and volume resistivity of Hughson H322 paint with Lesanol primer. ESA TM 173 September 1977.
7. Froggatt M.F.
Specification for application of Hughson H322 black electrically conductive coating. ESA PSS-24/QRM-18P issue 1.
8. Froggatt M.F.
Application of chemglaze H322 black electrically conductive coating utilizing Lesanol 01-66050 as primer. ESA QRM-34P Draft issue.
9. Froggatt M.F.
Prequalification tests on two thermal control coatings for OTS/ISEE-B. ESA EWP 1003.
10. Froggatt M.F.
Application of chemglaze L300 conductive coating, utilizing pyrolac P123 as primer. ESA QRM-35P Draft issue.
11. Froggatt M.F.
Prequalification of the paint system chemglaze L300/pyrolac P123 as applied on 4 MIL aluminium/kapton laminate. ESA EWP 1140.
12. Froggatt M.F.
Prequalification of chemglaze L300, black electrically conductive paint utilizing pyrolac P123 as primer. ESA EWP 1163.
13. Levy L.
Irradiations par électrons de revêtements de contrôle thermique.
ESTEC contract 2638/76/NL/MD October 1976.
14. Bosma S.J., Froggatt M.F., Gourmelon G.
Evaluation of a conductive adhesive system for the grounding of aluminised kapton tape. ESA STM 204. June 1978.
15. Gourmelon G., Froggatt M.F.
Evaluation of three conductive adhesives for use on ECS. EWP 1010 May 1976.

16. Bosma S.J. et.al.
Investigation of electrostatic discharge phenomena on conductive and nonconductive optical solar reflectors. 2nd spacecraft charging technology. Conference November 1978.
17. Minier C.F. Microscopic examination of the behaviour of nonconductive optical solar reflectors after electrical breakdown.
ESA TM-172, September 1977.
18. Paillous A. Sarraill D.
Comportement d'osr en verre et cerium et d'osr en silice sous irradiation par électrons de 5 à 20 keV. Etude Cert 4086, Rapport final, décembre 1978.
19. Bosma S.J.
Microscopic investigation of electrostatic discharge phenomena on non-conductive optical solar reflectors with a conductive adhesive.
ESA SIM 211 March 1979.
20. Bosma S.J.
Electrostatic simulation test of the improved outer aluminised kapton layer as proposed for the OTS VHF-shield. ESA SIM 203 April 1978.
21. Levadou F. Froggatt M.F.
Prequalification of conductive white paint
GSFC-NS 43C. ESA EWP 1046 November 1976.
22. Bosma S.J.
Theoretical evaluation of a grounding configuration for an indium oxide coated thermal control material. ESA SIM 212
23. Bosma S.J. Froggatt M.F.
Evaluation of a conductive adhesive system for the grounding of an indium-tin-oxide coated aluminised kapton. ESA SIM 213
24. Paillous A.
Mise au point de matériaux combinant la qualité de réflecteur solaire et une bonne conductibilité électrique. ESTEC contract 3184/NL/77/HP(SC)
Phase I Janvier 1978.
25. Paillous A.
Mise au point de matériaux combinant la qualité de réflecteur solaire et une bonne conductibilité électrique ESTEC contract 3184/NL/77/HP(SC)
Phase II Février 1979.
26. Lévy L.
Essai de claquage sur un échantillon de panneau OSR. Estec contract 63636 1976.
27. Paillous A.
Dégradations des revêtements de contrôle thermique par irradiations ultra-violettes et partielles. ESTEC contract 2558/75/JS October 1976.

TABLE I: ELECTRON IRRADIATION OF OTS
THERMAL CONTROL COATINGS

	Discharge		Minimum conditions for discharge	Surface potential at time of discharge	Number of discharges over 6 hours	Degradation	UV effect
	Small	Large					
Silver teflon mounted with transfer tape	X	X	20 keV - 1nA/cm ²	11U<13	(20keV,1nA) 21 large discharges	Visual for the eye	?
Aluminised kapton with vent holes, mounted with conductive adhesive		X	10 keV - 1nA/cm ²	2U<4	(30keV,2nA) 200 small discharges	Microscopic	Yes
Thermal blanket (VHF-Shield)	X	X	20 keV - 1nA/cm ²	2U<6.5	(25keV,2nA) 19 large, 200 small discharges	Microscopic	Yes
OSR	X	X	25 keV - 2nA/cm ²	4U<9	(30keV,2nA) 65 large discharges	Microscopic	?
Honeycomb with S13GLO white paint	X	X	10keV - 1nA/cm ²	6.5U<7.5	(10keV,1nA) 126 large discharges	Microscopic ?	?
Aluminised kapton without vent holes mounted with conductive adhesive		X	10keV - 1nA/cm ²	7U<10	(30keV,2nA) 180 small discharges	Microscopic ?	Yes
Aluminised kapton with vent holes with non-conductive adhesive		X	10keV - 1nA/cm ²	8U<12	(30keV,2nA) 400 small discharges	Visual for the eye	Yes

TABLE II: RESISTANCE OF ALUMINISED FEP TEFLON WITH BALZERS I.T.O.

Resistance before test (k Ω)	Resistance (k Ω) after bending over a cylinder of diameter (mm)									Remarks
	25	20	15	10	10	8	6	4	2	
8.8	10	10.7	11.2	17	-	140	300	750	750	
7.0	7.8	8.5	10	22	65	120	200	700	900	
18	22	25	40	60	145	500	1000	8000	8000	

ANNEX

SURVEY OF EUROPEAN LABORATORIES WITH FACILITIES TO CHARACTERIZE ELECTROSTATIC BEHAVIOUR OF SPACE MATERIALS

1. SCOPE

The survey was limited to five laboratories in Europe which have facilities and instrumentation to perform electrostatic tests of space materials.

The emphasis was on small scale testing facilities rather than large set-ups for irradiation of spacecraft structures or models.

2. FACILITIES

- Giessen University (Germany) 1st Institute of Physics
Contact: K.Groh.
- I.P.W. Freiburg (Germany)
Contact: Schmidtke, Seidl, Kist
- A.E.R.E. Harwell (U.K.)
Contact: D.Verdin
- E.S.A. ESTEC Noordwijk (Holland)
Contact: J.Dauphin, F.Levadou, J.Bosma, M.Froggatt
- Onera/Cert/Derts Toulouse (France)
Contact: Berry, Paillous, Levy, Sarraill

3. GENERAL OBSERVATIONS

The approached organisations have been requested to submit relevant information of spacecraft charging facilities for the survey. This information has been annexed as received.

4. ACTIVITIES ON SPACECRAFT CHARGING EXPERIMENTS AT GIESSEN UNIVERSITY (1st INSTITUTE OF PHYSICS)

In November 1978 the activities in the field of Spacecraft Charging started at Giessen University by concluding a contract between ESA/ESTEC and the university.

The goal of the research project is to perform ground tests on the possibility of controlling spacecraft charging phenomena via electric propulsion systems. That means, emphasis will be put on the active control of a charged spacecraft.

The research project, running over a scheduled period of about 15 months, is divided in three main parts:

- a) A literature and physical survey.
That means, in this phase all available literature will be studied to achieve an up-to-date knowledge of phenomena as the behaviour of a spacecraft immersed in a plasma, the ground simulation of such charging phenomena, the analysis of discharging, and the effects to be expected for operation of ion and/or electron sources in the proximity of charged surfaces.
- b) Electron and irradiation experiments.
That means, different samples of material used at present as spacecraft surfaces including thermal coatings and solar panel parts will be irradiated by an electron flux corresponding to the worst case conditions occurring

in magnetic substorms. After the preparatory studies and experiments the most important part follows, namely

- c) the test with an electric propulsion system on irradiated samples.
That means, in the proximity of the samples an ion thruster and/or its neutralizer (electron source) will be operated. The interaction between the charged sample and the thruster's exhaust plasma will be studied. The possibility of lowering the sample's potential or clamping the potential will be examined.

The test will be carried out in a big vacuum facility which fulfils the requirements of such experiments especially the magnetic cleanliness.

Some data of the chamber:

Length : 5,3 m
Diameter : 2,6 m
Pumping speed: 10^3 l/sec.
Vacuum : $= 2,10^{-6}$ mbar.

Figure 11 shows the vacuum facility in which the tests will be carried out and figure 12 the diagnostic device.

5. LARGE PLASMA CHAMBER AT I.P.W. FREIBURG

The chamber is 5.5 m long and 2.5 m diameter which would allow the testing of large samples.

A vacuum of better than 10^{-6} torr is achieved with 2 turbomolecular pumps in combination with a primary pump system. A cryopanel is included to trap contaminants and improve the vacuum. The total chamber can be baked to 120°C .

The plasma-source is a generator of the Kauffman type. The plasma has a long term stability and is variable for plasma density and temperature.

The plasma is characterized by different measurement methods:

- a) Impedance Probes,
- b) Langmuir Probes,
- c) Potential Analyzers,
- d) Ion Traverse Measurements.

A flexible system exists for the mounting of test samples and scanning probes. The position of probes and sample is indicated by an electronic co-ordinate system.

IPW also has an Electron Canon for high energy electrons (KeV-range), which can be mounted to the plasma chamber.

This option creates the possibility of immersing a test sample in a low energy plasma and simultaneous charging of the material to high potential levels by means of irradiation with high energy electrons.

Helmholtz coils are applied to guarantee a homogeneous magnetic field inside the chamber. The facility has already been applied to test prototypes and flight models of several plasma experiments of satellite payloads.

Relevant data:

Background pressure without plasma source	10^{-7} torr
with plasma source	2×10^{-6} torr
electron density	$10 \dots 5 \times 10^{12} \text{ cm}^{-3}$
electron temperature	400...3000 °K
ion beam energy	2....100 eV
ion beam velocity	3.....22 km/sec
magnetic field	0.....3.5 gauss

Figure 13 and 14 give an impression of the plasma chamber.

6. LOW ENERGY ELECTRON IRRADIATION FACILITY AT AERE, HARWELL, ENGLAND

To study the electrostatic discharging phenomenon in satellite components a facility has been constructed in which dielectric materials can be irradiated under vacuum at controlled temperatures with mono-energetic electrons of up to 30 keV energy at beam fluxes up to 30 nA.cm^{-2} . The surface voltage profiles of samples can be determined during irradiation and the leakage currents and the frequency and magnitude of electrical discharges can be continuously measured. Samples may be observed visually and photographed during irradiation, and the electromagnetic radiation accompanying discharges may also be monitored.

The irradiation chamber has an internal diameter of 460 mm and is 370 mm high and may be baked under vacuum at 70°C and is continuously flushed with dry nitrogen gas when at atmospheric pressure. It incorporates cryogenic panels and the pressure may be maintained at about 2×10^{-7} torr for long periods, the residual atmosphere being monitored up to mass number 60 with a quadrupole mass spectrometer.

Samples for irradiation are usually in the form of 140 mm diameter circles of material having projections for electrical connections. The samples are held horizontally and the lower surface is aluminised to form a central current collector which is surrounded by an uncoated strip of material and an outer concentric guard ring. The sample holder is a copper block through which water may be purged from a thermostatically controlled unit to maintain the sample at temperatures from ambient up to 75°C, or it may be filled with liquid nitrogen to give a sample temperature of $-178 \pm 5^\circ\text{C}$.

The electron gun is a triode unit mounted vertically above the top of the vacuum chamber. It employs thermionic emission from a tungsten filament giving an emitting area of 23 mm diameter. The electron beam diverges as it accelerates towards the earthed anode located 120 mm above the sample and the accelerating voltage is continuously variable from 3 to 30 kV. The beam distribution which is constant to within 30% is determined by a rotatable multipoint collector which can be substituted for the sample holder. During the irradiation of samples the beam flux is continuously monitored by a wire grid which collects 5% of the beam incident on the sample.

The surface voltage profiles of samples are measured with an electrostatic feedback voltmeter (Trek Inc., model 340HV) using a probe (type 4031S) swept about 3 mm above the surface of the

material. The probe passes over an earthed reference zone at each end of the sweep which takes 12 seconds.

The leakage current from samples is measured by connecting the sample to earth via an electrometer (Keithley Instruments Ltd., model 610C) and the output is displayed on a potentiometric recorder which also provides a measure of the frequency of current pulses from the sample. The magnitude and shape of these pulses are obtained with an inductively coupled current probe (Tektronix Inc., model P 6302) the output of which is displayed on a 100 MHz oscilloscope (Tektronix model 466). The electromagnetic radiation associated with the discharges is monitored with a circular loop antenna mounted adjacent to the sample. The voltage induced in the loop is displayed on a second model 466 oscilloscope triggered separately.

7. ESTEC MATERIALS SECTION "BISE" SIMULATION CHAMBER.

The Bise chamber is a combined irradiation chamber which is equipped for simultaneous particle and ultra-violet irradiation. Fig. 15 shows the main elements of this facility, viz.:

- proton source,
- electron source,
- ultra-violet irradiation source,
- vacuum chamber,
- in-situ measuring system.

Proton Source

The proton source consists of a 'Sames' high frequency generator which produces H⁺ and D⁺ ions. A hydrogen plasma is ionised by free electrons which oscillate with an electromagnetic field induced by a 100 MHz oscillator.

The extracted beam consists of 80% mono-atomic and 20% diatomic ions. The ions are accelerated by means of a stabilised power supply (0 to 50 kV) and analysed by an electro-magnet which permits separation of protons from molecular ions. Before entering the transfer system, the protons pass through a cryogenic trap which condenses volatile materials.

Electron Source

The electron source is a 'Sames' electron gun with a directly heated filament. The energy range is 0 to 50 KeV with a maximum current of 100 mA.

Transfer System

The transfer system deviates the protons into the deflection system and eliminates the recombined molecules from the beam. Simultaneously, the electrons can be transferred through the lower channel of the system.

Deflection System

Both protons and electrons are scanned over the target area by two alternating electric fields (E_1 and E_2) which are diagonally opposed to each other. The scanning frequency is approximately 1000 Hz with a phase difference in the order of 80 Hz between E_1 and E_2 .

Vacuum Chamber

The main section of the chamber is a stainless steel cylinder with a diameter of 740 mm and a height of 450 mm. The vacuum is maintained by a 2-stage primary pump and a 6501/s turbo-molecular pump in combination with a liquid nitrogen shroud. The main purpose of this shroud is to trap contaminants. A vacuum of better than 10^{-7} torr is achieved.

The sample-holder is situated inside the chamber and consists of a hollow disc of 230 mm diameter. Two pipelines circulate the temperature-regulating fluid through the disc. The temperature of the sample-holder can be regulated from -20 to +130°C with an accuracy of $\pm 1^\circ\text{C}$. The capacity of the sample-holder during a test is 21 samples (2 by 2 cm).

For the electrostatic simulation tests, the in-situ optics measuring system is replaced by a potential probe (type Trek 4031S) in connection with a Trek model 340 HV electrostatic voltmeter (0 - 20 kV).

The probe is mounted on a mechanical system which permits movements in 2 axes. These movements in X and Y directions are controlled by a relay panel on which the sphere's position is indicated in coordinates relative to the sample holder.

The probe is used for measuring surface potential profiles on the test sample. A stainless steel plate is mounted on the sample holder, electrically insulated from the holder and provided with a high tension feedthrough and power supply (0-5 kV). The plate is used as a means of in-situ calibration for the probe during tests.

The electron beam current is monitored continuously at the level of the sample holder by three Faraday cups (aperture 1cm²), one on each side of the holder and one on top. In addition, two more Faraday cups (apertures 1cm² and 0.5cm² respectively) were mounted on the X-Y system for homogeneity measurements over the sample holder.

The sample is electrically insulated from the sample holder and the sample grounding wire is brought out of the chamber via a double-insulated high-tension feedthrough and grounded.

The sample leakage current is measured by connecting the sample to ground via an electrometer (Keithly Model 602B) and the output is displayed on a recorder. This recording is also used to determine the number of discharges.

If a discharge occurs, the electrometer is protected by a spark gap which leads the pulse directly to ground.

A current probe is clamped around this direct path and used in combination with a fast storage oscilloscope to measure the discharge pulse.

The UV irradiation source can be utilised to study solar illumination effects.

In conclusion, the test data comprises:

- surface potential or potential profiles,
- sample to holder current (leakage current)
- discharge pulse (shape and magnitude)

- total discharge rate,
- visual inspection and photography during irradiation,
- illumination effects,
- temperature effects.

8. THE DERTS ELECTROSTATIC CHARGING FACILITY

General Requirements for Substorm Simulation

Electrostatic testing of coatings requires adequate substorm environment simulation and associated instrumentation for characterization of the induced effects.

Simulation of the electrons of the plasma can be achieved by means of quasi-monoenergetic electrons in the 5 to 25 keV energy range and fluxes up to 10 nA/cm². These electrons can be produced by the scattering of a focused beam delivered by an electron gun and directed to an aluminium thin foil. The transmitted beam is enlarged enough to irradiate a (200 x 200) mm² surface with a good homogeneity.

Due to scattering the transmitted beam is no longer monoenergetic. Its energy spectrum has been measured for various incident energies and foil thicknesses. Fig. 22 shows the energy spectrum for an incident primary energy of 18 keV. This spectrum is widened in the range of the low energies compared to the direct primary beam spectrum.

Simulation necessitates also possibility of illuminating the irradiated samples with ultra-violet light (sun light simulation), performance of irradiation under vacuum at controlled temperature.

The simulation chamber used at DERTS is founded upon the afore mentioned statements.

Parameters of interest

The main expected information are the following (Fig. 16)

- surface potentials or surface potential profiles 1)
- volume leakage currents (or sample-to-holder currents 2)
- breakdown currents (shape and magnitude of the current pulse generated by sudden discharging) 3)
- radiated EMI picked up by an in-situ Antenna 4)
- visual inspection and photography of samples under electron irradiation (localization of arcing) 5).

The Electrostatic testing facility can be used in two different configurations, "CEDRE", and "MELESE".

"CEDRE" Configuration

Fig. 17 is a schematic view of the "CEDRE" (Chambre pour l'Etude Des Revêtements sous Electrons) facility used to assess the electrostatic behaviour of dielectric coatings in simulated geosynchronous substorm environment.

General structure of the vacuum chamber is cylindrical. Turbomolecular pumping units allow the chamber and the electron gun to be operated at pressure levels less than 5×10^{-7} Torr. The electron gun (SAMES manufacturer) works in the range 4

to 25 keV, with fluxes at the sample level up to 10 nA cm^{-2} . An aluminum foil $1,2 \mu\text{m}$ thick is used in order to scatter the electrons.

The sample holder is made up of 4 plates ($200 \times 200 \text{ mm}^2$) each maintained at fixed temperature with a circulating fluid. This holder is fixed onto a rotating shaft allowing the presentation of any of the four plates in front of the energetic electron beam. In normal conditions, two faces can receive samples, the two others being used as Faraday cup holder, energy and surface potential measurement calibration systems.

Two samples of $(200 \times 200) \text{ mm}^2$ can be tested without opening the chamber so as to perform comparative tests on them.

The surface potential is measured by a potential probe held by a mechanical scanner. An electronic instrumentation is fed by the signal emitted by the probe and moves with it under vacuum. A potentiometer system yields its vertical position and allows recording on a X-Y plotter the surface potential profile of the electrically charged coating.

"MELESE" Configuration (Fig. 18)

Scope: In order to assess some basic properties such as secondary emission, surface leakage and volume leakage (the three manners electrons can escape from the irradiated surface sample) a special setting was designed called "MELESE" (Mesure d'ELECTrons SEcondaires).

It varies from the "CEDRE" configuration by an hemispheric electrode surrounding the irradiated sample with a solid angle very near of 2π .

The secondary electrons can be measured together with the backscattered electrons by means of a collecting hemispheric electrode 1) surrounding the irradiated area.

The fixation system of the sample allows measurement of the surface leakage current on a circular ring 3) on the sample surface but out of the irradiated area. A guard circular ring electrically insulated from the ring 3) by a 125 micrometer thick FEP film covers the whole ring 3). Note that in case of measurements using electrodes 3) and 5), the sample under irradiation is grounded by its periphery. However it is possible to disconnect from ground the rings 3) and 5) in order to provide a sample grounding only by its back face.

The coating is fixed onto a metallic plate 2) which is grounded to earth by means of a nanoammeter giving the volume leakage current plus the capacitor charging current. 1), 3) and 5) are also grounded by means of other nanoammeters. All the currents are simultaneously recorded.

Two fixed Faraday cups 4) are used to continuously monitor the electron flux during the irradiation.

Under certain circumstances, a current measured on a metallic plate 6) next to the sample but set back from the sample surface needs also to be measured.

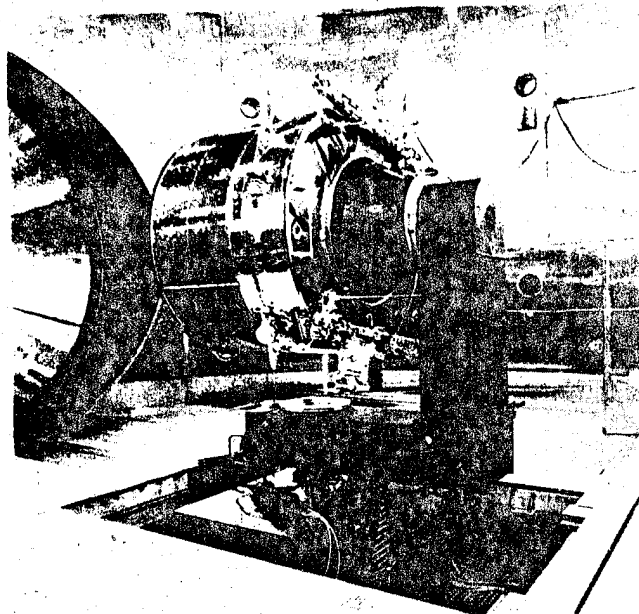


Figure 1: GEOS in the ESTEC Dynamic Test Chamber

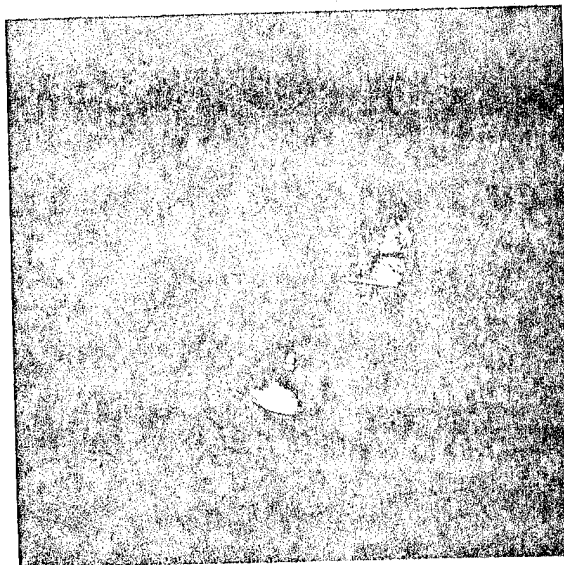


Figure 2: METEOSAT Model during Electron Irradiation (White spots on central band are discharges)



Figure 3: OCL1 OSR: Top of quartz layer (x 144) pyrolysed adhesive deposit due to discharges

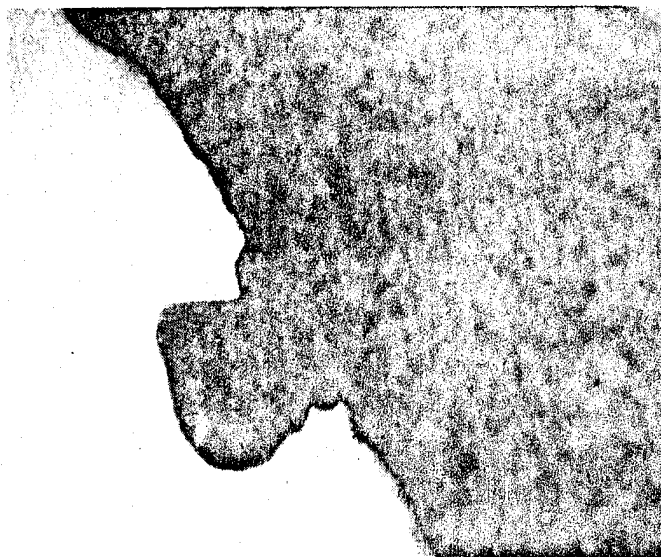


Figure 4: OCL1 OSR: Bottom of silver layer (x 144) silver evaporation due to discharges



Figure 5: Kapton with 1000Å Aluminium layer: Aluminium evaporation due to discharges (x 400)

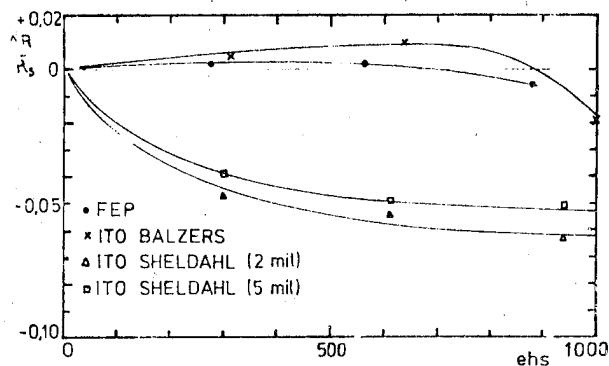


Figure 6: Variation of Solar Reflectance of SSM as a function of UV irradiation time

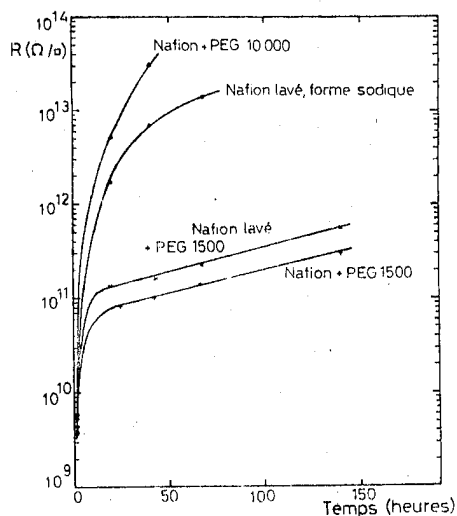


Figure 7: Variation of electrical resistance of different types on nafion as a function of vacuum exposure time

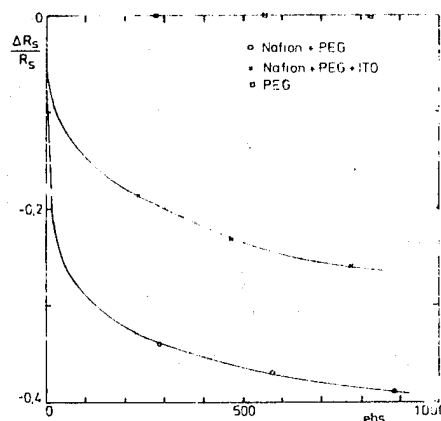


Figure 8: Variation of Solar Reflectance of different types of nafion as a function of UV irradiation time.

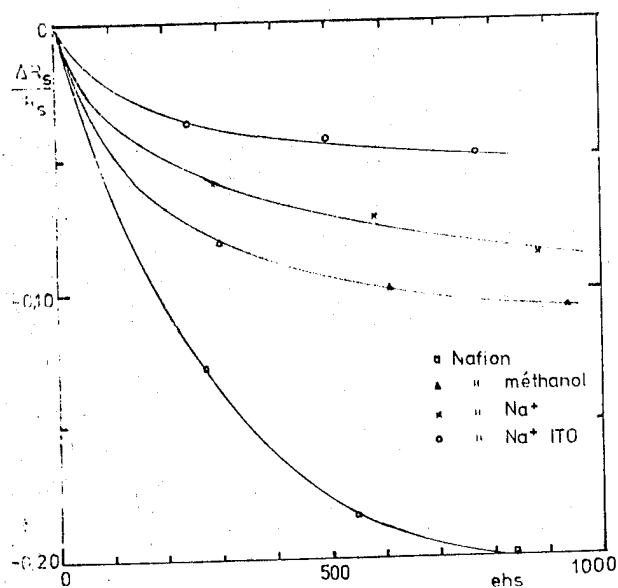


Figure 9: Variation of Solar Reflectance of different types of nafion as a function of UV irradiation time.

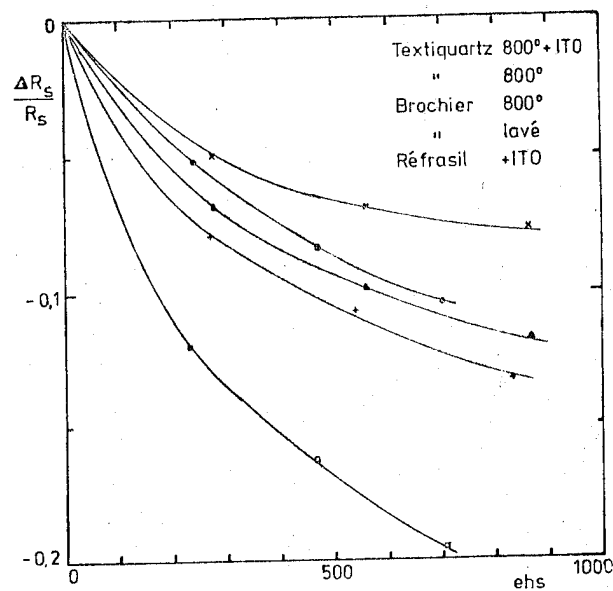


Figure 10: Variation of Solar Reflectance of Silica Fabrics as a function of UV irradiation time

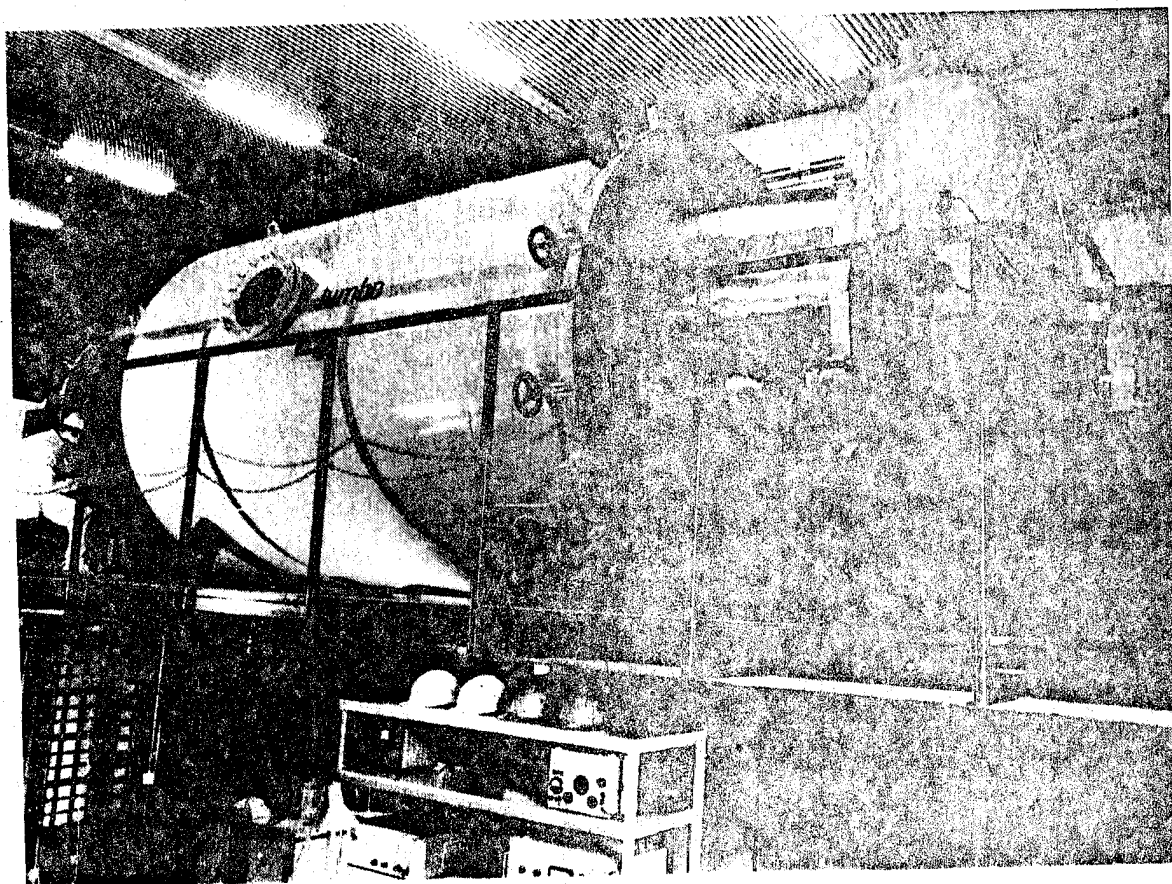


Figure 11: Irradiation facility at University of Giessen

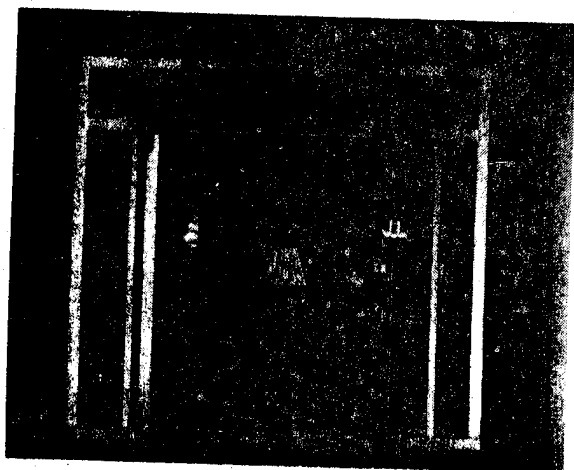


Figure 12: Diagnostic device of University of Glengen

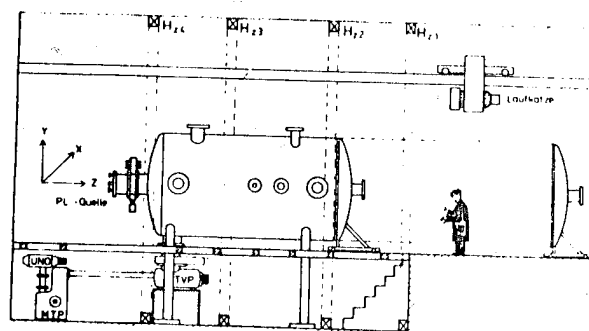


Figure 14: Schematic view of Freiburg Facility

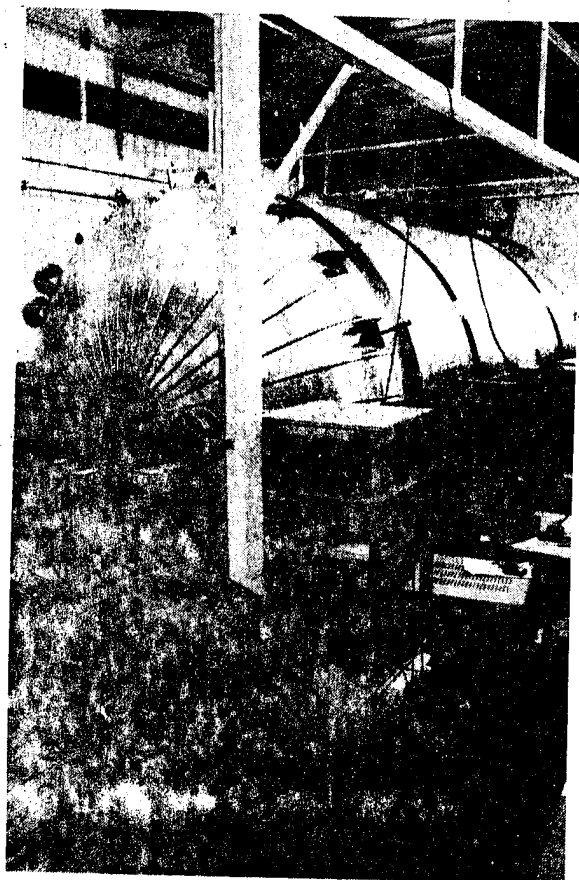


Figure 13: Irradiation Facility at I.P.W. Freiburg

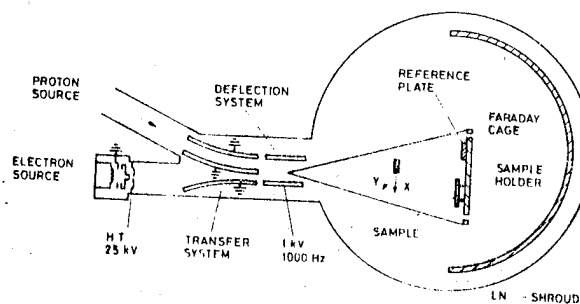


Figure 15: Schematic view of ESTEC "BISH" Chamber

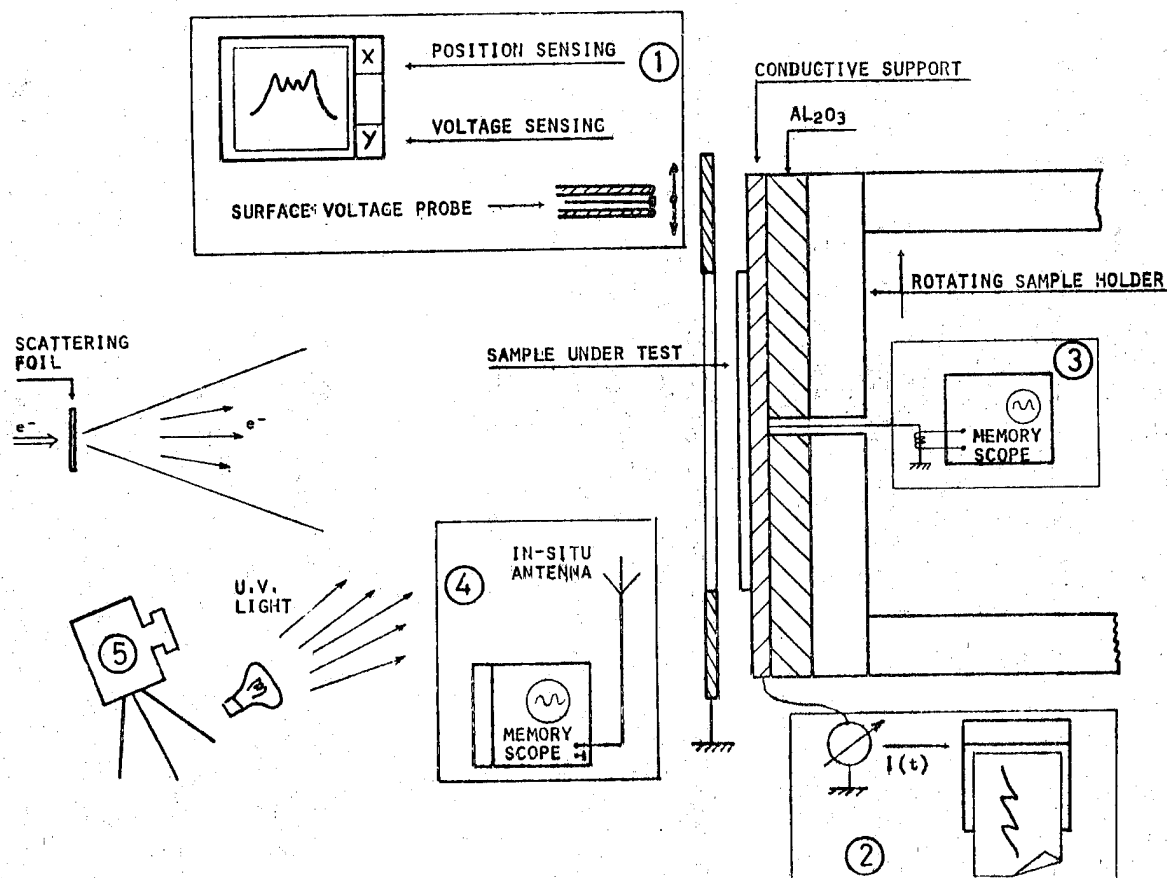


Figure 16: Diagram of D.E.R.T.S. measurement set-up

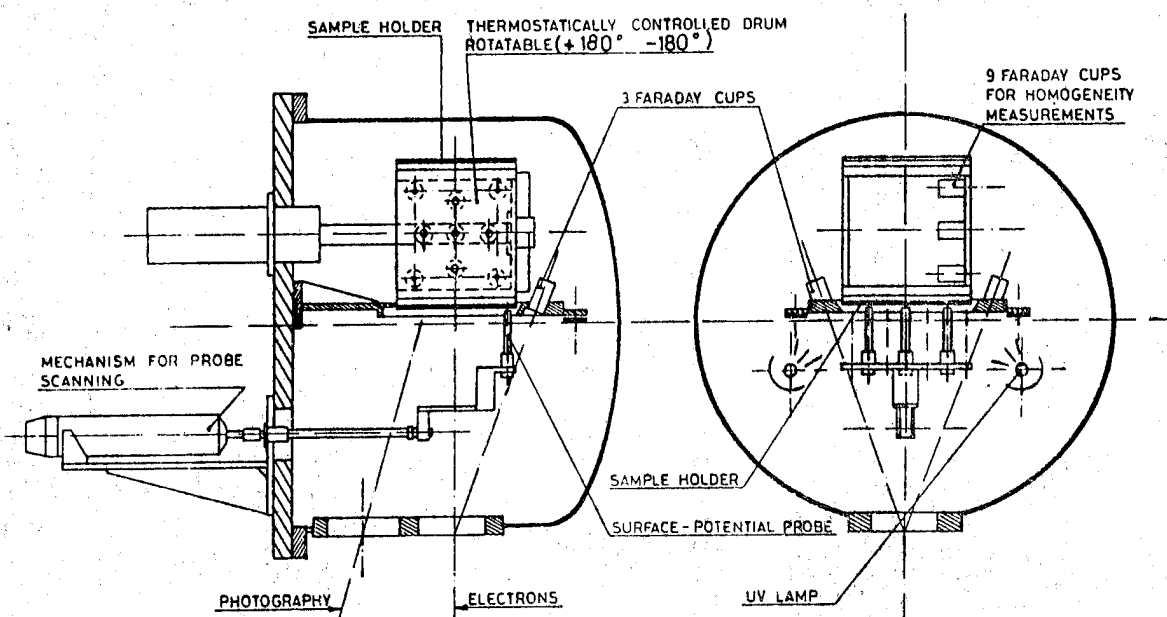


Figure 17: Schematic view of D.E.R.T.S. "CEDRE" Chamber

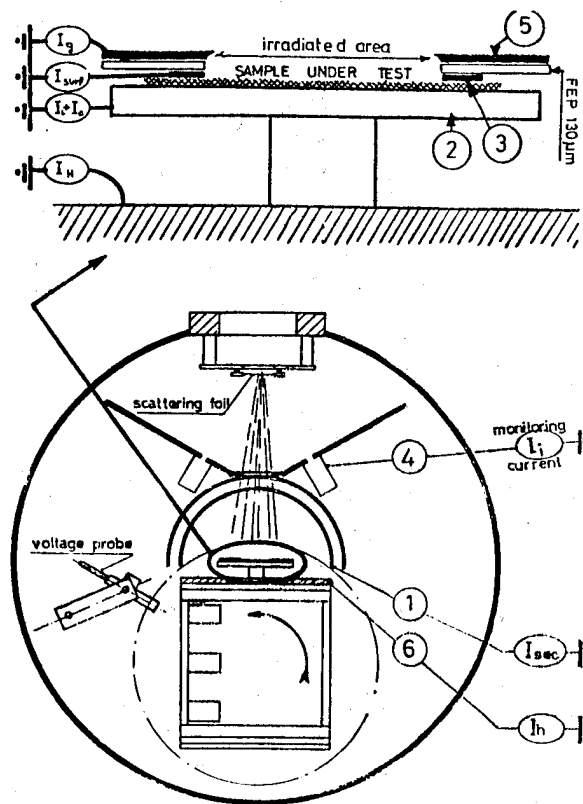


Figure 18: Schematic view of D.E.R.T.S. "MELESE" Configuration

N80-21440

SURFACE DISCHARGE ARC PROPAGATION AND DAMAGE ON SPACECRAFT DIELECTRICS

K G Balmain

University of Toronto

Department of Electrical Engineering, Toronto, Canada

ABSTRACT

The propagation of a surface discharge arc or flashover on dielectrics such as Mylar, Teflon and Kapton is the mechanism by which 10-30 keV deposited electronic charge is mobilized to produce damaging arc current densities. A propagation mechanism is discussed, in which the progress of the surface arc is controlled by the rate of removal of excess charge along filamentary tunnels filled with an overdense plasma of ionized discharge debris. Supporting evidence is drawn from area-scaling measurements of discharge electrical properties, and from microscope photographs of permanent damage in the form of sub-micron-diameter subsurface tunnels and surface grooves.

Keywords: Dielectric Arc Propagation, Dielectric Arc Damage, Dielectric Flashover, Spacecraft Discharge, Spacecraft Charging.

1. INTRODUCTION

Spacecraft charging by incident energetic electrons and consequent arc discharging are now reasonably well-established phenomena (Refs. 1-4) which apparently have caused synchronous-orbit satellites to exhibit various types of operational anomalies. To date, retrieval of synchronous-orbit spacecraft has not been possible, so the relevant experimental research results have come largely from ground-based laboratories. These measurements have shown that the incident electrons become embedded a few microns beneath the surface of any exposed dielectric materials on the spacecraft outer surface. When a sufficient charge has accumulated, breakdown occurs and propagates swiftly over the charged region as a surface "flashover". This discharge is accompanied by electron ejection with corresponding replacement current flow into the interior of the spacecraft, current which very probably can reach peak values of hundreds of amperes for dielectric sheet areas of the order of one square meter.

Laboratory measurements of the replacement current pulses resulting from these discharges have shown that the peak current and as well the released charge, pulse duration and energy dissipated in a load resistor all follow well-defined scaling laws as the specimen area is varied (Refs. 5,6,7), and furthermore these scaling laws are similar for Kapton, Teflon and Mylar (Ref. 8). For example, the peak discharge current has been found to scale in proportion to the area raised to the power 0.5

approximately, or in other words 0.5 is the slope of the corresponding log-log graph of peak current versus area. Similarly the log-log graphs of released charge, pulse duration and energy dissipated in a load resistor respectively exhibit slopes of 1.0, 0.5 and 1.5 approximately.

Discharge surface damage has also been identified on Kapton, Mylar and Teflon (Refs. 6,7,8,9). This damage takes the form of surface grooves, subsurface tunnels, "punchthrough" holes, and "blowout" holes. The appearance of this damage and the lightning-like appearance of the light emitted from a flashover arc suggest that the discharge arc propagates across the dielectric surface, and the velocity of propagation has been estimated (Refs. 6,8) by dividing the specimen radius by the pulse duration, giving approximately 3×10^5 m/s. The discharge propagation mechanism has been postulated to be due to "electron-hopping" (Ref. 10), to be controlled by the inductance and capacitance of a conducting channel (Ref. 11), and to involve wave propagation along a plasma channel (Ref. 8).

This study contains a further examination of the plasma channel propagation concept, and includes additional evidence in the form of photographs of damage patterns all having the forms of surface or subsurface channels.

2. THE PLASMA CHANNEL

That a discharge in a solid dielectric could develop in the form of a plasma channel was argued in considerable detail by Budenstein (Ref. 12), but the velocity of propagation of the arc is yet to be explained. Whatever the mechanism for propagation, the existence of a finite velocity is probably what determines the 0.5 slope of the peak current versus area curve. This can be seen by imagining the discharge to be in the form of a wave expanding from an ignition point, the resultant replacement current being proportional to the length of the wavefront. Clearly the maximum length of the wavefront is proportional to the linear dimensions of the specimen or in other words proportional to the square root of the area as observed. It would appear that an arc discharge propagating along straight, branching paths produces the same area-scaling effect.

To devise a model for discharge propagation, one must first take note of the experimental configuration shown in Figure 1. The charged area on

the dielectric sheet is defined by a tight-fitting metal mask which has a bevelled edge to reduce emitted-electron interception. The incident electrons become embedded in a diffuse layer 5 to 8 μm below the surface, with resultant high electric field being set up both above and below the charge layer (Refs. 13,14) and adjacent to the mask edge. Breakdown can be initiated at any high-field point, resulting in a punchthrough arc to the substrate (bulk breakdown), a blowoff arc to the surface, or a flashover arc consisting of a propagating subsurface discharge terminating in either a blowout hole or a punchthrough hole.

Such a propagating subsurface discharge is sketched in Figure 2. It is postulated that enough energy is released in the breakdown process to maintain a plasma channel of ionized debris connecting the point of discharge to the outside vacuum region. Because breakdown requires a high local field, it is further postulated that the excess charge must be removed via the plasma channel before each step in the breakdown process can proceed. The extent of the high field region ahead of the point of discharge should be about the same as the distance travelled by the excess charge along the channel, in a given time interval, so that the velocity of propagation of the discharge should be approximately equal to the velocity of propagation of the excess charge along the plasma channel.

In earlier work (Ref. 8) it was noted that an electromagnetic wave on a highly conducting channel over a highly conducting ground plane would propagate at the velocity of light in the dielectric medium, but the observed velocity appears to be almost three orders of magnitude lower. It was postulated in the earlier work that the required wave slowing could be produced by the added inductance per unit length provided by an overdense plasma channel, the inductance per unit length contributed by the plasma being

$$L_p = \frac{1}{\pi a^2 \epsilon_0 \omega_p^2} = \frac{m}{\pi a^2 N e^2} \quad (1)$$

for a plasma relative permittivity given by

$$\epsilon_p = 1 - \frac{\omega_p^2}{\omega^2} \quad (2)$$

$$z = -\frac{\omega_p^2}{\omega^2} \quad \text{in the overdense case} \quad (3)$$

in which ω is the wave frequency (radians/s) for an $\exp(j\omega t)$ time variation, $\omega_p = (Ne^2/m\epsilon_0)^{1/2}$ is the plasma frequency, N is the electron density (m^{-3}), e is the electron charge magnitude (coul.), m is the electron mass (kg.), a is the channel radius and ϵ_0 is the permittivity of a vacuum. It was indicated in the earlier work that the other contributions to the inductance per unit length were negligible, and therefore that the propagation velocity is

$$v_p = \frac{1}{(LC)^{1/2}} \quad (4)$$

where C is the capacitance per unit length given by $C = 2\pi\epsilon/[\cosh^{-1}h/a]$, h being the height of the plasma channel over the ground plane and $\epsilon = \epsilon_0\epsilon_d$ being the dielectric permittivity. Taking the logarithm approximation for \cosh^{-1} and setting $\omega_p = 2\pi f_p$ gives

$$v_p \approx \frac{2\pi a \sqrt{\ln(2h/a)}}{\sqrt{\epsilon_d}} f_p \quad (5)$$

$$\approx 2\sqrt{2} \pi a f_p \quad (6)$$

$$\approx 9 a f_p \quad (7)$$

in which the values $\epsilon_d = 3$, $h = 6 \times 10^{-5}$ m and $a = 3 \times 10^{-7}$ m have been used. Thus a velocity of 3×10^5 m/s would be produced by a plasma frequency f_p of 100 GHz, corresponding to an electron density of approximately 10^{20} m^{-3} .

The above calculation involves both elementary transmission-line theory and the inclusion of the ground plane. Conceivably these two constraints might in some way limit the accuracy of the calculated results, so there is reason to consider propagation along a cylindrical plasma channel of radius "a" and with relative permittivity $\epsilon_p = 1 - \omega_p^2/\omega^2 = -\omega_p^2/\omega^2$ inside an infinite dielectric of relative permittivity ϵ_d . The azimuthally symmetric Bessel-function TM solution is appropriate (Ref. 15) and its longitudinal electric field is

$$E_z = A J_0(\gamma_p \rho) e^{-j\beta z} \quad \rho < a \quad (8)$$

$$E_z = C K_0(\gamma_d \rho) e^{-j\beta z} \quad \rho > a \quad (9)$$

$$\text{where } \gamma_p^2 + \beta^2 = k_p^2, \quad k_p = \omega \sqrt{\mu_0 \epsilon_0 \epsilon_p} \quad (10)$$

$$-\gamma_d^2 + \beta^2 = k_d^2, \quad k_d = \omega \sqrt{\mu_0 \epsilon_0 \epsilon_d} \quad (11)$$

The procedure of matching all tangential fields at

$$\rho = a \text{ gives } \gamma_p a \frac{J_0(\gamma_p a)}{J_1(\gamma_p a)} = -\frac{\epsilon_p}{\epsilon_d} \gamma_d a \frac{K_0(\gamma_d a)}{K_1(\gamma_d a)} \quad (12)$$

On the assumption that a is small, the small-argument and overdense-plasma approximations give for equation (12)

$$-\frac{2\omega^2 \epsilon_d}{\omega_p^2} = (\gamma_d a)^2 \ln(\gamma_d a) \quad (13)$$

Also, (11) can be written as

$$\frac{\omega^2}{v_p^2} = \frac{\omega^2}{c^2} \epsilon_d + \gamma_d^2 \quad (14)$$

To a first order of approximation, the slowly varying $-\ln(\gamma_d a)$ can be set equal to a constant M lying in the range 4.6 to 9.2 for values of $\gamma_d a$ in the range 10^{-2} to 10^{-4} . Thus (13) becomes

$$\frac{2}{M} \frac{\omega^2}{\omega_p^2} \epsilon_d = \gamma_d^2 a^2 \quad (15)$$

Eliminating γ_d from (15) and (14) gives

$$\frac{1}{v_p^2} = \frac{\epsilon_d}{c^2} + \frac{2\epsilon_d}{M\omega_p^2 a^2} \quad (16)$$

The term involving the velocity of light c is negligible, so that the plasma channel propagation velocity v_p is given by

$$v_p = \left(\frac{M}{2\epsilon_d}\right)^{1/2} a \cdot 2\pi f_p \quad (17)$$

$$\text{or for } M=8, v_p \approx 7 a f_p \quad (18)$$

which is almost identical to equation (7). Setting the logarithm in (13) equal to a constant implies the disregard of a small amount of wave dispersion and therefore the disregard of a small amount of resultant pulse distortion as the wave propagates. It is therefore clear that the use of transmission-line theory and the consideration of a nearby ground plane do not unduly restrict the original simplified analysis (Ref. 8), so that comparison with other theories (eg. Ref. 16) may be facilitated.

3. SURFACE DAMAGE

In the manner indicated in Figure 1, specimens of Kapton H, FEP Teflon and Mylar were exposed to a 20 kV electron beam of $\pm 15\%$ worst-case nonuniformity over the aperture and current density of 80 nA/cm². This current density is at least an order of magnitude higher than at synchronous orbit and was chosen in part to produce a high enough discharge repetition rate for convenient pulse averaging. Experiments suggested no significant change in individual discharge pulse properties from current densities of 10 μ A/cm² down to 75 nA/cm², but more recent results (Ref. 17) suggest possible current density dependence of released charge and peak current below 8 nA/cm².

A typical arc discharge is shown in Figure 3. In general, every arc on a given specimen exhibited a different pattern compared to all other arcs, although some parts of an arc might repeat, especially near an edge. In addition, when punchthrough holes occurred, they repeatedly formed bright focal points for the discharges.

The Kapton damage photographs were all taken on a single specimen 75 μ m thick which had been subjected to 11 discharges. Figure 4 shows a groove disappearing into a heaved-surface tunnel, indicating that groove and tunnel damage both result from the same basic physical process. Figure 5 includes the area of Figure 4 in its lower right quadrant and shows that the heaved-surface tunnel comprises a narrow central channel bordered by a damaged fringe. Figures 6 and 7 show surface grooves crossing heaved-surface tunnels, while Figures 8 and 9 for the same region show additional tunnels with no surface heaving.

The Teflon specimen examined was 50 μ m thick and had been subjected to 9 discharges, but nevertheless damage was difficult to find except at a punchthrough and near an edge. The latter damage is shown in Figure 10 in which discharge tunnel heaving and cracking is clearly evident.

The Mylar specimen tested was 75 μ m thick and had been subjected to 12 discharges, resulting in damage which was relatively easy to find. Figures 11 and 12, taken near the mask edge, show a variety of surface patterns which are displayed at higher magnification in Figures 13 and 14. Figure 15 is a good example of a branched groove crossing a heaved-surface tunnel, while Figure 16 shows both straight grooves and a leafy pattern of irregular grooves. Finally, Figures 17, 18 and 19 provide close-up views of blowout holes in a heaved-surface tunnel, the appearance of the holes suggesting localized

melting of the Mylar.

4. CONCLUSIONS

Damage photographs on Kapton, Teflon and Mylar consistently reveal channel-like patterns. The sub-surface channels (or tunnels) are always irregular and often result in surface heaving and cracking with occasional blowout holes. The surface channels are usually grooves in a pattern of straight branching lines suggesting surface crystallization effects, but sometimes an irregular leafy pattern of surface grooves can be seen interspersed amongst the straight grooves. Surface grooving on Teflon can sometimes be seen in microscopic examination but the grooves are too faint to photograph well.

Damage in the form of channels suggests the ejection of ionized discharge debris along these channels, especially in the case of tunnels. It is postulated that the rate of excess charge removal along the plasma channel determines the rate at which the discharge is permitted to progress, and that the transport of charge along the channel involves an approximately dispersionless wave propagation mode which is much slower than the velocity of light. It is shown that this mode can propagate in the case of an overdense plasma, and that the presence of a nearby ground plane does not strongly influence the properties of the mode.

5. ACKNOWLEDGMENTS

The author expresses his gratitude to G.R. Dubois for his contributions to the experiments and the photography. The research was supported by the Natural Sciences and Engineering Research Council of Canada under Grant A-4140.

6. REFERENCES

1. Rosen, A. (Ed.), *Spacecraft Charging by Magnetospheric Plasmas*, Progress in Astronautics and Aeronautics, Vol. 47, 1976.
2. Pike, C.P., and Lovell, R.R. (Eds.), *Proceedings of the 1976 Spacecraft Charging Technology Conference*, Report AFGL-TR-77-0051/NASA TMX-73537, 24 Feb. 1977.
3. Goodman, J.M. (Ed.), *Effect of the Ionosphere on Space and Terrestrial Systems*, Proceedings of an NRL/ONR-sponsored conference held in Arlington, Va., January 24-26, 1978. U.S. Gov't. Printing Office Stock No. 008-051-00069-1.
4. *Spacecraft Charging Technology - 1978*, Proceedings of a conference held at Colorado Springs, Oct. 31 to Nov. 2, 1978, edited by R.C. Finke and C.P. Pike, NASA Conference Publication 2071/AFGL-TR-79-0082.
5. Balmain, K.G., Kremer, P.C., and Cuchanski, M., "Charged-Area Effects on Spacecraft Dielectric Arc Discharges", in Reference 3, pp. 302-308.
6. Balmain, K.G., "Scaling Laws and Edge Effects for Polymer Surface Discharges", in Reference 4, pp. 646-656.

7. Yablowsky, E.J., Hazelton, R.C., and Churchill, R.J., "Characterization of Electrical Discharges on Teflon Dielectrics Used as Spacecraft Thermal Control Surfaces", in Reference 4, pp. 632-645.
8. Balmain, K.G., and Dubois, G.R., "Surface Discharges on Teflon, Mylar and Kapton", paper G-10 presented at the 1979 IEEE Nuclear and Space Radiation Effects Conference, Santa Cruz, California, July 17-20, 1979.
9. Amore, L.J., and Eagles, A.E., "Materials and Techniques for Spacecraft Static Charge Control", in Reference 2, 621-654.
10. Inouye, G.T., and Sellen, J.M., "A Proposed Mechanism for the Initiation and Propagation of Dielectric Surface Discharges", in Reference 3, pp. 309-312.
11. Leadon, R., and Wilkenfeld, J., "Model for Breakdown Process in Dielectric Discharges", in Reference 4, pp. 704-710.
12. Budenstein, P.P., "Dielectric Breakdown in Solids", Report AD-A012 177, prepared for the U.S. Army Missile Command, Redstone Arsenal, Alabama, 20 December 1974.
13. Meulenbergh, A., "Evidence for a New Discharge Mechanism for Dielectrics in a Plasma", in Reference 1, pp. 237-246.
14. Beers, B.L., Hwang, H.-C., Lin, D.L., and Pine, V.W., "Electron Transport Model of Dielectric Charging", in Reference 4, pp. 209-238.
15. Johnson, C.C., Field and Wave Electrodynamics, McGraw-Hill Book Co., N.Y., 1965, pp. 173-176.
16. Beers, B.L., Pine, V.W., Hwang, H.C., and Bloomberg, H.W., "Negative Streamer Development in FEP Teflon", Paper G-7 presented at the 1979 IEEE Nuclear and Space Radiation Effects Conference, Santa Cruz, California, July 17-20, 1979.
17. Flanagan, T.M., Denson, R., Mallon, C.E., and Treadaway, M.J., "Effect of Laboratory Simulation Parameters on Spacecraft Dielectric Discharges", paper G-8 presented at the 1979 IEEE Nuclear and Space Radiation Effects Conference, Santa Cruz, California, July 17-20, 1979.

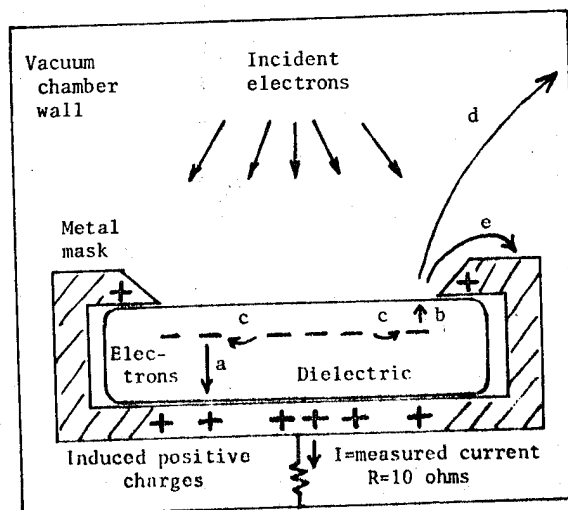


Figure 1. Possible charging and discharging phenomena: a) punchthrough arc with top surface of dielectric blown off, b) blowoff arc to surface, c) flashover arc or propagating subsurface discharge, d) ejected electrons going to chamber wall, e) ejected electrons going to mask.

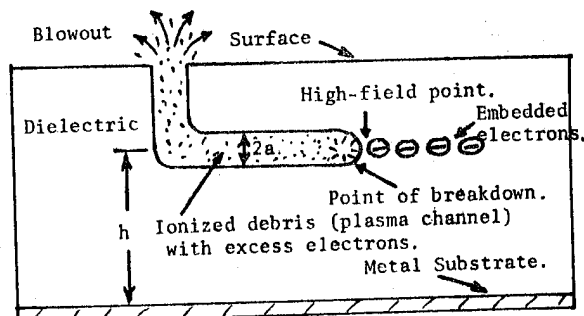


Figure 2. The propagation of a breakdown channel through a subsurface layer of electrons embedded in a dielectric sheet.

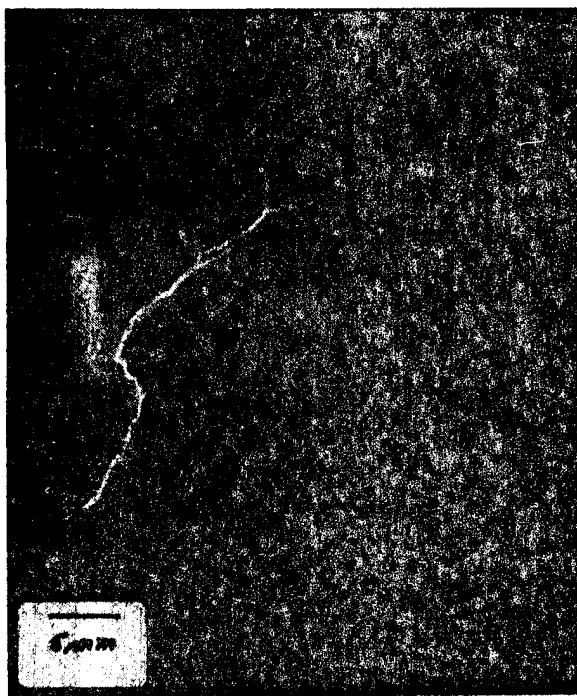


Figure 3. Typical arc discharge on Mylar.

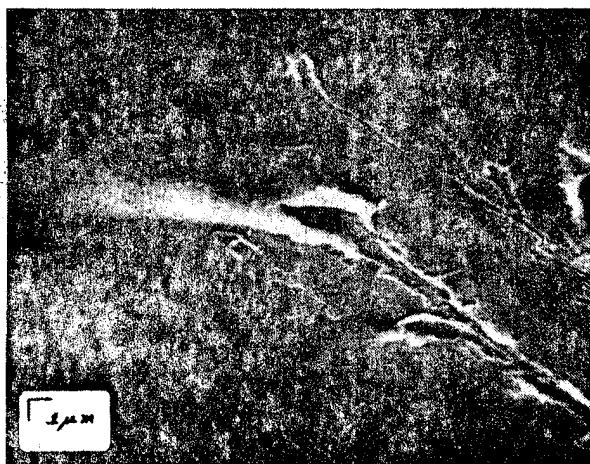


Figure 4. Kapton; scanning electron microscope.

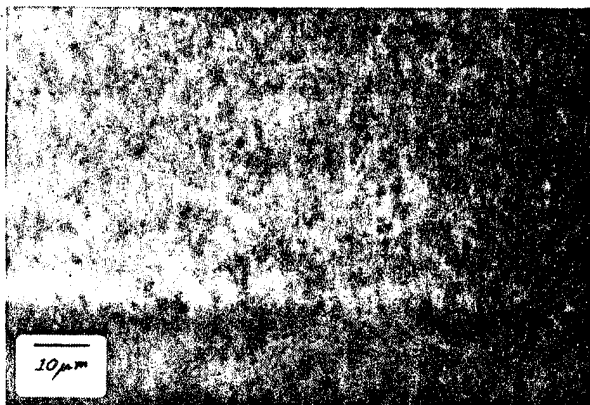


Figure 5. Kapton; reflected light.

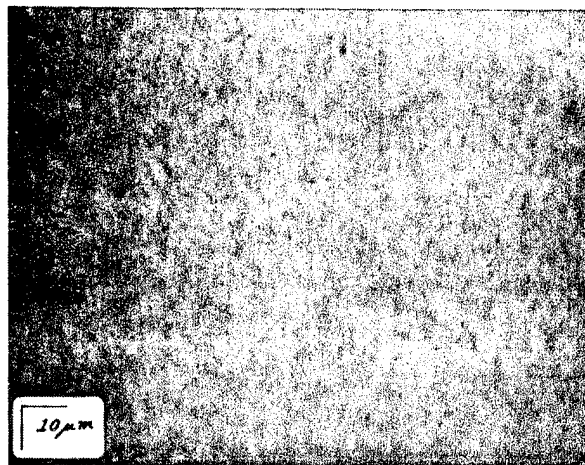


Figure 6. Kapton; scanning electron microscope.

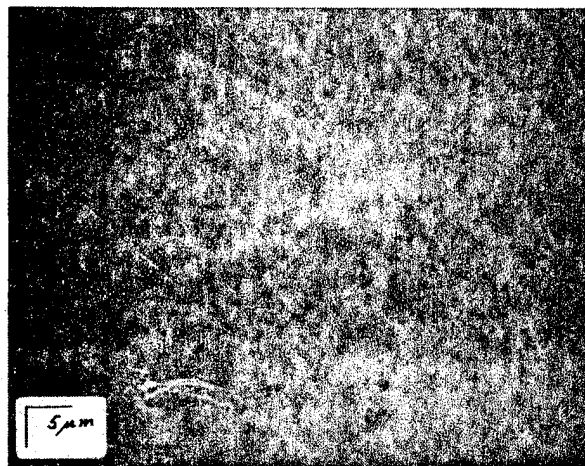


Figure 7. Kapton; scanning electron microscope.

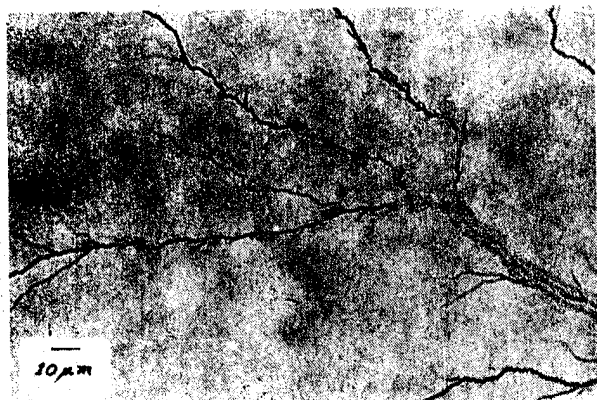


Figure 8. Kapton; transmitted light.

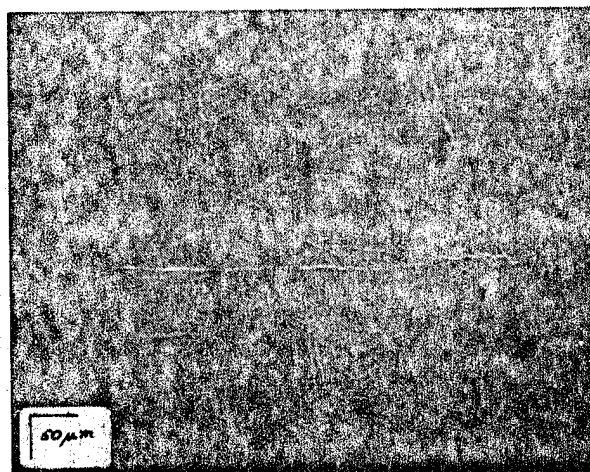


Figure 11. Mylar; scanning electron microscope.

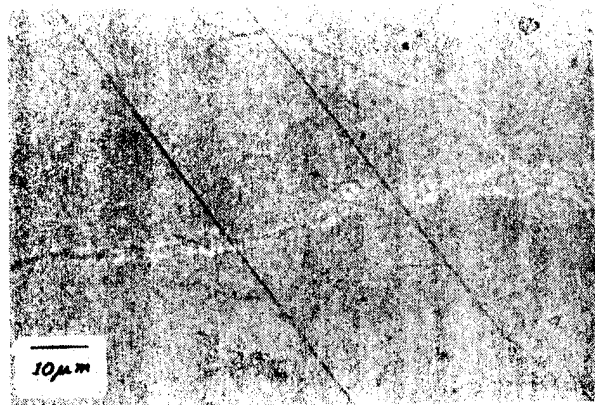


Figure 9. Kapton; reflected light.

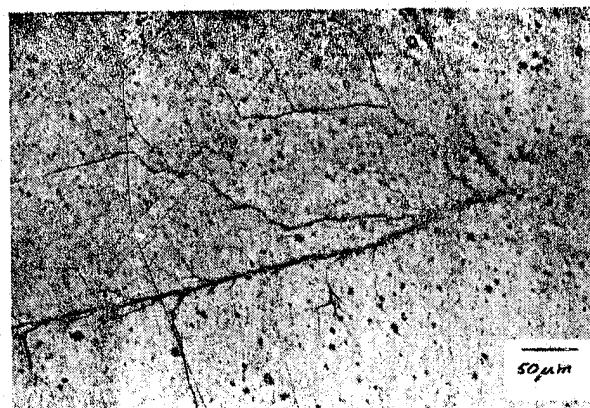


Figure 12. Mylar; transmitted light.

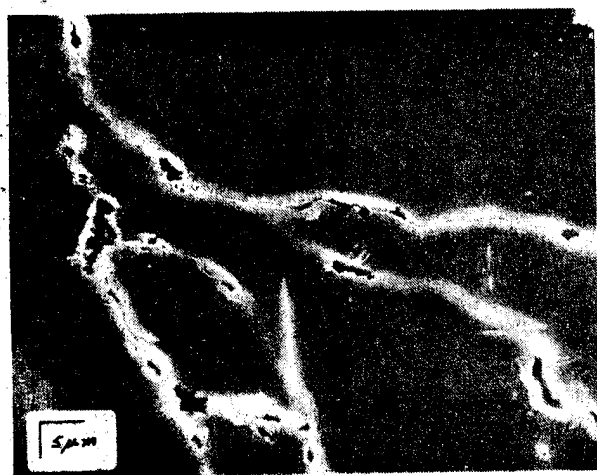


Figure 10. Teflon; scanning electron microscope.

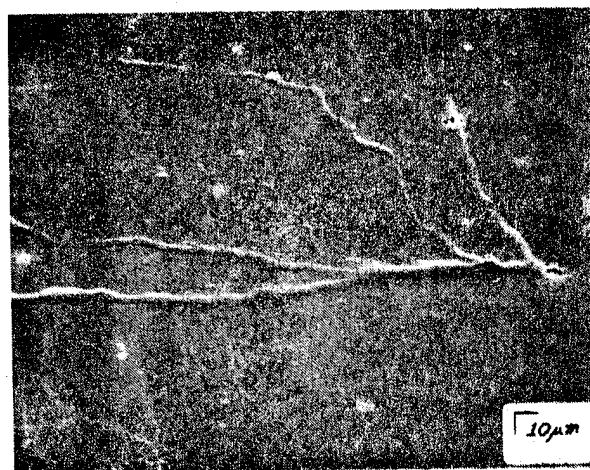


Figure 13. Mylar; scanning electron microscope.

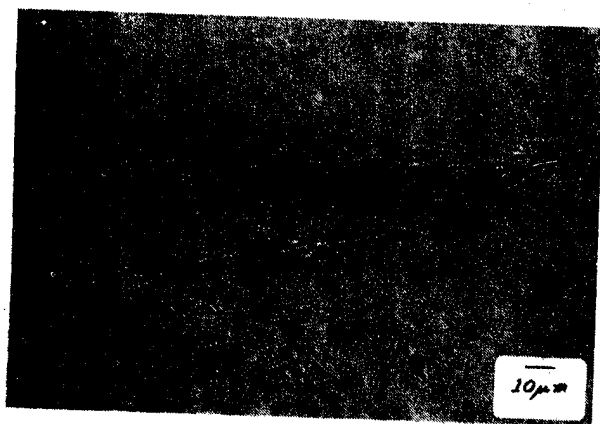


Figure 14. Mylar; reflected light.

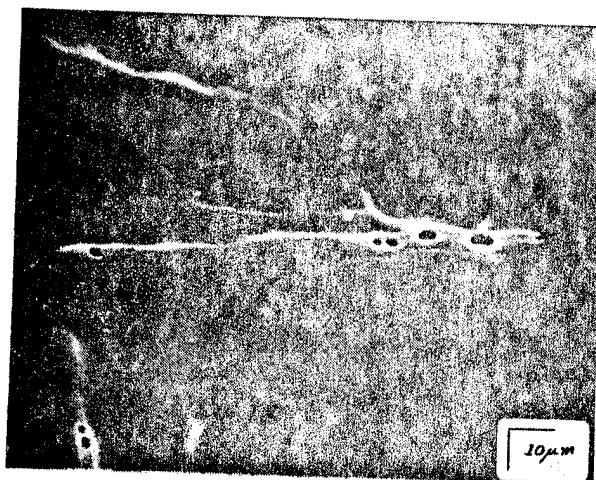


Figure 17. Mylar; scanning electron microscope.

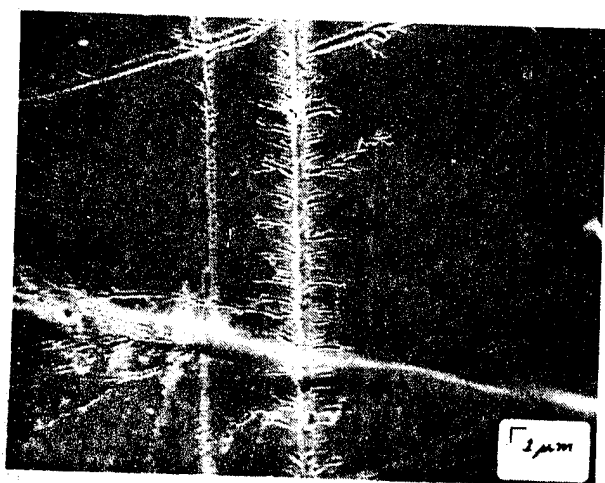


Figure 15. Mylar; scanning electron microscope.

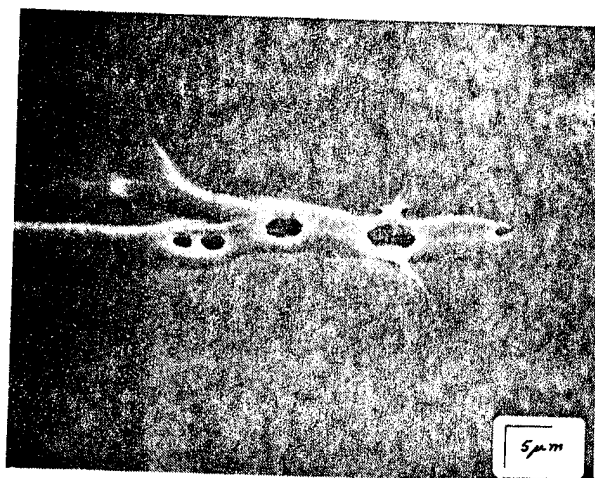


Figure 18. Mylar; scanning electron microscope.

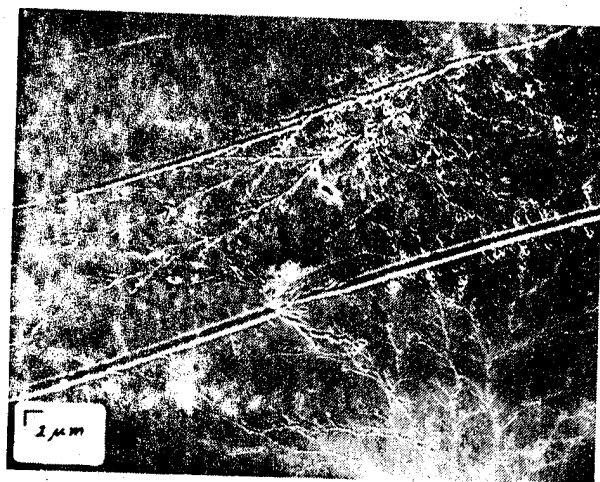


Figure 16. Mylar; scanning electron microscope.

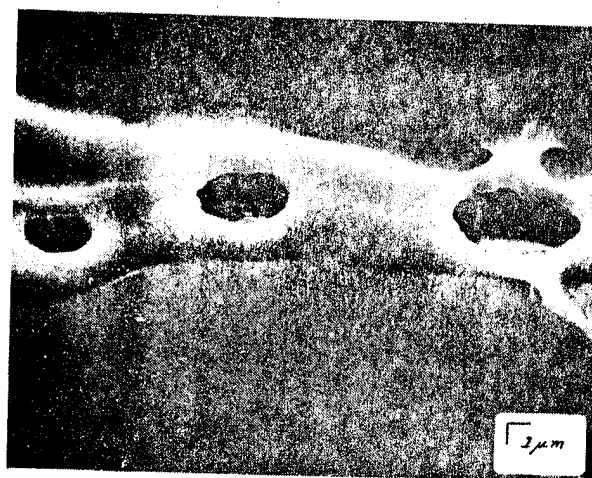


Figure 19. Mylar; scanning electron microscope.

N80-21441

THE CHARGING AND DISCHARGING OF SPACECRAFT DIELECTRICS

D K Davies

Electrical Research Association Ltd., Leatherhead, Surrey, UK

ABSTRACT/RESUME

Previous analyses of spacecraft charging under electron and ion bombardment are discussed briefly and shown to be inconsistent with recent experimental data. The processes underlying charge equilibration in insulators under electron bombardment, which include backscattering, secondary emission and radiation-induced conductivity, are reviewed. It is shown that the contribution of each of these processes is not unequivocally established. The observed discharges are discussed in terms of a demonstrable dependence of insulator electrical breakdown on indeterminate structural defects or impurities. The conceptual conditions for minimising charge levels are discussed but the prime conclusion is, however, that further experimental investigation must precede practical solutions.

Keywords: Spacecraft charging, insulators, electron bombardment, secondary emission, radiation, discharges

1. INTRODUCTION

Numerous spacecraft operational anomalies attributed to surface charging and subsequent discharge effects have justified considerable effort on modelling these phenomena.

The aim in the derivation of a theoretical model is to describe the charging of highly insulating materials under irradiation by electron or ion beams of prescribed energy and flux ranges. Charging rates and surface potentials must be predictable in terms of recognised, or determinable, materials parameters and the characteristics of the incident radiation and emitted electrons. The charge and energy deposition profiles, and hence, the internal electric fields, must be calculable, the objective being the delineation of the prime parameters governing the probability and energy of electrical discharges within the material, hence, yielding the possibility of controlling these phenomena by materials or structural modification.

Several theoretical analyses of electron bombardment charging have been made and these previous models of the charging process are assessed and the underlying processes of interaction of energetic electrons with materials reviewed in the present

paper. Ion interactions are also reviewed briefly and the rôle of radiation induced conductivity in the charge equilibration process is discussed.

Attainable accuracies in modelling the detailed physical processes must be tempered by the awareness of the significance of largely unpredictable impurities on the electrical properties of insulators particularly electrical breakdown.

Emergent novel model concepts are presented which indicate possible means of control. The prime conclusion is, however, that further experimental investigation of the basic interactions must precede realistic solution.

2. THE INTERACTION OF CHARGED SPECIES WITH INSULATORS

Despite considerable research motivated by the development of techniques such as scanning electron microscopy and the advent of practical devices - electrets - based on electron irradiation, the basic processes involved in the charging of insulators are poorly understood. The several mechanisms involved in the interaction of energetic electrons with solids, represented schematically in Fig. 1 together with their conventional detection methods, are well recognised but the significance of each to the charging of insulators has not been unequivocally established. Models of the charging process are therefore necessarily approximate.

2.1 Models of Electron Beam charging of Insulators

The charging process is generally considered capacitative, that is, the charge results from a nett current difference between the incident electron flux and the total dissipative current comprising the electron back-scattering and secondary emissive processes, and the neutralising electrical conductivity of the materials. The rate of surface potential increase of a material of capacitance, C , per unit area, is given by:

$$\frac{dv_s}{dt} = \frac{1}{C} (j_i - j_{bs} - j_{se} - j_c),$$

where, j_i , j_{bs} , j_{se} and j_c are the incident, back-scattered, secondary emitted and material conduc-

tion current densities, respectively. The inadequacies of current models generally arise owing to improper description of the physical processes underlying these disparate interactions.

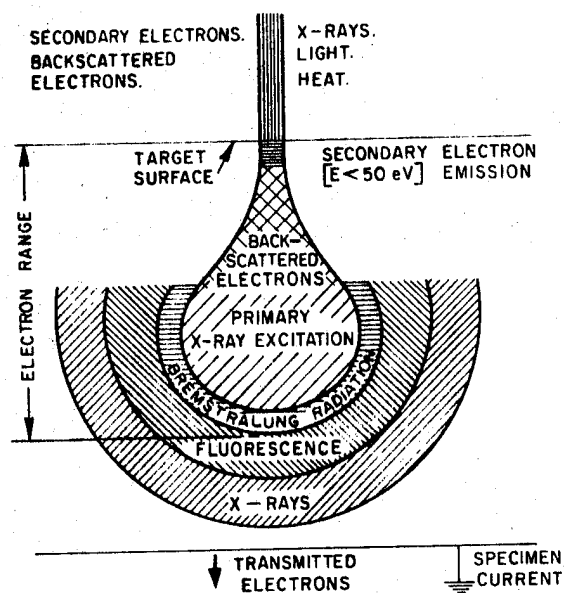


Figure 1. Representational diagram of interaction of energetic electrons with a solid (after Beaman and Asasi (Ref. 1)).

The significant effect of the surface charge on the incoming electrons has been ignored (Ref. 2) or inadequately described (Ref. 3, 4), a uniform volume density of charge having been assumed and an incorrect description given for the incoming current, respectively. Beers et al. (Ref. 4) pointed out that the primary current is not reduced by the surface charge field as described by Purvis et al. Both models, however, effectively assume that equilibrium is attained when the energy of the incoming electrons is zero, that is, when the retarding surface charge field is equivalent to the primary electron energy. This is not the case. As has long been known, and recently demonstrated experimentally by the author (Ref. 5), equilibrium obtains in highly insulating materials largely when dynamic balance is achieved between the incoming and secondary emitted electrons.

Figure 2 shows the equilibrium surface potential measured for electron irradiated 'Kapton' film plotted against the appropriate electron energy. It is evident that the surface charges to a potential representative of 'second crossover energy', (see Fig. 3) that is, where the secondary emission coefficient is unity. The equilibrium surface potentials extracted from the experimental data presented by Purvis et al. (Ref. 3) also presented in Fig. 2, exhibit precisely the same characteristics. This effect is not described by the present models. It is interesting to note that the threshold surface potential is apparently different for silvered and uncoated 'Kapton' and also for the aluminium plate. The former difference may indicate the influence of the coating metal and a possible avenue for controlled modification of the interaction. The slope of the plots in Fig. 2 are not unity which suggests that a second charge dissipation process must be involved. Clearly, accurate modelling

requires proper description of these detailed processes.

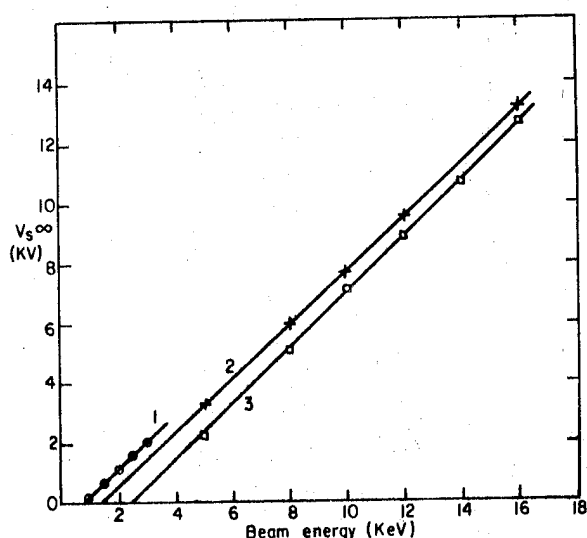


Figure 2. Measured equilibrium surface potential plotted against beam energy for electron irradiated Kapton, (Ref. 5), (1) silvered Kapton, (Ref. 3), (2) and aluminium, (Ref. 3), (3).

2.2 Backscattering

For metals, the backscattering coefficient, for a normally incident beam, increases with target atomic number but changes only gradually with energy for a given material (ref. 6). The coefficient decreases slowly with increasing energy for low atomic numbers, the variation becoming less for intermediate materials (silver) and reversing for high atomic numbers. Most of the data available for polymers follow the earlier trend, being described approximately (Ref. 7) by the empirical expression, $n = 0.1E^{-0.2}$, E being the beam energy.

Two approaches have been made to describe backscattering in low atomic number materials (ref. 8). In one, a single, large-angle scattering process has been assumed; while in the other, the electrons penetrate along straight paths in high atomic number materials until reaching a certain depth whereupon they diffuse again in straight lines isotropically in all directions. Recent measurements suggest that both single and diffusion scattering must be considered.

In view of the apparent significance of the surface coating in charge equilibration indicated by the data in Fig. 2, a thorough analysis of backscattering must be included in future models.

2.3 Secondary Electron Emission

Electrons emitted from solids under electron bombardment usually have a distinctly bimodal energy distribution. The backscattered electron energies are very similar to those of the primary electrons while the low energy, < 50 eV, say,

electrons are those emitted following ionization of the solid. The number of these secondary electrons per incident electron - the secondary emission coefficient, δ , can far exceed unity. The form of the variation of δ with incident electron energy is shown schematically in Fig. 3.

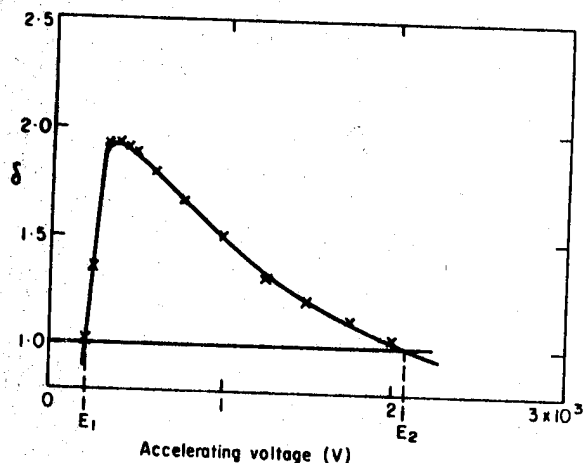


Figure 3. Schematic diagram of variation of secondary emission yield as a function of beam energy showing E_1 and E_2 the first and second "crossover" energies.

The energies V_1 and V_2 at which $\delta = 1$ are known as the first and second crossover points. Physically, these may be interpreted as the onset of energies for ionization and the energy at which the depth of primary beam penetration precludes emission of the secondary electrons. For $V_1 < V < V_2$, $\delta > 1$, and so in principle the insulator may charge positively. The emission energy is so small, however, that a small positive excursion of the surface is sufficient to inhibit further emission. A positive extracting field, such as may be provided by a deeply trapped negative charge, however, could cause the surface to charge positively, the equilibrium charge density being defined only by the extracting field (Ref. 5).

Despite considerable investigation, there is no complete theory describing secondary emission, (Ref. 9). The secondary emission yield may be defined in terms of the primary energy by

$$\delta = n(x, E_0) f(x) dx,$$

where $n(x, E_0)$ is the number of secondary electrons produced at a distance x from the surface by the primary electron of energy E_0 and $f(x)$ is the probability of emission through that distance x .

If β is the energy required to produce a secondary electron and $-dE/dx$ is the energy loss per unit path length normal to the surface, then:

$$n(x, E_0) = -\frac{1}{\beta} \frac{dE}{dx}$$

The function $f(x)$ may be expressed as:

$$f(x) = AB e^{-x/L},$$

where, A is the fraction of electron diffusing towards the surface; B is the probability of emission having arrived at the surface; and, L is the mean free path for absorption of the electrons or the effective escape depth. Penetration experiments have suggested that the energy loss of the primary electrons per unit path length is approximately constant, then:

$$\frac{dE}{dx} = \frac{E_0}{R},$$

where R is the range of electrons of energy E_0 . Substitution and integration yields:

$$\delta = \frac{A B E_0 L}{\beta R} (1 - e^{-R/L})$$

Expressed in terms of the maximum yield, δ_{\max} , and the energy for maximum emission, E_{\max} , this describes the universal yield curve which is generally accepted but does not wholly describe the data for insulators. Many expressions for the range of the primary electrons in terms of materials parameters have been derived, (Ref. 1). Typically (Ref. 10), for primary energy in kilovolts and material density, ρ , in gm cm^{-3} , then $R = 1.15 \times 10^{-6} E_0^{1.35} / \rho$ cm, empirically describes the observed range in alumina.

Experiment, (Ref. 11) has shown that the effect of changing the angle of incidence of the primary electrons is consistent with the escape depth model. Increasing the angle of incidence decreases the normal distance from the surface at which the secondaries are produced and so increases the yield, the increased yield with angle being clearly larger for higher beam energies.

Trapped primaries retard subsequent electrons, hence, reducing their penetration and consequently changing the secondary emission characteristics. This escape depth concept may, therefore, be important in describing the temporal growth of charge particularly near equilibrium.

Such concepts must be pursued in future modelling but clearly more experimental data are also required.

2.4 Radiation Induced Conductivity

The power law relationship between equilibrium conductivity, C_R , and irradiation dose rate ϕ is well established, (Ref. 12), i.e.

$$C_R = \epsilon K \phi^\Lambda$$

where ϵ is the permittivity; K and Λ are constants, the latter usually having value between 0.5 and 1. There is a wide spread in published values for K for polymers and measurements at low dose rates generally yield lower values for Λ than higher dose rates, (Ref. 2).

The dose rate is usually assumed to be constant over the irradiated volume and given by $\phi = 10^5 IV/R \rho$, I and V being the beam current density (A cm^{-2}) and energy (V). It is evident that the assumed range may be greatly overestimated and,

hence, local dose rate underestimated, for a charged dielectric. The radiation induced conductivity is dependent on both dose rate and time, the conductivity increasing over a period of seconds. Little is known about the latter effect, (Ref. 2), however, but this is again significant in describing transient charging phenomena.

Charge leakage is confined to the irradiated region which would inevitably be reduced as the dielectric charges. Circuit models based on the trapping of injected monoenergetic electrons in a plane layer at a depth defined by the beam energy have been successful in describing the observed currents. As such, they may prove useful in modelling the internal fields established within the irradiated dielectrics, as well as aiding the description of macroscopic charging phenomena. However, the assumption of a uniform ohmic conductivity throughout an irradiated volume defined by the initial beam energy must be treated cautiously.

2.5 Ion Bombardment

There is a paucity of information on the effect of ion bombardment of synthetic polymers. It has been shown (Ref. 13), that at low kinetic energies electron emission by Auger neutralisation, which is familiar for metals, (Ref 14), also occurs in inorganic insulators. At higher energies penetration of the material probably occurs and radiation induced conductivity has been observed.

Controlled charging of P.E.T. has been achieved in air by both positive and negative ions generated by a Nernst filament (Ref. 15). However, the nature of the ions and of the interaction process both remain to be established.

2.6 Electrical Breakdown of Insulators

The intrinsic electric strength of insulators, and in particular synthetic polymers, has long been investigated. Several theories based variously on thermal runaway, electromechanical distortion or trap saturation concepts, have been advocated but the cataclysmic breakdown phenomenon remains to some extent unpredictable. The latest, (Ref 16) in the long series of reports shows that this arises owing to the very great influence of defects in the polymer film on the breakdown process. Figure 4 presents experimental data showing the number of breakdowns per unit area as a function of the applied electric stress for two differing polypropylene films. Such an effect can only result from random non-uniformities in the materials. The whole range of breakdown stress for these materials, however, is about 4 to 8 Megavolt cm^{-1} and so a degree of consistency is evident. Pretensions to accuracy in predicting breakdown in polymers must be treated with caution.

It has been shown (Ref. 17) that the discharge rate under electron bombardment is proportional to the electron flux and that large areas of dielectric are apparently discharged in single events. Grounding any surface metallisation causes little reduction in discharge activity although reducing metallisation loss from that observed with ungrounded specimens. This effect presumably results from less energetic discharges consistent with more local effects in the former circumstance. The local erosion of surface metallic films by discharges - both within the dielectric and across the surface - is commonly observed in capacitors.

In fact, it is a practice to "clear" thin film capacitors by deliberately breaking down defects by overvoltage application, thus promoting such discharge erosion of the adjacent electrode material. Evidently the incidence of discharges decreases at a given electric stress following such treatment. The initiation and energetics of surface breakdown effects are clearly also unpredictable being equally dependent on local field distortions caused by material defects, electrode irregularities (where present) or non-uniform charges.

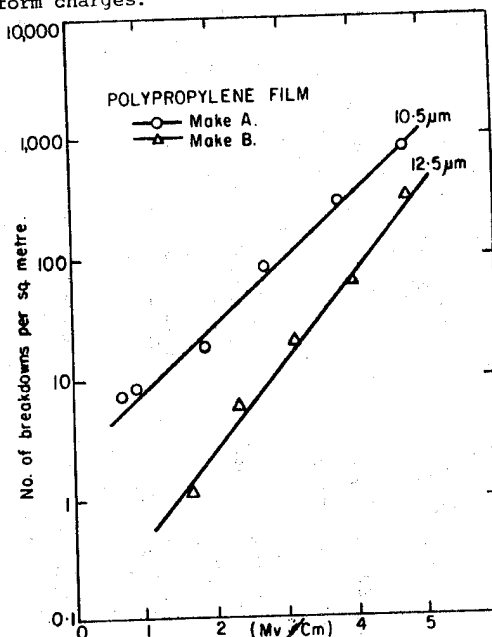


Figure 4. Plot of experimentally observed number of breakdowns plotted against applied electric stress for polymer films.

3. DISCUSSION - MINIMISING CHARGE ACQUISITION

The analysis has shown several conceptual avenues which may be sensibly pursued in order to minimise charge acquisition.

Increasing electron-backscatter by using high atomic number coatings, for instance, would evidently reduce electron-dielectric interaction. Likewise, incorporation of electron-retarding species into the insulating materials would decrease electron penetration for a given incident energy, thereby raising the upper secondary emission threshold (second crossover). Since the low emission energy of secondaries precludes large positive potential excursions of the surface, extension of the range of secondary emission results in reduced accumulated charge densities.

The use of special surface profiles to increase the effective angle of incidence of the primary electrons would also seem indicated. This, however, may not be practicable owing to the frequently over-riding prime requirement of the surfaces - optical reflectivity, for instance.

Increasing the insulator conductivity to an appropriate level would inhibit charge growth. However, the physical or chemical "doping" of polymers, in general, radically changes wanted mechanical characteristics. Optimisation of radiation-induced conductivity may offer a feasible alternative means.

All the proposals are, however, somewhat speculative, since there is a dearth of information on many aspects of these interactions.

A parameter wholly ignored in most analysis is temperature. Certainly, changes in temperature have a very great influence on the electrical properties of insulators. The conductivity of polyimide, for example, increases by an order of magnitude between 20°C and 50°C. Spacecraft surface materials can experience large temperature excursions between sunlight and shade. Very different charge migration characteristics would certainly obtain at these extremes.

There appears to be little data available with regard to the influence of material temperature on the charge acquisition processes, although it is evident that there must be some influence on the equilibrium levels obtained.

4. CONCLUSIONS

The present brief review has underlined some of the inadequacies of present simple models of insulator charging. Also, the general lack of understanding of the basic processes involved in the interaction of ionized species with insulators - particularly synthetic polymers - has been emphasised. In fact, there is a paucity of experimental data on many aspects arising probably owing to the difficulty in applying conventional techniques to highly insulating materials.

A cautionary note must also be introduced with regard to attainable accuracies. While an individual experiment may provide an acceptable - say 5% - level of accuracy, it is probably inevitable that, owing to the sensitivity of these processes to indeterminate impurities and defects in the materials, the degree of reproducibility for multiple samples is far less. This is certainly the case with electrical breakdown - a factor of two difference in breakdown stress is possible between small area specimens of the same material.

The experiments indicate that at room temperature the predominant (but not exclusive) equilibrating process is that of secondary electron emission. It has also emerged that if a uniform charge density on the specimen is assumed, then any variation in input current reflects the influence of the surface field on the emission properties of the source only. The surface charge reduces only the energy of the incoming electrons. An improved model of the temporal growth of surface charge, the equilibrium surface potential and internal fields must take account of the fact that:

1. The energy and charge deposition profiles are influenced by temporal changes in the volume and surface fields;
2. The secondary emission process and radiation induced conductivity are both space and time variable owing to these changes;
3. Equilibrium obtains when a dynamic balance exists between the primary electron current and the several - but predominantly secondary emission - processes and not through total repulsion of the primary electrons;

4. The primary electron interaction with the material may be significantly influenced by surface films (either deliberate or inadvertent), and
5. The indeterminate defect properties of polymer films play a significant rôle in their electrical characteristics particularly electrical breakdown strength.
6. The material temperature significantly influences the electrical breakdown mechanism and may play an important rôle in the charge acquisition and equilibration process.

5. REFERENCES

1. Beaman D R and Asasi J A 1971, *Mat. Res. and Stds.*, 11, 14-17.
2. Gross B, Sessler G M and West J E, 1974, *J. Appl. Phys.* 45, 2841-51.
3. Purvis C K, Stevens N J and Oglebay J C, 1977, *Proc. Spacecraft Charging Tech. Conf.*, AFGL-TR-0051, NASA TMX-73537, USAF Academy, Colorado, 459-86.
4. Beers B L and Pine V W, 1978, *Interim Contract Report*, SAI-102-78-002, Science Applications Inc.,
5. Davies D K, 1976, *Nature*, 262, 279.
6. Bishop, H E, p.85 et. seq. Ref. 8
7. Wall, J A Burke E A and Frederickson A R, 1977, *Proc. Spacecraft Charging Tech. Conf.* AFGL-TR-0051, NASA TMX - 73537, USAF Academy, Colorado, 569-91.
8. Thornton, P R 1968, *Scanning Electron Microscopy*, (London; Chapman and Hall)
9. Simon R E and Williams B F, 1968, *IEEE Trans. Nuc. Sci.* NS-15, 167-70
10. Young J R, 1956, *Phys. Rev.* 103, 292-3.
11. Hill, G E, 1976, *Adv. Electronics and Electron Phys.* 40A, 153-65.
12. Fowler, J F, 1956, *Proc. Roy. Soc. A* 236, 464.
13. Vance D W, 1971, *J. Appl. Phys.*, 42, 5430-43.
14. Hagstrom, H D, 1956, *Phys. Rev.* 91, 543.
15. Baum E A and Lewis T J, *Static Electrification 1975, Inst. Phys. Conf. Ser. No. 27*, 130-40. (Ed. A R Blythe, London Inst. Phys. 1975)
16. Parkman N, 1978, *ERA Report*, 78-21, 23. *IEEE Trans. Elec. Ins.* No.105 (Aug. 1978)
17. Stevens N J and Lowell, R R, 1975, *NASA Tech. Memo TMX-71795*.

PRECEDING PAGE BLANK NOT FILMED

DISCUSSION

S. J. Bosma :

We at ESTEC have irradiated aluminised kapton samples. In general, it was found that for incident energies lower than 30 keV, discharges occurred over the whole surface of the samples, with 'Lichtenberg' patterns towards the edges. For energies higher than 30 keV, discharges were very concentrated at points and caused 'punctures'. Do you think that 'discharges' you photographed are caused by edge effects on the punctures?

K. G. Balmain:

None of the photographs shown involved punctures through to the substrate, all of these experiments have been carried out using 20 keV electrons. We did see some punctures, however, especially in materials 50 μ m thick and thinner. Once a puncture had occurred, it became the 'focal point' for subsequent discharges. It is possible that the puncture point, being at ground potential, would produce incident-beam focussing in its vicinity and consequent high embedded-charge density with discharge initiation there. Similar remarks could apply to discharge initiation at the mask edge.

Discharge area appear brightest and thickest at the mask edge or at a punch through, but it is not clear that the electron flow is strongly to the mask or down the puncture hole. It is at least as probable that most of the electrons are propelled into space through surface holes near the mask or at the puncture edge.

D. Verdin :

We have observed reductions in the surface potential of electron-irradiated aluminised Kapton on simultaneous exposure to visible light. Since unaluminised Kapton does not show any reduction in surface potential, the effect does not appear to result from photoemission. I therefore wish to ask if you have any information on the extent to which photoconduction contributes to the charge equilibration process in irradiated dielectrics?

D. K. Davies:

All polymers are photoconductive to a degree, and so illumination would increase charge dissipation rates. However, charge carrier mobility in insulators is a thermally activated process, and so the observed decrease in surface potential could result from temperature increase.

J. Dauphin (ESA) :

Do you know of a white pigment that is UV stable and has a high secondary emission?

D. K. Davies:
No.

S.J. Bosma :

If the second cross-over of the secondary emission curve is moved to the kV-range, is there still a problem of positive charging due to high secondary yields caused by electrons in space with lower incident energies than this second cross over? In other words, must the secondary emission yield between the two cross-overs be >1 ?

D. K. Davies:

No, the secondary emission yield need not be unity since the low (say <50 eV) emission energy of secondary electrons would preclude any large positive excursion of the surface potential, even for high yield values.

S.A. Greenberg :

In view of your facility's radiation output of a few thousands rads per day, can you reasonably expect to reach threshold levels in reasonable time?

R. C. Tennyson:

If we use a 500 mc source unfiltered, then it has been estimated that we can achieve about 3.3×10^4 rads/day. Consequently, it is possible with this S90 - Y90 natural source to achieve simulated electron doses of 10^7 rads in about one year of actual exposure. However, to reach levels of 10^9 rads becomes impractical.

J. Dauphin (ESA) :

How is the UV intensity inside the chamber measured?

R. C. Tennyson:

We have two sensors for monitoring the UV radiation: 220-280 nm and 300-400 nm, respectively. Due to our facility design, the UV lamp can easily be raised through the top of the quartz cylinder, and calibrated. At present such calibration measurements will be made every 100 hrs.

R. Moss (Ford Aerospace) :

Have you cross-checked your strain gauge calibrations of the composites against known stable standards such as NBS quartz rods?

R. C. Tennyson:

No, however, we have checked our strain gauge measurements against several metal tubes and correlated these results with actual micrometer measurements of the tube displacements. For comparative purposes these calibration specimens are also included in the thermal-vacuum long duration tests. At present, we are also making comparisons with laser interferometer displacement data in-situ.

Preceding page blank

225

SESSION VII

ENVIRONMENTAL EFFECTS – RADIATION

Co-chairmen: J. Guillin & M.L. Minges

PRECEDING PAGE BLANK NOT FILMED

N80-21448

EFFECT OF RADIATIONS ON POLYMERS AND THERMAL CONTROL COATINGS

J Bourrieau & A Paillous

*Centre d'Etudes et de Recherches de Toulouse**Département d'Etudes & de Recherches en Technologie Spatiale, Toulouse, France*

ABSTRACT

An overall survey of the problems encountered with polymers and thermal control coatings submitted to radiations in space is presented.

A theoretical study that modelizes the degradations of the solar absorptance under electron and proton irradiations is described. The model takes the absorbed energy dose repartition within the material into account and assumes that the solar absorptance variation is imputed to color centers, the concentration of which can be expressed in terms of dose. The relevance of such a correlation is corroborated by measurements performed on two polymers and two white paints.

An example of a radiation qualification test program carried out for OTS is given. Predicted degradations of the thermal control coatings are compared to data obtained after one year in orbit.

Keywords: Radiation damage, thermal control coatings, electron irradiation, proton irradiation, space environment simulation.

1. INTRODUCTION

The external surfaces of a satellite are submitted to the various components of the space environment (particles, ultraviolet radiation, vacuum, thermal conditions). As a consequence of these components acting together, it is well known that a degradation of the physical properties is observed. For polymeric materials and thermal control coatings for instance, a change in colour is observed that leads most often to an increase of the solar absorptance. It is obvious that such a change is principally due to the energetic protons and electrons encountered in orbit as well as to the severe ultraviolet radiation flux out of atmosphere.

Spacecraft system designers are most concerned about these changes and in order to take them into account they wish to know the variation law in terms of time in orbit. Advanced space projects involve very long mission durations (five to ten years becoming often a requirement) for which short time experiments in laboratory must be representative of a far longer exposure to space.

Economic constraints strongly incite to look for the appraising of the possible degradation, at the lowest cost. That is to say that all the previous experience must be used in order to lighten the costly simulation procedures and that it is necessary to be fully aware of the tests validity as well of its limits.

In a first part we will make an overall survey of the problem encountered when laboratory experiment are performed in order to simulate the effects of space radiation : purpose, approach and facilities. Some data concerning the prediction of degradations on board the OTS 2 satellite will be compared to the one obtained in orbit.

In a second part a model that could help to predict the degradation in orbit will be presented. This model correlates the reflectance degradation of paints and SSMS to the absorbed energy dose. A verification of this model is given.

2. STATE OF ART TECHNIQUES OF SIMULATION

2.1 General comments

The techniques and procedures that are being used in USA or in Europe have not appreciably changed for the five last years (Ref 1, 2, 3). Ultraviolet radiation, electrons and protons are simultaneously directed onto the samples that are maintained under a high vacuum (less than 10^{-6} Torr) for all the irradiation time as well as for the optical measurement period. Contamination-free pumping systems and chambers are of prime importance in order to prevent a parasitic degradation of the optical properties of sample under test. An extreme care must be exerted in order to control the sample temperature that could modify the degradation kinetics and its nature. For instance the infrared energy excess of sun simulators using Xenon arc lamps must be suppressed or limited by appropriate means in order to prevent the sample overheating.

The optical reflectance must be spectrally measured at least in all the solar range (0.35 to $2.3 \mu\text{m}$), if one wishes to evaluate the solar absorptance variations.

For the last three years a growing interest has been expressed for conductive coatings ; so there is now some requirements for in-situ electrical conductivity measurements as the irradiation gets on. The conductivity values can be largely modified in presence of ultraviolet and visible light (e.g. Kapton) or in presence of particle radiation (many dielectrics).

Free standing polymeric films (that is to say, films not bonded by an adhesive to a substrate, have recently been of concern for various external use in space : large reflectors, solar sail, thermal blankets, solar cells substrates. The experiments have shown that the mechanical properties (ultimate strength, impact strength, modulus, shrinkage, dimensional stability) of irradiated polymeric films were largely modified by UV or electron irradiation (Ref. 4, 5, 6). There is some evidence that a very fast variation of mechanical properties happens during the very earliest minutes following the beginning of exposure to air of an in-vacuum irradiated film : Ref. 7. That would suggest the need of an in-situ mechanical testing of irradiated polymers.

It has been widely demonstrated for the last few years (Ref. 8,9) that an electrostatic charge of the satellite dielectric surfaces can build up under certain circumstances until the point that discharges can occur. This phenomenon has been experienced by many geosynchronous satellites the particle environment of which has been shown to vary considerably during magnetic substorms. During these substorms at synchronous orbits the relatively cold plasma (about 1 eV) of density 10 to 100 cm^{-3} is rapidly swept away and replaced transiently by an energetic electron plasma: electron energies from 3 to 20 keV density 0.1 to 10 cm^{-3} (Ref. 10). It is these latter energetic electrons which give rise to the high potentials (up to 20 000V) that have been measured in space and also to the differential charging of contiguous surfaces when some of them are illuminated. Discharges are observed when the differential voltage exceeds a certain threshold value. Such arcing phenomena, among other detrimental effects, can severely degrade some parts of the satellite surfaces because they are repetitive (Ref. 11, 12, 13, 14). Material breakdown can lead to charring, matter volatilization or ejection ... For some coatings, like FEP second surface mirrors, the optical degradation that is due to these discharge phenomena can be more important than the one that is due to the pure radiation damage in the bulk (Ref 14, 15): discharge paths can be seen on the top of their surface, leading to a diffuse reflection of light and to greatly enhanced absorption. Therefore it is of prime importance to include in the radiation qualification tests of materials to be flown in geosynchronous orbits, the low energy electron component of the environment (5 to 20 keV). In this case, one must try to oblige the sample to undergo the same number of breakdown (or discharge) phenomena that are expected on a statistical basis for a certain time in orbit without altering their physical nature. That is to say, one must use in laboratory electron fluxes and electron energies that are nearly the same as the ones encountered in substorm conditions (i.e. 0.1 to $0.8 \text{ nA cm}^{-2}\text{s}^{-1}$, 5 to 25 keV). Moreover the sample configuration must be carefully chosen in order to be representative of the actual technique used in space.

Besides these low energy electrons, the qualification test must obviously be performed with electrons and protons the energy and the fluences of which are chosen, depending on the orbit conditions, in such a way as to ensure a high level of concordance between the energy doses absorbed and those calculated for the mission (Ref. 2).

An example of a simulation performed at DERTS for the space qualification of OTS coatings is given hereafter.

2.2 Qualification of the OTS thermal control coatings

Under contracts of ERNO and ESTEC, two qualification programs of thermal control coatings for the geosynchronous environment of OTS were carried out (Ref 16, 17, 18). The aim of the first was to simulate the environment conditions of materials placed on the North and South faces of the satellite ; the second was related to materials on the equatorial belt of the same satellite. These conditions corresponded to two different levels of solar exposure.

An absorbed energy dose calculation was performed at DERTS (Ref 16), for the various materials to be tested, after computation of the spectral particle fluxes. Fig. 1 and 2 give the dose repartition in Silica for a 7 years exposure to space. Dose at surface is mainly due to protons; dose in the bulk is mainly due to electrons. From these results, one electron energy (200 keV) and two proton energies (40 and 150 keV) were selected, together with the respective fluences, in order to give to the sample the same absorbed energy dose distribution as the one in space. Fig. 3 gives a comparizon of these dose distributions for Silica.

The irradiation parameters that were chosen for both tests are reported in Table 1. Samples are also described in Table 1. A continuous UV exposure (3 suns intensity) was applied for all the test duration. Electrons and protons irradiations were performed at selected times allowing an exact equivalence with UV corresponding to various exposures in orbit. Fig. 4 indicates the procedure that has been followed for the second test. Fluences rates range from $1.3 \cdot 10^9$ to $8.8 \cdot 10^9 \text{ e cm}^{-2} \text{ s}^{-1}$ for electrons, from 4.5 to $2.9 \cdot 10^8 \text{ p cm}^{-2} \text{ s}^{-1}$ for 150 keV protons, from $1.3 \cdot 10^9$ to $8.8 \cdot 10^9 \text{ p cm}^{-2} \text{ s}^{-1}$ for 40 keV protons.

The DERTS combined environment facility was used (Photo 1). A high vacuum (less than 10^{-6} Torr) was maintained for all the irradiations and measurements.

A spectral in-situ measurement of the optical reflectance was performed and the solar absorptance variations were computed. From the degradation values, a variation curve showing predicted degradations in terms of time in orbit was given for each sample (Ref. 17,18). Some examples are given in Fig. 5 to 9.

Some limited and preliminary analysis of OTS 2 thermal surface degradation is becoming available at ESTEC (Ref. 19). The temperatures of 14 spot beam antenna dish sensors have been used, normalising for seasonal solar intensity and seasonal solar vectors angle to sensor positions

on curved dish. The view factors at each sensor plus struts and rest of dish are ignored; thus it is only possible to give averages of the maximum solar absorptance of the S13G/LO on the antenna dishes.

The corresponding degradation values are reported in Fig. 8. For the OCLI silvered quartz, the temperature of 11 sensors on TWT and control radiators were used for the steady state spacecraft tests of May 26, 1978 and May 26, 1979 for approximately equal and similar spacecraft dissipations. Using both maxima and minima, the mean annual increase of the solar absorptance was calculated to be 0.0035; this value can be compared with our predicted value in Fig. 7.

These results are the only available from in orbit OTS measurements. They confirm the validity of tests performed at DERTS for the radiation qualification of thermal coatings. An other evidence of the validity of the procedure that is used currently was given three years ago by in flight experiments on board the French satellite SRET 2 (Ref. 20).

3. MODELING OF DEGRADATIONS DUE TO PARTICLES

3.1 Introduction

Spacecraft system designers need to know the solar absorptance variation during exposure to space conditions in order to effectively control the satellite temperature by use of appropriate coatings. Such a variation is due to absorption bands that are observed in the reflectance spectrum in consequence of color centers formation or of molecular evolutions that are induced by ionizing (and ultraviolet) radiations.

To be practical, the solar absorptance variations must be correlated to the particle fluences that are expected in orbit for a given coating.

Generally at first one computes the energy spectrum of electrons and protons that will be encountered in space. Then irradiations are performed under vacuum with monoenergetic particles whose energies and fluences are thought to simulate the most active in space. In-situ optical measurements allow to know the spectral reflectance variation due to irradiations.

Such a method has several drawbacks : a) the choice of energies and fluences is rather empirical, b) the isotropic distribution of particles in space is not simulated in the laboratory c) previous experience is worthless because each simulation specifically describes the environment of one orbit.

A degradation model that would take the physical processes into account could reduce the influence of the test parameters, allow a better choice of simulation conditions and allow to use data obtained in other laboratories and in other experiment conditions.

Degradation data that can be found in literature as a consequence of particle irradiations are seldom comparable at the first glance because they have been obtained with various particle nature, energies, fluences and flux rates.

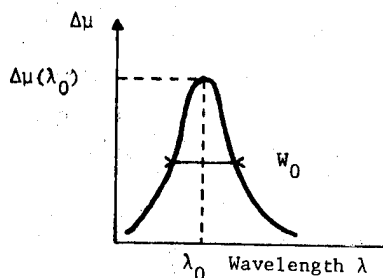
A literature search was decided in order to gather degradation data for the coatings in current use: S13G (ZnO/silicone paint), 293 (ZnO/silicate paint), Alumine/silicate paint, aluminized Kapton, Terphane film (polyethylene terephthalate) : see Ref. 21. A model was tested for the aluminized Kapton and the S13G paint for which there was a sufficient amount of results in the published technical papers. Complementary systematic experiments were performed for some materials (Terphane, PSG 120 (ZnO/silicone), PSZ 183 (ZnO/silicate); FEP Teflon SSM, Kapton) in order to incorporate reliable and coherent data: see Ref. 22,23.

3.2 Model

3.2.1 Preliminary remarks

Degradation of the thermal control coatings due to electrons and protons encountered in space is mainly due to low energy particles : a few tens to a few hundreds kiloelectron volts. That is to say that the degraded zone is very near to the surface.

In the degraded zone an increase of the optical absorptance in the solar range (0.3 to 2.4 μm) is measured in the form of an absorption band as a consequence of the creation of defects (color centers, molecular products) under irradiation. In a variety of cases the defect concentration N_D has been correlated to the intensity and the shape of the absorption band variation by the SMAKULA relation (Ref. 24)



$$N_D = A(\lambda_0) W_0 \Delta\mu(\lambda_0) \quad (1)$$

where

W_0 is the full band width between half amplitude points, $\Delta\mu(\lambda_0)$ is the maximum amplitude of the spectral absorption coefficient variation and $A(\lambda_0)$ is a constant.

Very often the defect concentration is only related to the energy density (or "dose") that is locally absorbed by the material under irradiation. That is especially the case for defects that are created by ionisation process. At a macroscopic scale the degradations are expected to depend only on the dose distribution within the material. This absorbed energy dose is not uniform for low energy particles when expressed in terms of depth, but its distribution within the matter can be calculated using computation codes - see for instance Ref. 25, 26, 27 and also a general description in Chapter 3 of Ref.23.

3.2.2 Model basis

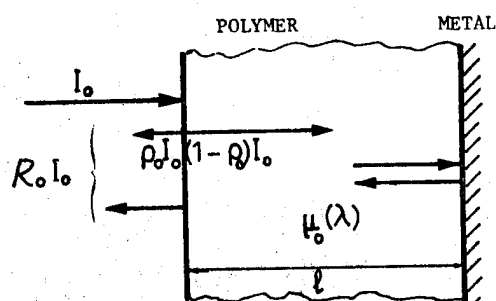
The following assumptions are made:

- the defect density is only related to the local absorbed dose
- the optical degradation is due to an absorption band the intensity of which depends only on the defect density and it follows the SMAKULA relation (1).

The absorption band can be measured by comparing the reflectance spectra $R(\lambda)$ of the irradiated and unirradiated coating. From the spectra the solar absorptance (or reflectance) can be computed.

3.3 Development of a model for SSM

3.3.1 Calculation



The SSM is made of a polymeric film (the thickness of which is l , the absorption coefficient is $\mu_0(\lambda)$) and a metal layer.

The reflectance at the front surface is $\rho_0(\lambda)$ and at the polymer-metal interface is $R_0(\lambda)$.

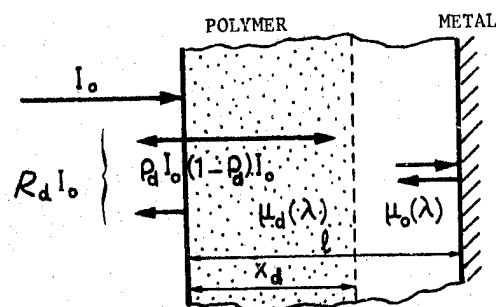
$R_0(\lambda)$ is assumed to be equal to 1.0.

The intensity of a light beam impinging on the surface is I_0 . The reflectance $R_0(\lambda)$ of the SSM is

$$R_0(\lambda) = \rho_0(\lambda) + [1 - \rho_0(\lambda)] \exp[-2\mu_0(\lambda)l] \quad (2)$$

After irradiation: A zone near to the surface is supposed to be uniformly degraded. Its thickness is x_d and its "absorption coefficient" is μ_d .

$$\mu_d(\lambda) = \mu_0(\lambda) + \Delta\mu(\lambda)$$



Beyond this zone, the material keeps the initial properties.

The reflectance $\rho_d(\lambda)$ at the front surface (degraded zone) is assumed to be equal to the one of the unirradiated polymer: $\rho_d(\lambda) = \rho_0(\lambda)$.

The reflectance of the degraded SSM is:

$$R_d(\lambda) = \rho_0 + (1 - \rho_0) \exp[-2\mu_0(\lambda)l] \exp[-2x_d\Delta\mu(\lambda)] \quad (3)$$

From (2) and (3)

$$\Delta\mu(\lambda) = \frac{1}{2x_d} \ln \frac{R_0(\lambda) - \rho_0}{R_d(\lambda) - \rho_0} \quad (4)$$

Therefore the spectral absorption coefficient variation $\Delta\mu(\lambda)$ can be calculated if the degraded thickness is known and the reflectances $R_0(\lambda)$ and $R_d(\lambda)$ are measured (ρ_0 can be calculated from the index or estimated from the spectrum in a high absorptance zone). Thus the product $W\Delta\mu$ (see section 3.2.1) can be obtained for each set of irradiation parameters (particle nature, particle energy, fluence). The absorbed energy dose \bar{D} and the particle penetration x_d can also be computed by the usual codes for each set.

A plot of $W_d\Delta\mu(\lambda_0)$ versus \bar{D} must give a unique curve if the defect number depends only on the mean absorbed energy dose, that is to say if our modeling basis is valid.

Moreover the solar absorptance variation $\Delta\alpha_s$ should be given by a unique curve if it was plotted versus the product $x_d W_d\Delta\mu$.

3.3.2. Results for aluminized Kapton

Many data can be found in the literature concerning aluminized Kapton irradiated either by electrons or by protons. A result compilation was performed (Ref. 21). The main irradiations that we selected because sufficient spectral data were available, are described in Table 2 with the mention "literature results". An absorption band whose maximum is at 600 nm is exhibited by irradiated aluminized Kapton samples (Fig. 10). ρ_0 was assumed to be 0.08.

After computation of the degraded range x_d and of the mean dose \bar{D} (Table 2) the product $W_{600}\Delta\mu(600)$ was plotted versus the mean dose \bar{D} : Fig. 11 shows that a straight line is obtained. Such a result suggests that the created defects depend only on the mean dose in the aluminized Kapton.

This was confirmed by results obtained at DERTS (Ref. 22) after irradiation of an aluminized Kapton film 75 μm thick bonded with a 3M467 adhesive to an aluminum platelet: Table 2. Fig. 12 where the latter results are given, shows exactly the same variation law for $W_d\Delta\mu$ in terms of absorbed dose.

Furthermore Fig. 13 indicates that it is possible to correlate directly the solar absorptance variation $\Delta\alpha_s$ (calculated from the in-situ

spectral measurements of reflectance) with the total number of defects that have been created by irradiation:

$$\Delta\alpha_s \text{ (in percent)} \approx 8.6 \cdot 10^{-2} \cdot W\Delta\mu \cdot x_d^{1.28} \quad \text{where}$$

$W\Delta\mu \cdot x_d$ is expressed in nm

3.3.3 Results for aluminised FEP Teflon

An aluminized FEP Teflon 75 μm thick was bonded with a 3M467 adhesive to an aluminum substrate and was irradiated at DERTS (Ref. 22): see Table 3. The in-situ reflectance spectrum was not continuously recorded but obtained at discrete wavelength that did not allowed an accurate localization of the absorption band maximum after irradiation. So the $W\Delta\mu$ value was calculated as:

$$W\Delta\mu \approx \int_{280}^{600} \Delta\mu(\lambda) d\lambda$$

Fig. 14 shows that all the $W\Delta\mu$ values are on the same curve when plotted versus the absorbed energy doses that can be computed for the various irradiations. However the linear relationship is only obtained for the highest energy densities.

As in the case of the aluminized Kapton, a curve giving $\Delta\alpha_s$ in terms of the total number of created defects can be drawn: Fig. 15. In this figure some $\Delta\alpha_s$ values at low irradiation doses seem too high. This is probably due to a deformation of the SSM that was noticed at the end of irradiations (see Ref. 22).

3.3.4 Results for Terphane films

A variety of thicknesses of polyethylene terephthalate, Terphane transparent film (*) (between 3.5 and 125 μm) were tested under irradiation at DERTS. For irradiation, the film were fixed (without adhesive) on a polished aluminum platelet and the in-situ reflectance measurements were performed with the same aluminum platelet that ensured the second surface reflexion.

Table 5 gives the irradiation parameters. The front surface reflexion is assumed to be $\rho_0 = 0.059$. As in the case of FEP film the maximum of the absorption band was not easily located due to the lack of a continuous spectrum recording, so instead of $W\Delta\mu$ we used:

$$W\Delta\mu = \int_{320}^{600} \Delta\mu(\lambda) d\lambda$$

The results are reported in Fig. 16. It can be seen that the degradations due to protons (45, 75 and 150 keV) and to 210 keV electrons seem to belong to a same curve. There is a very large spread of values for the 80 and 40 keV electron irradiation. This spread is probably due to the heterogeneity of dose in the irradiated zone (**).

(*) From 125 to 12 μm , Terphane films were available in the quality "D"; Terphane 3,5 μm and 6 μm thick was only available with the quality "D".

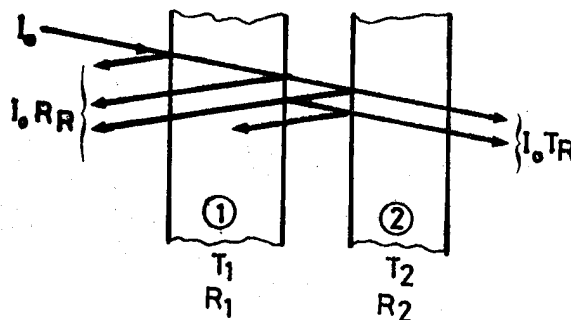
(**) It would also be due, for a part, to the different qualities ("P" and "D") of the Terphane films we used.

However the 20 keV and above all the 40 keV electrons lead to rather small degradations.

This trend suggests that there is possibly a reaction threshold for degradation. In any case, the proposed model does not hold for this material.

3.4 Development of a model for paints

3.4.1 Model



Let us consider a coating made up of two layers, the reflectance and transmittance of each being known: R_1, R_2, T_1, T_2 . The resulting reflectance R_R and transmittance T_R are:

$$R_R = R_1 + T_1 R_2 T_1 + T_1 R_2 R_1 T_2 + \dots + T_1 R_2 (R_1 R_2)^{n-1} T_1 + \dots$$

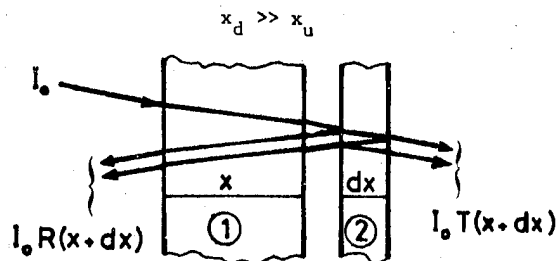
$$+ R_R = R_1 + \frac{R_2 T_1^2}{1 - R_1 R_2} \quad (5)$$

$$T_R = T_1 T_2 + T_1 R_1 R_2 T_2 + \dots + T_1 (R_1 R_2)^{n-1} T_2 + \dots$$

$$+ T_R = \frac{T_1 T_2}{1 - R_1 R_2} \quad (6)$$

3411 Paints : case of a bulk degradation

Let us consider a paint that is degraded by high energy particles or at very large irradiation doses, that is to say a paint where the zone of photon absorption and scattering (characterized by a mean penetration depth x_u) is small compared with the zone of particle penetration (characterized by a range x_d). In other terms:



If $R(x)$ and $T(x)$ are the reflectance and transmittance of the first layer the thickness of which is x and if r and μ are the "reflexion" and "absorption coefficient" of the second layer whose thickness is dx , (5) and (6) can be used:

$$\begin{aligned} R_1 &= R(x) & \mu_2 &= \mu \\ T_1 &= T(x) & R_2 &= r dx \\ & & T_2 &= 1 - (\mu + r) dx \end{aligned}$$

$$\text{yielding } R(x+dx) = R(x) + \frac{T^2(x) r dx}{1 - R(x) r dx} \quad (7)$$

$$\text{and } T(x+dx) = \frac{T(x) [1 - (\mu + r) dx]}{1 - R(x) r dx} \quad (8)$$

Neglecting second order terms:

$$\frac{dR}{dx} \approx r T^2(x) \quad (9)$$

$$\frac{dT}{dx} = -T(x) [rR(x) + (\mu + r)] \quad (10)$$

With the boundary conditions

$$T(0) = 1 ; R(0) = 0 ; \left[\frac{dR}{dx} \right]_{(0)} = R ; \left[\frac{dT}{dx} \right]_{(0)} = -\mu + r$$

these equations give:

$$R(x) = 1 + k + \alpha(k) \frac{1 - \frac{\alpha(k)+1+k}{\alpha(k)-1-k} \exp(x/x_u)}{\frac{\alpha(k)+1+k}{\alpha(k)-1-k} \exp(x/x_u)} \quad (11)$$

$$\text{with } x_u = \frac{1}{2\alpha(k)r} \quad \text{"optical range"}$$

$$\alpha(k) = [k(k+2)]^{0.5}$$

$$\text{and } k = \mu/r$$

If the paint thickness x is far greater than x_u , (11) becomes

$$R(x) = 1 + k - [k(k+2)]^{0.5} \quad (12)$$

$$= 1 + \frac{\mu}{r} - \left[\frac{\mu}{r} - \left(\frac{\mu}{r} + 2 \right) \right]^{0.5}$$

In the case of an irradiated paint with $x_d \gg x_u$, relation (12) is:

$$\text{before irradiation: } R_0 = 1 + k_0 - \alpha(k_0) \quad (13)$$

$$\text{after irradiation: } R_d = 1 + k_d - \alpha(k_d) \quad (14)$$

The measurement of $R_0(\lambda)$ and $R_d(\lambda)$ allows to obtain directly (Fig. 17):

$$k_0 = \frac{\mu_0}{r_0} \quad \text{and} \quad k_d = \frac{\mu_d}{r_d}$$

This leads to the optical range value:

$$\text{before irradiation: } x_{u0} = \frac{1}{2r_0} [k_0(k_0+2)]^{-0.5} \quad (15)$$

$$\text{after irradiation: } x_{ud} = \frac{1}{2r_d} [k_d(k_d+2)]^{-0.5} \quad (16)$$

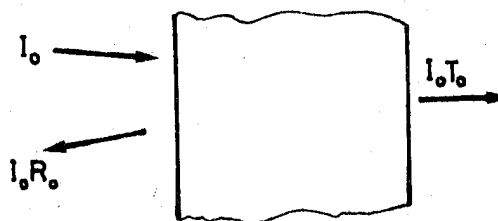
See Fig. 18.

3412 Paints: case of a surface degradation

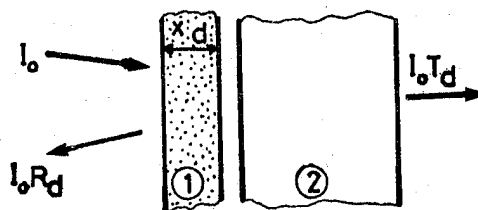
We consider now a paint that is degraded by low energy particles (electrons or protons) or at very low irradiation doses. In such a case

$$x_u \gg x_d$$

Before irradiation:



The reflectance and transmittance of the paint are R_0 and T_0 , and the absorption coefficient is μ_0 . After irradiation, two layers can be considered:



The layer 2 is a non degraded medium whose thickness is $\ell - x_d$

$$R_2 = R_0 ; \mu_2 = \mu_0$$

The layer 1 is the degraded medium whose thickness is x_d

$$\mu_1 = \mu_d = \mu_0 + \Delta\mu$$

$$R_1 = r_d x_d \quad r_d \text{ is the "reflexion coefficient"}$$

$$T_1 = 1 - r_d x_d - \mu_d x_d$$

(5) becomes:

$$R_d = r_d x_d + R_0 \frac{[1 - (r_d + \mu_d) x_d]^2}{1 - R_0 r_d x_d} \quad (17)$$

Neglecting μ_0 (small compared with $\Delta\mu$), the second order terms, and assuming that the reflexion coefficient is unchanged ($r_d = r_0$), (17) yields

$$\Delta\mu \approx \frac{1}{2x_d} \frac{R_0 - R_d}{R_0} \quad (18)$$

3413 Paint absorption variation in terms of reflectance

a) The results of the two preceding subsections can be summarized as follows :

- If $x_d \ll x_u$: From the in-situ spectral measurements, the initial reflectance $R_0(\lambda)$ and its variation during irradiation $R(\lambda)$ can be obtained.

. A dose repartition computation by the usual codes allows to know the mean absorbed dose \bar{D} in the particle penetration zone whose thickness is x_d .

. Then, relation (18) can be applied

$$\Delta\mu(\lambda) = \frac{1}{2x_d} \frac{\Delta R(\lambda)}{R_0(\lambda)}$$

- If $x_d \gg x_u$

. Spectral measurements allow to get the reflectances before and after irradiation $R_0(\lambda)$ and $R_d(\lambda)$.

. The classical methods allow to know the dose repartition from which the mean dose \bar{D} and the degraded thickness x_d can be obtained.

. Assuming that the reflexion coefficient is not changed by irradiation ($r_0 = r_d = r$), one can use the relation (12)

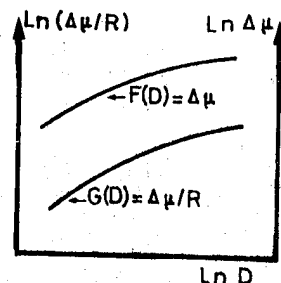
$$R(k) = 1 + k - [k(k+2)]^{0.5} \quad \text{where } k = \frac{\mu}{r}$$

in order to calculate k_0 (before irradiation) and $k = k_0 + \Delta k$ (after irradiation).

b) For a given dose, it is thus possible:

. in the $x_d \gg x_u$ range to calculate $\Delta k = \frac{\Delta\mu}{k}$ for each absorbed dose \bar{D} and to draw the curve $\frac{\Delta\mu}{r} = F(\bar{D})$

. in the $x_d \ll x_u$ range to calculate $\Delta\mu$ for each dose \bar{D} and to draw the curve $\Delta\mu = G(\bar{D})$



REMARKS

. These curves must verify $\frac{F(D)}{G(D)} = r = \text{constant}$ (i.e. the hypothesis previously made: $r_0 = r_d = r$ not dependent on dose D)

. Provided the particle nature and energy were not significant in the degradation, the values $\Delta\mu = F(\bar{D})$ and $rG(\bar{D})$ must be identical.

3.4.2 Results for the Si3G paint

Degradation data in the literature concerning the Si3G paint have been compiled : see Ref.21. Table 5 gives the various irradiation conditions as well as the degraded thickness and the mean dose \bar{D} .

Two absorption bands are noticed in the spectra of irradiated specimen at 410nm and 2100nm.

In a first phase, a linear relation is observed for the variation of reflectance under irradiation in terms of increasing degraded thickness x_d : Fig. 19. In a second phase, degradation seems to keep a constant level, once the degraded thickness exceeds the optical range x_u .

As indicated at Section 4.1.3b, the reflexion coefficients r can be calculated after being shown not dependent on dose:

$$r_{410} = 776 \text{ cm}^2 \text{ g}^{-1} \quad r_{2100} = 167 \text{ cm}^2 \text{ g}^{-1}$$

From these values one can estimate the initial optical thicknesses:

$$x_{uo 410} = 3.17 \cdot 10^{-3} \text{ g cm}^{-2} \quad (\text{i.e. } 14.4 \mu\text{m})$$

$$x_{uo 2100} = 7.66 \cdot 10^{-3} \text{ g cm}^{-2} \quad (\text{i.e. } 35 \mu\text{m})$$

Fig. 20 and 21 give the variation of the absorption coefficient in terms of dose. The degradation does not depend on the particle nature or energy. It depends only on the absorbed energy dose. Accordingly the model seems to be validated.

3.4.3 Results for the PSG 120 paint

A PSG 120 paint (ZnO/Silicone, manufactured by Astral Sikkens) applied on an aluminum substrate by ESTEC was irradiated at DERTS in the conditions that are reported in Table 6.

Two absorption bands are in evidence after irradiation: a very large one at 2050 nm and another at 410 nm. However the in-situ measurements of the reflectance were performed at discrete wavelengths and did not allow a good characterization of the 410 nm band. So the 2050 nm data only was used.

Fig. 22 indicates a tendency towards saturation, that is similar to the one recorded for the S13G paint (Fig. 19), but is less distinct.

Fig. 23 reports $\Delta\mu$ and $\frac{\Delta\mu}{x_d}$ values that have been calculated respectively in the $x_d \ll x_u$ and in the $x_d \gg x_u$ range. In spite of the little number of points in the second range, it seems possible to deduce as indicated at Section 4.1.3 b from Fig. 23, a value of the reflexion coefficient: $r_{2050} \approx 17 \text{ cm}^2 \text{ g}^{-1}$. The absorption variation $\Delta\mu$ recorded after irradiation seems to depend only on the absorbed dose. It is worth to note that the apparent initial optical thickness x_u that can be calculated as an average for 5 samples is about 170 μm . Here too the model seems to be validated.

3.4.4 Results for the PSZ 184 paint

A PSZ 184 paint (ZnO/Silicate, manufactured by Astral Sikkens) applied by CNES on an aluminum substrate with a silicate priming was irradiated by electrons and protons. The irradiated samples (Ref. 21 and Table 7) exhibited severe cracks. These cracks were due to a bad priming of the substrate as it was made clear by the fact that a specimen using PSZ 184 on a P 113 primer did not crack under a proton irradiation at 45 keV. In any case the quality of the optical measurements was rather bad for all the samples we tested, especially for those irradiated by protons. Absorption bands were noticed at 2100nm and at about 600nm. Only the first one was workable, the second being overlapped by a drift of the absorption threshold of the paint.

The degradation due to protons seems nearly independent of the dose, probably owing to the cracks. The irradiations by 40 keV electrons seem to belong to the $x_d \ll x_u$ zone; the irradiations by 210 keV electrons to the $x_d \gg x_u$ zone. The latter electron results are given in Fig. 24, they seem to be consistent with a $r = 31 \text{ g}^{-1} \text{ cm}^2$ value. Obviously however definite results cannot be given concerning the fact that the absorption variation does not depend on particle nature or energy.

3.5 Conclusion

- A model that correlates the optical degradation to the absorbed energy dose during particle irradiations is proposed for thermal control coatings.

From the experiments performed on six usual coatings, for five among them, this model has been verified (four coatings: S13G, PSG 120, aluminized FEP, aluminized Kapton) or seems plausible (one coating: PSZ 184). However the model does not seem appropriate for a Terphane SSM.

- The consequences are the following:

A good simulation of the action of particles encountered in space seems to be achievable in the laboratory without duplicating the exact nature of the acting particles and their angular and spectral repartition. A reproduction of the absorbed energy dose repartition within the material is sufficient.

The solar absorptance variation during irradiation that is the value of prime importance for the satellite system designer can be correlated with the physical parameters: absorption coefficient μ , band width W , degraded thickness x_d , absorbed energy dose.

For a given coating,

- . if the sensitivity to irradiation (defined by the product $W\Delta\mu$ or by $\int \Delta\mu d\lambda$, or by $\Delta\mu(\lambda_{\text{max}})$, values that are representative of the number of created defects) has been proved to only depend on the absorbed energy dose and

- . if the dose that is predicted for a given orbit can be assumed uniform (its mean value being \bar{D}) in the thickness x_d ,

then the sensitivity curve [e.g. $W\Delta\mu = f(D)$] and the empirical relation between α_d and $W\Delta\mu x_d$ allow to obtain directly the predicted solar absorptance variation due to the in-orbit irradiation.

If the predicted dose is not uniform, three or four irradiations at the laboratory are required in order to evaluate experimentally the optical degradation.

If the sensitivity to irradiation is not known, it must be obtained from literature results or experiments giving the spectral reflectance for a variety of conditions and doses (electrons and protons, some tens to some hundreds keV, 10^{12} to 10^{16} particles cm^{-2}).

If the particle energy and the particle nature modify the degradation, modelling is not possible.

Synergistic effects of particles acting with UV radiation have been excluded from the present study, their modelling is not possible.

We must remind that flux rate and temperature effects could be observed in certain circumstances.

4. REFERENCES

1. L.B. FOGDALL, S.S. CANNADAY - Radiation effects on thermal control coatings polymers and optical materials. International Seminar Simulation and Space - CERT Toulouse, September 1973.
2. J. BOURRIEU, A. PAILLOUS, J.P. PHILIPPON, J.C. GIACOMONI, A. ZILIANI - Methodology concerning the simulation of ionizing radiations with special reference to coating when in geostationary orbit - Int. Seminar Simulation and Space - CERT Toulouse, September 1973.

3. L.B. FOGDALL, S.S. CANNADAY, W.S. SLEMP
AIAA Paper 77-741 (1977)
4. L.B. FOGDALL, S.S. CANNADAY, W. M. ROWE
A.I.A.A. Paper 78-1622
5. D.F. HALL (Aerospace Corp.) - Private
communication (1979)
6. J.D. BRODER, S.J. MARSIK - NASA TM 78926
(1978)
7. P. FAYET, A. PAILLOUS - Paper n° 23 -
5th Space Simulation Conference - Gaithers-
burg Md (1970)
8. C.P. PIKE, R.R. LOVELL - Proceedings of the
Spacecraft Charging Technology Conf.
Colorado Springs NASA TMX 73537 (1977)
9. Proceedings of the Spacecraft Charging
Technology Conference 1978 - NASA Conference
Public. 2071 (1979)
10. A. ROSEN - AIAA Paper 75-91 (1975)
11. C.F. MINIER - ESA ESTEC - Internal Working
Paper n° 937 (1975)
12. C.F. MINIER - ESA ESTEC - TM 172 (1972)
13. S.J. BOSMA - ESA ESTEC - TQM/SARL/98/78
14. A. PAILLOUS, D. SARRAIL - Rapport final sur
contrat ESTEC 83584 - Note ONERA/CERT/DERTS
(1978)
15. J.B. SCHUTT - Paper n° 25 at the 5th Space
Simulation Conference - Gaithersburg Md
(1970)
16. Performance of an investigation of the
space radiation stability of OTS thermal con-
trol materials - Study Phase A Final Report
Bestellung Nr 102010/A 378880 ERNO - Note
ONERA/CERT/DERTS (1974)
17. A. PAILLOUS - Rapport final sur contrat
ESTEC 2015/73/JS - Qualification des revête-
ments de contrôle thermique aux rayonnements
UV et particuliers de l'Espace - Doc. N°29
ONERA/CERT/DERTS (1975)
18. A..PAILLOUS - Degradation des revêtements de
contrôle thermique par irradiations UV et
particulaires - Rapport final sur contrat
ESTEC 2558/75/JS - Note ONERA/CERT/DERTS
(1976)
19. D.H. HOWLE (ESTEC) Private Communication
TXNO 14193/TK 14.9.79
20. A. PAILLOUS - Experience "films polymériques"
embarquée sur SRET 2 - Note ONERA/CERT/DERTS
NT/03/12 (1977)
21. J. BOURRIEU, A. PAILLOUS, M. ROMERO -
Degradations de revêtements de contrôle
thermique sous l'effet des rayonnements
ultraviolets et particuliers - Rapport
final sur contrat ESTEC 2515/75/HP - Docu-
ment ONERA/CERT/DERTS (1976)
22. A. PAILLOUS, M.T. AMAT, J. MARCO,
G. PANABIERE - Irradiations par protons et
irradiations par électrons de revêtements de
contrôle thermique et de films polymériques
TOME 1 - Partie expérimentale - Document
ONERA/CERT/DERTS - Rapport final sur contrat
23. J. BOURRIEU - Irradiations par protons et
irradiations par électrons de revêtements de
contrôle thermique et de films polymériques
TOME 2 - Partie théorique - Document
ONERA/CERT/DERTS - Rapport final sur contrat
ESTEC 2838/6/NL/HP/SC - Février 1978
24. A. SMAKULA - Zeitschrift für Physik -
59, 603 (1930)
25. J. BOURRIEU, R. SCHUTTLE - Transmission
des électrons par les écrans plans épais
Programme MONA 1 - Document ONERA/CERT/DERTS
NT/02/24
26. J. BOURRIEU, R. SCHUTTLE - Programme Eldose
pour le calcul des répartitions de doses
absorbées dans les écrans minces - Document
ONERA/CERT/DERTS NT/02/20
27. J. BOURRIEU - Répartition de doses indui-
tes par protons - Cas de l'environnement
spatial et des simulations à l'accélérateur
Programme PRODOS - Note ONERA/CERT/DERTS
(to be published)
28. L.B. FOGDALL, S.S. CANNADAY - Final Report
for contract NAS-5 - 11219 - Nasa CR 110715
(1970)
29. R.J. ANDRES, P.M. BLAIR, J.C. SMITH -
AIAA Paper 71.453 (1971)
30. L.B. FOGDALL, S.S. CANNADAY, AIAA Paper
69-643
31. L.B. FOGDALL, S.S. CANNADAY, R.R. BROWN -
Final report for contract NAS-5 - 9650 (1970)
32. M.T. LAFOND, A. PAILLOUS - Note ONERA/CERT/
DERTS CR/03/51)
33. J. BROADWAY - Radiation effects design
handbook - Section 2 - Thermal control coa-
tings - NASA CR 1786 (1971)
34. J.P. MILLARD - AIAA Paper 68-794 (1968)
35. G.A. ZERLAUT, J.E. GILLIGAN, N.A. ASHFORD
Final report contract - NAS-8 5379 (1971)
36. J.E. GILLIGAN, G.A. ZERLAUT - A 71 26520
(1971)

ACKNOWLEDGEMENT

This work has been supported in part under ERNO Contract 102010/A/37880 and ESA/ESTEC Contracts 2015/74, 2558/75, 2515/75, 2838/76, 3184/77. We are indebted to Messrs. J. DAUPHIN and F. LEVADOU for valuable discussions and also to Mr. D. HOWLE for his effort on the OTS2 coatings degradation investigation. We are also grateful to CNES and especially to J. SIMON and J.C. GUILLAUMON for their interest.

	STAGE	Years in Space	E.S.H. number	UV simulation duration (h)	Electron fluence (45° incidence 200 keV) $e \cdot cm^{-2}$	Proton fluences (normal incidence 40 keV) $p \cdot cm^{-2}$	Proton fluences (normal incidence 150 keV) $p \cdot cm^{-2}$	Samples
1st TEST (North&South PACS)	A ₁	0.7	192	96	$1.43 \cdot 10^{14}$	$6.92 \cdot 10^{13}$	$2.51 \cdot 10^{12}$	a) OCLI silvered OSR, fixed with RTV 560
	B ₁	1.11	1224	612	$0.94 \cdot 10^{15}$	$0.46 \cdot 10^{15}$	$1.65 \cdot 10^{13}$	b) OCLI silvered OSR, without adhesive
	C ₁	2.05	2268	1134	$1.78 \cdot 10^{15}$	$0.88 \cdot 10^{15}$	$2.91 \cdot 10^{13}$	c) Aluminized Kapton
	D ₁	3.15	3480	1740	$2.69 \cdot 10^{15}$	$1.35 \cdot 10^{15}$	$4.49 \cdot 10^{13}$	d) Aluminum Mystik 7492 (with adhesive)
	E ₁	4.05	4480	2240	$3.46 \cdot 10^{15}$	$1.74 \cdot 10^{15}$	$5.78 \cdot 10^{13}$	e) Aluminized FEP
	F ₁	5.40	5964	2982	$4.65 \cdot 10^{15}$	$2.34 \cdot 10^{15}$	$7.76 \cdot 10^{13}$	f) 3M Black VELVET 41C10
	G ₁	7.14	7892	3946	$6.09 \cdot 10^{15}$	$3.04 \cdot 10^{15}$	$1.01 \cdot 10^{14}$	g) CHEMGLAZE Z 306 h) CUVERTIN 306 i) Z 93 IITRI
2nd TEST (EQUATORIAL FACE)	A ₂	0.18	508	160	$0.15 \cdot 10^{15}$	$0.77 \cdot 10^{14}$	$0.27 \cdot 10^{13}$	a) OCLI OSR with ITO layer
	B ₂	1	2443	893	$0.86 \cdot 10^{15}$	$0.43 \cdot 10^{15}$	$1.44 \cdot 10^{13}$	b) PPE OSR (Cerium doped) with ITO layer
	C ₂	2.11	5604	1868	$1.81 \cdot 10^{15}$	$0.91 \cdot 10^{15}$	$3.02 \cdot 10^{13}$	c) Conductive HUGHSON H322 on Kapton
	D ₂	3	7949	2650	$2.57 \cdot 10^{15}$	$1.30 \cdot 10^{15}$	$4.29 \cdot 10^{13}$	d) Conductive HUGHSON H322 on aluminized Kapton e) Conductive HUGHSON H322 on aluminized Mylar f) S13G/LO IITRI g) PSG 120 ASTRAL h) PSZ 184 ASTRAL i) 293 IITRI j) Vacuum deposited aluminum over glass

TABLE 1 - OTS SIMULATION - IRRADIATION PARAMETERS

	Litterature ref.	Particle Nature	Energy (keV)	x_d ($g \cdot cm^{-2}$)	\bar{D} (Gy/Particle)	Fluence rate ($p \cdot cm^{-2} \cdot s^{-1}$)	Irradiation temperature $^{\circ}C$	Fluence $p \cdot cm^{-2}$
LITERATURE RESULTS	30	ELECTRONS	20	$8 \cdot 10^{-4}$	$4 \cdot 10^{-9}$?	8	10^{16}
	28	ELECTRONS	35	$2.2 \cdot 10^{-3}$	$2.5 \cdot 10^{-9}$	$1 \text{ to } 7 \cdot 10^{10}$	18	$3 \cdot 10^{14} \text{ to } 10^{16}$
	31	ELECTRONS	50	$4.2 \cdot 10^{-3}$	$1.9 \cdot 10^{-9}$	$2 \cdot 10^{10} \text{ to } 5 \cdot 10^{11}$	22	10^{15}
	30	ELECTRONS	80	$> 7 \cdot 10^{-3**}$	$1.5 \cdot 10^{-9}$?	8	$3 \cdot 10^{14} \text{ to } 10^{16}$
	32	ELECTRONS	850	$> 7 \cdot 10^{-3**}$	$2.7 \cdot 10^{-10}$	$2.3 \cdot 10^{12}$	10	$10^{16} \text{ to } 8 \cdot 10^{17}$
	28	PROTONS	40	$2.2 \cdot 10^{-4}$	$1.3 \cdot 10^{-7}$	$1 \text{ to } 5 \cdot 10^{10}$	10	$3 \cdot 10^{14} \text{ to } 10^{16}$
	29	PROTONS	140	$8.5 \cdot 10^{-5}$	$8 \cdot 10^{-8}$	$2 \cdot 10^{11}$?	$6 \cdot 10^{13}$
DEXIS RESULTS	22	ELECTRONS	40	$2.7 \cdot 10^{-3}$	$2.3 \cdot 10^{-9}$	$2.7 \text{ to } 5.4 \cdot 10^{10}$	30 ± 1	* $2 \cdot 10^{14} \text{ to } 2 \cdot 10^{15}$
	22	ELECTRONS	80	$8.5 \cdot 10^{-3}$	$1.35 \cdot 10^{-9}$	$2.9 \text{ to } 5.3 \cdot 10^{10}$	30	* $2 \cdot 10^{14} \text{ to } 10^{15}$
	22*	ELECTRONS	210	$1.06 \cdot 10^{-2} **$	$1.01 \cdot 10^{-9}$	$3 \text{ to } 6.3 \cdot 10^{10}$	30	* $2 \cdot 10^{14} \text{ to } 10^{15}$
	22	PROTONS	45	$9 \cdot 10^{-5}$	$8 \cdot 10^{-8}$	$1.3 \text{ to } 6.2 \cdot 10^{10}$	30	$10^{13} \text{ to } 2.8 \cdot 10^{15}$
	22	PROTONS	75	$1.2 \cdot 10^{-4}$	$1 \cdot 10^{-7}$	$1.3 \text{ to } 6.2 \cdot 10^{10}$	30	$10^{13} \text{ to } 2.8 \cdot 10^{15}$
	22	PROTONS	150	$2.4 \cdot 10^{-4}$	$1 \cdot 10^{-7}$	$1.3 \text{ to } 6.2 \cdot 10^{10}$	30	$10^{13} \text{ to } 2.8 \cdot 10^{15}$

** Material thickness is less than the particle penetration

* 45° incidence

TABLE 2 - IRRADIATION PARAMETERS FOR ALUMINIZED KAPTON

Littera- ture reference	Particle nature	Particle energy (keV)	x_d (g cm ⁻²)	\bar{D} (Gy/particle)	Fluence rate p cm ⁻² s ⁻¹	Irradiation temperature (°C)	Fluence p cm ⁻²
22	ELECTRONS	40	$2.2 \cdot 10^{-3}$	$1.6 \cdot 10^{-9}$	2.7 to $5.4 \cdot 10^{10}$	30 + 1	$2 \cdot 10^{14}$ to $2 \cdot 10^{15}$ *
22	ELECTRONS	80	$8.3 \cdot 10^{-3}$	$1.2 \cdot 10^{-9}$	2.9 to $5.3 \cdot 10^{10}$	30	$2 \cdot 10^{14}$ to $2 \cdot 10^{15}$ *
22	ELECTRONS	210	$1.6 \cdot 10^{-2}$	$1.1 \cdot 10^{-9}$	3 to $6.3 \cdot 10^{10}$	30	$2 \cdot 10^{14}$ to $2 \cdot 10^{15}$ *
22	PROTONS	45	$1.3 \cdot 10^{-4}$	$5.5 \cdot 10^{-8}$	1.3 to $6.2 \cdot 10^{10}$	30	10^{13} to $2.8 \cdot 10^{15}$
22	PROTONS	75	$1.9 \cdot 10^{-4}$	$6.3 \cdot 10^{-8}$	1.3 to $6.2 \cdot 10^{10}$	30	10^{13} to $2.8 \cdot 10^{15}$
22	PROTONS	150	$3.5 \cdot 10^{-4}$	$7.6 \cdot 10^{-8}$	1.3 to $6.2 \cdot 10^{10}$	30	10^{13} to $2.8 \cdot 10^{15}$

* 45° incidence

TABLE 3 - IRRADIATION PARAMETERS FOR ALUMINIZED FEP TEFLON

REF	Particle nature	Particle energy (keV)	Film thickness (μm)	x_d (g cm ⁻²)	\bar{D} (Gy/Particle)	Fluence rate p cm ⁻² s ⁻¹	Irradiation temperature (°C)	Fluence p cm ⁻²
22	ELECTRONS	210	3.5 6 12 23 50 75 125	$8.6 \cdot 10^{-4}$ $1.47 \cdot 10^{-3}$ $2.94 \cdot 10^{-3}$ $5.6 \cdot 10^{-3}$ $1.22 \cdot 10^{-2}$ $1.84 \cdot 10^{-2}$ $3.06 \cdot 10^{-2}$	$6.7 \cdot 10^{-10}$ $7.8 \cdot 10^{-10}$ $8.3 \cdot 10^{-10}$ $9.6 \cdot 10^{-10}$ $10.6 \cdot 10^{-10}$ $10.5 \cdot 10^{-10}$ $9.8 \cdot 10^{-10}$	3 to $6 \cdot 10^{10}$	30	* $2 \cdot 10^{14}$ to 10^{15}
22	ELECTRONS	80	3.5 6 12 23 50 and more	$8.57 \cdot 10^{-4}$ $1.47 \cdot 10^{-3}$ $2.94 \cdot 10^{-3}$ $5.63 \cdot 10^{-3}$ $8.5 \cdot 10^{-3}$ *	$1.5 \cdot 10^{-9}$ $1.6 \cdot 10^{-9}$ $1.8 \cdot 10^{-9}$ $1.7 \cdot 10^{-9}$ $1.4 \cdot 10^{-9}$	2.9 to $5.3 \cdot 10^{10}$	30	* $2 \cdot 10^{14}$ to 10^{15}
22	ELECTRONS	40	3.5 6 12 and more	$8.57 \cdot 10^{-4}$ $1.47 \cdot 10^{-3}$ $2.50 \cdot 10^{-3}$	$2.75 \cdot 10^{-9}$ $2.7 \cdot 10^{-9}$ $2.1 \cdot 10^{-9}$	2.7 to $5.4 \cdot 10^{10}$	30	* $2 \cdot 10^{14}$ to 10^{15}
22	PROTONS	150	3.5 and more	$2.3 \cdot 10^{-4}$ **	$1.04 \cdot 10^{-7}$	1.3 to $6.2 \cdot 10^{10}$	30	10^{13} to $2.8 \cdot 10^{15}$
22	PROTONS	75	3.5 and more	$1.3 \cdot 10^{-4}$ **	$9.6 \cdot 10^{-8}$	1.3 to $6.2 \cdot 10^{10}$	30	10^{13} to $2.8 \cdot 10^{15}$
22	PROTONS	45	3.5 and more	$9.0 \cdot 10^{-5}$ **	$8 \cdot 10^{-8}$	1.3 to $6.2 \cdot 10^{10}$	30	10^{13} to $2.8 \cdot 10^{15}$

* 45° incidence

** degraded zone less than the film thickness

TABLE 4 - IRRADIATION PARAMETERS FOR TERPHANE

Littera- ture reference	Particle nature	Particle energy (keV)	x_d (g cm ⁻²)	\bar{D} (Gy/particle)	Fluence rate p cm ⁻² s ⁻¹	Irradiation temperature (°C)	Fluence p cm ⁻²
31	ELECTRONS	20	$1.0 \cdot 10^{-3}$	$3.2 \cdot 10^{-9}$			10^{13} to 10^{15}
28	ELECTRONS	35	$2.5 \cdot 10^{-3}$	$2.2 \cdot 10^{-9}$	1 to $7 \cdot 10^{10}$	18°	$4 \cdot 10^{13}$ to 10^{16}
31	ELECTRONS	50	$4.8 \cdot 10^{-3}$	$1.65 \cdot 10^{-9}$	$2 \cdot 10^{10}$ to $5 \cdot 10^{11}$	22°	10^{14} to $8 \cdot 10^{15}$
30	ELECTRONS	80	$9.9 \cdot 10^{-3}$	$1.3 \cdot 10^{-9}$?	8°	10^{16}
36	PROTONS	1.2	$1.0 \cdot 10^{-5}$	$1.9 \cdot 10^{-8}$	$4.9 \cdot 10^9$	12°	$2.5 \cdot 10^{15}$
35	PROTONS	1.2	$1.0 \cdot 10^{-5}$	$1.9 \cdot 10^{-8}$	$5 \cdot 10^9$?	$8 \cdot 10^{15}$
34	PROTONS	2 or 10	$6 \cdot 10^{-5}$	$2.7 \cdot 10^{-8}$?	?	$2.5 \cdot 10^{15}$
33	PROTONS	10 or 20	$6 \cdot 10^{-5}$ or 10^{-4}	2.7 or $3.2 \cdot 10^{-8}$	$7.3 \cdot 10^9$	Amb	$2 \cdot 10^{15}$
31	PROTONS	20	$1.0 \cdot 10^{-4}$	$3.2 \cdot 10^{-8}$?	20°	10^{14} to 10^{16}
28	PROTONS	40	$1.8 \cdot 10^{-4}$	$3.6 \cdot 10^{-8}$	1 to $5 \cdot 10^{10}$	18°	10^{14} to 10^{16}

TABLE 5 - IRRADIATION PARAMETERS FOR SL36

Littera- ture reference	Particle nature	Particle energy (keV)	x_d (g cm ⁻²)	\bar{D} (Gy/particle)	Fluence rate p cm ⁻² s ⁻¹	Irradiation temperature (°C)	Fluence p cm ⁻²
22	ELECTRONS	40	$2.5 \cdot 10^{-3}$	$1.7 \cdot 10^{-9}$	2.7 to $5.4 \cdot 10^{10}$	30 ± 1	* $2 \cdot 10^{14}$ to $2 \cdot 10^{15}$
22	ELECTRONS	80	$9 \cdot 10^{-3}$	$1 \cdot 10^{-9}$	2.9 to $5.3 \cdot 10^{10}$	30	* $2 \cdot 10^{14}$ to 10^{15}
22	ELECTRONS	210	$5 \cdot 10^{-3}$	$5.8 \cdot 10^{-10}$	3 to $6 \cdot 10^{10}$	30	* $2 \cdot 10^{14}$ to 10^{15}
22	PROTONS	45	$2.4 \cdot 10^{-4}$	$3 \cdot 10^{-8}$	1.3 to $6.2 \cdot 10^{10}$	30	10^{13} to $2.8 \cdot 10^{15}$
22	PROTONS	75	$3.4 \cdot 10^{-4}$	$3.6 \cdot 10^{-8}$	1.3 to $6.2 \cdot 10^{10}$	30	10^{13} to $2.8 \cdot 10^{15}$
22	PROTONS	150	$5.6 \cdot 10^{-4}$	$4.3 \cdot 10^{-8}$	1.3 to $6.2 \cdot 10^{10}$	30	10^{13} to $2.8 \cdot 10^{15}$

* 45° incidence

TABLE 6 - IRRADIATION PARAMETERS FOR PSG 120

Littera- ture reference	Particle nature	Particle energy (keV)	x_d (g cm ⁻²)	\bar{D} (Gy/particle)	Fluence rate p cm ⁻² s ⁻¹	Irradiation temperature (°C)	Fluence p cm ⁻²
22	ELECTRONS	40	$2.5 \cdot 10^{-3}$	$2.6 \cdot 10^{-9}$	2.7 to $5.4 \cdot 10^{10}$	30	$2 \cdot 10^{14}$ to $2 \cdot 10^{15}$
22	ELECTRONS	80	$9.0 \cdot 10^{-3}$	$1.3 \cdot 10^{-9}$	2.9 to $5.3 \cdot 10^{10}$	30	$2 \cdot 10^{14}$ to 10^{15}
22	ELECTRONS	210	$4.5 \cdot 10^{-2}$	$6 \cdot 10^{-10}$	3 to $6.3 \cdot 10^{10}$	30	$2 \cdot 10^{14}$ to 10^{15}
22	PROTONS	45	$1.5 \cdot 10^{-4}$	$4.8 \cdot 10^{-8}$	1.3 to $6.2 \cdot 10^{10}$	30	10^{13} to $2.8 \cdot 10^{15}$
22	PROTONS	75	$2.3 \cdot 10^{-4}$	$5.2 \cdot 10^{-8}$	1.3 to $6.2 \cdot 10^{10}$	30	10^{13} to $2.8 \cdot 10^{15}$
22	PROTONS	150	$4.1 \cdot 10^{-4}$	$5.8 \cdot 10^{-8}$	1.3 to $6.2 \cdot 10^{10}$	30	10^{13} to $2.8 \cdot 10^{15}$

* 45° incidence

TABLE 7 - IRRADIATION PARAMETERS FOR PS7 184

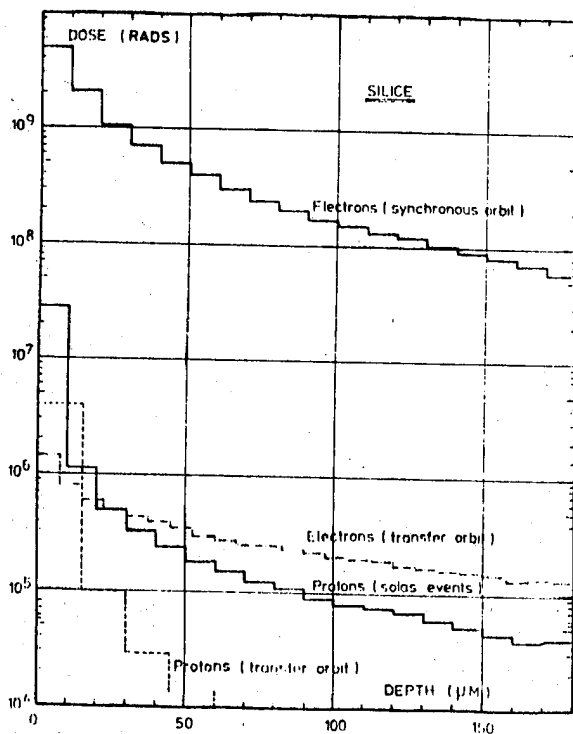


FIG. 1 OTS: DOSE REPARTITION FOR ELECTRON IN SPACE

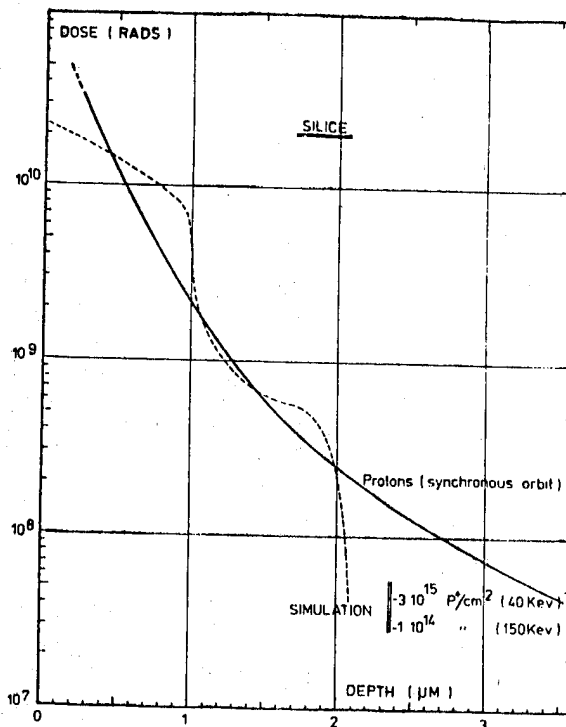


FIG. 3 COMPARISON BETWEEN THE DOSE REPARTITION IN SPACE AND IN LABORATORY (PROTONS)

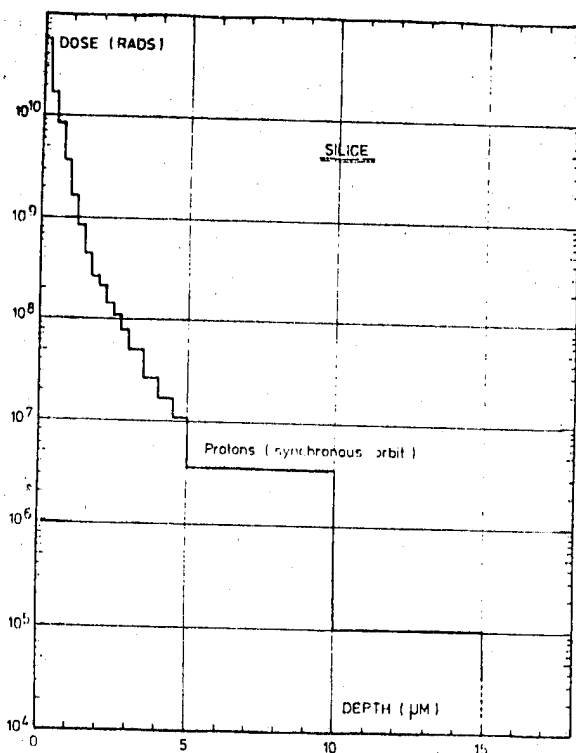


FIG. 2 OTS: DOSE REPARTITION FOR PROTONS IN SPACE

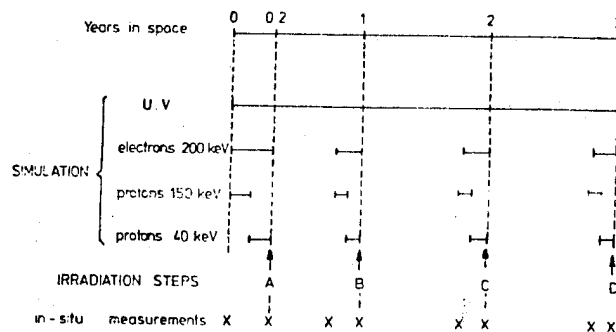


FIG. 4 RADIATION QUALIFICATION OF OTS COATINGS (2nd TEST)

ORIGINAL PAGE IS
OF POOR QUALITY

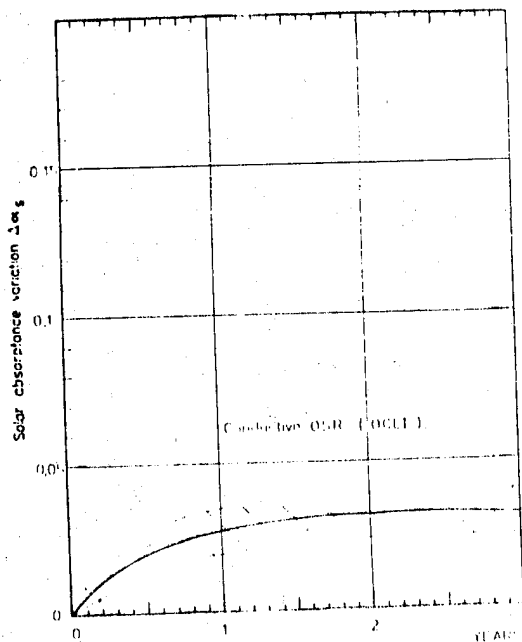


FIG. 5 PREDICTED DEGRADATION OF A CONDUCTIVE OCLI OSR (EQUATORIAL FACE OF OTS)

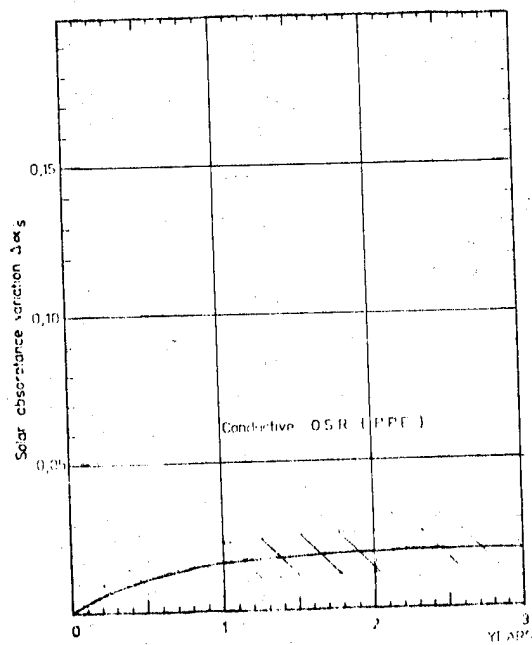


FIG. 6 PREDICTED DEGRADATION OF A CONDUCTIVE PPE OSR (EQUATORIAL FACE OF OTS)

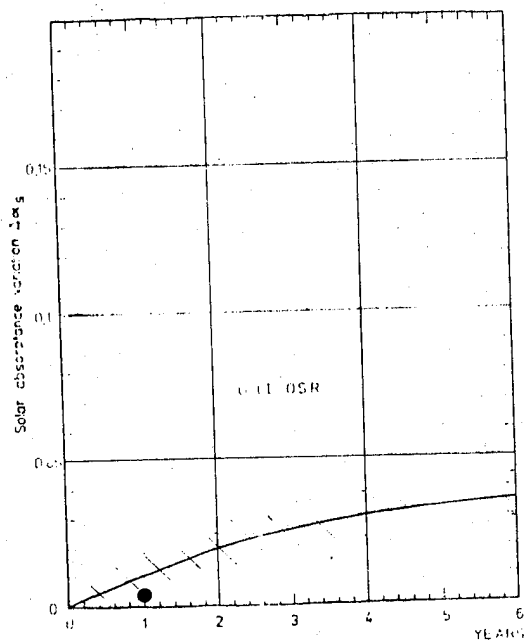


FIG. 7 PREDICTED DEGRADATION OF AN OCLI OSR (NORTH AND SOUTH FACE OF OTS)
THE DOT CORRESPONDS TO THE DEGRADATION MEASURED IN-ORBIT

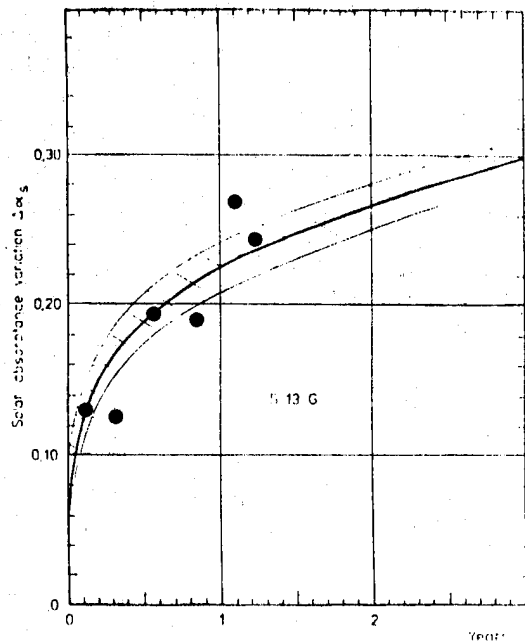


FIG. 8 - DEGRADATION OF THE S13G PAINT ON THE EQUATORIAL FACE OF OTS
THE LINE CORRESPONDS TO THE PREDICTED DEGRADATION, THE DOTS CORRESPOND TO THE DEGRADATION ESTIMATED FROM IN-ORBIT DATA

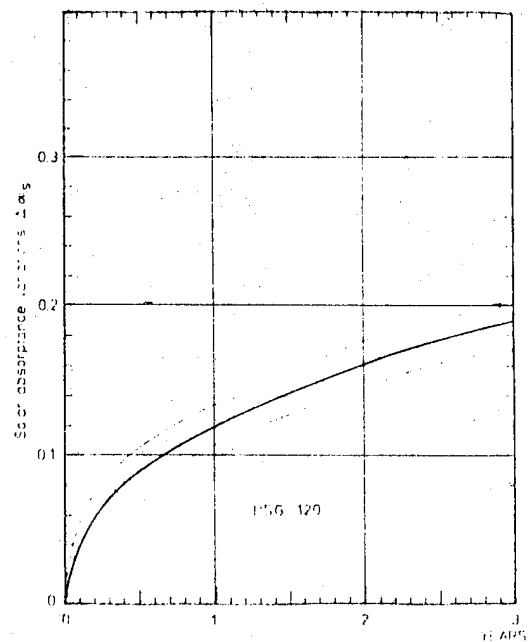


FIG. 9 - ESTIMATED DEGRADATION OF A PSG 120 PAINT ON AN EQUATORIAL FACE OF OTS

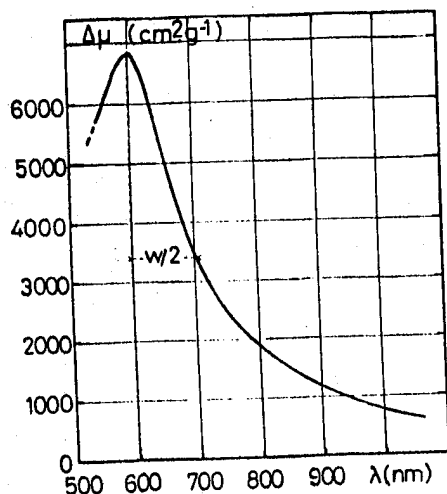


FIG. 10 ABSORPTION BAND OF AN IRRADIATED KAPTON

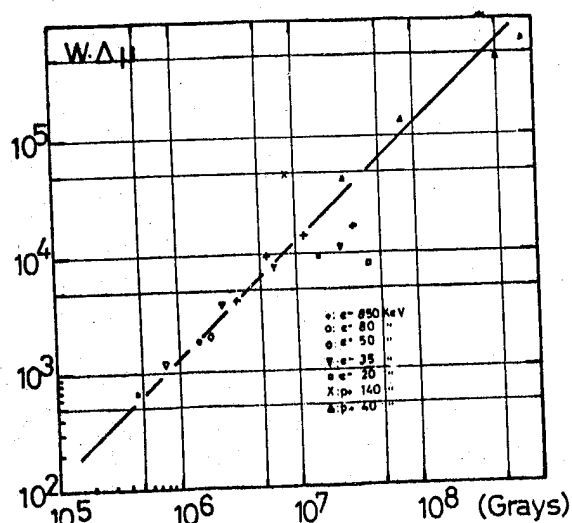


FIG. 11 SENSITIVITY CURVE FOR KAPTON (FROM LITERATURE DATA)

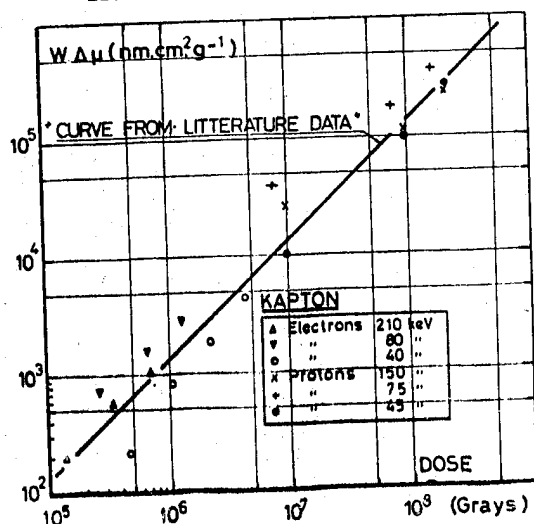


FIG. 12 SENSITIVITY CURVE FOR KAPTON (FROM DERTS EXPERIMENTS)

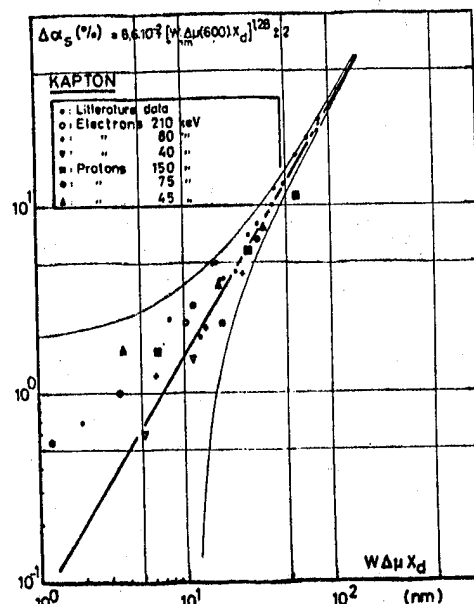
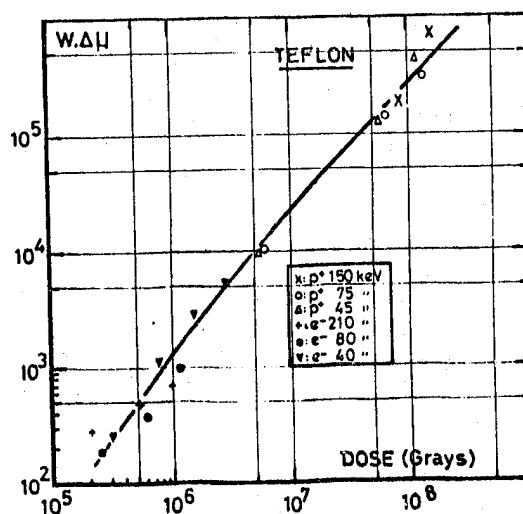
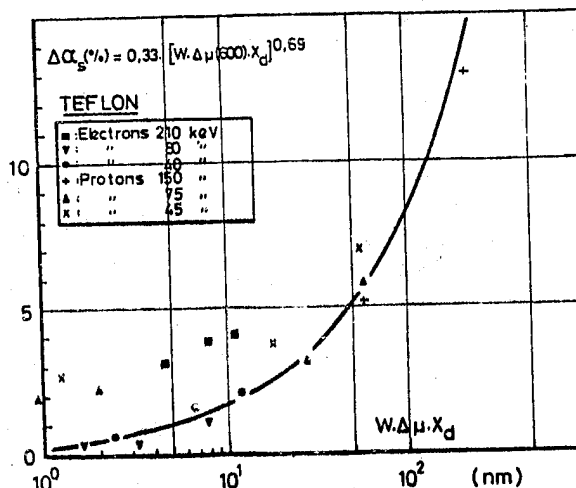
FIG. 13 SOLAR ABSORBANCE DEGRADATION VERSUS $W\Delta\mu x_d$ 

FIG. 14 SENSITIVITY CURVE FOR FEP TEFLON

FIG. 15 SOLAR ABSORBANCE DEGRADATION VERSUS $W\Delta\mu x_d$ FOR FEP TEFLON

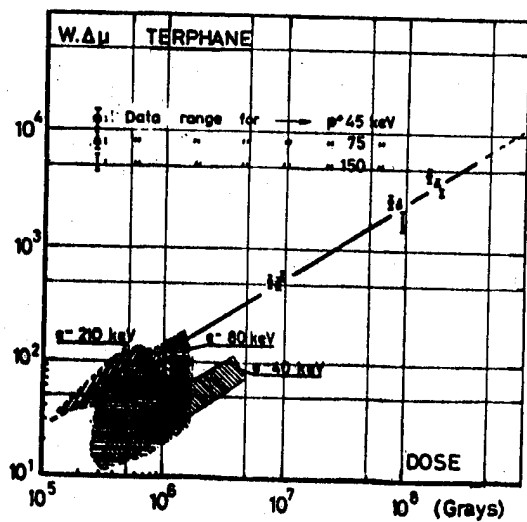


FIG. 16 SENSITIVITY CURVE FOR TERPHANE

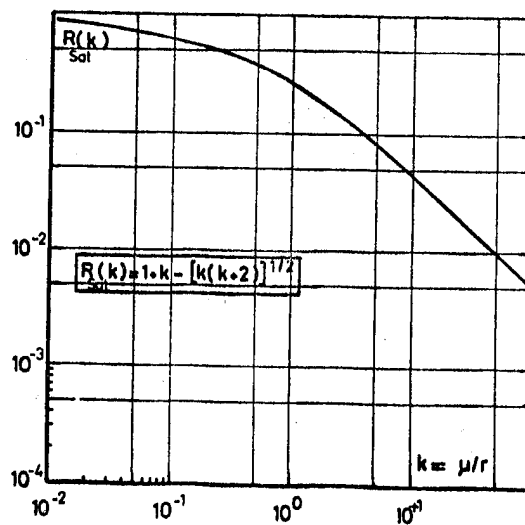
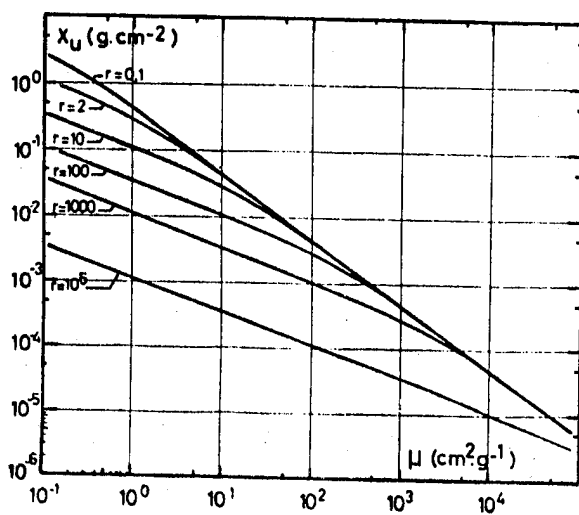
FIG. 17 REFLECTANCE IN TERMS OF μ/r 

FIG. 18 OPTICAL RANGE VERSUS ABSORPTANCE COEFFICIENT

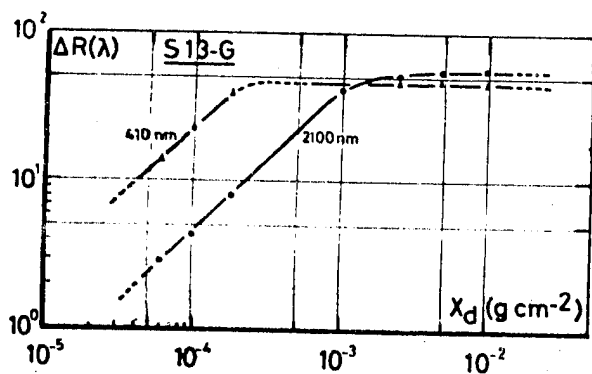


FIG. 19 REFLECTANCE VARIATION COMPARED TO THE DEGRADED ZONE THICKNESS OF S13G PAINT

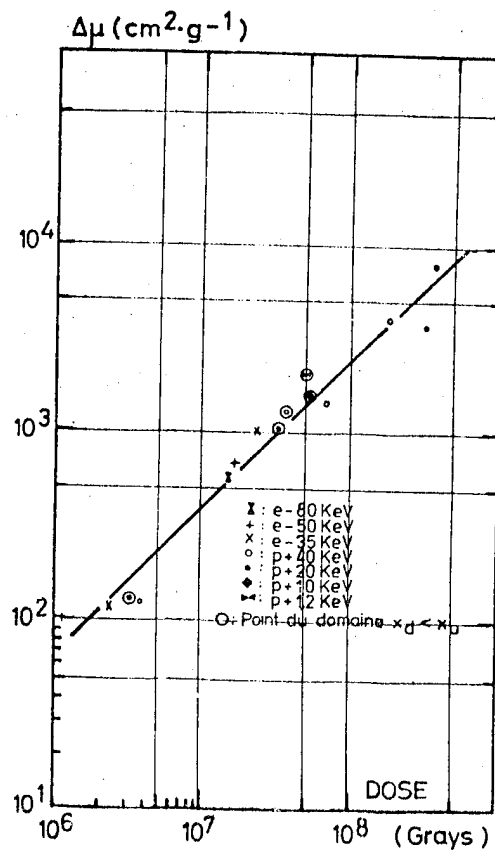


FIG. 20 SENSITIVITY CURVE OF S13G AT 410 NM

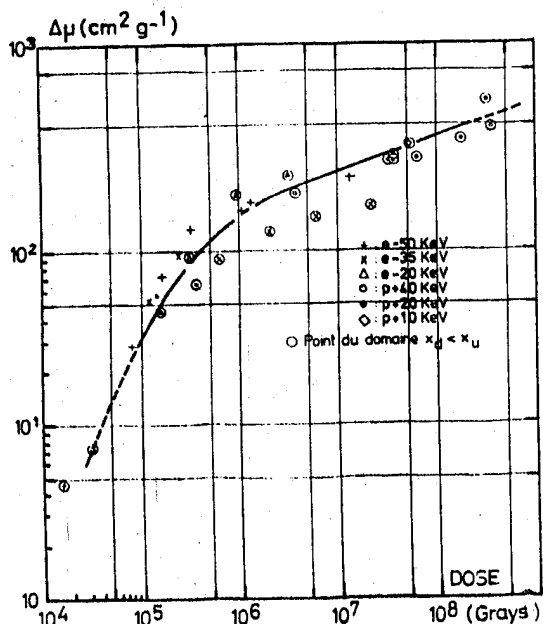


FIG. 21 SENSITIVITY CURVE OF S13G AT 2100 NM

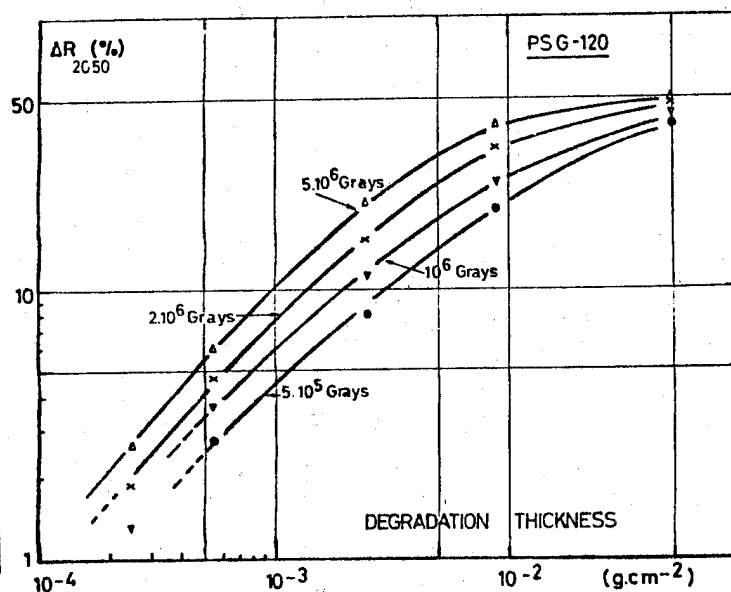


FIG. 22 REFLECTANCE VARIATIONS COMPARED TO THE DEGRADED ZONE THICKNESS OF PSG 120

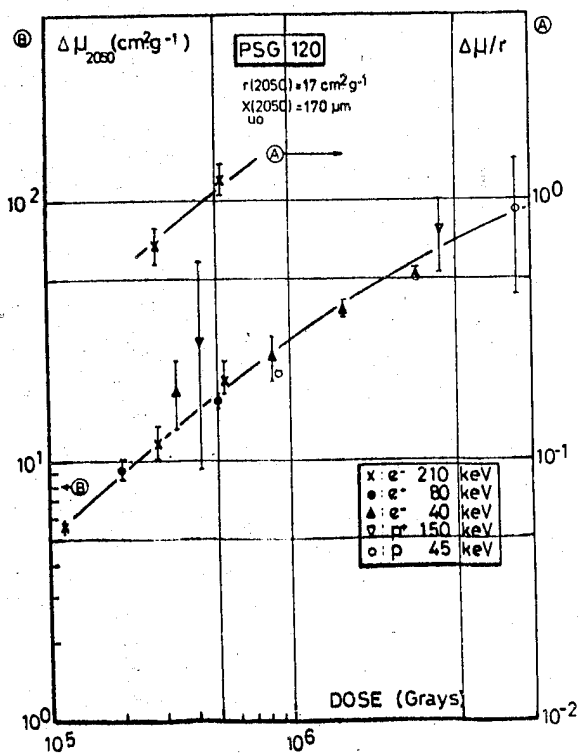


FIG. 23 SENSITIVITY CURVE OF PSG 120

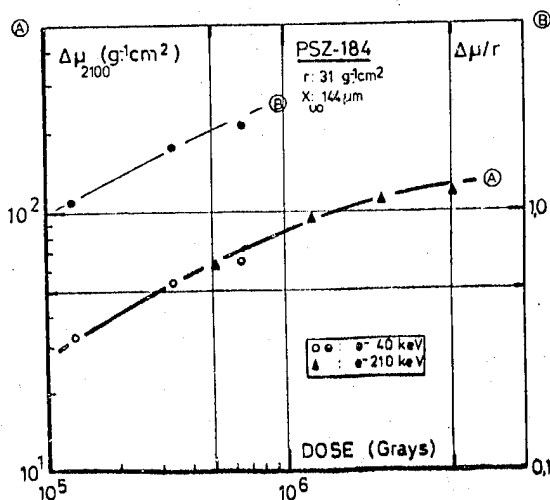


FIG. 24 SENSITIVITY CURVE OF PSZ 184

ORIGINAL PAGE IS
OF POOR QUALITY

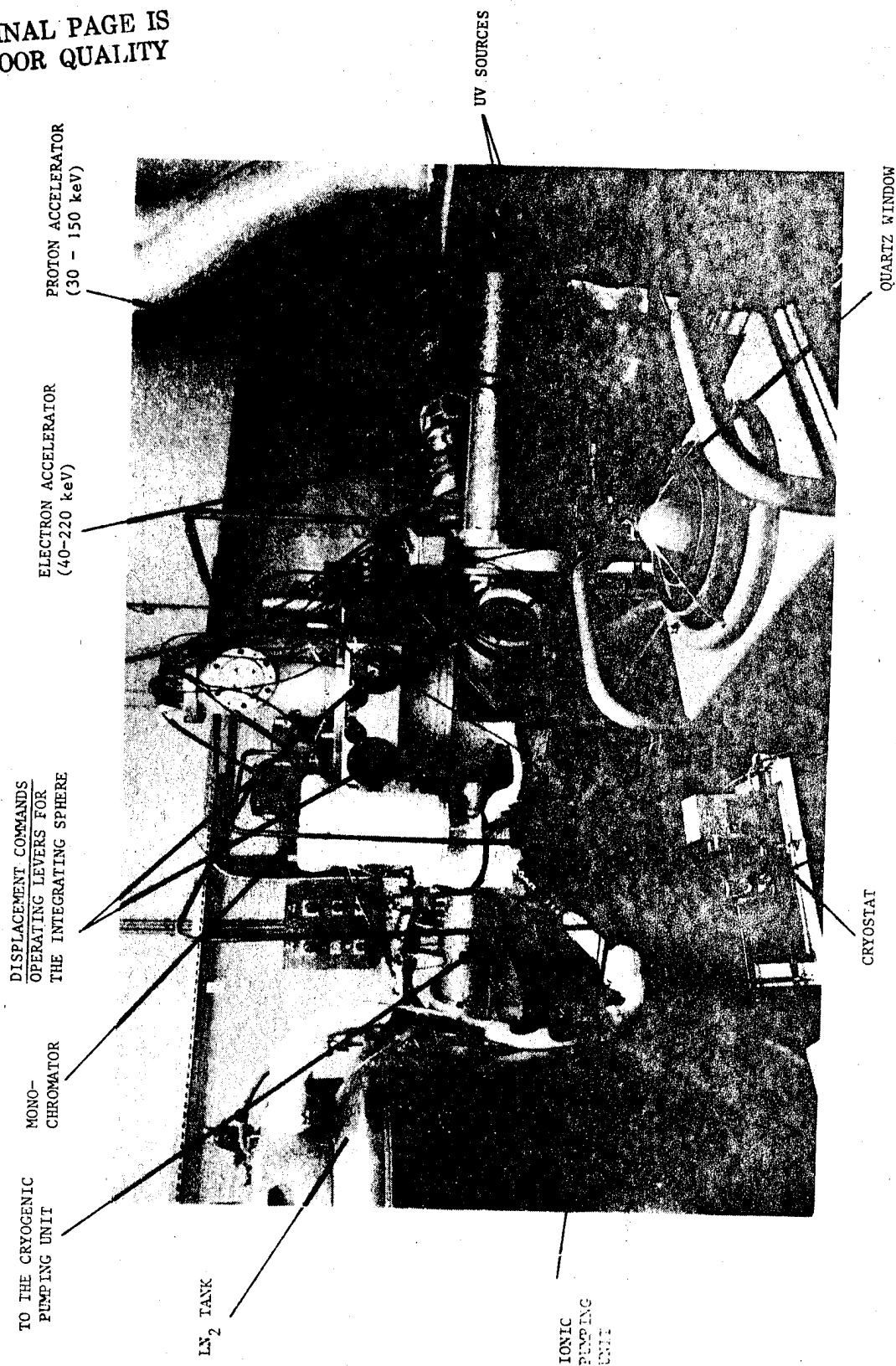


PHOTO 1 - COMBINED RADIATION FACILITY AT DERTS

N80-21443

RANGE AND INTERACTION OF LOW ENERGY PROTONS IN METAL AND METAL OXIDE
THERMAL CONTROL MATERIALS

S A Greenberg & M McCargo

Lockheed Palo Alto Research Laboratory, Palo Alto, California, USA

ABSTRACT

The effects of low-energy protons on the properties of typical metal and metal-oxide thermal-control materials are addressed from a fundamental mechanistic standpoint. A novel, direct method for evaluating range-energy relationships for protons in a variety of stopping media is described. Comparison of the results for metals of diverse atomic numbers has led to modification of existing range theory incorporating corrected electronic-stopping cross sections. A phenomenological model for the proton-induced coloration of zinc-oxide pigments has been formulated. Experimental results indicate that optically active defect centers are created which do not undergo self-annihilation even at very high-proton fluence.

1. INTRODUCTION

Keywords: Thermal-Control Materials, Proton Range, Straggling, Metals and Metal Oxides, Damage Mechanisms, Energy Deposition, Zinc-Oxide Pigments, Optical Properties

Conventional spacecraft thermal-control materials have been shown to undergo degradation upon exposure to the low-energy proton component of the solar-wind environment. Although sufficient laboratory simulation and flight data exist to quantify the magnitude of this degradation, meaningful phenomenological models that explain or predict the pertinent damage mechanisms are lacking currently. In particular, there is scant range data for low-energy protons in typical spacecraft-functional surfaces, which precludes adequate correlation of the changes in optical properties with lattice-defect concentrations and spatial distributions.

While considerable attention has been given to the depth distribution of heavy ions in a variety of stopping media, little information is available for light ions in metals and metal oxides. Andersen and Ziegler (Ref. 1) recently summarized and discussed the results of low-energy protons and helium ions in a number of target materials, while Lindhard et al (Ref. 2) and Schiott (Ref. 3) have performed a theoretical treatment for the passage of energetic ions through matter. Schiott (Ref. 3) specifically directed his analytical approach to the range of light ions in metals. In order to understand the degradation phenomena, it is

necessary to elucidate the mechanism of energy loss along the path which controls the depth distribution of the impinging ion, as well as the radiation damage which ensues as the energy is transferred to the atoms of the stopping medium, thereby causing lattice defects and color-center formation.

2. EXPERIMENTAL TECHNIQUE

Conventional methods for determining range-energy relationships of low-energy protons in a variety of target materials have been limited to indirect depth profile determination techniques including optical property changes (Ref. 4) ion-back scattering (Ref. 5) and nuclear resonance (Ref. 6). This study is based on a new approach for direct measurement of proton transmission spectra of thin-metallic and dielectric films.

The traditional problems of producing, supporting, and characterizing very thin films is circumvented by deposition of the target material directly upon the proton-detector surface. The method is based on the principle that a beam of charged particles, stopped in a conductive medium, will generate a current proportional to the particle flux, as in a simple Faraday cup. If the conducting surface is a thin-metallic film on an insulating substrate, the current measured from the film to ground, should decrease as the proton energy increases sufficiently to permit incident particles to penetrate the film and deposit in the insulating layer. Similarly, for the case of a thin insulating film deposited on a conductive substrate, the current induced in the substrate should increase as the protons penetrate the dielectric and come to rest in the conductive medium.

Metallic films (aluminum, copper, and gold) were produced by vacuum evaporation onto previously cleaned one-inch square fused-silica wafers. Electrical contact was made to the films by means of 0.003 inch copper wires cemented to one corner of the film with silver epoxy. Film thickness determinations were made using a Sloan interferometer. The lower limit for metal film thickness was governed by the ability to produce coherent coatings. In practice, it was determined that below a few hundred Å, the metal films were frequently physically discontinuous and agglomerated. This prevented accurate thickness determinations from being made.

Aluminum oxide films were made by non-aqueous anodic oxidation of 99.99 percent purity aluminum discs of one-inch diameter. The technique for producing reproducible oxide layers of controlled thickness has been previously described (Ref. 7). Electrical contact was made to the unanodized back surface of the aluminum substrate.

Direct range measurements of protons in zinc oxide were not practical by the method utilized in this study. Consequently, only the optical property effects of protons were studied. Potassium-silicate stabilized zinc-oxide specimens were prepared by compacting the powder in recessed aluminum holders. Formulation procedures for the $\text{ZnO/K}_2\text{SiO}_3$ material have been previously described, together with details of the optical property measurement techniques (Ref. 8).

A Texas Nuclear Model 9400 low-energy accelerator was used in conjunction with an ORTEC Mass Analyzer to produce a mass analyzed proton beam. Figure 1 shows the vacuum exposure chamber, sample mounting arrangement and associated equipment in schematic form. The proton beam, produced from a radio-frequency ion source, was focused through an Einzel lens mass-analyzer unit to provide a collimated essentially pure H^+ beam. The protons were assumed to be monoenergetic corresponding to the sum of the impressed extraction and acceleration potentials. Proton fluxes varied from $2 \times 10^8 \text{ p}^+/\text{cm}^2\text{-s}$ at the lowest energies to $5 \times 10^{10} \text{ p}^+/\text{cm}^2\text{-s}$ at high energies.

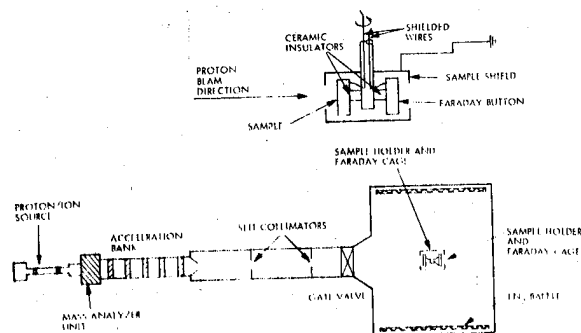


Figure 1. Schematic Representation of Facility

The Faraday cup and samples were mounted on a rotatable table and alternately exposed to the proton beam at each energy. The induced currents were measured with a Keithley Model 610A electrometer.

For metallic films on insulating substrates, the proton transmittance (T_p) at a discrete energy was defined as:

$$T_p = 1 - \frac{(\text{Sample current})}{(\text{Faraday cup current})} \frac{(\text{Faraday cup area})}{(\text{Sample area})} \quad (1)$$

For insulating films on metal substrates

$$T_p = \frac{(\text{Sample current})}{(\text{Faraday cup current})} \frac{(\text{Faraday cup area})}{(\text{Sample area})} \quad (2)$$

Figures 2 and 3 show typical proton transmittance spectra (integral and differential) for aluminum and aluminum-oxide films respectively. The experimental spectral-energy parameters characteristic of this technique for each film thickness, are defined as

- E_0 = Threshold energy for proton penetration (incipient transmittance)
- $E_{1/2}$ = Median proton penetration energy (50 percent transmittance)
- E_1 = Limiting proton penetration energy (100 percent transmittance)

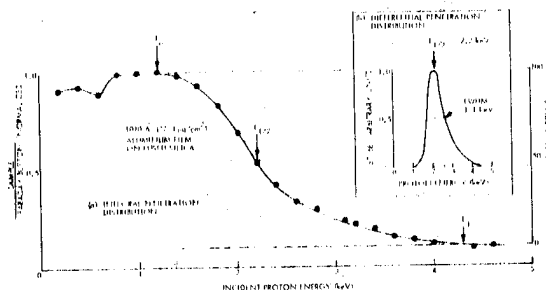


Figure 2. Typical Proton Transmission Spectrum for Aluminum

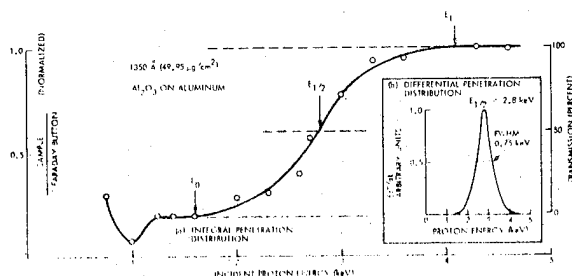


Figure 3. Typical Proton Transmission Spectrum for Aluminum Oxide

For this study, the median proton penetration energy ($E_{1/2}$) has been chosen as the principal parameter, because of its natural relationship to the conventional theoretical and practical concept of median projected range. However, E_0 and E_1 retain significance with respect to defining boundary values for the elastic and inelastic scattering processes associated with proton straggling.

3. EXPERIMENTAL RESULTS

3.1 Metals

Median proton ranges in aluminum, copper, and gold as a function of incident proton energies are shown in Figure 4. For each metal, the range decreases monotonically with energy. The data are presented in terms of geometric penetration normal to the sample plane (projected range). Consequently, for each proton energy, the range decreases as the density of the stopping medium is increased (i.e., $R_{Al} > R_{Cu} > R_{Au}$).

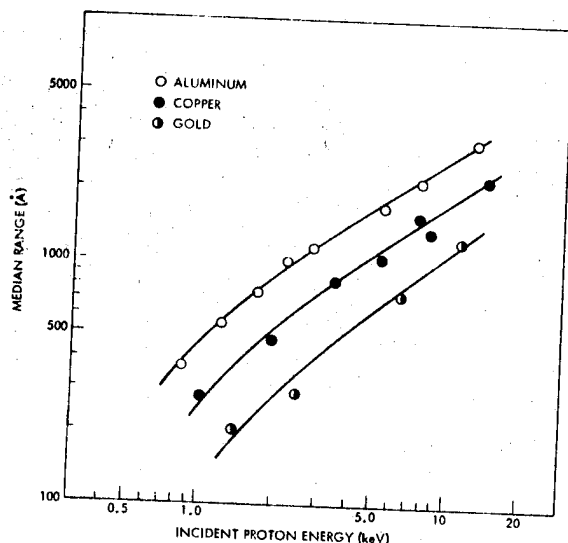


Figure 4. Proton Ranges in Metals

The quantitative results are particularly significant in that they provide a unique opportunity to compare theoretical predictions with experimental data obtained by a single technique over a wide range of proton energies and target atomic numbers.

3.2 Aluminum Oxide

Figure 5 presents the proton range-energy results for aluminum oxide films. The target-preparation technique permits much thinner films to be studied than is the case with metals. Consequently, the penetration parameters of very low-energy protons have been measured for the first time.

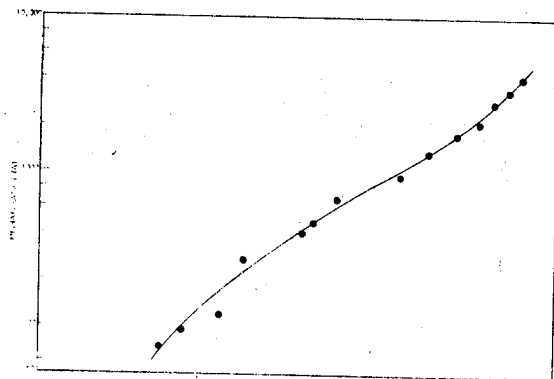


Figure 5. Proton Range in Aluminum Oxide

The character of the proton range-energy relationship in Al_2O_3 is significantly different from that of Al. Despite the fact that the density of Al_2O_3 is greater than that of Al, the median range of protons is greater in the oxide. In addition, an inflection in the range-energy plot occurs in the low-keV region, suggesting that a change in the stopping mechanism occurs.

3.3 Zinc Oxide

Typical degradation of the reflectance properties of a $\text{ZnO}/\text{K}_2\text{SiO}_3$ powder specimen exposed to 1.2 keV

protons is illustrated in Figure 6. Two regions of induced optical absorption occur, in the visible and near infrared. The visible absorption band increases dramatically with proton fluence and dominates changes in solar absorptance (α_s).

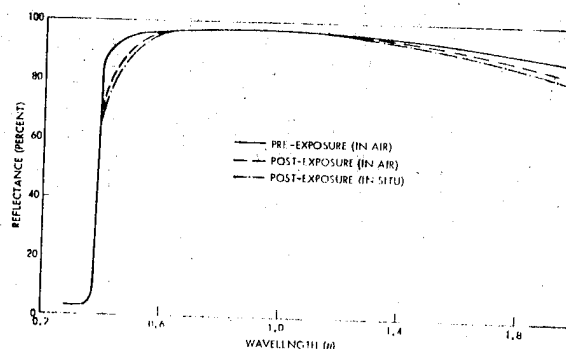


Figure 6. Proton Induced Degradation in Zinc-Oxide Powder

Figure 7 demonstrates the effect of proton fluence on α_s for $\text{ZnO}/\text{K}_2\text{SiO}_3$ powders. It is notable that there appears to be little effect of incident proton energy on the degradation pattern over the range of solar-wind energies (0.25 - 3.2 keV). This result is a significant indication that the optical damage mechanism is essentially energy independent in this limited region.

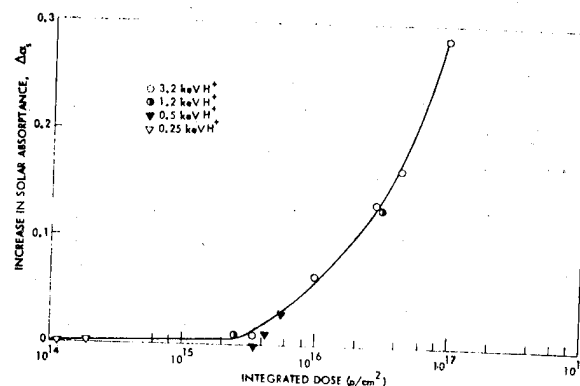


Figure 7. Effect of Proton Fluence on Zinc-Oxide Solar Absorptance

4. DISCUSSION

The major processes responsible for energy losses of energetic ions are

- (i) Nuclear Stopping: Screened Coulomb collisions between the moving ions and the target atoms
- (ii) Electronic Stopping: Interactions between the electrons associated with the moving ions and the various electrons (both bound and free) in the stopping medium
- (iii) Charge Exchange: Between the moving ion and the atoms of the stopping medium.

All three processes are energy dependent and therefore make different contributions to the energy loss along the ion path. They may be treated independently and expressed thus:

$$\left(\frac{dE}{dx}\right)_{\text{Total Loss}} = \left(\frac{dE}{dx}\right)_{\text{Nuclear}} + \quad (3)$$

$$\left(\frac{dE}{dx}\right)_{\text{Electronic}} + \left(\frac{dE}{dx}\right)_{\text{Exchange}}$$

so that the predicted total path covered by an ion as it is brought to rest from an initial energy E is expressed as

$$R_{\text{Total}} = \int_0^E - \frac{dE}{(dE/dx)_{\text{total}}} \quad (4)$$

At higher energies, where electronic losses dominate, the particle is only slightly deflected, but at the end of the path the elastic nuclear collisions produce large-angle scattering, so the average depth is less than the total range. The more important parameter, the projected range R_p , is the average depth to which an ion will penetrate when the incident direction is normal to the surfaces. It is related to the total range and the lateral spread R_L , of the beam as shown in Figure 8.

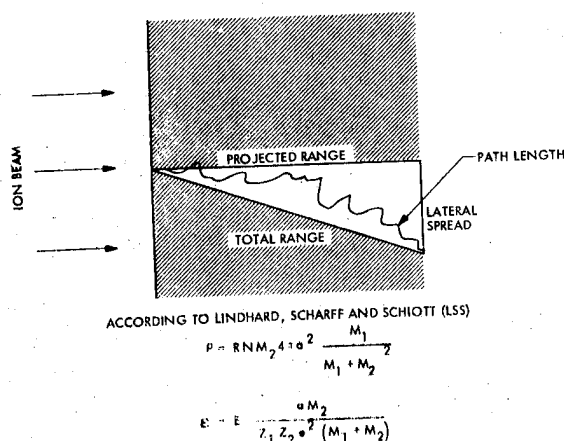


Figure 8. Range Parameters

The basic principals governing these processes have been developed into a comprehensive theory of atomic stopping by Lindhard and Scharff (Ref. 9) and a more detailed analysis including electronic losses by Lindhard, Scharff, and Schiott (LSS) (Ref. 2). Numerical solutions to the LSS equations have been developed by Schiott (Ref. 3) in his treatment of light ions in metals; he predicted the projected range R_p was significantly less than the total path of the projectile, due to importance of nuclear stopping.

For application of the LSS theory, it is more appropriate to derive a universal relationship for the nuclear stopping (S_n) in terms of dimensionless parameters ρ and ϵ , defined as

$$\rho = RNM_2 4 \pi a^2 \frac{M_1}{(M_1 + M_2)^2} \quad (5)$$

and

$$\epsilon = E \frac{aM_2}{Z_1 Z_2 e^2 (M_1 + M_2)} \quad (6)$$

where

$$a = 0.8853 a_0 \left(Z_1^{2/3} + Z_2^{2/3} \right)^{-1/2}$$

where

- a = screening radius
- a_0 = first Bohr radius of hydrogen atom (0.529×10^{-8}) cm
- R = Range
- E = Energy
- N = number of target atoms per unit volume
- Z_1 & Z_2 = atomic number of the incident particle and target atom, respectively
- M_1 & M_2 = atomic weight of the incident particle and target atom, respectively
- e = electronic charge

To obtain the stopping contribution due to electronic events, LSS derived a velocity proportional stopping power (S_e) given by

$$S_e = k\epsilon^{1/2} \quad (7)$$

where

$$k = \left[\frac{\xi 0.0793 Z_1^{1/2} Z_2^{1/2} (M_1 + M_2)^{3/2}}{(Z_1^{2/3} + Z_2^{2/3})^{3/4} M_1^{3/2} M_2^{1/2}} \right]$$

and

$$\xi \approx Z_1^{1/6}$$

These electronic calculations do not produce a universal (S_e) curve, but rather a family of curves each characterized by a particular value of k , where k is of the order of 0.1 to 0.25 for $Z_1 > Z_2$, and only where $Z_1 < Z_2$ can k become greater than unity. In the case of protons, ($Z_1 = 1$), $k > 1$ for all target materials with $Z_2 \geq 8$. Thus, nuclear stopping, the stopping process at low energies, reaches a maximum value around $\epsilon = 0.35$ and then decreases. Electronic stopping increases linearly with velocity over a wide range, and, therefore, becomes the dominant stopping process for energies greater than $\epsilon = 3$.

The range of the proton, evaluated by integrating the basic LSS stopping power curves, is the total distance R that the proton travels in coming to rest. In these experiments, it is the projected range R_p which is of interest and the relationship between R_p and R is illustrated in Figure 8. This correction has been discussed in detail by LSS and by Schiott. They express the correction term in the form $R/R_p = \rho/\rho_p = (1 + bM_2/M_1)$ where b is a slowly varying function of E and R . In the case of protons where $M_1 < M_2$, large-scale scattering makes the correction between R_p and R somewhat larger than the value given by the above approximation. Under these circumstances, electronic stopping is usually appreciable and partially

offsets the increase in the correction term and $1 + M_2/3M_1$ (i.e., $b \approx 1/3$) is a useful empirical correction. In his paper, Schiott (Ref. 12) discusses the procedure to be followed in obtaining a more quantitative correction, whereby his correction for values of R_p/R for light ions is shown to be strongly energy dependent. As Z_2 increases, the range decreases due to the strong atomic number dependence of the nuclear stopping cross section.

Figure 9 shows the excellent agreement between the experimental results of this work with the theoretical curve for protons in Al ($k = 2$). Data from the prior work of Young (Ref. 9), Hines (Ref. 4), and Freeman and Latimer (Ref. 8) at higher energies show reasonable consistency. Young's (Ref. 8) data indicates shorter ranges at low ϵ due to his method, which only accounts for measurement of transmitted protons with sufficient energy to excite the phosphor detector.

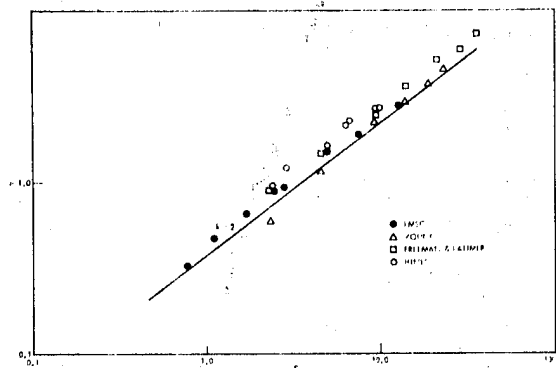


Figure 9. $\rho - \epsilon$ Comparison for Protons in Aluminum

The range-energy data generated in this study permit direct comparison with Schiott's (Ref. 11) analysis. Figure 10 shows the results for protons in Al, Cu, and Au plotted in $\rho - \epsilon$ parameters. It is readily apparent, that Schiott's approach over-emphasizes nuclear stopping. Rather, the experimental results can be represented by a modified total stopping cross section of the form.

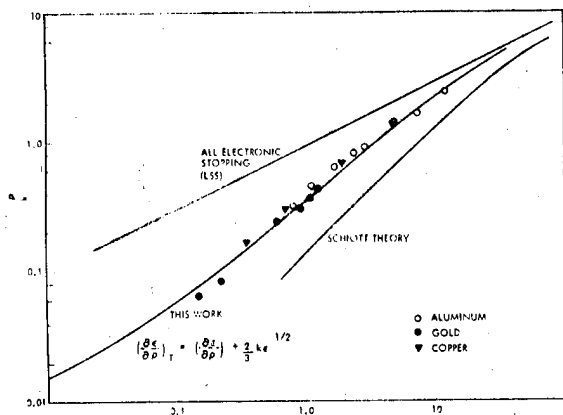


Figure 10. Universal $\rho - \epsilon$ Plot for Protons in Metals

$$\left(\frac{d\epsilon}{d\rho}\right)_T = \left(\frac{d\epsilon}{d\rho}\right)_N + \frac{2}{3} k\epsilon^{1/2} \quad (8)$$

In this analysis, the average value of the electronic stopping cross section $\frac{2}{3} k\epsilon^{1/2}$ is used, rather than the initial value ($k\epsilon^{1/2}$) as proposed by LSS theory.

The analytical treatment is more complicated when the target consists of two (or more) different atomic species. In many cases, these species are sufficiently close in atomic number that one substitutes the mean atomic number into the LSS formulas and proceeds as for a monoatomic target. In the case of Al_2O_3 where the two atomic numbers are appreciably different, a simple range formula can be derived, provided that the stopping powers for the aluminum and oxygen atoms exhibit the same energy dependence. For example, the two ϵ/E conversion factors are sufficiently similar, ($-d\epsilon/d\rho$) has almost the same slope for both species. LSS have shown that the R in a target composed of two species A & B, having relative abundances X_A and X_B may be expressed as

$$R = R_A R_B (X_A R_A + X_B R_B)^{-1} \quad (9)$$

where R_A and R_B are the corresponding ranges in pure monoatomic targets. Domeij et al (Ref. 13) have used Eq. (8) to interpret their experimental data in Al_2O_3 and WO_3 . Schiott (Ref. 12), Sanders and Winterbon et al (Ref. 15), have recently given a detailed treatment of projected ranges (R_p) in polyatomic targets, and in the absence of channeling, the mean penetration depth R_p can be estimated with reasonable precision, i.e., to within about 10 percent.

Comparing the experimental data for Al_2O_3 with theory (Figure 11), it becomes evident that while the analysis qualitatively agrees, some characteristic features are neglected. In particular, the Al_2O_3 range-energy data show a change in slope in the low keV region which may be related to its electronic structure. For low proton energies, sufficient energy may not be available for excitation of the valence-band electrons across the band gap (~ 7 eV). This effect could result in increased nuclear stopping and concomitant reduction of the projected range.

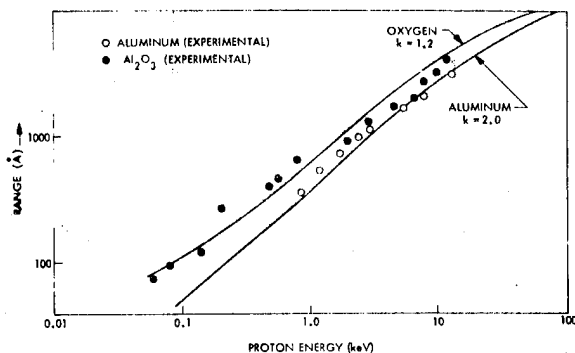


Figure 11. $R - E$ Comparison of Aluminum and Aluminum Oxide

So far, only the analytical approach to deriving the projected range R_p has been considered, but in correlating the changes in optical properties with defect concentration, it is important to have some

knowledge of the range straggling. In polycrystalline and amorphous materials, the differential range distribution is approximately Gaussian (see Figure 2) in shape, and therefore, can be described by a single parameter, namely the average fluctuation ΔR_p in projected range. LSS have developed a framework for treating the problem in terms of the dimensionless energy parameter ϵ . Their predictions showed that the straggling is not strongly energy dependent except when electronic stopping is dominant, but, in the case where $M_1 < M_2$ as for protons, their approximations do not hold due to the dominance of large-angle scattering. The large value of $\Delta R_p/R_p$ for light ions is expected, because R_p is much less than the total path length R . Schiott (Ref. 12) pointed out that for $M_1 < M_2 < 20M_1$, it is difficult to obtain a single-parameter approximation, and, therefore, each ion-substrate combination must be treated separately. In the case of protons, the contribution from electronic stopping usually lower the value of $\Delta R_p/R_p$ below the predicted values.

Figure 12 shows that the experimental values for straggling obtained in this study are in excellent agreement with the predicted values. Straggling results were obtained from the differential transmittance data (as illustrated in Figure 2b using FWHM values).

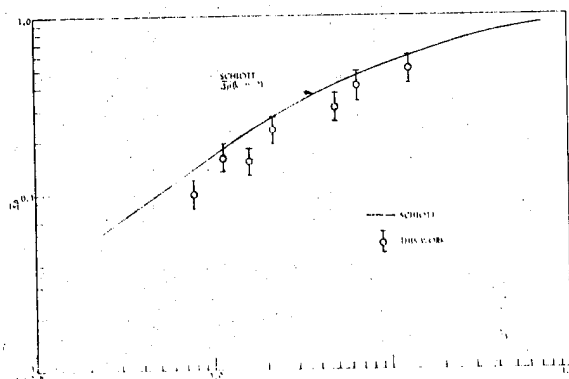


Figure 12. Proton Straggling in Aluminum

Although understanding of the stopping processes of low energy protons in various media provides a basis for quantitative estimation of range-energy relationships, it does not, in itself, provide the details necessary to attempt to correlate proton-induced optical changes with lattice defect concentrations and spatial distributions.

Of specific interest, is the behavior of zinc oxide, which is used extensively as a pigment for thermal-control coatings on spacecraft. Extensive studies during the past decade have shown that ZnO degrades under exposure to electromagnetic and charged particle radiation. The mechanism for ultraviolet degradation in vacuum appears to be related to the generation of hole-electron pairs, followed by field-assisted hole migration to the surface, hole capture by surface oxygen, and desorption leaving surface oxygen vacancies. The surface defects manifest themselves by absorption in the near-infrared spectral region which is reversible in air. Additional absorption also appears near the band edge which has been attributed to the residual excess zinc in the interstitial

positions. The infrared absorption can be significantly diminished by encapsulating the individual ZnO particles in a thin shell of potassium silicate (~ 50 Å) which inhibits oxygen desorption.

Low-energy proton irradiation of silicate-treated ZnO produces spectral features similar to UV effects. This is understandable in terms of the significant portion of the particle energy expended in electronic excitation analogous to the valence band-conduction band transitions imparted to the ZnO semiconductor material by photon absorption. In addition, the stopping mechanism for protons includes a provision for displacement of atoms from lattice sites, resulting in interstitial components which may act as absorption centers.

The foregoing experimental and analytical treatments provide a basis for estimating the projected range of solar-wind protons in zinc-oxide particles coated with thin layers of potassium silicate.

Knowledge of the range of protons in ZnO, together with an insight into the damage mechanism, permits the formulation of a phenomenological model for optical degradation. However, it is not possible to *a priori* estimate either the number of optically active defect sites generated per incident proton or annihilation rate of defects without making some assumptions relative to the model.

The geometry of the closely packed ZnO powders can be approximated as continuous strata of zinc oxide as shown in Figure 13. Since the low energy protons have a range less than the particle diameter (~ 3000 Å), optical damage is generated exclusively in the outmost layer of particles. The spectral reflectance is governed by the scattering properties of the powder compact for the undegraded ZnO. Under proton irradiation, the outer layer of particles show an increased absorption coefficient. Hence, to a first approximation, the reflectance characteristics can be analyzed in terms of established theory for an absorbing film on a reflective substrate (Ref. 16), if the absorption coefficient is determinable. For particulate materials, this quantity is difficult to measure directly. However, it can be deduced from single crystal data. The spectral characteristics of the proton-induced absorption in ZnO powders and paints (Figure 6) are very similar to the absorption band in ZnO single crystals produced by heating in zinc vapor. Indeed, it is very likely that interstitial zinc is responsible for the absorption in both cases. Scharowsky (Ref. 17) has measured this absorption coefficient (Figure 14), and computed the corresponding concentration of absorption centers in the concentration range $6.6 \times 10^{17} - 6.8 \times 10^{18}$ centers/cm³. As shown in Figure 15, a linear relationship between absorption coefficient and excess zinc concentration permits extrapolation to the higher-defect densities generated by proton bombardment.

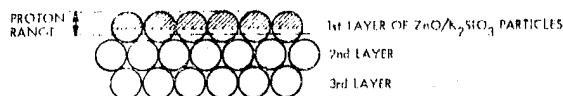


Figure 13. Geometry of Zinc-Oxide Powder

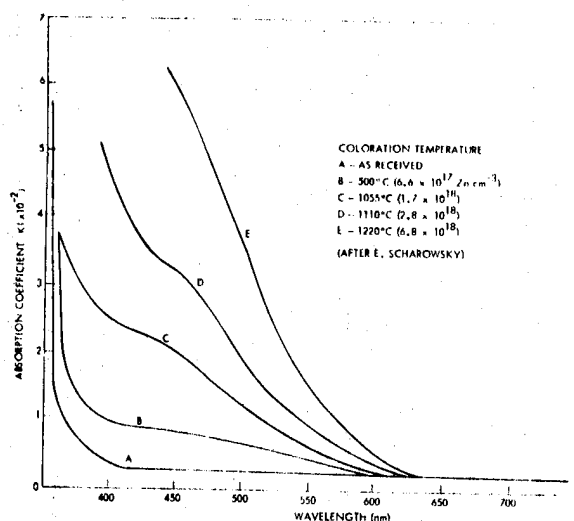


Figure 14. Coloration of Zinc-Oxide Crystals

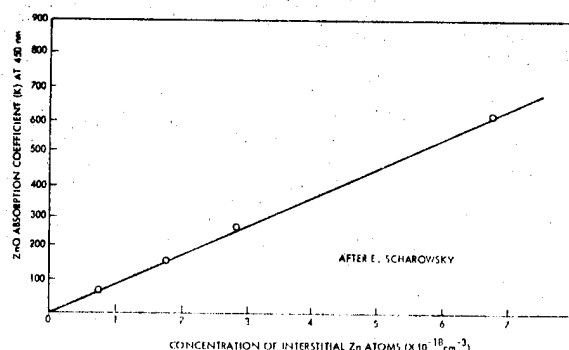


Figure 15. Relationship of Spectral Absorption Coefficient in ZnO to Excess Zinc Concentration

In order to utilize the relationship shown in Figure 15, it is necessary to know the defect concentration in the proton damaged region (i.e., the number of optically active absorption centers generated per incident proton). This quantity can be expressed as

$$[C] = \frac{F}{R_p} \phi \quad (10)$$

where

F = Proton fluence
 R_p = Projected range
 ϕ = Yield of defects per proton

The quantity ϕ is difficult to compute directly with any degree of confidence from strictly theoretical arguments. In particular, for high-proton fluences there is no valid basis for predicting the constancy of ϕ , in view of the possibility of defect self-annihilation.

In order to assess the magnitude of ϕ , Eq. (10) was utilized, together with values of constant ϕ between

1 and 10, to compute reflectance values at $\lambda = 450$ nm. Figure 16 shows the results of these calculations together with the experimental points. For each proton energy, the corresponding calculated range was used to compute defect concentrations. The experimental points are in excellent correlation with a value of $\phi = 1/3$ defect/proton. The close correspondence between the shape of experimental and theoretical curves conclusively establishes that self-annihilation of defects does not occur (i.e., $\phi = \text{constant}$) up to the limits of the experimental-proton fluences ($1 \times 10^{17} \text{ p}^+/\text{cm}^2$). For the highest-proton fluences, the calculated defect concentration in the damaged layer corresponds to 6.7×10^{21} defects/cm³ or greater than 15 percent of the ZnO lattice sites.

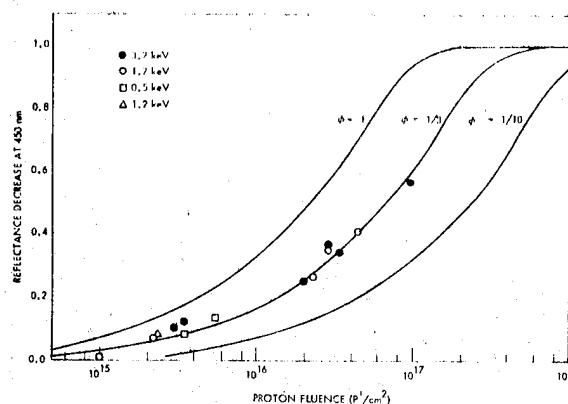


Figure 16. Effect of Proton Fluence on ZnO Reflectance at 450 nm

- Andersen H H & Ziegler J F 1977, Stopping powers and ranges in all elements Vols I & II, Pergamon Press, New York.
- Lindhard J, Scharff M & Schiott H E 1963, Kgl. Danske Videnskab Selskab Mat. Fys. Medd. 33, No. 14.
- Schiott H E 1966, Kgl. Danske Videnskab Selskab Mat. Fys. Medd., 35, No. 9.
- Hines R C 1963, Phys. rev, 132, 701.
- Jarvis G N & Sherwood A C, Nucl. instr. methods, 115, 271.
- Ligeon E & Guivarc'h A 1975, Rad effects, 27 129.
- Davies J A, McIntyre J D, Cushing R L & Lounsbury M 1960, Canad J. Chem, 38, 1535.
- McCargo M, Greenberg S A & Douglas N J 1970, Progress in astronautics and aeronautics, Vol. 23, 189, Academic Press, New York.
- Lindhard J & Scharff M 1961, Phys. rev, 124, 128.
- Freeman N J & Latimer J D 1968, Canad J. Phys., 46, 467.
- Young J R 1956, J. Appl. Phys., 27, 1
- Schiott H E 1968, Can. J. Phys., 46, 449.

13. Domeij B, Brown F, Davies J A & McCargo M 1964,
Can J. Phys., 42, 1624.
14. Sanders J B 1968, Can J. Phys., 46, 445.
15. Winterbon K B, Sigmund P & Sanders J B 1970,
Kgl. Danske Videnskab Selskab Mat. Fys. Medd.,
37, 14.
16. Born M & Wolf E 1959, Principles of optics,
Pergamon Press, New York, 60 -- 61.
17. Scharowsky E 1953, J. fur Physik, 135, 318.

N80-21444

AN ANALYTICAL APPROACH TO EVALUATION OF SPACE RADIATION EFFECTS ON MATERIALS FOR LONG-LIFE MISSIONS

J Moacanin, A Gupta & W F Carroll

*Jet Propulsion Laboratory
California Institute of Technology, Pasadena, California, USA*

ABSTRACT

An analytical model was developed which quantifies effects on organic composite matrix materials of high energy electrons and of UV as well as interactions between the two radiations. Literature data on polyethylene were used to construct a degradation kinetics scheme corresponding to an earth orbit at L=3. Analysis of the model showed that steady state concentrations of radicals put limits on accelerated test conditions. These conclusions were validated by an experimental study on polymethylmethacrylate using UV laser excitation. Relationships for balancing electron and UV radiations to equal acceleration factors are derived, estimates of errors included. Pulse radiolysis using an electron-beam along with time-resolved spectroscopy is shown to be able to separate primary from secondary reactions. Implications of these reactions to changes in engineering material properties are indicated. The use of mechanistic studies is discussed in the context of general test strategies for evaluating materials for space applications.

Keywords: Composites, Space Radiation Effects, Analytical Modeling, Polyethylene, Polymethylmethacrylate, Pulse Radiolysis

1. INTRODUCTION

Uncertainty in the effect of space radiation on composites is a key obstacle to the cost-effective design and reliability of future large space structures (Ref. 1) for long-life missions (10-30 years). Laboratory duplication of the space environment within reasonable cost and time constraints is impractical. Hence, space simulation "compromises" must be made in developing test facilities and optimized test strategies. Key issues to be resolved include test conditions, practical limits to acceleration factors, assessment of interactive effects between environmental stresses and relative merits of sequential vs. simultaneous application of stresses. Moreover, it would be beneficial to develop a systematic data base which could be used for estimations of life of materials for a variety of orbits for space missions. To meet these needs a comprehensive materials evaluation program must combine both analytical and engineering approaches.

A methodology was developed which utilizes an analytical model for material degradation in space to define a test and qualification program (Ref. 2).

Data in the literature are used in an initial analytical process to define critical test parameters and outline a mechanistic test program which leads ultimately to a definition of test facilities, critical test conditions for accelerated/real time simulative testing and prediction of degradation rates in real time for a given space environment. The outputs of combined mechanistic and simulative tests would lead to an improved model. This paper details mechanistic aspects of the modeling approach along with experimental techniques under development.

2. BASIC CONSIDERATIONS

Real time or accelerated simulation of environmental effects is the central issue in testing. It is convenient to separate causative interactions with the environment from effects on materials caused by these interactions (Fig. 1).

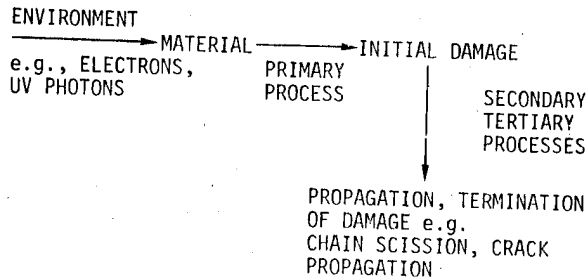


Figure 1. Damage Center Formation

Environmental stresses such as high-energy electrons or UV photons create initial damage centers in the material; these primary processes are responsible for the direct environment-material interactions. The fate of the reactive species in the damage centers depends on the chemistry and physics of the material; the resulting secondary, tertiary and higher order reactions lead to changes in the chemistry and morphology of the material and are responsible for degradation in engineering properties. This provides the logical framework for the definition of a mechanistic test program.

Primary processes (electronic excitation, 10^{-10} - 10^{-6} sec) can be studied using ultrafast electron (or UV) pulses (see below for description). These

studies yield data on mechanisms and rates of formation of damage centers; this information is critical in developing test condition criteria (Fig. 2 and Ref. 2). Study of secondary and other

DEGRADATION PROCESSES	EXPTL. TECHNIQUES	MECHANISMS, RATES	MODEL INPUTS
PRIMARY	PULSE RADIOLYSIS	DAMAGE INITIATION	ACC/SIM. TEST CRITERIA
SECONDARY TERTIARY	TIME RESOLVED SPECTROSCOPY, STEADY STATE RATE MEASUREMENTS	DAMAGE PROPAGATION, QUENCHING/ TERMINATION	STABILIZATION CRITERIA; ENG. PROPERTY CHANGES

Figure 2. Experimental Inputs to Analytical Model

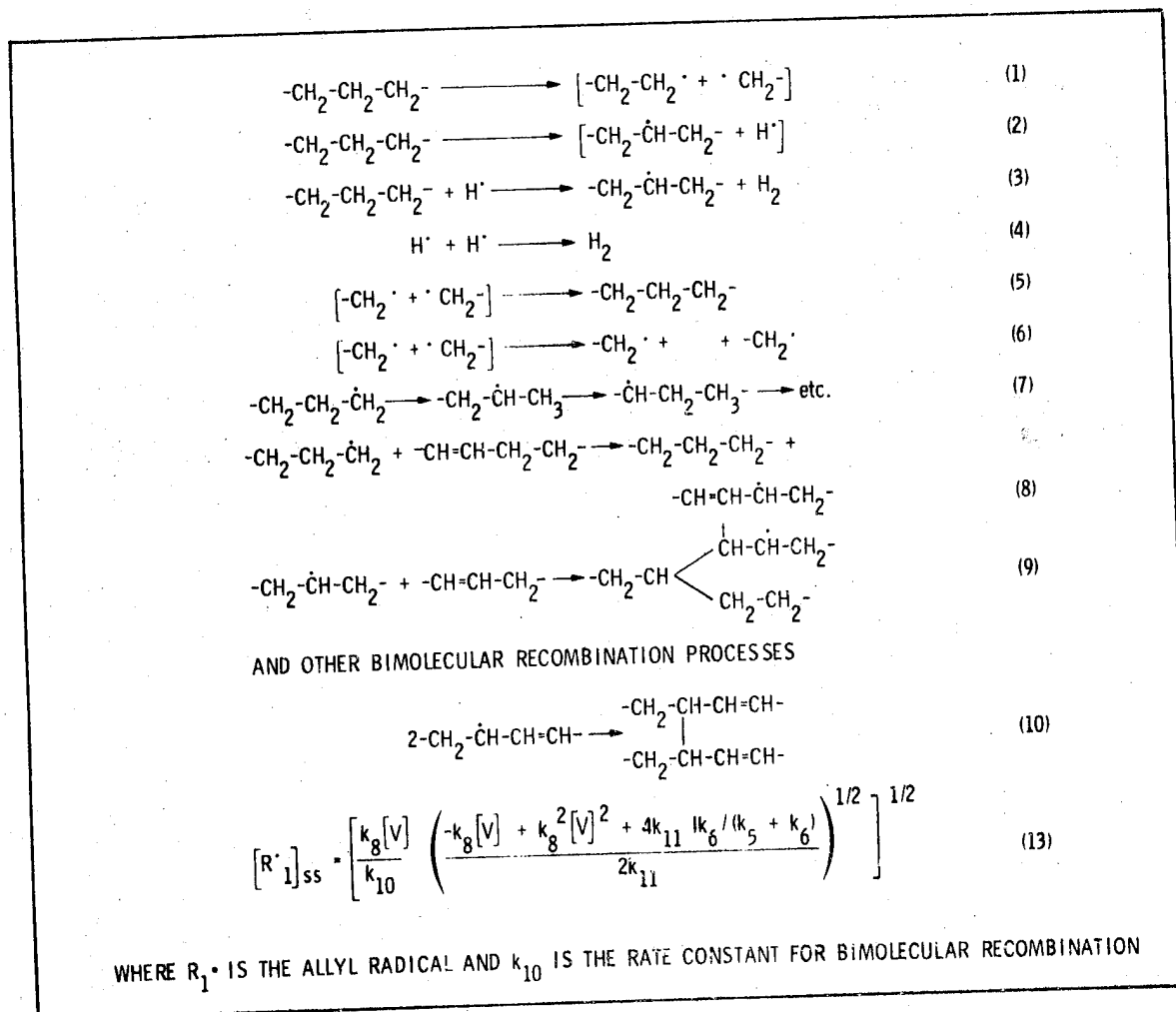


Figure 3. Analytical Model of Degradation of Polyethylene on High Energy Electron Impact

processes (chemical reactions, 10^{-3} - 10^5 sec) requires time resolved spectroscopy for fast reactions and conventional chemical methods for slower processes. This part of the study provides information on the fate of damage centers, (viz., quenching, propagation and termination processes), and on reactions which determine changes in engineering properties; it also guides approaches to improving material stability. For example, it is known that crosslink reactions cause embrittlement and that certain aromatic compounds are capable of dissipating electronic excitation energy by radiative or non-radiative processes. These effects are dominated by kinetic rather than thermodynamic equilibrium criteria and indicate the need for using transient kinetic data and why conventional steady state chemical and engineering inputs are insufficient.

3. METHOD VALIDATION

An analytical model was developed which quantifies effects of high energy electrons as well as interactions between electrons and UV photons. Proton effects were omitted, although their incorporation into the overall scheme should be straightforward. Our intent is to apply our methodology to evaluation of space effects on epoxy, polyimide and polysulfone graphite composites, but the methodology had to be validated before commitments of resources were made. Validation studies follow in the order in which they were performed.

3.1 Polyethylene Model

The model was applied to polyethylene (PE) exposed to radiation corresponding to an earth orbit at L=3. Data from literature were used to construct a degradation kinetics scheme (Ref. 2) which is summarized in Fig. 3.

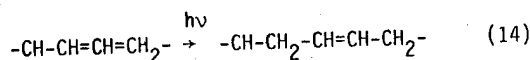
The primary degradation product is the alkyl radical, $R\cdot$, $(-CH_2-\dot{C}H-CH_2-)$ which is usually formed in spurs or regions of high concentration and may undergo primary recombination or may migrate along or across chains until it comes across a double bond where it forms an allyl radical, R_i , $(-\dot{C}H-CH=CH-CH_2-)$. Concordant with allyl radical formation, hydrogen radicals are also formed which either recombine with another hydrogen radical to form H_2 or abstract a hydrogen atom from the polymer backbone again forming H_2 , and generating another alkyl radical (eq. 3). Thus we may have two different types of alkyl radicals in the system; primary alkyl radical pairs caged in damage centers or free alkyl radicals. Hydrogen is thus a principal decay product.

In this scheme equations 1 and 2 represent formation of alkyl and hydrogen radicals via ion radical recombination or other primary excitation routes. Crosslinking processes (eqs. 9, 10 and 12) are quite important and cause brittleness to develop in polyethylene or exposure to e-beam radiation. Decay of free alkyl radicals, i.e., those which escape the primary cage, can take place by recombination but at realistic dose rates recombination is very inefficient. Similarly R_i does not efficiently combine with $R\cdot$, since $[R\cdot]_{ss}$, the steady state concentration of $R\cdot$, is expected to be small (eq. 11). Ultimately $R\cdot$ starts interacting with conjugated double bonds which may be formed by recombination of R_i and form polyene radicals (eq. 12) which are strongly colored and diffuse very slowly, being essentially stable.

The observed failure modes of PE exposed to space radiation can be readily modeled in terms of the proposed scheme. Thus polyethylene becomes brittle, loses mass in the form of H_2 and becomes strongly colored. The brittleness is directly related to processes represented by eqs. 9, 10 and 11, mass loss to eqs. 3 and 4 and coloration by eq. 12. Hence, the rate of increase in crosslink density (related to an increase in brittleness), is proportional to the square of the steady state allyl radical concentration. Thus, by linking modulus with crosslink density one can plot the rate of change of modulus since change in crosslink density is proportional to $k_{10}[R_i]_{ss}^2 + k_9[R\cdot]_{ss} + k_{11}[R_i]_{ss}[R\cdot]_{ss}$, the last term being relatively unimportant. Further, we see a correlation between H_2 evolution yield and alkyl radical yield. Hence we can establish a correlation between two failure rates such as brittleness and coloration through mechanistic considerations which eliminate stress as a variable. This is of practical consideration, since it may be convenient to measure rate of coloration and predict the rate of brittleness from this analysis instead of relating these two failure modes individually to magnitude of stress. These relationships between two failure modes are expected to be independent of stress parameters up to the limit of valid acceleration. Hence this model provides us with a simple technique to measure acceleration factors, and to also verify this model.

The literature shows that only about 3.6% of the alkyl radicals become "free alkyl radicals" up to a dosage of 110 Mrads, which is approximately equivalent to 30 years or more exposure in an environment which deposits 6×10^{-2} MeV per second in the form of e-beam excitation. However, the steady state concentration of allyl radicals (Eq. 13) goes through a plateau at about 80 Mrad, since at these dosages (Ref. 4), eq. 11 becomes important. In eq. 13, $k_6/(k_5 + k_6)$ is approximately .036. 1 is the steady state rate of generation of alkyl radicals, equaling $PG \times 10^4$, when P is the incident energy of electron beam in MeV/sec [V] is the end group (double bond) concentration. All of this modeling is based on rates measured at 293°K. The activation energy of k_5 is about 72×10^3 J/mol and that of k_3 is about $(64-72) \times 10^3$ J/mol⁵. Analysis of these data also yields values of R_i concentration as function of e-beam energy. Fig. 4 indicates that at a dose rate of 50×10^4 MeV/sec, accelerated exposure rates start deviating from real time exposure conditions, thus defining limits to practical accelerated test conditions.

In regard to UV effects, it is known that allyl radicals absorb UV at 238 nm and at wavelengths greater than 390 nm. From literature data (Refs. 3 and 4), approximate extinction coefficient values of 10^4 and 10^3 may be assigned as an upper limit at these wavelengths. Since $[R_i]_{ss} = 5.8 \times 10^{-6}$ moles/lit at 10^4 MeV/sec of e-beam excitation, it follows that absorbance due to R_i will not exceed .058 and .0058 at these two wavelengths. This means that approximately 14% of solar irradiance at 238 nm will be absorbed by allyl radicals and 0.6% of solar irradiance in the range 390-500 nm will be absorbed. It is known that the long wavelength excitation converts the allyl radicals back to alkyl radicals of the same type.



Hence there is some measurable effect of UV on transients generated by e-beam excitation. This effect is much more pronounced in a combined accelerated exposure, which will therefore unduly emphasize this "cross term." Thus a 10x acceleration of e-beam intensity will produce a $[R]_{ss}$ of $\sim 2 \times 10^{-5}$ moles/lit which will have an absorbance of 0.2 at 238 nm resulting in 40% absorption at 238 nm. Simultaneous acceleration of e-beam and UV should thus be avoided, and if acceleration of e-beam excitation is desired, UV should be attenuated relative to real time values. Fig. 5 shows the calculated ratios of e-beam and UV fluxes which preserve the proper balance of free radical concentrations, and preserve reaction mechanisms, and thus allow correct extrapolations of accelerated test data; a ratio of 1.0 corresponds to real time conditions.

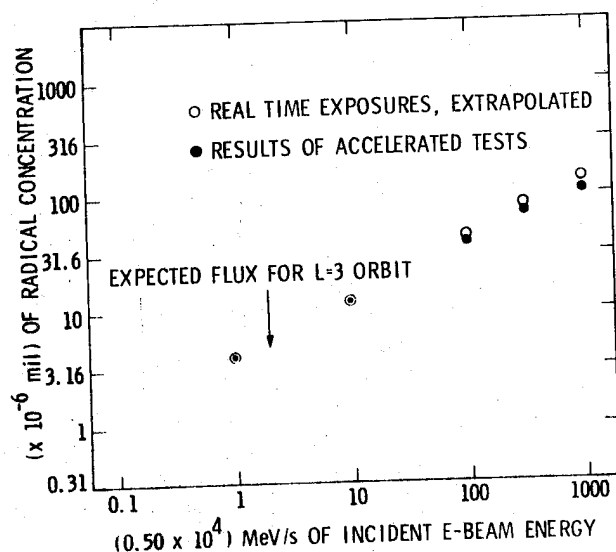


Figure 4. Deviation from predicted degradation rate as a function of acceleration factor in polyethylene

3.2 Experimental Model Validation

The analysis of the PE model showed the role played by free radicals in limiting acceleration factors (Fig. 4). For an experimental validation of the concept a study was carried out on polymethylmethacrylate (PMMA) because of the extensive literature on its photochemistry. A pulsed UV laser was used as the excitation source in order to simplify experimental procedures. To be sure, the chemistry induced by a e-beam would differ in detail, but the generic problem would be the same. From literature and from our recent results, mechanisms for primary and secondary PMMA reactions were defined (Fig. 6). Laser pulsing was performed at 77°K and radical measurements were made at the same temperature using e.s.r.; by stabilizing radicals at low temperature one could study the effect of increasing flux by simply increasing the number of pulses. Fig. 7 shows the concentration of the propagating chain radical as function of flux. The downward bend of the curve is similar to that for PE (Fig 4); at

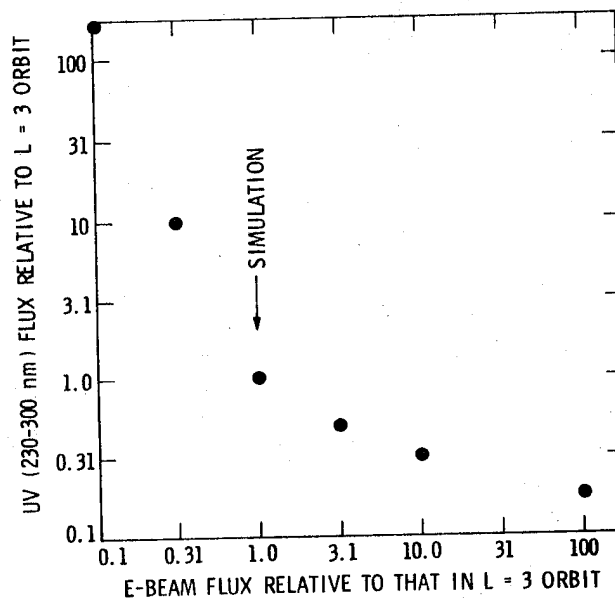


Figure 5. Proposed strategy for multistress exposure of polyethylene

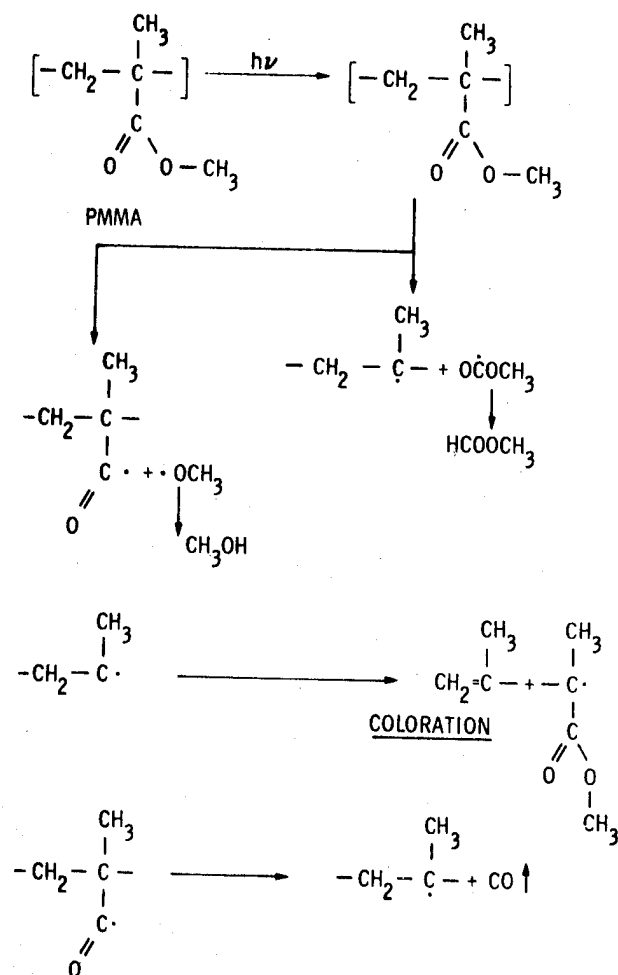
high flux values the curve reaches a maximum and finally bends downward. This behavior is controlled by competitive secondary photolysis products (Fig. 8 dashed line); the effect starts to be noticeable at fluxes corresponding to 150-200 pulses, and clearly saturation is reached at about 600 pulses (Fig. 7). Thus, how free radical concentrations limit acceleration was demonstrated experimentally, in accordance with predictions made on the PE model.

3.3 Pulse Radiolysis

Development of the pulse radiolysis method is in progress. Preliminary experiments were performed on poly(1-vinylnaphthalene), P1VN, and poly(2-vinylnaphthalene), P2VN, as model systems because of the existing background on their electronic excited states.

Pulse radiolysis experiments were carried out by 3 ns 600 KEV electron beam pulses from a Featron (Hewlett Packard) (Fig. 9). This linear accelerator was modified by inserting a precision delay generator in its pulse circuit to improve pulse shape and pulse synchronization with optical pulses from a Xenon flash lamp which is used to monitor transient absorption. Time resolved emission spectra were recorded using a ASI monochromator and a shielded Hamamatsu photomultiplier. Output of the photomultiplier was fed into a 500 MHz scope. Transient absorption was detected using a Xenon Flash lamp and collimating optics using the same detection assembly as above. Dosimetry was carried out by monitoring H₂ evolution from cyclohexane.

From our results a mechanism for primary processes was proposed (Fig. 10). Ion radicals decay through recombination within spurs, hence avoid degradation, although it is known that they are thermodynamically unstable. When these ion radicals are prepared at lower concentration by conventional techniques, they lead to relatively rapid depolymerization (Ref. 9). In the present case degradation products



are H_2 and formation of unsaturation.

Partial support for the proposed mechanism was provided by emission spectroscopy on P1VN (Fig. 11). The prompt emission comes from excited states (first excited singlet at 400 nm and first triplet at 500 nm) generated by ion radical recombination inside spurs while delayed emission comes from these excited states generated by recombination of "free" ion radicals, presumably through long range interactions such as hopping or tunnelling. These preliminary results give us confidence that pulse radiolysis studies will provide quantifiable data on primary processes.

4. CONCLUSIONS

Implications of the results of our analytical approach to testing are that certain boundaries to test design parameters can be defined even from preliminary models, which otherwise would have required extensive long-term real-time and accelerated tests.

Maximum permissible acceleration factors were calculated from steady state concentrations of free radicals. This criterion was first predicted analytically and then validated experimentally. Similar considerations of free radicals kinetics provide a criteria for using a raster electron-beam instead of continuous beam (Ref. 2). It is concluded that repeat frequencies of less than 1 sec^{-1} only are acceptable for temperatures not exceeding 373°K .

There are advantages to carrying out sequential (e-beam and UV) rather than simultaneous tests, since errors can be estimated and are likely to be relatively small. If simultaneous testing is used, the ratio of the two fluxes must be selected carefully, otherwise "cross-term" effects may dominate.

AT HIGH UV FLUXES THE RADICALS CAN UNDERGO SECONDARY PHOTOLYSIS.

Figure 6. Analytical model of degradation of PMMA induced by pulsed UV laser

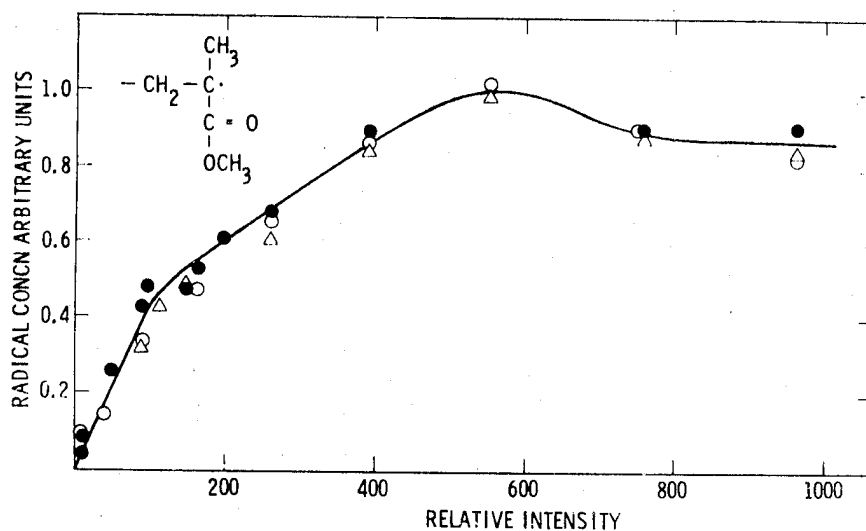


Figure 7. Dependence of radical concentration on intensity

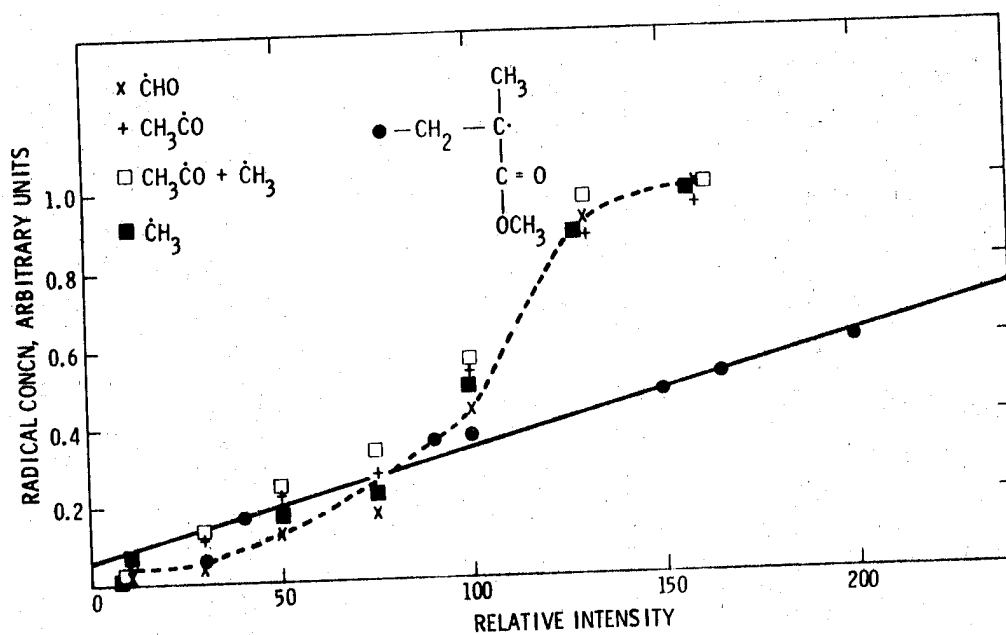


Figure 8. Secondary photolysis of primary photoproducts at high intensities

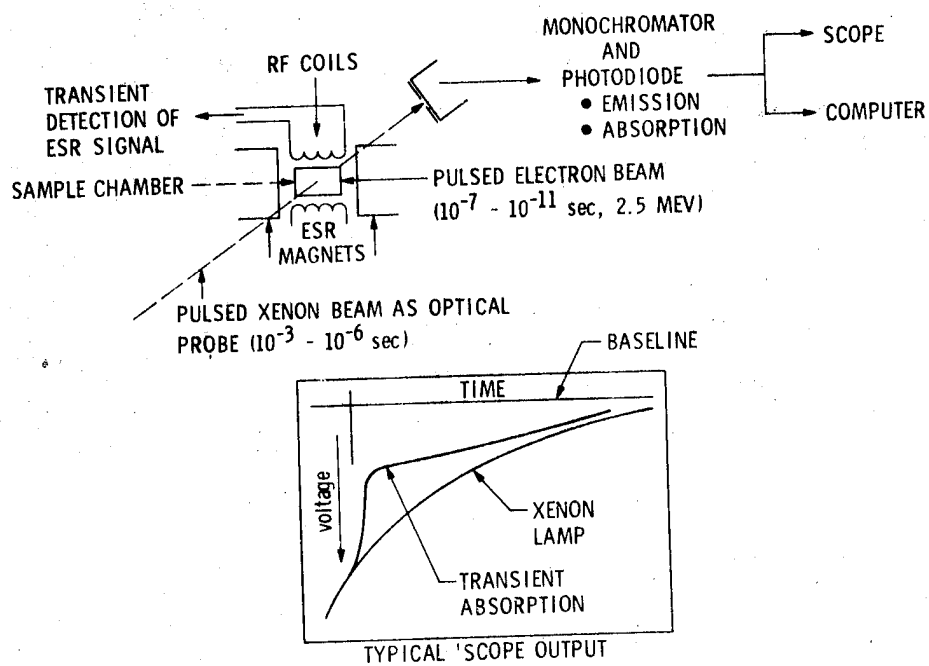


Figure 9. Pulse radiolysis

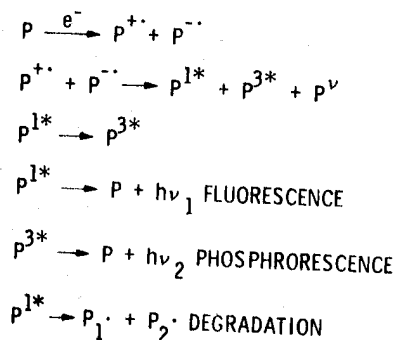


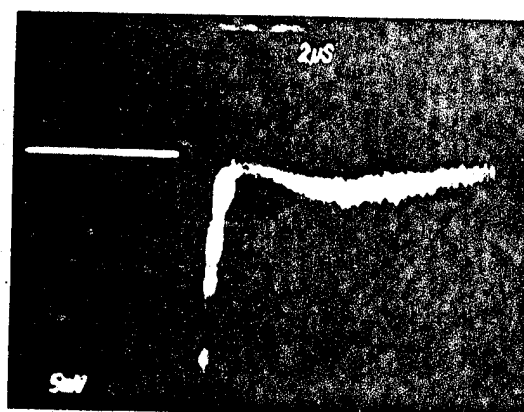
Figure 10. Proposed mechanism for primary processes in P1VN and P2VN

If in the course of long-term testing, there is need to interrupt periodically exposure to radiation, an estimate of the time needed for radicals to reach steady state should be estimated. For polyethylene at ambient temperature this time is about 200 hours for 10x acceleration, and hence in this case this can be considered to be the minimum period of uninterrupted exposure.

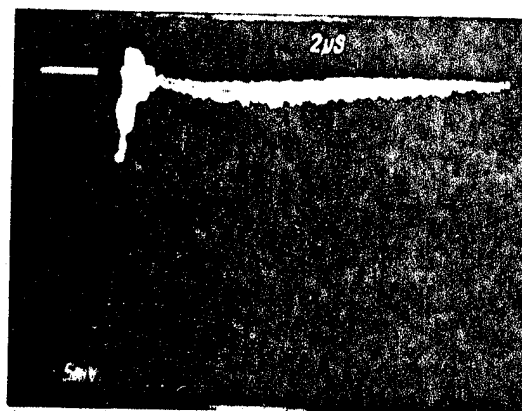
Because of the large stopping power for low energy electrons, there will be a wide spectrum of electron energies corresponding to $L=3$ (Ref. 2). Therefore, we conclude that mechanistic experiments should be done at two energy levels at least.

5. REFERENCES

1. Freeland, R. E., and Campbell, T. G., "Deployable Antenna Technology Development for the Large Systems Technology Program," Paper No. 79-0932, Proceeding of AIAA/NASA Conference on Adv. Technology for Future Space Systems, Hampton, Virginia, March 1979.
2. Gupta, A., Carroll, W. F. and Moacanin, J., "Effects of Space Environment on Composites: An Analytical Study of Critical Experimental Parameters," JPL Publication 79-47, National Aeronautics and Space Administration, July 1979.
3. Shimada, S., Kashiwabara, H., and Sohma, J., Ref. Progr. Polym. Phys. Jap. 13, 475 (1970) and references therein.
4. Doe, M. and Waterman, D. C., J. Phys. Chem., 74, 1913 (1970).
5. Dole, M. and Waterman, D. C., *ibid* 74 1906 (1970).
6. Tsuji, K., Seiki, Polymer J. 2, 606 (1971).
7. Tsuji, K., J. Polymer Sci., A1, 11, 1407 (1973).
8. Tsuji, K., Takeshita T., J. Polym. Sci., B10, 185 (1972).
9. Rembaum, A. and Moacanin, J., Exchange Reactions, pp. 173-190, published by International Atomic Energy Agency, Vienna (1965).



TIME
400 nm



TIME
500 nm

Figure 11. Transient emission from poly 1 vinyl naphthalene

ACKNOWLEDGEMENT

This paper represents one phase of work performed at the Jet Propulsion Laboratory, California Institute of Technology under Contract NAS7-100 of the National Aeronautics and Space Administration.

N80-21445

SPACE ENVIRONMENTAL EFFECTS ON POLYMER MATRIX COMPOSITES

R C Tennyson, JS Hansen, B Uffen, D Morison & G Mabson

University of Toronto
Institute for Aerospace Studies, Toronto, Ontario, Canada

ABSTRACT

This paper presents some experimental results from one phase of a research programme which is investigating short and long term behaviour of fiber reinforced polymer matrix composite materials subjected to a simulated space environment. The present work is concerned with the influence of thermal-vacuum conditions on mechanical stiffness (E_{22}), strength (σ_{2u}) and coefficient of thermal expansion (CTE). One important feature of these experiments is that all tests involving the vacuum environment have been made *in-situ*, thus eliminating the possibility of specimen contamination by reaction with the atmosphere (ex: moisture re-absorption). CTE data have been accumulated as a function of number of thermal cycles in a vacuum exceeding six months duration. The resulting information will be useful in the design of spacecraft structures fabricated from this class of composite materials.

Keywords: Space Environment, Polymer Matrix Composites, Thermal-vacuum, Coefficient of Thermal Expansion, Strength Stiffness.

1. INTRODUCTION

In the design of present and future spacecraft, especially large space structures envisaged for extensive exploitation of space, lightweight fiber reinforced polymer matrix composites are seriously being considered as construction materials. They offer very attractive strength/weight and stiffness/weight ratios (compared to most metals) and perhaps more importantly, the possibility of dimensional stability over a wide temperature range. For example, materials such as graphite/epoxy and Kevlar/epoxy provide the opportunity to design structural components with essentially a zero coefficient of thermal expansion (CTE) in prescribed directions over much of the thermal environment normally encountered by spacecraft. Another aspect of importance for large space structures is their enormous cost and consequently the requirement for long life (~ 30 years). During the life cycle, every component of the structure will experience exceedingly harsh conditions composed of temperature extremes, ultra hard vacuum, a broad spectrum of intense radiation, micro-meteorite impact and impingement by various atomic and molecular species. Thus one is faced with the difficult task of assessing the degree to which this environment will affect material properties over a

prolonged time period. This is of particular concern since many organic/polymeric materials are used as matrix or bonding agents in composite materials. In addition, most commercial polymers are mixtures of basic polymeric material and various additives such as solvents, catalysts, antioxidants, manufacturing aids, etc. Consequently, in the presence of hard vacuum alone, the loss of adsorbed and absorbed gases as well as sublimation or evaporation of the more volatile constituents of the material can occur, all of which will be accelerated by elevated temperature. Finally, the cumulative effects of radiation and thermal fatigue also raise serious questions regarding the long term behaviour of polymer matrix composites in space.

By necessity, realistic ground-based simulation is of high priority. In this context, it seems that a complete simulation is impossible; however the combined effects of temperature, vacuum, U.V. radiation together with selected high energy and molecular beam bombardment can be attained. While providing an appropriate simulation, it is the philosophy of the present programme that all testing must be done *in-situ*, i.e., with the samples remaining in the space environment. This approach eliminates ground handling effects and re-absorption of ambient moisture or contaminants, as well as chemical changes when re-exposed to the atmosphere.

The following report describes three simulators being used to evaluate composite materials *in-situ* and provides some test data on graphite/epoxy (3M, SP288 T300), Kevlar/epoxy (3M SP306, PRD-49-III) and boron/epoxy (3M SP290). Up to the present, emphasis has been placed on determining the long-term effect of thermal-vacuum cycling on the CTE response with some short term results given for strength and stiffness. It should further be noted that this work represents only a portion of a more extensive programme, a complete description of which is given in the flow chart of Fig. 1. To provide comparative data with that obtained from the simulators, experimental packages (Fig. 2) containing a variety of composite samples (i.e., tubes and flat plate specimens fabricated from the same materials) were assembled to fly on the first NASA Long Duration Exposure Facility (LDEF) satellite. Together, the combined simulation and flight test results should provide a comprehensive set of design data.

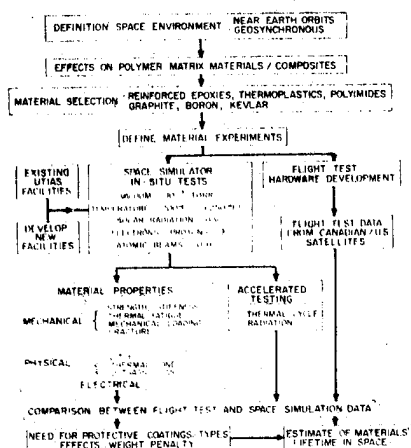


Figure 1. Flow chart illustrating research programme at UTIAS



Figure 2. UTIAS composite flight package for LDFF mission.

2. DESCRIPTION OF UTIAS SPACE SIMULATORS

The central parameter in a space environment is an extremely hard vacuum combined with an infinite pumping capacity. Pressures of approximately 10^{-12} torr and lower can be encountered at orbital altitudes. For simulation purposes, maintaining a working vacuum of 10^{-12} torr is extremely difficult. However, the same outgassing effects can be obtained at somewhat higher, more easily obtained pressures. The effect of a total vacuum (0 torr) is that each molecule leaving an exposed surface never returns. In this case, the molecular loss rate is a function only of the nature of the material (i.e., vapor pressure and molecular weight) and absolute temperature. This effect is closely approached when the mean-free-path is sufficiently large in comparison to system dimensions. In actual practice, this can be achieved at pressures of about 10^{-4} or 10^{-5} torr (mean-free-path for air .5 to 5 meters). On this basis, a system maximum operating pressure of 10^{-5} torr is considered sufficient for the proposed simulation. In this pressure range, radiation is by far the dominant thermal energy transfer mechanism, therefore, heating/cooling effects similar to those encountered in space can be achieved. However the three simulators described below are all capable of maintaining a working vacuum ranging from 10^{-6} to 10^{-8} torr.

2.1 Thermal-Vacuum Facility With In-Situ Mechanical Loading (SS1)

A photograph of the space simulator facility with in-situ loading capability, designed and constructed at UTIAS, is shown in Fig. 3.

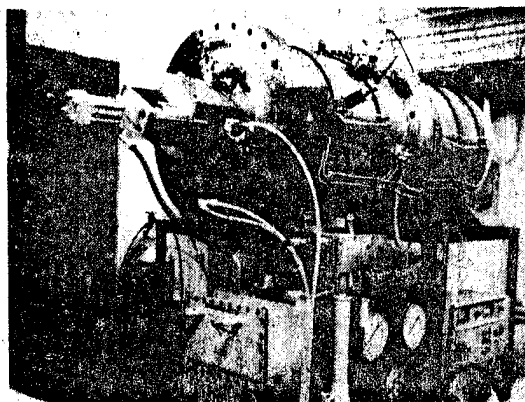


Figure 3. UTIAS space simulator with in-situ mechanical loading.

The vacuum system is composed of several major components for pumping, valving, pressure measurement, baking, trapping and piping, a complete description of which can be found in Ref. 1. The stainless steel test chamber is cylindrical in shape, measuring 51 cm in diameter x 117 cm in length. Combined action of roughing and oil diffusion pumps with a liquid nitrogen cryogenic trap above the diffusion pump permits 10^{-6} torr to be achieved in about one hour. Of particular interest is the mechanical loading fixture attached to the chamber door (Fig. 4) which can supply in-situ uniaxial or torsional loading of specimens. Universal gimbals ensure alignment of the load which is transmitted via hydraulic pistons acting through flexible stainless steel bellows.

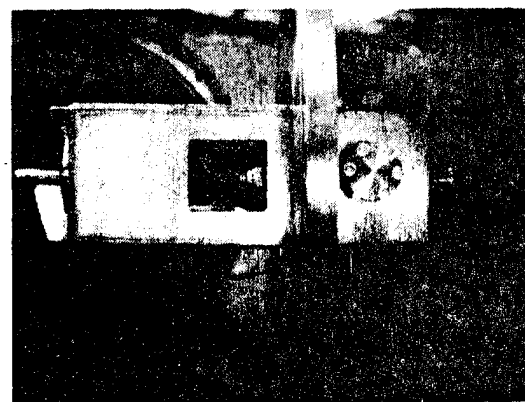


Figure 4. Hinged chamber door with load fixture attached.

2.2 Long Term Thermal-Vacuum Cycling Facility (SS2)

Much of the work reported in this paper was based

on continuous thermal cycling ($75^{\circ}\text{F} \leq T \leq 200^{\circ}\text{F}$) at 10^{-7} - 10^{-8} torr over a period exceeding 6 months using the facility shown in Fig. 5.



Figure 5. Long term thermal-vacuum cycling facility.

This ultra high vacuum chamber has a working volume of approximately 66 cm diameter x 76 cm in height. Employing a roughing pump, two Zeolite adsorption pumps and an ion getter pump yields a vacuum close to 10^{-8} torr in a fully loaded state. Currently, 158 composite specimens (120 flats + 38 tubes) are mounted in a tray structure slung below the top chamber closure plate (see Fig. 6).

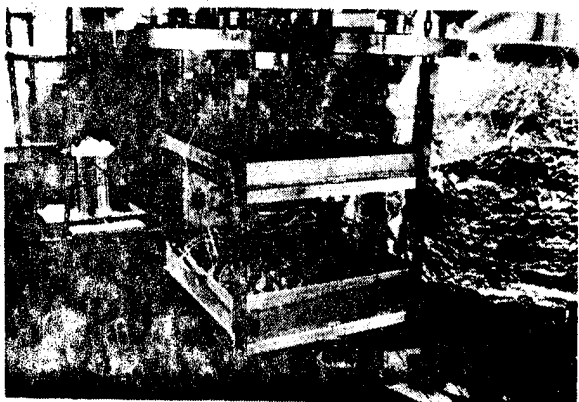


Figure 6. Tray structure containing instrumented flat and tubular composite specimens.

Of this number, 33 were strain gauged for monitoring thermal response of the materials. Both levels of the tray contain 3 thermocouples each to record temperature. A description of these specimens can

be found in Table 1. Note that the 'cracked' samples will be studied at a later date to assess fracture toughness.

This facility is also equipped with a mass spectrometer capable of resolving species in the range of 13 - 80 AMU and partial pressures of the order of 10^{-10} torr. Although a variety of outgassing products were observed, the dominant contribution was H_2O^+ . Figure 7 presents the measured partial pressure for H_2O^+ as a function of time and it was found that an acceptable vacuum was attained in about two weeks.

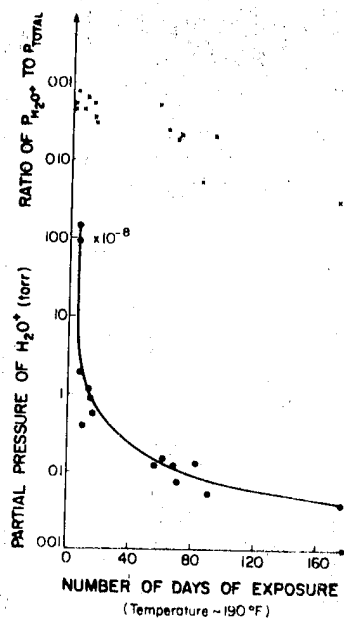


Figure 7. Mass spectrometer data on H_2O^+ as a function of vacuum duration.

2.3 Thermal-Vacuum Radiation Facility With In-Situ Mechanical Loading (SS3)

A third thermal-vacuum facility (Fig. 8) has been developed* containing a U.V. source and a β -emitter. The working volume within the cylindrical chamber is about 45 cms diameter x 34 cms in height. Using a 1000 watt Xenon D.C. arc lamp (Conrad-Hanovia, USA; ~ 1000 HR lifetime) in conjunction with a variable current regulated power supply provides a capability of simulating about 1 solar constant over the wavelength range 200 nm - 400 nm. Measurements of the actual U.V. intensity will be made with both short (220 nm - 280 nm) and long wave (300 nm - 400 nm) sensor cells ("Blak-Ray" meters UVP Int. Inc., USA). This system is mounted vertically in an air cooled quartz tube centered in the chamber, thus providing 360° of exposure (see Fig. 9). Electron bombardment will be obtained by natural emission from S90 sources attached to the inside wall of the facility. At present two source strengths of 1 and 500 millicuries provide peak energies of approximately 1.5 Mev, taking into account the existence of an aluminium foil protective window. One other feature includes a carousel arrangement (see Fig. 9) which can support 30 flat coupons (about

*Designed by Mr. B. A. Smith and Mr. L. P. Hébert, Research Assistants at UTIAS.

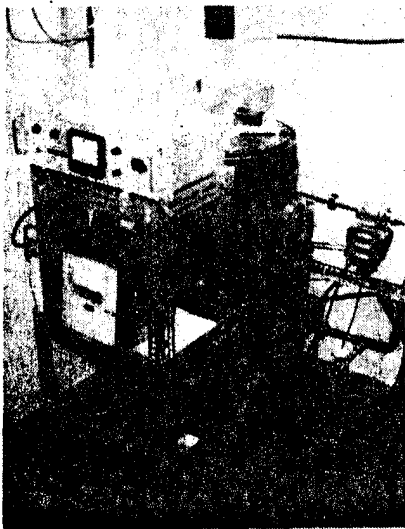


Figure 8. Thermal-vacuum radiation facility.

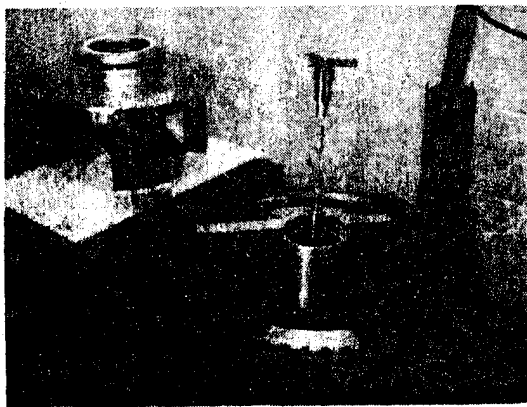


Figure 9. View of (1) Xenon U.V. lamp centered in quartz tube window; (2) rotating carousel containing composite flat plate specimens.

2.54 cms in width), each of which can be rotated into a gimbal mounted load grip having 4500 N capacity. The carousel can be turned externally, thus permitting test data to be obtained for varying radiation exposures on individual specimens. In addition to CTE measurements, this permits the determination of modulus and strength as well. Uniaxial loading is again supplied by an external hydraulic piston acting through flexible bellows. Extensive radiation safety equipment has yet to be assembled but it is anticipated that tests should be underway shortly.

3. TEST RESULTS

As stated earlier, in-situ testing of polymer matrix materials is regarded as necessary to ensure that results are unaffected by such factors as contamination and re-absorption. For example, it has been found that even 24 HRS exposure in vacuum ($\sim 10^{-6}$ torr) at elevated temperature ($\sim 250^\circ\text{F}$) can produce significant outgassing for thin laminates. Figures 10 and 11 illustrate the short and long term % mass gain of a 4-ply graphite/

epoxy tube (~ 0.51 mm thick) when re-exposed to ambient laboratory conditions. The excess in weight above its initial value (prior to exposure) is probably due to moisture diffusion into the composite, occupying molecular sites vacated by other lower mass number polymer molecules. Because of this, measurements of CTE, strength and stiffness were made in-situ, as described in the following sections.

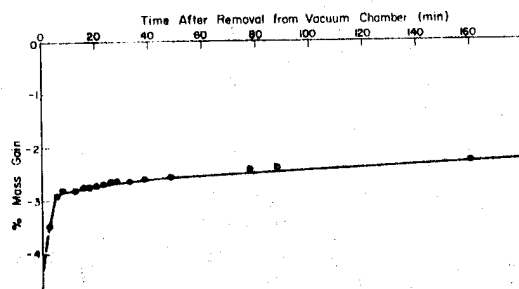


Figure 10. Variation in % mass gain with time after removal from vacuum (graphite/epoxy, SP 288-T300)

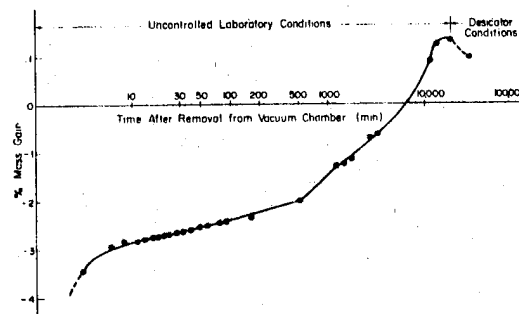


Figure 11. Long term change in % mass gain for graphite/epoxy after removal from vacuum.

3.1 Coefficient of Thermal Expansion (CTE)

All thermal response data were obtained using bonded foil strain gauges (type EA-06-250-BB120, Micro-Measurements, USA) after extensive calibration under ambient pressure and vacuum conditions. The apparent response of a strain gauged structure or material sample undergoing a temperature change (ΔT) (i.e., the reading one obtains from a strain indicator) is given by

$$\epsilon_A = \epsilon_M - \epsilon_g \quad (1)$$

where 'M' and 'g' refer to the 'material' and strain 'gauge', respectively. If the material and gauge strains vary linearly over the tempera-

ORIGINAL PAGE IS
OF POOR QUALITY

ture range of interest, then we can re-write Eq.(1) as

$$\Delta m = \frac{\epsilon A}{\Delta T} + \alpha g \quad (2)$$

where αm and αg denote the material and strain gauge coefficients of thermal expansion, respectively.

The determination of an average value for αg at ambient pressure was made by bonding three gauges on separate metal tubes; steel (4140), copper and aluminum, subjecting each sample to uniform heating and measuring the axial displacement as a function of temperature. This was done in a small oven (containing a glass window) mounted in a travelling microscope, as can be seen in Fig. 12*.

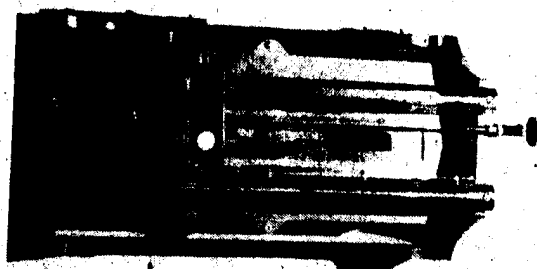


Figure 12. Travelling microscope calibration of strain gauge on metal tube in oven.

At the same time, the apparent strains were recorded to correlate with the actual strains at different temperature increments. After many repeat tests, a least squares fit yielded an average value of $\alpha g = 6.93 \times 10^{-6}$ in/in/°F (Fig. 13).

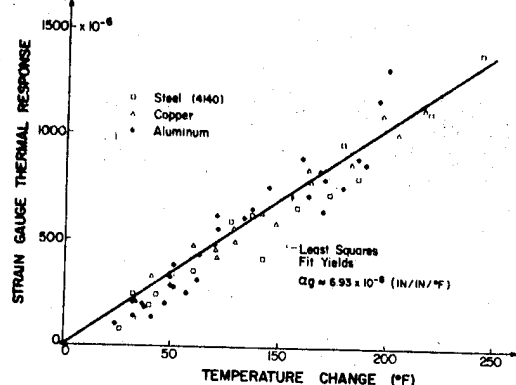


Figure 13. Calibration of strain gauge at ambient pressure (MM EA-06-250-BB120)

The next step involved calibrating the strain gauge-metal tube system in vacuum. As shown in Fig. 14, the calibration for αg shifted due to outgassing and the final value used throughout the remainder of this report was taken as 6.55×10^{-6} (in/in/°F) under vacuum conditions.

Using the long term thermal-vacuum facility (SS2), thermal strain measurements were made as a function of vacuum duration and number of thermal cycles (T/C). Initially, substantial outgassing occurred. This work was carried out by Mr. J. A. Catalano, Research Assistant, UPTAS.

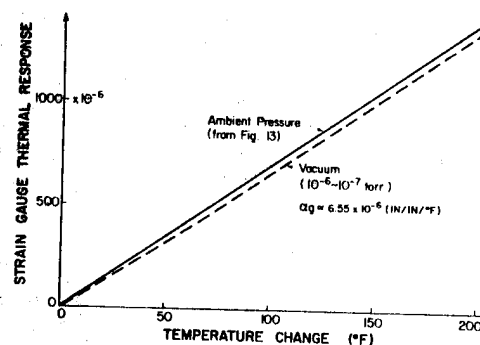


Figure 14. Thermal-vacuum response of strain gauge

with the major component being water moisture. However, in less than two weeks, steady state vacuum of 10^{-8} torr was achieved at 75°F , increasing to 10^{-7} torr at 200°F . Note that throughout this experiment, a calibrated steel tube containing the same type of bonded strain gauge was inside the facility undergoing the same thermal-vacuum cycling as the composite samples. It was found that no significant deviation in the measuring system occurred, thus providing the necessary confidence for interpreting the composite materials' response.

Figures 15, 16 and 17 present the CTE data obtained on 4 ply, ± 8 symmetric balanced laminates as a function of the number of thermal cycles for varying vacuum exposure times. The three materials investigated include Kevlar/epoxy, graphite/epoxy and boron/epoxy.

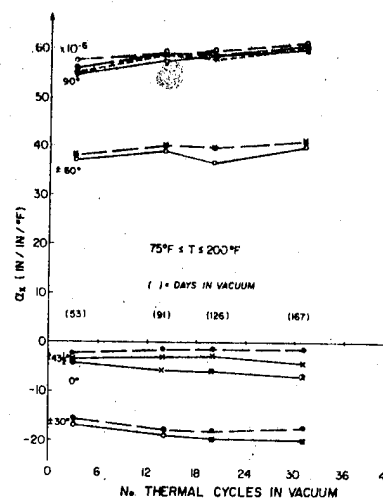


Figure 15. Effect of thermal-vacuum cycling on thermal response of Kevlar/epoxy (3M GP306, PRD49) at 10^{-7} - 10^{-6} torr.

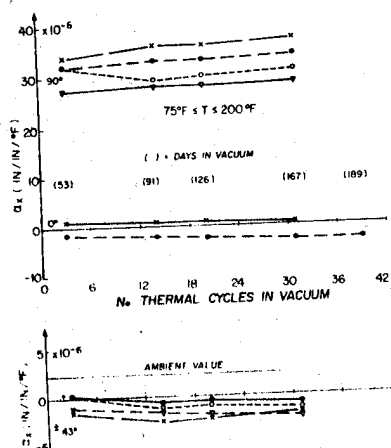


Figure 16. Effect of thermal-vacuum cycling on thermal response of graphite/epoxy (3M SP288 T300) at $10^{-7} \sim 10^{-8}$ torr.

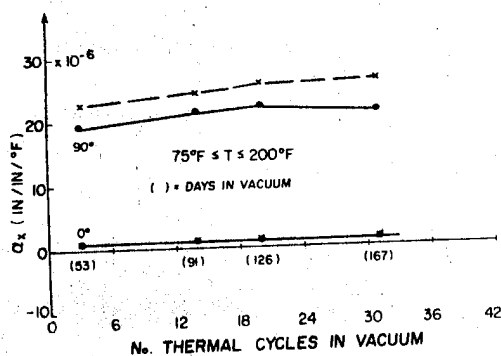


Figure 17. Effect of thermal-vacuum cycling on thermal response of boron/epoxy (3M SP290) at $10^{-7} \sim 10^{-8}$ torr.

It is quite apparent that substantial changes occur in CTE due to the combined effects of vacuum and thermal cycling. Since the development and accumulation of microcracks together with bulk material outgassing probably account for this behaviour, it is reasonable to expect that the 'drift' in CTEs should level off with time. Clearly knowledge of the asymptotic values is required for design purposes. Independent measurements on a $\pm 43^\circ$ graphite/epoxy tube in SS1 confirm the vacuum effect change (see Fig. 16) after only two thermal cycles for 48 HRS at $\sim 10^{-7}$ torr. Based on these results it is possible to estimate the initial change in CTE due to prolonged vacuum exposure alone, prior to thermal cycling. This was done for Kevlar/epoxy and graphite/epoxy using previous ambient CTE measurements for reference purposes (see Table 2). It is evident once again that large changes occur for both materials, due to bulk outgassing effects.

To assess test data consistency, it is possible to calculate the theoretical variation in CTE with fiber angle based on knowing α_1 ($\equiv \alpha_{00}$), α_2 ($\equiv \alpha_{90}$) and the four elastic orthotropic constants, E_{11} , E_{22} , G_{12} , ν_{12} . This was done for ambient pressure and vacuum conditions, the latter corresponding to 167 days at $10^{-7} \sim 10^{-8}$ torr after 31 thermal cycles. A listing of the relevant material properties used in the analysis is given in Table 3 for both Kevlar/epoxy and graphite/epoxy. Figures 18 and 19 provide comparisons of the experimental results with predictions and it can readily be seen that excellent correlation was achieved. Note that for the graphite/epoxy vacuum tests, only one set of data at $\pm 43^\circ$ (other than α_1 and α_2) was available for comparative purposes.

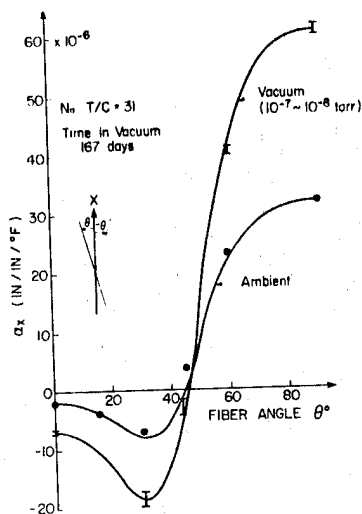


Figure 18. Effect of thermal-vacuum cycling on the CTE for Kevlar/epoxy (symmetric balanced $\pm \theta$ laminates)

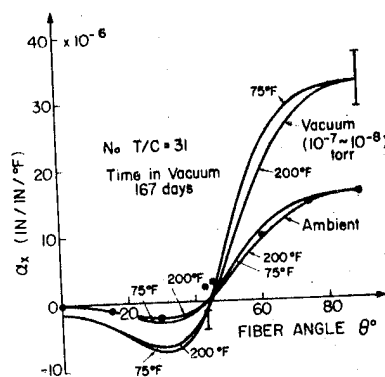


Figure 19. Effect of thermal-vacuum cycling on the CTE for graphite/epoxy (symmetric balanced $\pm \theta$ laminates)

One other factor that should be considered in these calculations is the variation in orthotropic elastic constants with temperature and vacuum. However, at present, the authors have only been able to accumulate graphite/epoxy test results on

the change in E_{22} with temperature at 10^{-6} - 10^{-7} torr up to ~ 214 HRS (see Fig. 20). Nonetheless, using the values in Table 3 at ~ 200°F, curves were constructed to compare with the room temperature (75°F) modulus analysis, as shown in Fig. 19. From a design viewpoint, no apparent effect occurs at the zero CTE crossing.

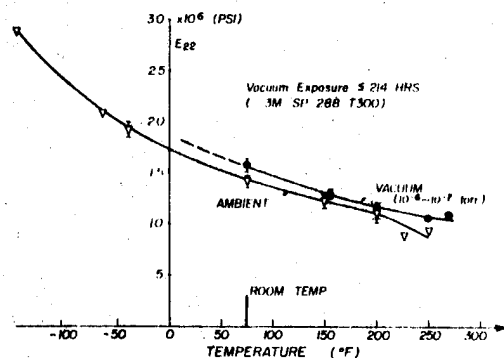


Figure 20. Effect of thermal-vacuum environment on tensile modulus of graphite/epoxy modulus ($\theta = 90^\circ$)

3.2 Orthotropic Stiffness (E_{22}) and Tensile Strength (σ_{2u})

It is fairly certain that for most fiber reinforced polymer matrix materials, the existence of any thermal-vacuum effect should be most pronounced in terms of the matrix response, as evidenced by the CTE data for $\theta = 90^\circ$. Consequently, test configurations were selected consisting of graphite/epoxy 90° layups (i.e., circumferential fiber orientation) using thin-walled tubes (0.38 mm - 0.58 mm thick) manufactured in-house with a belt-wrapper apparatus (Ref. 1). It should be noted that the ambient data were obtained from specimens stored under "normal" laboratory conditions, with no regard for moisture content.

Using bonded foil strain gauges, the variation in E_{22} was measured at ambient and vacuum conditions for varying temperatures. If one now compares the mean results, it would appear that an increase in stiffness occurs in the vacuum state. Because of the limited test data for $T > 200^\circ\text{F}$, it is premature to speculate on whether the large differences in E_{22} exist or not. However, it is well known that moisture content within the epoxy matrix can result in drastic strength reductions as one approaches the glass transition temperature for the resin system. Since no precautions were taken with the "ambient" specimens to limit or reduce their moisture absorption, there may well be a significant effect in terms of E_{22} as indicated. Confirmation of this behaviour must await tests which will be performed on the specimens currently being studied in the long term facility (SS2).

Based on the previous rationale that the existence of any thermal-vacuum effect would exhibit the largest change in the matrix (i.e., loading normal to the fibers), ultimate tensile strengths (σ_{2u}) were also measured for the same graphite/epoxy specimens. From a design viewpoint, although this parameter is the "lowest" of the strength tensor

components, its effect on the ultimate strength of any laminate configuration can be quite severe, depending of course on the nature of the loading (see Ref. 2 for example).

A comparison between ambient pressure and vacuum strength data for varying temperatures is given in Fig. 21, where the results have been nondimensionalized by the ambient pressure, room temperature strength ($\bar{\sigma}_{2RT}$). Based on the mean value

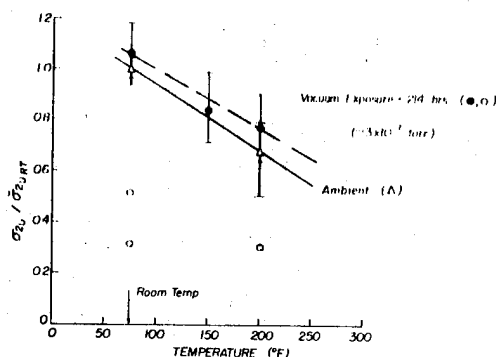


Figure 21. Effect of thermal-vacuum environment on tensile strength of graphite/epoxy laminates ($\theta = 90^\circ$).

comparison, it would appear that an increase in the matrix strength parameter occurs in vacuum, although substantial scatter in the test data is evident. Despite this scatter, three anomalous failure loads were obtained in the vacuum environment that fell well below the "scatter" range. From a design point of view, the rather limited results available indicate a 20% probability of the occurrence of such low loads within a group of test specimens fabricated at the same time, from the same material batch under highly controlled conditions. Since this anomalous behaviour has never been observed in our multitudinous ambient pressure tests conducted over the past five years using various batches of materials, it seems that some random "flaw" characteristic might be present whose effect is amplified under vacuum conditions. However, elucidation of this effect should be forthcoming based on the number of specimens presently residing in the long term thermal-vacuum facility. They should provide statistically valid data when strength tests are carried out in the near future for the three materials of interest.

4. CONCLUSIONS

Substantial CTE test data for three polymer matrix composite materials have been obtained from thermal cycling them in hard vacuum (10^{-7} - 10^{-8} torr) over a time period exceeding six months. The results, which were determined from in-situ measurements, indicated that large changes had occurred in the CTE's compared to ambient values for the specimen configurations investigated. Furthermore, these differences can be accurately predicted for any fiber orientation once the principal CTE values α_1 , α_2 are known for the given environmental conditions. Such results permit the design

engineer to estimate the correct zero CTE configuration for long term spacecraft structural applications based on a minimal number of tests.

Although only preliminary short-term data have been obtained on the stiffness (E_{22}) and tensile strength (σ_{2u}) for one material system (graphite/epoxy) in a thermal-vacuum environment, considerably more statistically significant data will be soon obtained from specimens which have currently accumulated over six months exposure in our long term space simulator. Indications are at present that both parameters increase in magnitude over their ambient values for a given temperature. However, some anomalous low failure loads were found that must await further confirmation.

Acknowledgements

The authors wish to gratefully acknowledge the financial support of our composite materials space

simulation programme by the National Research Council of Canada (Grant No. A2783) and the United States Air Force Office of Scientific Research (AFOSR-78-3694-A). In addition, all of the composite materials used in this investigation were supplied by the 3M Co., St. Paul, Minnesota, U.S.A.

References

1. Tennyson, R. C., Hansen, J. S., Holzer, R. P., Uffen, B. and Mabson, G., Thermal-Vacuum Facility With In-Situ Loading, Proc. AIAA/IES/ASTM 10th Space Simulation Conf., Bethesda, Md., Oct. 1978.
2. Tennyson, R. C., MacDonald, D. and Nanyaro, A., Evaluation of the Tensor Polynomial Failure Criterion for Composite Materials, J. Composite Materials, Vol. 12, 1978.

Table 1

Specimen Configurations Subjected to Long Term Thermal-Vacuum Cycling

Fiber Orientation (deg)	Graphite/Epoxy No. Spec.			Kevlar/Epoxy No. Spec.			Boron/Epoxy No. Spec.		
	T	F	F _c	T	F	F _c	T	F	F _c
[0] _{4S}		5	5		5	5		5	5
[±30] _{2S}				6					
[±43] _{2S}	8	5	5		5	5			
[±43½] _{2S}								5	5
[±45] _{2S}				6					
[±60] _{2S}									
[90] _{4S}	6	5	5	6	5	5		5	5
[60,-60,0] _{2S}	6	5	5		5	5		5	5

NOTE: T = tube, 10.2 cm long x 4.45 cm dia.

F, F_c = flat coupon, uncracked and cracked, respectively
12.7 cm long x 5.08 cm wide

Thickness: 4 ply = 0.508 mm and 6 ply = 0.762 mm

Table 2

Estimated Initial Change in CTE Due to Vacuum Outgassing Prior to Thermal-Cycling

Fiber Orientation (°)	Material α_x (in/in/°F)10 ⁻⁶			
	Kevlar/Epoxy (3M SP 306)		Graphite/Epoxy (3M SP 288 T300)	
	Ambient	Vacuum	Ambient	Vacuum
0	-1.7	-3.5	-0.2	~0
± 30	-7	-10.5	-2.5	-
± 43	-	-	2.3	~0
± 43½	0	-2.5	-	-
± 60	23.3	37.5	9.8	-
90	32	55.5	15.8	31.5

NOTE: All specimens were 4 plies thick (0.508 mm thick), ±0 symmetric balanced laminates

Table 3

Material (State)	Material Properties Used to Calculate Variation of CTE With θ					
	α_1 (in/in/°F)10 ⁻⁶	α_2 (in/in/°F)10 ⁻⁶	E_{11} (psi)10 ⁶ [N/M ²]10 ¹⁰	E_{22} (psi)10 ⁶ [N/M ²]10 ¹⁰	G_{12} (psi)10 ⁶ [N/M ²]10 ¹⁰	ν_{12}
<u>Kevlar/Epoxy</u>						
Ambient @ R/T	-1.7	32.0	12.6 [8.69]	0.8 [0.55]	0.3 [0.21]	0.34
Vacuum @ R/T	-7.0	61.0	-	-	-	-
<u>Graphite/Epoxy</u>						
Ambient @ R/T	-0.2	15.8	20.5 [14.14]	1.4 [0.97]	0.59 [0.41]	0.26
Ambient @ 200°F(93°C)	-0.2	15.8	-	1.1 [0.76]	-	-
Vacuum @ R/T	-1.5	32.5	-	1.6 [1.10]	-	-
Vacuum @ 200°F(93°C)	-1.5	32.5	-	1.175 [0.81]	-	-

R/T \equiv Room Temperature @ 75°F

PRECEDING PAGE BLANK NOT FILMED

SESSION VIII
MATERIALS FOR SPECIFIC APPLICATIONS

Co-chairmen: L. Preuss & D. Verdin

N80-21446

EFFECT OF SPACE CHARGED PARTICLE ENVIRONMENT ON OPTICAL COMPONENTS AND MATERIALS

J Bourricau & M Roméro

Centre d'Etudes et de Recherches en Technologie Spatiale, Toulouse, France

ABSTRACT

After a brief review of permanent and transient effects induced by charged particles on optical materials we describe models of material swelling and transmission losses, tests performed in these fields for METEOSAT and SPOT, and results concerning the background noise induced in one D2h experiment.

Swelling is characterized by the linear contraction coefficient, it has been found that its variations with the absorbed dose is not function of exposure conditions for vitreous-ceramics; for silicas dose rate influence has been observed.

Transmission losses described by the variations of the absorption coefficient versus dose, have been studied for some silica and glasses; as for swelling the exposure conditions have been found weightless for some materials.

Keywords: Radiation damages - optical materials - models - swelling - transmission losses - background noise.

1. INTRODUCTION

Glasses and other transparent materials are often directly exposed to space radiation environment (front lenses of optical systems, solar cell filters, SSM, as examples). Interactions with UV and charged particles induce various kinds of effects:

- permanent or transient damages,
- light emission (giving spurious background in optical measurements)
- electrical charging and breakdown (often involving disturbances or failures into electronic circuits and surface damages of coatings).

Furthermore exposed optical components generally are cold zones collecting outgassing products and radiations can affect the rate of formation and the optical absorption of the polluting.

Various studies, mainly sponsored by CNES and ESA are performed at DERTS in the field of radiation effects (damages and charging) on materials and components used in space applications.

In order to improve the laboratory tests validity our main objective is the development of radiation damages models.

These models are based on the dose repartition profile; in space, as well as in laboratory tests, the radiations impinging the samples have a limited range (trajectory length) and stopping power of materials are function of the particle energy. Consequently when the thickness of the active part (i.e. the part where defects creation induces damages) or when the shielding in front of it is not a negligible fraction of the particle mean penetration depth, the dose and damage distributions cannot be considered as constant in the bulk material.

In the case of monocinetic particles impinging a sample under one incidence we can approximate these distributions by the following method: when all the material can be damaged, we consider the bulk material as divided into two sheets after irradiation:

- the first is made of damaged material, its thickness is the mean penetration depth of particles, in this part dose and damages are supposed constant and equal to the mean values ;

- the second is made of undamaged material.

One of our objectives in these models is to choose a parameter physically linked to the radiation damage process (i.e. directly related to the defect concentration) and to follow its variations with the absorbed dose.

The choice of the dose as main parameter describing the exposure is made in order to eliminate the apparent influences of the nature of particles and of their energetic and angular distributions.

The general rules above exposed are used at DERTS in order to modelise damages of thermal control coatings (Ref. 1, 2, 3) of MOS electronic devices (Ref. 4) and of optical materials.

The latter are the object of the following part.

2. CHARGED PARTICLES EFFECTS ON OPTICAL MATERIALS

2.1 Damage review

Permanent or cumulative damages of optical components can be classified into two categories; surface damages and bulk material effects.

Surface damages occur on directly exposed components (solar cell filters, thermal control coatings, reflecting layer of mirrors, etc....). They are mainly induced by UV and low energy electrons and protons, doses are often in the $10^6 - 10^7$ grays range into the first micron of an exposed material. These damages can be the following:

- optical absorption (discrete or continuous), brittleness increase and sputtering of deposited layers,
- pulverisation during electrical breakdown,
- darkening and polymerisation of contaminant layers.

Bulk material damages are mainly induced by large range charged particles, consequently they can occur in shielded or unshielded components. These bulk effects are the following:

- transmission losses (they can be continuous or located in narrow absorption bands connected with color centers);
- swelling and strain linked to density variations in the exposed sheet of the material,
- index variations and shattering unusual in space application because the required dose levels are over the range of space induced doses.

Damage decreases are often observed after irradiation; they are either true recoveries (rearrangement between induced complementary defects - vacancies and interstitials for example) or apparent bleaching (linked to defect binding, in this case the primary absorption band disappears for the benefit of another). The recovery time constant is generally a function of the material nature (impurities content), of the sample temperature (defect mobilities), of the nature and concentration of defects.

Transient effects, connected with flux (dose or fluence rate), are the following:

- transmission losses induced by free carriers and moving defects (i.e. having a short recovery time constant),
- light emission (fluorescence, luminescence or Cerenkov effects).

This kind of damages linked to high fluence rate is mainly relevant to military applications. Yet background noise constraining for low photon intensity measurements can be observed (see for example the following part concerning the D2B experiments).

2.2 Material swelling under irradiation

These studies have been performed mainly for the primary and folding mirrors of the METEOSAT radiometer (CNES and ESA contracts).

2.2.1 Swelling model

One aspect of radiation damages of glasses is the swelling under irradiation (Ref. 5, 6). The heterogeneity of dose repartition can explain the phenomenon if radiation effect is a density change in the irradiated part.

Swelling model of circular samples have been made (Ref. 7) with this hypothesis. We could define a mean linear expansion - or contraction - coefficient as follows:

$$\bar{a}_l = k \cdot \frac{C e^3}{x_d (e - x_d) R^2}$$

C = rise of camber (measured by the Newton rings methods)

e = total sample thickness,

R = radius of the sample,

x_d = damaged depth (computed as the mean penetration depth or measured if coloration occurs)

k = parameter linked to the dose distribution form (values between 0.83 and 1.03)

2.2.2 Results

Studies have been carried out on the following materials

CERVIT (OWENS)	{ VITREOUS CERAMICS
ZERODUR (SCHOTT)	
PYREX	
PURSIL	{ SILICA (ELECTRO QUARTZ) (Ref. 8)
PURIPSIL (A)	
TETRASIL (A)	
TETRASIL (SE)	

The relation between linear expansion (or contraction) and mean \bar{D} is always (see Fig. 1):

$$\bar{a}_{li} = \alpha_i \bar{D}^{1/2}$$

where α_i is a characteristic constant of the materials. Vitreous ceramics (Cervit and Zerodur) are more susceptible (two magnitude orders on \bar{a}_{li}) than silica; this can be compared to results obtained with HERASIL 3 (HERAEUS) and PURASIL (QUARTZ ET SILICE); on these silica, swelling is not observed under irradiation (Ref. 9).

For PYREX as silica (except TETRASIL A) tests have been performed with monocinetic electrons and only one fluence rate, the weight of these parameters is not defined.

For TETRASIL A fluence rate (or dose rate) and electronic energy variations were performed.

The weight of these parameters are indicated in the following table:

DOSE RATE (Gy/s)	ENERGY (MeV)	α_i (Gy ⁻¹)
2.6 10 ²	1.5	6.5 10 ⁻⁹
2.8 10 ²	1.0	4 10 ⁻⁹
2.3 10 ²	0.3	4 10 ⁻⁹
2.6 10 ¹	1.5	2.1 10 ⁻⁹

Lower dose rate and electron energies induce weaker shrinkage.

Thorough studies have been carried out on Cervit and Zerodur (Ref. 9) for the METEOSAT project, the conclusion is that particles energy and nature, as fluence rate, are weightless parameters.

2.2.3 Space qualification of METEOSAT mirrors

Radiation effects were expected on two exposed mirrors of the radiometer of METEOSAT (the primary mirror made of Cervit and the first folding mirror made of Zerodur).

Tests, sponsored by CNES and ESA, have been carried out for these two components.

The above conclusion concerning the vitreous ceramics (Zerodur and Cervit) involves that ground simulation of the in flight swelling of these materials can be made without problem; the exposure conditions can be defined easily in order to reproduce the dose profile estimated for the duration of the mission.

Codes available at DERTS (Ref. 20, 11, 12) have been used in order to:

- compute proton and electron fluences in flight (NASA models used are AE 4 and AE 6 for electrons and AP 8 for protons);
- define the dose profile corresponding to three years in space at the mirrors levels (after various shieldings - baffles - structures); it could be noted that introduction of the up-to-date AEI 7 model for electrons gives higher dose at depth greater than 1 g.cm⁻² (Ref. 13);
- compute the dose profiles induced by various monoenergetic electron beams (for the determination of the simulation parameters).

Tests have been performed with three electron energies (see Fig. 2). Swelling was obtained on the folding mirror made of Zerodur (Camber 3 μ m).

In the case of the primary mirror lightened structure (equivalent to a 400 mm diameter and 80 mm thickness disc) made of Cervit, aggregate swelling was, a priori, non measurable and buckling was not observed at the lightened places.

2.2.4 Thermal recoveries

Swelling recoveries can occur, as for other radiation induced damages; the ruling parameter of this effect is the defect mobility or - directly related with it - the temperature.

Recoveries have been studied on Cervit (see Fig. 3) and Zerodur; they are not obtained at room temperature, but partially observed at 170°C, and rapidly and totally carried out at 450°C.

It can be noted that, for all materials studied, swelling is on a part with transmission losses and the recoveries of these two kinds of damages are also connected.

2.3 Transmission losses

2.3.1 Model

As for SSM and OSR damage studies (Ref. 1, 2, 3) the model rules are the following:

- irradiation is not uniform in the bulk material, consequently induced transmission losses occur in the irradiated sheet (its thickness is x_d);
- the dose profile can be approximated by the mean dose, \bar{D} , in the damaged sheet (\bar{D} is computed);
- transmission losses at wavelength λ_i can be characterized by the absorption coefficient variation $\Delta\mu(\lambda_i)$ around the band maximum, $\Delta\mu(\lambda_i)$ is directly connected with the density of defects responsible of the absorption band.

These variations can be obtained from spectral transmittance measurements, before $T_o(\lambda_i)$, and after, $T_d(\lambda_i)$, exposure

$$\Delta\mu(\lambda_i) = \frac{1}{x_d} \log \frac{T_o(\lambda_i)}{T_d(\lambda_i)}$$

where x_d can be sometimes measured (coloration depth) or, in all case, computed with codes giving the penetration, diffusion and slowing down of protons and electrons.

2.3.2 Results

Various transparent materials have been studied under electronic irradiations at room temperature; they are the following:

- Kf1, LF1, LLF1 and FK5 glasses (SCHOTT),
- TETRASIL (A), TETRASIL (SE), PUOPSIL (A) and PURSIL (K) (ELECTRO QUARTZ) silica

2.3.2.1 Silica transmission losses

The transmission losses of silica are observed during swelling studies described above; electronic irradiations induce in these materials various absorption bands (see Fig. 4 to 7):

- 215 and 270 nm in TETRASIL (A) and (SE),
- 215, 295 and 525 nm in PUOPSIL (A) and PURSIL (K).

Three of these can be identified with known absorption bands:

- 215 nm: C band probably connected with O^{-2} vacancies (Ref. 14)
- 295 nm: B band linked to unidentified impurity (Ref. 15)
- 525 nm: A band probably related to aluminum impurity (Ref. 16).

Dose rate and electron energy effects on transmission losses at 215 nm are studied on TETRASIL (A). (see Fig. 8):

- in spite of a large dispersion it seems that the absorption coefficient variations are not relevant to these parameters;
- $\Delta\mu(215)$ is a linear function of the mean dose between 10^5 and 10^7 Grays;
- the 270 nm band behaviour is probably similar for the higher doses.

Partial tests are carried out on two samples of each of other silica; the Figure 9 gives $\Delta\mu(215)$ versus dose for TETRASIL (SE):

- proportionality between dose and $\Delta\mu(215)$ is possible under 10^4 Grays;
- it can be noted that for space applications (doses generally lower than $4 \cdot 10^6$ Grays) TETRASIL (A) is better than TETRASIL (SE).

Concerning the two other silica, PURSIL (K) and PUOPSIL (A), their susceptibilities are so high that we could not follow the growth of the absorption at 215 nm; some results concerning the 295 and 525 nm bands are given (see Fig. 10).

2.3.2.2 Glasses transmission losses

Several SCHOTT glasses (FK5, KF1, LF1 and LLF1) samples have been exposed to electron beams; two absorption bands are obtained around 350 and 700 nm (see Fig. 11 to 14).

Various electronic exposure conditions have been used in order to observe the influence of energy and fluence rate:

- energy 1.2 MeV, fluence rates: $2 \cdot 10^{10}$, $8 \cdot 10^{10}$ and $5 \cdot 10^{11} \text{ e.cm}^{-2} \text{ s}^{-1}$
- fluence rate $8 \cdot 10^{10} \text{ e.cm}^{-2} \text{ s}^{-1}$, energies 0.3, 0.8, 1.2 MeV.

Various difficulties have been encountered:

- the first step of irradiation was sufficient, to saturate the absorption band around 350 nm,

we could not follow its growth with the dose increase;

- insufficient polish of sample surfaces induces discrepancy on transmission measurements;
- tests made at 0.3 MeV are not valid either because instabilities of the accelerator beam at low energy or because the influence of the sample surface heterogeneity.

In practice for all these glasses results have been obtained only on the absorption around 700 nm (see Fig. 15 to 18):

- the absorption coefficient grows as $\bar{D}^{1/3}$ except for LF1 glass,
- a weak influence of dose rate seems to be observed at the lower dose rate (8 Grays per second), except for FK 5 glass,
- the electronic energy weight is not evidenced between 0.8 and 1.2 MeV but the variation range of this parameter is insufficient in order to observe a possible effect.

2.3.2.3 Space qualification tests (SPOT mission) of SCHOTT glasses

Pure technologic study, sponsored by CNES for SPOT project, has been made at DERTS in order to qualify SCHOTT glasses (FK 51, FK 52 and KZFS 6) to be used for the initial dioptric version of the HRV instrument. All samples had an anti-reflexion coating (MATRA manufacturer) (Ref. 17).

Charged particles fluences (electrons and protons) and dose induced distributions have been computed for circular orbit (altitude 800 km, inclination $98^\circ 7'$) (Ref. 10) from the following NASA data:

- AP 8 for protons,
- AE 4 and AE 6 for electrons.

It can be noted that NASA data change (AE1 7 model for electrons) induces an increase of dose for penetration depth greater than 0.5 g.cm^{-2} . Three accelerating voltages (0.8, 1.3 and 1.8 MV) have been used in order to reproduce (see Fig. 19) the expected dose profile. Six irradiation steps at fluence rate $10^9 \text{ e.cm}^{-2} \text{ s}^{-1}$ have been made in order to obtain the damage growth in a direct exposure configuration during a six years mission.

Transmission measurements between 300 and 2500 nm have been carried out before and after each irradiation step.

The damages are located at wavelength lower than 900 nm (see Fig. 20 to 22).

For all these components recoveries occur at room temperature (see Fig. 23), after a fast initial step, observed in samples with high defect concentrations (6 years mission simulation) the transmission recovery rate is about $2.5 \cdot 10^{-4}$ /hour.

These recoveries indicate that transmission losses obtained with high fluence rate ($10^9 \text{ e.cm}^{-2} \text{ s}^{-1}$) are probably over estimated.

The tests have been carried out in the direct exposure configuration; in practice an Invar structure has been planned; its thickness has been fixed to 1 mm in order to protect the lenses; the front lens, unshielded by the Invar structure could be guarded against radiation by a silica window.

This study was made during the feasibility phase of the HRV instrument, the dioptric version is out of date and some tests are planned at DERTS on the components of the new catadioptric solution.

2.4 Example of transient effects

Other source of failure on optical experiments in space is the transient background noise induced by high fluence rate, particularly for low photon intensity measurements. It is the case for the D2B Zodiacal light experiment, where a photomultiplier 541N (EMR) associated with an UV converter has been used as detector.

Very often the orbit (500 - 700 km - inclination 37°) crossed the South Atlantic anomaly where high electron fluxes are encountered and spurious backgrounds are observed.

DERTS has carried out study, sponsored by CNES, in this field before the mission (Ref. 18-19).

Fluence rate variations with time are computed along the trajectory, during one day (see Fig. 24); for some orbits, during few minutes, electron fluence rate over $10^6 \text{ e}^- \cdot \text{cm}^{-2} \cdot \text{s}^{-1}$ are forecast with energy greater than 0.5 MeV.

The energy distribution after shielding has been computed at the PM level for the maximum indicated (Δ) on the Figure 24. The energy spectra is close to that of Sr^{90} beta ray source, chosen for simulation. Tests have been performed with a 34 mc source at a fluence rate equal to $2 \cdot 10^5 \text{ e}^- \cdot \text{cm}^{-2} \cdot \text{s}^{-1}$ in front of the detector or on one side.

Evidence of background noise source into the MgF_2 window or into the photocathode of the photomultiplier (without the UV converter) has been obtained.

In front exposure has been made, the variations of counting rate versus aluminum shielding thickness with and without the UV converter (see Fig. 25) have proved that this component acts for one part as a shielding for the background noise induced at the first stage of the PM, for other part as a photon source (luminescence) under electronic bombardment.

Induced background, without aluminum shielding under the Sr^{90} beta ray source exposure, has given an estimation of the detection system susceptibility to electron bombardment. For the maximum fluence rate indicated (Δ) on Fig. 24 the expected background noise was 900 pulses per second.

In flight measurements gave values between 300 and 9000 pulses per second (mean value 2700 pulses per second) for 13 South-Atlantic anomaly crossings at various altitudes during one week

3. CONCLUSION

With the results mentioned above, we have seen that the main parameter describing most of the exposure conditions (fluence, nature of particles, energy and angular distributions) is the induced dose repartition, but other characteristic of irradiation are not included in this parameter such as temperature and fluence rate; consequently the models cannot resolve all possible problems. Synergetic effects, fluence (or dose) rate and temperature influences, defect creation with energy threshold, recoveries are all difficulties to be still resolved. They can be coped with only through the knowledge of the true physical processes (nature and mobility of defects, interactions with impurities, etc.)

The models, in numerous favourable cases, can reduce the cost of qualification tests, the simulation of the dose profile is easier than reproduction of all energetic and angular distributions for each kind of particles. They can simplify the comparison of results obtained by laboratories working with various exposure conditions and, consequently, increase the amount of consistent informations concerning material behaviour under irradiation.

They require some theoretical means such as computer codes in order to forecast the charged particle environment in all kind of orbits and the dose distribution in the bulk materials exposed to these radiations or to accelerator beams.

II. REFERENCES

1. J. BOURRIEAU, A. PAILLOUS, M. ROMERO - Degrada-tions des revêtements de contrôle thermique sous l'effet des rayonnements UV et particulaires - Rapport final Contrat ESTEC 2515/75/HP
2. J. BOURRIEAU, A. PAILLOUS - Irradiations par protons et irradiations par électrons de revêtements de contrôle thermique et de fibres polymériques - Rapport final Tomes 1 et 2 - Contrat ESTEC 2838/76/NL/HP/SC
3. J. BOURRIEAU, A. PAILLOUS - Effect of radiations on polymers and thermal control coatings - Spacecraft materials in space environment - ESTEC Symposium Noordwijk - October 1979
4. A. ROIZES - Evaluation de la dégradation des dispositifs MOS, C. MOS et LOC.MOS et des composants opto-électroniques soumis à irradiation dans un environnement spatial - Contrat ESTEC 2352/74/HP - Documents 1 à 14.
5. W. PRIMAK - Swelling of refractory materials and silicate glasses on proton deutérium and helium ion bombardment - J1. Nucl. Materials 74, 84-92 (1978)
6. J. BOURRIEAU - Dégradation du Cervit sous irradiation électronique - Publ. ONERA/CERT/DERTS CR/02/38
7. M. ROMERO - Disque bilame, application au Cervit - Publ. ONERA/CERT/DERTS NF/02/14

8. M. ROMERO - Comportement sous irradiation de silices Electro-Quartz - Publ. ONERA/CERT/DERTS CR/OPT/03.
9. J. BOURRIEU - Etude expérimentale sur l'irradiation par les particules à haute énergie des miroirs utilisés dans le télescope radiomètre METEOSAT - Rapport final Contrat ESTEC N° 2145/74/CA
10. J.P. PHILIPPON - Estimation des flux "protons et électrons" reçus par un satellite d'observation sur trois types d'orbite - Publ. ONERA/CERT/DERTS CR/ENV/05
11. J. BOURRIEU, R. SCHUTTLER - Transmission des électrons par les écrans plans épais - Programme MONA 1 - Publ. ONERA/CERT/DERTS NT/02/24
12. J. BOURRIEU - Répartition des doses induites par les protons - Cas de l'environnement spatial et des simulations à l'accélérateur - Programme PRODOS - Document ONERA/CERT/DERTS (à paraître)
13. J. BOURRIEU - Doses électroniques sur orbite géostationnaire - Comparaison des modèles de flux AE 4 - AE17 (Lo) et AE17 (Hi) - Conséquences sur les dégradations des composants électroniques de METEOSAT - Publ. ONERA/CERT/DERTS NT/02/40
14. E.N.J. MITCHELL, E.G.S. PAIGES - Proc. Phys. Soc. 67B, 262 ()
15. E. LELL - Phys. and Chem. Glass 3, 84-94 ()
16. J.H. SCHULMAN and W.D. COMPTON - Color centers in solids - Publ. Pergamon Press (1963)
17. J. BOURRIEU, G. PANABIERE - Irradiations électroniques de verres SCHOTT FK 51 - FK 52 et KZFS 6 - Publ. ONERA/CERT/DERTS CR/ENV/10.
18. J. BOURRIEU, J. SIFFRE - Bruit de fond et vieillissement du photomultiplicateur RTC 413 F et du Spiraltron Bendix 3199 sous irradiation électronique - Publ. ONERA/CERT/DERTS CR/D2B/01
19. J. BOURRIEU, J. SIFFRE - Dégradation du photomultiplicateur EMR 541 N irradié par une source de Sr^{90} - Publ. ONERA/CERT/DERTS CR/D2B/03
20. J.-P. PHILIPPON - Evaluation théorique et calcul des flux de particules dans la zone stable de la magnétosphère - Thèse d'université n° 258 - Toulouse (1970)

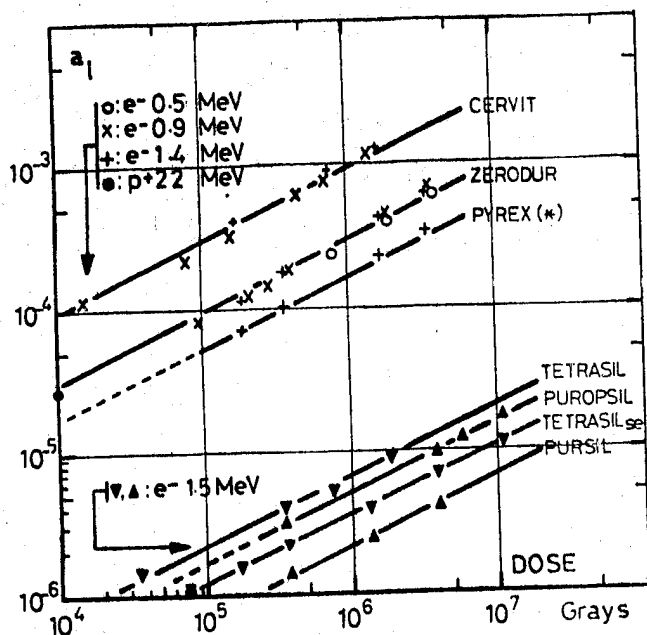


FIG-1: Linear contraction-or expansion (*) coefficient vs dose for various materials

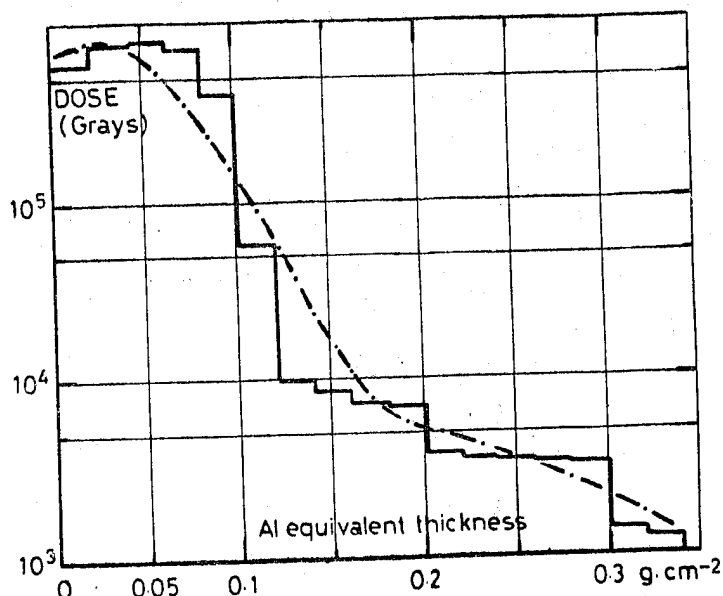


FIG-2: Dose distributions in METEOSAT mirrors
— : 3 years in space

--- : Simulation

$5.0 \cdot 10^{14} e^- \cdot cm^{-2}$	0.6 MV + 0.7 MV
$1.2 \cdot 10^{14} e^- \cdot cm^{-2}$	0.8 MV
$1.0 \cdot 10^{13} e^- \cdot cm^{-2}$	1.2 MV

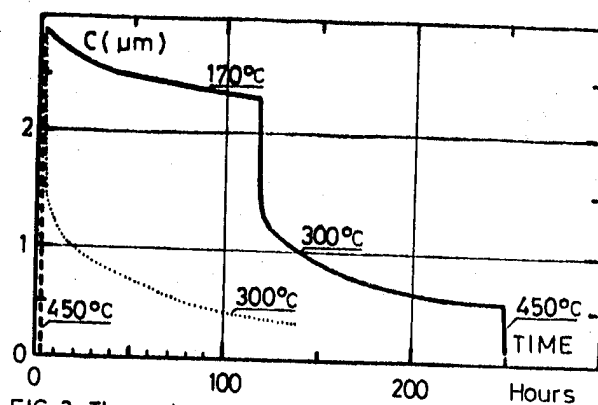


FIG-3: Thermal recovery of irradiated CER VIT samples

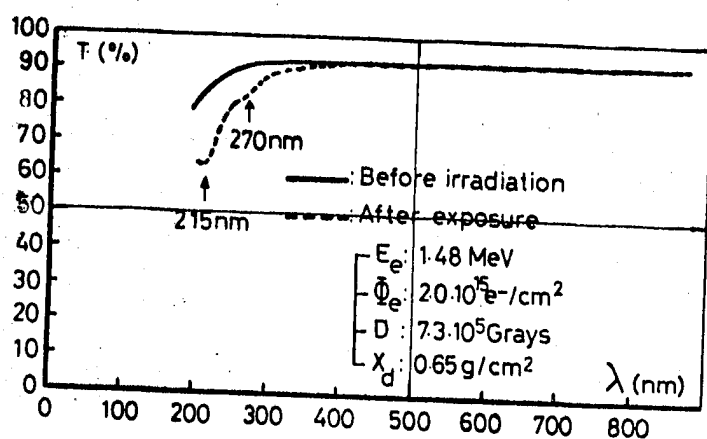


FIG-4: TETRASIL (A) Thickness: 7.5 mm

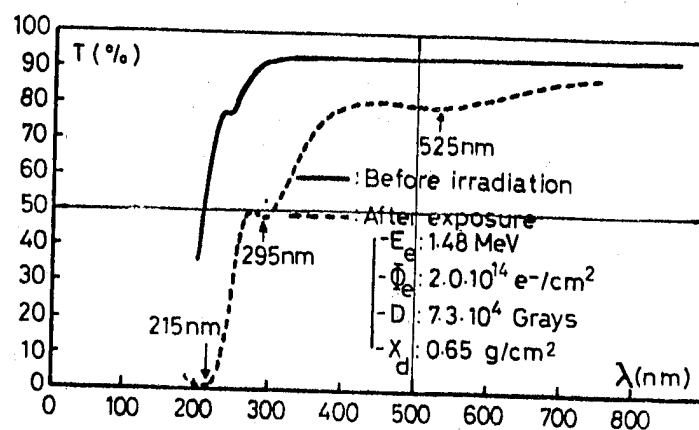


FIG-6: PUROPSIL (A) Thickness: 7.5 mm

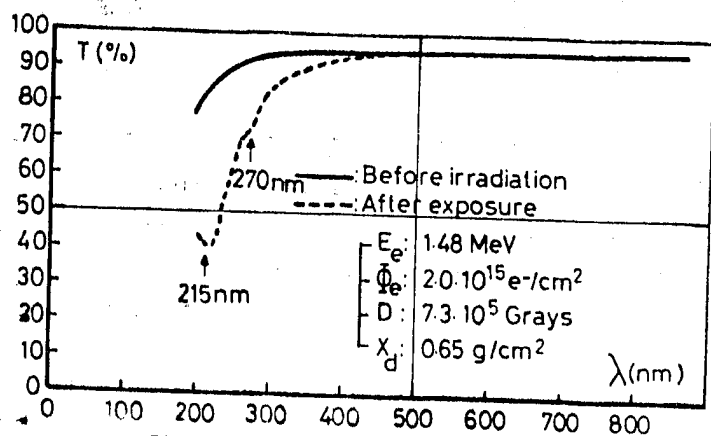


FIG-5: TETRASIL (SE) Thickness: 7.5 mm

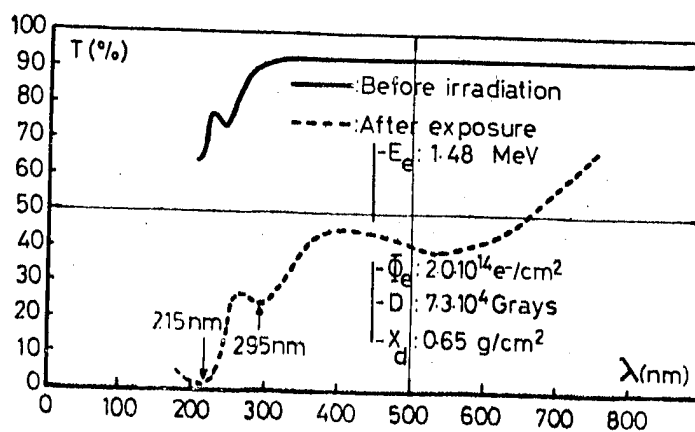


FIG-7: PURSIL (K) Thickness: 7.5 mm

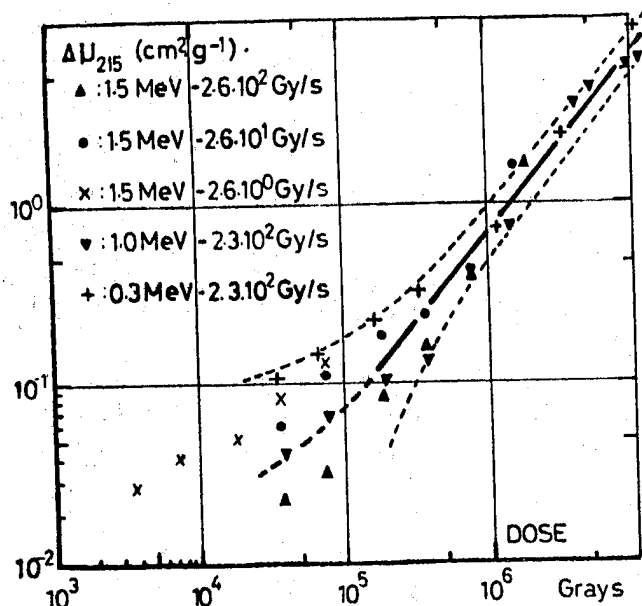


FIG-8: TETRASIL(A) - Absorption coefficient at 215nm vs dose (dashed line: $\pm 2\%$ on transmission) Electron irradiations

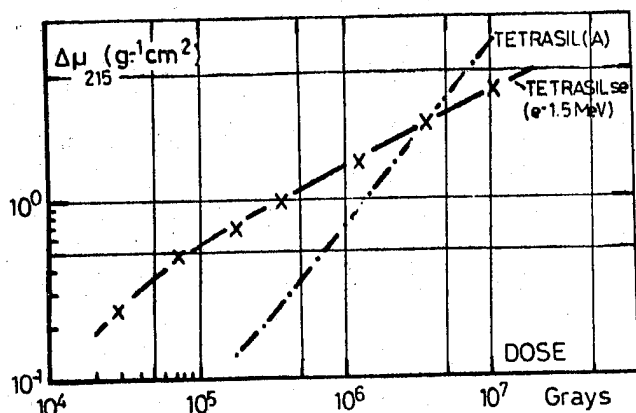


FIG-9: TETRASIL and TETRASIL(SE): Absorption at 215nm vs dose (Electron irradiations)

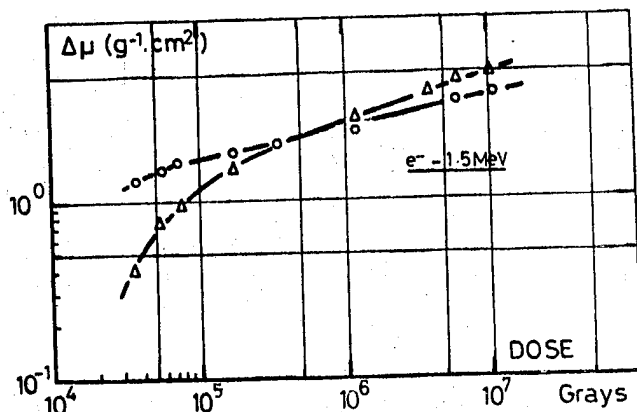


FIG-10: PUROPSIL: Absorption coefficients at 295nm(Δ) and 525nm(Δ) vs dose (Electron irradiations)

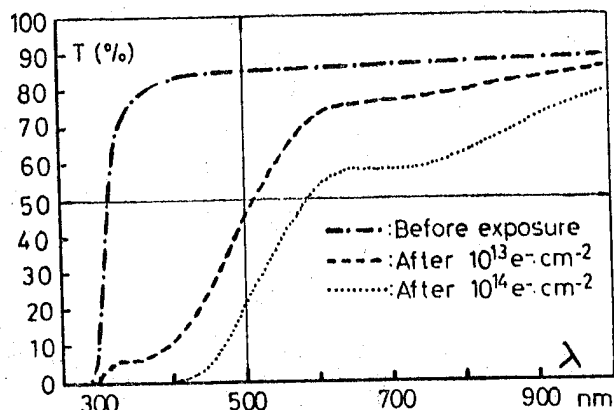


FIG-11: KF1 glass - Electron irradiations (1.2 MeV)

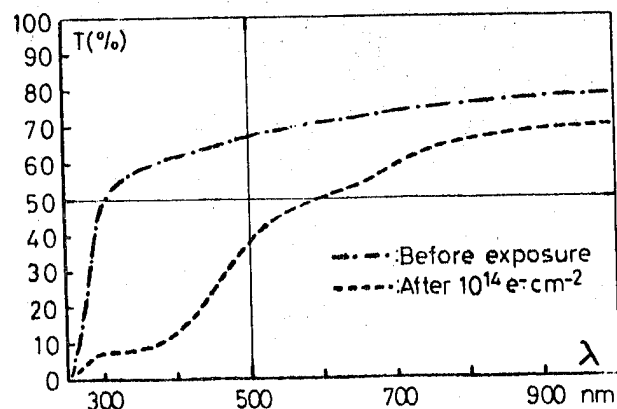


FIG-12: FK5 glass - Electron irradiations (1.2 MeV)

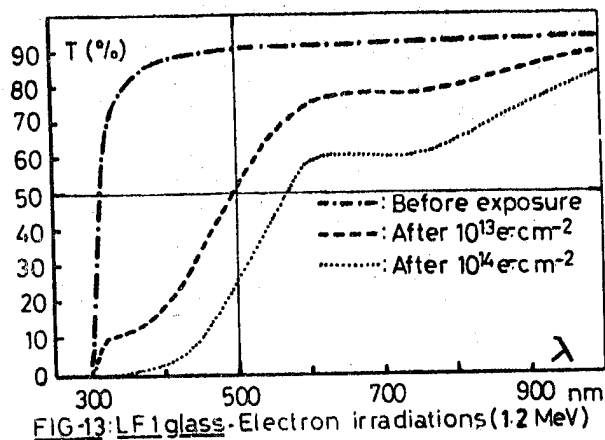


FIG-13: LF1 glass - Electron irradiations (1.2 MeV)

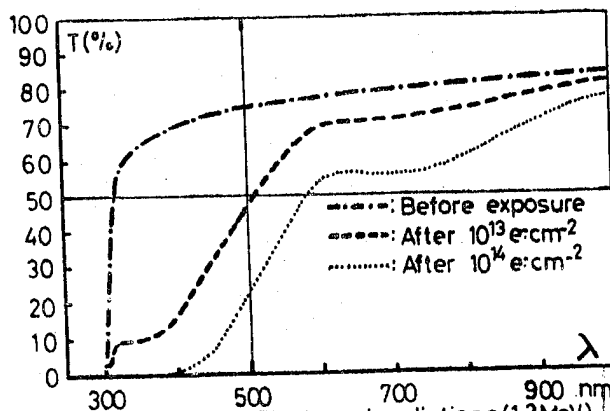
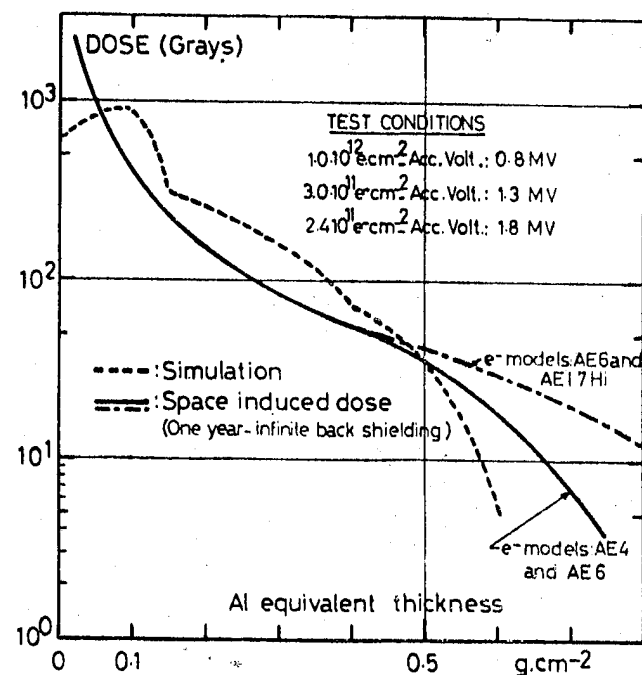
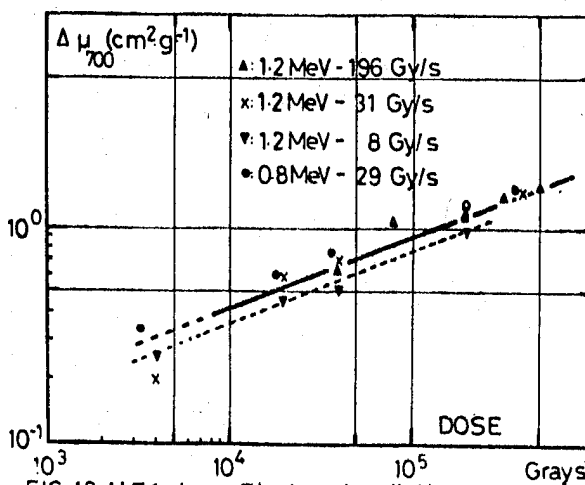
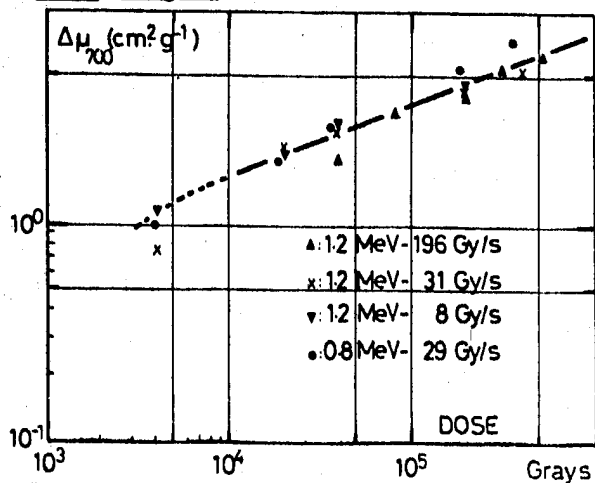
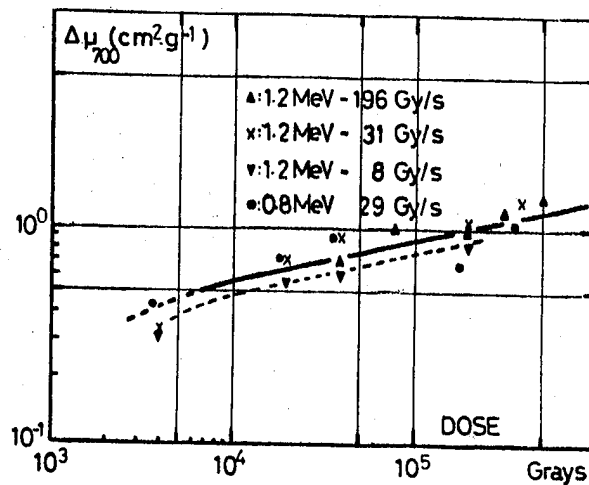
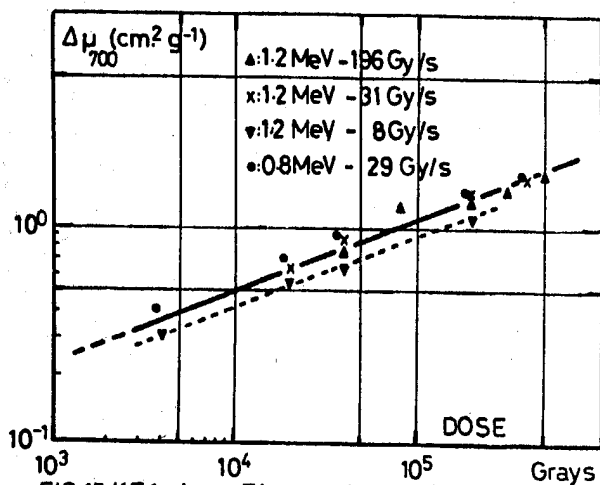


FIG-14: LLF1 glass - Electron irradiations (1.2 MeV)



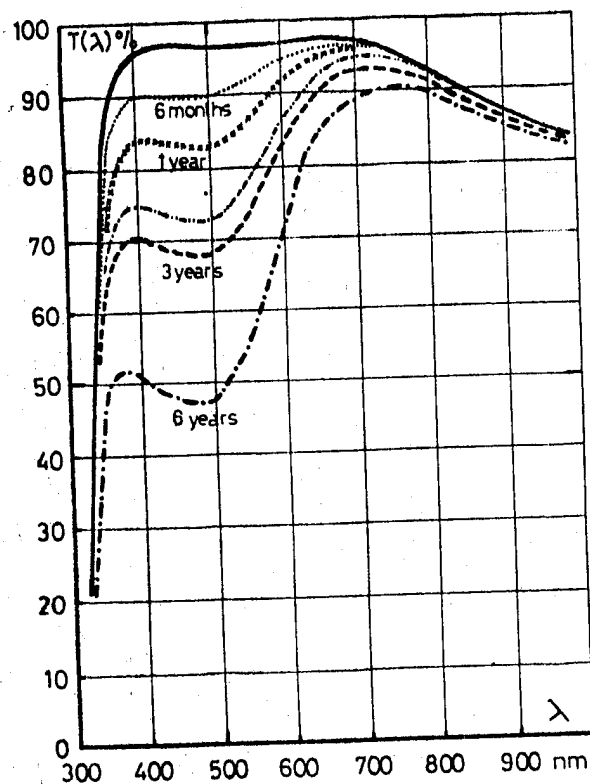


FIG-20: FK 51 Radiation damages (SPOT mission)

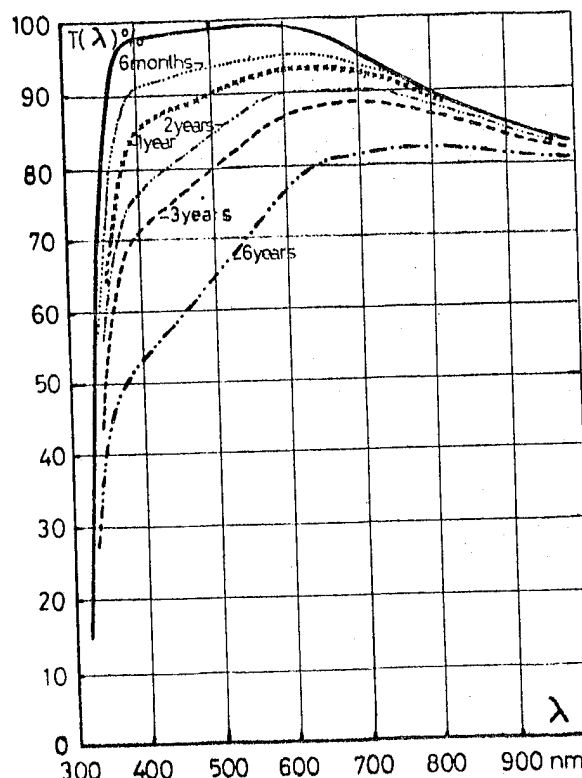


FIG-22: KZFS 6 Radiation damages (SPOT mission)

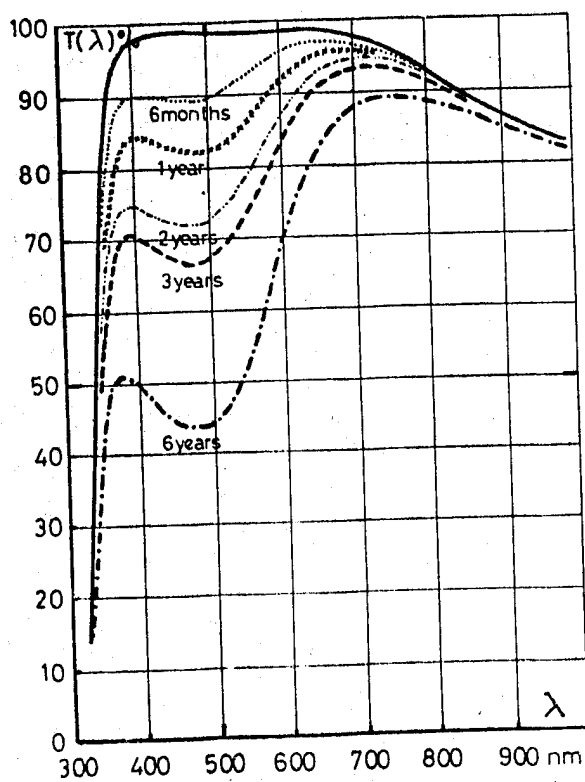
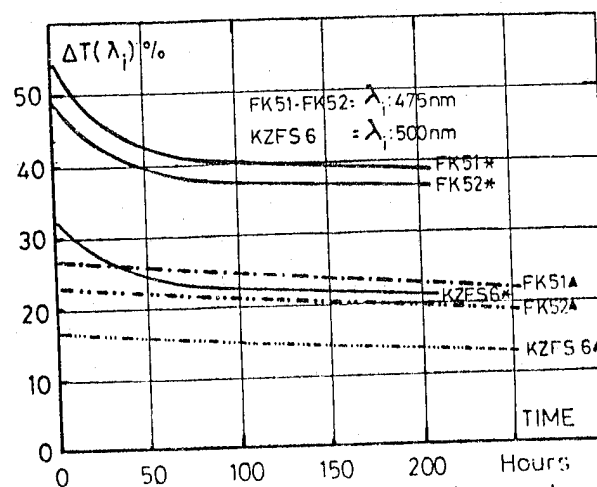


FIG-21: FK 52 Radiation damages (SPOT mission)

FIG-23: Transmission recovery at room temperature
(Influence of the concentration of defects)
* High concentration (6 years tests)
▲ Low concentration (2 years tests)

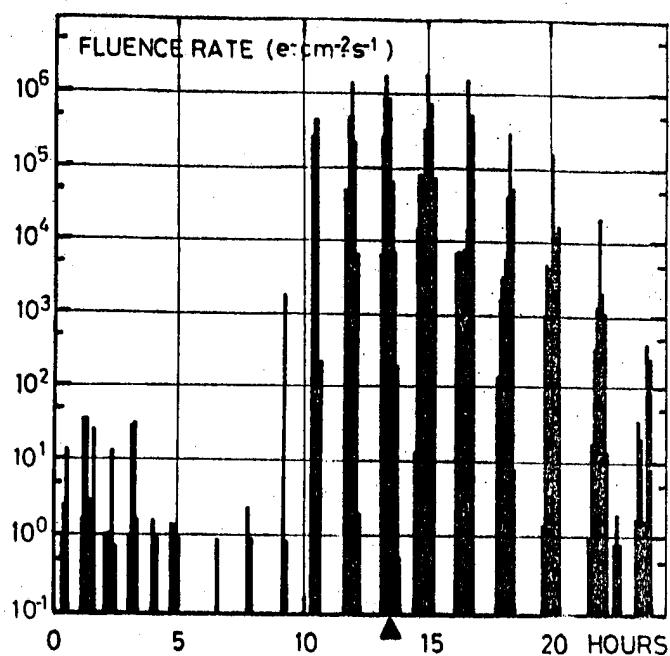


FIG-24: Electronic fluence rate variations
($E > 0.5$ MeV) D2B orbits

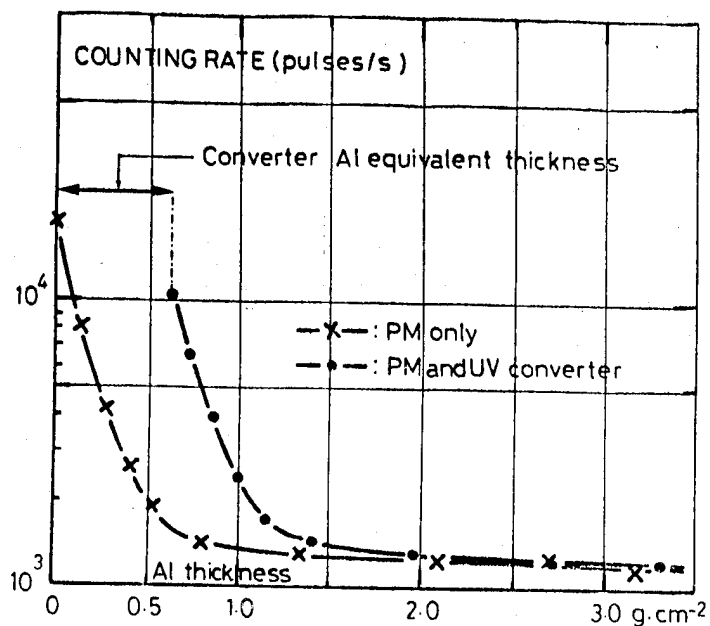


FIG-25 Spurious background in PM 541N

N80-21447

USE OF ULTRA-LIGHT ADHESIVE FOR THE METAL HONEYCOMB BONDING

J Chanteranne

*Aérospatiale, Space & Ballistic Systems Division, Les Mureaux, France*Abstract

The design of satellite panels in sandwich structures has to be optimized, in order to reduce the mass, by fitting the strength of the bonding menisci to the strength of the honeycomb core. This optimization applied to the satellite structures of the Intelsat V family has led to the use of an adhesive of very low surface mass (100 g/m²), which is unusual for the bonding of honeycomb. In the serial production, in order to get an invariability of quality in such a particular technology, it is advisable to determine and supervise with precision the most sensitive operational parameters.

We inform you about our experience in the manufacture of such structures with adhesive films "Redux 312 UL", and show the influence of the hygrometry of the bonding room, and of the use of a primer on the geometry and strength of the adhesive menisci formed on the honeycomb.

1. INTRODUCTION

The structure panels of the satellites Intelsat V are characterized by :

- a low mass,
- great dimensions (2m x 2m),
- a correct and reproducible flatness,
- a quality assurance of high level.

The quality of the bonded joints between the honeycomb core and the coating is tested for each panel with flatwise tensile specimens bleeded off the openings.

The results we are reporting here come from the analysis of defects established during the development and manufacture of the first serial models and from the interpretation which could be given thanks to the excellent traceability of this product on a great quantity of parameters, which can interfere in the result during the manufacture.

2. OPTIMIZATION OF THE ADHESIVE QUANTITY ACCORDING TO THE DIMENSIONS OF THE HONEYCOMB MESH

As the art and thickness of the liner ($20\text{ }\mu\text{m}$) forming the honeycomb do not change, it would be false to think that the necessary mass of adhesive is independent of the mesh dimensions.

As a matter of fact, we have established a reduction in the height of the adhesive menisci, when the dimensions of the mesh are reduced (fig. 1).

This phenomenon, which is explained by the progressive reduction of the adhesive reserve available inside the cell will be all the more important as the mass of the used adhesive is smaller.

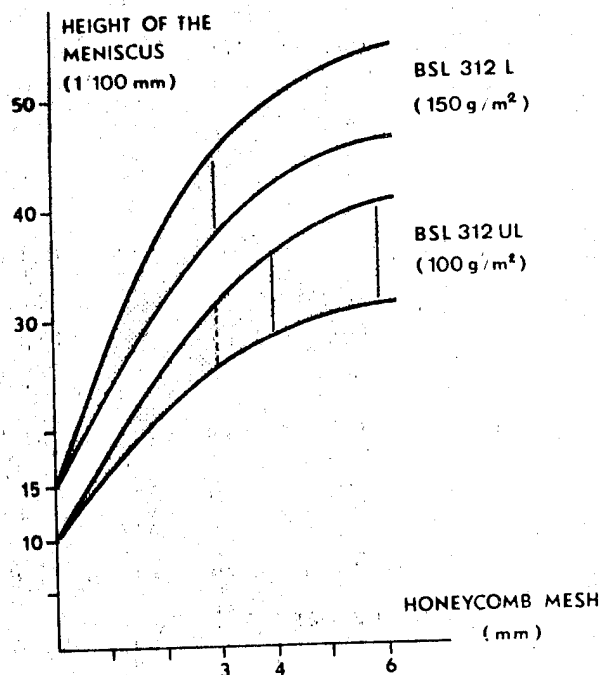


Fig. 1 - Menisci height of adhesive "REDUX 312 UL and L" according to the dimension of the honeycomb mesh.

The analysis of this phenomenon allowed us to understand why with an equal mass of adhesive the menisci strength was less on the honeycomb mesh of 3mm than on the honeycomb mesh of 4 and 6mm and has therefore led us to use a film of 100g/m² for the honeycomb of 4 and 6mm and use a film of 150g/m² for the honeycomb of 3mm.

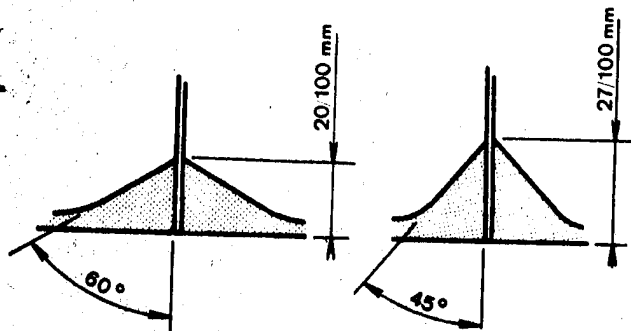
3. CHOICE OF THE HYGROMETRY IN THE ADHESIVE BONDING ROOM

The use of an adhesive of very low surface mass shows also the sensitivity of the polymer to the water quantity it contains at the curing time. This quantity of water has neither to be too great (case of adhesive bonding in hygrometric environment more than 70%, nor too dry (case of adhesive bonding in environment with a degree of hygrometry less than 30%). It seems otherwise that the humidity rate of the adhesive film depends on the hygrometry of the environment, but also on of the time spent in this environment and that this phenomenon is reversible.

When the adhesive film stays some hours in a relative hygrometric environment lower than 30%, we have stated a reduction of 10 to 20% of the resin shear strength and a reduction of 15 to 25% of the adhesive menisci height, and therefore an important strength reduction of the bonded joints of about 25 to 45%.

These values are founded on a great deal of specimens observed and statistically processed (fig. 7).

The maximal characteristics have been obtained with Redux 312 for hygrometric rates of the adhesive bonding rooms comprised between 40 and 60%.



24 h. to 30% H.R. 24 h. to 50% H.R.
Without primer

Fig. 2 - Development of the adhesive meniscus geometry according to the hygrometry of the adhesive bonding room, in case of adhesive bonding of honeycomb 5056 of $20\mu\text{m}$, with mesh of 4mm, with "Redux 312 UL" 100 g/m².

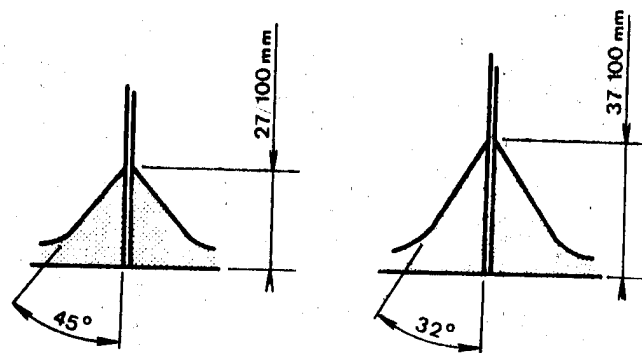
4. USE OF THE PRIMER "REDUX 112"

The problem whether to use the primer or not on the honeycomb meshes has been raised on account of a degassing out of the norms in space environment, the quantity to be used being some hundred grammes per satellite.

The comparison tests run out after staying of the adhesive film within different hygrometries have shown a clear strength increase of the

adhesive menisci, when the primer "Redux 112" is applied on the honeycomb liner.

The macrographic cross-sections show well enough the height increase of the adhesive meniscus and therefore the better conditions of damping obtained with the primer.



Without primer

With primer
"Redux 112"

Fig. 3 - Geometry development of the adhesive meniscus with use of the primer "Redux 112", in case of adhesive bonding of honeycomb 5056 of $20\mu\text{m}$, with meshes of 4mm, with "Redux 312 UL" (100 g/m²).

In an adhesive bonding environment having an hygrometry lower than 30%, the increase of adhesive damping on the liner with primer - also the height increase of the meniscus - compensates for, but does not suppress, the deterioration of the polymer characteristics, which is due to a drying before curing.

4. CONCLUSIONS

The serial manufacture of sandwich panels of high quality for satellite structure is feasible with an adhesive film of very low surface mass of 100 g/m² (Redux 312 UL).

This delicate manufacture will be mastered provided that the classic operational parameters be well supervised, such as quality of the adhesive batch, parameters of surface treatment and of curing, but it will be necessary not to neglect the primer use on the honeycomb which increases by 40%

the meniscus height, as the hygrometry control of the bonding rooms between 40 and 60%, a too low hygrometry, lower than 30%, reducing between 25 and 45% the strength of the adhesive menisci.

5. BIOGRAPHY

J. Chanteranne is graduate of "l'Ecole Nationale Supérieure d'Ingénieurs des Arts et Métiers". He joined Aerospatiale in 1970 and occupies a post of responsibility within the Production Department for the development of special industrial technologies applied to the resistant and light structures of satellites and space vehicles.

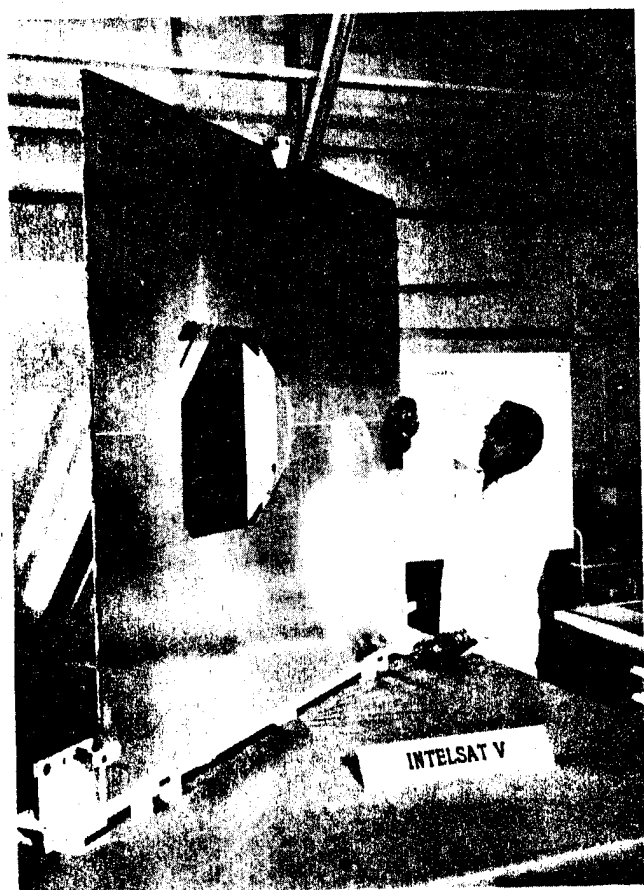


Figure 4

Structure panels INTELSAT V after bonding

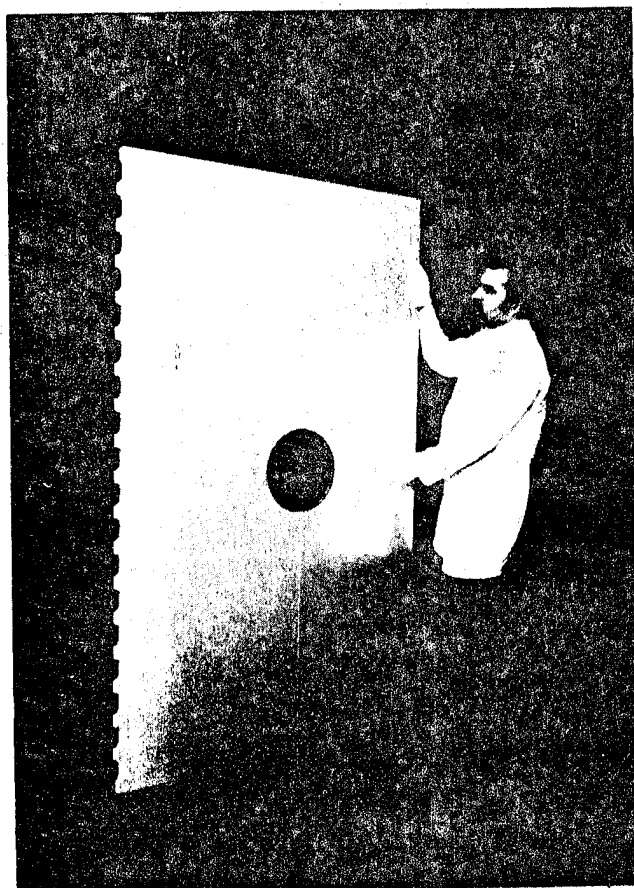
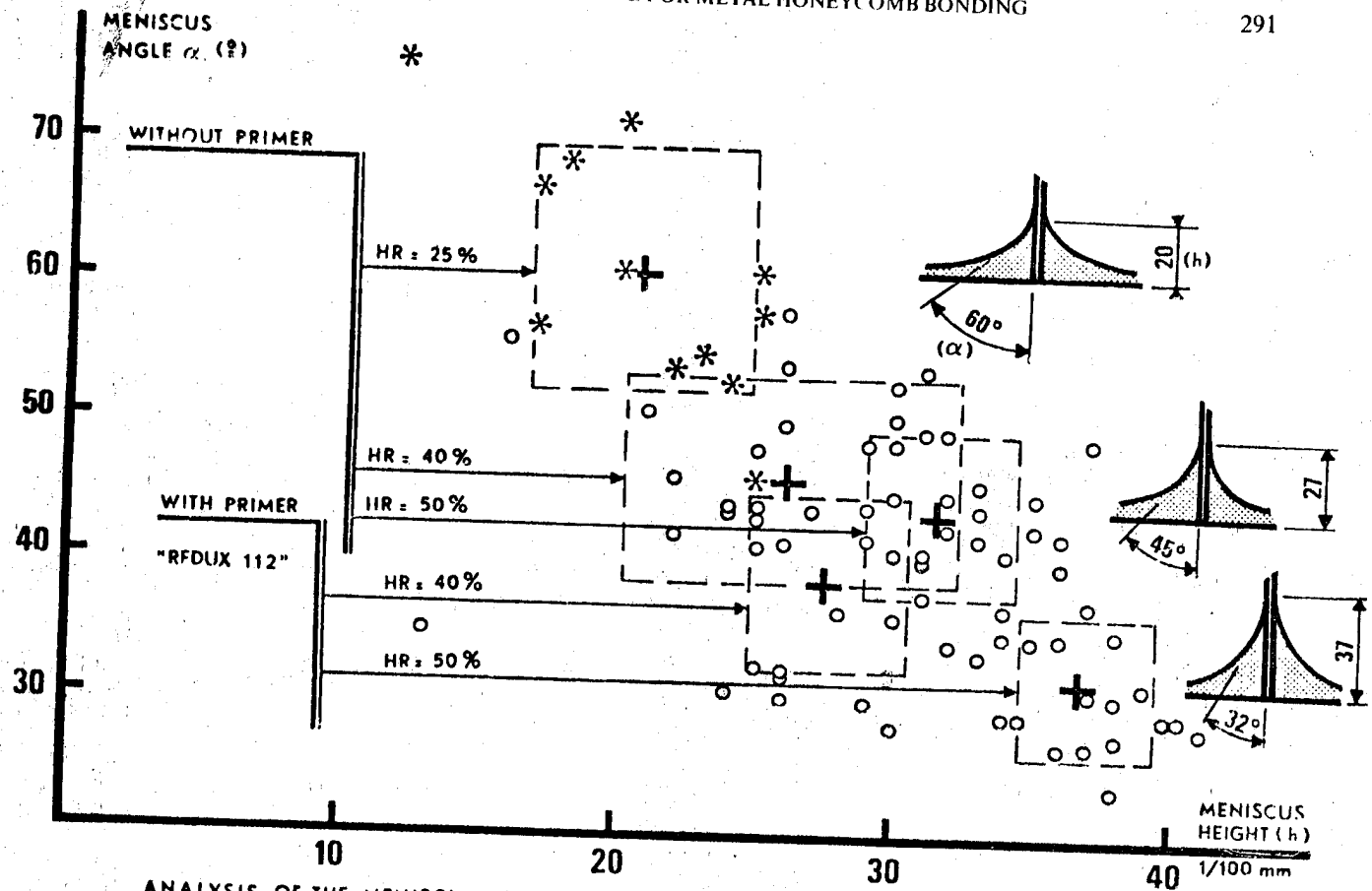
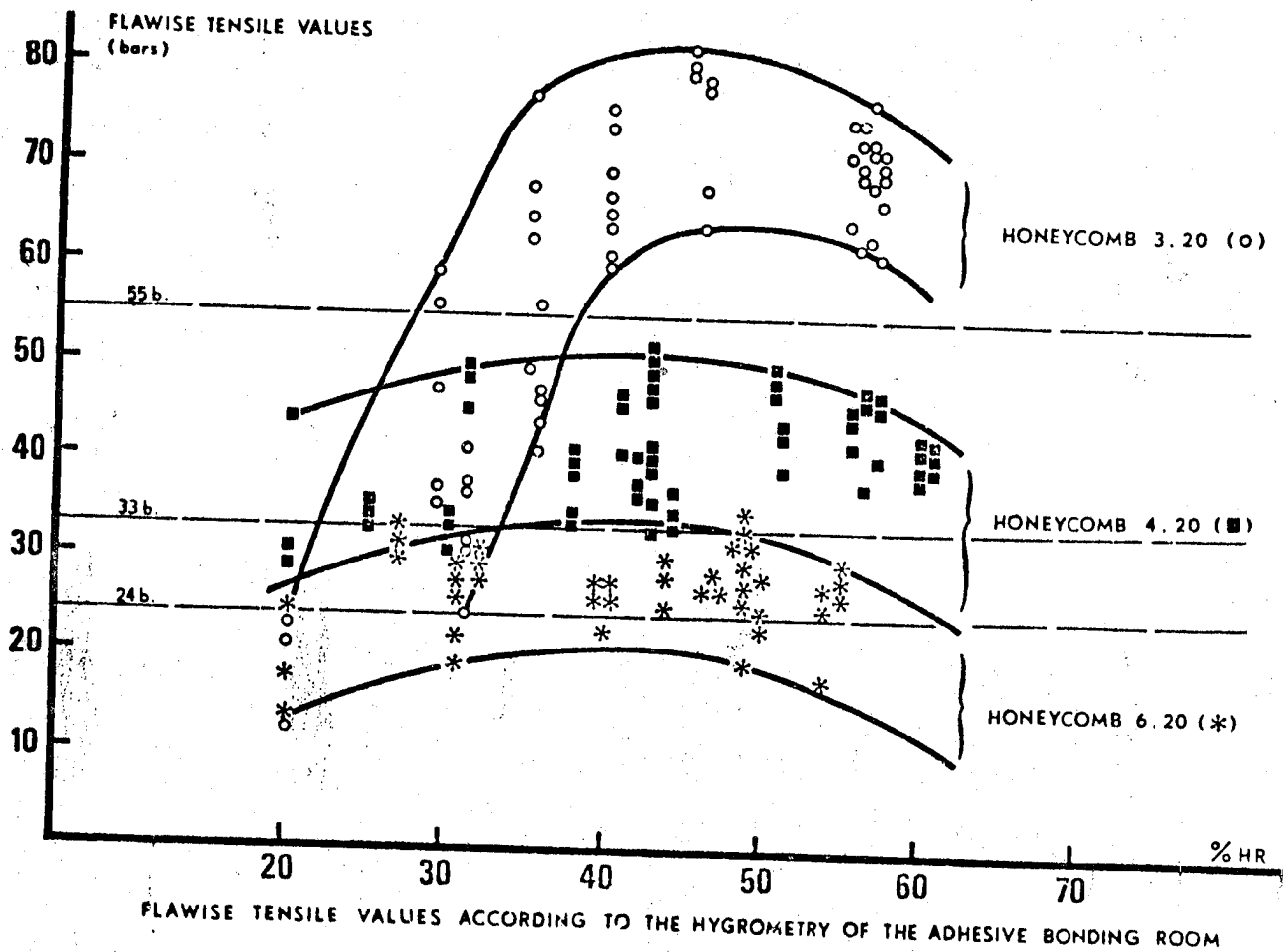


Figure 5



ANALYSIS OF THE MENISCI ANGLES AND HEIGHTS. BSL 312 UL (100 gr/m²) ON HONEYCOMB 4.20



N80-21448

HIGH-TEMPERATURE RESISTANT MATERIALS FOR SPACE MOTORS

J J Choury

*Société Européenne de Propulsion (SEP), Saint-Médard-en-Jalles, France*ABSTRACT

Evolution of the Apogee Boost Motor and particularly of the nozzle design for solid propellant motors over the last 15 years.

Corresponding evolution of throat materials used for high temperatures : phenolic composites, carbon-carbon composites developed by SEP (sepcarb). General thermomechanical characteristic - Ablation resistance - Advantages of carbon-carbon materials.

Future prospects : improvement of materials - increased application field in space.

Key words

Apogee Boost Motors - Nozzle - Phenolic composites - Carbon-carbon composites - Thermal Protection.

1. INTRODUCTION

Since fifteen years the solid propellant rocket motor nozzles have very much changed because of the progresses concerning ablative materials.

The nozzle is, in fact, one of the main component of the rocket motor and its performance depends on the characteristics of the materials.

For the rocket motors of ballistic missiles the evolution of the nozzles resulted in an increasing of their dimension and in designs utilizing more and more submerged architectures. Because of the more and more severe thermomechanical sollicitations, these nozzles were gradually obliged to use new high performances materials able to resist to a more and more aggressive environment.

The use of these new materials had a great influence on the nozzles architecture which evolution also greatly depended on the different designs of rocket motor vector control. So we gradually passed from rotative nozzles to fixed nozzles with gaz injection in the exit cone then to the flexible nozzles of the actual generation.

Concerning the materials exposed to important heat transfer flow, we have passed, as shown in table 1, from heavy materials (tungsten) or not very resistant to thermal shocks (polycrystallin graphites) or highly anisotropic (pyrographites) or thermodegradable (phenolic composites) to thermostable materials very well resisting to thermal shocks and few anisotropic.

Table 1.

	ROTATED NOZZLES	FIXED NOZZLES (GAZ INJECTION)	FLEXIBLE NOZZLE
<u>ABLATIVE MATERIALS</u>			
. High heat transfert	Tungsten	Pyrographite	carbon-carbon (sepcarbs)
	Graphite ($d \sim 1.75$)	Graphite ($d \sim 1.85$)	
. Low heat transfert	Phenolic carbon**	Phenolic graphite***	carbon-carbon (sepcarbs)
		Phenolic carbon***	Phenolic graphite***
<u>INSULATING MATERIALS</u>	Refractory cements	Phenolic carbon***	Phenolic carbon***
	Phenolic carbon**	Phenolic silica	
	Phenolic silica		
	Phenolic asbestos		

** short fibers

*** Fabrics

These progresses in the development of ablative materials and in the nozzles design enabled SEP to have a good place in the world for the apogee boost motors. SEP has had, for instance, an important role in the development of the apogee boost motor of the European satellite GEOS put in orbit on april 1977. Actually SEP is developping as main contractor and with the collaboration of SNIA VISCOSA (Italy) and MAN (Germany) a series of apogee boost motors called MAGE 1, 2 and 3, under contract of the European Space Agency.

In this paper we proposed to show the materials which enabled to change so quickly the design of the apogee boost motors nozzles which are now very much performant. Although we also intend to speak of materials for insulation, we shall particularly insist on the development of phenolic composites with carbon reinforcements and on sepcarbs (carbon-carbon materials) at SEP. We shall present the known characteristics of these materials that we shall compare to those of more classical materials such as polycrystallin graphites and pyrographite. In particular we shall demonstrate the interest of sepcarbs as nozzles materials, because their ablation resistance can vary in a large range, according to their characteristics.

2. EVOLUTION OF THE APOGEE BOOST MOTORS NOZZLES

The apogee boost motor has a fixed non vectored nozzle. The apogee boost motor and its satellite (spacecraft), usually spin stabilized, is injected into a transfert orbit by a launcher. The goal of the apogee boost motor is to create a velocity increment at a point near the apogee of the transfert orbit apogee in order to inject the spacecraft into a circular geostationary orbit. The velocity increment and the total weight of the spacecraft are requirements imposed by the launcher. To increase the payload there are two ways of reducing the weight of the motor inerts and increasing the specific impulse.

For an apogee boost motor, such as MAGE 1, the influence coefficients of the payload in relation with the weight of the inerts of the motor and with the specific impulse are the following :

$$\frac{\Delta(\text{weight of the payload})}{\Delta(\text{weight of the inerts})} = \frac{1.06 \text{ kg/kg}}{(1.06 \text{ lbs/lbs})}$$

$$\frac{\Delta(\text{weight of the payload})}{\Delta(\text{specific impulse})} = \frac{0.85 \text{ kg/sec}}{(1.87 \text{ lbs/lbs})}$$

Of course the nozzle design has a great influence on the improvement of the specific impulse and on the weight reduction of inerts.

The throat behaviour is, in particular, a main parameter to be taken in account. In this nozzle area the convective heat transfer and therefore the erosive conditions are maximum.

Because of the small diameter of the throat nozzle in apogee boost motor, a slight variation of this diameter (due to the erosion) leads to a rather large variation of the throat area. This variation of area is detrimental because it reduces the expansion ratio and therefore the thrust efficiency and also changes the flow rates of the motor.

The growing use of higher specific impulse propellants increases the erosivity of the combustion products therefore a low erosion rate of the throat is all the more difficult to obtain.

That is why we are looking for light materials with a more and more high resistance to erosion. This explains that we have passed from phenolic composites to the polycrystallin graphites then to the pyrographite. Unfortunately these materials (we will see it later) cannot be manufactured in large parts and are very sensitive to thermal shocks. For these reasons they are generally used as inserts in the nozzle. The change between the resistance to erosion of the throat insert and the throat extension may induce a step or a discontinuity in the contour then turbulences in the gas flow which are detrimental to the thrust efficiency. The best solution is to have a good smooth erosion profile from the entrance cap to the exit cone ; hence the development of sepcarbs with multidirectional textures.

The motor specific impulse deeply depends on the gas side contour of the nozzle, mainly of the exit cone. For maximum performance all the combustion products must be accelerated to a maximum velocity in the direction of the axis. Therefore the expansion ratio must be as high as possible. Unfortunately during this expansion two adverse effects occurred : divergence and two phases losses. The contoured shape of the exit cone is a compromise between the divergence losses and the axial velocity within the limited length of envelope. The two phases flow losses occur mainly in the throat area where the acceleration is maximum. An appropriate shape of the throat area allows to reduce these losses. Finally it is necessary to avoid particle impingements in the aft part of the exit cone. For the exit cone we chiefly need good mechanical properties materials, not too much conductor and easy to be manufactured in this special shape, hence the generalized use first of phenolic composites and nowadays of sepcarb which are moreover thermostable.

We can sum up the evolution of the apogee boost motor nozzles as follows.

a) First generation nozzles

Three examples are given in figures 1, 2 and 3. These nozzles whose development began at the end of 1960's are principally using phenolic composites and polycrystallin graphites like the nozzles of the big rocket motors of ballistic missiles produced at the same time.

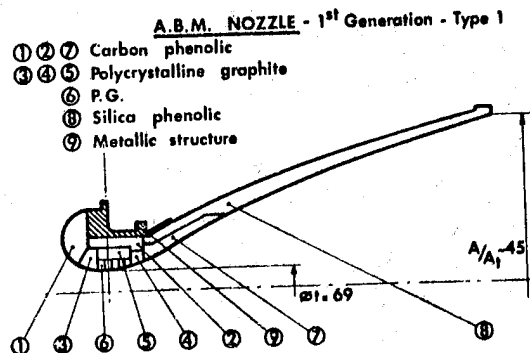
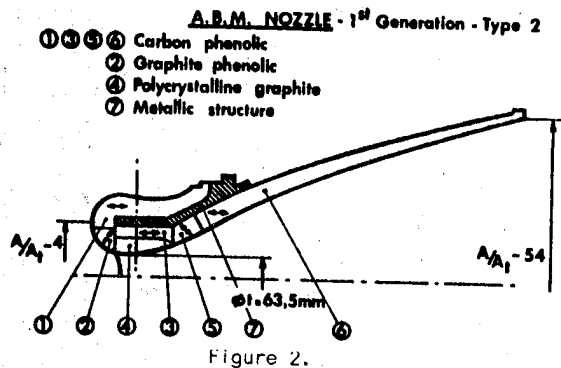


Figure 1

In figure 1 we present a sketch of one of the first nozzles developed for apogee boost motors. The metallic structure (9) is made of aluminium alloy ; the entrance cap (1), the external insulation (2) and exit cone entrance (7) are made of phenolic carbon ; the aft part of the exit cone (8) is in phenolic silica ; the throat (6) in pyrographite is surrounded by three pieces (3, 4, 5) in polycrystalline graphite. In such a nozzle the three functions (structural resistance, insulation, erosion resistance) are well separated and so they lead to the use of materials with very different characteristics. The temperatures of the metallic structure and the external part of the exit cone are generally low during the firing tests.



The nozzle in figure 2 uses the same technology as the nozzle of GEOS satellite motor. In comparison with the nozzle described here before, the main differences are :

- a less massive metallic structure (7),
- a more simple architecture for throat area with only two pieces : one throat (4) in polycrystalline graphite with a phenolic carbon insulation (3) ;
- the use of phenolic graphite more performant than the phenolic carbon for the input throat approach (2),
- the use of only one material (phenolic carbon) for the two pieces (5,6) of the exit cone

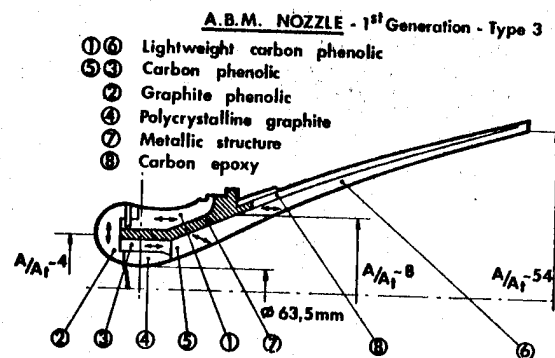
In this nozzle we used phenolic composites of better quality developed by SEP between 1968 and 1972 and using, in peculiar, more reliable and more performant reinforcements (carbon and graphite fabrics) manufactured now by GEPEM in France. In spite of these improvements, this nozzle with a weight of about 11 kg was still very heavy.

The erosion of the nozzle throat depends, of course, on the used propellant. For example we have noticed the two following values :

- Propellant PBCT 15/14 (15 % Al, 14 % binder)
T 3450°K → erosion rate = 0.048 mm/sec
- Propellant PBCT 16/12 (16 % Al, 12 % binder)
T 3620°K → erosion rate = 0.091 mm/sec

This throat erosion is in a great part due to the bad behaviour in erosion of input throat approach materials and to the induced turbulences in the combustion products flow.

To reduce the weight of such a nozzle we have used low density materials in all the areas where heat transfers are low. This new nozzle has been developed under CNES contract. It is described by the sketch of figure 3.



The main differences, in comparison with the precedent one, are the following :

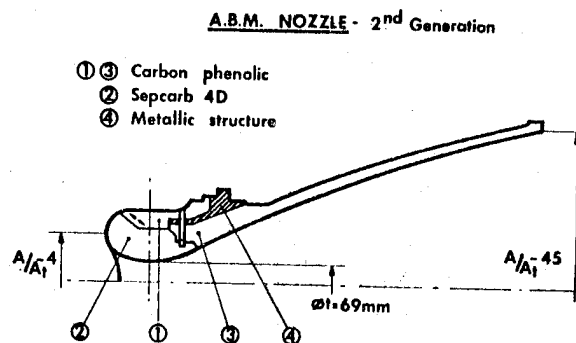
- The phenolic carbon of the external insulation (1) of the structure and of the aft part of the exit cone (6) is made of tape wrapped phenolic carbon lightened by addition of microballoons the density of which being close to 1 g/cc.
- To improve the behaviour in erosion of the nozzle part before the throat we have used phenolic graphite in the entrance cap (2). This entrance cap is made of phenolic-graphite fabric molded in an helicoidal rosette mechanically fastened to the external insulation by phenolic carbon fastener.
- On the outside of the exit cone a high strength carbon epoxy overwrap is used for structural strength. The parting of the structural and thermal functions is due to the poor mechanical characteristics of the lightweight material.

With these improvements we were able to reduce the nozzle weight to 9.3 kg which did not seem to be sufficient to test the nozzle at firing because of the progresses made in parallel in the development of sepcarbs and of the foreseen improvements of nozzles with these last materials.

b) Second generation nozzles

The characteristics outline of these nozzles stay on the fact that the ablative materials has also a structural function which is possible thanks to the use of sepcarbs with multidirectionnal textures, which mechanical properties are retained or even improved up to high temperatures.

A sketch of this type of nozzle is given in figure 4.



It is the same nozzle that those used on apogee boost motor MAGE 1.

The entrance cap and the throat (2) are made with one single sepcarb piece with 4D texture (SEP patent) of a density near 2.0.

This piece can withstand the external pressure without being reinforced by a metallic structure, on the other hand the multidirectional texture of this piece prevents it from cracking or delamination which is a great advantage in comparison with classical materials.

The structure (6) in titanium alloy is protected on its external face by phenolic carbon (1).

The exit cone (4) is also made with phenolic carbon. Such a new design allows not only a weight reduction but also an improvement in the erosion resistance of the contour mainly in the throat area. The depth of erosion is reduced at the throat and the erosion smoothness is enhanced compared with the previous multipiece design. The result is a better specific impulse.

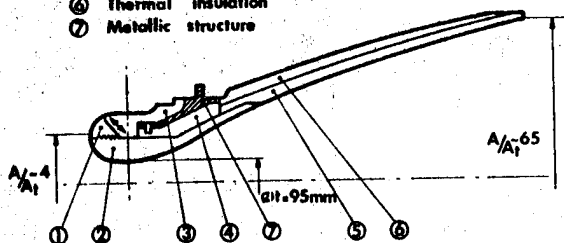
Only pyrolytic graphite (PG) insert on the throat may reduce the erosion, but the erosion of the contour from the throat approach to the throat extension would be very irregular and probably the specific impulse would be reduced. On the other hand, with PG the nozzle design would be more complicated and therefore less reliable.

c) Third generation nozzles

A sketch of this type of nozzle, developed for example for apogee boost motor MAGE 3 is given in figure 5.

Figure 5. A.B.M. Nozzle (3rd Generation)

- ① ② Sepcarb 4D
- ③ ④ Carbon phenolic
- ⑤ Sepcarb "rosette"
- ⑥ Thermal insulation
- ⑦ Metallic structure



The submerged part of the nozzle is made with two sepcarbs 4D (1, 2) pieces going from the entrance cap to the exit cone entrance. The exit cone (5) is in sepcarb "rosette" directly screwed to the throat piece. This exit cone is insulated on its outside with a felt (6) made either from carbon fibers or silica alumina fibers to protect the motor bottom from heating. Phenolic carbon (3, 4) only protects titanium alloy structure (7) against a too important heating. Such a nozzle weighs about 7 kg.

3. GENERALITIES ON NOZZLES MATERIALS

In this paper we are not going to speak of polycrystalline graphites and pyrographites (which are well known and widely described elsewhere) and of phenolic silica which was unused except for the first nozzles.

We will particularly insist on phenolic composites with carbon reinforcements and sepcarbs developed and manufactured by SEP.

3.1 Phenolic composites with carbon reinforcements

These materials, made of a carbon reinforcement, a phenolic matrix and eventually fillers, are known and used now since more than fifteen years in propulsion field.

The carbon reinforcements are made of carbon or graphite fibers under various forms: short fibers, mats, felts, fabrics. These fabrics are got by pyrolysis under a controlled atmosphere from cotton, rayon, viscose, preoxydized polyacrylonitrile (PAN), preoxydized pitch etc. For its phenolic composites, SEP essentially uses rayon precursor carbon or graphite fibers. Graphite fibers are in fact carbon fibers treated at a high temperature which changes amorphous initial structure of the carbon into a more oriented structure which is called turbostratic. These fibers are light, their evaporation temperature is about 3650 °C and their thermal conductivity is relatively low for the carbon fibers. They have good mechanical properties but a bad oxydation resistance (graphite fibers being however better than carbon fibers).

These low modulus fibers are different than high strength and high modulus carbon and graphite fibers which are also obtained by pyrolysis under controlled atmosphere from the same precursors but under tension, the main applications of which being structural materials.

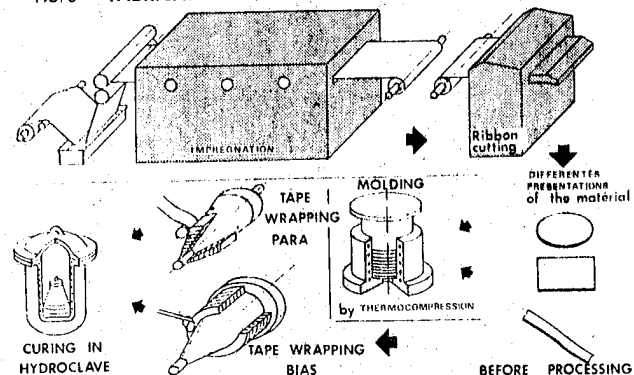
In its actual phenolic composites, SEP essentially uses carbon and graphite fabrics made in France by GEPEM. These fabrics are associated with phenolic resins which give a high rate char which has good mechanical properties. These resins are obtained by polycondensation of phenol and formol.

There are two main processes to make parts with phenolic composites:

- thermocompression molding,
- tape wrapping of a preform and curing of these one in an autoclave or hydroclave.

Sketches of these two techniques are given in figure 6.

FIG. 6 FABRICATION of PHENOLIC COMPOSITES



Generally the curing temperature is between 150 and 160 °C and the curing duration between 5 and 10 h. With these two techniques, parts of different shape and size are made as shown in the figures 7 and 8.

Fig. 7: Molding parts

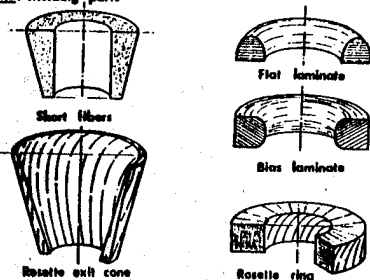
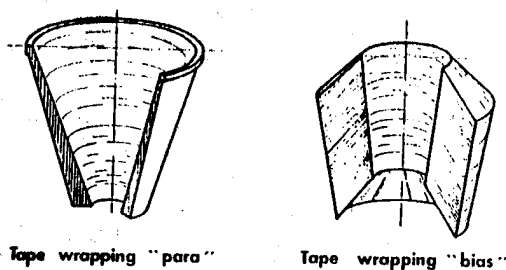
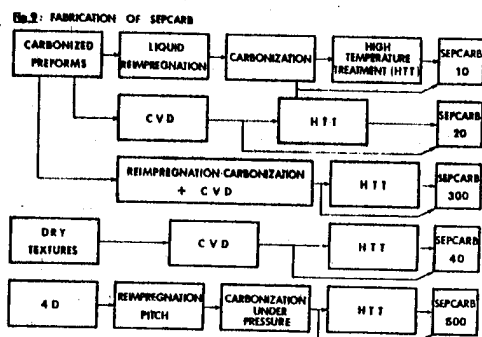


Fig. 8: Tape wrapping parts



3.2 Sepcarbs

As shown in figure 9, five main families of sepcarbs have been developed and industrially produced by SEP.



The three first sepcarbs families (10, 20, 300) which are made from carbonized preforms lay out on a very large experience of SEP in production of composite preforms. Of course the first works in the field of carbon-carbon were made with these kinds of sepcarbs.

These first works begun in 1969 and first they exclusively concerned reimpregnated pyrolysed materials (sepcarbs serie 10). Two types of resins have been studied to make these materials: phenolic and furfurylic resins. Even if they are better known (they composed in part classical composites) phenolic resins have been quickly let down, to the benefit of furfurylic resins, of a superior quality. The most difficult steps in the development of these sepcarbs have been:

- prepegging
- preforms curing
- pyrolysis of these preforms

For several years now the manufacturing technique of sepcarbs 10 is well known and we regularly get, in two or three reimpregnation, sepcarbs with a density between 1.50 and 1.60 on large parts (external diameter > 500 mm and thickness > 50 mm) the reinforcement of which being a rayon precursor graphite fabric.

The second family of sepcarbs which has been developed is those of sepcarb 20 obtained by densification of carbonized preforms by CVD. We generally use the "isothermal" process and the technique consists in filling the pores of preforms with pyrolytic carbon resulting of cracking of light hydrocarbons.

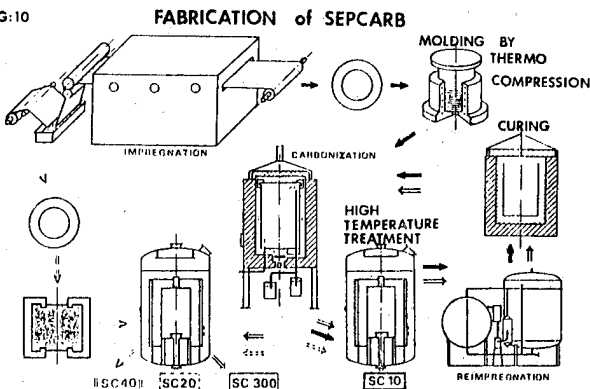
The third family of sepcarbs was developed in combining for the densification of carbonized preforms resin char and pyrolytic carbon (CVD). This kind of sepcarb is called sepcarb 300. This technique offers the best solution to fill the pores (the size and the distribution of which being generally very different from one part to the other) of the preforms. Addition of pyrolytic carbon in the matrix of carbon-carbon changes the thermal and the mechanical characteristics of these materials and affords to enlarge their range of applications.

Actually we easily produce large parts in sepcarb 20 or sepcarb 300 with density between 1.50 and 1.65 when they are reinforced with rayon precursor graphite fabric.

In parallel to this work on sepcarbs 10, 20, 300 we have developed a fourth family of carbon-carbon (sepcarbs 40) which is obtained by CVD densification of dry carbon textures. Since five years SEP has done a big effort in this field and today we are able to reach on large size parts densities between 1.60 and 1.67 with rayon precursor graphite fabric and between 1.75 and 1.90 with PAN precursor graphite fabric. If we use pitch precursor graphite fabric we can reach densities higher than 1.95.

A sketch of the manufacturing of these 4 families of sepcarbs is given on the figure 10.

FIG. 10



To complete our range of sepcarbs we have developed during the last three years a fifth family of carbon-carbon (sepcarbs 500) which is obtained by densification with pitch, under high pressure and temperature, of multidirectional textures (4D, 5D, 6D) patented by SEP.

In comparison with the perhaps better known textures 3D, these textures have many advantages such as :

- a better isotropy,
- a greater ability for densification (due to their open porosity)
- a more homogeneous densification resulting in no density gradient in the parts,
- a smaller porosity hence a minor roughness for the same quality of fiber,
- a better conservation of mechanical characteristics of fibers.

Generally with the sepcarbs500 we obtain density between 1.90 and 2.05. A sketch of their manufacturing is given on the figure 11.

4. GENERAL CHARACTERISTICS OF NOZZLES MATERIALS

4.1. Phenolic composites

We show down the characteristics of the three main materials used in the nozzles of apogee boost motors :

- a molded phenolic graphite,
- a molded phenolic carbon,
- a tape wrapped phenolic carbon parallelly to the piece axis.

Table 2.

CHARACTERISTICS	UNITS	P.G	GRAPHITES	PHENOLIC CARBON	PHENOLIC GRAPHITE
Density		2.15-2.23	1.65-1.85	1.50	1.47
Compressive resistance	MPa	350 100	56-158 // 51-163 ⊥	400 ⊥ 150 //	250 ⊥ 150 //
Tensile resistance	MPa	105-140 //	13-46 // 19-53 ⊥	150 // 150 ⊥	250 ⊥ 120 //
Flexural resistance	MPa	240 ⊥	20-76 // 29-79 ⊥	200 //	150 //
Flexural modulus				18000	16000
Shear resistance	MPa			35	25
Specific heat	Kj/Kg °C	~ 0.96	0.62-0.75	0.96	0.96
Conductivity (room temperature)	W/m2 °C	"a" direct. ~ 363 "c" direct ~ 1.25	80-150 80-150	2 // 1.35 ⊥	4 // 2 ⊥

a) Thermal expansion

Heating rate has a great influence on expansion values got with phenolic composites. In fact the expansion measured with high heating rates is more a swelling of the sample due to the outgassing during the pyrolysis of the resin than a real expansion.

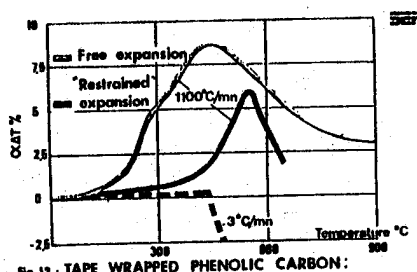
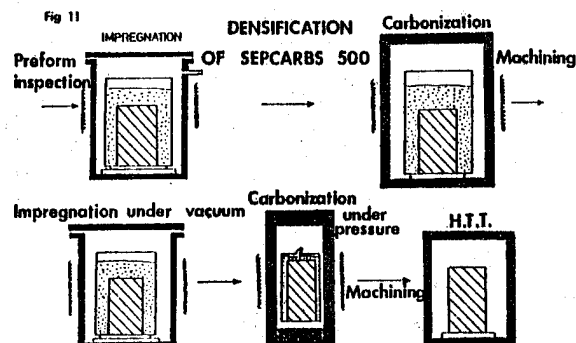


Fig 12 : TAPE WRAPPED PHENOLIC CARBON : FREE AND RESTRAINED EXPANSION
Figure 12.



The thermal and mechanical properties at room temperature of these materials are given in table 2. The evolution of some characteristics versus temperature is given by the curves of figures 12, 13, 14, 15, 16, 17

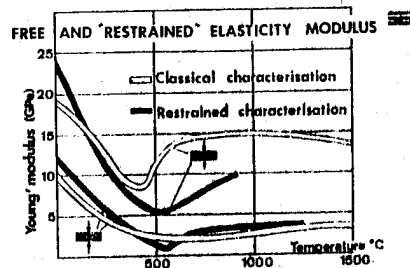


Fig 13 : TAPE WRAPPED PHENOLIC CARBON :

Figure 13.

The got α values are not homogeneous with the correspondent values of modulus measured or stabilized in temperature after a low rate heating and restrained samples.

Homogeneous characteristics (E, α) are obtained by restrained thermal growth tests. The values obtained in these conditions (see figures 12 and 13) are representative of characteristics of materials which have been pyrolyzed under a multi-axial compression.

b) Thermal conductivity

Phenolic carbon has a lower thermal conductivity than phenolic graphite till 300°C. The difference is reduced when the temperature grows up.

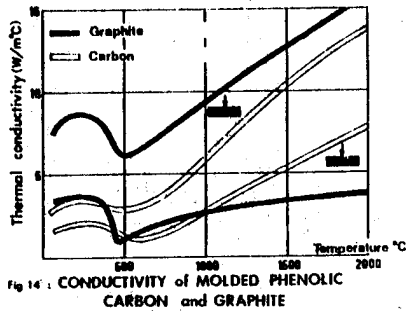


Figure 14.

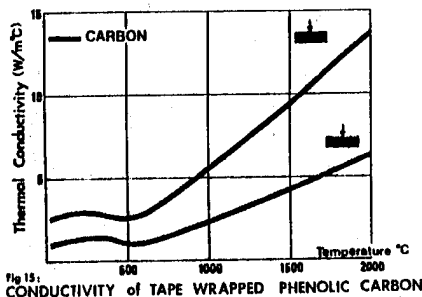


Figure 15.

In all the cases the conductivity in the direction of the lamina is higher than these across the lamina, the difference being more important when the material is more conducting. Phenolic composites are less conducting than polycrystallin graphites, that is why they are generally used for insulating materials in nozzles.

c) Mechanical characteristics

In a general way, phenolic composites have better mechanical characteristics at room temperature than polycrystallin graphites. On the contrary, because of their thermodegradable nature, their characteristics vary very much at high temperatures.

Unlike polycrystallin graphites and pyrographite the mechanical properties of which are increasing with temperature (Figures 18, 19), those of phenolic composites fall down dramatically between 300 and 500 °C (resin pyrolysis) and recover with difficulty their original values at high temperatures.

In a general way, above 1000 °C phenolic composites behave like carbon-carbon materials. This evolution at high temperatures of phenolic composites characteristics sometimes justifies their use as materials for nozzles contour when thermal heat transfers are low and mechanical sollicita-

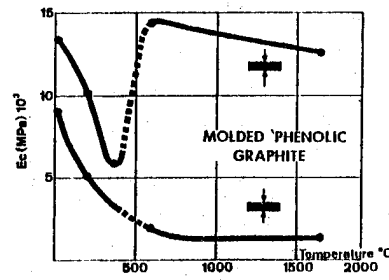


Fig 16: COMPRESSIVE MODULUS

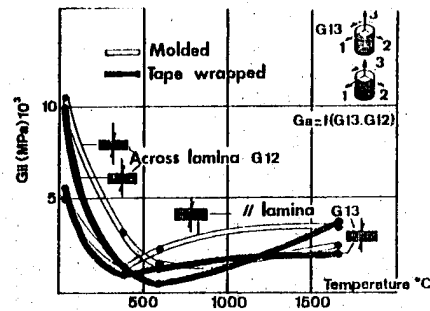


Fig 17: SHEAR MODULUS of PHENOLIC CARBONS

Fig 18: Tensile resistance of graphites and P.G

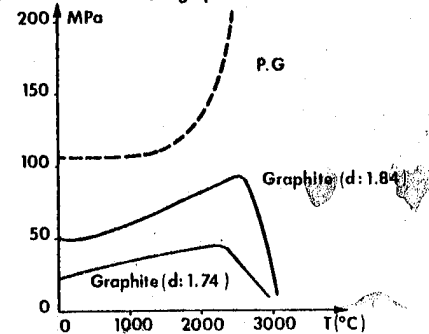
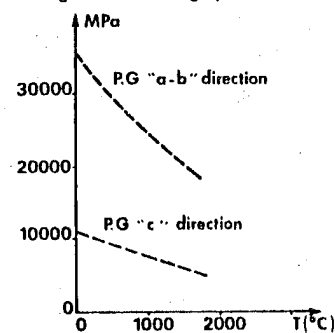


Fig 19: Young modulus of graphites and P.G



tions not too much severe. In this case the possibility to manufacture large parts can be interesting compare to the difficulties which are encountered with polycrystallin graphites and pyrographites.

4.2. Sepcarbs

Tables 3 and 4 give the characteristics at room temperature of the main sepcarbs 2D and nD which

are industrially manufactured by SEP.

CHARACTERISTICS	UNITS	SEPCARB 300 RAY	SEPCARB 40 RAY	SEPCARB 40 PAN	SEPCARB 40 PAN HR
Specific gravity	kg/m ³	1450-1550	1400-1730	1500-1850	1700-1900
Compressive resistance	MPa	70-80 105-115	50-160 90-135	55-140 50-250	200-270 260-300
Compressive modulus	MPa	12100-14900 2700-3000	12000-21800 5000-6100	25000-40000 -	46000-49000 -
Tensile resistance	MPa	45-60	35-70	40-150	160-180
Tensile modulus	MPa	10400-12800	12000-22700	25000-47000	45000-72000
Flexural resistance	MPa	-	70-110	65-220	260-360 360-535
Shear resistance	MPa	7-11	13-26	8-20	5-7
Expansion $\Delta l/l$	%	0.18-0.20 0.55	0.20-0.30 0.60-0.85	0.07-0.12 0.75-1.15	-
Thermal diffusivity	10 ⁻⁶ m ² s ⁻¹	65-90 18-26	150 40	130 60	-

Table 3 - Characteristics at room temperature of sepcarbs 2 D

CHARACTERISTICS	DIRECTION	UNITS	Z	X'	F
Specific gravity		kg/m ³	2000		
Compressive resistance		MPa	50	50	80
Compressive modulus		MPa	8500	23000	65000
Tensile resistance		MPa	-	30	100
Tensile modulus		MPa	-	18000	62000
Torsionnal resistance		MPa	45	20	-
Torsionnal modulus		MPa	11800	3500	-
Expansion $\Delta l/l$	1000°C 1500°C 2000°C	%	0.5 1.8 4.0	0.5 1.4 2.0	0.6 1.0 1.4
Thermal conductivity	100°C 500°C 800°C	W m ⁻¹ s ⁻¹	180 85 70		

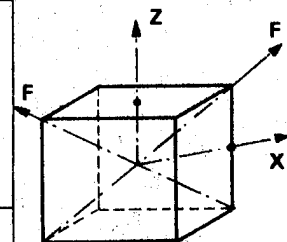
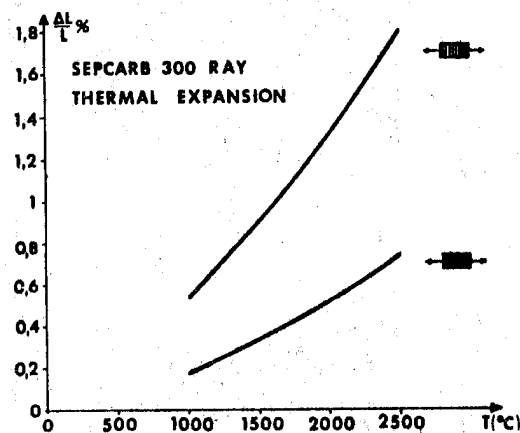


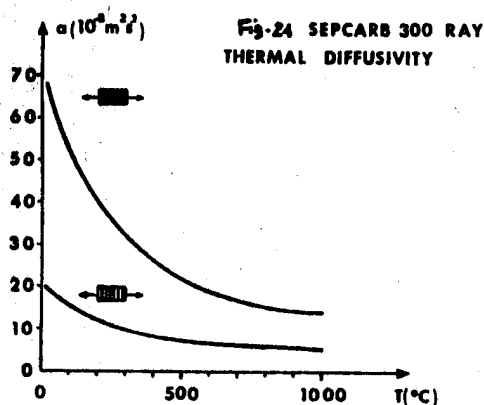
Table 4 - Characteristics at room temperature of sepcarbs 4D

These physical, thermal and mechanical characteristics of sepcarbs represent only a first approach of the possibilities of these materials and our aim is only to prove, that by opening the range of manufacturing technics of carbon-carbon materials, we have increased chances to find out the adequate material for a given function.

For each family of sepcarbs we can improve one or several thermomechanical properties of a given material by using a different reinforcement or matrix. We have an example of it by comparing sepcarb 40 PAN made from classical fibers and sepcarb 40 PAN made from high mechanical resistance fibers. Beyond high mechanical characteristics this last materials family proved a high fatigue resistance (more than 10⁶ cycles at 70 % of the ultimate strength and more than 2000 cycles at 90 % of the ultimate strength). Concerning high temperatures sepcarbs characteristics, most measurements are being done. However on figures 20,

21, 22, 23 we give for example the results got till now.





These curves show that sepcarbs behave like polycrystallin graphites. We can sum up the main known advantages of sepcarbs in comparison with polycrystallin graphites and PG as follows :

- At a given density sepcarbs have higher mechanical properties and a greater thermal shock resistance than polycrystallin graphites ;
- Sepsarbs ruptures are less brittle than those of polycrystallin graphites ;

High density sepcarbs 4D are potentially better (in peculiar, as we shall see it later for applications to nozzles) than PG, because of their best isotropy, of their low expansion coefficient in all the directions and of their ability to be manufactured in high size and big thickness.

Concerning the measure of erosion resistance of the sepcarbs used in the solid propellant rocket motor nozzles an important work has been done by SEP, which results are presented hereafter.

The first problem to solve has been to define the erosion tests. Indeed during these tests we must be sure that the material behaviour is similar to its behaviour in a scale 1 nozzle.

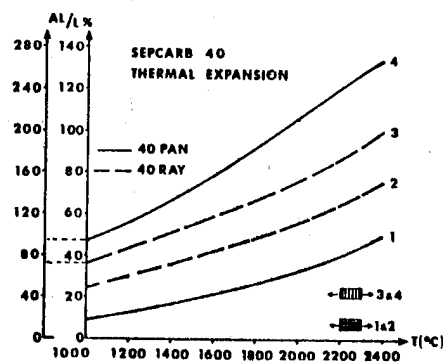


Figure 22

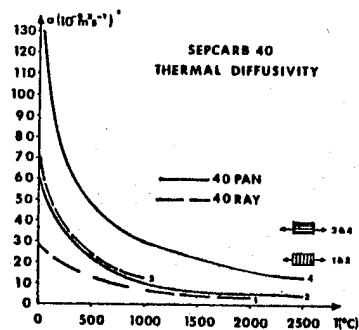


Figure 23

Several types of tests have been used, particularly a plasmajet (20 000 KW/m²) and a minirocket (diameter 200 mm, length 1000 mm, throat diameter 35 mm, duration 8.5-10 sec, pressure 30 bar) but these ones were not satisfactory. Finally only reduced scale rocket motors have given correct results. Two types of rocket motors have been used. Their characteristics are given in table 5.

Table 5

	ROCKET MOTORS	
	N° 1	N° 2
Rocket motor length	~ 3000 mm	~ 2000 mm
Rocket motor diameter	390 mm	800 mm
Throat diameter	54 mm	75 mm
Propellant grain weight	~ 350 kg	500 - 800 kg
Pressure	~ 50 bar	~ 50 bar
Duration (polyurethane propellant 3350 °K - 3500 °K)	~ 30 sec	~ 50 sec
Duration (PBCT propellant 3650 °K)	-	~ 50 sec

These two types of tests have given similar results with phenolic composites, the reproducibility being better with N° 2. Taking into account the US experience and the fact that a test erosion must be more severe when the material is more performant, we have chosen the rocket motor N°2 to test the sepcarbs.

Moreover, this choice enables to evaluate in firing test higher size parts, consequently a material more representative of those that will be used in scale 1 nozzles.

Indeed we cannot forget that the final characteristics of a composite material, such as carbon-carbon, partly depend on the shape and the dimensions of these parts.

Erosion resistance of sepcarbs

Table 6 gives the different firing test results and the characteristics of tested sepcarbs. All these materials have been treated at high temperatures.

Table 6

Table 6					$\bar{K} = \bar{V} re^{0.2} pe^{-0.8}$ bar.mm.sec
TEST NUMBER	CHARACTERISTICS OF SEPCARBS		DENSIFICATION PROCESS	AVERAGE DENSITY IN THE PARTS	
	PREFORM				
	RE INFORCEMENT	MATRIX			
1	Graphite fabric (rayon) square weave	furfurylic	resin	1.48	0.0363
2	Graphite fabric (rayon) 8 HS	without	CVD	1.68	0.0209
3	Graphite knit (PAN)	without	CVD	1.77	0.0163
4	Graphite mat (pitch)	without	CVD	1.82	0.0119
5	Graphite fabric (rayon) 8 HS	furfurylic	CVD	1.55	0.0233
6	3D (rayon)	without	pitch	1.93	0.0096
7	Graphite fabric (rayon) 8 HS	furfurylic	resin + CVD	1.50	0.0185
8	Graphite fabric (rayon) 8 HS	furfurylic	resin + CVD	1.50	0.0165
9	Graphite fabric (PAN) 8 HS	without	CVD	1.68	0.0139
10	4D (PAN)	phenolic	pitch	1.92	0.0121
11	Graphite fabric (PAN) 8 HS	without	CVD	1.73	0.0160
12	4D (PAN)	phenolic	pitch	1.91	0.0126
13	4D (PAN)	phenolic	pitch	1.88	0.0129

To try to set up laws giving the erosion resistance of carbon-carbon materials versus their density, we must take into account the fact that there is some density gradient in these materials. Only the average density of the eroded portion of the parts during the firing test has to be taken in account. Density gradients in the tested parts

have been estimated from density gradients measured in similar parts. After correction the values of table 6 give the correlation between erosion resistance and the real density of eroded portion of sepcarbs that we have represented in figure 24.

On this figure erosion resistance is expressed by a coefficient \bar{K} which is related with test conditions and the average erosion rate by the relation

$$\bar{K} = \bar{V} re^{0.2} pe^{-0.8}$$

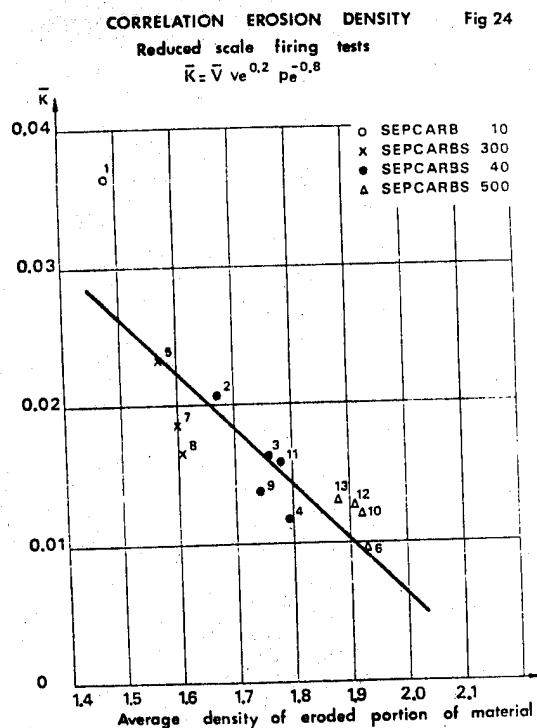
pe : efficiency pressure
re : efficiency throat radius
 \bar{V} : average erosion rate expressed by

$$\bar{V} = \frac{\Delta r}{t_{ce} - t_o}$$

where t_{ce} = efficiency combustion duration

t_o = response duration of erosion

Before giving conclusions on these results we must remember that the erosion resistance of a material used as nozzle throat does not only depend on its physico-chemical and thermomechanical characteristics but also on the behaviour of materials surrounding it and of the nozzle architecture. For the results we have presented here before we cannot affirm that all these materials have been tested in rigorously similar conditions. Taking into account that density gradients in parts were perhaps a little bit different from those we measured, it appears in first approximation that the erosion resistance of a carbon-carbon material varies in a linear way with its real density. This seems to be logical for the carbon material density strongly depends on the cristallin organization of carbon elements. Indeed the carbon density grows up with its orga-



nization degree. Now more a carbon is organized higher is its conductivity and higher is the necessary energy to destroy its structure.

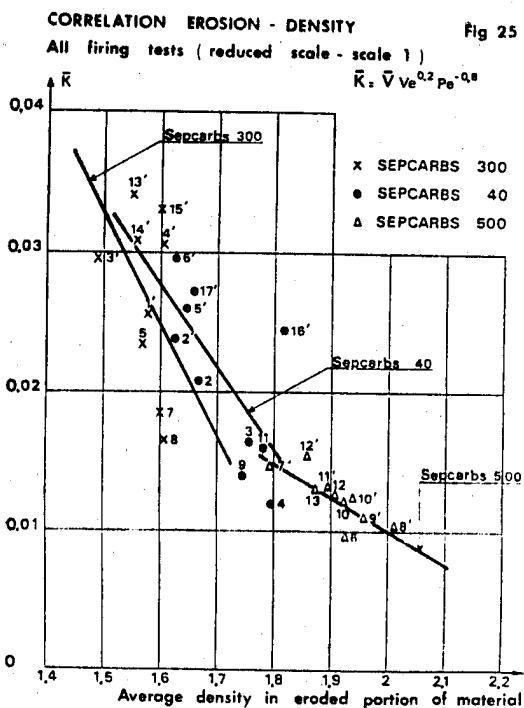
This explains the tight relationship existing between erosion resistance and density. However we see on figure 24 that some points much diverge from the straight line erosion = f (density). It means that this above correlation is not rigorous.

We can suppose with these first results that in fact the different sepcarbs families don't behave on the same way in erosion. To improve the erosion/density correlation we have been led to take into account some scale 1 tests results.

Two types of correction for these last results must be considered :

- density gradients in the parts
- firing tests parameters

After corrections, and for the same conditions, we could set up the correlations shown in the figure 25.



These results confirm that, for a given density, the different considered sepcarbs types don't behave in the same way in erosion and show us that we have much to do to perfectly control the laws giving the erosion resistance of sepcarbs. Probably parameters such as nature and percentage of fibers and matrix, total porosity, pore sizes and distribution have also an influence on erosion resistance of sepcarbs ; so it seems that into the same sepcarbs family the erosion/density correlation is not so rigorous that our expose supposes it. However, because of the tight links between parameters above and density we can consider that these erosion/density correlations for the different sepcarbs families, even if they give an approximative idea of reality, are an interesting characteristic of these materials and a good guide to use them in the nozzles.

4.3. External insulation materials

The use of sepcarb in exit-cones nozzles of apogee boost motors has a single disadvantage linked to the thermal conductivity of the material, i.e a too important overheating of the external face of these exit-cones which is not acceptable. Then it is necessary to insulate these exit cones to reduce dramatically their external temperature. So we first used carbon felt, which conductivity is 0.05 Kcal/m.h°C at room temperature and 0.15 Kcal/m.h°C at 1000 °C. Carbon felt pieces were sewed and bonded to the exit cone sepcarb with a graphite adhesive able to withstand at high temperature. This solution presented two main drawbacks :

- carbon felt burns with oxygen at low temperature (it was the case during firing tests in atmosphere),
- emissivity of carbon felt is high, chiefly in front of the sewing.

That is why we made efforts to develop an insulation with silica-alumina fibers the thermal conductivity of which being from 0.05 Kcal/m.h.°C at room temperature and 0.13 Kcal/m.h.°C at 1000°C. This type of material which may be continuously used till 1400 °C is bonded to the exit cone sepcarb with a refractory cement which hardens in the air and withstands till 1260 °C in permanent duty.

Tests with a propane/oxygen gas torch able to increase the sepcarb exit cone temperature up to 1650 °C have shown that the external face temperature can decrease to about 150 °C with 12.5 mm and 40 °C with 25 mm of this insulation and that on the other hand the binding between exit-cone and insulation was satisfactory.

This type of material which is non flammable and has a very low emissivity has been definitively chosen to replace carbon felt. It has one single inconvenient in comparison with carbon felt : a lightly higher specific gravity : 128 kg/m³ instead of 90.

During the firing tests, in nominal conditions, an important inconvenient was discovered for both carbon fibers and silica alumina fibers. It is their weak power to filtrate under vacuum the IR radiation. To improve this characteristic we have developed "sandwich-materials". The insulation is made now with layers of silica-alumina fibers and aluminum sheets. The tests show that this new insulation is totally satisfactory. In developing this new insulation we were conducted to use low specif. gravity silica-alumina fibers (96 kg/m³ instead of 128) that suppresses the only inconvenient of this kind of insulation compare to the carbon felt.

Advantages of carbon-carbon materials

These advantages may be summarized as follows :

- 1) Great heat of ablation, can be greater than 20 000 Kcal/kg.
- 2) Good ratio of mechanical resistance/density.
- 3) Improvement of the mechanical resistance at high temperatures.
- 4) Good resistance to thermal shock.
- 5) Low coefficient of expansion.
- 6) Low thermal conductivity.
- 7) Ability to control the erosion resistance by appropriate selection of materials.

Item 7, developed above is the principal advantage of the carbon-carbon materials in comparison with other rocket nozzles materials which shall be compared, type by type, as follows :

Low density carbon-carbon and phenolic composites

Phenolic composites are unstable materials which decompose at low temperature and consequently have thermomechanical properties for which the change with temperature is not easily controlled. Thereby, the use of the materials in rocket nozzles leads to design whose performance is not easily calculated.

The erosion behaviour of composite materials and particularly the phenolic composites, depends on their state of stresses. This state of stresses in a nozzle during firing is due to forces caused by the internal pressure and the thermal expansion of the materials. The stresses due to thermal expansion are generally the most critical in a nozzle design, depending not only upon time temperature parameters, but also upon effects of chemical reactions on thermal expansion. Influence of the state of stresses of phenolic composites of their ablation resistance has been measured. We have shown for example that the erosion rate of a phenolic graphite composite can vary of more than 25% depending upon its state of stresses.

This phenomenon of variation of erosion due to the effect of stresses, particularly those due to the decomposition gases of the resin (composite matrix) of phenolic composite, is greater with the phenolic carbons, less conductive, and result in very irregular erosion pattern (with big cracks). For these reasons such materials are not good for critical areas in the nozzle flamefront.

These results show that it is difficult to design a nozzle using phenolic composites as flamefront materials. It is better when the performance requirements for the materials are relatively low, at the level of phenolic graphites, to use thermally stable material with easily measured thermomechanical characteristics at any temperature. Such is the case for low density carbon-carbon materials.

The use of such materials simplifies nozzle design enabling improved design calculations to be prepared giving more reproducible results because of the narrow connection between density of these materials (controllable characteristic) and their ablation resistance.

Intermediate density (about 1.8) carbon-carbons and polycrystallin graphite

Among the best known advantages of the carbon-carbon materials, are noted :

- 1) For the same erosion resistance, their mechanical properties and their resistance to thermal stresses are greater than those of graphites
- 2) For some of these materials, the rupture mode is ductile compared with the brittle rupture mode for graphites.

However, it has been shown that for a same mean density, the erosion resistance of a carbon-carbon material was greater than that of a polycrystallin graphite.

High density (more than 1.9) carbon-carbon and pyrolytic graphite

In mentioning this type of carbon-carbon materials it is the multidirectional textures densified under high pressures which reach densities closed or greater than 2.0 which are mainly considered. These materials which have given until now the best results among the sepcarbs present, compare to the PG, the following advantages : improved isotropy, low expansion coefficient in the C direction and capability to manufacture large sizes and great thicknesses. These materials have already revolutionized the nozzles design by an extreme simplification. With these materials the nozzles erosion is more regular and reproducible, therefore their performance is better than those which use P.G.

5. FUTURE TRENDS AND CONCLUSION

It has been shown in this paper how much the nozzles design of apogee boost motors have changed during the last 10 years, thanks to the sepcarbs development. We have particularly insisted on the narrow relationship between the density of a carbon-carbon material and its erosion resistance. This principal characteristic together with their physical and thermomechanical properties explain that the carbon-carbons are the optimum materials for nozzle flamefronts, whatever the performances of these nozzle might be. Most particularly for each range of performances, the measured or potential superiority of these materials has been shown when compared with more classical materials : phenolic graphite composites, polycrystallin graphites, pyrolytic graphite. Now it is necessary to perfect our understanding in the field of erosion resistance of these materials in order to obtain more precise relationships than those stated in this paper and to improve these materials.

These sepcarbs can be improved in different ways :

For sepcarbs 2D

- in utilizing resins with chars more performant,
- in improving the CVD process,
- in controlling much better the use of high resistance fibers.

For sepcarb nD

- in utilizing, in certain cases, 5D and 6D to mechanically reinforce one or several directions in the materials.

For all these sepcarbs an other way to improve them is to put in their matrices ultrarefractory products. The main known improvements are :

- higher mechanical properties,
- a better oxydation resistance at high temperatures.

These proven improvements are the results of several years of research and development in SEP. They permit to imagine now nozzles with improved performance in utilizing a "free standing" architecture or deployable exit cone. The weight reduction of the submerged part of the nozzle and the increase of the expansion ratio permit a big increase of the specific impulse. These two important changes in the design of the nozzles having being already successfully tested by SEP we can hope in the future to improve again the propulsion of the apogee boost motors thanks to the development of the sepcarbs.

N80-21449

WACKER RTV-S691, A SILICONE ADHESIVE WITH LOW OUTGASSING RATE

W Hechtl

Wacker-Chemie GmbH, Munich, Germany

ABSTRACT

RTV-S 691 is a flowable, at room temperature curable silicone rubber, consisting of two components. Processing, properties and bonding performance are described.

Keywords: RTV-S 691 silicone rubber, addition curing system, processing, properties, bonding.

1. INTRODUCTION

In cooperation of Wacker-Chemie and AEG-TELEFUNKEN a silicone adhesive was developed which is suitable for space applications and especially for the bonding of solar cells to the supporting structure (Ref. 1 and 2). This adhesive, RTV-S 691, is a flexible material and represents a room temperature curable RTV-2 silicone rubber. It is characterized by the following properties:

It remains flexible at very high and very low temperatures which enables it to balance different thermal expansions and contractions of solar cell and structure.

It has a very low content of volatile components.

Bonding on various substrates is obtained by using Primer G 790.

2. THE ADDITION CURING SYSTEM

Various crosslinking systems are applied in the field of RTV-2 silicone rubber; the most important ones are the so-called condensation cure and the so-called addition cure. RTV-S 691 is an addition-curing RTV-2 silicone rubber. Addition cure was chosen because it offers many advantages compared to condensation cure.

An important advantage of the addition-curing RTV-2 silicone rubber is that during cure no decomposition products are evolved. So there is no need for post-treatment of the material in order to remove volatile components, as for instance open storage at room temperature or at elevated temperatures. Besides that the shrink is very low. Linear shrink values of less than 0.1 % were measured at 23°C. Furthermore there is no influence of volatile components on other materials which would cause a change of their properties.

A further advantage of addition-curing RTV-2 silicone rubber is that in the curing reaction the flexible final product is formed exclusively. The reaction is definite, a reverse reaction, for example upon thermal stress, is not possible. Therefore, there is no danger of reversion. A practical consequence of this fact is that heat cure is also possible, that the film thickness must not be considered, and furthermore, that the material can also be cured in absolutely sealed systems.

A further aspect is the catalyst quantity which is very small with addition-curing RTV-2 silicone rubber. The concentration of the platinum catalyst it contains is about 10 ppm. Since the catalyst may migrate

to the border area of the vulcanizate and cause negative effects, the lowest possible concentration is of advantage.

A further feature is the fact that addition-curing RTV-2 is absolutely harmless to handle and therefore requires no special safety precautions for processing.

3. PROCESSING AND CURE OF RTV-S 691

Adhesive RTV-S 691 is a pourable rubber. Both components A and B are liquids. The A-component is a filler/polymer compound. Since the filler may settle at storage, component A must be stirred prior to processing in order to obtain a homogenous compound. The B-component solely consists of a polymer and does not contain any fillers.

Both components A and B are mixed at a weight ratio of 9:1. Air bubbles which may form during stirring, can be removed preferably under reduced pressure.

Cure starts as soon as both components have been mixed together which is indicated by a raised viscosity. As working time the period of time is defined within which the viscosity at 23°C rises to 200,000 mPa.s; which is within a range of 90...110 minutes. (Fig. 1)

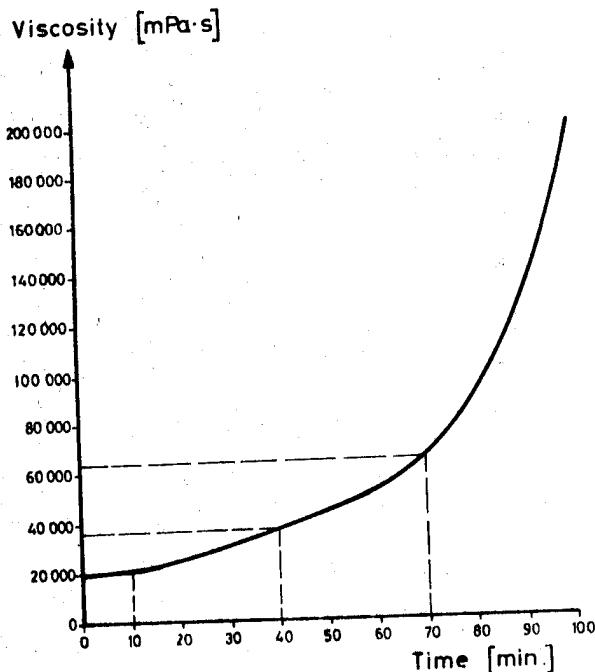


Fig. 1: Slope of viscosity of RTV-S 691 at 23°C after mixing both components

Here must be considered that the viscosity increase and consequently the working time, are highly influenced by the temperature. A temperature increase of 1°C reduces the working time for about 10%; a temperature decrease of 1°C extends the working time for about 10%.

By adding a so-called inhibitor, the working time may be extended; thus a working time of 6 or more hours is possible.

The material may not only be cured at room temperature but also at elevated temperatures. By raising the temperature the curing can be significantly reduced (Fig. 2).

Vulcanization time

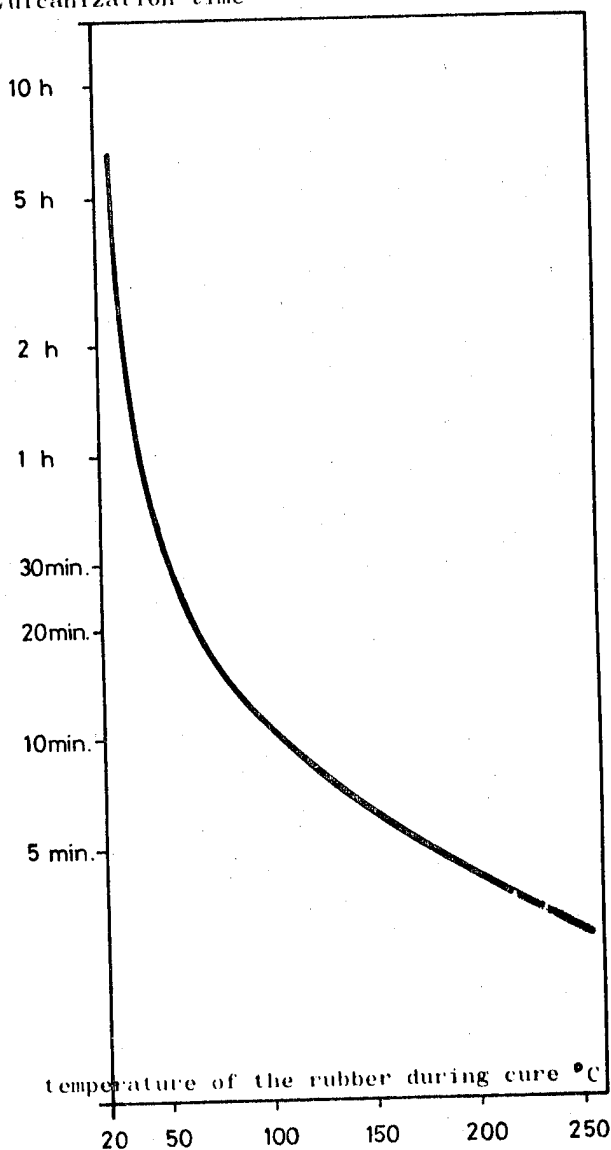


Fig. 2: Curing time of RTV-S 691 versus temperature

Adhesive RTV-S 691 is a very durable product. There is no change to observe in viscosity and curing performance, even after prolonged storage. That's why a storage life of one year is guaranteed.

4. PROPERTIES

A special property of adhesive RTV-S 691 is its low outgassing rate. This low outgassing rate is necessary to avoid contamination of solar cell cover glasses, which would reduce the energy yield. The values were measured by ESTEC. The following rates were established:

TWL (total weight loss):	0.27-0.47 %
VCM (volatile condensable material):	0.03-0.10 %

Another special property of RTV-S 691 is its ability to retain the flexibility even at low temperatures. The brittle point is at -104°C . Young's Modulus is approx. 1.4 N/mm^2 in the range of $+100^{\circ}\text{C}$ to -100°C and increases at temperatures below -100°C to about 9000 N/mm^2 .

The thermal coefficient of expansion of RTV-S 691 is $2 \times 10^{-4} \text{ deg}^{-1}$ above and 4×10^{-5} below the brittle point.

The mechanical property values (Fig. 3) as for instance Shore A, elongation and tensile strength are typical for RTV-2 silicone rubber. Equally typical is the electrical insulating effect, which is for example indicated by the high reading for volume resistivity. It is remarkable that the electrical properties only slightly depend on the temperature.

viscosity of component A (23°C): $55000-70000 \text{ mPa}\cdot\text{s}$

viscosity of component B (25°C): $200-240 \text{ mm}^2/\text{s}$

mixing ratio component A/component B (by weight): 9/1

viscosity of the mixed components (23°C):

$18000-26000 \text{ mPa}\cdot\text{s}$

working time (23°C): 90-110 minutes

total weight lost: 0.27-0.47%

volatile condensable material: 0.03-0.10%

density: $1.41-1.43 \text{ g/cm}^3$

hardness shore A: 50-60

tensile strength: $4.0-6.0 \text{ N/mm}^2$

elongation: 100-160%

young's modulus at 23°C : $1.33-1.53 \text{ N/mm}$

brittle point: -104°C

volume resistivity: $10^{14} \text{ Ohm}\cdot\text{cm}$

Fig. 3: Some typical properties of RTV-S 691

We especially checked the heat stability and the mechanical properties, i.e. Shore A, elongation and tensile strength after storage at 180°C (Fig. 4). Initially there are relatively insignificant changes. However, the values stabilize with increasing storage.

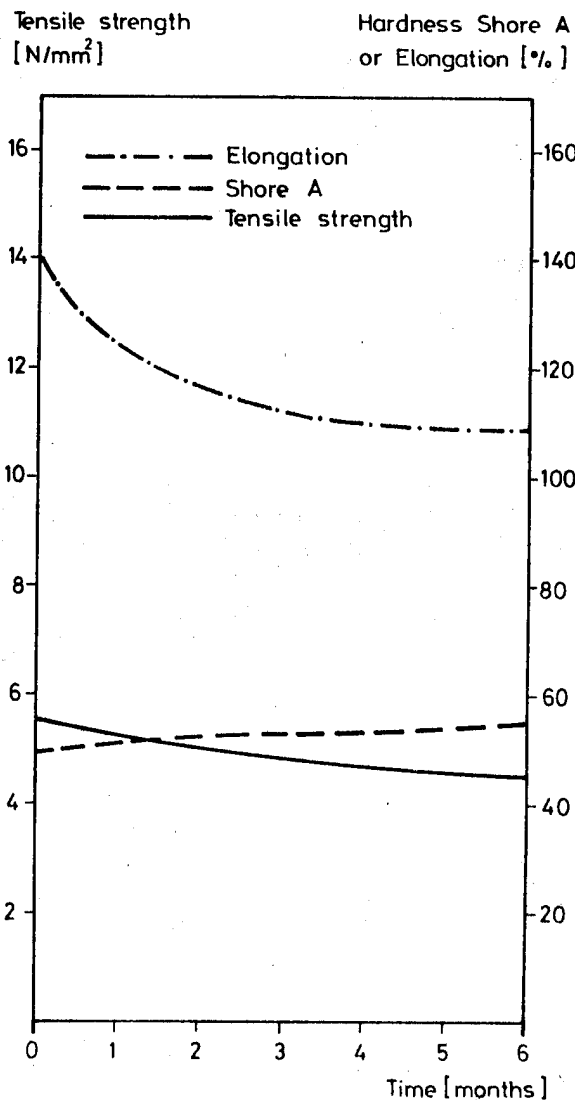


Fig. 4: Change of mechanical properties at 180°C storage

5. BONDING

The stability of the addition-curing rubber RTV-S 691 is based on the fact that only a small content of reactive chemical groups remains in the network of the cured material. The consequence however is its poor capability of adhering to other substrates. Therefore it is essential that a primer be used when RTV-S 691 is applied as an adhesive.

Therefore, two operations are necessary:

1. Treatment of surface with a primer.
2. Application and cure of the rubber.

Primer G 790 has proven quite successful. G 790 is a liquid which is applied on the surface of the substrate in a thin layer by dipping, spraying or brushing. After drying for 1 hour at room temperature, the solvent has evaporated and a thin resin film has formed. Subsequently the silicone rubber is poured and cured.

In order to establish the qualification of RTV-S 691, the bonding properties in connection with primer G 790 were tested quite extensively. At this the bond with materials like glass, aluminum, polyester-coated Kapton, solar cell silver etc. was tested. Besides that the test specimens were exposed to the following conditions:

1000 thermal cycles (+100/-180°C);
high temperature storage (+200°C, 50 h);
humidity storage (+60°C, 96 h, over
95 % rel. humidity).

When peel tests were performed to check the bond, it was found that the rubber could only be peeled off the substrate by destroying the rubber. This indicates that the bond is stronger than the mechanical strength of the rubber.

Further bonding tests were performed on various plastics (acrylate, epoxide, polyester, polyurethane resins) and metals (iron, steel, copper, zinc) with positive results. It was found that occasionally baking of the primer (10 minutes at 100-150°C) is preferable to drying at room temperature to obtain better bonding to metal.

6. CONCLUSION

RTV-S 691 was developed for a special application, that is bonding of solar cells to the structure. This application called for special product properties of viscosity, Shore A, elongation or Young's Modulus etc. These properties can be varied within an extensive range should this be essential for the solution of other application problems.

7. REFERENCES

1. J. Koch: Some current developments in solar array technology at AEG-TELEFUNKEN, Proc. 1. ESTEC Symposium, Noordwijk, 1978
2. W. Hechtl: Development of a low outgassing silicone adhesive, BMFT-Research Report 01TO 075A-Z12 WRT 2075 (1977)

THE USE OF MoS_2 LOADED GREASES IN ANTENNA
DESPIN MECHANISMS UNDER SIMULATED SPACE CONDITIONS

B. H. Baxter

British Aerospace, Dynamics Division,
Stevenage, Herts, England

ABSTRACT

Ball bearings, lubricated with MoS_2 lubricated grease, and test run at 100 rpm and 10^{-6} torr have been examined after running periods of 13,000 to 50,000 hours. One pair, having minimum lubricant levels showed an increase in torque during the test, and analysis showed extensive chemical modification to the lubricant. In contrast the second two pairs of bearings which had been lubricated with an excess of the same grease ran for 38,000 and 50,000 hours respectively. No chemical degradation was found and the bearings were in near perfect condition. The role of the MoS_2 under the conditions of this test is questioned in the light of the results obtained.

Keywords: Lubrication, Space Conditions, Molybdenum Disulphide, Ball Bearings.

1. INTRODUCTION

As part of the continuing programme of technological research, the Space Mechanism Group at ESTEC, placed a contract (No. 763/69 AA) on The Marconi Company Ltd., Space and Defence Division. Part of this contract called for the design and construction of bearing test rigs to simulate space conditions for the life testing of lubricants for antenna despin bearings. The basic requirement of the test programme was to compare the two main lubricant techniques available for this application, namely dry metal coated and grease lubricated bearings. A possible variant of the organic lubricant technology, a capillary feed oil reservoir, was not included in the programme.

Details of the mechanical design of the test rigs, the testing conditions, and the results obtained are contained in Contractor Report ESRO C.R. 91.

As the MDSR results began to accrue, the need arose for the 'surface chemical' examination of bearings which had either been rejected at an intermediate stage in the tests, or had completed the intended life period.

This work was carried out under ESTEC contracts, by The Materials Science Group of British Aerospace, Stevenage (previously British Aircraft Corporation). This small laboratory situated within Precision Products Group had built up the facilities and experience essential to the support of the Company's own defence contracts in the instrument development and manufacturing field, and we were pleased to assist ESTEC in their work.

Owing to the protracted time scale of the tests, the M.S.G. bearing examinations also spanned a considerable length of time. The first pair of bearings was reported on in May 1975 (1), the second pair in July 1977 (2) and the third and final pair in January 1978 (3). Furthermore the first report* described the results of the first pair of bearings, and the implications therefrom in isolation, and it was not until all three sets of bearings had been examined that a better overall picture emerged. This paper therefore provides a useful opportunity to describe the work in its entirety, and consequently to present a better summary than might be obtained from a study of the three individual reports.

2. TECHNICAL DESCRIPTION OF BEARINGS

All the bearings were of the same type, manufactured by the Fafnir Bearing Corporation (catalogue No. 3MM 9112 W1/CR) as specified below:-

Semi separable type
25° contact angle
60 mm bore
95 mm Outer diameter
18 mm width
Ball complement 19 (single row)
Ball diameter 10.31 mm
Retainer: One piece fabric
reinforced phenolic resin
Ring and ball material: vacuum
degassed 52100 steel

Each test rig contained four identical bearings, and the design of the rig was such that two of the bearings carried combined axial and radial load, and two radial loads only.

* This report provided the basis for a previous presentation by the Author at the First Space Tribology Conference in Frascati in April 1975.

In all of the tests the axial and radial loads were the same at 40N, and the rotational speed was 100 r.p.m. In each case one bearing with radial load and with radial and axial load was submitted.

3. EXAMINATION OF THE FIRST BEARING PAIR

This set comprised bearing no. 19 (axial and radial loads), and bearing no. 21 (radial load only). Each had been lubricated with minimum levels (100 mg) of BR2-S, Molybdenum Disulphide loaded grease, and the retainers had been preimpregnated with approximately 50 mg of lubricant base oil.

The test had been run at ambient temperature and 10^{-6} torr. The initial, satisfactory period of the test was 9000 hours (one year orbital life) but on continuation of the test, the combined torque of the four bearings in the test rig rose sharply and the test was discontinued after 13,000 hours (one year five months orbital life).

3.1. Laboratory Examination

A standard sequence was established for the bearing examination as follows:-

- (a) Preliminary low power examination and macro-photography.
- (b) Controlled disassembly.
- (c) Detailed microscopy and micro-photography of bearing raceways, ball surfaces and retainers.
- (d) Micro infra-red spectrophotometry of lubricant residues.
- (e) Methylation gas chromatography of lubricant residues.

3.2. Description of Results Physical Examination

(The most significant changes to the lubricant had occurred in bearing no. 19 which had run with a combined axial and radial load, and thus to simplify the description, the results are confined to this bearing).

Both inner and outer raceways carried a viscous, apparently non-wetting residue of lubricant. At higher power the non-wetting nature of the lubricant was shown by the fact that regions of the surface film disturbed by bearing disassembly did not re-spread over the bearing surface, (Figure 1).

A small sample of lubricant residue removed from the inner track and examined as a thin film in light transmission microscopy showed none of the features of the unused grease. Instead of the birefringent particles of soap thickener and characteristic lamellar particles of the disulphide, the 'worked' lubricant in the raceways showed an array of barely resolvable particles of MoS₂ and no thickener.



Figure 1. Modified Lubricant:
Track of Bearing 19

Ball contact with the retainer pocket had produced a highly characteristic witness (Figure 2). This consisted of grey relatively greasy zones on either side of an inner dark brown polished zone, which varied in width due probably to small variations in ball pocket geometry.

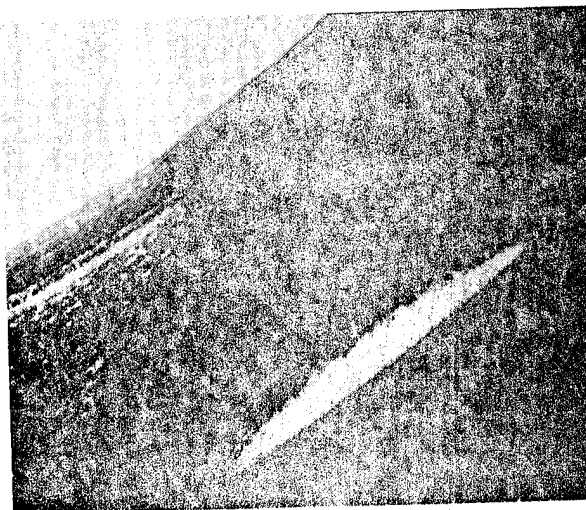


Figure 2. Retainer Ball Pocket
Witness: Bearing 19

3.3. Chemical Examination of Lubricant Residues

3.3.1. Infra-red. The complete list of infra-red spectra obtained in this phase of the work is shown in Table I.

Table I. IR Spectra from Low Level
BR2S Grease Bearings

IR1	BR2-S	Grease (unused)	(thin film)
IR2	BR2-S	Grease (unused)	(KBr microdisc)
IR3	BR2-S	Base oil	(thin film)
IR4	BR2-S	Base oil	(KBr microdisc)
IR5	Nylon Reservoir oil		(thin microfilm)

Table I. continued

IR6	Oil from 100 rpm rig end-flange	(thin microfilm)
IR7	Outer land Bearing 19	(microdisc)
IR8	Inner track Bearing 19	(microdisc)
IR9	Ball deposit Bearing 19	(microdisc)
IR10	Brown deposit from ball pockets Bearing 19	(microdisc)
IR11	Grey deposit from ball pockets Bearing 19	(microdisc)
IR12	Outer land Bearing 21	(microdisc)
IR13	Inner track Bearing 21	(microdisc)
IR14	Ball deposit Bearing 21	(microdisc)
IR15	Brown deposit from ball pockets Bearing 21	(microdisc)
IR16	Grey deposit from ball pockets Bearing 21	(microdisc)

The IR compositional changes seen are clearly shown in Figure 3 which contain a group of five of the IR spectra listed in Table I. A was obtained from a static unworked grease sample from the land of bearing 19, and was virtually identical with a spectrum of unused grease, except for a slightly increased relative abundance of thickening agent (sharp bands 1585 and 1565 cm⁻¹) due to evaporative loss of base oil fractions. In contrast spectrum B, of worked samples from the raceways of bearing 19 shows almost total loss of thickening agent and considerable degradation of the hydrocarbon CH deformation bands near 1400 cm⁻¹. The retainer ball pockets from bearing 19 provided the samples for IR D

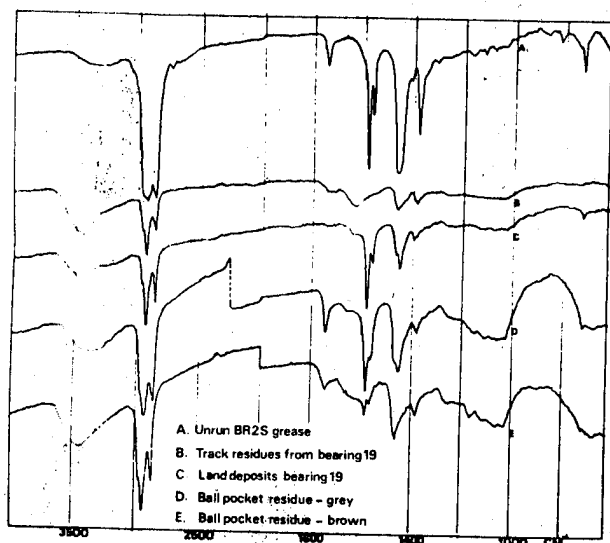


Figure 3. Micro IR of Bearings 19 and 21 Residues

and E. In this pair, curve D, from the grey grease residues, shows an enhancement of the thickening agent, whilst the central brown witness curve E exhibits the same degradation effects found in the bearing tracks.

3.3.2. Gas chromatography. The composition of BR2-S grease was given as 85% mineral oil, 3.5% ester oil, 9% lithium soap thickening agent and 3% molybdenum sulphide (% w.w.). Since the fatty

Table II. Relative Fatty Acid Abundance in BR2-S Grease

FATTY ACID	FROM ESTER	FROM Li. SOAP	% FATTY ACID IN GREASE	RELATIVE ABUNDANCE IN GREASE
Lauric	C12	0.60	0.00	4.76
Myristic	C14	1.00	0.09	8.65
Palmitic	C16	1.72	0.72	19.4
Stearic	C18	0.16	1.17	10.6
Oleic	C18	0.12	0.27	3.10
Linoleic	C18	0.00	0.27	2.14
12 Hydroxy Stearic	C18	0.00	6.48	51.4
TOTAL		3.60	9.00	100.05

Table III. Relative Abundances of Major Fatty Acids in Bearing Samples and Unused Lubricants

Sample	Lauric	Myristic	Palmitic	Oleic	Stearic	12-OH Stearic
Theory	4.8	8.7	19.4	10.6	5.2	51.4
BR2-S Grease	1.6	4	13	14	14	53
Land Bearing 19*	0.5	3	13	23	45	15
Ball Bearing 19	2.9	7	31.5	22	33	3.3
Track Bearing 19	3.2	10	26	28	27	6.5
Land Bearing 21*	1.6	7	20	17	51	2.5
Track Bearing 21	1.9	6.5	27	20	33	11

* Sample consisted of running debris not unused grease

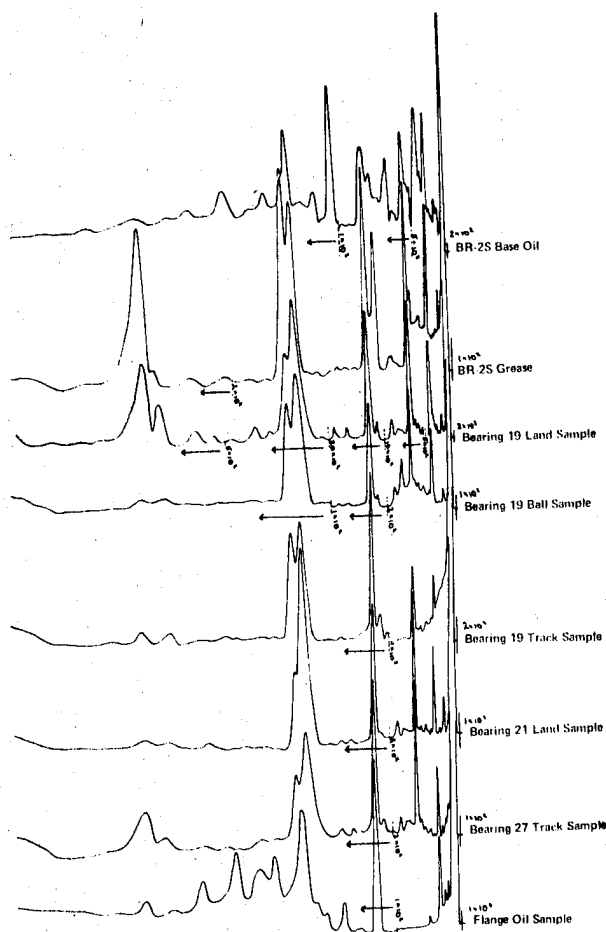


Figure 4. Gas Chromatograms of residues from Bearings 19 and 21

acid composition of both the ester oil component and the thickening agent were known in detail, the final fatty acid distribution and relative abundancies in the whole grease could be calculated.

Free fatty acids and fatty acid derivatives such as higher esters are not ideal subjects for gas chromatography owing to their low vapour pressure. Fatty acid soaps are completely non-volatile. However, if the fatty acids are converted to methyl ester derivatives, good separation and detection can be achieved in sensible times, using reasonable column temperatures.

Using a micromethylation technique, which converts any fatty acid derivative into the corresponding methyl ester, the fatty acid distribution in lubricant samples taken from various locations within the bearings was determined.

The results obtained are shown both in Table III and Figure 4, which is a composite of gas chromatograms of lubricant samples.

4. DISCUSSION OF RESULTS FROM EXAMINATION OF BEARINGS 19 AND 21 (MINIMUM BR2-S GREASE)

It was obvious from the physical examination of this pair of bearings that considerable chemical alteration of the lubricant had occurred during test running in vacuum. These changes, which were confined to the worked lubricant on balls and raceways had resulted in the formation of a thick and immobile product which would explain adequately the increase in running torque.

Micro-infra red analysis of samples taken specifically from sites on the raceways which showed the highest levels of physical changes, also indicated considerable compositional change. The major characteristic of the IR of the worked grease was however, a loss of thickening agent which should have caused a reduction in lubricant body rather than the stiffening described.

It was in the methylation gas chromatographic analysis results that the most dramatic changes were found.

As shown in Table II above, the thickening agent in BR2-S grease was almost entirely lithium 12 hydroxy stearate, and this acid therefore comprised 51.5% of the total fatty acids of the finished lubricant. In Table III (and Figure 4) it will be seen that methylation GC of the unused grease gave a result of 54% 12 hydroxy stearic acid, in reasonable agreement with the theoretical figure.

However, identical analysis of worked samples from the raceways of bearings 19 and 20 (Table III) showed that the abundance of this acid fell to very low values, especially on the track samples (e.g. bearing 19, 3.3%). At the same time the abundance of C₁₈ fatty acids, both saturated and unsaturated showed a very significant increase over the determined values in the unused grease.

The simple explanation that the running lubricant in the test bearings, that is the lubricant confined to the surfaces of ball and raceways, had become diluted with base oil by transfer from the retainer, could not be reconciled with the analytical results obtained. Since the base oil contained 5% of esters, only 7% of which were C₁₈ acids, this is the maximum abundance of these acids which could be reached even if the running lubricant were composed entirely of base oil from the retainer.

The interesting possibility was proposed therefore, that the 12 hydroxy stearic acid in the initial grease charge had been decomposed during the life test of the bearing, and further that this decomposition had led to the formation of C₁₈ derivatives. It was suggested that metal to metal contact under vacuum was the most likely cause of this degradation.

In addition to the chemical alteration to the major fatty acid of the thickening agent it appeared that the lithium soap structure had been lost and that some degree of lubricant polymerisation had occurred.

5. CONCLUSIONS FROM THE FIRST STAGE OF THE BEARING STUDY

The results described in summary above, pointed to the simple conclusion that thin organic lubricants were incompatible with the space environment. Lubricant decomposition in 'zero oxygen' conditions had been demonstrated previously (4) and these results appeared consistent with established opinion. The argument in favour of dry, metal coated bearings appeared therefore to have gained ground as a result.

A further significant result from this preliminary examination, was that the molybdenum sulphide did not appear to have contributed significantly to the life of the lubricant.

6. EXAMINATION OF THE SECOND PAIR OF BEARINGS

During 1977 our laboratory received the second pair of bearings from the MSDS tests. This pair (Nos. 16 and 17), which had run under identical load, pressure and speed conditions as for the first pair, had in contrast been lubricated with 3.7g of BR2-S lubricant per bearing, and the retainer had, as previously been vacuum impregnated with approximately 70 mg of base oil.

The bearings had been run at satisfactory torque levels for 38,500 hours (approximately four and one half years of orbital life) and the test was terminated at the end of the contractual period.

6.1. Physical Examination of Bearings 16 and 17

The same sequence was applied to this bearing pair as described above for the first pair.

After preliminary low power examination the bearings were dismantled. The best illustration of the condition of the running surfaces was afforded by the periphery camera photographs of the inner races and retainers which are shown in Figures 5 and 6.

As can be seen from these photographs, which comprised 90° segments of each bearing component, the majority of the BR2-S lubricant had not been directly involved in the bearing lubrication.

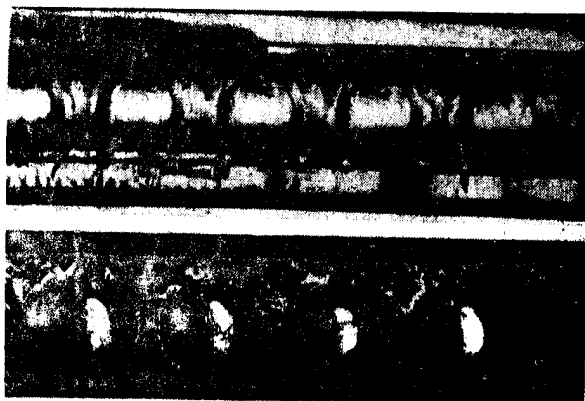


Figure 5. Periphery Photographs of Bearing 16, Inner Race and Retainer

Most of the grease, which was applied mechanically to the bearings, had remained on both sides of the retainer forming, as it were, an extension to the retainer which surrounded the balls almost completely.

The surface of the balls and both raceways were coated with a thin mobile film of lubricant which differed markedly from the opaque grey BR2-S in that it was a light red-brown in colour and almost transparent. (These effects will not be apparent in the monochrome reproductions of this reprint, but show clearly in the colour slides which will accompany the presentation).

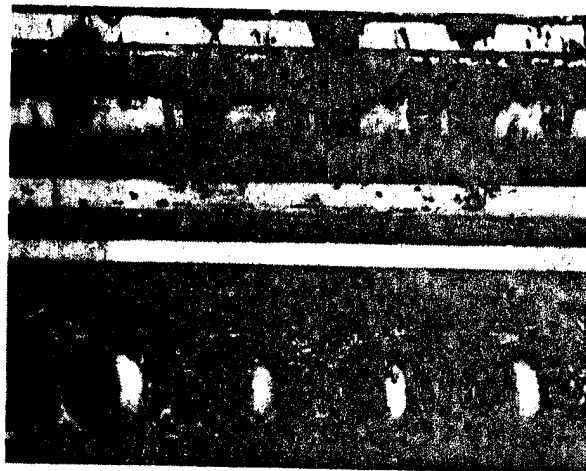


Figure 6. Periphery Photographs of Bearing 17, Inner and Retainer

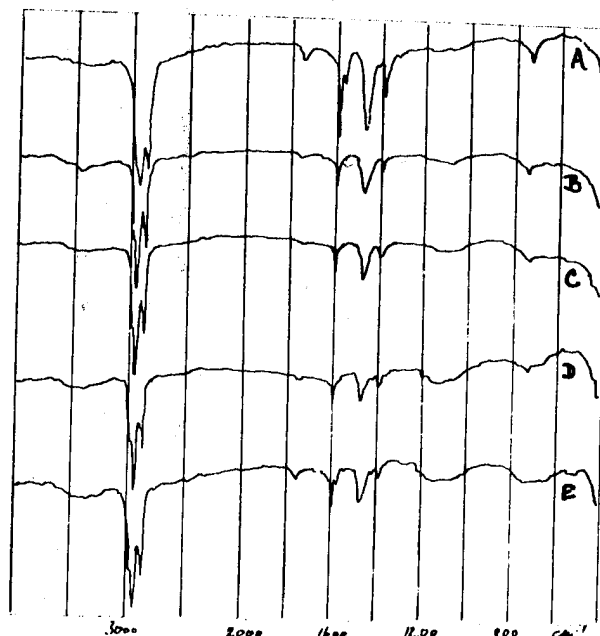


Figure 7. IR Spectra of Bearing 16
Lubricant Samples: A Unused
B/C Track 16 D/E Track 17

High power microscopic examination of parts of the raceways and ball surfaces, which had been washed free of lubricant indicated that virtually no wear had occurred. There was evidence however of some wear on the inner race retainer contacting land, which had been worn smooth. Some transfer of retainer material was found in this region of the bearing also.

The retainer pockets were perfectly lubricated by a thin film of the 'worked' lubricant described above. No wear was found and the visual evidence indicated a low friction ball/pocket contact through the whole of the test.

6.2. Chemical Analysis of the Lubricant

6.2.1. Infra-red analysis. As before, micro-samples were collected at specific sites across the bearing raceways and tracks. In fact six samples were taken per 'transit', three on the lands and three in the raceway. The results obtained are shown in Figure 7, which is a composite of spectra, comparing an unused grease (Curve A) with worked samples from a single transit of the inner raceway.

6.2.2. Methylation gas chromatography. Further land and track samples were collected and analysed as before by micromethylation and gas-chromatography.

It should be emphasised that this analytical technique detects and measures only the fatty acids present in the lubricants. The results, expressed as relative abundancies of the

Table IV. Relative Abundancies of Fatty Acids in Bearings 16 and 17 (High Level BR2-S)

Bearing No.	Sample	Relative Abundance (%)				
		Lauric	Myristic	Palmitic	C18*	120 H Stearic
16	2	1.7	3.9	10.6	24.2	59.6
16	3	1.2	4.9	12.3	15.5	66.0
16	4	0.85	3.0	14.0	32.9	49.0
16	5	1.25	3.0	13.4	21.1	61.1
16	6	1.2	2.7	13.5	28.5	53.9
17	(2	1.3	3.8	28.7	59.4	6.7)
17	3	0.7	2.8	11.6	25.7	59.0
17	4	0.5	2.6	10.6	43.7	9.2
17	5	0.6	2.8	10.9	48.3	37.3
17	6	0.2	2.3	8.4	47.2	41.8
Unrun BR2-S Theory		4.8	8.7	19.4	15.8	51.4
As measured		1.6	4.0	13.0	28.0	53.0

* Combined stearic and oleic acids

important fatty acids are collected, together with information on their respective site within the bearings in Table IV below.

6.3. Physical Examination of Lubricant Samples

6.3.1. Optical microscopy. As described above, the active lubricant, that is the relatively small portion of the total bearing lubricant charge which had been in use during the test, had a totally different appearance to that of the original. Small samples were taken from different sites within the bearings, dispersed gently in a transparent medium, and viewed by transmission optical microscopy.

The results obtained are shown in Figures 8 and 9. In Figure 8 a sample from the bearing land (virtually unused) and in Figure 9 a highly worked sample from the centre of the ball track in Bearing 16.

6.3.2. Electron micro-probe analysis. Samples of active lubricant, similar to that shown in Figure 9 were collected from the retainer ball pockets and the tracks, transferred to a micro-probe sample holder and carbon shadowed.

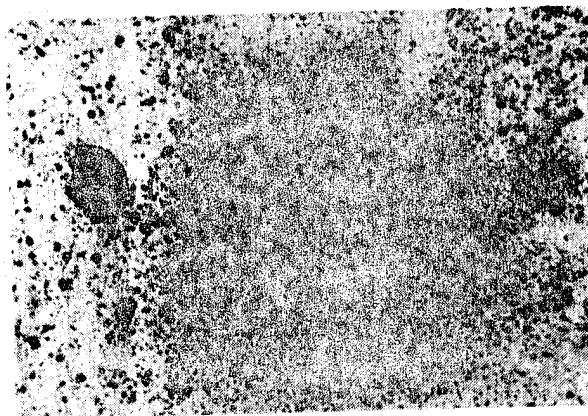


Figure 8. Unused Lubricant: Bearing 16

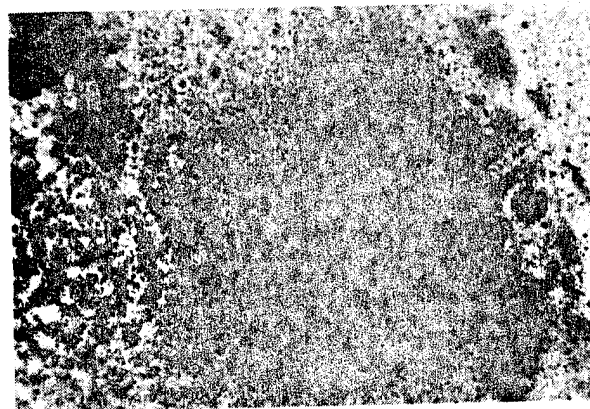


Figure 9. Used Lubricant: Bearing 16

The X-ray output from the ball pockets and the raceways and a sample of unused grease are shown in Figure 10.

From this analysis it was shown that in addition to molybdenum from the MoS₂ additive, and iron present as low level wear debris, both the ball pocket sample and, to a lesser extent, the track samples contained significant levels of lead. As examined, i.e. as a thin film in EMPA, the unused BR2-S grease gave no lead X-ray output.

(Subsequently atomic absorption analysis was applied to these, and lubricant samples from the third bearing. The results of this later work are described in the next section).

6.4. Electron Microprobe Analysis of Raceway Surface

The final stage of the examination of these bearings was to remove the grease, and lubricant residues from the outer raceway, using simple solvent washing; the surface was not scrubbed. A 5mm wide section was then cut transversely through the race, and mounted on the EMPA specimen holder.

Element scans from 0 to 20 KeV were then made across the ball track, but no elements other than the alloying constituents were found. High sensitivity checks were made both for molybdenum and lead, but neither element was detected.

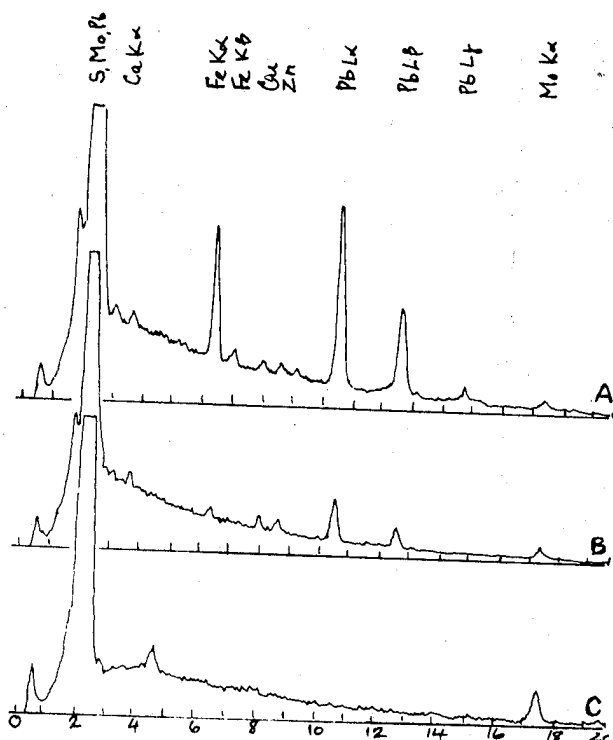


Figure 10. EMPA of Bearing 16 Residues:
A retainer B track C unused grease

7. DISCUSSION ON EXAMINATION OF HIGH LEVEL BR2-S LUBRICATED BEARINGS

The simplest description of this pair of bearings, when examined after 38,500 hours of running (in vacuo) was that they were in near perfect condition. In marked contrast to the first pair of minimally lubricated bearings, in which the BR2-S grease had been converted into a firm rubbery product, the active lubricant in this later pair was unchanged and fully fluid.

Both the IR analysis, Figure 7, and the gas chromatographic analysis in Table , confirmed that the lubricant had suffered little if any chemical degradation. Comparison of curve A Figure 7, the IR spectrum of unused grease, with each of the other spectra, which were of worked track samples shows that each was virtually identical to the unused oil.

Each track sample showed the sharp band at 1585cm⁻¹ due to the lithium soap at virtually constant ratio to the CH deformation band alongside. Comparison of these four spectra of worked lubricant with the IR spectra of track samples taken from the minimally lubricated bearing 19, (Figure 3) clearly illustrates the extent of the degradation which had occurred in the first pair of bearings, and serves to accentuate the remarkable stability achieved with the same grease in the second bearing pair.

Similarly an examination of the quantitative gas chromatographic data in Table IV shows that the 12 hydroxy stearic acid was retained unchanged in the samples from bearing 16, in fact its abundance was slightly higher than that in the unused grease, due probably to slight evaporative loss of base oil.

There was a greater tendency for loss of 12 hydroxy stearic acid to be apparent in the bearing 17 samples. Only one sample (3) was close to the unused level, two others were slightly reduced, and two were very low. At the same time the C18 acid abundance in the samples was significantly greater than that of the unused grease. It is possible that the lubricant degradation which had occurred in the first bearing pair had begun to be apparent, albeit to a lesser extent, in bearing 17.

The differences in lubricant life between the minimally lubricated bearings and the second pair, appeared to be related solely to the presence of excess grease in bearings 16 to 17. However, the whole of this grease charge was not used in a continuous circulating process in which all the grease in the bearing was continuously exposed to ball/race shearing. The greater part of the grease remained where it had been placed when the bearings were loaded, and only a thin film of lubricant on ball and track surfaces was "active" during the test.

Whether there was continuous exchange between this "active" lubricant zone and the liquid (base oil + some thickener) phase within the grease reservoirs must remain a subject for conjecture, but if this were the mechanism then it would help to explain the remarkable chemical

stability exhibited by this grease after 38,500 hours running, since by a process of constant renewal the "contact time" in the bearing load zone would be significantly reduced and hence the rate of chemical degradation would also be less.

The examination of these bearings showed very clearly that, notwithstanding the possibility of oil interchange between the static grease and the active working lubricant film, there was no transfer of molybdenum disulphide from the static grease into the ball/track load region. The micrographs of unused grease (Figure 8) and worked lubricant (Figure 9) demonstrates clearly that the original particles of molybdenum disulphide had been considerably reduced in size by the rolling action of the balls, and had not been replaced with fresh material during the life of the test.

8. EXAMINATION OF THIRD BEARING PAIR, NUMBERS 11 AND 14

This pair of bearings had also been lubricated with an excess of molybdenum disulphide loaded grease, but instead of the BR2-S used in the previous two bearing pairs, Molykote LT-2 was applied.

The lubricant charge was 3.66g of grease per bearing, and as before the retainers had been vacuum impregnated, prior to assembly with approximately 50mg of base oil.

The bearings had completed some 50,000 hours of test under vacuum in MSDL rig no. 4. This test, equivalent to 5.7 years of orbital life was a highly satisfactory demonstration of lubricant and bearing durability.

9. EXAMINATION OF BEARINGS

This followed exactly the same sequence as that described for the previous bearing pairs except for the addition of the atomic absorption measurement of lead in the lubricant and the electron-microprobe analysis of heavy metals in the lubricant residues in the bearing raceways.

9.1. Optical Microscopy and Microphotography

The condition of the raceways and the lubricant condition and distribution within the bearings are best summarised by the periphery photographs of segments of the inner races and retainers of the two bearings, which are shown in Figures 11 and 12.

As in the high-level BR2-S lubricated pair the bearings showed the large excesses of greases adhering to the retainer and surrounding the balls. The ball surfaces and the tracks were evenly coated with a fluid film which was red/brown in colour.

The contacting land of the inner raceway was liberally coated with a thin film of transparent oil, apparently transferred from the retainer.

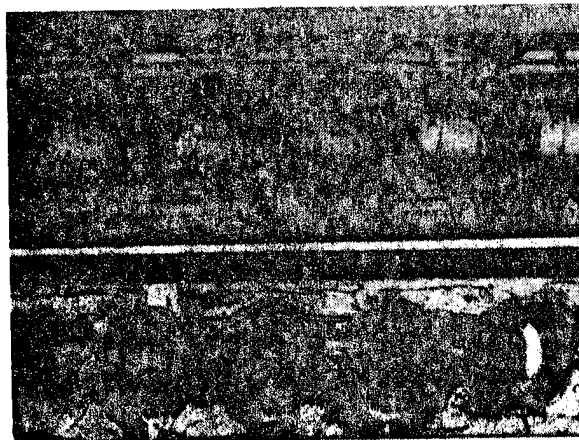


Figure 11. Periphery Photographs of Bearing 11



Figure 12. Periphery Photographs of Bearing 14

9.2. Transmission Microscopic Examination of Lubricant Samples

Small samples taken from the lands and across the raceways of the bearings showed the same variations as those described in the previous bearing pair. The 'unused' grease of the lands was identical with fresh samples of the grease, MoS₂ particles ranging in size from 1 to 50 μ m were visible together with the brightly birefringent particles of lithium soap.

A corresponding sample from the centre of the ball track was quite different, very few recognizable MoS₂ particles were detected, but the lithium soap particles remained at a readily detectable level.

9.3. Micro Infra-Red Spectroscopy

Selected, low volume samples taken from characteristic sites in the bearings were analysed by IR spectroscopy and the results obtained are shown in Figure 13 in comparison with two spectra of unused LT-2 grease.

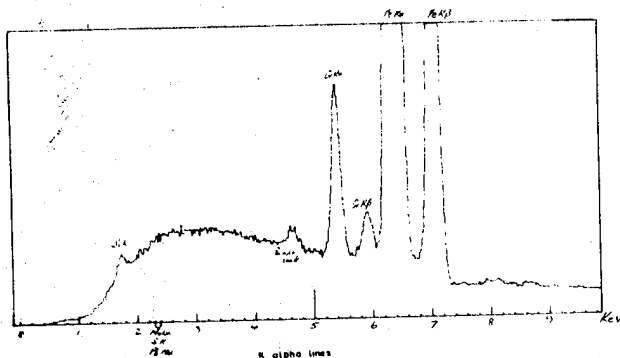


Figure 14. EMPA of Bearing Surface (Rinsed)

10. DISCUSSION OF RESULTS FROM EXAMINATION OF BEARINGS 11 AND 14

This examination showed that a virtually identical lubrication mechanism had operated in this pair of bearings as that found in the other high level lubricant pair, nos. 16 and 17.

The same static distribution of the majority of the grease was found, surrounding the balls, and apparently acting as a lubricant reservoir, maintaining a good fluid film to the ball/raceway contact.

One slight difference was found in comparison with the BR2-S lubricated pair, in that the active lubricant in the LT-2 lubricated bearings was low in lithium soap thickening agent and appeared to consist of a high proportion of free base oil.

Very little evidence was found in this pair of bearings for transfer of particulate molybdenum disulphide from the static lubricant in the working regions of the bearing. Electron microprobe analysis of worked samples of the lubricant confirmed that both molybdenum and sulphur were present, but the characteristic lamellar particles of MoS_2 were not detectable optically. It is concluded that the MoS_2 present originally in the working regions of the bearings was reduced in size by the grinding actions of the balls, until the average particle size was less than the resolving power of the light microscope ($< 1\mu\text{m}$).

Atomic absorption analysis of both BR2-S and LT-2 greases confirmed that they both contained lead at approximately 1%.

However, electron microprobe analysis of the ball tracks failed to show any evidence of preferential deposition of any of the elements lead, molybdenum or sulphur. It is possible that the method employed was not sufficiently sensitive, or that the geometry of the analyser prevented the detection or "seeing" the X-ray output from the lowest part of the raceway groove.

11. GENERAL DISCUSSION OF THE RESULTS OF LUBRICANT ANALYSIS OF THE THREE BEARING PAIRS

It must be concluded that the failure of the first pair of bearings which resulted in severe lubricant degradation and a resultant rise in running torque, was due simply to an inadequate level of lubricant in the bearing. This low level (100 mg of grease per bearing) meant that

virtually all of the lubricant charge was in constant contact with the running surfaces of the bearing. Consequently lubricant degradation was relatively rapid, and was in an advanced stage after 1300 hours.

The contrast, both in performance and the condition of the lubricant between the low level grease pair, and the bearings with high levels of grease, was very marked.

In both the high level BR2-S lubricated and LT-2 lubricated bearings, the excess grease appeared to have acted as an effective lubricant reservoir, maintaining a near perfect level of fluid lubricant to the active sites in the bearings. Very little evidence was found of lubricant degradation and this technique would appear to offer a cheap and easily applied method for the lubrication of space mechanisms.

There remains however the question of the role of the molybdenum disulphide in both the test greases.

In his review of molybdenum disulphide lubrication (5) Professor Lansdown reports very little on the use of this additive in rolling element lubricants.

If one takes the normally accepted view that the MoS_2 acts as a solid lubricant by virtue of its low basic plane shear, and that effective dry (and lubricated) sliding has been achieved by buffed-on films of the sulphide, then the presence of this material in the test lubricants could be seen as the intentional addition of a 'back up' lubricant. If this were the case, then some evidence of surface deposition in areas of high load in the bearings could have reasonably been expected.

In none of the six bearings examined was there any evidence of this effect. Furthermore there was no renewal of MoS_2 in the active lubricant of the bearing, and the material present initially in this 'working' lubricant was reduced in particle size such that it was below the resolution limit of the microscope. Since a reduction in average particle size increases the proportion of edge (non OOl plane) surface of the MoS_2 , its effectiveness as a lamellar lubricant would also be reduced.

From the results of our investigation of the six bearings described, it appears that the MoS_2 did not contribute significantly to the results achieved.

11. REFERENCES

- (1) BAe Technical Report ST: 13510
- (2) BAe Technical Report ST: 18573
- (3) BAe Technical Report ST: 19509
- (4) J.A. Jones, H.D. Moore and N.A. Scarlett. Grease lubrication of ball bearings in helium. Paper 1 Symposium of lubrication in hostile environments
- (5) Swansea Tribology Centre Report 77/363. Molybdenum Disulphide Lubrication, a continuation report. A.R. Lansdown.

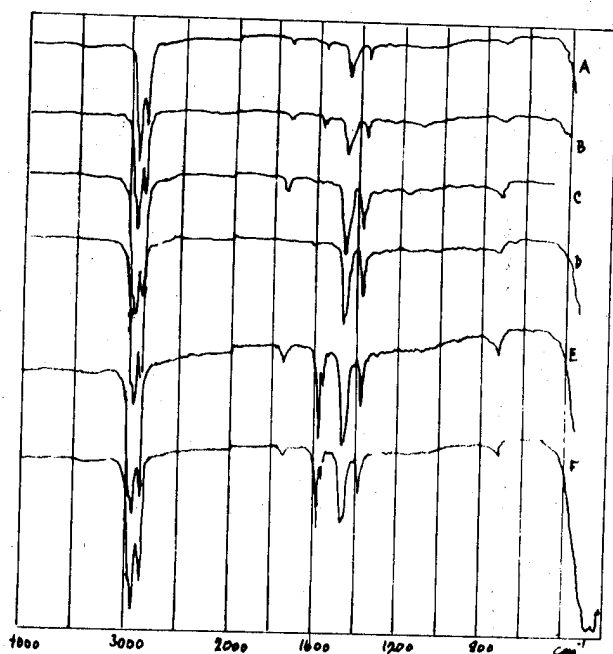


Figure 13. Micro IR of Bearings 11 and 14:
A bearing 11 outer, B track 14
inner: C free oil bearing 11
retainer: D pump end oil Reservoir:
E unused grease from retainer 11
F land of 11 outer

All the samples examined showed a consistent pattern; the unused grease from a non-active part of the bearing showed the normal distribution of band intensities for the thickening agent and the base oil. All samples from active sites, e.g. track, inner retainer contacting land inner surface of retainer etc., showed a considerable reduction in soap intensity relative to the hydrocarbon band at 1460 and 1380 cm⁻¹. This was a clear indication of a high concentration of free base oil in the active lubricant of the bearing.

9.4. Methylation Gas Chromatography

As described above this analytical technique allows the fatty acid distribution of micro-samples from the bearing to be determined, and hence the relative contribution of various lubricant components at a given site can be estimated. The results obtained by this method, and shown in Table V confirmed the dilution effect shown in the micro IR analysis.

9.5. Atomic Absorption Analysis

EMPA analysis of bearing residues from both bearings 11 and 14 showed the presence of lead, as was reported from a similar analysis of bearings 16 and 17 (BR2-S grease).

To establish finally the source of this element, fresh samples of both LT-2 and BR2-S grease were ashed down repeatedly with concentrated nitric acid and the resulting solution diluted and analysed by atomic absorption. The results are shown in Table VI.

9.6. Electron Microprobe Analysis of Bearing Surfaces

The lubricant layer was removed from the outer race of bearing eleven by solvent washing and a transverse section was then prepared. This was mounted in the analyser such that the electron beam impinged normal to the ball track. Element scans were then made across the track but no elements other than the constituents of the bearing material were found. Molybdenum sulphur and lead were searched for at high sensitivity but none was found. The EMPA output is shown in Figure 14.

Table V. Fatty Acid Distribution in Bearing Samples from Bearings 11 and 14

Bearing and Sample Site	Relative Abundance			
	C ₁₆	C _{18:1}	C ₁₈	12 OH Stearic
Bearing 11				
Inner				
land	8.5	35.6	8.4	47.5
track	8.7	34.5	16.2	40.6
land	7.2	14.7	16.7	61.8
Bearing 14				
Inner				
land	16.8	37.5	23.1	18.6
track	9.3	17.0	18.7	55.0
land	6.2	9.3	15.4	69.1
land	6.7	8.7	14.0	70.6
Unused LT-2 Grease	2.6	17.5	14.2	65.7
LT-2 base-oil extracted	18.8	73.2	8	-

Table VI. Atomic Absorption Determination of Lead in Grease Samples

SAMPLE	NO.	% LEAD	MEAN RESULT
LT-2 BASE OIL	1	0.0014	0.001% Pb.
	2	0.0013	
	3	0.0012	
LT-2 GREASE	1	1.02	1.01% Pb.
	2	0.96	
	3	1.06	
BR2-S GREASE	1	0.78	0.79% Pb.
	2	0.77	
	3	0.81	
LT-2 GREASE THEORY			1.2% Pb

DISCUSSION

Dr. A.J. Clarke (Marconi Space & Defence Systems) :

Nearly two years ago there was a failure in the Marecs L-band antenna. The failure investigation revealed the cause to be the film adhesive between the carbon fibre skin and the honeycomb. The antenna is being manufactured by a different division of Aerospatiale, who, to the best of my knowledge, do not employ special humidity conditions, they certainly do not prime the honeycomb and they may not be aware of your work. My question is, are you going to interact with your colleagues, who are engaged in the same kind of work, in order to improve the quality assurance of these structures?

J. Chanteranne:

The group in which I am working and the laboratory that studied the Marecs antenna are now integrated. I think that our experience with Intelsat-5 and the experience with the Marecs antenna should be shared.

Mr. Duploux :

During the manufacture of the Marots L-band antenna a few years ago, the hygrometric level was known, because the antenna was not manufactured in the usual workshop but in a special painting room which had a hygrometric level of 50-55%. Now we can assure a hygrometric level of 50% because the Marecs L-band antenna will be manufactured in the same workshop as Sylva which requires a hygrometry of nearly 50% and a temperature of about 21 °C. The Marecs L-band antenna will be manufactured under the same conditions, and in the same room and by the same people, so I think there is no longer a problem. Anyway, I hope not.

H.E. Hintermann (LSRH) :

In your CVD process for C-deposition, what kind of gases, what temperature and pressure do you use?

J. J. Choury:

This process is proprietary. All that I can say is that we use an isothermal process, with very light hydrocarbon, generally natural gas, methane or propane and that temperature is about 1000°C. The pressure is below normal, and some mm of Hg.

R. Moss (Ford Aerospace) :

Since it is evident that low loadings of grease gave a starved bearing, and about 3½ grams gave acceptable lifetimes, would you be comfortable with any reduction in grease loading below this level? Also, please comment on the advisability of increasing the proportion of oil to grease.

B. H. Baxter:

It would not be my choice, I can only offer advice. I think, if the level chosen of about 3½ gram was found satisfactory, for all other considerations that should be left as it was. Further reductions would probably go in towards the starved condition and we know that from a chemical point of view working in a starved condition means rapid oil decomposition. If you look in the printed paper, you will see that for the second pair of bearings the 3.77 gram of BR2S showed in some places slight loss of thickening agent after 30 000 hours. With the slightly increased viscosity of LT2, and the same charge these bearings went on to 50 000 hours. So, I think, that this is just about the right charge. I do not know how this was chosen, but I think it is a good figure.

R. Moss :

So there is evidence that the loading does satisfy, and anything less than that would be marginal.

B. H. Baxter:

Yes, it would be.

PRECEDING PAGE BLANK NOT FILMED

LIST OF PARTICIPANTS

S. ADAMY (MRS)	ESA/ESTEC, Zwarteweg 62, Noordwijk, Netherlands	J.J. CHOURY	SEP, B.P. No. 37 33160 Saint Médard en Jalles, France
A. ALONSO	INTA, Torrejón de Ardoz Madrid, Spain	A. CLARK	MSDS, Materials Lab Brown's Lane Portsmouth, England
K.G. BALMAIN	UNIVERSITY OF TORONTO, Toronto, Canada M5S 1A4	D.S. COLLINS	ESA/ESTEC, Zwarteweg 62 Noordwijk, Netherlands
B.H. BAXTER	BADG, P.O. Box 181, Six Hills Way Stevenage, England	C.B. CONNOR	ESA/ESTEC, Zwarteweg 62 Noordwijk, Netherlands
G. BEERE	ESA/ESTEC, Zwarteweg 62, Noordwijk, Netherlands	C. CORTI	MONTEDISON, Via Principe Eugenio 1/5 Milano, Italy
A. BELLOT	ESA HEADQUARTERS, 8-10 Mario Nikis 75738 Paris, France	H.M.A. VAN DAALEN	FOKKER-VFW, P.O. Box 7600 Schiphol-Oost, Netherlands
J.E. BENNETT	ESA/ESTEC, Zwarteweg 62 Noordwijk, Netherlands	J. VAN DAALEN	ISA, P.O. Box 42 Hengelo (Ov), Netherlands
J. BERRY	CERT, 2, av. E. Belin 31055 Toulouse, France	J. DAUPHIN	ESA/ESTEC, Zwarteweg 62 Noordwijk, Netherlands
P.W. BLAKE	ERNO, Huenefeldstr. 1-5 2800 Bremen 1, Germany	D.K. DAVIES	ERA, Cleeve Road Leatherhead, Surrey, England
F. BOERSMA	FOKKER-VFW, Postbus 7600 Schiphol-Oost	R.W. DAVIS	ESA/ESTEC, Zwarteweg 62 Noordwijk, Netherlands
K. BOGUS	ESA/ESTEC, Zwarteweg 62 Noordwijk, Netherlands	M. DEBEIR	ESA/ESTEC, Zwarteweg 62 Noordwijk, Netherlands
J. BOSMA	ESA/ESTEC, Zwarteweg 62 Noordwijk, Netherlands	E.J. DEBUSSON	AEROSPATIALE, 12, rue Pasteur 92152 Suresnes, France
J. BOURRIEAU	CERT, 2, av. E. Belin 31055 Toulouse, France	M. DESLOIRE	CNES, Rue Charles Beaudelaire 91000 EVRY, France
X. BOUTIN	SAGEM, 72, rue de la Tour Billy 95101 Argenteuil, France	J. DOL	FOKKER-VFW, P.O. Box 7600 Schiphol-Oost, Netherlands
D.H. BOWEN	AERE Harwell, Oxfordshire, OX11 0RA, England	B.D. DUNN	ESA/ESTEC, Zwarteweg 62 Noordwijk, Netherlands
G. BROWN	BADG, Bristol BS99 7AR, England	J. DUPLOUX	AEROSPATIALE, B.P. No. 2 78130 Les Mureaux, France
E. BUXTON	BADG, Stevenage SG11 2AB, England	A. DUVAL	INCA-MEC, B.P. No. 8 B-6000 Charleroi, Belgium
M.P. CANEVET	AEROSPATIALE, 12, rue Pasteur 92152 Suresnes, France	D.A. EBYON	ESA/ESTEC, Zwarteweg 62 Noordwijk, Netherlands
J. CHANTERANNE	SNIAS, B.P. No. 2 78130 Les Mureaux, France		

W.R. ECKERT	NATEC, Behringstrasse 154 D-2000 Hamburg 50, Germany	K. HUEHN	ESA/ESTEC, Zwarteweg 62 Noordwijk, Netherlands
P.G. EDWARDS	ESA, 18, rue E. Belin 31055 Toulouse, France	R.W. JAEGER	CNES, Rue Charles Baudelaire F-91 Evry, France
M. VAN EESBEEK	ESA/ESTEC, Zwarteweg 62 Noordwijk, Netherlands	F. JAMIN CHANGEART	CNES, 18, av. E. Belin 31055 Toulouse, France
C.N. FELLAS	BADG, Site B, Gunnels Wood Road Stevenage, England	F. JOO	DFVLR, 5000 Koeln 90 Linder Hoehe, Germany
M. FROGGATT	ESA/ESTEC, Zwarteweg 62 Noordwijk, Netherlands	M.D. JUDD	ESA/ESTEC, Zwarteweg 62 Noordwijk, Netherlands
R. GIBSON	FOKKER-VFW, P.O. Box 7600 Schiphol-Oost, Netherlands	H.J. JURASCHEK	DFVLR, 5000 Koeln 90 Linder Hoehe, Germany
C. GIORI	IIT RESEARCH INSTITUTE, 10W 35th Street Chicago, Ill. 60616, USA	J.F. LAFAY	ESA/ESTEC, Zwarteweg 62 Noordwijk, Netherlands
P. GOEDTKE	MBB, Postfach 801169 8 Muenchen 80, Germany	W.L. LEHN	AIR FORCE MATERIALS LABORATORY, Wright-Patterson AFB, Ohio 45433, USA
G. GOURMELON	ESA/ESTEC, Zwarteweg 62 Noordwijk, Netherlands	F. LEVADOU	ESA/ESTEC, Zwarteweg 62 Noordwijk, Netherlands
S.A. GREENBERG	LOCKHEED, 3251 Hanover Street Palo Alto, CA 94304, USA	L. LEVY	CERT, 2, av. E. Belin 31055 Toulouse, France
K. GROH	UNIVERSITY OF GIESSEN, Heinrich-Buff-Ring 16 6300 Giessen, Germany	R.G. VAN MARSDEN	FOKKER-VFW, P.O. Box 7600 Schiphol-Oost, Netherlands
C.J. GUILLAUMON	CNES, 18, av. E. Belin 31055 Toulouse, France	M. MC CARGO	LOCKHEED, 3251 Hanover Street Palo Alto, CA 94304, USA
J. GUILLIN	CNES, 18, av. E. Belin, 31055 Toulouse, France	A. MECHKAK	SNIAS, B.P. No. 2 78130 Les Mureaux, France
N. GUSTAFFSON	ESA/ESTEC, Zwarteweg 62, Noordwijk, Netherlands	H. MENGES	ESA/ESTEC Zwarteweg 62 Noordwijk, Netherlands
T.D. GUYENNE	ESA/ESTEC, Zwarteweg 62, Noordwijk, Netherlands	G. MENOZZI	CROUZET, B.P. 1014, 26010 Valence, France
G. TER HAAR	FOKKER-VFW, P.O. Box 7600 Schiphol-Oost, Netherlands	M.L. MINGES	AIR FORCE MATERIALS LABORATORY, Wright-Patterson AFB, Ohio 45433, USA
D.F. HALL	THE AEROSPACE CORP., P.O. Box 92957 Los Angeles, CA 90009, USA	J. MOACANIN	JPL, 4800 Oak Grove Drive Pasadena, CA 91103, USA
J.A. HANEKAMP	FOKKER-VFW, P.O. Box 7600 Schiphol-Oost, Netherlands	P.J.H. MOLLOY	BADG, Site B, Gunnels Wood Road Stevenage, England
W. HECHTIL	WACKER-CHEMIE 8263 Burghausen, Germany	D. MOREAU	ESA/ESTEC, Zwarteweg 62 Noordwijk, Netherlands
H. HINTERMANN	LSRH, Rue Breguet 2, Case Postale 42 CH-2000 Neuchâtel, Switzerland	H. MÖRTBERG	SAAB-SCANIA AB, Fack, S-58188 Linköping, Sweden
C. HOFKAMP	FOKKER-VFW, P.O. Box 7600 Schiphol-Oost, Netherlands	R. MOSS	FORD AEROSPACE & COMMUNICATIONS CORP., 3939 Fabian Way Palo Alto, CA 94303, USA
R. HONLAT	SOPEMEA, 31029 Toulouse, France	M. MUISAERTS (MRS)	ESA/ESTEC, Zwarteweg 62 Noordwijk, Netherlands
K. HOULBERG (MRS)	ESA/ESTEC, Zwarteweg 62 Noordwijk, Netherlands		

S.H. NEGRE (MRS)	ESA/ESTEC, Zwarteweg 62 Noordwijk, Netherlands	B. SERENE	ESA, 18, av. E. Belin 31055 Toulouse, France
D.T. NEWELL	BOARD, 223 Old Marylebone Road London NW5 1TH, England	H. SEUBERT	ESA/ESTEC, Zwarteweg 62 Noordwijk, Netherlands
D.A. NUTT	ESA/ESTEC, Zwarteweg 62 Noordwijk, Netherlands	I. SIMMERMAN (MRS)	ESA/ESTEC, Zwarteweg 62, Noordwijk, Netherlands
S. ORTAKEUYLI	EMD, 55 Quai Carnot 92214 St. Cloud, France	J. SOUFFRIEAU	EMERSON & CUMING, Nijverheidsstraat 24 2431 Oevel, Belgium
A. PAILLOUS	CERT, 2, av. E. Belin 31055 Toulouse, France	H.D. STENZENBERGER	TECHNOCHEMIE GMBH, Gutenbergstr. 2, Postfach 40 6901 Dossenheim, Germany
D.C. PATEL	ESA/ESTEC, Zwarteweg 62 Noordwijk, Netherlands	B. SCHWARZ	ERNO, Huenefeldstr. 1-5 2800 Bremen 1, Germany
N.H. PENNINGS	FOKKER-VFW, P.O. Box 7600 Schiphol-Oost, Netherlands	B. TATRY	CNES, 18, av. E. Belin 31055 Toulouse, France
A. PEYRAUD	MATRA, 37, av. L. Breguet 78140 Vélizy, France	R.C. TENNYSON	UNIVERSITY OF TORONTO, 4925 Dufferin St. Downsview, Toronto M3H 5T6, Canada
G. PREMAT	ESA/ESTEC, Zwarteweg 62 Noordwijk, Netherlands	R. THOMAS	ESA/ESTEC, Zwarteweg 62 Noordwijk, Netherlands
L. PREUSS	MBB, Postfach 801169 8000 Muenchen 80, Germany	M. TRELLA	ESA/ESTEC, Zwarteweg 62 Noordwijk, Netherlands
J. REDDY	ESA/ESTEC, Zwarteweg 62 Noordwijk, Netherlands	M. TUNBRIDGE	ESA/ESTEC, Zwarteweg 62 Noordwijk, Netherlands
A. REMONDIERE	CNES, 18, av. E. Belin 31055 Toulouse, France	M. URBAIN	SNIAS, B.P. No. 52 06322 Cannes La Bocca, France
M. REY	SNIAS, B.P. No. 52 06322 Cannes La Bocca, France	M. VERAIN	ESA/ESTEC, Zwarteweg 62 Noordwijk, Netherlands
M.L. REYNOLDS	ESA, 18, av. E. Belin 31055 Toulouse, France	D. VERDIN	UNITED KINGDOM ATOMIC ENERGY AUTHORITY HARWELL, Oxfordshire OX11 0RA, England
H.B. ROUMS	FOKKER-VFW, P.O. Box 7600 Schiphol-Oost, Netherlands	A. VAN 'T ZAND	FOKKER-VFW, P.O. Box 7600 Schiphol-Oost, Netherlands
J. SAGE	BADG, P.B. 181, Six Hills Way Stevenage, England	A. ZWAAL	ESA/ESTEC, Zwarteweg 62 Noordwijk, Netherlands
W. SCHAEFER	MBB, Postfach 801169 8000 Muenchen 80, Germany		
H.P. SCHMIDT	DEVLR, 5000 Koeln 90 Linder Hoehe, Germany		
H.G. SCHROEDER	DORNIER, Postfach 1360 7990 Friedrichshafen, Germany		
J. SCHUFE	DELFT UNIVERSITY, Kluyverweg 1 2629 HS Delft, Netherlands		
J.G. SCIALDONE	NASA/GODDARD SPACE FLIGHT CENTER, Greenbelt, MD 20771, USA		
P. SEIDL	IPW, Heidenhofstr. 8 7800 Freiburg, Germany		